

Non-normal forms

Présentée le 24 mai 2024

Faculté des sciences et techniques de l'ingénieur
Laboratoire de mécanique des fluides et instabilités
Programme doctoral en mécanique

pour l'obtention du grade de Docteur ès Sciences

par

Yves-Marie François DUCIMETIÈRE

Acceptée sur proposition du jury

Prof. L. G. Villanueva Torrijo, président du jury
Prof. F. Gallaire, directeur de thèse
Prof. S. Fauve, rapporteur
Prof. R. Kerswell, rapporteur
Prof. M. Wyart, rapporteur

A ma mère Régine, en souvenir de tous ces moments.

Acknowledgements

*J'ai plus de souvenirs que si j'avais mille ans.*¹

I am grateful to Stéphan Fauve, Rich Kerswell, and Matthieu Wyart for taking the time to read this thesis, as well as for a very insightful discussion on the occasion of a stimulating defense ! I also wish to acknowledge Guillermo Villanueva for presiding over the jury.

Merci Saviz, d'avoir toujours su me rassurer et me conseiller, de mes premiers à mes derniers moments à l'EPFL. Tes paroles encourageantes ont compté pour moi, ainsi que ton amour très fondamental et contagieux pour la science et la recherche, qui, dans l'angoisse des examens des premières années, m'ont laissé penser que le meilleur restait à venir et m'ont porté. Grâce à tes mots et à ton exemple, j'ai eu foi en l'avenir.

Merci Gioele, tout d'abord pour avoir été un assistant formidable en "Ecoulement des fluides" puis en "Hydrodynamique". Il émanait de toi une telle passion pour ta matière et un tel bonheur de faire de la recherche, que tu donnais assurément envie de faire partie du labo. Merci, ensuite, d'avoir supervisé mon premier projet en instabilité : j'étais fier de travailler avec toi sur ce beau sujet. Je me remémore la joie que m'ont procurée les lectures des premiers papiers sur l'optimisation adjointe et la non-normalité, ainsi que mes premiers calculs de recherche. J'eus l'impression d'avoir trouvé ma place. Alors, merci pour tout ça, ainsi que pour toute ta délicatesse et pour l'attention que tu portais à toujours donner aux étudiants confiance en eux.

Merci Elise, d'avoir guidé avec mansuétude mes premiers pas au labo et dans la recherche ! Merci, grâce à vos mots toujours biens choisis, de m'avoir donné confiance en moi et de m'avoir encouragé à poursuivre. L'approbation, les compliments, vous marquent parfois si profondément qu'ils fixent votre avenir (c'est à garder en tête dans nos rapports aux étudiants et aux jeunes chercheurs).

Merci Jérôme, de m'avoir ouvert les portes de votre laboratoire pour un stage d'été mémorable avec Debbie, Maura et Andrea. Je retourne à Carouge parfois, et je pense à vous tous avec

¹Charles Baudelaire, *les Fleurs du Mal*

nostalgie.

Thank you Colm and Adrien, for allowing me to come to Cambridge. I have invested so much in my studies, that concluding my Master with a project at “the Mecca” of instabilities gave me a deep sense of accomplishment and I felt extremely proud. Thank you for making this possible.

Merci Hervé, Martin, Gaétan, Ludovic et Eunok, d’avoir formé une équipe de postdocs de choc, toujours prêts à transmettre, et échanger sur une pléthore de sujets différents (échanges qui devenaient d’ailleurs rapidement nerveux dès lors qu’ils impliquaient Gaétan et la politique, pour le plus grand bonheur de mon oeil spectateur !). J’ai beaucoup appris de chacun d’entre vous, et, à mon arrivée au labo, vos présences m’ont rassuré et la belle dynamique que vous aviez créée a largement contribué au bien-être des doctorants. Merci Ludo, tout particulièrement, pour ta douceur et ta bienveillance, et pour tous les bons moments partagés (un jour peut-être, on comprendra ce qu’il se passait dans cette maudite T-junction !). Merci Eunok, d’avoir partagé ton expertise théorique et numérique sur le resolvent et, en effet, d’avoir toujours su comment maximiser le gain d’énergie du labo ! Merci Jesùs, Alice et Tomas, pour ces beaux moments.

Merci à tous nos étudiants, Tristan, Guillaume, Yohann, Julien, Samy, Matteo, Matthias, Tigrane, Sara, Filippo, Giovanni, Cédric, Edoardo (“Dodo d’amore”, al quale avrei voluto rubare un cielo di perle), Alberto (“Toto”), Inès, Valentin et Antoine d’avoir fait partie de la bande pendant de trop courts moments. Votre détermination sincère, et le plaisir simple que vous aviez à faire de la recherche sont à préserver, et, justement, m’ont souvent ramené à ce qu’avec le temps, j’eus égaré. Je porte le souvenir de chacun de vous.

Thank you Pier Giuseppe, Shahab, and Alessandro, for the countless moments we spent together. This has been a very intense period of our lives, and I cherish the memories of when you were still there with me, now that it has become evident to me that time has passed. Your successive departures saddened me greatly.

Grazie Giuseppe, pour ta présence calme et rassurante, et ta sensibilité. J’admire ton immense talent pour la science et le courage avec lequel tu portes tes idées. J’ai été honoré d’être ton collègue du début à la fin de nos aventures respectives au labo, et je te considérerai toujours comme un modèle.

Merci Petra, en premier lieu pour avoir réussi à rendre le labo fonctionnel malgré nos fâcheuses tendances à procrastiner ! Merci de toujours veiller à notre bien-être et pour toutes tes attentions qui ont largement contribué à rendre le labo si spécial, puisque nous prenons soin les uns des autres. Merci également pour toute l’aide que tu m’as apportée ces derniers mois très difficiles : ça n’était pas de ta responsabilité, et tu l’as fait par pure générosité. Le labo ne saurait exister sans toi.

Grazie Kevin (“Gavino d’amore”), to have been such an adorable colleague. I couldn’t imagine a better colleague than you, and it was a genuine joy to work by your side. I will miss your endless culture, sincerity, humility, goodwill, humor, and our morning discussions in the coffee room. I admire your creativity (although don’t forget: il est interdit de faire du feu sur le gazon !) and your curiosity, and I sometimes wish I was able to appreciate things as much as you do. Grazie per tutte le risate e i momenti di gioia, and for the infernal duo we have formed, specialized in the embarrassing thesis defenses ! I will miss you greatly, amico.

Merci Simeon (plutôt “Mer-Simeon” ou “Merci-meon”), principalement pour m’avoir introduit à la commande `mathcal` de `latek`. Accessoirement, j’aimerais aussi te remercier de m’avoir honoré de ton amitié. Parmi les meilleurs souvenirs de mon doctorat, demeureront notre randonnée à Trubelstock dans un silence englobant, nos moments à Sat à discuter de tout mais surtout d’amour, et nos sessions pétanque-pastis pleines de mélancolie les soirs d’été. A ce propos, crois bien que je regrette que “les boules-en-jet” aie dû être dissoute pour des raisons compliquées de politique interne, il faut dire que tu n’as jamais eu beaucoup de chance avec les sphères, mais je suis sûr que “l’étreinte boulière” ira loin (bien que je ne sois pas tellement sûr du patronyme ...). Avec un peu d’entraînement, peut-être même qu’on arrivera à se faire un nom à Ecublens ! J’ai beaucoup appris de toi, de ta capacité géniale à observer et à révéler le monde, scientifiquement et poétiquement. Je n’oublierai pas ta profondeur, ta délicatesse, et cette faculté que tu as à nous aimer (et donc, à nous faire nous aimer) pour ce que nous sommes, sans nous juger. Ton amitié fut très précieuse pour moi, et quand je repense à toutes nos discussions sur les bancs de l’Unil, mon coeur se serre. Merci d’avoir été là mon grand. Je suis sûr que nous nous reverrons souvent, surtout si tu vas faire un postdoc au Luxembourg ! (Ou était-ce en Belgique ?)

Merci Timothée, pour ta belle énergie et ton incroyable esprit de camaraderie ! Ton enthousiasme et ton talent apportent énormément au labo, et je suis sûr que tu feras une superbe thèse !

Mahbod, I envy you for starting your PhD with François: try to enjoy it before you reach the end !

Merci Edouard, pour une multitude de raisons, incluant ta supervision toujours bienveillante et la ferveur avec laquelle tu transmets tes innombrables connaissances (j’aimerais avoir la patience de lire autant que toi !). Merci pour ton soutien inaltérable lors de projets pourtant très compliqués, et de toujours chercher à nous donner confiance en nous. Je ne doute pas un instant que tu seras un directeur de thèse exceptionnel ! Merci aussi pour tous ces excellents moments passés ensemble au labo, à Tinos (même si on a réussi à se perdre en allant chercher du pain), à Athènes et à Alghero: c’était un réel plaisir de te côtoyer et d’avoir ta vision des choses toujours éclairée, humaniste et nostalgique. Sacré Edouard !

Thank you Tobias, for your inimitable humor and presence ! Also, thanks to you, I felt less

alone when I went to work on Saturdays (although I really think we should stop doing that).

Thank you Lebo, the sunshine of the MED corridor, for your joy, your positivity, your energy, and your witty remarks ! And good luck in the throes of the French language ! (Although I hope you keep your American accent).

Merci Aliénor et Sebastien, pour ce mois idyllique à Boulder ! (Même si, bizarrement, j'ai peu de souvenirs de notre dernier soir au White Horse ...)

Merci Florence, pour tous tes conseils et tes encouragements. En particulier, encore merci pour l'invitation à Nice : le premier "invited talk", ça ne s'oublie pas !

Merci Jean, Léonard, Sandra et Marine, du fond du coeur, pour ces treize ans d'amitié, récemment ponctués par des soirées mémorables à la Riponne, à la Jonction et aux Acacias, et un week-end hors du temps à Marseille ! Dans nos moments de joie, de fête, de communion, j'ai l'impression de vivre plus fort. Lorsque nous sommes ensemble, j'oublie le sentiment de la fuite du temps, et je suis simplement heureux. Merci Jean, aussi, pour nos soirées escalade-pizza-bière (dans cet ordre, je vous rassure) les jeudis soir, ces moments authentiques comptaient beaucoup pour moi. Enfin, Sandra, je compte bien figurer aussi très prochainement dans les remerciements de ta thèse !

Merci Yael et Seginus, mes frères : je bénis le destin qui nous a fait nous retrouver en première. Dans cet amas de doutes et de remises en question que sont nos vies, j'aurai toujours la certitude de notre amitié et de votre présence à mes côtés. Nous avons partagé tellement de choses depuis tant d'années, que je n'ose imaginer ce qu'aurait été ma vie sans vous. Pour nos intenses années lycée, nos discussions le soir sur CDA pour pallier les angoisses de nos premières années respectives, nos retrouvailles l'été à Prévessin avec Tutur et Manny, nos sorties vélos, nos promenades nocturnes à Genève, nos nuits gaming à Saint-Sulpice, et puis pour tout ce qu'on s'est dit, nos rêves, nos blessures, nos amours, nos mélancolies, j'aimerais vous remercier les gars : grâce à vous, j'ai souvent trouvé la force d'être heureux et d'espérer.

Merci Papa, de m'avoir pris dans ton bureau avec toi quand j'étais petit : c'est sur ton grand tableau noir que j'ai lu ma première formule. Grâce à toi, j'ai pu errer dans les couloirs du CERN, et c'est précisément dans cette errance que le monde de la recherche scientifique a commencé à devenir le mien. Plus récemment, merci pour des vacances d'été mémorables, de glorieuses randonnées dans les montagnes Haut-Savoyardes, et des promenades contemplatives dans la belle Annecy !

Merci Laura, d'avoir parcouru avant moi la voie du doctorat. J'ai souhaité l'emprunter à mon tour, fidèle à mon habitude d'être un petit frère compétitif et peu satisfaisant. Mais je suis sûr que tu ne m'en veux pas, et même que tu es fière de moi ! Merci d'avoir organisé toutes ces belles journées à Zurich et à Bâle qui m'ont réchauffé le coeur, et pour tout ton soutien ces

dernières semaines.

Thank you Vadim, for being always so sweet, for your sensitivity and kindness. I always learn something discussing with you and I admire your culture ! Thank you for all these unforgettable and familial moments we spent together with Laura.

Merci Maman, indéniablement, pour toute l'énergie que tu as déployée à nous soutenir depuis tant d'années. L'amour que tu nous portes semble absolu et inconditionnel, et je n'aurais pas pu avancer sans cette certitude que je pourrais toujours te trouver. Merci d'avoir, seule, assumé tes responsabilités et de n'avoir jamais renoncé malgré de nombreux moments difficiles. Je n'oublie pas que tu étais là pour nous, pas seulement dans la réussite et les moments de détente, mais aussi dans les moments d'angoisse et de doute. Merci d'avoir toujours fait tout ton possible pour nous garantir un avenir. En particulier, merci pour ton exigence et de nous avoir transmis le goût du travail, sans lequel je ne me serais pas engagé dans cette thèse, et j'aurais eu bien tort ! Merci pour tous ces souvenirs : je n'oublierai jamais l'époque où nous vivions tous les deux à Saint-Julien puis à Ferney-Voltaire, et où, grâce à toi, j'ai été tellement heureux et si plein d'envies et d'espoir. Au fond, c'est là que tout a commencé. Alors, merci pour ces innombrables moments passés tous les deux. Qu'ils furent tristes ou joyeux, je puise aujourd'hui ma force et ma volonté dans leurs souvenirs. Lorsque je poursuis à l'envers les fils de tout ce qui m'est arrivé de constructif et de durable, je te retrouve toujours à leurs commencements. Tu luis dans mon coeur, petite maman.

Merci François, *O Captain! My Captain! our fearful trip is done*^{II}. Nous nous sommes rencontrés il y a maintenant neuf ans, à l'occasion de votre cours de deuxième année, et j'ignorais à l'époque la grande aventure qui nous attendait, et à quel point vous alliez compter pour moi. On pourra dire ce fut épique ! Comme toute aventure digne de ce nom, cette thèse nous a fait passer par tous les états possibles, entre les moments d'échec, de découragement, d'errance, d'exaltation, et enfin de joie d'avoir *trouvé du nouveau*. Comme toute aventure digne de ce nom encore, on en ressort avec l'impression d'avoir vécu intensément, c'est-à-dire, poétiquement. Alors, merci d'avoir eu l'audace de nous lancer sur ce sujet infernal et magnifique, d'avoir cru en mes capacités et d'avoir cru en mon courage. Merci chef pour votre grand coeur, pour tous les moments passés à nous rassurer, à nous donner confiance en nous et en l'avenir, et à nous transmettre votre force et votre envie, qui semblent inépuisables. Merci de toujours faire en sorte qu'on se sente bien et qu'on ait plaisir à faire de la recherche (c'est-à-dire, même dans la difficulté). Merci pour votre tolérance extraordinaire envers nos états d'âme, et de toujours trouver les mots pour nous faire avancer sans nous brusquer. Merci d'être si peu rancunier, pour votre esprit de solution à toutes épreuves et pour votre humour. Merci de nous avoir incités à voyager, pour que nous pûmes nous créer tant de souvenirs. Merci de toujours faire les choses gratuitement, par générosité, par gentillesse, tout simplement. Merci pour votre magnanimité et, parfois, pour votre mélancolie. Plus prosaïquement, merci pour votre aide technique, vos idées eurêka (ou presque !), vos intuitions fabuleuses (que je ne

^{II}Walt Whitman, *O Captain! My Captain!*

comprenais que quelque temps après, à condition d'une intense réflexion) et votre capacité à vous plonger instantanément dans nos problèmes ! Merci pour toutes nos discussions improvisées, de science ou de comment les egos de certains l'instrumentalisme. Merci de m'avoir apporté tellement de choses depuis toutes ces années. Vraiment, du fond du coeur, merci de nous offrir ces quatre ans de doctorat, qui restera l'une des plus belles périodes de ma vie. Je suis fier de ce que l'on a accompli. Je vous admire sincèrement pour tout ce que vous avez réussi à construire, et qui demeurera.

Abstract

In this thesis, we propose to formally derive amplitude equations governing the weakly nonlinear evolution of non-normal dynamical systems, when they respond to harmonic or stochastic forcing, or to an initial condition. This approach reconciles the non-modal nature of these growth mechanisms and the need for a centre manifold to project the leading-order dynamics. Under the hypothesis of strong non-normality, small operator perturbations suffice to make singular the inverse of the operator which is relevant to the considered problem. The adjective “small” is relative to the choice of an induced norm, under which the operator induces a large input-output amplification. Such operator perturbation can be encompassed in a multiple-scale asymptotic expansion, closed by a standard compatibility condition. The resulting amplitude equations are tested in parallel and non-parallel two-dimensional flows, where they bring insight into the weakly nonlinear mechanisms that modify the gains as we increase the amplitude of the harmonic or stochastic forcing, or that of the initial condition

Key words: Instability, Nonlinear Dynamical Systems.

Résumé

Dans cette thèse, nous procédons à la dérivation formelle d'équations d'amplitude gouvernant l'évolution faiblement nonlinéaire de systèmes dynamiques non-normaux, lorsqu'ils sont sujets à un forçage harmonique ou stochastique, ou à une condition initiale. Notre approche réconcilie la nature non-modale des mécanismes d'amplifications, avec la nécessité d'une variété centrale sur laquelle projeter la dynamique à l'ordre dominant. Sous hypothèse de forte non-normalité, une petite perturbation suffit à rendre singulier l'opérateur pertinent pour le problème considéré. L'adjectif "petite" réfère ici au choix d'une norme induite, selon laquelle l'opérateur provoque une forte amplification entrée-sortie. Une telle perturbation d'opérateur peut être incorporée dans une expansion à échelles multiples, fermée par l'alternative de Fredholm. Les équations d'amplitude résultantes sont testées sur des écoulements fluide en deux dimensions, parallèles ou non. Il permettront d'interpréter les mécanismes faiblement nonlinéaire à l'origine de la modification des gains tandis que nous augmentons l'amplitude des forçages harmonique ou stochastiques, or celle de la condition initiale.

Mots clés : Instabilité, Systèmes Dynamiques Nonlinéaires.

Riassunto

In questa tesi si propone la derivazione formale di equazioni di ampiezza che governano l'evoluzione debolmente non lineare di sistemi dinamici non normali soggetti a una forzante armonica o stocastica o a una condizione iniziale. L'approccio considerato concilia la natura non modale dei meccanismi di amplificazione con la necessità di una varietà centrale su cui proiettare la dinamica all'ordine dominante. Nell'ipotesi di non normalità forte, è sufficiente una piccola perturbazione per rendere singolare l'operatore rilevante per il problema trattato. L'aggettivo "piccola" è relativo alla scelta di una norma indotta, per la quale l'operatore produce una grande amplificazione tra ingresso e uscita. Tale perturbazione dell'operatore può essere incorporata in un'espansione multi-scala, chiusa dall'alternativa di Fredholm. Le equazioni dell'ampiezza risultanti vengono testate su flussi bidimensionali paralleli e non-paralleli, in modo da interpretare i meccanismi debolmente non lineari che modificano i guadagni all'aumentare dell'ampiezza delle forzanti armoniche o stocastiche o delle condizioni iniziali.

Parole chiave: Instabilità, Sistemi Dinamici Nonlineari.

Contents

Acknowledgements	i
Abstract (English/Français/Italiano)	vii
1 Introduction	1
1.1 Linear dynamics with nonlinear consequences	1
1.1.1 Response to an initial perturbation	6
1.1.2 Response to a harmonic forcing	19
1.1.3 Response to a stochastic forcing	27
1.2 Weakly nonlinear dynamics	35
1.3 In this thesis: deriving weakly nonlinear amplitude equations for non-normal responses	47
I Response to a harmonic forcing	51
2 A non-modal weakly nonlinear amplitude equation for the response to a harmonic forcing	53
2.1 Introduction	53
2.1.1 Strong non-normality	53
2.1.2 Weak nonlinearity	55
2.1.3 Amplitude equations without eigenvalues	56
2.2 Response to Harmonic Forcing	57
2.2.1 Application case: the flow past a BFS	63
2.2.2 Application case: Orr mechanism in the plane Poiseuille flow	66
2.3 Conclusions	72
2.4 Appendix	73
2.4.1 Harmonic gain sensitivity and comparison with the WNNh model.	73
2.4.2 Applying the WNNh model to the Navier–Stokes equations.	74
2.4.3 Higher-order corrections of the WNNh equation.	75
2.4.4 Modal amplitude equation for harmonic forcing.	78
2.4.5 Uniqueness of the operator perturbation	79
	xiii

II	Response to a stochastic forcing	81
3	A non-modal weakly nonlinear amplitude equation for the variance maintained by a stochastic forcing	83
3.1	Introduction	83
3.2	Linear regime	86
3.3	Weakly nonlinear regime	91
3.4	Application to the backward-facing step flow	96
3.5	Conclusion	100
3.6	Appendix	102
3.6.1	Link between the PSD and the auto-correlation function	102
3.6.2	Norm in the frequency domain	102
3.6.3	Norm of the perturbation operator	102
3.6.4	Kernel of the adjoint operator	103
3.6.5	Linear gain for a generic forcing structure	103
3.6.6	Numerical implementation	103
4	Weakly nonlinear evolution of stochastically driven non-normal systems	105
4.1	Introduction	105
4.2	Linear regime	105
4.3	Weakly nonlinear regime	109
4.3.1	Generic nonlinear system and application to a toy model	109
4.3.2	Bilinear system and application to the backward-facing step flow	114
4.4	Conclusions	118
4.5	Appendix	120
4.5.1	discretisation of the amplitude equation in the frequency domain	120
4.5.2	The particular case of the NSE: discretisation of the amplitude equation in the frequency domain	121
5	Noise-induced transitions past the onset of a steady symmetry-breaking bifurcation: the case of the sudden expansion	129
5.1	Introduction	129
5.2	Problem definition	132
5.3	Weakly nonlinear expansion	135
5.4	Application case: the flow past a sudden expansion	139
5.4.1	Deterministic regime	140
5.4.2	Stochastic regime: amplitude statistics	141
5.4.3	Stochastic regime: escape time statistics	143
5.4.4	Stochastic regime: choice of the cut-off frequency	148
5.5	Summary and perspectives	150

6 Coupling modal and non-modal stochastic responses past the onset of a steady symmetry-breaking bifurcation	153
6.1 Introduction	153
6.2 Problem definition and linear regime	154
6.3 Weakly nonlinear expansion	162
6.4 Application to a toy model	168
6.5 Conclusions and perspectives	174
6.6 Appendix	177
6.6.1 Fredholm alternative imposed at second order	177
6.6.2 Fredholm alternative imposed at third order	178
III Response to an initial perturbation	181
7 A non-modal weakly nonlinear amplitude equation for the transient response	183
7.1 Introduction	183
7.2 Transient Growth	185
7.2.1 Application case: the flow past a backward-facing step	191
7.2.2 Application case: lift-up in the plane Poiseuille flow	193
7.3 Conclusions	196
7.4 Appendix	197
7.4.1 Applying the WNNt model to the Navier–Stokes equations.	197
7.4.2 Higher-order corrections of the WNNt equation.	199
7.4.3 Transient gain sensitivity and comparison with the WNNt model.	200
8 A weakly nonlinear amplitude equation approach to the bypass transition in the two-dimensional Lamb–Oseen vortex	203
8.1 Introduction	203
8.2 Linear formulation	207
8.3 Weakly nonlinear formulation	210
8.4 Linear and fully nonlinear transient growth in the diffusing, two-dimensional, Lamb-Oseen vortex	218
8.4.1 Flow geometry	218
8.4.2 Numerical methods	218
8.4.3 Linear results	219
8.4.4 Fully nonlinear results	224
8.5 Weakly nonlinear transient growth in the diffusing Lamb-Oseen vortex in dimension two	227
8.5.1 Transient change from nonlinear saturation to nonlinear amplification	227
8.5.2 Comparison of fully and weakly nonlinear gains	229
8.5.3 Bifurcation thresholds	231
8.5.4 Physical interpretation of the nonlinear “anti-saturation”: mean flow distortion and inversion of the vorticity gradient	233

8.6	Summary and perspectives	240
8.7	Appendix	242
8.7.1	Kernel of the adjoint of the perturbed inverse propagator	242
8.7.2	Temporal integration of the third-order equation.	242
8.7.3	Transient gain sensitivity in time-varying base flow and comparison with the amplitude equation.	243
8.7.4	The pseudo-forcing method	245
8.7.5	Expression of the adjoint operator	246
9	Weakly nonlinear optimization	249
9.1	Introduction	249
9.2	Flow configuration and governing equations	251
9.3	Weakly nonlinear Lagrangian optimization	253
9.4	Application case: the plane Poiseuille flow	258
9.5	Conclusions	269
9.6	Appendix	271
9.6.1	Variations with respect to the first order field.	271
9.6.2	Variations with respect to the second harmonic order field.	273
9.6.3	Variations with respect to the mean flow distortion field.	273
9.6.4	Variations with respect to the third order field.	273
9.6.5	Adjoint advection operator	274
10	Summary and perspectives	275
10.1	Application to a harmonic resolvent analysis	279
10.2	Application to a wavelet-based resolvent analysis	280
10.3	Some methodological clarifications	283
10.3.1	Coupling with sub-optimal responses	283
10.3.2	Coupling with harmonic optimal responses	284
10.4	Mathematical clarification	285
	Bibliography	303
	Curriculum Vitae	305

1 Introduction

Fluid flows have proven to be of considerable phenomenological richness, including pattern formation, spatiotemporal chaos, turbulence, and many others. The will to order these phenomena in a comprehensive analysis framework progressively has led to what is known today as the hydrodynamic stability theory. Over the years, this theory has benefited from theoretical and numerical advances in mathematics, particularly in the fields of linear algebra, partial differential equations, and dynamical systems. Many observed phenomena could thus find at least a partial explanation by characterising the linear response of the Navier-Stokes equations to infinitesimally small disturbances, in a quiet surrounding or under a sustained forcing. Such linear response, however, has sometimes proven to be too simplistic, and substantial progress has been made in extending the hydrodynamic stability theory to fully nonlinear regimes.

In this introductory part, we propose a review of some concepts stemming from the hydrodynamic stability theory, and that have been necessary in constructing this thesis. We mostly focus on linear and weakly nonlinear techniques, but also give some elements of fully nonlinear extensions.

1.1 Linear dynamics with nonlinear consequences

We consider the situation of a fluid flow in a spatial domain Ω , of dimension two or three. Its velocity field $\mathbf{U}(\mathbf{x}, t)$ is governed by the incompressible Navier-Stokes equations

$$\partial_t \mathbf{U} = -(\mathbf{U} \cdot \nabla) \mathbf{U} - \nabla p + \text{Re}^{-1} \Delta \mathbf{U} + \mathbf{F}, \quad \text{subject to } \mathbf{U}(\mathbf{x}, 0) = \mathbf{U}_0(\mathbf{x}), \quad (1.1)$$

where $p(\mathbf{x}, t)$ is the pressure field, $\mathbf{F}(\mathbf{x}, t)$ is some body forcing, and Re is the Reynolds number, built on relevant length and velocity scales. Because of the (hypothetical) incompressibility of the flow, the pressure field is such that the velocity field is divergence-free

$$\nabla \cdot \mathbf{U} = 0. \quad (1.2)$$

Both pressure and velocity fields are linked through a linear Poisson equation. Therefore, it is understood in (1.1) that $p = p[\mathbf{U}]$ (the brackets for a functional dependency) and (1.2) will not be written explicitly in what follows. For the problem to be well-posed, appropriate boundary conditions must be appended at the domain boundary, noted $\partial\Omega$.

A relevant starting point in analyzing the phase space trajectories of (1.1), is to compute exact solutions by enforcing simplifying symmetry in time and/or in space. These solutions include exact invariant states, also called exact coherent states, which encompass equilibrium states (fixed points and traveling waves) and periodic orbits. Often determined numerically, invariant states correspond to generally non-trivial flow structures that may be relevant in that, locally in the phase space, the full trajectory may project well on their associated manifolds and/or non-normal optimal responses. To illustrate this, let us develop in this introductory part the case of the linearized dynamic around a fixed point.

In the case of a steady body forcing $\mathbf{F}(\mathbf{x}, t) = \mathbf{F}_b(\mathbf{x})$ in (1.1), a fixed point, also called "base flow", solution $\mathbf{U}_b(\mathbf{x})$ solves

$$\mathbf{0} = -(\mathbf{U}_b \cdot \nabla)\mathbf{U}_b - \nabla p + \text{Re}^{-1} \Delta \mathbf{U}_b + \mathbf{F}_b. \quad (1.3)$$

We assume such a solution to be accessible, at least numerically and with good accuracy, using for instance the Newton method. The dynamics of an infinitesimal perturbation \mathbf{u} to the base flow, externally excited by an infinitesimal perturbation \mathbf{f} to the body forcing, and initialized by an infinitesimal perturbation \mathbf{u}_0 to the initial condition, is governed by

$$\partial_t \mathbf{u} = L\mathbf{u} + \mathbf{f}, \quad \text{subject to} \quad \mathbf{u}(\mathbf{x}, 0) = \mathbf{u}_0(\mathbf{x}). \quad (1.4)$$

This system is equipped with appropriate boundary conditions on \mathbf{u} , and L is a linear operator acting on \mathbf{u} according to

$$L\mathbf{u} = -(\mathbf{u} \cdot \nabla)\mathbf{U}_b - (\mathbf{U}_b \cdot \nabla)\mathbf{u} - \nabla p + \text{Re}^{-1} \Delta \mathbf{u}. \quad (1.5)$$

The operator L is defined over the Hilbert space $L^2(\Omega)$. The field \mathbf{u} must belong to the said "domain" of L , a function space denoted $\mathcal{D}(L) \subseteq L^2(\Omega)$, which is characterized by boundary and appropriate regularity conditions on \mathbf{u} . These latter for instance consist of requiring \mathbf{u} to belong to the $C^2(\Omega)$ function space, as a consequence of the presence of the Laplacian in (1.5), and generically make $\mathcal{D}(L)$ more restrictive than $L^2(\Omega)$.

The operator L is sometimes referred to as the "direct" linearized evolution operator or more simply the linearized evolution operator. Owing to the independence of L with respect to time, the formal solution to (1.4) can be written as

$$\mathbf{u}(\mathbf{x}, t) = e^{Lt} \mathbf{u}_0(\mathbf{x}) + e^{Lt} \int_0^t e^{-Ls} \mathbf{f}(\mathbf{x}, s) ds, \quad (1.6)$$

the linear operator e^{Lt} being the operator exponential of Lt . It is also called the "propagator"

for, in the absence of forcing in (1.6), e^{Lt} would directly map the initial condition onto its evolution at time t .

When \mathbf{u} was introduced as a "perturbation" to the base flow, we implicitly referred to a size measure without specifying it. This specific measure of \mathbf{u} must be much smaller than the one of \mathbf{U}_b for the former to be considered as a perturbation to the latter, thereby for (1.4) to hold. A natural choice of measure is the norm induced by the L^2 inner product for continuous and generally complex-valued functions on Ω , writing

$$\langle \mathbf{u}_a | \mathbf{u}_b \rangle = \int_{\Omega} \mathbf{u}_a^H \mathbf{u}_b d\Omega, \quad (1.7)$$

the superscript "H" designating the Hermitian transpose. In this manner, $\langle \mathbf{u} | \mathbf{u} \rangle$ is directly proportional to the kinetic energy of the disturbance field. The perturbation could be measured by other norms, although, for this specific thesis work, this norm must be *induced* by an inner product. In other terms, in this thesis, all fields are required to belong to a Hilbert space. This is more restrictive than solely requiring them to belong to a Banach space and precludes, for example, the use of L^p norm with $p \neq 2$.

The choice of an inner product makes possible the construction of the adjoint operator of L , denoted L^\dagger , and being such that

$$\langle L\mathbf{u} | \mathbf{v} \rangle \doteq \langle \mathbf{u} | L^\dagger \mathbf{v} \rangle, \quad \forall \mathbf{u} \in \mathcal{D}(L), \mathbf{v} \in \mathcal{D}(L^\dagger). \quad (1.8)$$

The function space $\mathcal{D}(L^\dagger) \subseteq L^2(\Omega)$ is the domain of the operator L^\dagger and contains appropriate boundary regularity conditions on the adjoint field \mathbf{v} . The adjoint operator L^\dagger is determined upon performing integration by part of the term at the left-hand side in (1.8). The arising boundary terms, when they do not vanish thanks to the boundary conditions on \mathbf{u} , are canceled by enforcing appropriate boundary conditions on \mathbf{v} . Together with regularity conditions, this fully characterizes the domain $\mathcal{D}(L^\dagger)$, provided the latter is chosen as large as possible. The domain of the adjoint operator $\mathcal{D}(L^\dagger)$ need not be the same as the domain of the direct one $\mathcal{D}(L)$, particularly because different boundary conditions may need to be imposed on the direct and adjoint fields. The adjoint of the operator L in (1.5), under the inner product (1.7), is such that

$$L^\dagger \mathbf{u}^\dagger = (\mathbf{U}_b \cdot \nabla) \mathbf{u}^\dagger - (\nabla \mathbf{U}_b)^T \mathbf{u}^\dagger - (\mathbf{U}_b \cdot \nabla) \mathbf{u}^\dagger + \nabla p^\dagger + \text{Re}^{-1} \Delta \mathbf{u}^\dagger, \quad \mathbf{u}^\dagger \in \mathcal{D}(L^\dagger), \quad (1.9)$$

and where p^\dagger is such that \mathbf{u}^\dagger is divergence-free. The following terminology is recalled

- L is said to be "self-adjoint" if and only if $L = L^\dagger$ (where the equality also implies $\mathcal{D}(L) = \mathcal{D}(L^\dagger)$). Equivalently, L is self-adjoint if and only if $\mathcal{D}(L) = \mathcal{D}(L^\dagger)$ and $\langle L\mathbf{g} | \mathbf{h} \rangle = \langle \mathbf{g} | L\mathbf{h} \rangle$, $\forall \mathbf{g}, \mathbf{h} \in \mathcal{D}(L) = \mathcal{D}(L^\dagger)$.
- L is said to be "normal" if and only if $LL^\dagger = L^\dagger L$ (where the equality also implies that the domains are equal). Equivalently, L is normal if and only if $\mathcal{D}(L) = \mathcal{D}(L^\dagger)$ and $\langle L\mathbf{g} | L\mathbf{h} \rangle =$

$$\langle L^\dagger \mathbf{g} | L^\dagger \mathbf{h} \rangle, \forall \mathbf{g}, \mathbf{h} \in \mathcal{D}(L) = \mathcal{D}(L^\dagger).$$

- L is said to be "non-normal" if and only if $LL^\dagger \neq L^\dagger L$, either because the domains differ, or $\mathcal{D}(L) = \mathcal{D}(L^\dagger)$ holds but there exist at least one pair (\mathbf{g}, \mathbf{h}) such that $\langle L\mathbf{g} | L\mathbf{h} \rangle \neq \langle L^\dagger \mathbf{g} | L^\dagger \mathbf{h} \rangle$, for $\mathbf{g}, \mathbf{h} \in \mathcal{D}(L) = \mathcal{D}(L^\dagger)$.

Note that a self-adjoint operator is necessarily normal, but the reciprocal is not true. From this classification follows properties concerning the eigenmodes and eigenvalues of the direct and adjoint operators. We assume the spectra of L and L^\dagger not to contain a continuous part, and denote $\mathbf{q}_i \in \mathcal{D}(L)$ (with $\|\mathbf{q}_i\| = 1$) the eigenmode of the operator L . It is associated with an eigenvalue σ_i , which possesses the i th largest real part of all, such that $L\mathbf{q}_i = \sigma_i \mathbf{q}_i$. Accordingly, we denote $\mathbf{q}_i^\dagger \in \mathcal{D}(L^\dagger)$ (with $\|\mathbf{q}_i^\dagger\| = 1$) the eigenmode of the operator L^\dagger . It is associated with the eigenvalue σ_i^* ("*" the complex conjugation), such that $L^\dagger \mathbf{q}_i^\dagger = \sigma_i^* \mathbf{q}_i^\dagger$. Indeed, if we denote instead by κ_i the eigenvalues of the adjoint operator, then we have

$$\begin{aligned} L\mathbf{q}_i = \sigma_i \mathbf{q}_i &\Rightarrow \langle \mathbf{q}_i^\dagger | L\mathbf{q}_i \rangle = \sigma_i \langle \mathbf{q}_i^\dagger | \mathbf{q}_i \rangle \Leftrightarrow \\ &\langle L^\dagger \mathbf{q}_i^\dagger | \mathbf{q}_i \rangle = \sigma_i \langle \mathbf{q}_i^\dagger | \mathbf{q}_i \rangle \Leftrightarrow \\ &\kappa_i^* \langle \mathbf{q}_i^\dagger | \mathbf{q}_i \rangle = \sigma_i \langle \mathbf{q}_i^\dagger | \mathbf{q}_i \rangle, \quad \forall i, \end{aligned} \quad (1.10)$$

thereby it is clear the eigenvalues of the adjoint operator must be the complex conjugates of the eigenvalues of the direct one.

- If L is self-adjoint, then $\sigma_i \in \mathbb{R}$, $\forall i$ and the eigenmodes of L constitute an orthonormal set under the inner product (1.7), i.e. $\langle \mathbf{q}_i | \mathbf{q}_j \rangle = \delta_{ij}$. In addition, \mathbf{q}_i also is the eigenmode of L^\dagger associated with an eigenvalue σ_i^* , implying that for each i holds $\mathbf{q}_i^\dagger = \mathbf{q}_i$.
- If L is normal, the properties mentioned above for the self-adjoint case also hold at the only difference that eigenvalues and eigenmodes are generally complex, $\sigma_i \in \mathbb{C}$, $\forall i$ (which doesn't affect the orthonormality property).
- If L is non-normal, $\sigma_i \in \mathbb{C}$, $\forall i$, and the eigenmodes do not form an orthogonal set under the inner product (1.7). Furthermore, for each i the adjoint eigenmode \mathbf{q}_i^\dagger is generally different from \mathbf{q}_i .

In all cases, a bi-orthogonality property between the direct and adjoint eigenmode

$$\langle \mathbf{q}_i^\dagger | \mathbf{q}_j \rangle = 0 \quad \text{if } i \neq j. \quad (1.11)$$

More generally if a mass matrix M had been included in the eigenvalue problem, specifically if we had had instead $L\mathbf{q}_i = \sigma_i M\mathbf{q}_i$ and $L^\dagger \mathbf{q}_i^\dagger = \sigma_i^* M\mathbf{q}_i^\dagger$, then the bi-orthogonality property would have become $\langle \mathbf{q}_i^\dagger | M\mathbf{q}_j \rangle = 0$ if $i \neq j$.

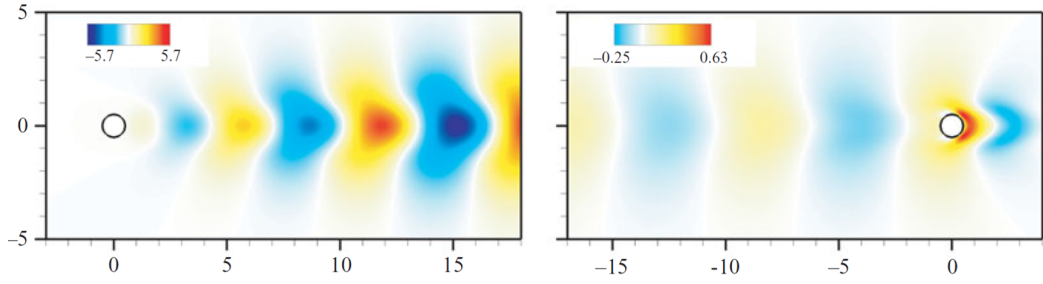


Figure 1.1: Cross-wise velocity distribution (left) for the leading eigenmode \mathbf{q}_1 of the linearized Navier-Stokes operator (1.5) corresponding to the two-dimensional cylinder flow at $\text{Re} = 46.6$ and (right) its associated leading adjoint eigenmode \mathbf{q}_1^\dagger . Only the real parts are shown. Reproduced from Sipp and Lebedev (2007).

The specification of the domain of the operators is essential in determining if L is normal or not. First because if $\mathcal{D}(L) \neq \mathcal{D}(L^\dagger)$, due for instance to different boundary conditions on the direct and adjoint fields, L must be non-normal. Indeed, it is not possible to have equality between direct and adjoint eigenmodes if they are subject to different boundary conditions. In addition, even in the configuration where $\mathcal{D}(L) = \mathcal{D}(L^\dagger)$, the operator L could be normal in an unbounded domain but non-normal in a bounded one. The boundary conditions would then act as a source of non-normality. To illustrate this, Trefethen and Embree (2005) (in § 12) proposes the example of the advection-diffusion operator $Lu = u'' + u'$, whose domain is the set of functions in $L^2([0, 1])$ with absolutely continuous derivative and subject to $u(0) = u(1) = 0$; it is easily shown that $L^\dagger u = u'' - u'$ and $\mathcal{D}(L) = \mathcal{D}(L^\dagger)$. Thereby $\langle Lf | Lg \rangle - \langle L^\dagger f | L^\dagger g \rangle = 2\langle f'' | g' \rangle + 2\langle f' | g'' \rangle = 2[f'g']_0^1$ for $f, g \in \mathcal{D}(L) = \mathcal{D}(L^\dagger)$. This last boundary term would be null in an infinite domain (replacing $[0, 1]$ by $]-\infty, \infty[$) for all the functions f, g , and their derivatives must vanish at infinity, thereby making the operator L normal. However, this boundary term has no reason to be null on a bounded domain, which makes L non-normal.

The linearized Navier-Stokes operator in (1.5) is generally non-normal under the inner product (1.7) whenever the base flow \mathbf{U}_b is non-zero. That is because the sign of the term representing the advection of the perturbation by the base flow has been reversed in (1.9) with respect to (1.5). Consequently, the direct and adjoint eigenmodes present different spatial support, for they have been advected in opposite directions. As an illustration, we reproduce from Sipp and Lebedev (2007) in figure 1.1 the leading eigenmode \mathbf{q}_1 of L and its associated adjoint mode \mathbf{q}_1^\dagger , for the cylinder wake flow at $\text{Re} = 46.6$. If the direct eigenmode presents oscillations in the far wake, the adjoint eigenmode is concentrated upstream and in the separating shear layer at the cylinder boundary. Clearly, \mathbf{q}_1 and \mathbf{q}_1^\dagger are not identical (in fact they project very poorly on each other), which indicates that the operator L must be non-normal.

The non-normality of the linearized Navier-Stokes operator has numerous and important consequences for the flow dynamics (Chomaz, 2005; Kerswell, 2018; Reddy & Henningson, 1993; Schmid & Henningson, 2001; Trefethen et al., 1993). Some of them will be briefly recalled in the following lines. Nonetheless, it is important to realize that the degree of non-normality of

an operator depends on the choice of the (induced) norm. That is because the characterization of non-normality involves the adjoint operator. In the context of plane parallel shear flows, Heifetz and Methven (2005) have shown a certain measure of the flow non-normality differs if the adjoint is constructed under the inner product (1.7), or if it is under another inner product inducing the enstrophy norm (L^2 norm of the vorticity). In what follows, only the non-normality with respect to the energy inner product (1.7) will be discussed.

1.1.1 Response to an initial perturbation

The following section focuses on the flow response to an initial perturbation in a perfectly quiet surrounding, where the forcing term \mathbf{f} is null in (1.6). In other terms, we will study the behavior of the solution

$$\mathbf{u}(\mathbf{x}, t) = e^{Lt} \mathbf{u}_0(\mathbf{x}), \quad (1.12)$$

in the most general case where L is non-normal. Assuming that L is diagonalizable and that its eigenmodes \mathbf{q}_i form a complete basis of $\mathcal{D}(L)$ (i.e. every function in $\mathcal{D}(L)$ can be represented as a linear combination of the eigenmodes), we define the operator P

$$P = [\mathbf{q}_1, \mathbf{q}_2, \dots], \quad \text{and its inverse} \quad P^{-1} = \begin{bmatrix} \frac{\langle \mathbf{q}_1^\dagger | \bullet \rangle}{\langle \mathbf{q}_1^\dagger | \mathbf{q}_1 \rangle} \\ \frac{\langle \mathbf{q}_2^\dagger | \bullet \rangle}{\langle \mathbf{q}_2^\dagger | \mathbf{q}_2 \rangle} \\ \vdots \end{bmatrix}, \quad (1.13)$$

where the operator $\langle \mathbf{g} | \bullet \rangle$ applied to some \mathbf{h} reads $\langle \mathbf{g} | \mathbf{h} \rangle$. In other terms, $\langle \mathbf{g} | \bullet \rangle \equiv \langle \mathbf{g} |$ in the quantum mechanics formalism. The expression of P^{-1} in (1.13) follows directly from the bi-orthogonality of the direct and adjoint eigenmodes

$$P^{-1}P = \begin{bmatrix} \frac{\langle \mathbf{q}_1^\dagger | \mathbf{q}_1 \rangle}{\langle \mathbf{q}_1^\dagger | \mathbf{q}_1 \rangle} & \frac{\langle \mathbf{q}_1^\dagger | \mathbf{q}_2 \rangle}{\langle \mathbf{q}_1^\dagger | \mathbf{q}_1 \rangle} & \dots \\ \frac{\langle \mathbf{q}_2^\dagger | \mathbf{q}_1 \rangle}{\langle \mathbf{q}_2^\dagger | \mathbf{q}_2 \rangle} & \frac{\langle \mathbf{q}_2^\dagger | \mathbf{q}_2 \rangle}{\langle \mathbf{q}_2^\dagger | \mathbf{q}_2 \rangle} & \dots \\ \vdots & \vdots & \ddots \end{bmatrix} = \begin{bmatrix} 1 & 0 & \dots \\ 0 & 1 & \dots \\ \vdots & \vdots & \ddots \end{bmatrix}, \quad (1.14)$$

which indeed is the identity operator with domain $\mathcal{D}(L)$. In addition

$$PP^{-1} = \sum_j \mathbf{q}_j \frac{\langle \mathbf{q}_j^\dagger | \bullet \rangle}{\langle \mathbf{q}_j^\dagger | \mathbf{q}_j \rangle}, \quad (1.15)$$

which also must correspond to the identity operator since the eigenmodes \mathbf{q}_i constitute a complete basis of $\mathcal{D}(L)$. By introducing the diagonal operator

$$\Lambda = \begin{bmatrix} \sigma_1 & & \\ & \sigma_2 & \\ & & \ddots \end{bmatrix}, \quad (1.16)$$

(σ_i the eigenvalues of L) such that $L = P\Lambda P^{-1}$ thus $e^{Lt} = Pe^{\Lambda t}P^{-1}$, the solution (1.12) re-writes

$$\mathbf{u} = Pe^{\Lambda t}P^{-1}\mathbf{u}_0 = \sum_j \mathbf{q}_j e^{\sigma_j t} \frac{\langle \mathbf{q}_j^\dagger | \mathbf{u}_0 \rangle}{\langle \mathbf{q}_j^\dagger | \mathbf{q}_j \rangle}. \quad (1.17)$$

It is associated with a kinetic energy

$$\|\mathbf{u}\|^2 = \sum_j e^{2\Re(\sigma_j)t} \frac{|\langle \mathbf{q}_j^\dagger | \mathbf{u}_0 \rangle|^2}{|\langle \mathbf{q}_j^\dagger | \mathbf{q}_j \rangle|^2} + \underbrace{\sum_j \sum_{k \neq j} e^{(\sigma_j^* + \sigma_k)t} \frac{\langle \mathbf{q}_j^\dagger | \mathbf{u}_0 \rangle^* \langle \mathbf{q}_k^\dagger | \mathbf{u}_0 \rangle}{\langle \mathbf{q}_j^\dagger | \mathbf{q}_j \rangle^* \langle \mathbf{q}_k^\dagger | \mathbf{q}_k \rangle} \langle \mathbf{q}_j | \mathbf{q}_k \rangle}_{=0 \text{ if } L \text{ is normal or if } \mathbf{u}_0 = \mathbf{q}_i}. \quad (1.18)$$

We further discuss the temporal evolution of $\|\mathbf{u}\|^2$ making an important distinction between the asymptotic and the finite-time regimes.

Asymptotic response

As a consequence of the exponential dependencies, the kinetic energy in (1.18) is dominated by the term corresponding to the eigenvalue with the largest real part in the regime $t \rightarrow \infty$. This corresponds to σ_1 (as well as σ_2 if we have $\sigma_2 = \sigma_1^*$). Supposing $\Re(\sigma_1) > \Re(\sigma_2)$ (the conclusions drawn below being easily generalizable if $\Re(\sigma_1) = \Re(\sigma_2)$), expression (1.18) reduces to

$$\|\mathbf{u}\|^2 \sim e^{2\Re(\sigma_1)t} \frac{|\langle \mathbf{q}_1^\dagger | \mathbf{u}_0 \rangle|^2}{|\langle \mathbf{q}_1^\dagger | \mathbf{q}_1 \rangle|^2} \quad \text{as } t \rightarrow \infty, \quad (1.19)$$

thereby the kinetic energy of the linear perturbation eventually evolves exponentially at a rate $2\Re(\sigma_1)$.

- If $\Re(\sigma_1) < 0$, the perturbation eventually vanishes ($\|\mathbf{u}\|^2 \rightarrow 0$) and the fixed point \mathbf{U}_b is then said to be "linearly stable" or to be an "attractor". In other terms, any trajectory initiated or passing sufficiently close to \mathbf{U}_b will end up at \mathbf{U}_b from the direction given by \mathbf{q}_1 . Quantifying how small should the perturbation be for the trajectory to end up at \mathbf{U}_b eventually amounts to computing the basin of attraction of \mathbf{U}_b , for which nonlinearities have to be reintroduced.

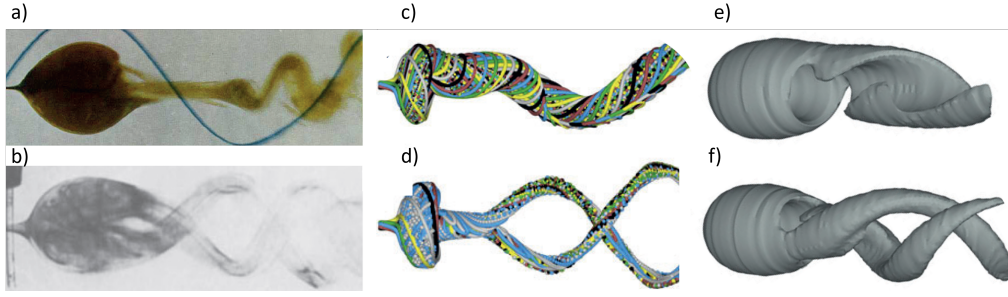


Figure 1.2: Selected example of emerging unsteadiness in fluid flow. Frames (a) and (b) show experimental visualizations of single double helical vortex breakdown modes from Sarpkaya (1971) and Escudier and Zehnder (1982), respectively. Frames (c) and (d), reproduced from Meliga et al. (2012), imitate an experimental dye visualization and show numerically computed dye lines transported from an analytic solution; the latter consists of a superposition of the base flow \mathbf{U}_b and the linearly unstable mode multiplied by an amplitude determined analytically. Frames (e) and (f) are alternative representations to (c) and (d), respectively, and depict an isosurface of azimuthal vorticity.

- If $\Re(\sigma_1) > 0$, the linear perturbation eventually grows exponentially and the fixed point \mathbf{U}_b is then said to be "linearly unstable". In other terms, any trajectory initiated or passing sufficiently close to \mathbf{U}_b (but not at \mathbf{U}_b exactly) will eventually deviate from it exponentially following the direction given by \mathbf{q}_1 . The linear perturbation \mathbf{u} ultimately reaches a critical size where it can't be considered a perturbation anymore, thereby nonlinearities can't be neglected rigorously and have to be taken into account.

Whenever σ_1 evolves from $\Re(\sigma_1) < 0$ to $\Re(\sigma_1) > 0$ (i.e. crosses the real axis), by changing the external parameter intervening in the operator, is called a "bifurcation". Whereas the nonlinear dynamics subsequent to the instability still bear symptoms of \mathbf{q}_1 , in terms for instance of frequency or structure, is found to be without a general answer. As will become clear in section 1.2, it depends on the nature of the bifurcation and on the distance to the latter in the parameter space. In the configuration where a complex conjugate pair of eigenvalues is unstable $\sigma_1 = \sigma_2^*$, it is possible that the nonlinear dynamics reaches a limit cycle at a prescribed frequency close to $\Im(\sigma_1)$. The associated flow topology could qualitatively match the structure of the complex unstable eigenmode. This scenario, although far from being generic, is illustrated in figure 1.2. In this figure, the superposition of the base flow and the real part of the linearly most unstable mode, multiplied by an amplitude determined analytically through weakly nonlinear considerations (Meliga et al., 2012), shows qualitative agreement with experimental visualizations (Escudier & Zehnder, 1982; Sarpkaya, 1971).

Note that a fixed point might still be relevant in the flow dynamics despite its linearly unstable nature. One of the reasons is that the dimension of the unstable manifold often is significantly lower than the dimension of the stable one; therefore a trajectory could still spend a lot of time in the vicinity of \mathbf{U}_b , in which case the latter would have a signature in the whole flow statistics in case of a chaotic dynamics. Another

reason is that the unstable manifold tangent to \mathbf{q}_1 in the linear regime could follow a homo/heteroclinic orbit, which would cause the nonlinear trajectory to return to \mathbf{U}_b cyclically.

However, even if a trajectory is initiated sufficiently close to \mathbf{U}_b , it is possible that the exponential growth along \mathbf{q}_1 is not observed. The reason is that, as will be elaborated further in a moment, the double-sum term in (1.18) can't be neglected if L is non-normal. In fact, it may lead to transient algebraic growth of \mathbf{u} sufficient for nonlinearities to set in, thus for (1.18) to lose its validity even *before* the exponential term in contains has time to declare.

- If $\Re(\sigma_1) = 0$, the present linear theory does not conclude as to the stability of the equilibrium, and \mathbf{U}_b is said to be "linearly neutral". The associated neutral eigenmode \mathbf{q}_1 is nevertheless essential in the construction of the center manifold (Guckenheimer & Holmes, 1983), as we shall develop shortly in section 1.2.

It can be deduced from (1.19) that, in the limit $t \rightarrow \infty$, the kinetic energy of the perturbation is maximized by selecting $\mathbf{u}_0 = \mathbf{q}_1^\dagger$. Thereby, the adjoint eigenmode \mathbf{q}_1^\dagger can be interpreted intuitively as the optimal manner to excite the direct eigenmode \mathbf{q}_1 . Accordingly, selecting $\langle \mathbf{q}_1^\dagger | \mathbf{u}_0 \rangle = 0$ guarantees that the asymptotic behavior of $\|\mathbf{u}\|^2$ is not $\propto e^{2\Re(\sigma_1)t}$ but contains only exponential of lower growth rate or larger decay rates.

In the rest of this document, whenever the adjectives "stable", "unstable" or "neutral" are used, they will systematically refer to linear stability analysis. Furthermore, we insist that it characterizes a behavior that is asymptotic in time, whereas we argue thereafter that the finite time behavior might be just as relevant if L is non-normal.

Finite time response

Coming back to expression (1.18) for the kinetic energy of the linear perturbation, the double-sum term is identically null if L is normal; that is because $\langle \mathbf{q}_i | \mathbf{q}_k \rangle = \delta_{ik}$, which cancels when summed over $k \neq j$. It is also null in the specific case where \mathbf{u}_0 is purely along one of the eigenmodes, for, by construction, dynamics initiated along an eigenmode remain along it. In these cases, $\|\mathbf{u}\|^2$ decays monotonously if $\Re(\sigma_1) < 0$, for it is the sum of decaying exponentials pondered by positive coefficients.

However, precisely because the eigenmodes do not form an orthonormal set, the double sum term in (1.18) generally is non-zero if L is non-normal (and if \mathbf{u}_0 projects over more than one eigenmode). Thenceforth, since the coefficients multiplying the terms $\propto e^{(\sigma_j^* + \sigma_k)t}$ can be negative, their decreases can imply the energy $\|\mathbf{u}\|^2$ to grow algebraically fast at finite times. Algebraic growth means that it remains bounded by a low degree polynomial in t . Eventually, the exponential behavior mentioned in the previous section takes over if the linearization is still valid. This phenomenon is referred to as "transient growth".

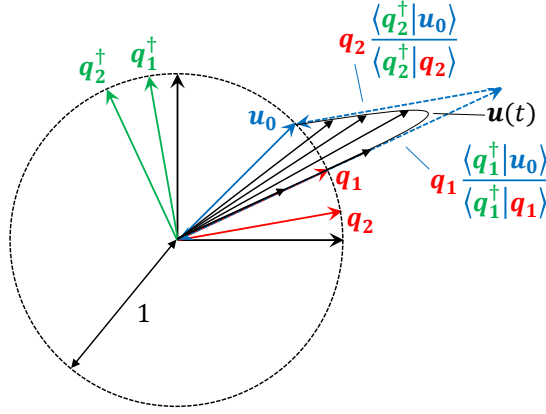


Figure 1.3: Schematic representation of the decomposition of an initial condition \mathbf{u}_0 in the eigenbasis of a matrix L , in the scenario where L is a 2×2 non-normal matrix with real and eigenvalues. Red arrows are direct eigenvectors whereas green arrows are adjoint eigenvectors. Blue arrows are \mathbf{u}_0 (full) and its decomposition (dotted) in the eigenbasis. Black arrows are the solution $\mathbf{u}(t)$ as some consecutive times.

Let us illustrate it with a simple example, in the spirit of that proposed in Chomaz (2005). If L is a 2×2 matrix with purely real and stable eigenvalues, the perturbation \mathbf{u} represented in the eigenbasis in (1.17) reduces to

$$\mathbf{u} = \mathbf{q}_1 e^{\sigma_1 t} \frac{\langle \mathbf{q}_1^\dagger | \mathbf{u}_0 \rangle}{\langle \mathbf{q}_1^\dagger | \mathbf{q}_1 \rangle} + \mathbf{q}_2 e^{\sigma_2 t} \frac{\langle \mathbf{q}_2^\dagger | \mathbf{u}_0 \rangle}{\langle \mathbf{q}_2^\dagger | \mathbf{q}_2 \rangle}. \quad (1.20)$$

This representation is sketched in figure 1.3 for $t = 0$. Since L is non-normal, \mathbf{q}_1 and \mathbf{q}_2 are non-orthogonal and $\langle \mathbf{q}_1^\dagger | \mathbf{q}_1 \rangle$ is smaller than one. As a consequence, the component of \mathbf{u}_0 along \mathbf{q}_1 , writing $\mathbf{q}_1 \langle \mathbf{q}_1^\dagger | \mathbf{u}_0 \rangle / \langle \mathbf{q}_1^\dagger | \mathbf{q}_1 \rangle$, is of larger norm than \mathbf{u}_0 itself. If in addition $\Re(\sigma_2) < \Re(\sigma_1)$, $\mathbf{u}(t)$ in (1.20) converges towards $e^{\sigma_1 t} \mathbf{q}_1 \langle \mathbf{q}_1^\dagger | \mathbf{u}_0 \rangle / \langle \mathbf{q}_1^\dagger | \mathbf{q}_1 \rangle$ faster than it decays along it. This must correspond to an increase in the energy of \mathbf{u} for sufficiently small times. This can also be seen directly by writing the energy

$$\|\mathbf{u}\|^2 = e^{2\sigma_1 t} \frac{|\langle \mathbf{q}_1^\dagger | \mathbf{u}_0 \rangle|^2}{|\langle \mathbf{q}_1^\dagger | \mathbf{q}_1 \rangle|^2} + e^{2\sigma_2 t} \frac{|\langle \mathbf{q}_2^\dagger | \mathbf{u}_0 \rangle|^2}{|\langle \mathbf{q}_2^\dagger | \mathbf{q}_2 \rangle|^2} + 2e^{(\sigma_1 + \sigma_2)t} \frac{\langle \mathbf{q}_1^\dagger | \mathbf{u}_0 \rangle \langle \mathbf{q}_2^\dagger | \mathbf{u}_0 \rangle}{\langle \mathbf{q}_1^\dagger | \mathbf{q}_1 \rangle \langle \mathbf{q}_2^\dagger | \mathbf{q}_2 \rangle} \langle \mathbf{q}_1 | \mathbf{q}_2 \rangle. \quad (1.21)$$

The first two terms in the right-hand side of (1.21) are decaying exponential pondered by positive coefficients. If the third term also is a decaying exponential, it is multiplied by a coefficient that, in the configuration illustrated in figure 1.3, is negative through $\langle \mathbf{q}_2^\dagger | \mathbf{u}_0 \rangle / \langle \mathbf{q}_2^\dagger | \mathbf{q}_2 \rangle < 0$. If $\Re(\sigma_2) < \Re(\sigma_1)$ the negative third term vanishes faster than the positive first one, therefore $\|\mathbf{u}\|^2$ must increase initially.

The description proposed above suggests that particularly large transient growth is expected in

cases where $\langle \mathbf{q}_1^\dagger | \mathbf{q}_1 \rangle \ll 1$, and where $\Re(\sigma_2) \ll \Re(\sigma_1)$. Indeed, in the latter case, $\mathbf{u}(t)$ converges so rapidly towards $e^{\sigma_1 t} \mathbf{q}_1 \langle \mathbf{q}_1^\dagger | \mathbf{u}_0 \rangle / \langle \mathbf{q}_1^\dagger | \mathbf{q}_1 \rangle$, that the amplitude along the later did not have time to decay much in the meantime. Note also that transient growth could as easily happen in an unstable system.

Transient growth phenomena generalize to high (including infinite-) dimensional systems. Contrarily to the two-dimensional example treated above, a generally vast number of eigenmodes are then needed to characterize the transient gain. That is because the double sum term in (1.18) involves mode-mode interactions through the inner product $\langle \mathbf{q}_j | \mathbf{q}_k \rangle$, which can take significant values over a large range of indices. As an example, Åkervik et al. (2007) considered the transient growth in the energy of a fluid flow over a separated boundary-layer flow. Using eigenmodes as a projection basis for analyzing the flow dynamics, they have shown that about one hundred modes are required for converged results of optimal growth (see their figure 4a).

For this reason, instead of computing directly eigenmode, the paradigm is modified to find the initial condition that maximizes the gain in energy at a certain time t_o (called a "temporal horizon"). This way, the full potential of the system for transient growth is directly revealed. We aim to solve the maximization problem

$$\begin{aligned} G(t_o) &= \max_{\mathbf{u}_0} \frac{\|\mathbf{u}(t_o)\|}{\|\mathbf{u}_0\|} = \max_{\mathbf{u}_0} \frac{\|e^{Lt_o} \mathbf{u}_0\|}{\|\mathbf{u}_0\|} = \|e^{Lt_o}\| \\ &= \max_{\mathbf{u}_0} \sqrt{\frac{\langle (e^{Lt_o})^\dagger e^{Lt_o} \mathbf{u}_0 | \mathbf{u}_0 \rangle}{\langle \mathbf{u}_0 | \mathbf{u}_0 \rangle}}. \end{aligned} \quad (1.22)$$

This amounts to computing the norm of the propagator e^{Lt_o} , or, equivalently, the largest eigenvalue associated with the problem

$$(e^{Lt_o})^\dagger e^{Lt_o} \check{\mathbf{u}}_j = \kappa_j^2 \check{\mathbf{u}}_j, \quad j = 1, 2, \dots \quad (1.23)$$

The eigenvalue problem (1.23) is self-adjoint, implying the eigenvalues κ_j^2 , sorted by decreasing magnitude, to be real and positive. The eigenmodes $\check{\mathbf{u}}_j$ are normalized as $\|\check{\mathbf{u}}_j\| = 1$. The maximum transient gain $G(t_o) = \kappa_1$, and the optimal initial condition directly corresponds to $\check{\mathbf{u}}_1$. The eigenmode $\check{\mathbf{u}}_j$ also coincides with the j th right "singular" mode of e^{Lt_o} , associated with the singular value κ_j

$$\kappa_j \check{\mathbf{u}}_j^\dagger = e^{Lt_o} \check{\mathbf{u}}_j, \quad \kappa_j \check{\mathbf{u}}_j = (e^{Lt_o})^\dagger \check{\mathbf{u}}_j^\dagger, \quad (1.24)$$

where $\check{\mathbf{u}}_j^\dagger$ (normalized as $\|\check{\mathbf{u}}_j^\dagger\| = 1$) is the j th left singular mode of e^{Lt_o} . Most importantly, inherited from the fact that the operator in (1.23) is self-adjoint, both the $\check{\mathbf{u}}_j$ and the $\check{\mathbf{u}}_j^\dagger$ families are orthonormal. Thereby the initial condition \mathbf{u}_0 can be decomposed as

$$\mathbf{u}_0 = \sum_j \langle \check{\mathbf{u}}_j | \mathbf{u}_0 \rangle \check{\mathbf{u}}_j, \quad (1.25)$$

leading to a response at $t = t_o$

$$\mathbf{u}(t_o) = e^{Lt_o} \mathbf{u}_0 = \sum_j \langle \check{\mathbf{u}}_j | \mathbf{u}_0 \rangle e^{Lt_o} \check{\mathbf{u}}_j = \sum_j \langle \check{\mathbf{u}}_j | \mathbf{u}_0 \rangle \kappa_j \check{\mathbf{u}}_j^\dagger. \quad (1.26)$$

We understand now why the change of paradigm operated from computing the eigenmodes of L to solving (1.23) is fruitful. In doing so, we moved from a poor, non-orthogonal eigenbasis, to two orthonormal ones into which both the initial condition and the response at $t = t_o$, respectively, can be projected. The component of $\mathbf{u}(t_o)$ onto $\check{\mathbf{u}}_j^\dagger$ is directly given by the component of \mathbf{u}_0 onto $\check{\mathbf{u}}_j$, multiplied by the associated gain κ_j . This permits to rank the relative importance of each structure $\check{\mathbf{u}}_j^\dagger$ in the response $\mathbf{u}(t_o)$. For instance, in a configuration where $G(t_o) = \kappa_1 \gg \kappa_2 > \kappa_3 > \dots$ (i.e. where e^{Lt_o} is close to being of unitary rank), and where the actual and uncontrolled initial condition \mathbf{u}_0 does not project particularly well on one of the sub-optimal $\check{\mathbf{u}}_j$ for $j \geq 2$, the response in (1.26) is well approximated by

$$\mathbf{u}(t_o) \approx \langle \check{\mathbf{u}}_1 | \mathbf{u}_0 \rangle \kappa_1 \check{\mathbf{u}}_1^\dagger. \quad (1.27)$$

This simple result has profound consequences: the structure (not the amplitude) of the response does not depend on the structure of the initial condition, but becomes inherent to the propagator itself. Indeed, $\check{\mathbf{u}}_1^\dagger$ is computed solely from the knowledge of e^{Lt_o} . As soon as few structures $\check{\mathbf{u}}_j^\dagger$ are associated with gains much larger than all the others (i.e. e^{Lt_o} is low-rank), these leading structures are expected to emerge in the response, regardless of how it was initiated. They are expected to be distinguishable at least for some times around t_o . This conclusion is all the more relevant in that it permits to make predictions even in an uncontrolled environment where \mathbf{u}_0 can't be known or prepared. In this perspective, note that the configuration where solely $\check{\mathbf{u}}_1^\dagger$ has a much larger gain than all the others, is particularly favorable.

Some transient growth mechanisms: Orr, Lift-up, convective non-normality

Again due to the non-normality of the linearized Navier-Stokes operator (1.5), fluid flows furnish numerous examples of transient growth phenomena. The first step in studying these generally consists of computing the maximum gain in (1.22) and the associated sets of optimal initial conditions and responses. This has been first carried out in the context of parallel shear flows by Butler and Farrell (1992) and by Corbett and Bottaro (2000). The optimal structures emerging from these calculations can be interpreted physically, and suggest two main mechanisms for the transient growth in the flow kinetic energy: the Orr and the lift-up mechanisms.

In the Orr mechanism (Orr, 1907), perturbative vorticity layers are initially oriented against the base shear. As time evolves, these layers are advected by the base shear and, for purely kinematic reasons, become more compact in doing so. In virtue of the conservation of the circulation, this must be associated with an increase in velocity, hence the transient increase

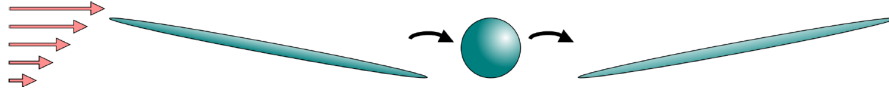


Figure 1.4: Explicative sketch of the Orr mechanism: a patch of vorticity perturbation initially oriented against the base shear flow is materially advected by the latter. In virtue of the conservation of the circulation $\int \mathbf{u} \cdot d\mathbf{l} \sim U(t)L(t) = \text{cst}$, ($L(t)$ the perimeter of the vorticity patch and $U(t)$ some associated characteristic velocity) the kinetic energy gain $G(t) \sim U(t)^2/U(0)^2 = L(0)^2/L(t)^2$ must increase with the perimeter diminishing (between the first and the second snapshot in the sketch). The gain will then decrease again as the vorticity patch is reoriented and stretched in the direction of the base advection (between the second and the third snapshot in the sketch). This sketch and the associated explanation have been reproduced from Antkowiak (2005).

Table 1.1: Summary of the dependence of the optimal transient gain on the Reynolds number, in wall-bounded shear flow. This table has been reproduced from Schmid and Henningson (2001)

Flow	$G_{max} \times 10^{-3}$	t_{max}
plane Poiseuille (Trefethen et al., 1993)	0.20 Re^2	0.076 Re
plane Couette (Trefethen et al., 1993)	1.18 Re^2	0.117 Re
circular pipe (Schmid & Henningson, 1994)	0.07 Re^2	0.048 Re
Blasius boundary layer (Butler & Farrell, 1992)	1.50 Re^2	0.778 Re

in kinetic energy (see in figure 1.4 for a schematic representation)

In the lift-up mechanism, streamwise-invariant vortices advect the base velocity successively upward and downward. This creates strong streamwise velocity perturbations (forming what is called "streaks"), thus a considerable increase in the kinetic energy of the perturbation field. In a purely linear regime, the perturbations subsequent to both the Orr and the lift-up mechanisms will eventually vanish exponentially with time. That is because the associated base flows, at least those considered in Butler and Farrell (1992) and Corbett and Bottaro (2000), are linearly stable. Several years of research concerned about transient growth in parallel shear flows have revealed the optimal gain (1.22) to be increasing with the Re number as Re^2 , as summarized in table 1.1 reproduced from Schmid and Henningson (2001). Both the Orr and the lift-up mechanisms will be analyzed in greater detail in this thesis, with special attention paid to their effects in a weakly nonlinear regime.

Non-parallelism of the base flow, designating the fact that it varies in the streamwise direction, was shown in Cossu and Chomaz (1997) and later in Marquet et al. (2008, 2009) to be an additional source of non-normality. This was also formalized in Trefethen and Embree (2005) (§11), in the more general framework of variable-coefficients operators. Cossu and Chomaz (1997) argue that this additional source non-normality is related to the presence of a (locally) convectively unstable pocket in the flow. This is exemplified in figure 1.5 for the backward-

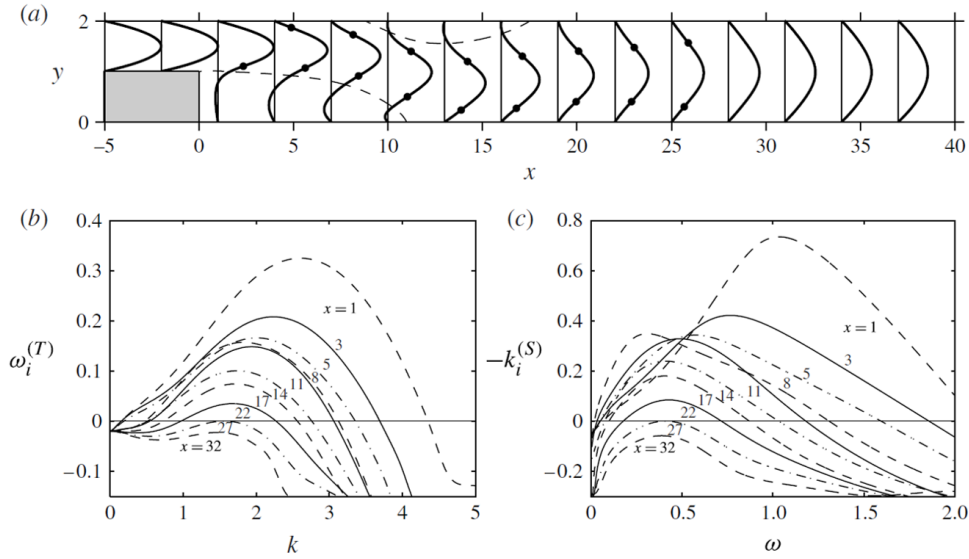


Figure 1.5: (a) Profiles of the streamwise base velocity of the backward-facing step flow at $Re = 500$. The dots highlight the inflection points. (b) Temporal and (c) spatial growth rates arising from a local stability analysis at different streamwise locations. Figure reproduced from Boujo and Gallaire (2015)

facing step at $Re = 500$. There, a recirculation zone with negative streamwise velocity is created past the discontinuous step at $x = 0$, creating an intense shear layer. Solving a uni-dimensional Orr-Sommerfeld eigenvalue problem at each streamwise location x , reveals the flow to be (locally) unstable from $x = 0$ to $x = 27$ to a shear (Kelvin-Helmholtz) instability. For each streamwise location, the instability is further characterized as being "convective". This means that, locally, a perturbative wavepacket is advected faster than it is growing, thereby it is decaying if observed from a fixed spatial location. Performing a stability analysis that fully takes into account the streamwise direction (i.e., that is two-dimensional), and does not treat it as a parameter for local (one-dimensional) analysis, is called a "global" stability analysis. Due to the convective nature of the local instability for each streamwise location, the global analysis would reveal flow to be stable (Huerre & Monkewitz, 1990). And yet, as argued in Cossu and Chomaz (1997), an initial perturbation initially located upstream, can draw energy from the base flow and thus grow as it is advected downstream across the convectively unstable pocket. This pocket being of finite size, the energy of the perturbation will then decay as the latter is advected out of the pocket, and eventually be washed out of the flow domain. This scenario is associated with a transient growth in the perturbation. It is illustrated in figure 1.6 for the backward-facing step flow at $Re = 500$.

Note also in figure 1.6 the large values taken by the optimal gain in figure 1.6b. In fact, it was found in Boujo and Gallaire (2015) to increase exponentially with the Re number for the backward-facing step flow, thereby more rapidly than for parallel shear flows. A considerable body of work has been devoted to the computation of transient growth properties of non-parallel flows. Among them, could be mentioned the work of Åkervik et al. (2008) and

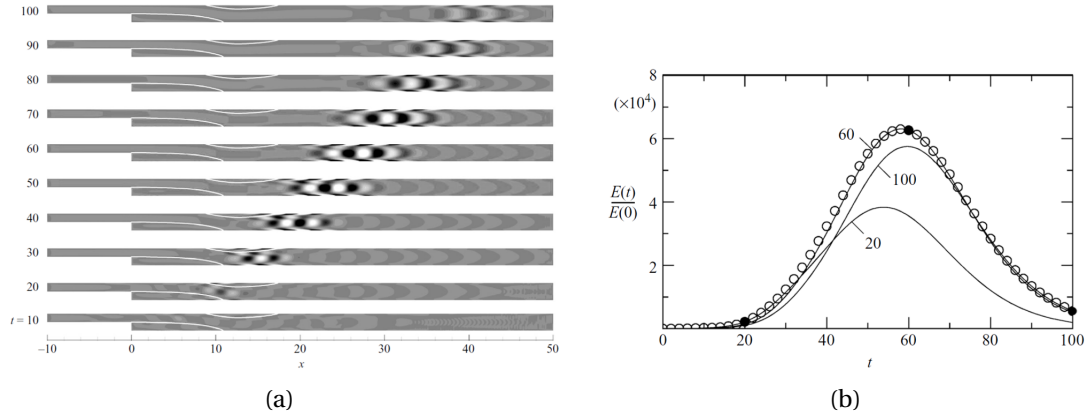


Figure 1.6: (a) Contour of the vorticity perturbation evolution seeded by the optimal initial condition $\tilde{\mathbf{u}}_1$ (optimized for $t_o = 58$) for the backward-facing step at $Re = 500$ shown in figure 1.5. As the perturbation progresses in the convectively unstable pocket from $x = 0$ to $x = 27$, it grows in energy, to eventually decay as it leaves the pocket. (b) The circles are the "envelope", meaning the maximum gain in the kinetic energy $G(t_o)^2$, as defined (1.22), and plotted as a function of the temporal horizon $t = t_o$. The continuous lines are the amplification of the kinetic energy along a trajectory, each being seeded by the optimal condition for $t_o = [20, 60, 100]$, respectively. At the black bullets, the optimization time equals the instantaneous time and the continuous line seeded must collide with the envelope. Both (a) and (b) have been reproduced from Blackburn et al. (2008).

Ehrenstein and Gallaire (2005) and Monokrousos et al. (2010) for a spatially evolving (Blasius) boundary layer flow. The works of Ehrenstein and Gallaire (2008) and Alizard et al. (2009), for their part, were concerned about a separated boundary layer flow.

Nonlinear effects and possible bypass transition

The relevance of linear optimal transient growth and its associated structures $\tilde{\mathbf{u}}_i$ and $\tilde{\mathbf{u}}_i^\dagger$ in nonlinear flow regimes is a highly complicated question without a general answer. Nevertheless, a well-accepted specific nonlinear scenario where transient growth plays a crucial role is illustrated in figure 1.7a. Reproduced from Trefethen et al. (1993), figure 1.7a shows the temporal evolution of the norm of a perturbation over a linearly stable toy system. If the initial perturbation has a very small (the linearization is still valid at the initial time) yet sufficiently large amplitude, the gain in energy associated with the transient growth is sufficient to trigger nonlinearities, which makes the solution escape from its original attractor. In fluid flows, this can for instance happen as the perturbation nonlinearly feedback onto the base flow, thus modifying it to render it unstable. This could also be due to the effects of nonlinearly generated harmonics which feedback on the perturbation itself.

In other terms, through transient growth, the non-normality property of a linearized operator tends to reduce the size of the basin of attraction of the stable coherent states. If figure 1.7a shows an example where non-normality helps escape a linearly stable solution, transient

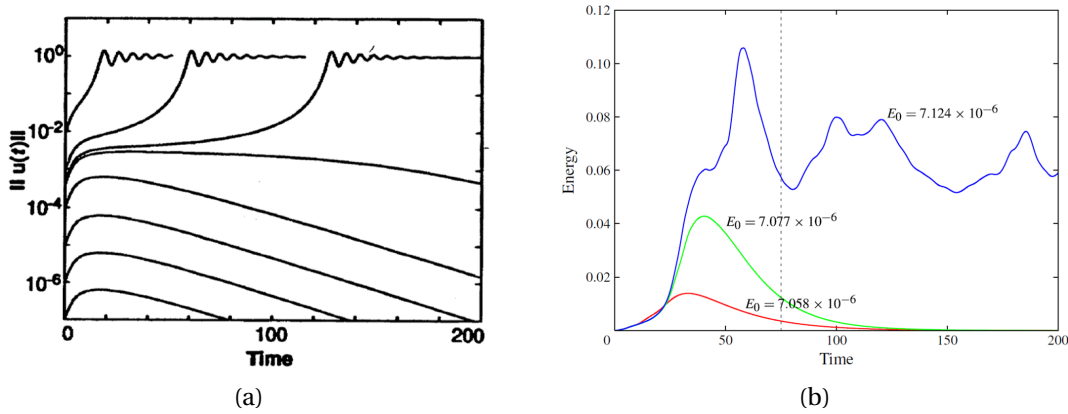


Figure 1.7: Nonlinear "bypass" transition. (a) Illustration on a toy model, reproduced from Trefethen et al. (1993). (b) Bypass transition towards turbulence in a pipe Poiseuille flow at $Re = 1750$ (the initial condition is not \tilde{u}_1 but results from a linear optimization problem). Reproduced from Pringle et al. (2012).

growth may be as relevant in escaping a linearly unstable one by triggering nonlinearities before the unstable mode emerges.

Figure 1.7b exemplifies the bypass transition mechanism towards turbulence in the linearly stable pipe Poiseuille flow at $Re = 1750$ (Pringle et al., 2012). If the perturbation is initialized with kinetic energies equal $E_0 = 7.058 \times 10^{-6}$ and $E_0 = 7.077 \times 10^{-6}$, the flow relaminarizes after a strong transient growth episode. If it is initialized with slightly larger kinetic energy $E_0 = 7.124 \times 10^{-6}$, the transient growth is this time just sufficient to make the flow transit to a turbulent regime. However, the initial conditions in Pringle et al. (2012) do not correspond to \tilde{u}_1 but result from a nonlinear optimization parametrized by E_0 . That is why the curves in figure 1.7b differ slightly in the initial, linear regime. This does not mean that a bypass transition would not occur if the perturbation was initiated with \tilde{u}_1 . Simply, it would require a larger E_0 (Pringle & Kerswell, 2010). The Lamb-Oseen vortex flow also is subject to a bypass transition (Rossi et al., 1997), as will be studied in detail in this thesis.

In boundary layer flow, the non-normal lift-up mechanism is also found to be an essential ingredient for the transition to turbulence, but also for its role played in the so-called self-sustained cycle. In figure 1.8a the streaky structures are observable in a smoke flow. The authors Matsubara and Alfredsson (2001) report that their initial growth is "closely related to algebraic or transient growth theory". The streaks are linearly unstable and, further downstream, the flow transits to a self-sustained turbulent state. Hamilton et al. (1995) argue that during the streaks breakdown, nonlinear interactions re-energize the streamwise vortices, which in turn generate streaks through the lift-up mechanism (although occurring over the non-linearly distorted mean flow). The loop is closed, proposing a scenario for the turbulent state to self-maintain (see in figure 1.8b). In this last sense, transient growth, although linear, can be extended into characterizing turbulent states by considering the coupling between the mean flow and the most amplified response which feeds back on it through nonlinearities.

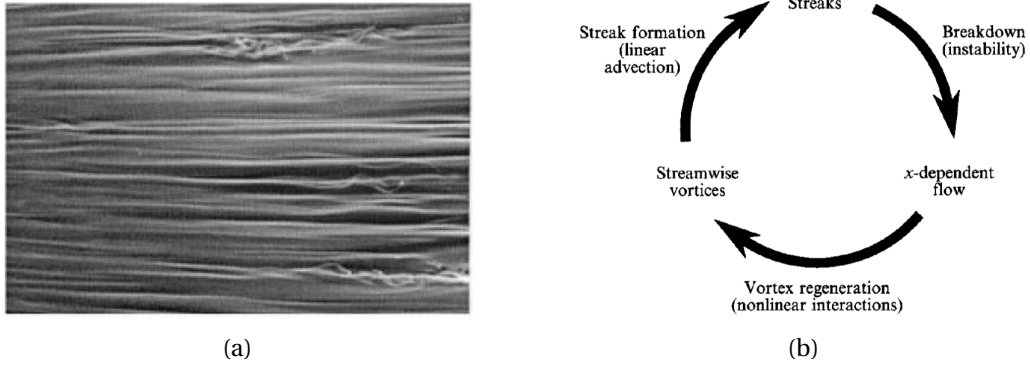


Figure 1.8: (a) Visualization of a smoke boundary layer flow subjected to free-stream turbulence; streaky structures resulting from the lift-up mechanism are observable. Reproduced from Matsubara and Alfredsson (2001). (b) Mechanism of self-sustained near-wall turbulence proposed in Hamilton et al. (1995).

In the bypass mechanism presented above, the perturbation is even more amplified in a nonlinear regime than in a purely linear one, but this need not be the case. In fact, nonlinearities can have a "saturating" effect on the energy of the perturbation, inducing a decrease in the transient gain with the amplitude of the initial perturbation. This is for instance occurring in the backward-facing step at $Re = 500$ considered in Blackburn et al. (2008) (see their figure 12). In this scenario, precisely because the flow did not transit to another structurally different state, the nonlinear response is expected to still bear symptoms of the linear optimal response $\tilde{\mathbf{u}}_1^\dagger$, at least in a weakly nonlinear regime. In this thesis, a method will be derived to assess *a priori* (before doing the nonlinear computations) if weak nonlinearities have a saturating or an amplifying effect on the optimal transient response.

To finalize this section concerned with the response to an initial perturbation, we propose in figure 1.9 an iconographic, non-exhaustive summary. It is based on the simulation of a slightly modified version of the 2×2 toy system proposed in Trefethen et al. (1993)

$$\frac{d\mathbf{u}}{dt} = A\mathbf{u} + \|\mathbf{u}\|^2 B_{1,2}\mathbf{u}, \quad A = \begin{bmatrix} \gamma R^{-1} & 1 \\ 0 & -2R^{-1} \end{bmatrix}, \quad B_1 = R \begin{bmatrix} 0 & -1 \\ 1 & 0 \end{bmatrix}, \quad B_2 = R \begin{bmatrix} -1 & 0 \\ 0 & -1 \end{bmatrix}, \quad (1.28)$$

and R is a constant parameter. The non-normal matrix A has eigenvalues $[\gamma R^{-1}, -2R^{-1}]$. In figure 1.9 are shown simulations of the linearized system (i.e. with simply $A\mathbf{u}$ at the right-hand side in (1.28)) as well as fully nonlinear simulations where both B_1 and B_2 were used respectively in the nonlinear terms, leading to different nonlinear behaviors. We distinguish the results as follows

- If we select $\gamma = -1$, corresponding to figure 1.9a, both eigenvalues of A are negative and the system is linearly stable. Therefore, the linear simulation decays exponentially asymptotically, with a decay rate equal to the largest eigenvalue. In addition, since A is non-normal, the linear trajectory presents a transient growth episode at a finite

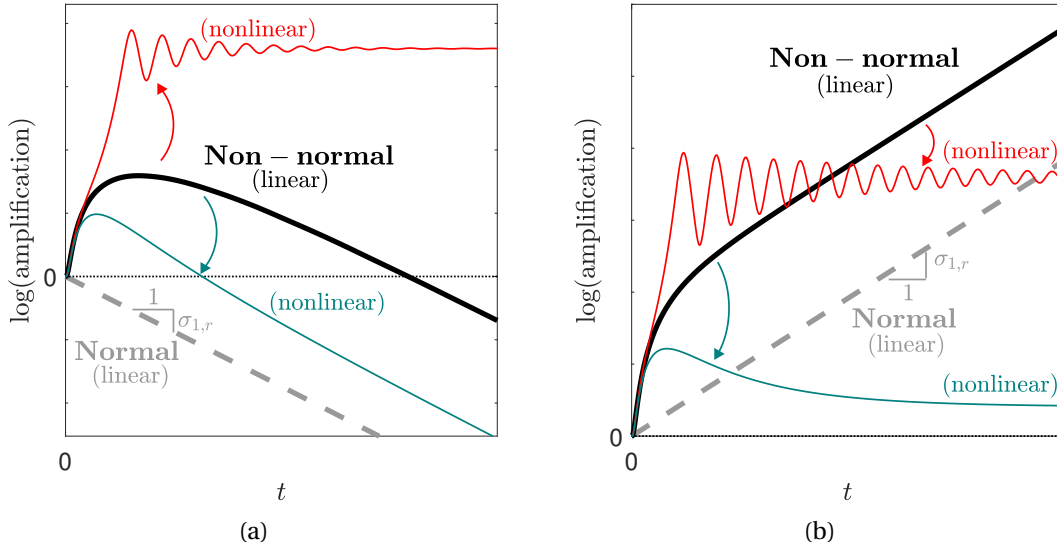


Figure 1.9: Linear (bold continuous lines) and fully nonlinear amplification $\|\mathbf{u}(t)\|^2/\|\mathbf{u}(0)\|^2$ (y-axis in log scale) for the toy system (1.28). The nonlinear simulations were performed for $\|\mathbf{u}(0)\|^2 = 10^{-3.2}$, and both the matrices B_1 (red continuous line) and B_2 (blue continuous line) were used, leading to different nonlinear behaviors. We set $R = 25$ and in (a) $\gamma = -1$, leading to a linearly stable system, whereas in (b) $\gamma = 1$ leading to a linearly unstable system. The gray dashed is the linear behavior that would follow a normal system with the same eigenvalues, namely, by replacing the component A_{12} by 0 (instead of 1) in (1.28).

time. Triggering nonlinearities by increasing $\|\mathbf{u}(0)\|$ can mitigate this transient gain (blue curve). On the contrary, it can also amplify the perturbation even more at the point of making the solution transit to another attractor (red curve, showing the bypass mechanism). It may also be that the amplifying or saturating character of nonlinearities depends both on the time t for a given $\|\mathbf{u}(0)\|$, and/or on the amplitude $\|\mathbf{u}(0)\|$ for a given time t (clearly, not all possible scenarios are shown in figure 1.9a).

- If we select $\gamma = 1$, corresponding to figure 1.9b, one eigenvalue of A is positive and the system is linearly stable. Therefore, the linear simulation increases exponentially asymptotically, with a growth rate equal to the largest eigenvalue. In addition, since A is non-normal, the initial growth of the perturbation is not exponential but algebraic, which can be faster than exponential at finite times. By re-introducing nonlinearities, the exponential growth observable for sufficiently small $\|\mathbf{u}(0)\|$ will saturate eventually. If $\|\mathbf{u}(0)\|$ is sufficiently large (as in figure 1.9b), the exponential growth might not even be observable, and nonlinearities will directly be brought about by the algebraic growth, the system then leaves the unstable fixed point not along its most unstable mode, but along the most amplified singular one. While nonlinearities necessarily have a saturating character at long times since the linear gain is infinite there, they might magnify the amplification at finite times (red curve). Again, not all possible scenarios are shown in figure 1.9b.

1.1.2 Response to a harmonic forcing

We now proceed by studying the behavior of the linear perturbation (1.6) when subject to an external and sustained disturbance, i.e. when $\mathbf{f}(\mathbf{x}, t) \neq 0$. In what follows, the initial perturbation \mathbf{u}_0 is set to zero. This falls into the so-called "receptivity analysis". We shall first consider the response to a monochromatic, harmonic forcing. This will serve as a building block for the ensuing analysis of the response to stochastic forcing.

A harmonic forcing at a frequency ω expresses

$$\mathbf{f}(\mathbf{x}, t) = \hat{\mathbf{f}}(\mathbf{x})e^{i\omega t} + \text{c.c.}, \quad (1.29)$$

which, injected in (1.6), leads to

$$\begin{aligned} \mathbf{u}(t) &= e^{Lt} \int_0^t e^{-Ls} e^{i\omega s} \hat{\mathbf{f}} ds + \text{c.c.} = e^{Lt} \int_0^t e^{(i\omega I - L)s} ds \hat{\mathbf{f}} + \text{c.c.} \\ &= e^{Lt} P \int_0^t e^{(i\omega I - \Lambda)s} ds P^{-1} \hat{\mathbf{f}} + \text{c.c.} \end{aligned} \quad (1.30)$$

where only temporal dependencies have been highlighted in the notation. We further distinguish between two cases: in the first (i), $i\omega$ also is an eigenvalue of L , whereas in the second (ii), it is not.

(i) If $i\omega$ is an eigenvalue of L , the forcing is said to be "resonant", as it excites the system at an eigenfrequency which is not subject to any damping (or growth). Say that $i\omega$ is the k th (i.e. $\sigma_k = i\omega$) eigenvalue of L ; if L is further assumed to be real, $-i\omega$ is the $(k+1)$ th eigenvalue, and the operator $e^{(i\omega I - \Lambda)s}$ expresses

$$e^{(i\omega I - \Lambda)s} = \text{diag}(\dots, e^{(i\omega - \sigma_{k-1})s}, 1, e^{2i\omega s}, e^{(i\omega - \sigma_{k+2})s}, \dots). \quad (1.31)$$

Thereby

$$\int_0^t e^{(i\omega I - \Lambda)s} ds = \text{diag}(\dots, \frac{e^{(i\omega - \sigma_{k-1})t} - 1}{(i\omega - \sigma_{k-1})}, t, \frac{e^{2i\omega t} - 1}{2i\omega}, \frac{e^{(i\omega - \sigma_{k+2})t} - 1}{(i\omega - \sigma_{k+2})}, \dots), \quad (1.32)$$

and the response (1.30) reads

$$\begin{aligned} \mathbf{u}(t) &= e^{Lt} P \int_0^t e^{(i\omega I - \Lambda)s} ds P^{-1} \hat{\mathbf{f}} + \text{c.c.} \\ &= e^{Lt} \left[t \mathbf{q}_k \frac{\langle \mathbf{q}_k^\dagger | \hat{\mathbf{f}} \rangle}{\langle \mathbf{q}_k^\dagger | \mathbf{q}_k \rangle} + \mathbf{q}_{k+1} \frac{e^{2i\omega t} - 1}{2i\omega} \frac{\langle \mathbf{q}_{k+1}^\dagger | \hat{\mathbf{f}} \rangle}{\langle \mathbf{q}_{k+1}^\dagger | \mathbf{q}_{k+1} \rangle} + \sum_{j \neq k, k+1} \mathbf{q}_j \frac{e^{(i\omega - \sigma_j)t} - 1}{(i\omega - \sigma_j)} \frac{\langle \mathbf{q}_j^\dagger | \hat{\mathbf{f}} \rangle}{\langle \mathbf{q}_j^\dagger | \mathbf{q}_j \rangle} + \text{c.c.} \right] \\ &= t \mathbf{q}_k \frac{\langle \mathbf{q}_k^\dagger | \hat{\mathbf{f}} \rangle}{\langle \mathbf{q}_k^\dagger | \mathbf{q}_k \rangle} + \mathbf{q}_{k+1} \frac{e^{i\omega t} - e^{-i\omega t}}{2i\omega} \frac{\langle \mathbf{q}_{k+1}^\dagger | \hat{\mathbf{f}} \rangle}{\langle \mathbf{q}_{k+1}^\dagger | \mathbf{q}_{k+1} \rangle} + \sum_{j \neq k, k+1} \mathbf{q}_j \frac{e^{i\omega t} - e^{\sigma_j t}}{(i\omega - \sigma_j)} \frac{\langle \mathbf{q}_j^\dagger | \hat{\mathbf{f}} \rangle}{\langle \mathbf{q}_j^\dagger | \mathbf{q}_j \rangle} + \text{c.c.} \end{aligned} \quad (1.33)$$

where we used $e^{Lt} \mathbf{q}_j = e^{\sigma_j t} \mathbf{q}_j$, $\forall j$. The first term at the right-hand side of (1.33) grows algebraically $\propto t$, such that the energy of the perturbation diverges with time $\lim_{t \rightarrow \infty} \|\mathbf{u}\| = \infty$. This is called a "resonance", for it is a consequence of the resonant nature of the forcing. Specifically, the presence of this term is solely due to the fact that the forcing frequency also is a neutral frequency of the system. Nevertheless, it appears clearly in (1.33) that the divergence of the response can be prevented if $\hat{\mathbf{f}}$ is such that $\langle \mathbf{q}_k^\dagger | \hat{\mathbf{f}} \rangle = 0$. In other words, the resonance does not occur if the forcing is orthogonal to the adjoint mode associated with the neutral frequency. This result is sometimes referred to as the "Fredholm alternative", "compatibility condition", or even "solvability condition", and will be widely evoked along this thesis.

(ii) If $i\omega$ is not an eigenvalue of L , the said "resolvent" operator $R(\omega) = (i\omega - L)^{-1}$ exists and can be used to directly compute the integral in (1.30) as

$$\begin{aligned} \mathbf{u}(t) &= e^{Lt} \int_0^t e^{(i\omega I - L)s} ds \hat{\mathbf{f}} + \text{c.c.} = e^{Lt} R(\omega) [e^{(i\omega I - L)s}]_{s=0}^{s=t} \hat{\mathbf{f}} + \text{c.c.} \\ &= e^{Lt} R(\omega) [e^{(i\omega I - L)t} - I] \hat{\mathbf{f}} + \text{c.c.} \\ &= \underbrace{e^{i\omega t} R(\omega) \hat{\mathbf{f}}}_{\text{harmonic response}} - e^{Lt} R(\omega) \hat{\mathbf{f}} + \text{c.c.} \end{aligned} \quad (1.34)$$

where we used that the resolvent and the propagator operators commute (which can be shown using their respective series or dyadic representation). Note that (1.34) and (1.33) are completely equivalent in the absence of a resonant frequency (i.e., if the two first terms vanish in (1.33) and the third, summation term is made over all indices j). It is easily shown using the dyadic representation of the resolvent

$$R(\omega) = \sum_j \mathbf{q}_j \frac{1}{(i\omega - \sigma_j)} \frac{\langle \mathbf{q}_j^\dagger | \cdot \rangle}{\langle \mathbf{q}_j^\dagger | \mathbf{q}_j \rangle}. \quad (1.35)$$

The second term at the right-hand side in (1.34), $e^{Lt} R(\omega) \hat{\mathbf{f}}$, involves the propagation of $R(\omega) \hat{\mathbf{f}}$. It is understood as the non-stationary response, which must be present to enforce that the perturbation is initially null $\mathbf{u}(0) = \mathbf{0}$. It would be identically null upon choosing $\mathbf{u}_0 = R(\omega) \hat{\mathbf{f}} + \text{c.c.}$, for the solution is then directly initiated in the stationary regime. This non-stationary response term diverges exponentially if L is linearly unstable. This is true regardless of the forcing frequency. Furthermore, the exponential growth is associated with its own eigenfrequency and eventually dominates over the harmonic response $e^{i\omega t} R(\omega) \hat{\mathbf{f}}$. The latter is the first term on the right-hand side in (1.34) and oscillates at the forcing frequency ω with bounded energy. This capacity of an unstable system (in a global sense) to respond with its own unstable frequency, dominating over the excitation frequency, is referred to as the "signaling problem" in the literature (Huerre & Monkewitz, 1990). Again, the dyadic representation of the response in (1.33) informs that the exponential divergence can be precluded if the forcing is orthogonal to all unstable adjoint mode(s).

In the configuration where L is linearly neutral or stable, the term $e^{Lt} R(\omega) \hat{\mathbf{f}}$ remains of

bounded energy. If L is stable, it eventually decays with time and this term represents nothing more than a transient response. As a side comment, this transient response could in fact, as we argued in the previous section, have drastic nonlinear consequences among which the system could transit even before the harmonic response has time to develop. Turning back to the linear realm, after the transient response fades away, the linear response relaxes towards its harmonic response oscillating at the forcing frequency. If the forcing is switched off, this harmonic response also fades away and the flow relaxes towards the base state. We assume L to be linearly stable in the following lines, and we solely consider the asymptotic response

$$\lim_{t \rightarrow \infty} \mathbf{u}(t) = \hat{\mathbf{u}}(\omega) e^{i\omega t} + \text{c.c.}, \text{ where } \hat{\mathbf{u}}(\omega) = R(\omega) \hat{\mathbf{f}}. \quad (1.36)$$

It is associated with a kinetic energy $\|\hat{\mathbf{u}}(\omega)\|^2 = \|R(\omega) \hat{\mathbf{f}}\|^2$. Using the dyadic representation of the resolvent (1.35), and remembering that in the case where L is non-normal the \mathbf{q}_j s do not constitute an orthonormal set, the energy $\|\hat{\mathbf{u}}(\omega)\|^2$ again is determined by a potentially large number of mode-mode interactions. In other words, the harmonic response of a stable system results from the cooperation of a potentially very large number of eigenmodes. Therefore, these latter generically constitute an inappropriate basis for the description of the flow. An exception to this could be found in the very specific case where ω is close to an eigenfrequency with a vanishing damping rate. Say that $\sigma_1 = i\omega_1 + \gamma$, with γ a negative real number with $\gamma \rightarrow 0$. Then

$$\hat{\mathbf{u}}(\omega) \rightarrow \frac{\mathbf{q}_1 \langle \mathbf{q}_1^\dagger | \hat{\mathbf{f}} \rangle}{i(\omega - \omega_1) - \gamma \langle \mathbf{q}_1^\dagger | \mathbf{q}_1 \rangle} \text{ if } \omega \rightarrow \omega_1 \text{ and } \gamma (< 0) \rightarrow 0 \quad (1.37)$$

which simply is a Lorentzian response, along the weakly damped eigenmode \mathbf{q}_1 . Actually, even if in (1.37) the response is modal, non-normality plays a role through the denominator $\langle \mathbf{q}_1^\dagger | \mathbf{q}_1 \rangle$. It is generically smaller than one for non-normal systems (see for instance figure 1.1) thus enhancing the amplitude of the Lorentzian response.

Harmonic optimal gain

Since in all generality the harmonic response is not well described by a single or even a few eigenmodes, we shall rely upon the same non-modal tools employed to compute the transient growth. Specifically, we seek the largest possible response-to-forcing amplification, also called "harmonic gain" $G(\omega)$ as

$$G(\omega) = \max_{\hat{\mathbf{f}}} \frac{\|\hat{\mathbf{u}}(\omega)\|}{\|\hat{\mathbf{f}}\|} = \max_{\hat{\mathbf{f}}} \sqrt{\frac{\langle R(\omega)^\dagger R(\omega) \hat{\mathbf{f}} | \hat{\mathbf{f}} \rangle}{\langle \hat{\mathbf{f}} | \hat{\mathbf{f}} \rangle}} = \|R(\omega)\|. \quad (1.38)$$

Thereby the optimal gain $G(\omega)$ is the largest eigenvalue η_1 ($G(\omega) = \eta_1$) of the self-adjoint problem

$$R(\omega)^\dagger R(\omega) \tilde{\mathbf{u}}_j = \eta_j^2 \tilde{\mathbf{u}}_j, \quad j = 1, 2, \dots \quad (1.39)$$

where the strictly positive eigenvalues η_j^2 are sorted by decreasing values. The associated eigenmodes $\tilde{\mathbf{u}}_j$ (normalized as $\|\tilde{\mathbf{u}}_j\| = 1$) constitute an orthonormal family of forcing structures. Among them, $\tilde{\mathbf{u}}_1$ is the most amplified one, and the rest constitutes sub-optimal forcing structures. The mode $\tilde{\mathbf{u}}_j$ also is j th right singular mode of $R(\omega)$, associated with eigenvalue η_j and a left singular mode $\tilde{\mathbf{u}}_j^\dagger$ (normalized as $\|\tilde{\mathbf{u}}_j^\dagger\| = 1$)

$$\eta_j \tilde{\mathbf{u}}_j^\dagger = R(\omega) \tilde{\mathbf{u}}_j, \quad \eta_j \tilde{\mathbf{u}}_j = R(\omega)^\dagger \tilde{\mathbf{u}}_j^\dagger. \quad (1.40)$$

This makes $\tilde{\mathbf{u}}_1^\dagger$ the most amplified harmonic response.

Note the analogy between the problem of finding the optimal initial conditions in (1.23), parameterized by the temporal horizon t_o , and the current problem of finding the optimal forcing structures, parameterized by the frequency ω .

Decomposing a generic harmonic forcing $\hat{\mathbf{f}}$ into the orthonormal basis formed by the $\tilde{\mathbf{u}}_j$ s, then applying the resolvent leads to the following decomposition of $\hat{\mathbf{u}}(\omega)$

$$\hat{\mathbf{u}}(\omega) = \sum_j \eta_j \langle \tilde{\mathbf{u}}_j | \hat{\mathbf{f}} \rangle \tilde{\mathbf{u}}_j^\dagger. \quad (1.41)$$

Again, the (non-modal) decomposition of $\hat{\mathbf{u}}(\omega)$ in the singular mode basis (1.41) appears more fruitful than the dyadic (modal) one in (1.33). The first reason is that the $\tilde{\mathbf{u}}_j^\dagger$ are orthonormal thus there is no redundancy in their respective information and the sum in (1.41) is expected to converge much faster than the one in (1.33). The second is that the contribution of each $\tilde{\mathbf{u}}_j^\dagger$ is weighted by η_j , and two different η_j s can be separated by a ratio of several orders of magnitude. This is again the low-rank approximation. In the most favorable case where $\eta_1 \gg \eta_2 > \dots$, and if $\hat{\mathbf{f}}$ is sufficiently generic in the sense that it does not promote a particular sub-optimal structure, $\hat{\mathbf{u}}(\omega)$ is well approximated by

$$\hat{\mathbf{u}}(\omega) \approx G(\omega) \langle \tilde{\mathbf{u}}_1 | \hat{\mathbf{f}} \rangle \tilde{\mathbf{u}}_1^\dagger. \quad (1.42)$$

Thereby the harmonic response is along $\tilde{\mathbf{u}}_1^\dagger$, regardless of the exact shape of $\hat{\mathbf{f}}$. Only the amplitude of the response requires the knowledge of $\hat{\mathbf{f}}$. In other words, at a prescribed frequency, the structure of the response becomes intrinsic to the operator itself, while the form of the excitation is unimportant (apart from the fact that it should be non-zero).

The computation of the harmonic gain (1.38) and associated optimal structures were widely performed in fluid mechanics literature, both for parallel (see Schmid (2007) for a review) and non-parallel shear flows (Åkervik et al., 2007; Alizard et al., 2009; Boujo & Gallaire, 2015; Sipp, 2012). Very large values for the harmonic gain are often found. Sometimes, this can be simply

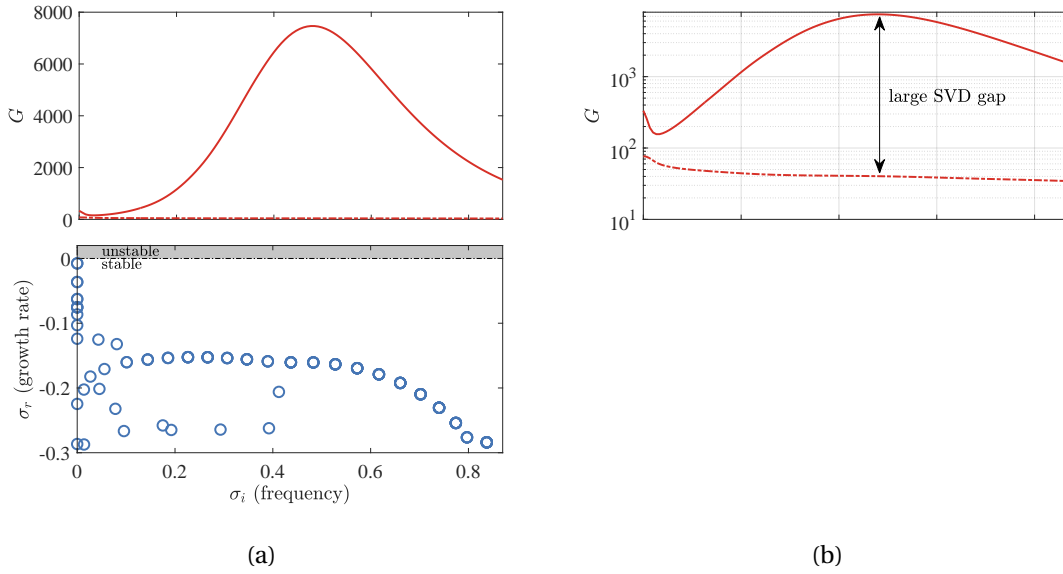


Figure 1.10: (a) Top: harmonic gain $G(\omega)$ ($= \eta_1(\omega)$), as defined in (1.38), as a function of the frequency, and for the flow past a backward-facing step at $Re = 500$ (shown in figure 1.5). The first sub-optimal $\eta_2(\omega)$ is also included as the dash-dotted line. Bottom: spectrum of the flow in the complex plane. (b) The same figure as the top figure in (a) (just at its left) but shown in a logarithmic scale for the y -axis to better quantify the ratio between η_1 and η_2 .

linked to the presence of a very weakly damped eigenvalue, moreover associated with a direct and adjoint mode having poor spatial support $\langle \mathbf{q}_1^\dagger | \mathbf{q}_1 \rangle \ll 1$, through the Lorentzian response (1.37). This scenario is exemplified in figure 4 in Symon et al. (2018), for the cylinder flow at $Re = 47$. However, as argued, a huge $G(\omega)$ may not be linked to any outstanding eigenvalue with a frequency close to ω . This last configuration is illustrated in figure 1.10 for the flow past a backward-facing step at $Re = 500$.

The harmonic gain curve reaches very large values up to $G = 7480$ over a relatively selective range of frequency, the most amplified being located at $\omega = 0.47$. Over this frequency range, the spectrum is essentially flat and reveals only largely damped eigenvalues. Therefore the harmonic gain can't be linked to a specific eigenmodal mechanism, but results from an interaction between a vast amount of eigenmodes. This was also shown in Garnaud et al. (2013b) to occur in a jet turbulent mean flow. Figure 4 in Garnaud et al. (2013b) shows large harmonic gain up to $G = 200$ over a range of frequencies for which, in their figure 3, no eigenvalues are standing out.

Convective non-normality

As for the transient gain, large values of harmonic gain in non-parallel flows can be linked to the presence of a convectively unstable region. Under the assumption that the base flow varies slowly in the streamwise direction, this can be quantified by a formal weakly non-parallel

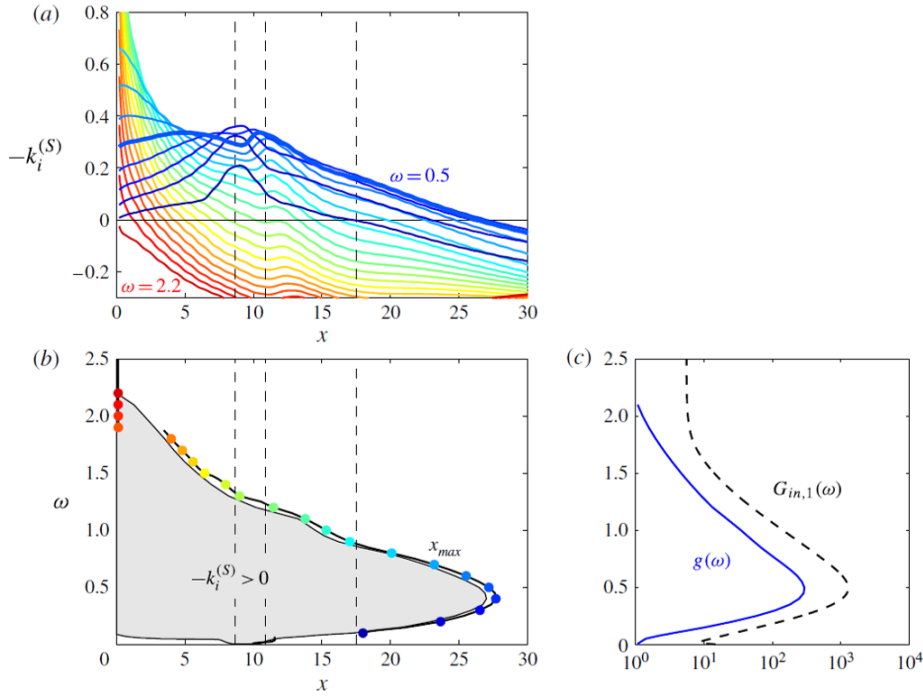


Figure 1.11: (a) Spatial growth rate at different frequencies. (b) The shaded area is the region of local, convective instability. (c) Amplification factor in thick blue line compared with the harmonic gain in dashed line. Reproduced from Boujo and Gallaire (2015)

(WKBJ) analysis (Huerre & Rossi, 1998). It leads to an integral amplification factor $g(\omega)$ directly as the exponential of the integral of the spatial growth rate, over the convectively unstable region (thus the boundaries of the integral depend on the frequency)

$$g(\omega) = \exp\left(\int -k_i^{(S)}(\omega, x) dx\right). \quad (1.43)$$

For the backward-facing step at $Re = 500$, the amplification factor is reported in figure 1.11, where it is seen to compare well with the harmonic gain (whereas the latter does not make any assumptions about the base flow weak non-parallelism). Specifically, it predicts well the most amplified frequency $\omega = 0.47$, which can then be interpreted as the frequency leading to the largest integral of $-k_i^{(S)}$ over space. Because it is linked to a convective instability, the global spectrum in figure 1.10a does not show any outstanding eigenvalue at this frequency.

The work of Beneddine et al. (2016) argues that if a large harmonic gain at a given frequency is associated with a convective instability mechanism, such as in the scenario we just presented for $\omega = 0.47$, there is a strong gap between it and the sub-optimal gains at this frequency (i.e. $\eta_1 \gg \eta_2 > \dots$). Figure 1.10b corroborates this conclusion, for at $\omega = 0.47$ the ratio between $G = \eta_1$ and η_2 is particularly important ≈ 200 . Thereby, following (1.42), the response of the backward-facing flow at $Re = 500$ to a structurally unspecified forcing, at the frequency close to $\omega = 0.47$, will systematically and accurately resemble the most amplified response $\tilde{\mathbf{u}}_1^\dagger$. This

is an appreciable conceptual progress: by changing the paradigm from computing eigenmode to computing singular modes, we could reduce the dynamics of the flow to a single (singular) mode. This is despite the fact that the spectrum in figure 1.10a reveals the dynamics to result from the combination of a large number of eigenmodes.

A large harmonic gain over some frequency interval implies the flow to largely amplify any sustained small external disturbance whose Fourier decomposition contains these frequencies. Therefore, as for the transient gain, it also indicates the propensity for the flow to trigger nonlinearities which could make it transit to another state or regime, for instance, turbulence. This motivated the development of methods aiming at extending the resolvent analysis in nonlinear regimes.

Going nonlinear

Among them, the "self-consistent" method outlined in Mantič-Lugo and Gallaire (2016b) considered the effect of nonlinearities on the harmonic response to an external harmonic forcing, under some simplifying hypothesis. The method consists of splitting the flow into a mean (in time) component and a fluctuation. Both the mean flow and the fluctuation are unknown to be solved for. The problem is closed by assuming the fluctuation to be monochromatic (which can't be exactly true in a nonlinear regime), so as to neglect the effect of all harmonics. Under this hypothesis the fluctuation, oscillating at a pulsation ω , obeys a linear equation. That is because the quadratic nonlinearity of the Navier-Stokes equations generates terms oscillating at 2ω and $\omega - \omega = 0$ (forcing the mean flow), which don't feedback on ω . The system of equations in Mantič-Lugo and Gallaire (2016b) then consists of a linear, externally forced, equation for the fluctuation at ω , and a nonlinear equation for the mean flow, forced by the Reynolds stress divergence of the fluctuation. This closed system is solved iteratively for the flow past a backward-facing step at $Re = 500$. It revealed the harmonic gain to decrease with nonlinearities, as the mean flow presented a smaller recirculation region, corresponding to a convectively unstable pocket of reduced size.

The technique advanced in Mantič-Lugo and Gallaire (2016b) can be generalized by including an arbitrary number of harmonics, at the cost of making the equation for the fluctuations nonlinear (Rigas et al., 2021). The work of Bengana and Tuckerman (2021) proceeds from the same generalization of Mantič-Lugo et al. (2014) in the case of an unforced but unstable flow (the fundamental frequency is that of the unstable mode). If for instance the 2ω harmonic is included in the fluctuation, the nonlinear fluctuation-fluctuation term will produce in particular $-\omega + 2\omega = \omega$ and $\omega + \omega = 2\omega$ interactions. Both feedback on their respective component of the fluctuation, thus their governing equations are nonlinear. The resulting system is made of N nonlinear coupled equations for N harmonics, and a nonlinear equation for the mean flow, over which all perturbation feeds back through Reynolds stress divergence. Solving this system is sometimes also referred to as the "harmonic balance" method. The number N of harmonics to be included for an accurate description of the nonlinear flow is case-dependent and the truncation is difficult to justify *a priori*. Indeed, contrary to asymptotic expansion methods,

the self-consistent method does not formalize a hierarchical ordering between the amplitude of the harmonics. In practice, harmonics are gradually included until the convergence of the results (see figure 7 in Bengana and Tuckerman (2021)). Convergence curves are generally found to be non-monotonous.

Since it describes a nonlinear response state, it can also be used for a nonlinear extension of the problem of finding the maximum harmonic gain (1.38) (Rigas et al., 2021). Again, the convergence of the optimal structures with the number of included harmonics needs to be verified *a posteriori*. To the knowledge of the author, there are no conceptual differences between the "harmonic balance" method and the "self-consistent" method.

In another context, the structures associated with the harmonic gain have sometimes proven to be successful in reproducing the main feature of self-sustained, statistically steady turbulent flows (Abreu et al., 2020; Amaral et al., 2021; McKeon & Sharma, 2010; Nogueira et al., 2019; Pickering et al., 2020, 2021; Towne et al., 2018). In these analyses, the flow is not subject to an external harmonic forcing but the turbulent fluctuations play the role of an endogenous source of excitation. More precisely, the Navier-Stokes equations are reformulated as a nonlinear equation for the mean flow, forced by the Reynolds stress divergence of the turbulent fluctuations, and an equation for the turbulent fluctuations (or several, one per wavenumber, if written in the Fourier domain). The latter can be seen as an input-output problem through the resolvent operator linearized around the mean flow, forced by the nonlinear fluctuations-fluctuations term (see equations (2.11) and (2.12) in McKeon and Sharma (2010)). Say the resolvent operator around the mean flow is close to being unit-rank for a given frequency, which often proves to be the case for a turbulent flow with a strong mean advection. Then, we know from (1.42) that the response is necessarily along its most amplified harmonic response regardless of the forcing. Therefore, if only the structure (and not the amplitude) of the response is sought, the nonlinear fluctuations-fluctuations forcing term needs not to be computed. The amplitude of the fluctuation would remain unknown though, as it involves the inner product between the most amplified forcing and the nonlinear fluctuations-fluctuations forcing. This leads to a closure problem, for the mean flow equation requires knowledge of the fluctuations through the Reynolds stress divergence term. This problem is typically contoured by computing the mean flow with a turbulent eddy-viscosity model or reconstructing it from data McKeon and Sharma (2010). An approximate manner to compute the amplitude of the fluctuations from weakly nonlinear arguments has also been proposed Rosenberg et al. (2019).

In figure 1.12, are reproduced resolvent modes on a turbulent jet mean flow at $M = 0.4$ and computed including an eddy-viscosity model. They are compared with the leading SPOD modes, which optimally reproduce the flow statistics. The agreement is reasonable, particularly at $St = 0.6$ where the low-rank assumption was found in Pickering et al. (2020) to be particularly well verified. The authors relate this to the fact that the large optimal response results from a convective instability mechanism of the same (Kelvin-Helmholtz) nature as the one presented below for the backward-facing step. This interpretation is in accordance with the conclusions drawn in Beneddine et al. (2016).

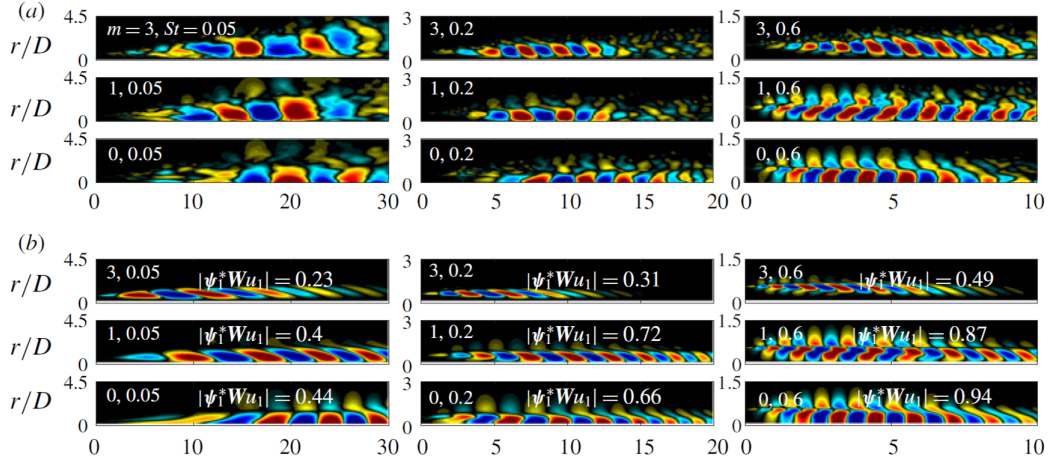


Figure 1.12: Streamwise velocity perturbation of a turbulent jet flow at $M = 0.4$ and corresponding to (a) the most energetic SPOD mode and (b) the resolvent response associated with the largest gain on an eddy-viscosity mean flow. Included azimuthal wavenumbers are $m \in [0, 1, 3]$ and frequencies $St = [0.05, 0.2, 0.6]$. The inner product between the SPOD and the resolvent mode is also shown (the amplitude of the resolvent mode is chosen such as to maximize this inner product). Reproduced from Pickering et al. (2020).

Thereby, just as transient growth has proven to be an important ingredient in the self-sustaining of wall-bounded turbulent flow in figure 1.8b, linear non-normal mechanisms at work in the harmonic response are here found essential in the self-sustained of a turbulent jet flow. In both cases, the price to pay for linear analysis to be valid in a turbulent regime is that the relevant operator (propagator or resolvent) should be constructed around a mean flow instead of a base flow (which renders the adjective "linear" somewhat inappropriate), which goes with a closure problem.

1.1.3 Response to a stochastic forcing

In this section, we appraise the effect of a stochastic sustained forcing on the linear perturbation by solving (1.6) without an initial perturbation, but under the specific forcing

$$\mathbf{f}(\mathbf{x}, t; \theta) = \mathbf{f}_s(\mathbf{x}) \xi(t; \theta), \quad (1.44)$$

where $\mathbf{f}_s(\mathbf{x})$ is a spatial structure and $\xi(t; \theta)$ is a statistically steady scalar stochastic process, not necessarily a white noise for the moment. The symbol θ designates a random variable, following a certain probability law. As an example, we could have $\xi(t; \theta) = \sin(\omega t + 2\pi\theta)$ with θ a random phase following an uniform distribution $\theta \sim \mathcal{U}_{[0,1]}$. We insist that the shape of the forcing in (1.44) is far from being general, and a more complete stochastic excitation would consist of the sum $\mathbf{f}(\mathbf{x}, t; \theta) = \sum_j \mathbf{f}_{s,j}(\mathbf{x}) \xi_j(t; \theta_j)$ together with spatio-temporal covariance matrices.

In order to describe the forcing and the response in a statistical sense, the ensemble averaging

operation, denoted $\{\bullet\}$, is introduced. It consists of averaging over all processes, each corresponding to a different value of θ . The temporal averaging operation over a finite-time signal of length T

$$\bar{\bullet} = \frac{1}{T} \int_0^T \bullet dt \quad (1.45)$$

is also introduced, as well as the finite-time Fourier transform and its inverse

$$\hat{\xi}(\omega; \theta) = \frac{1}{\sqrt{T}} \int_0^\infty \xi(t; \theta) e^{-i\omega t} dt, \quad \xi(t; \theta) = \frac{\sqrt{T}}{2\pi} \int_{-\infty}^{+\infty} \hat{\xi}(\omega; \theta) e^{i\omega t} d\omega. \quad (1.46)$$

The process $\xi(t; \theta)$ being by assumption statistically steady, it is unambiguously given by its Fourier transform without loss of information about a transient regime. The linear response (1.6) to (1.44) (and without initial condition) reads

$$\begin{aligned} \mathbf{u}(t; \theta) &= \frac{\sqrt{T} e^{Lt}}{2\pi} \int_0^t \int_{-\infty}^{\infty} e^{-Ls} \mathbf{f}_s \hat{\xi}(\omega; \theta) e^{i\omega s} d\omega ds \\ &= \frac{\sqrt{T}}{2\pi} \int_{-\infty}^{\infty} e^{Lt} \int_0^t e^{(i\omega I - L)s} ds \hat{\xi}(\omega; \theta) d\omega \mathbf{f}_s. \end{aligned} \quad (1.47)$$

It is clear in (1.47) that if L possesses a neutral eigenvalue at a certain frequency and that $\hat{\xi}(\omega; \theta)$ does not vanish at this same frequency, the response is subject to a resonance phenomenon, namely, to an algebraic growth $\propto t$ of the neutral eigenmode. As we have shown, that is because $(i\omega I - L)$ will possess a null eigenvalue at this frequency, thus the exponential will contain a unit term which will become t after temporal integration. In the rest of this section, let us consider the scenario where L is stable, such that $(i\omega I - L)^{-1}$ exists for all frequencies ω . Thereby (1.47) becomes

$$\begin{aligned} \mathbf{u}(t; \theta) &= \frac{\sqrt{T}}{2\pi} \int_{-\infty}^{\infty} e^{Lt} R(\omega) [e^{(i\omega I - L)s}]_{s=0}^{s=t} \hat{\xi}(\omega; \theta) d\omega \mathbf{f}_s \\ &= \frac{\sqrt{T}}{2\pi} \int_{-\infty}^{\infty} \hat{\xi}(\omega; \theta) R(\omega) \mathbf{f}_s e^{i\omega t} d\omega - \frac{\sqrt{T} e^{Lt}}{2\pi} \int_{-\infty}^{\infty} \hat{\xi}(\omega; \theta) R(\omega) \mathbf{f}_s d\omega. \end{aligned} \quad (1.48)$$

It is also constituted of a transient response to the forcing (second term on the right-hand side in 1.48), due to the fact that \mathbf{u} must be initially null. Such transient response eventually decays in a linear regime since L is assumed to be linearly stable. The first term on the right-hand side is the steady response in which the response is characterized by its Fourier transform

$$\hat{\mathbf{u}}(\omega; \theta) = \hat{\xi}(\omega; \theta) R(\omega) \mathbf{f}_s. \quad (1.49)$$

In line with previous approaches concerning transient growth and the harmonic response, for a given process ξ , one can construct an orthonormal basis of forcing structure onto which an unspecified structure \mathbf{f}_s can be projected. These structures can be ranked by the respective contributions of their responses in the variance of the total response. This amounts

to maximizing the variance-to-intensity gain G_s as

$$G_s^2 = \max_{\mathbf{f}_s} \frac{\overline{\|\mathbf{u}(t; \theta)\|^2}}{\|\mathbf{f}_s\|^2}. \quad (1.50)$$

The variance of the response can be expressed in the Fourier domain as (Parseval's theorem)

$$\begin{aligned} \overline{\|\mathbf{u}(t; \theta)\|^2} &= \frac{T}{4\pi^2} \int_{-\infty}^{\infty} \int_{-\infty}^{\infty} \{\langle \hat{\mathbf{u}}(\omega; \theta) | \hat{\mathbf{u}}(s; \theta) \rangle\} \overline{e^{it(s-\omega)}} d\omega ds \\ &= \frac{1}{2\pi} \int_{-\infty}^{\infty} \{|\hat{\xi}(\omega; \theta)|^2\} \langle \mathbf{f}_s | R^\dagger(\omega) R(\omega) \mathbf{f}_s \rangle d\omega \\ &= \langle \mathbf{f}_s | B \mathbf{f}_s \rangle \end{aligned} \quad (1.51)$$

where we used the definition of the Dirac impulse $\overline{e^{it(s-\omega)}} = 2\pi\delta(s-\omega)/T$, and where we defined the self-adjoint, strictly positive definite operator

$$B = \frac{1}{2\pi} \int_{-\infty}^{\infty} \{|\hat{\xi}(\omega; \theta)|^2\} R^\dagger(\omega) R(\omega) d\omega. \quad (1.52)$$

Subsequently, the maximum stochastic gain (1.50) is also equal to

$$G_s^2 = \max_{\mathbf{f}_s} \frac{\langle \mathbf{f}_s | B \mathbf{f}_s \rangle}{\langle \mathbf{f}_s | \mathbf{f}_s \rangle}. \quad (1.53)$$

The orthonormal set of optimal and sub-optimal stochastic forcing (real) structures are then found as the eigenmodes $\tilde{\mathbf{f}}_j$ (normalized as $\|\tilde{\mathbf{f}}_j\| = 1$) of the operator B

$$B \tilde{\mathbf{f}}_j = \mu_j^2 \tilde{\mathbf{f}}_j, \quad j = 1, 2, \quad (1.54)$$

associated with real eigenvalues μ_j^2 . The stochastic forcing structure $\tilde{\mathbf{f}}_1$ leads to the largest variance amplification, equal to $G_s^2 = \mu_1^2$. The stochastic process $\xi(t; \theta)$ can be chosen as a delta-correlated white noise, characterized in the temporal domain as $\overline{\{\xi(t; \theta)\xi(t+s; \theta)\}} = \delta(s)$. Using Fourier transforms it is shown to correspond to $\{|\hat{\xi}(\omega; \theta)|^2\} = 1, \forall \omega$ in the frequency domain. In the latter case, the operator B in (1.52) is similar to the one derived in Farrell and Ioannou (1993).

Once again the orthonormal family $\tilde{\mathbf{f}}_j$ is found to be particularly informative if the operator B is low-rank. Say the linear system is subject to a more generic forcing

$$\begin{aligned} \mathbf{f}(\mathbf{x}, t; \boldsymbol{\theta}) &= \sum_{k=1}^N \mathbf{f}_k(\mathbf{x}) \xi(t; \theta_k) = \mathbf{F}(\mathbf{x}) \boldsymbol{\xi}(t; \boldsymbol{\theta}), \quad \text{with} \\ \mathbf{F}(\mathbf{x}) &= [\mathbf{f}_1, \mathbf{f}_2, \dots, \mathbf{f}_N], \quad \text{and} \quad \boldsymbol{\xi}(t; \boldsymbol{\theta}) = [\xi(t; \theta_1), \xi(t; \theta_2), \dots, \xi(t; \theta_N)]^T. \end{aligned} \quad (1.55)$$

where the \mathbf{f}_k s are some unspecified forcing structures. The random variables θ_k all follow the same probability law but are independent of each other, such that the processes $\xi(t; \theta_k)$ are uncorrelated (i.e. $\{\xi(t; \theta_i)\xi(t; \theta_j)\} = 0$ if $i \neq j$ and same in the Fourier domain). Thereby the

variance of the response is

$$\begin{aligned}
\overline{\|\mathbf{u}(t; \boldsymbol{\theta})\|^2} &= \frac{1}{2\pi} \int_{-\infty}^{\infty} \sum_k \sum_n \langle R(\omega) \mathbf{f}_k | \{ \hat{\xi}(\omega; \theta_k)^* \hat{\xi}(\omega; \theta_n) \} R(\omega) \mathbf{f}_n \rangle d\omega \\
&= \frac{1}{2\pi} \int_{-\infty}^{\infty} \sum_k \langle \mathbf{f}_k | \{ |\hat{\xi}(\omega; \theta_k)|^2 \} R^\dagger(\omega) R(\omega) \mathbf{f}_k \rangle d\omega \\
&= \sum_k \left\langle \mathbf{f}_k \left| \frac{1}{2\pi} \int_{-\infty}^{\infty} \{ |\hat{\xi}(\omega; \theta_k)|^2 \} R^\dagger(\omega) R(\omega) d\omega \mathbf{f}_k \right. \right\rangle \\
&= \sum_k \langle \mathbf{f}_k | B \mathbf{f}_k \rangle
\end{aligned} \tag{1.56}$$

In addition, each \mathbf{f}_k can be decomposed in the orthonormal $\tilde{\mathbf{f}}_j$ family simply as

$$\mathbf{f}_k = \sum_j \langle \tilde{\mathbf{f}}_j | \mathbf{f}_k \rangle \tilde{\mathbf{f}}_j, \tag{1.57}$$

which permits to write the variance of the response as

$$\overline{\|\mathbf{u}(t; \boldsymbol{\theta})\|^2} = \sum_k \sum_j \mu_j^2 \left| \langle \tilde{\mathbf{f}}_j | \mathbf{f}_k \rangle \right|^2. \tag{1.58}$$

If each \mathbf{f}_k does not favor a particular sub-optimal, and under the low-rank assumption for the operator B , $\mu_1 \gg \mu_2 > \dots$, and the variance of the response is well approached by

$$\overline{\|\mathbf{u}(t; \boldsymbol{\theta})\|^2} \approx \mu_1^2 \sum_k \left| \langle \tilde{\mathbf{f}}_1 | \mathbf{f}_k \rangle \right|^2. \tag{1.59}$$

Thereby, in a statistical sense (at least for the variance), the stochastic response is dominated by the response to $\tilde{\mathbf{f}}_1$, which greatly simplifies the description of the system. Note that if in addition the resolvent operator $R(\omega)$ also is low-rank, each ω component of the stochastic response (1.49) is well described by the leading singular modes of $R(\omega)$.

Extracting the relevance structures can also be made directly at the response level, by computing the covariance operator $C(\bullet) = \overline{\mathbf{u}(t; \boldsymbol{\theta}) \langle \mathbf{u}(t; \boldsymbol{\theta}) | \bullet \rangle}$ of the response to the forcing (1.55). The operator $C(\bullet)$ applies over some deterministic, time-independent field $\mathbf{g} = \mathbf{g}(\mathbf{x})$ as

$$\begin{aligned}
C(\mathbf{g}) &= \overline{\mathbf{u}(t; \boldsymbol{\theta}) \langle \mathbf{u}(t; \boldsymbol{\theta}) | \mathbf{g} \rangle} \\
&= \frac{1}{2\pi} \int_{-\infty}^{\infty} R(\omega) \mathbf{F} \{ \hat{\xi}(\omega; \boldsymbol{\theta}) \hat{\xi}(\omega; \boldsymbol{\theta})^H \} \langle \mathbf{F}^H R(\omega)^\dagger \mathbf{g} \rangle d\omega.
\end{aligned} \tag{1.60}$$

with $\langle \bullet \rangle$ the spatial integration. It was used that $\hat{\mathbf{u}}(\omega; \boldsymbol{\theta}) = R(\omega) \mathbf{F} \hat{\xi}(\omega; \boldsymbol{\theta})$ and $\hat{\xi}(\omega; \boldsymbol{\theta})$ does not depend on space. In case of white noise $\{ \hat{\xi}(\omega; \boldsymbol{\theta}) \hat{\xi}(\omega; \boldsymbol{\theta})^H \} = I$, leading to the same operator as in Farrell and Ioannou (1993). Note that the operator $C(\bullet)$ depends on \mathbf{F} whereas B does not. We can postulate the following decomposition of the response

$$\mathbf{u}(\mathbf{x}, t; \boldsymbol{\theta}) = \sum_k \zeta(t; \theta_k) \boldsymbol{\phi}_k(\mathbf{x}) = \Phi(\mathbf{x}) \boldsymbol{\zeta}(t; \boldsymbol{\theta}), \quad \Phi = [\boldsymbol{\phi}_1, \boldsymbol{\phi}_2, \dots] \tag{1.61}$$

with the ϕ_k s an orthonormal family and the $\zeta(t; \theta_k)$ s some *a priori* unknown uncorrelated (i.e. $\{\zeta(t; \theta_i)\zeta(t; \theta_j)\} = 0$ if $i \neq j$) stochastic processes. Decomposition (1.61) is associated with the covariance operator applied to \mathbf{g}

$$C(\mathbf{g}) = \overline{\mathbf{u}(t; \boldsymbol{\theta}) \langle \mathbf{u}(t; \boldsymbol{\theta}) | \mathbf{g} \rangle} = \Phi \underbrace{\frac{1}{2\pi} \int_{-\infty}^{\infty} \{\hat{\zeta}(\omega; \boldsymbol{\theta}) \hat{\zeta}(\omega; \boldsymbol{\theta})^H\} d\omega}_{=\Gamma} \langle \Phi^\dagger \mathbf{g} \rangle = \Phi \Gamma \langle \Phi^\dagger \mathbf{g} \rangle, \quad (1.62)$$

where $\Gamma = \text{diag}(\gamma_1^2, \gamma_2^2, \dots)$ is a diagonal operator since the $\zeta(t; \theta_k)$ s are uncorrelated, and where we defined $\gamma_k^2 = (2\pi)^{-1} \int_{-\infty}^{\infty} \{|\hat{\zeta}(\omega; \theta_k)|^2\} d\omega$, the variance of $\zeta(t; \theta_k)$. Since $\langle \phi_i | \phi_j \rangle = \delta_{ij}$, we have $\langle \Phi \mathbf{a} | \Phi \mathbf{b} \rangle = \langle \mathbf{a} | \mathbf{b} \rangle = \langle \mathbf{a} | \Phi^\dagger \Phi \mathbf{b} \rangle$ for all \mathbf{a}, \mathbf{b} . As a consequence, we directly have $\Phi^{-1} = \Phi^\dagger$. From (1.62),

$$C(\mathbf{g}) = \Phi \Gamma \langle \Phi^\dagger \mathbf{g} \rangle, \forall \mathbf{g} \in \mathcal{D}(C), \quad \text{then} \quad C\phi_k = \gamma_k^2 \phi_k, \quad k = 1, 2, \dots \quad (1.63)$$

easily shown by selecting $\mathbf{g} = \phi_k$ for $k = 1, 2, \dots$. Equation (1.63) provides both ϕ_k as the k th (real) eigenmode of the real, self-adjoint operator C , and γ_k^2 as k th (real) eigenvalue of C . Ranking γ_k^2 in decreasing order, the response \mathbf{u} is often found to be well approximated by a few of the leading γ_k^2 (again C is found to be low-rank). In practice, C is often computed directly from data, precisely because (1.60) requires the knowledge of the forcing structures which is difficult to estimate in realistic situations. Then, solving (1.63) amounts to perform the celebrated "POD" for Proper Orthogonal Decomposition (see Berkooz et al. (1993) for a review).

The theoretical framework for a non-modal stochastic forcing analysis of the linearized Navier-Stokes equation, as reconstituted above, was introduced in Farrell and Ioannou (1993, 1994, 1996). Taking the stochastic forcing as white noise processes, the stochastic gains μ_j and the associated forcing and response structures $\tilde{\mathbf{f}}_j$ and ϕ_j , respectively, were computed for the plane Poiseuille and Couette flow (Farrell & Ioannou, 1993). The analysis was also carried out for the Lamb-Oseen vortex flow (Fontane et al., 2008) and the non-parallel flow past a backward-facing step (Boujo & Gallaire, 2015; Dergham et al., 2013). In all these studies, the stochastic gains are often found to be enormous, revealing these flows to be extremely receptive to external stochastic disturbances.

Nonlinear extensions

Once again, the linear non-modal analysis of the receptivity to stochastic forcing can be extended to a nonlinear regime, upon considering fluctuations around a mean flow instead of a base flow. As mentioned, this approach is nonetheless subject to a closure problem, which can be circumvented by either modeling or neglecting some nonlinear terms. We presented in figure 1.12 a case where the mean flow was obtained by an eddy-viscosity model, which amounts to modeling the Reynolds stress divergence of the fluctuations forcing the mean flow. Around this mean flow, the structure of the most amplified perturbation can be computed. In

the following lines, we briefly present another, and presumably non-equivalent, manner to bypass the closure problem. This will result in a closed coupled system for both the mean flow and its fluctuations.

It is known under the name of SSST (Stochastic Structural Stability Theory) and was introduced in Farrell and Ioannou (2003) in the context of two-dimensional turbulent jets in a x -periodic domain. The idea is to decompose the flow into a mean $U(y)$, averaged in the x direction, and the sum of fluctuations (not necessarily small) $\mathbf{q}_k(y)$, each oscillating with wavenumber k in x . Under some hypotheses, they evolve according to the following system

$$\begin{aligned} \frac{dU}{dt} &= -\sum_k \frac{k}{2} \text{diag} \left[\Im(\mathbf{q}_k \mathbf{q}_k^H) \Delta^\dagger \right] - rU, \\ \frac{d\mathbf{q}_k}{dt} &= L_U \mathbf{q}_k + \sqrt{\epsilon} F_k \boldsymbol{\xi}_k, \quad k=1,2,\dots \end{aligned} \quad (1.64)$$

where L_U designates the linearized Navier-Stokes operator around the mean flow U . System (1.64) has been reproduced from Farrell and Ioannou (2019). The nonlinear Reynolds stress divergence of the fluctuations is included in the mean flow equation (summation term). However, in the equation for \mathbf{q}_k , the nonlinear forcing (convolution) term accounting for the fluctuations-fluctuations interactions (generating wavenumber k) has been modeled by a series of uncorrelated white (in time) noise processes $F_k \boldsymbol{\xi}_k$, parameterized by an intensity ϵ . The covariance matrix of the fluctuation $C = \{\mathbf{q}_k \mathbf{q}_k^H\}$ in the statistically steady regime obeys

$$\begin{aligned} \frac{dU}{dt} &= -\sum_k \frac{k}{2} \text{diag} \left[\Im(\mathbf{q}_k \mathbf{q}_k^H) \Delta^\dagger \right] - rU, \\ \frac{dC_k}{dt} &= L_U C_k + C_k L_U^\dagger + \epsilon Q_k, \quad k=1,2,\dots \end{aligned} \quad (1.65)$$

with $Q_k = F_k F_k^H$, F_k postulated *a priori* with physical arguments. In the equation for \mathbf{q}_k , modeling the nonlinear fluctuations-fluctuations forcing term by white noise processes is a strong hypothesis, often justified by the fact that L_U is generically strongly non-normal. Thereby the stochastic response \mathbf{q}_k is dominated by a few leading modes and does not depend on the details of the excitation. The mean flow is generally stable, but the equilibrium solution(s) of the coupled system (1.65), which includes a non-normally amplified fluctuation, has no reason to be. A stable fixed point of (1.65) corresponds to a statistically steady turbulent state. As represented in figure 1.13, the number and the stability of the equilibrium solution(s) (as well as their nature, fixed point, limit cycle, etc...) may be modified by increasing the parameter ϵ . In figure 1.13, the SSST successfully predicts the turbulent flow to reach a statistically steady state with $n=4$ zonal jets. In another context, it was also efficient in describing the interaction between rolls and streaks appearing in the transition to turbulence in the three-dimensional Couette flow (Farrell & Ioannou, 2012).

The fluctuations-fluctuations nonlinear interaction terms in the equation for the fluctuations, instead of being replaced by white noise, are sometimes simply ignored. This leads to a class

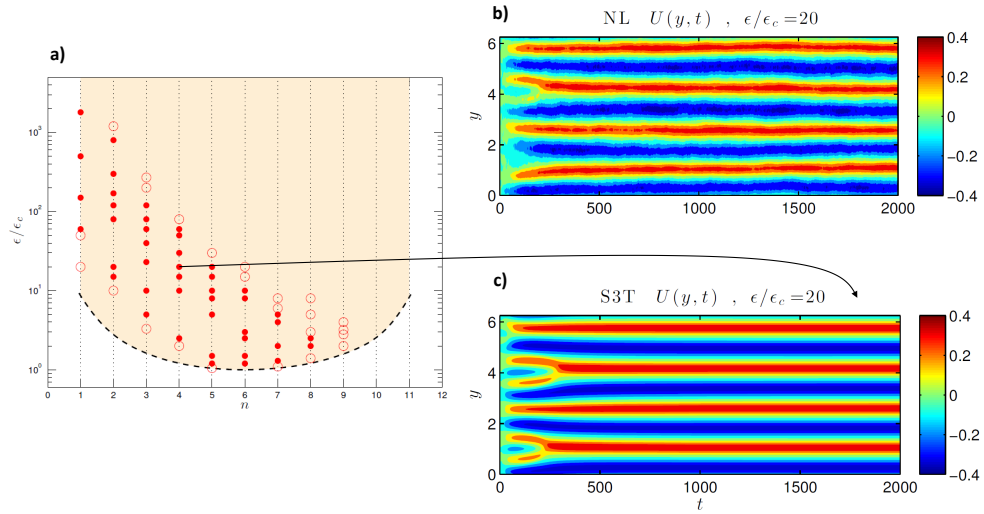


Figure 1.13: (a) Stability diagram of the system (1.65) as a function of the number of zonal jets n of and the normalized parameter ϵ/ϵ_c (ϵ_c the minimum value of ϵ on the dashed line). Below the dashed curve, the homogeneous state $U = 0$ is stable and no jets appear. Above, $U = 0$ is unstable and new statistically steady states appear as fixed points in (1.65), characterized by the number of zonal jets n . A full (resp. empty) circle corresponds to stable (resp. unstable) fixed points. For $\epsilon/\epsilon_c = 20$ and $n = 4$, the stable fixed point (finite amplitude equilibrium jets) is shown as the steady regime of the Hovmöller diagram in (c), which compares well with fully nonlinear simulations in (b). Reproduced from Farrell and Ioannou (2019).

of models called "semi-linear": nonlinear for the mean, and linear for the fluctuations. It was recently generalized in Marston et al. (2016) such as to include fluctuations-fluctuations interactions at the large scales only.

In considering the effect of nonlinearities on the response of the backward-facing step to external white noise forcing, Mantič-Lugo and Gallaire (2016a) also chose to neglect the fluctuations-fluctuations interaction terms, in the equation for the fluctuations. Specifically, the system was rewritten as (i) an equation for the (temporal) mean flow nonlinearly forced by a frequency (convolution) integral of the Reynolds stress divergence of the fluctuating part of the response, and (ii) a linear equation for the latter. Indeed the equation for the fluctuating part of the response had been linearized around the mean flow and was simply forced by the applied external forcing. Then, by discretizing the convolution integral in the frequency domain, the authors could solve the coupled system iteratively until the convergence of the fields and associated nonlinear stochastic gain. The latter was found to be in good agreement with fully nonlinear results and to significantly decrease while increasing the forcing amplitude. This was explained by the fact that the mean flow presented an increasingly reduced convectively unstable recirculation region.

As a summary, in the present section, we have reviewed the linear dynamics of a small perturbation, both under modal and non-modal aspects. In particular, we have briefly discussed

how non-modal analyses can lead to a greatly reduced yet accurate description of the flow dynamics in certain regimes. Aiming at projecting the flow dynamics, many attempts to import these linear modal and non-modal techniques in fully nonlinear regimes have been mentioned. They generally rely on a mean-fluctuation decomposition and are subject to closure problems, circumvented by either modeling or ignoring some nonlinear terms. Different closures between different models have no reasons to be equivalent, and, in fact, they are not Nivarti et al. (2022).

The following section also will be concerned with nonlinear effects. Although we will allow us a strong starting hypothesis, the procedure will enable a careful, mathematically justified, treatment of nonlinear terms.

1.2 Weakly nonlinear dynamics

Small amplitude disturbances over a linearly unstable system grow exponentially until nonlinearities can't be neglected anymore. A "weakly nonlinear" analysis unravels the leading-order nonlinear effects, sufficient to compute a finite-amplitude asymptotic solution in specific regimes. We briefly recall the procedure in the following lines, focusing on the most simple configuration. Remarkably, weakly nonlinear behaviors will be captured by solving linear problems only.

The very first assumption to be made in performing a weakly nonlinear analysis is that the external parameter should be asymptotically close to its "critical" value, where the system is linearly neutral. This assumption is primordial for the procedure to find proper closure, as will become clear in a moment. Thereby, a small quantity $\epsilon \ll 1$ is introduced to quantify some distance to criticality in the parameter space.

For the Navier-Stokes equations, the relevant external parameter is the Reynolds number Re . We denote L_c as the linearized Navier-Stokes operator for $Re = Re_c$, Re_c being the critical value at which L (assumed real) possesses a pair of (neutral) complex conjugate eigenvalues $\pm i\omega_1$. We further assume that these are the only neutral eigenvalues of L_c , all the others possessing a strictly negative growth rate.

The weakly nonlinear method imposes to consider Re numbers close to Re_c , rationalized as

$$\frac{1}{Re} = \frac{1}{Re_c} - \epsilon^2. \quad (1.66)$$

The scaling (1.66) applies to the inverse of the Reynolds numbers, as it appears in the Navier-Stokes equations. The reason for which the small parameter ϵ is raised to power two specifically will be clarified in a moment. At a Re number slightly larger than Re_c according to (1.66), the pair of neutral eigenvalues become unstable with a growth rate of $O(\epsilon^2)$. This can be quantified by relying on the sensitivity analysis of the eigenvalues $\pm i\omega_1$ to a $-\epsilon^2 \Delta$ operator perturbation of L_c . As a consequence, a pair of complex conjugate linearly unstable eigenmodes grow exponentially, until nonlinearities have an effect after a long time of $O(\epsilon^{-2})$. If the period $2\pi/\omega_1 = O(1)$, the response then possesses two time scales: a time scale of $O(1)$ over which it oscillates, and another of $O(\epsilon^2)$ over which the amplitude of the oscillations are modulated, both linearly and nonlinearly. This separation of time scales is illustrated in figure 1.14(g) for the cylinder flow at $Re = 100$ (unstable base flow shown in figure 1.14(a)), corresponding to $\epsilon^2 = 10^{-2}$. Oscillating eigenmodes grow exponentially until, at $t = O(10^2)$, nonlinearities set in.

Thereby the flow field is thought of as depending on two independent time variables. The first, τ , is referred to as the "fast" time and captures the phase variations. The second, T , is referred to as the "slow" time and aims at describing amplitude modulations. The solution will eventually depend only on t upon evaluating its two intrinsic variables τ and T over the lines $\tau = t$ and $T = \epsilon^2 t$. Under this description, the partial derivative with respect to t present

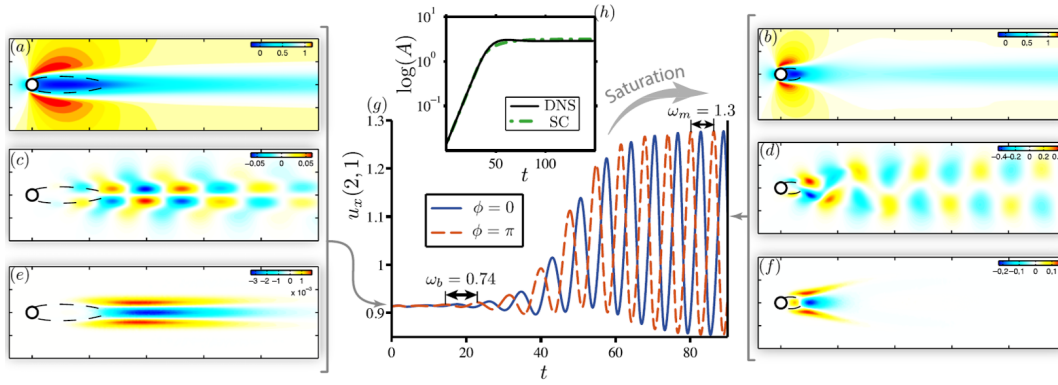


Figure 1.14: Some flow fields for the cylinder flow at $Re = 100$ (past a Hopf bifurcation at $Re_c = 47$). (a) Base flow and (b) temporal mean flow. (c) Linearly unstable mode around the base flow and (d) fluctuation instantaneous snapshot around the mean flow. Are also shown the streamwise component of the Reynolds stress divergence of (e) the unstable eigenmode and (f) the fluctuation around the mean flow. (g) Monitoring of the streamwise velocity, revealing its transient evolution from linear instability to nonlinear saturation (the flow was initiated along its unstable eigenmode with a small amplitude and two different phases). (h) Associated temporal evolution of the unstable mode amplitude (black is the fully nonlinear solution and green is the self-consistent approach). Figure reproduced from Mantić-Lugo et al. (2015).

in the original equation becomes

$$\begin{aligned} \frac{\partial \mathbf{u}_i(t)}{\partial t} &= \frac{\partial \tau}{\partial t} \frac{\partial \mathbf{u}_i(\tau, T)}{\partial \tau} \Big|_{(\tau, T)=(t, \epsilon^2 t)} + \frac{\partial T}{\partial t} \frac{\partial \mathbf{u}_i(\tau, T)}{\partial T} \Big|_{(\tau, T)=(t, \epsilon^2 t)} \\ &= \frac{\partial \mathbf{u}_i}{\partial \tau} + \epsilon^2 \frac{\partial \mathbf{u}_i}{\partial T}. \end{aligned} \quad (1.67)$$

By abuse of notation, τ is sometimes simply written t in the literature. Note that in all generalities, times scales that are even slower than T , for instance, $T_2 = \epsilon^4 t$, $T_4 = \epsilon^6 t$, etc... could be introduced, but won't be necessary in what follows.

Furthermore, the solution is sought as an asymptotic power series of ϵ , such that

$$\mathbf{u}(\tau, T) = \mathbf{U}_{b,c} + \epsilon \mathbf{u}_1(\tau, T) + \epsilon^2 \mathbf{u}_2(\tau, T) + \epsilon^3 \mathbf{u}_3(\tau, T) + O(\epsilon^4), \quad (1.68)$$

where the spatial dependence was implied, and where $\mathbf{U}_{b,c}$ is a neutral fixed point, solving the fully nonlinear steady Navier-Stokes equations at $Re = Re_c$. Expansion (1.68) will sometimes be referred to as "multiple scale asymptotic expansion". The relevance of multiple scale asymptotic expansion is well established, not only in fluid mechanics but more generally in the field of nonlinear partial differential equations (Bender & Orszag, 1978; Glendinning, 1994; Hinch, 1991).

Substituting (1.68), (1.67) and (1.66) in the Navier-Stokes equations (1.1), and factorizing terms

in powers of ϵ yields a cascade of linear problems to be solved successively. At order ϵ^0 the steady, fully nonlinear Navier-Stokes equation is recovered

$$\mathbf{0} = -(\mathbf{U}_{b,c} \cdot \nabla) \mathbf{U}_{b,c} - \nabla p + \text{Re}_c^{-1} \Delta \mathbf{U}_{b,c}. \quad (1.69)$$

which is satisfied by the construction of $\mathbf{U}_{b,c}$. At the next order ϵ , the equation corresponds to the unforced linearized Navier-Stokes equation around $\mathbf{U}_{b,c}$

$$\partial_\tau \mathbf{u}_1 = L_c \mathbf{u}_1. \quad (1.70)$$

The solution of this equation is given by (1.17), studied in more detail in the previous section. As we have seen, it is generally subject to transient growth phenomena before relaxing to its neutral mode, say $\hat{\mathbf{q}}$, associated with the eigenvalue $i\omega_1$ (i.e. $i\omega_1 \hat{\mathbf{q}} = L_c \hat{\mathbf{q}}$). Transient growth is avoided if the perturbation is initialized along $\hat{\mathbf{q}}$, corresponding to the solution

$$\mathbf{u}_1(\tau, T) = A(T) \hat{\mathbf{q}} e^{i\omega_1 \tau} + \text{c.c.}, \quad (1.71)$$

valid for all τ . The scalar $A(T)$ is a complex amplitude, for the moment undetermined. It can be included since τ and T are independent, thereby $\partial_\tau(A\mathbf{u}_1) = A\partial_\tau \mathbf{u}_1$ and A cancels out in (1.70).

At order ϵ^2 , is collected a linear but forced equation

$$\partial_\tau \mathbf{u}_2 = L_c \mathbf{u}_2 - \Delta \mathbf{U}_{b,c} - 2|A|^2 C[\hat{\mathbf{q}}, \hat{\mathbf{q}}^*] - (e^{2i\omega_1 \tau} A^2 C[\hat{\mathbf{q}}, \hat{\mathbf{q}}] + \text{c.c.}), \quad (1.72)$$

where we defined the advection operator

$$C[\hat{\mathbf{g}}, \hat{\mathbf{h}}] = \frac{1}{2} [(\hat{\mathbf{g}} \cdot \nabla) \hat{\mathbf{h}} + (\hat{\mathbf{h}} \cdot \nabla) \hat{\mathbf{g}}]. \quad (1.73)$$

Owing to the orthogonality of Fourier modes at distinct frequencies, the particular solution to (1.72) in the asymptotic limit $\tau \rightarrow \infty$ (i.e. in the steady regime after the transients have faded away) reads

$$\mathbf{u}_2(\tau, T) = \mathbf{u}_{2,0} + |A(T)|^2 \mathbf{u}_2^{|A|^2} + (e^{2i\omega_1 \tau} A(T)^2 \hat{\mathbf{u}}_2^{A^2} + \text{c.c.}), \quad (1.74)$$

with

$$L_c \mathbf{u}_{2,0} = -\Delta \mathbf{U}_{b,c}, \quad L_c \mathbf{u}_2^{|A|^2} = -2C[\hat{\mathbf{q}}, \hat{\mathbf{q}}^*], \quad \text{and} \quad (2i\omega_1 I - L_c) \hat{\mathbf{u}}_2^{A^2} = -C[\hat{\mathbf{q}}, \hat{\mathbf{q}}]. \quad (1.75)$$

By assumption, L_c does not possess an eigenvalue at either 0 or $2i\omega_1$, thereby linear problems in (1.75) can directly be solved for. The fields thus generated are associated with the following physical interpretations, respectively

- In evaluating the expansion (1.68), the non-oscillating part reads $\mathbf{U}_{b,c} + \epsilon^2 \mathbf{u}_{2,0} + \epsilon^2 |A|^2 \mathbf{u}_2^{|A|^2}$. Consequently, the field $\mathbf{u}_{2,0}$ corrects the base flow $\mathbf{U}_{b,c}$ with an amplitude ϵ^2 . It accounts

for the fact that we consider a Re number slightly above its critical value Re_c at which $\mathbf{U}_{b,c}$ was computed.

- The field $\mathbf{u}_2^{|A|^2}$ also is a correction to the base flow, with an amplitude $\epsilon^2|A|^2$. It accommodates the fact that the mode $\hat{\mathbf{q}}$, of amplitude ϵA and frequency ω_1 , nonlinearly interacts with its complex conjugate to bring about a non-oscillating term ($i\omega_1 - i\omega_1 = 0$). In this sense, $\epsilon^2|A|^2\mathbf{u}_2^{|A|^2}$ represents the difference between the base flow at a given Re (approximated by $\mathbf{U}_{b,c} + \epsilon^2\mathbf{u}_{2,0}$) and the time-averaged mean flow.

In (1.75), the forcing term $2C[\hat{\mathbf{q}}, \hat{\mathbf{q}}^*]$ at the origin of $\mathbf{u}_2^{|A|^2}$ is called the "Reynolds stress divergence".

- The field $\hat{\mathbf{u}}_2^{A^2}$ is a component of the overall solution with amplitude $\epsilon^2 A^2$, that oscillates at the first harmonic frequency $2\omega_1$. It results from the nonlinear interaction of the mode with itself.

At this second-order, the homogeneous solution along \mathbf{q} with an arbitrary amplitude (say A_2) can be left apart without loss of generality (Fujimura, 1991). This way, A alone carries the component of the flow field on $\hat{\mathbf{q}}$, without needing to redefine the latter as $A + \epsilon A_2 + O(\epsilon^2)$.

Pursuing the computation up to order ϵ^3 leads to solving the linear problem

$$\partial_\tau \mathbf{u}_3 = L_c \mathbf{u}_3 + (e^{3i\omega_1\tau} \hat{\mathbf{f}}_{3,nr} + e^{i\omega_1\tau} \hat{\mathbf{f}}_{3,r} + \text{c.c.}), \quad (1.76)$$

or, equivalently,

$$\begin{aligned} \partial_\tau \mathbf{u}_{3,nr} &= L_c \mathbf{u}_{3,nr} + (e^{3i\omega_1\tau} \hat{\mathbf{f}}_{3,nr} + \text{c.c.}), \\ \partial_\tau \mathbf{u}_{3,r} &= L_c \mathbf{u}_{3,r} + (e^{i\omega_1\tau} \hat{\mathbf{f}}_{3,r} + \text{c.c.}), \quad \text{with } \mathbf{u}_3 = \mathbf{u}_{3,r} + \mathbf{u}_{3,nr}. \end{aligned} \quad (1.77)$$

The operator L_c has no eigenvalue in $3i\omega_1$, thereby the first problem in (1.77) is non-resonant (hence the subscript "nr"). Its solution in the asymptotic limit $\tau \rightarrow \infty$, is found upon inverting

$$(3i\omega_1 I - L_c) \hat{\mathbf{u}}_{3,nr} = \hat{\mathbf{f}}_{3,nr} = -2A^3 C[\hat{\mathbf{q}}, \hat{\mathbf{u}}_2^{A^2}], \quad \text{and } \mathbf{u}_{3,nr} = e^{3i\omega_1\tau} \hat{\mathbf{u}}_{3,nr} + \text{c.c.}, \quad (1.78)$$

yields the third harmonic component of the flow field.

However, the second problem in (1.77) leads to a resonance as described in section 1.1.2, as the system is forced at its neutral eigenfrequency. We have shown in (1.33) that the solution of such a linear, resonant system contains a term $\propto \tau$ which diverges in the limit $\tau \rightarrow \infty$, of interest here. That is true except if its proportionality factor is identically null, which, according to (1.33), amounts to imposing

$$\begin{aligned} \langle \hat{\mathbf{q}}^\dagger | \hat{\mathbf{f}}_{3,r} \rangle &= 0, \\ \text{where } \hat{\mathbf{f}}_{3,r} &= -A\Delta\hat{\mathbf{q}} - 2AC[\hat{\mathbf{q}}, \mathbf{u}_{2,0}] - 2A|A|^2 \left(C[\hat{\mathbf{q}}, \mathbf{u}_2^{|A|^2}] + C[\hat{\mathbf{q}}^*, \hat{\mathbf{u}}_2^{A^2}] \right) - \hat{\mathbf{q}} \partial_T A. \end{aligned} \quad (1.79)$$

In other terms, the forcing structure $\hat{\mathbf{f}}_{3,r}$ must be orthogonal to the kernel of the adjoint operator $(-i\omega_1 I - L_c^\dagger)$, which also is the adjoint neutral eigenmode $\hat{\mathbf{q}}^\dagger$. This orthogonality condition must be imposed under the inner product (1.7), employed for computing the adjoint operator.

Note that, had the direct and adjoint eigenmodes been calculated by including a mass matrix in the eigenvalue problems, the condition (1.79) would still hold without including this mass matrix in the inner product.

The "non-resonance", "solvability", or "compatibility" condition (1.79), also sometimes called "Fredholm alternative", leads to an ordinary differential equation for A

$$\frac{dA}{dT} = \lambda A - (\mu_0 + \mu_2)A|A|^2, \quad (1.80)$$

where we have defined

$$\lambda = -\frac{\langle \hat{\mathbf{q}}^\dagger | 2C[\hat{\mathbf{q}}, \mathbf{u}_{2,0}] + \Delta \hat{\mathbf{q}} \rangle}{\langle \hat{\mathbf{q}}^\dagger | \hat{\mathbf{q}} \rangle}, \quad \mu_0 = \frac{\langle \hat{\mathbf{q}}^\dagger | 2C[\hat{\mathbf{q}}, \mathbf{u}_2^{|A|^2}] \rangle}{\langle \hat{\mathbf{q}}^\dagger | \hat{\mathbf{q}} \rangle}, \quad \text{and} \quad \mu_2 = \frac{\langle \hat{\mathbf{q}}^\dagger | C[\hat{\mathbf{q}}^*, \hat{\mathbf{u}}_2^{A^2}] \rangle}{\langle \hat{\mathbf{q}}^\dagger | \hat{\mathbf{q}} \rangle}. \quad (1.81)$$

The amplitude equation (1.80) corresponds to the celebrated Stuart-Landau equation (Stuart, 1960). It can be re-expressed in terms of t by evaluating $T = \epsilon^2 t$

$$\frac{dA(\epsilon^2 t)}{dt} = \epsilon^2 \frac{dA(T)}{dT} \Big|_{T=\epsilon^2 t} = \epsilon^2 \lambda A - \epsilon^2 (\mu_0 + \mu_2) A |A|^2, \quad (1.82)$$

which eventually gives for the rescaled amplitude $a(\epsilon^2 t) = \epsilon A(\epsilon^2 t) e^{i\omega_1 t}$

$$\frac{da}{dt} = (i\omega_1 + \epsilon^2 \lambda) a - (\mu_0 + \mu_2) a |a|^2. \quad (1.83)$$

The asymptotic expansion (1.67) for the flow field becomes

$$\mathbf{u} = \mathbf{U}_{b,c} + (a\hat{\mathbf{q}} + \text{c.c.}) + \epsilon^2 \mathbf{u}_{2,0} + |a|^2 \mathbf{u}_2^{|A|^2} + (a^2 \hat{\mathbf{u}}_2^{A^2} + \text{c.c.}) + O(\epsilon^3) \quad (1.84)$$

with $a = O(\epsilon)$, and where we have neglected some transient, decaying terms appearing at $O(\epsilon^2)$ and $O(\epsilon^3)$.

The physical interpretation of λ and μ_0 in (1.81) is unraveled by noticing that an infinitesimal displacement $\delta\sigma_j$ of an eigenvalue σ_j , induced by an infinitesimal perturbation δL of the

operator L writes

$$\begin{aligned}
& \delta(L\hat{\mathbf{q}}_j) = \delta(\sigma_j \hat{\mathbf{q}}_j) \\
& \Rightarrow (\delta L)\hat{\mathbf{q}}_j + L\delta\hat{\mathbf{q}}_j = \delta(\sigma_j)\hat{\mathbf{q}}_j + \sigma_j\delta\hat{\mathbf{q}}_j \\
& \Rightarrow \langle \hat{\mathbf{q}}_j^\dagger | (\delta L)\hat{\mathbf{q}}_j \rangle + \langle \hat{\mathbf{q}}_j^\dagger | L\delta\hat{\mathbf{q}}_j \rangle = \delta(\sigma_j) \langle \hat{\mathbf{q}}_j^\dagger | \hat{\mathbf{q}}_j \rangle + \sigma_j \langle \hat{\mathbf{q}}_j^\dagger | \delta\hat{\mathbf{q}}_j \rangle \\
& \Rightarrow \langle \hat{\mathbf{q}}_j^\dagger | (\delta L)\hat{\mathbf{q}}_j \rangle + \langle \sigma_j^* \hat{\mathbf{q}}_j^\dagger | \delta\hat{\mathbf{q}}_j \rangle = \delta(\sigma_j) \langle \hat{\mathbf{q}}_j^\dagger | \hat{\mathbf{q}}_j \rangle + \sigma_j \langle \hat{\mathbf{q}}_j^\dagger | \delta\hat{\mathbf{q}}_j \rangle \\
& \Rightarrow \delta(\sigma_j) = \frac{\langle \hat{\mathbf{q}}_j^\dagger | (\delta L)\hat{\mathbf{q}}_j \rangle}{\langle \hat{\mathbf{q}}_j^\dagger | \hat{\mathbf{q}}_j \rangle}.
\end{aligned} \tag{1.85}$$

Furthermore, a perturbation δL of the linearized Navier-Stokes operator induced solely by a perturbation $\delta \mathbf{U}_b$ in the base flow can be written using (1.5) as

$$(\delta L)\bullet = -2C[\delta \mathbf{U}_b, \bullet]. \tag{1.86}$$

It is associated with an eigenvalue perturbation

$$\delta(\sigma_j) = -\frac{\langle \hat{\mathbf{q}}_j^\dagger | 2C[\delta \mathbf{U}_b, \hat{\mathbf{q}}_j] \rangle}{\langle \hat{\mathbf{q}}_j^\dagger | \hat{\mathbf{q}}_j \rangle}. \tag{1.87}$$

The comparison between (1.87) and the expressions for λ and μ_0 in (1.81) directly suggest the following interpretations.

- The coefficient λ is the displacement (or "sensitivity") of the neutral eigenvalue $i\omega_1$ induced by the modification $\mathbf{u}_{2,0}$ to the base flow. Furthermore, the term in $\Delta\hat{\mathbf{q}}$ takes into account the effect of increasing the Re number on the mode $\hat{\mathbf{q}}$ itself. In other terms, the eigenvalue $i\omega_1$ of the linearized operator at Re_c , drifts to $i\omega_1 + \epsilon^2\lambda$ (at leading-order) by considering a Re number slightly above Re_c according to (1.66). For this reason, the real part of λ is expected to be positive, and the linear term in (1.83) to describe a linear instability.
- The coefficient μ_0 is the displacement of the neutral eigenvalue $i\omega_1$ that results from the nonlinearly-induced mean-flow correction $\mathbf{u}_2^{|A|^2}$ to the base flow. Note that μ_0 enters with a negative sign in (1.83). Thereby if it has a positive real part, the mean flow correction, with an amplitude $|a|^2$, has a stabilizing effect on the mode which counterbalances the linear instability when a has become sufficiently large.
- The coefficient μ_2 has no eigenvalue sensitivity translation, for it involves $\hat{\mathbf{q}}^*$ instead of $\hat{\mathbf{q}}$. It quantifies how the second harmonic field $\hat{\mathbf{u}}_2^{A^2}$ nonlinearly interacts with the complex conjugate of the mode $\hat{\mathbf{q}}^*$, which feeds back on the mode and brings about a modification of its eigenvalue. It enters in (1.83) the same way as μ_0 does, thus in effect it is their sum $\mu = \mu_0 + \mu_2$ that determines the weakly nonlinear behavior.

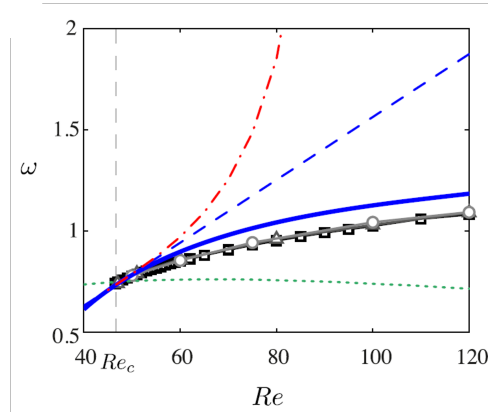


Figure 1.15: Oscillation frequency of the flow past a cylinder (same as in figure 1.14) as a function of the Re number. The continuous blue line is the weakly nonlinear frequency $\bar{\omega}$ given in (1.88), triangle markers are experimental data, circle markers are data from fully nonlinear simulations, and square markers results from self-consistent computations (Mantič-Lugo et al., 2014). Figure reproduced from Gallaire et al. (2016).

If μ_r the real part of μ is positive, equation (1.83) predicts nonlinearities to saturate the instability towards a limit cycle with equilibrium amplitude \bar{r} and frequency $\bar{\omega}$ given by

$$\bar{r} = \epsilon \sqrt{\frac{\lambda_r}{\mu_r}} \propto \sqrt{\frac{1}{Re_c} - \frac{1}{Re}}, \quad \text{and} \quad \bar{\omega} = \omega_1 + \epsilon^2 \lambda_i - \epsilon^2 \mu_i \frac{\lambda_r}{\mu_r}. \quad (1.88)$$

In addition to the linear drift $\epsilon^2 \lambda_i$ due to the change in Re number, the frequency ω_1 is nonlinearly corrected by $\epsilon^2 \mu_i \lambda_r / \mu_r$. For the flow past a cylinder, the comparison between the weakly nonlinear frequency predicted in (1.88), and the one extracted from fully nonlinear computations is shown in figure 1.15. The frequency predicted by a linear stability analysis over the base flow (captured at leading order by $\omega_1 + \epsilon^2 \lambda_i$) is also included. The latter fails to predict the limit cycle frequency both quantitatively and qualitatively, but the weakly nonlinear approximation brings a substantial amelioration.

It was shown in Sipp and Lebedev (2007) that, for this specific flow, $|\mu_0| \gg |\mu_2|$ such that weakly nonlinear saturating effects predominantly stem from the mean-flow correction $\mu_2^{|A|^2}$. That is why the self-consistent model introduced in Mantič-Lugo et al. (2014), and relying on the assumption that harmonics have no effects, is so effective in predicting the nonlinear frequency in figure 1.15. The saturating effect of the mean flow correction is physically understood by comparing figure 1.14(a) and figure 1.14(b). It appears to substantially reduce the extent of the (absolutely unstable) shear layer behind the cylinder, thereby tending to stabilize the flow.

In this sense, computing and comparing the weakly nonlinear coefficient μ_0 with μ_2 is a manner to assess *a priori* if the self-consistent method in its original form (Mantič-Lugo et al., 2014) is appropriate, or if it needs to be extended (Bengana & Tuckerman, 2021; Meliga, 2017).

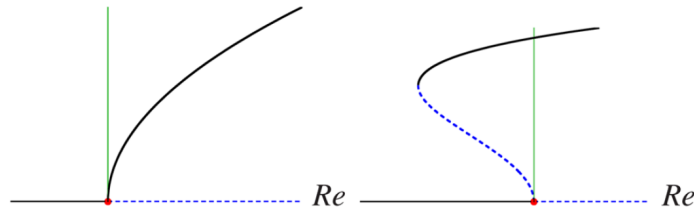


Figure 1.16: Sketch of a supercritical (left) and subcritical (right) bifurcation as a function of some external parameter (Re here). Dashed lines for unstable equilibrium solutions and full lines for stable ones. The vertical line denotes Re_{Re_c} . Figure reproduced from Schmid and Brandt (2014a).

For the flow past cavity Sipp and Lebedev (2007) demonstrate that $|\mu_0| \sim |\mu_2|$. For this reason, the self-consistent method needs to be extended by including the effect of second harmonic, to properly predict the nonlinear saturation (Meliga, 2017).

The equilibrium solution (1.88) characterizes a "supercritical Hopf" bifurcation. The name "Hopf" designates the fact that it is a pair of complex conjugate eigenvalues that become unstable, and not for instance a single real one. The adjective "supercritical" results from the fact that $\mu_r > 0$, therefore leading-order nonlinearities have a saturating effect and are sufficient to predict a nonlinear limit cycle (see the left frame in figure 1.16). If $\mu_r < 0$, the Hopf bifurcation is qualified as "subcritical", and the weakly nonlinear procedure needs to be pursued to $O(\epsilon^5)$ (at least). This would yield a term in $a|a|^4$ in the amplitude equation, from which a stable equilibrium solution could be predicted. The latter, if existing, can be shown to persist for Re inferior to Re_c , implying the possibility for the flow to transit towards another attractor before it becomes linearly unstable (see the right frame in figure 1.16). We thereby make the distinction between a transition and a bifurcation.

A word on the scaling in ϵ^2 appearing in (1.66). It is possible to replace, for instance, ϵ^2 by ϵ in (1.66). To be consistent, this requires introducing an intermediate slow time in ϵt . This results in the field $\mathbf{u}_{2,0}$ appearing as a particular solution at first-order. At second-order, it interacts with $\hat{\mathbf{q}}$ such as to create a resonant forcing term $\propto A$ oscillating at $i\omega_1$, and the Fredholm alternative needs to be imposed already. The computations then need to be pursued at third-order to capture the cubic nonlinearity in the Stuart-Landau equation. The final amplitude equation has the same form as (1.83), with a term in A and a term in $A|A|^2$, but both the computations and the ensuing expressions for the coefficients are significantly heavier. This is a consequence of Re being *a priori* permitted to make a larger excursion above Re_c . In this sense, the scaling in (1.66) is motivated as being the one leading the simplest possible expression for the coefficients, for the same minimal-order form of the amplitude equation (which in the case of a Hopf bifurcation is a term in A and a term in $A|A|^2$).

As reviewed in Fauve (1998) the reduction of the Navier-Stokes equations to an amplitude equation, by using weakly nonlinear expansions in the vicinity of a bifurcation point, has been early performed for a variety of parallel flows (Chiffaudel & Fauve, 1987; Chossat & Iooss, 1994;

Crawford et al., 1988; Cross, 1986; Golubitsky & Stewart, 1985). The first works of this kind date back to Gor'kov (1957) and Malkus and Veronis (1958) for thermal convection problems and to Stuart (1958, 1960) and Watson (1960) for parallel shear flows. The amplitude equation could systematically discriminate between the supercritical and subcritical nature of the considered bifurcation. It was for instance shown in Chossat and Iooss (1994) that the Taylor-Couette instability is supercritical, whereas the instability occurring in the plane Poiseuille flow at $Re_c = 5772$ is subcritical.

Accounting for non-parallelism in the base flow, by considering a second or even a third dimension, increases the size of the discretized operators and thus requires larger computational power. As a consequence, constructing amplitude equations non-parallel base flows was only performed recently. Among the first to do so were Sipp and Lebedev (2007), Meliga et al. (2009). Weakly nonlinear expansions still are the object of current research and were recently found to capture well the double crest swirling motion in a circular sloshing flow Bongarzone et al. (2022), extended to elliptic-type container excitation in Marcotte et al. (2023). As another example, Buza et al. (2022) recently derived an amplitude equation for the center-mode bifurcation of rectilinear viscoelastic shear flow, showing the nature of the bifurcation to depend on the Reynolds and Weissenberg numbers.

There exist some other techniques than the multiple scales weakly nonlinear expansion to derive amplitude equations. Among them, is the "center manifold theory", outlined for instance in Guckenheimer and Holmes (1983) or Haragus and Iooss (2011). The center manifold is a nonlinear invariant manifold in the phase space (W^c in figure 1.17) that, at the equilibrium point, is tangent to the neutral (linear) eigenspace (E^c in figure 1.17). We consider in what follows that the unstable manifold (E^u in figure 1.17) is empty (i.e., the linearized operator has no eigenvalues with strictly positive growth rates). The center manifold is characterized by the graph of a smooth function, say \mathbf{h} , that takes as arguments the coordinates along the neutral eigenspace E^c , say \mathbf{x} , and maps it into the phase space that includes coordinates along the stable eigenspace E^s , say \mathbf{y} . In mathematical terms

$$W^c = \{(\mathbf{x}, \mathbf{y}) \in \mathbb{R}^N : \mathbf{y} = \mathbf{h}(\mathbf{x}), \quad \mathbf{0} = \mathbf{h}(\mathbf{0}), \quad D_{\mathbf{x}}\mathbf{h}|_{\mathbf{x}=\mathbf{0}} = \mathbf{0}\}, \quad (1.89)$$

where N is the dimension of the system, $D_{\mathbf{x}}$ the Jacobian matrix and $(\mathbf{x}, \mathbf{y}) = (\mathbf{0}, \mathbf{0})$ is an equilibrium. In other terms, all along the center manifold W^c , the coordinates along the stable eigenmodes are enslaved into the coordinates along the neutral eigenmodes.

A generic nonlinear dynamical system, diagonalized such that \mathbf{x} and \mathbf{y} naturally appear as state variables, can be decomposed as

$$\begin{aligned} \frac{d\mathbf{x}}{dt} &= L^c \mathbf{x} + N^c(\mathbf{x}, \mathbf{y}), \\ \frac{d\mathbf{y}}{dt} &= L^s \mathbf{y} + N^s(\mathbf{x}, \mathbf{y}), \end{aligned} \quad (1.90)$$

where L^c and L^s designate the projection of the diagonalized version of the linearized operator

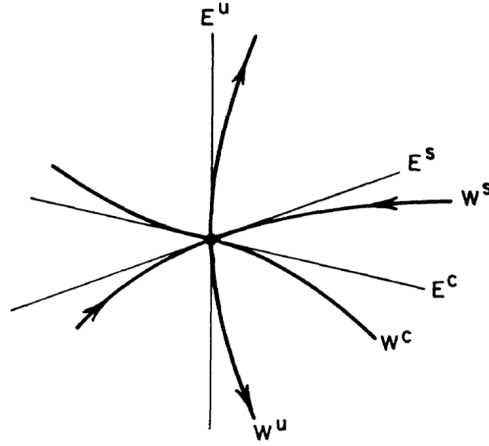


Figure 1.17: In the phase space are highlighted the stable, unstable, and center eigenspaces (E^s , E^u , and E^c , respectively) as well as the stable, unstable, and center manifolds (W^s , W^u , and W^c , respectively). Figure reproduced from Guckenheimer and Holmes (1983).

L onto the neutral and stable eigenspaces, respectively. The symbols N^c and N^s designate generic nonlinear terms, projected in the same way. By definition, W^c must be an invariant of the system thus the function \mathbf{h} must solve the governing equations (1.90). Consequently, it is determined by injecting $\mathbf{y} = \mathbf{h}(\mathbf{x})$ into the second equation (1.90), leading to an equation for \mathbf{h}

$$D_{\mathbf{x}}\mathbf{h}(\mathbf{x})\frac{d\mathbf{x}}{dt} = L^s\mathbf{h}(\mathbf{x}) + N^s(\mathbf{x}, \mathbf{h}(\mathbf{x})), \quad (1.91)$$

subject to the boundary conditions specified in (1.89). The ensuing dynamics along the manifold W^c is found by evaluating the first equation in $\mathbf{y} = \mathbf{h}(\mathbf{x})$, leading to

$$\frac{d\mathbf{x}}{dt} = L^c\mathbf{x} + N^c(\mathbf{x}, \mathbf{h}(\mathbf{x})). \quad (1.92)$$

Such dynamics are particularly relevant to the system, for the center manifold, if not necessarily unique, can be shown to be locally attracting.

Unfortunately, equation (1.91) for \mathbf{h} generally is as difficult to solve as the original one. Therefore its solution is typically sought as being polynomial in \mathbf{x}

$$\mathbf{h}(\mathbf{x}) = \sum_j A_j^{(1)} x_j + \sum_j \sum_k A_{jk}^{(2)} x_j x_k + \sum_j \sum_k \sum_l A_{jkl}^{(3)} x_j x_k x_l + \dots \quad (1.93)$$

where $A^{(n)}$ is a tensor of order n that contains polynomial coefficients (unknown and to be solved for). Expansion (1.93) typically is truncated at the minimal, relevant order, and the polynomial coefficients are determined by identification between the left-hand and the right-hand sides in (1.91). The amplitude equation is then found by evaluating (1.92) along this truncated polynomial approximation of \mathbf{h} . Indeed the coordinates \mathbf{x} , amplitudes along the neutral eigenspace, play the role of a and a^* according to our previous terminology for the

Hopf bifurcation (1.83).

As previously mentioned, the center manifold need not be unique. This motivated recent developments from Haller and Ponsioen (2016) and Li et al. (2022) on the computation of a "spectral submanifold" (sometimes abbreviated in "SSM"), which is the unique, smoothest possible of all the center manifolds. This was applied for instance in the context of solid mechanics in Jain et al. (2018) for reducing the dynamics of a Von-Karman beam. In fluids mechanics, the SSM theory was at the basis of the numerical tools deployed in Kaszas et al. (2022) for transitions among exact coherent states in the plane Couette flow.

The question of the equivalence between the center manifold and the weakly nonlinear methods, for the reduction of the Navier-Stokes equation, arises. In Knobloch and Guckenheimer (1983), concerned with the convection in a horizontal layer rotating about a vertical axis, the amplitude equations derived by using both methods were found to be identical to each other. In addition, the paper of Fujimura (1991) has demonstrated in a more general context the equivalence of both methods under the appropriate definition of the disturbance amplitude. In the case of the Hopf bifurcation, $\mathbf{x} = (a, a^*)$ and the polynomial expansion (1.93) for \mathbf{h} is expected to be equivalent to that in (1.84) (for $\mathbf{u} - \mathbf{U}_{b,c}$). Indeed, the weakly nonlinear expansion (1.84), like \mathbf{h} , takes solely the coordinates along the neutral mode as arguments, and the resulting field $\mathbf{u} - \mathbf{U}_{b,c}$ projects over all the stable modes through the higher-order fields. Thereby, the expansion (1.84) also computes the leading-order nonlinear curvature of E^c in the phase space, since higher-order fields are generically not along the neutral eigenmodes.

Note that the "normal form theory" (Guckenheimer & Holmes, 1983; Haragus & Iooss, 2011) is another technique to reduce a nonlinear dynamical system, of generic form

$$\frac{d\mathbf{x}}{dt} = N(\mathbf{x}), \quad (1.94)$$

to an amplitude equation. Without loss of generality, we assume $\mathbf{x} = \mathbf{0}$ to be a fixed point of (1.94), around which the system is expanded as

$$\frac{d\mathbf{x}}{dt} = L\mathbf{x} + \sum_i \sum_j \sum_k M_{ijk}^{(3)} x_j x_k \mathbf{e}_i + O(\|\mathbf{x}\|^3) \quad (1.95)$$

where L is assumed to be diagonal, again without loss of generality upon a change of variable. The symbol $M^{(n)}$ designates a tensor of order n that contains polynomial coefficients, and \mathbf{e}_i is a unit vector in the direction x_i (i.e. the eigenmode associated with the i th eigenvalue of the diagonal operator L). The idea behind the normal form theory is to perform a sequence of changes in variables such that, in the new variables after a change, the polynomial of smallest degree in (1.95) has one degree more. This way, by proceeding with the sequence of change in variables, nonlinear terms are found at higher and higher orders, i.e. are more and more negligible in the vicinity of the equilibrium point. As a simple example, let us consider the

following change of coordinates

$$\mathbf{y} = \mathbf{x} + \sum_i \sum_j \sum_k A_{ijk}^{(3)} x_j x_k \mathbf{e}_i, \quad \text{i.e.} \quad y_i = x_i + \sum_j \sum_k A_{ijk}^{(3)} x_j x_k \quad (1.96)$$

where $A^{(n)}$ is a tensor of order n that contains polynomial coefficients, unknown for the moment. Then the main point of the normal form theory is that these coefficients in $A^{(n)}$ can be chosen in such a way that, under the change of variable (1.96), the expansion (1.95) writes more simply

$$\frac{d\mathbf{y}}{dt} = L\mathbf{y} + O(\|\mathbf{y}\|^3). \quad (1.97)$$

This is convenient since, as compared with (1.95), nonlinear effects have been mitigated in (1.97) as long as $\|\mathbf{x}\| \ll 1$. Proper coefficients in $A_{ijk}^{(3)}$ can be found upon inverting the coordinate transform in (1.96) according to

$$\mathbf{x} = \mathbf{y} - \sum_i \sum_j \sum_k A_{ijk}^{(3)} y_j y_k \mathbf{e}_i + O(\|\mathbf{y}\|^3), \quad \text{i.e.} \quad x_i = y_i - \sum_j \sum_k A_{ijk}^{(3)} y_j y_k + O(\|\mathbf{y}\|^3) \quad (1.98)$$

Further injecting (1.98) in (1.95) leads to

$$\frac{dx_i}{dt} = \sigma_i y_i - \sigma_i \sum_j \sum_k A_{ijk}^{(3)} y_j y_k + \sum_j \sum_k M_{ijk}^{(3)} y_j y_k + O(\|\mathbf{y}\|^3) \quad (1.99)$$

with σ_i the i th eigenvalue of L . On the other hand, taking the temporal derivative of (1.96) leads to

$$\begin{aligned} \frac{dy_i}{dt} &= \frac{dx_i}{dt} + \sum_j \sum_k A_{ijk}^{(3)} \frac{dx_j}{dt} x_k + \sum_j \sum_k A_{ijk}^{(3)} x_j \frac{dx_k}{dt} \\ &= \frac{dx_i}{dt} + \sum_j \sum_k A_{ijk}^{(3)} x_j x_k (\sigma_j + \sigma_k) + O(\|\mathbf{x}\|^3) \\ &= \frac{dx_i}{dt} + \sum_j \sum_k A_{ijk}^{(3)} y_j y_k (\sigma_j + \sigma_k) + O(\|\mathbf{y}\|^3). \end{aligned} \quad (1.100)$$

By identifying (1.99) with (1.100), we obtain eventually

$$\begin{aligned} \frac{dy_i}{dt} - \sum_j \sum_k A_{ijk}^{(3)} y_j y_k (\sigma_j + \sigma_k) &= \sigma_i y_i - \sigma_i \sum_j \sum_k A_{ijk}^{(3)} y_j y_k + \sum_j \sum_k M_{ijk}^{(3)} y_j y_k + O(\|\mathbf{y}\|^3) \\ \frac{dy_i}{dt} &= \sigma_i y_i + \sum_j \sum_k \left(M_{ijk}^{(3)} - (\sigma_i - (\sigma_j + \sigma_k)) A_{ijk}^{(3)} \right) y_j y_k + O(\|\mathbf{y}\|^3). \end{aligned} \quad (1.101)$$

Therefore, if for the considered i the condition $\sigma_i \neq \sigma_j + \sigma_k$ holds for all j, k , then it is possible to eliminate the quadratic nonlinear terms in the equation for y_i simply by setting

$$A_{ijk}^{(3)} = \frac{M_{ijk}^{(3)}}{\sigma_i - (\sigma_j + \sigma_k)}. \quad (1.102)$$

However, if the system is neutral and, for instance, one of the eigenvalues is null, this condition cannot be verified. For instance if $\sigma_1 = 0$, then it is clearly not possible to satisfy the condition $\sigma_i \neq \sigma_j + \sigma_k$ for all j, k , since we can always choose $j = 1$ and $k = i$. This means that for each i , the quadratic nonlinear term cannot be removed by a polynomial change of coordinates.

Overall, the normal form theory develops a systematic procedure to identify which terms can and cannot be removed by successive polynomial changes of coordinates. The polynomial terms that can't be removed constitute the "normal form" of the system and extract the quintessence of the nonlinear behavior of the original equation in the vicinity of a bifurcation point. For this reason, amplitude equations, as derived by multiple scale expansions or center manifold theory, are considered as being normal forms in this thesis. Nevertheless, whether or not there exists strict mathematical equivalence between these two theories, and the normal form theory present above, remains unclear to the authors.

1.3 In this thesis: deriving weakly nonlinear amplitude equations for non-normal responses

All the reduction techniques mentioned in the previous section rely on the existence of a (non-empty) center eigenspace, and the ensuing amplitude equations describe bifurcations. However, as we have developed and illustrated in particular in figure 1.10a, there exist some systems that exhibit very rich dynamics even though they are significantly stable and without an outstanding eigenvalue. For this, they must be (i) non-normal and (ii) excited. The backward-facing step, for example, has an ample response to harmonic forcing around $\omega = 0.47$ whereas the spectrum only shows significantly stable, densely packed eigenvalues (except around $\omega = 0$ but these modes are irrelevant here). Consequently, center manifold or weakly nonlinear expansion methods cannot be applied to describing the harmonic response around $\omega = 0.47$, because there are no neutral or close to neutral eigenmodes around this frequency. More fundamentally, we have shown the harmonic response to result from an interaction between a large number of eigenmodes, such that reducing the dynamic to one or even a few of them is the wrong paradigm. Fortunately, by focusing the analysis on the computation of singular modes instead of eigenmodes, we have also shown in figure 1.10b that the dynamics could be reduced to a single one of these singular modes.

These facts motivated the present thesis aiming at computing amplitude equations (normal forms), not for amplitudes premultiplied by eigenmodes, but for non-normal optimal responses (hence its title).

For this purpose, an important property of non-normal operators is that their eigenvalues are not robust. That is to say, a perturbation of size ϵ of the operator L can lead to the displacement of an eigenvalue over a distance $\gg \epsilon$. This property, although it appeared implicitly in the previous section, was never mentioned so far. This is illustrated in figure 1.18, considering the

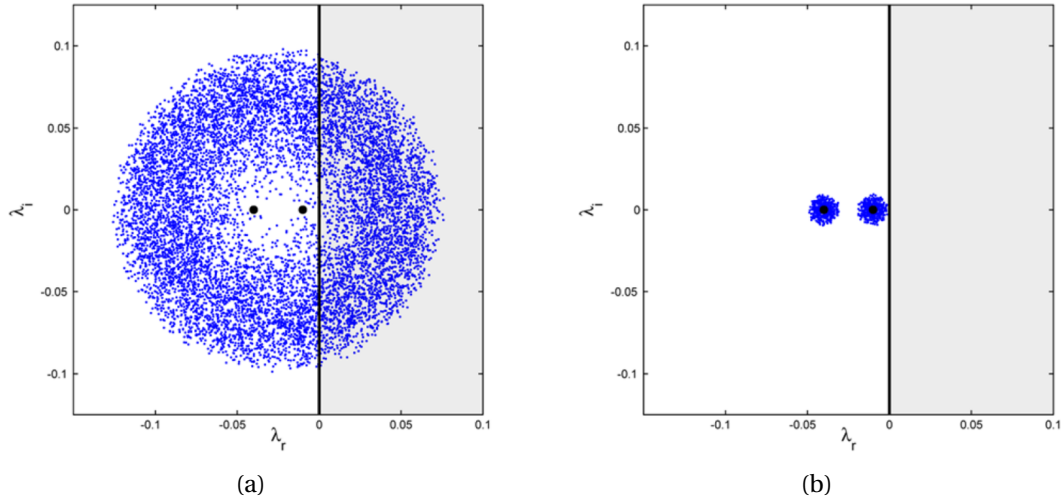


Figure 1.18: Spectrum of A for (a) $\mu = 1$, making A non-normal and (b) $\mu = 0$, making A normal. In both cases, the eigenvalues of A (black dots) are the same and equal to -0.04 and -0.01 . The blue dots are the eigenvalues of $A + \Delta A$ for one hundred, randomly generated matrices ΔA , each of norm $\|\Delta A\| = 10^{-2}$. In the gray zone, eigenvalues are unstable. Figure reproduced from Schmid and Brandt (2014a).

spectrum of the matrix

$$A = \begin{bmatrix} -0.01 & 0 \\ \mu & -0.04 \end{bmatrix}, \quad (1.103)$$

perturbed by one hundred random matrices ΔA , each being of norm $\|\Delta A\| = 10^{-2}$. The eigenvalues of A are independent from μ . However, the matrix is non-normal if $\mu \neq 0$, and normal otherwise. This has the effect that, for $\mu = 1$ in figure 1.18a, the eigenvalues of the perturbed operator $A + \Delta A$ can be located at significantly different positions than the eigenvalues of A . Specifically, by perturbing A , its eigenvalues can be dislodged over a distance that appears to be superior to 10^{-2} . That is why perturbed eigenvalues can be found to be significantly unstable, whereas the least stable eigenvalue of A is at -0.01 .

The fact that eigenvalues of a non-normal operator are substantially dislodged by perturbing the latter, is partially understood by the sensitivity formula in (1.85). As we have mentioned, for non-normal operators, $\hat{\mathbf{q}}_j^\dagger$ and $\hat{\mathbf{q}}_j$ are not identical and can effectively be very different (cf figure 1.1). This renders the denominator in (1.85) potentially very small, thus the displacement of the associated eigenvalue large. Note that this property is generally undesired for numerical purposes, for it implies that eigenvalues are difficult to make converge with the numerical discretization. This phenomenon does not occur if A is normal for $\mu = 0$ in figure 1.18b, and the perturbed eigenvalues remain closely around the original ones.

Quantifying how far the eigenvalues of an operator drift by perturbing it with some other operator of norm ϵ , amounts to computing the ϵ -pseudospectrum (H. Landau, 1976; Trefethen

& Embree, 2005). Contrarily to the sensitivity analysis in (1.85), the ϵ -pseudospectrum is not perturbative in ϵ and thus does not require the latter to be small. Three equivalent mathematical definitions of the pseudospectrum are given as follows (Trefethen & Embree, 2005)

Let $A \in \mathcal{C}(X)$ and $\epsilon \geq 0$ be arbitrary. The ϵ -pseudospectrum $\sigma_\epsilon(A)$ of A is the set of $z \in \mathbb{C}$ defined equivalently by any of the conditions

$$\|(z - A)^{-1}\| > \epsilon^{-1}, \quad (1.104)$$

$$z \in \sigma(A + E) \text{ for some } E \in \mathcal{B}(X) \text{ with } \|E\| < \epsilon, \quad (1.105)$$

$$z \in \sigma(A) \text{ or } \|(z - A)u\| < \epsilon \text{ for some } u \in \mathcal{D}(A) \text{ with } \|u\| = 1. \quad (1.106)$$

If $\|(z - A)u\| < \epsilon$ as in (1.106), then z is an ϵ -pseudoeigenvalue of A and u is a corresponding ϵ -pseudoeigenvector (or pseudoeigenfunction or pseudomode)

In this definition, $\sigma(A)$ stands for the spectrum of A and $\mathcal{C}(X)$ designates the set of closed operators on X where X is a complete normed vector space over the complex field \mathbb{C} . In addition, $\mathcal{B}(X)$ designates the set of bounded operators on X .

In figure 1.18, all the blue dots are contained in the 10^{-2} -pseudospectrum of A (definition (1.105) has been used). For the non-normal version of A in figure 1.18a, the 10^{-2} -pseudospectrum is very loose around the two eigenvalues of A , such as to make large excursions of the perturbed eigenvalues possible. From its definition (1.104), it appears linked to the fact that the resolvent gain, as introduced previously, is large. Indeed, the larger the resolvent gain is, the wider is part of the complex plane satisfying (1.104).

In figure 1.18b for the normal version of A , on the contrary, the 10^{-2} -pseudospectrum is closely around the eigenvalues. That is because for a normal operator (and considering the L^2 norm) $\|(z - A)^{-1}\| = 1 / \text{dist}(z, \sigma(A))$. Thereby definition (1.104) implies the ϵ -pseudospectrum to be the set of z such that $\text{dist}(z, \sigma(A)) < \epsilon$. Consequently, the displacement of an eigenvalue, by perturbing the operator A with some operator of norm 10^{-2} , is bounded by 10^{-2} .

Crucially, by identifying definition (1.104) with (1.38), we deduce that $i\omega$ is on the border of the $G(\omega)^{-1}$ ($G(\omega)$ the harmonic gain) pseudospectrum of the operator A . By now relying on definition (1.105), this means that an operator perturbation of norm $G(\omega)^{-1}$ is sufficient to make $i\omega$ a (neutral) eigenvalue. All along this thesis, this fact will make it possible to bridge non-modality with classical techniques to derive amplitude equations. To do so, we shall proceed as follows

- **Part I** is constituted of only one chapter, **chapter 2**. In the latter, we outline a methodology to derive an amplitude equation to capture the effect of weak nonlinearities on the optimal response to a harmonic forcing. The method is applied to both a parallel and a non-parallel flow and captures and helps understand different types of weakly nonlinear behaviors.

- **Part II** is constituted of four chapters and will deal with the response to stochastic forcing. In the first chapter of this part, **chapter 3**, we show that by selecting a different inner product, we can extend the methodology proposed in the first part to derive an equation for the weakly nonlinear evolution of the variance of the response to stochastic forcing. Results are illustrated on the backward-facing step flow.

In the second chapter of this part, **chapter 4**, we propose a more complicated procedure to derive a "spectral envelope" equation that, not only describes the weakly nonlinear evolution of the variance of the response, but also of its entire Fourier spectrum. The method is first tested on a toy model, then on the same backward-facing step flow as in the previous chapter, which makes possible a comparison between both approaches.

In the third chapter of this part, **chapter 5**, the classical modal approach to derive an amplitude equation is extended to cases where the flow is stochastically forced. The method is applied on the sudden expansion flow, subject to a supercritical pitchfork bifurcation above which two equilibria exist. This makes possible noise-induced transitions, which couldn't occur in the previous configurations where the system had only one global attractor. The mean return time of the transitions between one attractor to the other is captured by the amplitude equation, at a very low numerical cost.

The fourth chapter of this part, **chapter 6**, aims at coupling both approaches from chapter 3 and chapter 5, such as to derive a system of amplitude equation for both the bifurcated mode and the non-normal response. Both equations are nonlinearly coupled, which could help understand the role of non-normality in noise-induced transitions.

- **Part III** includes three chapters. In the first of them, **chapter 7**, we derive a weakly nonlinear amplitude equation for the optimal response to an initial perturbation, over a time-invariant base flow. The ensuing amplitude equation is tested both on the backward-facing step flow and on the streamwise-invariant plane Poiseuille flow.

In the second chapter of this part, **chapter 8**, the method is extended to time-varying base flows and applied to the Lamb-Oseen vortex flow, which exhibits bypass transition. The amplitude equation predicts and helps interpret the role of nonlinearities on the transient gain.

In the third and last chapter of this third part, **chapter 9**, inspired by the minimal seed paradigm we incorporate the amplitude equation in a Lagrangian optimization, yielding weakly nonlinear optimal structures. Their potential to trigger turbulence is tested on the three-dimensional plane Poiseuille flow.

Response to a harmonic forcing **Part I**

2 A non-modal weakly nonlinear amplitude equation for the response to a harmonic forcing

Remark: This chapter is largely inspired by the first half of the article Ducimetière et al. (2022a), in collaboration with Edouard Boujo and François Gallaire.

2.1 Introduction

Nonlinear dynamical systems can have one or several equilibrium solutions, which form one of the building blocks of the phase space (Strogatz, 2015). The linear stability of an equilibrium can be deduced from the eigenvalues of the linearised operator: linear modal analysis thus helps to detect bifurcations and distinguish between linearly unstable, neutral (marginally stable) and strictly stable equilibria, when the largest growth rate is positive, null and negative, respectively. It sometimes remains too simplistic, however, and has therefore been generalised over the last decades to account for nonlinear (Stuart, 1960) and non-modal (Trefethen et al., 1993) effects, although these two types of correction have generally been opposed, culminating into F. Waleffe’s paper entitled “*Nonlinear normality versus non-normal linearity*” (Waleffe, 1995). The objective of the present chapter is precisely to contribute to reconciling nonlinearity and non-normality, and to rigorously derive weakly nonlinear amplitude equations ruling non-normal systems when subject to a harmonic forcing.

2.1.1 Strong non-normality

Upon the choice of a scalar product, a linear operator is non-normal if it does not commute with its adjoint. Consequently, its eigenmodes do not form an orthogonal set, and the response to an initial condition or a sustained forcing may be highly non-trivial (see Trefethen and Embree (2005) for an exhaustive presentation). In particular, non-normal systems subject to harmonic forcing may exhibit strong amplification, much larger than the inverse of the

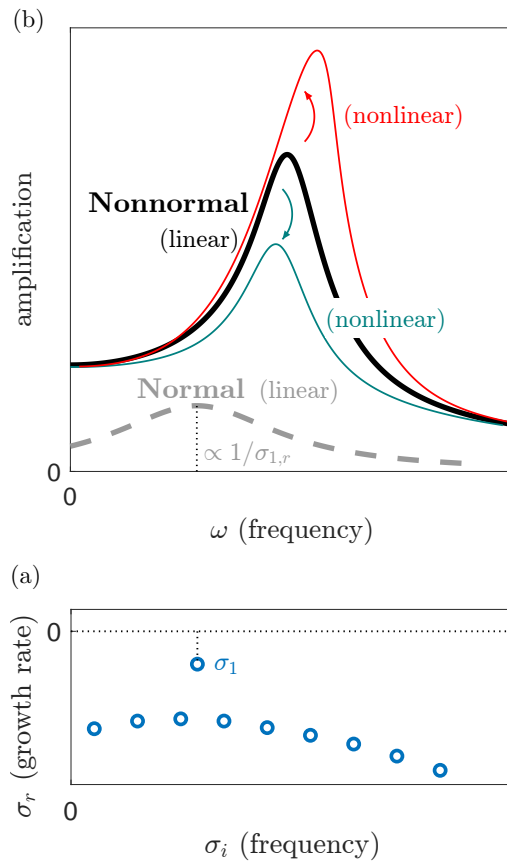


Figure 2.1: Cartoon representation of nonlinearity and non-normality, illustrated in the frequency domain for a linearly stable system; the least stable eigenvalue σ_1 of the eigenspectrum in (a) has indeed a negative growth rate. Normal systems subject to external forcing respond preferentially at frequency $\sigma_{1,i}$. Non-normal systems can respond at different frequencies, with an amplification much larger than predicted by $\sigma_{1,r}$. Nonlinearity may reduce or magnify the gain.

smallest damping rate, and at forcing frequencies unpredictable at the sight of the spectrum (figure 2.1). Non-normal operators are encountered in various fields. In laser physics (see Trefethen and Embree (2005) §60), H. J. Landau described non-normality by developing the concept of the *pseudospectrum*, as a pertinent alternative to modal analysis (H. Landau, 1976, 1977). Non-normality in an unstable laser cavity results in a substantial increase in the linewidth of the laser beam signal compared with a perfect resonator (Petermann, 1979). In astrophysics, Jaramillo et al. (2021) recently used a pseudospectrum analysis to study the stability of black holes. In network science, Asllani et al. (2018) have shown that many directed empirical networks in various disciplines (biology, sociology, communication, transport, etc.) present strong non-normality. For instance, the non-normality of the London Tube network can result in the outbreak of measles epidemic, although linear stability theory predicts an asymptotic decay of the number of contagions.

In hydrodynamics, non-normality is frequent and inherited from the linearisation of the advective term $(\mathbf{U} \cdot \nabla)\mathbf{U}$. This term gives a preferential direction to the fluid flow, which breaks the normality of the linear operator. In the context of parallel flows, non-normality is found for instance in the canonical plane Couette and Poiseuille flows (Butler & Farrell, 1992; Farrell & Ioannou, 1993; Gustavsson, 1991; Reddy & Henningson, 1993; Schmid & Henningson, 2001), in pipe flow (Schmid & Henningson, 1994) and in boundary layers (Butler & Farrell, 1992; Corbett & Bottaro, 2000). Non-normality is also found in non-parallel flows (Cossu & Chomaz, 1997), for instance spatially developing boundary layers (Åkervik et al., 2008; Ehrenstein & Gallaire, 2005; Monokrousos et al., 2010), jets (Garnaud et al., 2013a, 2013b) and the flow past a backward-facing step (Blackburn et al., 2008; Boujo & Gallaire, 2015). Exhaustive reviews of non-normality in hydrodynamics can be found in Chomaz (2005) and Schmid (2007). The crucial role played by non-normality in the transition to turbulence has become clear over the years (Baggett & Trefethen, 1997; Schmid, 2007; Trefethen et al., 1993). If the flow is non-normal, low-energy perturbations such as free-stream turbulence or wall roughness can be amplified strongly enough to lead to a regime where nonlinearities come into play, which may lead to turbulence through a sub-critical bifurcation. The toy system presented in Trefethen et al. (1993) is an excellent illustration of this so-called “bypass” scenario.

2.1.2 Weak nonlinearity

This illustrates the importance of combining nonlinearity and non-normality. In the bypass transition scenario, it is the conjunction of non-normality and nonlinearity which succeeds in shrinking the basin of attraction of a linearly strictly stable equilibrium, as strong amplification triggers nonlinearities (figure 2.1), and may radically change the behaviour of dynamical systems. Nonlinear effects can be introduced in the analysis either by weakly or fully nonlinear analyses. Notwithstanding the relevance and usefulness of fully nonlinear solutions (Hof et al., 2004; Schneider et al., 2010), as well as the existence of a fully nonlinear non-normal stability theory able to compute nonlinear optimal initial conditions via Lagrangian optimisation (Cherubini et al., 2010, 2011; Kerswell, 2018; Pringle & Kerswell, 2010), we believe that establishing a rigorous reduced-order model for weak nonlinearities is relevant. To the best of our knowledge, weakly nonlinear approaches all hinge on the fact that an amplitude equation can only be constructed close to a bifurcation point. Indeed, only linearised systems with a neutral or weakly damped eigenmode may experience resonance, whose avoidance condition results in the amplitude equation.

Following the insight of L. Landau, who introduced amplitude equations in analogy to phase transitions (L. Landau and Lifshitz (1987), §26), weakly nonlinear analyses using a multiple-scale approach were performed in some pioneering works in the context of thermal convection (Gor’kov, 1957; Malkus & Veronis, 1958), parallel shear flows (Stuart, 1958, 1960; Watson, 1960) and non-parallel shear flows (Sipp & Lebedev, 2007). In these studies, a so-called Stuart-Landau equation of the form $d_T A = \lambda A - \kappa A |A|^2$ is obtained for the bifurcated mode amplitude A as a condition for non-resonance. When the real part of the nonlinear coefficient is strictly

positive, $\Re(\kappa) > 0$, the cubic term $A|A|^2$ is sufficient to capture the saturation amplitude, and the Stuart-Landau equation is an accurate model for supercritical bifurcations; otherwise it can be extended to describe subcritical bifurcations as well.

Amplitude equations can be generalised to describe slow dependence on space (see Cross and Hohenberg (1993) for a review) and are also widely used to describe spatio-temporal pattern formation in physical systems near the bifurcation threshold. Beyond hydrodynamics, this occurs in plasma physics, solidification fronts, nonlinear optics, laser physics, oscillatory chemical reactions, buckling of elastic rods, and many other fields.

While the form of the amplitude equation can often be deduced from symmetry considerations (Crawford & Knobloch, 1991; Fauve, 1998), its coefficients (λ and κ in the case of the Stuart-Landau equation) are evaluated with scalar products of fields computed at the bifurcation point. Other approaches exist to deduce the normal form, i.e. the amplitude equation which distillates the quintessence of the nonlinear behaviour in the vicinity of a bifurcation point (Guckenheimer & Holmes, 1983; Haragus & Iooss, 2011; Manneville, 2004). Common to all these approaches is the concept of the centre manifold, along which the dynamics is slow, while, under a spectral gap assumption, an adiabatic elimination ensures the slaving of quickly damped modes.

2.1.3 Amplitude equations without eigenvalues

This indicates that the application of asymptotic approaches to describe the weakly nonlinear behaviour of non-normal systems is not straightforward, because of the absence of a neutral bifurcation point in many non-normal systems. Note that even when a system has a neutral or weakly damped mode, it can still exhibit large non-normality, which could jeopardise the relevance of a classical, single-mode amplitude equation.

The present work proposes to reconcile amplitude equations and non-normality. Specifically, a method is advanced to derive amplitude equations in the context of harmonic forcing. We systematically vary the amplitude of a given harmonic forcing at a prescribed frequency and predict the gain (energy growth) of the asymptotic response (§2.2). We perform an *a priori* weakly nonlinear prolongation of the gain, at a very low numerical cost. The applied harmonic forcing and initial condition are allowed to be arbitrarily different from any eigenmode. The method does not rely on the presence of an eigenvalue close to the neutral axis; instead, it applies to any sufficiently non-normal operator. If such an eigenvalue is nevertheless present on the neutral axis, we recover a classical, modal amplitude equation. The method is illustrated with two flows, the non-parallel flow past a backward-facing step (sketched in figure 2.2a) and the parallel plane Poiseuille flow (figure 2.2b). These two non-normal flows exhibit large harmonic forcing gains.

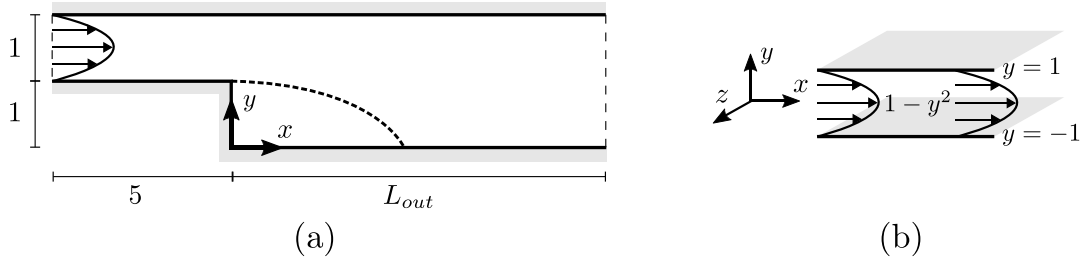


Figure 2.2: Sketch of the flow configurations. **(a)** Two-dimensional flow over a backward-facing step, with a fully developed parabolic profile of unit maximum centreline velocity at the inlet. **(b)** Three-dimensional plane Poiseuille flow, confined between two solid walls at $y = \pm 1$, and invariant in the x (streamwise) and z (spanwise) directions

In both contexts, a generic nonlinear dynamical system is considered,

$$\partial_t \mathbf{U} = N(\mathbf{U}) + \mathbf{F}, \quad \mathbf{U}(0) = \mathbf{U}_0, \quad (2.1)$$

where $N(*)$ is a nonlinear operator and \mathbf{F} is a forcing term. An appropriate and common step to begin the analysis of (2.1) is to linearise it around an unforced equilibrium. The latter is denoted \mathbf{U}_e and satisfies $N(\mathbf{U}_e) = \mathbf{0}$. Around this equilibrium are considered small-amplitude perturbations in velocity $\epsilon \mathbf{u}$, forcing $\epsilon \mathbf{f}$ and initial condition $\epsilon \mathbf{u}_0$, where $\epsilon \ll 1$. An asymptotic expansion of (2.1) in terms of ϵ can thus be performed, transforming the nonlinear equation into a series of linear ones. The fields \mathbf{u} , \mathbf{f} and \mathbf{u}_0 are recovered at order ϵ and linked through the linear relation

$$\partial_t \mathbf{u} = L\mathbf{u} + \mathbf{f}, \quad \mathbf{u}(0) = \mathbf{u}_0, \quad (2.2)$$

where L results from the linearisation of N around \mathbf{U}_e . For fluid flows governed by the incompressible Navier-Stokes equations, $L\mathbf{u} = -(\mathbf{U}_e \cdot \nabla)\mathbf{u} - (\mathbf{u} \cdot \nabla)\mathbf{U}_e + Re^{-1}\Delta\mathbf{u} - \nabla p(\mathbf{u})$, where the pressure field p is such that the velocity field \mathbf{u} is divergence free. Both fields are linked through a linear Poisson equation. In practice, pressure is included in the state variable, resulting in a singular mass matrix; it is omitted here, for the sake of clarity.

2.2 Response to Harmonic Forcing

We first derive an amplitude equation for the weakly nonlinear amplification of time-harmonic forcing $\mathbf{f}(\mathbf{x}, t) = \hat{\mathbf{f}}(\mathbf{x})e^{i\omega_o t} + c.c$ in a linearly strictly stable system. In the long-time regime, only the same-frequency harmonic response $\mathbf{u}(\mathbf{x}, t) = \hat{\mathbf{u}}(\mathbf{x})e^{i\omega_o t} + c.c$ persists. Injecting the expressions of \mathbf{f} and \mathbf{u} in (2.2) leads to $\hat{\mathbf{u}} = (i\omega_o I - L)^{-1} \hat{\mathbf{f}} \doteq R(i\omega_o) \hat{\mathbf{f}}$, where $R(z) = (zI - L)^{-1}$ is the resolvent operator. In the current context, it maps a harmonic forcing structure onto its

asymptotic linear response at the same frequency. A measure of the maximum gain is

$$G(i\omega_o) = \max_{\hat{\mathbf{f}}} \frac{\|\hat{\mathbf{u}}\|}{\|\hat{\mathbf{f}}\|} = \|R(i\omega_o)\| \doteq \frac{1}{\epsilon_o}. \quad (2.3)$$

In the following, we choose the L^2 norm (or “energy” norm) induced by the Hermitian inner product $\langle \hat{\mathbf{u}}_a, \hat{\mathbf{u}}_b \rangle = \int_{\Omega} \hat{\mathbf{u}}_a^H \hat{\mathbf{u}}_b d\Omega$ (the superscript H denotes the Hermitian transpose). The operator $R(i\omega_o)^\dagger$ denotes the adjoint of $R(i\omega_o)$ under this scalar product, such that $\langle R(i\omega_o) \hat{\mathbf{u}}_a, \hat{\mathbf{u}}_b \rangle = \langle \hat{\mathbf{u}}_a, R(i\omega_o)^\dagger \hat{\mathbf{u}}_b \rangle$, for any $\hat{\mathbf{u}}_a, \hat{\mathbf{u}}_b$. Among all frequencies ω_o , the one leading to the maximum amplification is noted $\omega_{o,m}$ and associated with an optimal gain $G(i\omega_{o,m}) = 1/\epsilon_{o,\max}$. The singular value decomposition of $R(i\omega_o)$ provides $G(i\omega_o) = \epsilon_o^{-1}$ as the largest singular value, and the associated pair of right singular vector $\hat{\mathbf{f}}_o$ and left singular vector $\hat{\mathbf{u}}_o$. The former represents the optimal forcing, whereas the latter characterises the long-time-harmonic response reached, after the transients fade away

$$R(i\omega_o)^{-1} \hat{\mathbf{u}}_o = \epsilon_o \hat{\mathbf{f}}_o, \quad \left[R(i\omega_o)^\dagger \right]^{-1} \hat{\mathbf{f}}_o = \epsilon_o \hat{\mathbf{u}}_o, \quad (2.4)$$

where $\|\hat{\mathbf{f}}_o\| = \|\hat{\mathbf{u}}_o\| = 1$. Smaller singular values of $R(i\omega_o)$ constitute sub-optimal gains, and the associated right singular vectors are sub-optimal forcing structures. Note that one can express $\langle \hat{\mathbf{u}}, \hat{\mathbf{u}} \rangle = \langle R\hat{\mathbf{f}}, R\hat{\mathbf{f}} \rangle$ as $\langle R^\dagger R\hat{\mathbf{f}}, \hat{\mathbf{f}} \rangle$, such that the singular values of $R(i\omega_o)$ are also the square root of the eigenvalues of the symmetric operator $R(i\omega_o)^\dagger R(i\omega_o)$. An important implication is that the singular vectors form an orthogonal set for the scalar product $\langle *, * \rangle$. The practical computation of ϵ_o , $\hat{\mathbf{f}}_o$ and $\hat{\mathbf{u}}_o$ is detailed for the Navier-Stokes equations in Garnaud et al. (2013b), for instance. Note that, if the operator L possesses a neutral eigenvalue, $\omega_{o,m}$, $\hat{\mathbf{f}}_o$ and $\hat{\mathbf{u}}_o$ respectively reduce to the frequency, the adjoint and the direct mode associated with this eigenvalue.

Since L is strongly non-normal, as assumed in the rest of the present study, none of ϵ_o , $\hat{\mathbf{u}}_o$ and $\hat{\mathbf{f}}_o$ are immediately determined from its spectral (modal) properties. Strong non-normality implies $\epsilon_o \ll 1$, such that the inverse resolvent $R(i\omega_o)^{-1}$ appearing in (2.4) is almost singular. We perturb it as

$$\Phi \doteq R(i\omega_o)^{-1} - \epsilon_o P, \quad \text{with} \quad P = \hat{\mathbf{f}}_o \langle \hat{\mathbf{u}}_o, * \rangle, \quad (2.5)$$

where the linear operator P is such that $P\hat{\mathbf{g}} = \hat{\mathbf{f}}_o \langle \hat{\mathbf{u}}_o, \hat{\mathbf{g}} \rangle$, for any field $\hat{\mathbf{g}}$ (note that $\langle \hat{\mathbf{u}}_o, * \rangle$ would write more simply “ $\langle \hat{\mathbf{u}}_o |$ ” in the quantum mechanics formalism). This leads to $\Phi \hat{\mathbf{u}}_o = \mathbf{0}$, such that Φ is exactly singular. The norm of the perturbation operator is small since $\|P\| = 1$. The field $\hat{\mathbf{u}}_o$ constitutes the only non-trivial part of the kernel of Φ , and its associated adjoint mode is $\hat{\mathbf{f}}_o$. Indeed, using that $P^\dagger = \hat{\mathbf{u}}_o \langle \hat{\mathbf{f}}_o, * \rangle$, we have

$$\begin{aligned} \Phi^\dagger \hat{\mathbf{f}}_o &= \left[R(i\omega_o)^{-1} \right]^\dagger \hat{\mathbf{f}}_o - \epsilon_o \hat{\mathbf{u}}_o \langle \hat{\mathbf{f}}_o, \hat{\mathbf{f}}_o \rangle \\ &= \left[R(i\omega_o)^\dagger \right]^{-1} \hat{\mathbf{f}}_o - \epsilon_o \hat{\mathbf{u}}_o = \mathbf{0}, \end{aligned}$$

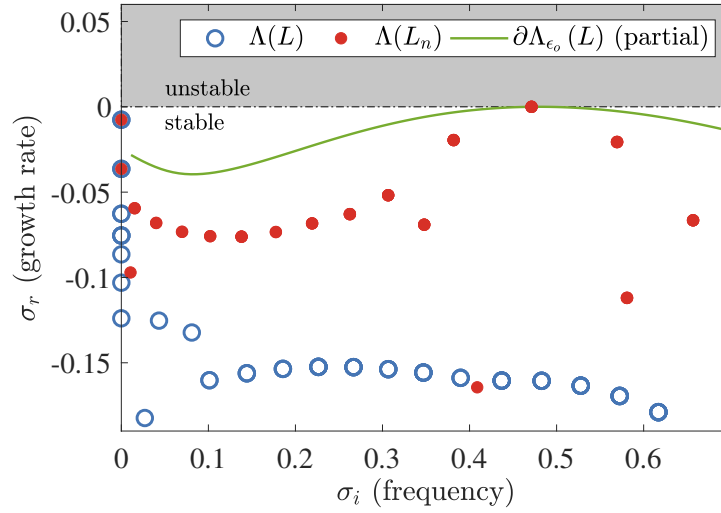


Figure 2.3: Natural and perturbed spectra of the flow past a backward-facing step (sketched in figure 2.2a) at $Re = 500$. Blue circles: eigenvalues of the linearised Navier-Stokes operator L . Red dots: eigenvalues of the linear operator perturbed with $\epsilon_o P = \epsilon_o \hat{\mathbf{f}}_o \langle \hat{\mathbf{u}}_o, * \rangle$. By construction, one eigenvalue of $L_n = L + \epsilon_o P$ lies on the imaginary axis. Green isocontour: part of the ϵ_o -pseudospectrum of L , where $\|R(z)\| = 1/\epsilon_o$. By construction, the ϵ_o -pseudospectrum is contained in the stable half-plane, except at $i\omega_o$ where it touches the neutral axis.

where we used the fact that the inverse of the adjoint is the adjoint of the inverse. We note that $\hat{\Phi}$ can be rewritten as $\hat{\Phi} = (i\omega_o I - L_n)$ where $L_n \doteq L + \epsilon_o P$, such that (2.5) seems to imply that the state operator L has been perturbed. In this process, the operator L_n has acquired an eigenvalue equal to $i\omega_o$, and therefore has become neutral. However, it has also lost its reality and therefore does not, in general, possess an eigenvalue equal to $-i\omega_o$. By construction, ϵ_o is the smallest possible amplitude of the right-hand side of (2.4) for a given $i\omega_o$, such that $\epsilon_o P$ is the smallest perturbation of L necessary to relocate an eigenvalue of L on $i\omega_o$. This fact can be formalised with the pseudospectrum theory outlined in Trefethen and Embree (2005). In the complex plane, $z \in \mathbb{C}$ belongs to the ϵ -pseudospectrum $\Lambda_\epsilon(L)$ if and only if $\|R(z)\| \geq 1/\epsilon$. If E is an operator with $\|E\| = 1$, eigenvalues of $L - \epsilon E$ can lie anywhere inside $\Lambda_\epsilon(L)$. Eigenvalues of L and singularities of $\|R(z)\|$ thus collide with the ϵ -pseudospectrum in the limit $\epsilon \rightarrow 0$. As ϵ increases, the ϵ -pseudospectrum may touch the imaginary axis, such that any $z = i\omega_o$ can be an eigenvalue of $L - \epsilon E$ if the amplitude of the perturbation is greater than or equal to $\epsilon = \|R(i\omega_o)\|^{-1}$. We recognise ϵ as the inverse gain ϵ_o defined in (2.3), and thus E as P . In particular, if $\omega_o = \omega_{o,m}$, the associated $\epsilon_{o,\max}$ is referred to as the stability radius of L since the $\epsilon_{o,\max}$ -pseudospectrum is the first to touch the imaginary axis.

As an illustration of the fact that a small-amplitude perturbation can easily “neutralise” a non-normal operator, we consider the Navier-Stokes operator linearised around the steady flow past a backward-facing step (BFS), sketched in figure 2.2, at $Re = 500$. The most amplified frequency $\omega_o = \omega_{o,m} \approx 0.47$ is associated with $\epsilon_o \approx 1.3 \cdot 10^{-4} \ll 1$. The spectra of L and L_n are shown in figure 2.3, together with part of the ϵ_o -pseudospectrum of L . Clearly, the very small

perturbation $\epsilon_o P$ locates an eigenvalue exactly onto $i\omega_o$, despite the strong stability of L . We stress that neither ω_o nor ϵ_o can be deduced only by inspecting the spectrum of L .

Nevertheless, in what follows, it is really the inverse resolvent and not the state operator L that we propose to perturb. Indeed, L is generally a real operator whereas L_n is necessarily a complex one, and only one side of the spectrum of L_n can generally be made neutral at a time, depending on whether L is perturbed with P or its complex conjugate P^* .

The inverse gain $\epsilon_o \ll 1$ constitutes a natural choice of small parameter. We choose the Navier-Stokes equations for their nonlinear term $(\mathbf{U} \cdot \nabla)\mathbf{U}$, which yields both a non-normal linearised operator and a rich diversity of behaviours. The flow is weakly forced by $\mathbf{F} = \phi\sqrt{\epsilon_o^3}\hat{\mathbf{f}}_h e^{i\omega_o t} + c.c.$, where $\hat{\mathbf{f}}_h$ is an arbitrary (not necessarily optimal) forcing structure, and $\phi = O(1)$ is a real prefactor. Imposing $\|\hat{\mathbf{f}}_h\| = 1$, the forcing amplitude is $F \doteq \phi\sqrt{\epsilon_o^3}$. A separation of time scales is invoked for the flow response: its envelope is assumed to vary on a slow time scale $T = \epsilon_o t$ (such that $d_t = \partial_t + \epsilon_o \partial_T$). This ensures a comprehensive distinguished scaling and suggests the following multiple-scale expansion:

$$\mathbf{U}(t, T) = \mathbf{U}_e + \sqrt{\epsilon_o}\mathbf{u}_1(t, T) + \epsilon_o\mathbf{u}_2(t, T) + \sqrt{\epsilon_o^3}\mathbf{u}_3(t, T) + O(\epsilon_o^2). \quad (2.6)$$

The velocity field at each order j is then Fourier expanded as

$$\mathbf{u}_j(t, T) = \bar{\mathbf{u}}_{j,0}(T) + \sum_m (\bar{\mathbf{u}}_{j,m}(T) e^{im\omega_o t} + c.c.), \quad (2.7)$$

with $m = 1, 2, 3, \dots$. This decomposition is certainly justified in the permanent regime, of interest in this analysis. The proposed slow dynamics does not aim to capture the transient regime but flow variations around the permanent regime. Introducing (2.6)-(2.7) into the Navier-Stokes equations and using (2.5) to perturb the operator $R(i\omega_o)^{-1}$ appearing from time derivation yields

$$\begin{aligned} & \sqrt{\epsilon_o} \left[\left(\Phi \bar{\mathbf{u}}_{1,1} e^{i\omega_o t} + c.c. \right) + \mathbf{s}_1 \right] + \epsilon_o \left[\left(\Phi \bar{\mathbf{u}}_{2,1} e^{i\omega_o t} + c.c. \right) + \mathbf{s}_2 + C(\mathbf{u}_1, \mathbf{u}_1) \right] + \\ & \sqrt{\epsilon_o^3} \left[\left(\Phi \bar{\mathbf{u}}_{3,1} e^{i\omega_o t} + c.c. \right) + \mathbf{s}_3 + 2C(\mathbf{u}_1, \mathbf{u}_2) + \partial_T \mathbf{u}_1 + \left(P \bar{\mathbf{u}}_{1,1} e^{i\omega_o t} + c.c. \right) \right] + O(\epsilon_o^2) \\ & = \phi\sqrt{\epsilon_o^3}\hat{\mathbf{f}}_h e^{i\omega_o t} + c.c., \end{aligned} \quad (2.8)$$

where

$$\mathbf{s}_j \doteq -L\bar{\mathbf{u}}_{j,0}(T) + \left[\sum_m (im\omega_o - L)\bar{\mathbf{u}}_{j,m}(T) e^{im\omega_o t} + c.c. \right]$$

for $m = 2, 3, \dots$, and $C(\mathbf{a}, \mathbf{b}) \doteq \frac{1}{2}((\mathbf{a} \cdot \nabla)\mathbf{b} + (\mathbf{b} \cdot \nabla)\mathbf{a})$. Note that the perturbation $\epsilon_o P$ modifying $R(i\omega_o)^{-1}$ into Φ at leading order is compensated for at third order. Terms are then collected at each order in $\sqrt{\epsilon_o}$, leading to a cascade of linear problems, detailed hereafter.

At order $\sqrt{\epsilon_o}$, we collect $(im\omega_o I - L)\bar{\mathbf{u}}_{1,m} = \mathbf{0}$ for $m = 0, 2, 3, \dots$, and $\Phi\bar{\mathbf{u}}_{1,1} = \mathbf{0}$. Since L is strictly stable, the unforced equation for $m \neq 1$ can only lead to $\bar{\mathbf{u}}_{1,m} = \mathbf{0}$. Conversely, the kernel of

Φ contains the optimal response $\hat{\mathbf{u}}_o$, therefore $\bar{\mathbf{u}}_{1,1}(T) = A(T)\hat{\mathbf{u}}_o$, where $A(T) \in \mathbb{C}$ is a slowly varying scalar amplitude verifying $\partial_t A = 0$. Finally, the general solution at order $\sqrt{\epsilon_o}$ is written

$$\mathbf{u}_1(t, T) = A(T)\hat{\mathbf{u}}_o e^{i\omega_o t} + c.c. \quad (2.9)$$

At order ϵ_o , we obtain the solution $\mathbf{u}_2 = |A|^2 \mathbf{u}_{2,0} + (A^2 e^{2i\omega_o t} \hat{\mathbf{u}}_{2,2} + c.c.)$, where

$$\begin{aligned} -L\mathbf{u}_{2,0} &= -2C(\hat{\mathbf{u}}_o, \hat{\mathbf{u}}_o^*), \\ (2i\omega_o I - L)\hat{\mathbf{u}}_{2,2} &= -C(\hat{\mathbf{u}}_o, \hat{\mathbf{u}}_o). \end{aligned} \quad (2.10)$$

The homogeneous solution of the system $\Phi \bar{\mathbf{u}}_{2,1} = \mathbf{0}$ is arbitrarily proportional to $\hat{\mathbf{u}}_o$, and written $A_2(T)\hat{\mathbf{u}}_o$. It can be ignored ($\bar{\mathbf{u}}_{2,1} = \mathbf{0}$) without loss of generality. It could also be kept, provided it is included in the definition of the amplitude, which would then become $A + \epsilon_o A_2$.

At order $\sqrt{\epsilon_o^3}$, we assemble two equations yielding the Fourier components of the solution oscillating at ω_o ,

$$\Phi \bar{\mathbf{u}}_{3,1} = -A|A|^2 [2C(\hat{\mathbf{u}}_o, \mathbf{u}_{2,0}) + 2C(\hat{\mathbf{u}}_o^*, \hat{\mathbf{u}}_{2,2})] - \hat{\mathbf{u}}_o \frac{dA}{dT} - A\hat{\mathbf{f}}_o + \phi\hat{\mathbf{f}}_h \quad (2.11)$$

(recalling $P\hat{\mathbf{u}}_o = \hat{\mathbf{f}}_o$) and at $3\omega_o$, $(3i\omega_o I - L)\bar{\mathbf{u}}_{3,3} = -2A^3 C(\hat{\mathbf{u}}_o, \hat{\mathbf{u}}_{2,2})$. The operator Φ being singular, the only way for $\bar{\mathbf{u}}_{3,1}$ to be non-diverging, and thus for the asymptotic expansion to make sense, is that the right-hand side of (2.11) has a null scalar product with the kernel of Φ^\dagger , i.e. is orthogonal to the adjoint mode $\hat{\mathbf{f}}_o$ associated with $\hat{\mathbf{u}}_o$. This is known as the ‘‘Fredholm alternative’’. As a result, the amplitude $A(T)$ satisfies

$$\frac{1}{\eta} \frac{dA}{dT} = \phi\gamma - A - \frac{\mu + \nu}{\eta} A|A|^2, \quad (2.12)$$

with the coefficients

$$\begin{aligned} \eta &= \frac{1}{\langle \hat{\mathbf{f}}_o, \hat{\mathbf{u}}_o \rangle}, \quad \gamma = \langle \hat{\mathbf{f}}_o, \hat{\mathbf{f}}_h \rangle, \\ \frac{\mu}{\eta} &= \langle \hat{\mathbf{f}}_o, 2C(\hat{\mathbf{u}}_o, \mathbf{u}_{2,0}) \rangle, \quad \frac{\nu}{\eta} = \langle \hat{\mathbf{f}}_o, 2C(\hat{\mathbf{u}}_o^*, \hat{\mathbf{u}}_{2,2}) \rangle. \end{aligned} \quad (2.13)$$

The coefficient γ is the projection of the applied forcing on the optimal forcing. The coefficient μ embeds the interaction between $\hat{\mathbf{u}}_o$ and the static perturbation $\mathbf{u}_{2,0}$, i.e. it corrects the gain according to the fact that $\hat{\mathbf{u}}_o$ extracts energy from the time-averaged mean flow rather than from the original base flow. In contrast, the coefficient ν embeds the interaction between $\hat{\mathbf{u}}_o^*$ and the second harmonic $\hat{\mathbf{u}}_{2,2}$. We show in Appendix 2.4.1 that, in the regime of small variations around the linear gain, the amplitude equation reduces to the standard sensitivity of the gain Brandt et al. (2011) to a base flow modification induced by $\mathbf{u}_{2,0}$, and embeds the effect of the second harmonic $\hat{\mathbf{u}}_{2,2}$ as well. Introducing the rescaled quantities $a \doteq \sqrt{\epsilon_o} A$ and $F = \phi\sqrt{\epsilon_o^3}$, such that the weakly nonlinear harmonic gain $G = \|\sqrt{\epsilon_o} \bar{\mathbf{u}}_{1,1}\| / \|\phi\sqrt{\epsilon_o^3} \hat{\mathbf{f}}_h\|$ is

simply $= |a|/F$, (2.12) becomes

$$\frac{1}{\eta\epsilon_o} \frac{da}{dt} = \frac{\gamma F}{\epsilon_o} - a - \frac{\mu + \nu}{\eta\epsilon_o} a|a|^2. \quad (2.14)$$

The gain associated with the linearised version of (2.14) is $G = |\gamma|/\epsilon_o$, as expected for the linear prediction. We recover $G = 1/\epsilon_o$ when the optimal forcing is applied ($\gamma = 1$). We also note that this expression predicts $G = 0$ when $\gamma = 0$, which merely indicates that the linear response is orthogonal to $\hat{\mathbf{u}}_o$, without stating anything on the gains associated with sub-optimal forcings except that they should be at most $O(\epsilon_o^{-1/2})$, assuming a sufficiently large “spectral” gap in the singular-value decomposition of the resolvent operator. For the rest of the chapter, we set $\gamma = 1$. Expressing a in terms of an amplitude $|a| \in \mathbb{R}^+$ and a phase $\rho \in \mathbb{R}$ such that $a(t) = |a(t)| e^{i\rho(t)}$, the time-independent equilibrium solutions, or fixed points, of equation (2.14), named $(|a_e|, \rho_e)$, solve

$$\frac{F}{\epsilon_o} e^{-i\rho_e} = |a_e| + \frac{\mu + \nu}{\eta\epsilon_o} |a_e|^3, \quad (2.15)$$

Squaring and adding the real and imaginary parts of (2.15) leads to a third-order polynomial for the equilibrium amplitude of (2.14):

$$DY^3 + 2BY^2 + Y = \left(\frac{F}{\epsilon_o}\right)^2 \quad \text{with} \quad D = \frac{|\mu + \nu|^2}{\epsilon_o^2 |\eta|^2} > 0 \quad \text{and} \quad B = \Re \left[\frac{\mu + \nu}{\epsilon_o \eta} \right] \quad (2.16)$$

and where $Y = |a_e|^2 > 0$. Let $p(Y) = DY^3 + 2BY^2 + Y$ be the left-hand side of (2.16). We further distinguish two cases: (i) if $B \geq 0$, $p(Y)$ is increasing monotonically with Y and can only cross the constant line $(F/\epsilon_o)^2$ once. We have in addition $p(Y) > Y$, thus the gain smaller than the linear prediction and monotonically decaying while F is increasing. Conversely, if (ii) $B < 0$, we have $p(Y) < Y$ in the interval $0 < Y < -2B/D$, and the gain should then be greater than the linear one in the corresponding range of forcing $0 < (F/\epsilon_o)^2 < -2B/D$. Furthermore, $p(Y)$ may vary non-monotonically over this interval and cross the constant line $(F/\epsilon_o)^2$ three times (leading to three solutions for Y); namely, $p(Y)$ may be decreasing on a certain interval of Y while dominated by the negative term $\propto Y^2$, bridging two other intervals where $p(Y)$ is increasing due to the respective positive terms $\propto Y$ and $\propto Y^3$. A necessary and sufficient condition for such a case to occur is that the equation $dP/dY = 3DY^2 + 4BY + 1 = 0$ possesses two real and positive solutions. This is guaranteed if and only if the determinant $\Delta \doteq 16B^2 - 12D$ is strictly positive. Finally, for $-2B/D \leq Y$, $p(Y)$ must be monotonically increasing again with $p(Y) \geq Y$, resulting in a gain smaller than the linear one and monotonically decreasing while F is increasing.

The stability of the equilibrium solution(s) $(|a_e|, \rho_e)$ can also be established from the amplitude equation (2.14). If an equilibrium becomes unstable for a given forcing amplitude, we expect the flow response to depart from the associated limit cycle. However, the stability of the equilibria of the amplitude equation does not directly conclude on the stability of the limit

cycle, for instance, to perturbations in the third dimension, which could be assessed with a Floquet stability analysis or a direct numerical simulation. Equation (2.14) can be expressed as a two-by-two amplitude/phase nonlinear dynamical system

$$\frac{d|a|}{dt} = F[\eta_r \cos(\rho) + \eta_i \sin(\rho)] - \eta_r \epsilon_o |a| - (\mu_r + \nu_r) |a|^3 \quad (2.17)$$

$$|a| \frac{d\rho}{dt} = F[\eta_i \cos(\rho) - \eta_r \sin(\rho)] - \eta_i \epsilon_o |a| - (\mu_i + \nu_i) |a|^3. \quad (2.18)$$

Perturbing this system around the equilibrium solution $(|a_e|, \rho_e) + (|a'(t), \rho'(t))$ and neglecting nonlinear terms leads to the following equation for the perturbation $d_t(|a'|, \rho')^T = J(|a'|, \rho')^T$, where J is the Jacobian matrix expressed as

$$J = \begin{bmatrix} -\epsilon_o \eta_r - 3(\mu_r + \nu_r) |a_e|^2 & F[\eta_i \cos(\rho_e) - \eta_r \sin(\rho_e)] \\ -\epsilon_o \eta_i |a_e|^{-1} - 3(\mu_i + \nu_i) |a_e| & -F[\eta_i \sin(\rho_e) + \eta_r \cos(\rho_e)] |a_e|^{-1} \end{bmatrix}. \quad (2.19)$$

If at least one of the two eigenvalues of J has a positive real part, the associated equilibrium is linearly unstable.

Note that equations (2.17) and (2.18), for the amplitude and the phase of the oscillating linear response, are similar to those that would be obtained for a classical Duffing-Van der Pol oscillator with appropriate parameters and harmonically forced around its natural frequency. If the latter is set to one, $\eta_r \epsilon_o$ and $\eta_i \epsilon_o$ are respectively proportional to the damping ratio and the detuning parameter. The coefficient $(\mu_i + \nu_i)$ is proportional to the cubic stiffness parameter (Duffing nonlinearity $\propto x^3$), and $(\mu_r + \nu_r)$ to the nonlinear damping parameter (Van der Pol nonlinearity $\propto \dot{x}x^2$).

For the sake of completeness, Appendix 2.4.3 shows how to compute higher-order corrections of (2.14). It is worth mentioning, in particular, that the Fredholm alternative ensures that higher-order solutions oscillating at ω_o are orthogonal to the optimal response $\hat{\mathbf{u}}_o$, and that the action of \mathcal{P} need not be computed explicitly and can be replaced by the action of $(i\omega_o I - L)$ for all practical purposes.

2.2.1 Application case: the flow past a BFS

Equation (2.14) is the first main result of this study and will be further referred to as the Weakly Nonlinear non-normal harmonic (WNNh) model. We discuss its performance when the stationary flow past a BFS sketched in figure 2.2 is forced harmonically with the optimal structure $\hat{\mathbf{f}}_o$. At $Re = 500$ and the optimal forcing frequency, $\hat{\mathbf{f}}_o$ is shown in figure 2.4a together with its associated response $\hat{\mathbf{u}}_o$ in figure 2.4b (see Appendix 2.4.2 for details about the geometry and the numerical method). As shown in Blackburn et al. (2008) and Boujo and Gallaire (2015), the BFS flow constitutes a striking illustration of streamwise non-normality. As seen in figure 2.4a, the optimal forcing structure is located upstream and triggers a spatially growing response along the shear layer adjoining the recirculation region, as the result of the

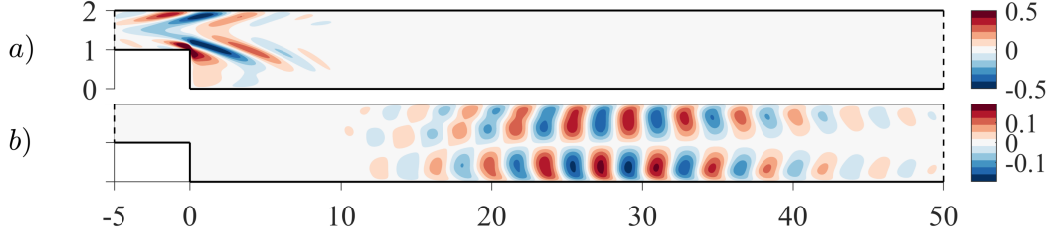


Figure 2.4: **(a)** Streamwise (x) component of the optimal harmonic forcing structure $\Re(\hat{\mathbf{f}}_o)$ for the BFS (sketched in figure 2.2a) at $Re = 500$ and at the optimal forcing frequency $\omega_o/(2\pi) = \omega_{o,m}/(2\pi) = 0.075$. **(b)** Streamwise component of the associated response $\Re(\hat{\mathbf{u}}_o)$. Both structures are normalised as $\|\hat{\mathbf{f}}_o\| = \|\hat{\mathbf{u}}_o\| = 1$.

Re	ϵ_0	η	$\mu/(\epsilon_0\eta)$	$\nu/(\epsilon_0\eta)$	B
200	73.9^{-1}	$3.66 - i \cdot 0.0163$	$5.13 - i \cdot 1.32$	$0.137 + i \cdot 1.13$	5.27
500	7456.6^{-1}	$117.1 - i \cdot 0.653$	$8.23 - i \cdot 2.60$	$0.364 - i \cdot 0.396$	8.59
700	148080^{-1}	$1626.7 - i \cdot 8.65$	$9.06 - i \cdot 4.38$	$-0.729 - i \cdot 1.39$	8.33

Table 2.1: WNNh coefficients for the backward-facing step flow, when the optimal forcing structure ($\gamma = 1$) is applied at the optimal frequency $\omega_o/(2\pi) = \omega_{o,m}/(2\pi) = 0.075$.

convectively unstable nature of the shear layer. We first set the Reynolds number Re between 200 and 700, and the frequency $\omega_o = 2\pi \times 0.075$ close to the most linearly amplified frequency $\omega_{o,m}$, which varies only slightly with Re . The linear gain grows exponentially with Re (Boujo and Gallaire (2015)), as seen in table 2.1. Since η scales like $O(\epsilon_o^{-1/2})$, the term in dA/dT in (2.11) is asymptotically consistent only close to equilibrium points where $dA/dT = 0$, which is the regime of primary interest in the context of harmonic forcing. In accordance, the temporal derivative dA/dT is kept in (2.12) to assess the stability of such equilibria, determined by the analysis of the Jacobian matrix (2.19).

Predictions from the WNNh model are compared with fully nonlinear gains extracted from direct numerical simulations (DNS) in figure 2.5a. The DNS gains are the ratio between the temporal root-mean-square (r.m.s) of the kinetic energy of the fluctuations at ω_o (extracted through a Fourier transform) and the *rms* of the kinetic energy of the forcing (for instance, the forcing $F\hat{\mathbf{f}}_o e^{i\omega_o t} + c.c.$, with $\|\hat{\mathbf{f}}_o\| = 1$ corresponding to an effective forcing *rms* amplitude of $\sqrt{2}F$). Since the coefficient B defined in (2.16) is strictly positive for all Re , the WNNh model predicts nonlinearities to saturate the energy of the response, and thus the gain to decrease monotonically with the forcing amplitude. This is confirmed by the comparison with DNS, displaying an excellent overall agreement. As shown in the inset (in logarithmic scale), the nonlinear gain transitions from a constant value in the linear regime to a $-2/3$ power-law decay when nonlinearities prevail, as predicted from (2.14). This transition is delayed when the Reynolds number (and therefore the linear gain) decreases, and compares well with DNS data. The main plot (in linear scale) confirms the agreement with the DNS, and the improvement over the linear model. Re-scaled WNNh curves appear similar for $Re = 200$ and $Re = 700$, and a

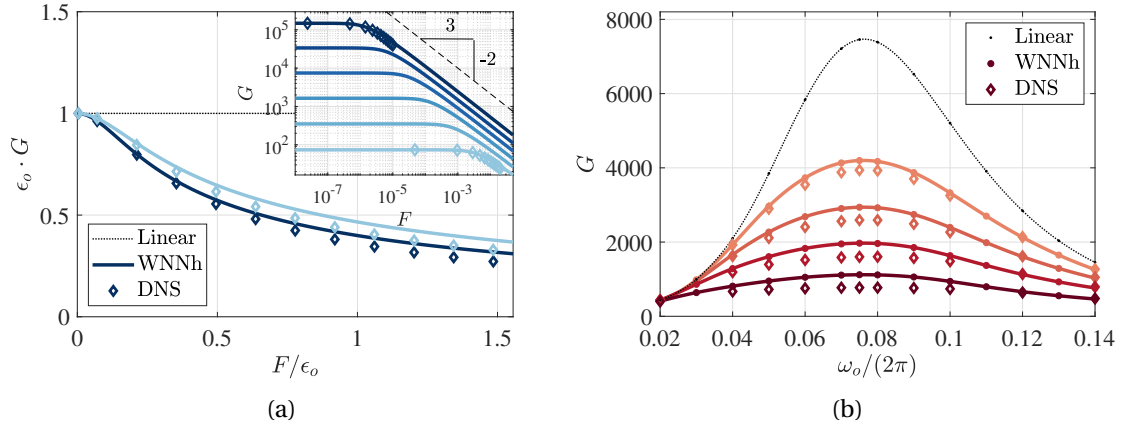


Figure 2.5: Weakly and fully nonlinear harmonic gain in the BFS flow (sketched in figure 2.2a). At each frequency and each Reynolds number, the optimal linear forcing structure $\hat{\mathbf{f}}_o$ is applied. **(a)** Fixed frequency $\omega_o/(2\pi) = 0.075$, varying Reynolds number $Re = 200$ and 700 (larger Re darker). Inset: log-log scale, $Re = 200, 300 \dots 700$. **(b)** Fixed Reynolds number $Re = 500$, varying forcing r.m.s amplitude $F = \sqrt{2}^{-1} [1, 2, 4, 10] \cdot 10^{-4}$ (larger amplitudes darker).

slight overestimate is observed as the forcing amplitude approaches ϵ_0 . Indeed, $F \sim \epsilon_0$ implies $\phi \sim 1/\sqrt{\epsilon_0}$, which jeopardises the asymptotic hierarchy. Nonetheless, the error remains small for this flow in the considered range of forcing amplitudes. Further physical insight is gained from the WNNh coefficients gathered in table 2.1. The nonlinear coefficients remain of order one, which confirms the validity of the chosen scalings. The real part of μ being larger than that of ν , the present analysis rationalises *a priori* the predominance of the mean flow distortion over the second harmonic in the saturation mechanism reported *a posteriori* in Mantič-Lugo and Gallaire (2016b).

Next, we select $Re = 500$ and report in figure 2.5b harmonic gains as a function of the frequency, for increasing forcing amplitudes. At each frequency, the corresponding optimal forcing structure $\hat{\mathbf{f}}_o$ is applied. The comparison between DNS and WNNh is conclusive over the whole range of frequencies. The saturating character of nonlinearities is well captured. Such a good agreement may appear surprising in the low-frequency regime, for instance at $\omega_o/(2\pi) = 0.04$ where the second harmonics at frequency $2\omega_o$ could, in principle, be amplified approximately four times more than the fundamental. It happens, however, that the associated forcing structure $-C(\hat{\mathbf{u}}_o, \hat{\mathbf{u}}_o)$ is located much farther downstream than the optimal forcing at $2\omega_o$, with a weak overlap region which results in a poor projection. Therefore, the second-order contribution does not reach amplitudes of concern in this flow, as a consequence of its streamwise non-normality. For $\omega_o/(2\pi) = 0.075$ the fully nonlinear and predicted weakly nonlinear structures are compared in figure 2.6. The energy centroid of the fully nonlinear response shows a clear migration upstream when increasing the forcing amplitude, as already reported in Mantič-Lugo and Gallaire (2016b). It is associated with a shortening of the mean recirculation bubble under the action of the Reynolds stresses, in turn explaining the reduction of the gain. Although some distortion of the structures due to higher harmonics is observed

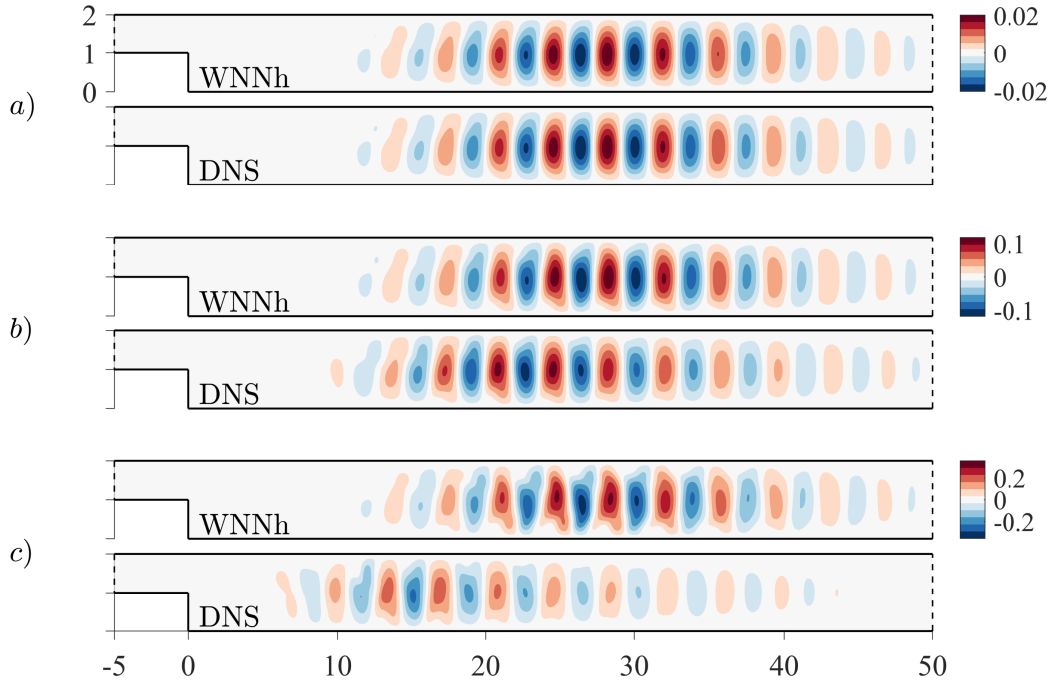


Figure 2.6: Snapshots of the weakly (WNNh) and fully (DNS) nonlinear cross-wise (y) component of the velocity perturbation around the mean flow in the BFS flow. The frequency is fixed to $\omega_o/(2\pi) = 0.075$ and the Reynolds number to $Re = 500$. Three increasing forcing amplitudes are considered: **a)**, **b)** and **c)** correspond respectively to $F = [10^{-5}, 10^{-4}, 10^{-3}]/\sqrt{2}$. The WNNh structures are evaluated as $2\Re(\sqrt{\epsilon_o} A e^{i\omega_o t} \hat{\mathbf{u}}_o + \epsilon_o A^2 e^{2i\omega_o t} \hat{\mathbf{u}}_{2,2})$, with A the equilibrium solution of (2.12); the DNS structures are obtained by taking the $n\omega_o$ ($n = 1, 2, 3, \dots$) Fourier components of a DNS simulation in the stationary regime, then by taking two times the real part of their sum weighted by $e^{in\omega_o t}$. In this manner, the phases can also be compared between WNNh and DNS.

when increasing the forcing amplitude, the fully nonlinear structure remains dominated by its ω_o -component. The weakly nonlinear structure does not capture the upstream migration since it does not include the $O(\epsilon_o^{3/2})$ corrections of the ω_o -component structure; thus, the latter is intrinsically restricted to $\hat{\mathbf{u}}_o$. However, the coefficient $\mu + \nu$ is constructed on forcing terms at $O(\epsilon_o^{3/2})$ and indeed embeds the nonlinear interactions responsible for the migration and the saturation, explaining why the predicted level of energy is correct even though the structure is not.

2.2.2 Application case: Orr mechanism in the plane Poiseuille flow

The weakly nonlinear evolution of the harmonic gain is now sought for the plane Poiseuille flow sketched in figure 2.2, a typical flow with component-wise non-normality (Schmid (2007) and Trefethen et al. (1993)). Periodicity is imposed in the streamwise and spanwise directions with wavenumbers k_x and k_z , respectively. The set of parameters $(Re, k_x, k_z) = (3000, 1.2, 0)$

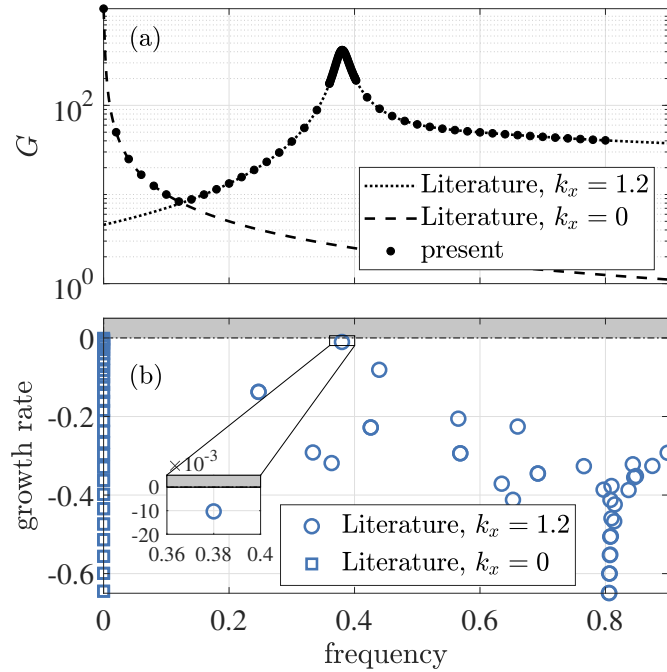


Figure 2.7: **(a)** Linear harmonic (optimal) gain as a function of the optimisation frequency. Present results are compared with those reproduced from Schmid and Henningson (2001), where perturbations are expressed as Fourier mode of streamwise wavenumber k_x . **(b)** Eigenspectra.

is selected. According to the classical work of Orszag (1971), the base flow at this Re number is linearly stable since instability first occurs at $Re_{cr} \approx 5772$ and $k_{x,cr} \approx 1.02$. In both the linear and nonlinear computations, the spanwise invariance $k_z = 0$ is systematically maintained. While the base flow $U(y)$ has only one velocity component and depends only on one coordinate, the perturbations are here two-dimensional (i.e. $\mathbf{u} = (u_x(x, y), u_y(x, y))$). The computations are performed in the streamwise-periodic box $(x, y) \in [0, 2\pi/1.2] \times [-1, 1] \equiv \Omega$. All the scalar products are taken upon integration inside this periodic box, in particular for the normalisation $\langle \hat{\mathbf{u}}_o, \hat{\mathbf{u}}_o \rangle = \langle \hat{\mathbf{f}}_o, \hat{\mathbf{f}}_o \rangle = 1$, and latter for the evaluation of the weakly nonlinear coefficients.

The linear optimal gain (2.3) is computed in the frequency interval $0 \leq \omega_o \leq 0.8$ (figure 2.7a), together with the associated optimal forcing and responses structures. Results are validated with the one-dimensional results of Schmid and Henningson (2001) based on a Fourier expansion of wavenumbers $k_x = 1.2$ and $k_x = 0$ in the streamwise direction. Eigenspectra are also reported in figure 2.7(b). The SVD algorithm applied to the periodic box automatically selects the most amplified wavenumber among all spatial harmonics $n1.2$ with $n = 0, 1, 2, \dots$. Below $\omega_o \approx 0.12$, the harmonic $0 \cdot 1.2 = 0$ is dominant due to the concentration of weakly damped eigenvalues along the imaginary axis. The gain $G(\omega_o = 0) = 1216$ is equal to the inverse of the smallest damping rate among all these spatially invariant modes. The large value of the gain associated with those modes is understood considering that the small pressure gradient

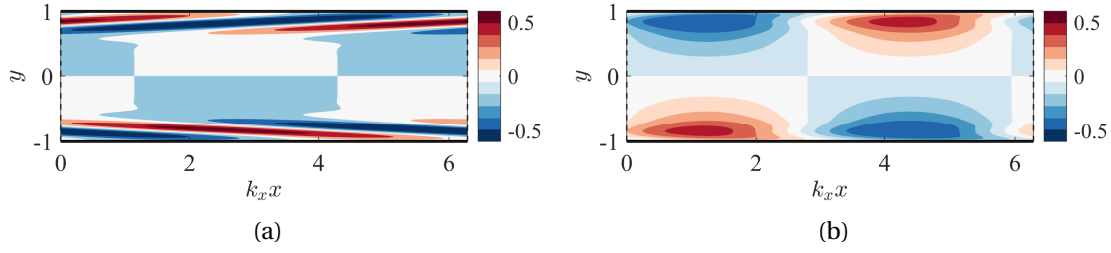


Figure 2.8: **(a)** Streamwise component of the optimal forcing $\Re(f_{o,x})$ for the plane Poiseuille flow (sketched in figure 2.2b) for $(Re, k_x, k_z) = (3000, 1.2, 0)$ and $\omega_o = 0.3810$. **(b)** Streamwise component of the response $\Re(\hat{u}_{o,x})$. Both fields are normalised as $\|\hat{\mathbf{f}}_o\| = \|\hat{\mathbf{u}}_o\| = 1$. Only one wavelength $0 \leq k_x x \leq 2\pi$ is shown.

$(2/Re, 0)^T = (2/3000, 0)^T$ is sufficient to induce the Poiseuille base flow (equal to unity in the centreline). Above $\omega_o \approx 0.12$, the fundamental wavenumber $1 \cdot 1.2 = 1.2$ prevails. The corresponding harmonic gain presents a local and selective maximum for $\omega_o = 0.38$, certainly linked to the presence of the weakly damped eigenvalue $\sigma_1 = -0.0103 + 0.380i$. Nevertheless, $G(\omega_o = 0.38) = 416$ is significantly larger than $1/0.0103 \approx 97$. This is a direct consequence of the non-normality of the plane Poiseuille flow. Unlike the BFS flow, the non-normality at play here is not due to the presence of a convectively unstable region but to the Orr mechanism, suggested for the first time in Orr (1907). Namely, an initial condition or forcing field constituted of spanwise vortices tilted towards the upstream direction (fig. 2.8a), tilts downstream under the action of the mean shear (fig. 2.8b), which leads to a significant gain in the kinetic energy of the perturbation. The coefficient B is shown in figure 2.9a, and the associated WNNh prolongation of the harmonic gain in figure 2.9b. The coefficient B is negative in the interval $0.378 \leq \omega_o \leq 0.486$, and B and D are such that three equilibrium amplitudes $|a_e|$ exist for some values of F in the sub-interval $0.389 \leq \omega_o \leq 0.428$. Among them, none or only one is found to be stable. Consequently, as the forcing amplitude is increased, the harmonic gain curve leans toward the higher frequencies in figure 2.9b; in the meantime, a frequency interval where no stable solution is predicted appears and grows larger.

Note that, in the absence of a stable equilibrium, it is natural to consider completing (2.14) up to $O(\sqrt{\epsilon_o^5})$. It is shown in Appendix 2.4.3, however, that such an approach is problematic in the present case, because the non-oscillating forcing terms appearing at $O(\epsilon_o^2)$ excite the largely amplified static modes visible in figure 2.7 for $\omega_o = 0$. The associated gains being of order $1/\epsilon_o$, the mean flow correction terms at $O(\epsilon_o^2)$ break the asymptotic hierarchy. This problem is not encountered at $O(\epsilon_o)$, because the forcing $-2C(\hat{\mathbf{u}}_o, \hat{\mathbf{u}}_o^*)$ in (2.10) projects poorly on the optimal one for $\omega_o = 0$, and $\|\mathbf{u}_{2,0}\|$ remains of order unity.

For comparison with DNS data, two different forcing frequencies with *a priori* distinct behaviours are selected: $\omega_o = 0.3810$ and $\omega_o = 0.4025$. These two frequencies are highlighted by the vertical dashed grey lines in figure 2.9. In both cases the coefficient B is negative, and for the case $\omega_o = 0.4025$ three equilibrium solutions exist for some values of F . The linear

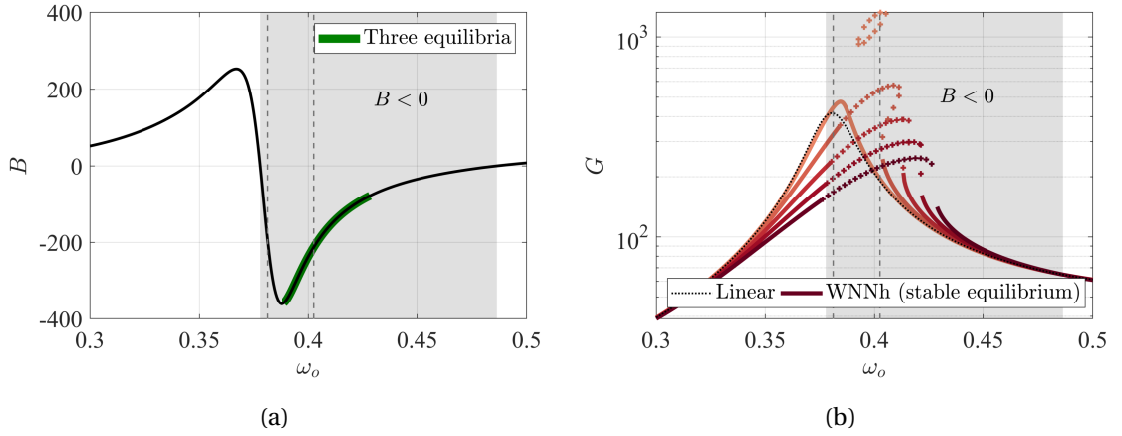


Figure 2.9: **(a)** Coefficient B defined in (2.16) as a function of the optimisation frequency. The superimposed bold green line indicates that B and D are such that three equilibrium solutions to (2.14) exist. **(b)** Weakly nonlinear harmonic gain predicted by the WNNh model for increasing forcing amplitude F in $[0.55, 1.45, 2.35, 3.25, 4.15] \cdot 10^{-4}$ (larger F darker). Solid lines denote stable equilibrium solutions of (2.14) whereas bold plus markers (+) denote the unstable ones. The vertical dashed grey lines highlight $\omega_o = 0.3810$ and $\omega_o = 0.4025$, frequencies for which comparison with DNS data is shown in figure 2.10. The grey zone denotes a negative B .

ω_o	ϵ_o	η	$\mu/(\epsilon_o\eta)$	$\nu/(\epsilon_o\eta)$	B
0.3810	$(415.6)^{-1}$	$4.06 + i \cdot 0.218$	$-177.0 - i \cdot 315.6$	$-17.4 - i \cdot 197.8i$	-194.4
0.4025	$(190.4)^{-1}$	$2.78 + i \cdot 3.89$	$-160.1 + i \cdot 24.3$	$-52.3 - i \cdot 10.6$	-212.4

Table 2.2: WNNh coefficients for the plane Poiseuille flow at $(Re, k_x, k_z) = (3000, 1.2, 0)$, and when the optimal forcing structure ($\gamma = 1$) is applied.

gains and weakly nonlinear coefficients are reported in table 2.2. The corresponding WNNh prolongation of the linear gain as a function of the forcing amplitude is shown in figure 2.10, together with DNS results. For comparison, the prediction of a "classical" (modal) amplitude equation constructed around the weakly damped eigenvalue σ_1 and its associated direct and adjoint modes is also added. Its derivation is briefly recalled in Appendix 2.4.4.

For $\omega_o = 0.3810$ (figure 2.10a), the WNNh gain initially increases with F due to the negativity of B . As visible in table 2.2, this is mostly due to the contribution of $\Re[\mu/(\epsilon_o\eta)]$ which is ten times larger than that of $\Re[\nu/(\epsilon_o\eta)]$. Thus, at this frequency, the principal factor for the initial increase of the WNNh gain is the Reynolds stress of the response $a\hat{u}_o$. The latter creates a mean flow that amplifies the linear forcing \hat{f}_o more than the base flow does. This may be interpreted considering the displacement of the eigenvalue σ_1 . Let \hat{q}_1 (respectively \hat{a}_1) denote the eigenmode (respectively adjoint mode) associated with the eigenvalue σ_1 . The sensibility

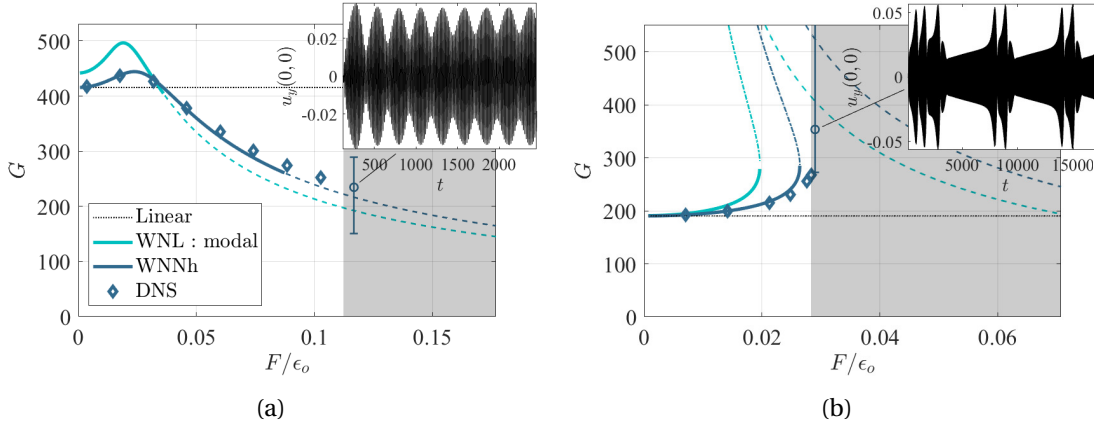


Figure 2.10: Evolution of the harmonic gain G with respect to F for (a) $\omega_o = 0.3810$ and (b) $\omega_o = 0.4025$ (frequencies highlighted by vertical dashed grey lines in figure 2.9). In both, the grey zone indicates that no harmonic gain could be properly defined, as the kinetic energy of the perturbation ceases to converge to a constant value. In particular, the inset shows the monitoring of $u_y(0,0)$ for the flow represented by the circle (the link is indicated by a thin line).

of the latter to the base flow deformation $\delta \mathbf{U}_b$ due to the Reynolds stress of $a \hat{\mathbf{u}}_o$ is written

$$\delta \sigma_1 = - \frac{\langle \hat{\mathbf{a}}_1, C[\hat{\mathbf{q}}_1, \delta \mathbf{U}_b] \rangle}{\langle \hat{\mathbf{a}}_1, \hat{\mathbf{q}}_1 \rangle} \quad (2.20)$$

where $\delta \mathbf{U}_b = |a|^2 \mathbf{u}_{2,0}$. For $\omega_o = 0.3810$, we obtain $\delta \sigma_1 = |a|^2 (1.2 + i \cdot 3.9)$. Since $\Re[\delta \sigma_1] > 0$, the eigenvalue is moving toward the unstable part of the complex plane under the action of the Reynolds stress. This is in accordance with the fact that the plane Poiseuille flow is subcritical, and may explain the initial increase in the gain with F . Meanwhile, $\Im[\delta \sigma_1] > 0$ and σ_1 is shifting toward higher frequencies. Thus ω_o ceases to be the least damped frequency, which could shed light on the fact that increasing F further leads to a monotonic decay in the WNNh gain at ω_o . Because of the flow non-normality, however, this explanation based solely on the location of σ_1 remains qualitative.

The overall agreement with the DNS results is excellent. Nevertheless, the WNNh model slightly underestimates the threshold in F above which a stable equilibrium does not exist anymore. It stands at $F/\epsilon_o = 0.087$ against $F/\epsilon_o = 0.11$ for the DNS. This loss of a proper harmonic response may be symptomatic of the fact that σ_1 eventually crosses the neutral line and becomes unstable. Indeed, for $F/\epsilon_o = 0.11$ (blue circle in the grey zone in figure 2.10a), the Fourier spectrum of the flow in its stationary regime presents two dominant neighbouring frequencies: the forcing one at $\omega = \omega_o$ and a second “natural” one at $\omega \approx 0.404$. As these two frequencies are very close, a beating behaviour is visible in the inset of figure 2.10a at a frequency consistent with $\Delta\omega = 0.404 - 0.381 = 0.023$.

The classical modal amplitude equation leads to a prediction that is only qualitative. Even for $F = 0$ the linear harmonic gain $|\langle \hat{\mathbf{f}}_o, \hat{\mathbf{a}}_1 \rangle / (\langle \hat{\mathbf{q}}_1, \hat{\mathbf{a}}_1 \rangle \sigma_{1,r})|$ (see Appendix 2.4.4 for its derivation)

is overestimated, as it is deduced from the modal quantities linked to σ_1 only. As mentioned earlier, in non-normal flows a high number of eigenmodes is generally necessary to describe its harmonic response, even in the presence of a weakly damped eigenvalue. Thus, relying on a single mode constitutes a poor description of the response to forcing.

We now consider $\omega_o = 0.4025$, and the associated results in figure 2.10b. The WNNh model yields multiple equilibrium solutions in the range $0 < F/\epsilon_o < 0.0264$. Only the one represented by a thick continuous line is stable, and corresponds to a monotonic growth of the gain with F . The DNS results validate the existence of this solution. The two other solutions, depicted by the dash-dotted and dashed lines, are unstable in one eigendirection and two eigendirections, respectively. Above $F/\epsilon_o = 0.0264$ the WNNh model predicts the loss of the stable equilibrium solution, which is accurately confirmed by the DNS whose threshold is located around $F/\epsilon_o = 0.0286$. Slightly above, the signal of $u_y(0,0)$ in the inset suggests again the presence of a “natural” frequency due to the subcritical destabilisation of σ_1 . Indeed, $u_y(0,0)$ alternates between an algebraic growth typical of a true resonance (both natural and forcing frequencies collapse), and a beating-like behaviour whose period is very long (the natural frequency drifts slightly from the forcing one).

Across this threshold, the evolution of the average kinetic energy of the response appears discontinuous. This loss of stable equilibrium is to be distinguished with its destabilisation encountered for $\omega = 0.3810$. Overall, the difference of behaviours between figures 2.10a and 2.10b may be explained by the difference of proximity between ω_o and $\Im[\sigma_1]$ of the mean flow. As the forcing is progressively increased above $F/\epsilon_o = 0.0286$, the flow response quickly becomes chaotic, and then turbulent.

It should be mentioned that, in some situations, the amplitude equation (2.14) may be in default. First, as just mentioned, when the optimal linear harmonic gain at frequency $2\omega_o$ is $\sim 1/\sqrt{\epsilon_o}$ or larger and projects well onto the optimal forcing, the asymptotic hierarchy is threatened as $\hat{\mathbf{u}}_{2,2}$ may be substantial enough to reach order $\sqrt{\epsilon_o}$ or above. It is thus important to assess that the norm of $\hat{\mathbf{u}}_{2,2}$ remains of order one. A second delicate situation arises, for the same reason, when a sub-optimal gain at the frequency ω_o is $\sim 1/\epsilon_o$. In both cases, the model could be extended by including in the kernel of Φ the optimal response at frequency $2\omega_o$, or the sub-optimal response at frequency ω_o , respectively.

Eventually, it should be noted that there are several manners to perturb $R(i\omega_o)^{-1}$ such as to include $\hat{\mathbf{u}}_o$ in the kernel. Among them, the one with the smallest amplitude, i.e. ϵ_o , has been chosen in (2.5). We demonstrate in Appendix 2.4.5 that this is the only choice that leads to a consistent amplitude equation. Choosing a higher perturbation amplitude is possible, but implies filling the kernel with another structure than $\hat{\mathbf{u}}_o$.

2.3 Conclusions

In summary, we have derived an amplitude equation for non-normal systems, describing the asymptotic response to harmonic forcing in a weakly nonlinear regime. The presence of a neutral or weakly damped mode was unnecessary. The approach is based on the following observation: in non-normal systems, the resolvent operator can be made singular by perturbing it slightly, therefore the small distance to singularity can be used as a multiple-scale expansion parameter. The resulting amplitude equation has been compared with fully nonlinear simulations, both in parallel and non-parallel two-dimensional flows. In all cases, it predicts accurately the supercritical or subcritical nonlinear evolution of the response and brings insight into the weakly nonlinear mechanisms that modify the gains as the amplitude of the harmonic forcing varies.

For future research, we believe that the proposed amplitude equation could be employed as a tool for a variety of different problems. (i) For instance, the efficiency of the WNNh model in capturing a subcritical behavior may prove useful in the search for optimal paths to chaos or turbulence. Indeed, equation (2.16) could be included as a constraint in a Lagrangian optimisation problem, whose stationary point would constitute a weakly-nonlinear optimal. Such an approach could complement fully nonlinear optimisations, proposed for instance in Pringle and Kerswell (2010), by providing physical understanding at a numerical cost close to the linear one. (ii) Amplitude equations could also be exploited for fully three-dimensional flows, where we expect them to still be valid since the hypothesis of two dimensionality has never been made in the developments. Again in their quality of reduced-order models, they would be all the more relevant here because assessing the three-dimensional finite-amplitude flow behavior from DNS is generally costly.

Furthermore, the method presents numerous possibilities for extension, in addition to higher-order corrections. For instance, the inclusion of multiple forcing structures or trajectories: the nonlinear interaction of multiple harmonic forcings or initial conditions is particularly relevant when distinct structures lead to comparable gains, for instance, perturbations of different spatial wavenumbers like in jet flows forced with different azimuthal wavenumbers (Garnaud et al. (2013b)). The ensuing system of coupled amplitude equations may bear a rich dynamics, such as hysteresis and chaos. Amplitude equations are useful for flow control and optimisation, as shown for instance in Sipp (2012) in the classical context of a marginally stable flow, displaying little non-normality, with a well-isolated eigenvalue and a sufficiently large spectral gap. In the next chapters, we derive amplitude equations for the response to stochastic forcing, as investigated in Farrell and Ioannou (1993) and Mantič-Lugo and Gallaire (2016a) with linear and self-consistent models, respectively.

2.4 Appendix

2.4.1 Harmonic gain sensitivity and comparison with the WNNh model.

Let $G_o = 1/\epsilon_o$ designate the linear harmonic gain. Then $R^\dagger R \hat{\mathbf{f}}_o = G_o^2 \hat{\mathbf{f}}_o$ holds by definition, and implies $G_o^2 = \langle R^\dagger R \hat{\mathbf{f}}_o, \hat{\mathbf{f}}_o \rangle$ thanks to the chosen normalisation $\|\hat{\mathbf{f}}_o\| = 1$. We are interested in the squared gain variation δG_o^2 (where this notation does not designate the square of the gain variation) induced by a small perturbation δL of the state operator. The latter results in the following perturbation δR of the resolvent:

$$\begin{aligned} \delta R &= (i\omega I - L - (\delta L))^{-1} - (i\omega I - L)^{-1} \\ &= [(i\omega I - L)(I - R(\delta L))]^{-1} - R \\ &\approx (I + R\delta L)R - R \\ &= R(\delta L)R. \end{aligned}$$

The gain variation is therefore

$$\begin{aligned} \delta G_o^2 &= \langle \delta(R^\dagger R) \hat{\mathbf{f}}_o, \hat{\mathbf{f}}_o \rangle = \langle (\delta R)^\dagger R \hat{\mathbf{f}}_o + R^\dagger (\delta R) \hat{\mathbf{f}}_o, \hat{\mathbf{f}}_o \rangle \\ &= \langle R^\dagger (\delta R) \hat{\mathbf{f}}_o, \hat{\mathbf{f}}_o \rangle + c.c. \\ &= \langle R(\delta L)R \hat{\mathbf{f}}_o, R \hat{\mathbf{f}}_o \rangle + c.c. \\ &= \langle (\delta L)G_o \hat{\mathbf{u}}_o, G_o^2 \hat{\mathbf{f}}_o \rangle + c.c., \end{aligned}$$

so finally

$$\delta G_o^2 = 2G_o^3 \Re [\langle (\delta L) \hat{\mathbf{u}}_o, \hat{\mathbf{f}}_o \rangle]. \quad (2.21)$$

For instance, a base flow modification $\delta \mathbf{U}_e$ results in $(\delta L) \hat{\mathbf{u}}_o = -(\hat{\mathbf{u}}_o \cdot \nabla) \delta \mathbf{U}_e - (\delta \mathbf{U}_e \cdot \nabla) \hat{\mathbf{u}}_o = -2C(\hat{\mathbf{u}}_o, \delta \mathbf{U}_e)$ yielding the same formula as in Brandt et al. (2011) with a different normalisation.

On the other hand, the WNNh model predicts

$$Y^3 \frac{|\mu + \nu|^2}{\epsilon_o^2 |\eta|^2} + 2Y^2 \Re \left[\frac{\mu + \nu}{\epsilon_o \eta} \right] + Y = \left(\frac{F}{\epsilon_o} \right)^2. \quad (2.22)$$

where $Y = |\bar{a}|^2$. We identify the weakly nonlinear harmonic gain as $G^2 = Y/F^2$, and multiply (2.22) by ϵ_o^2/Y :

$$Y^2 \frac{|\mu + \nu|^2}{|\eta|^2} + \frac{2Y}{G_o} \Re \left[\frac{\mu + \nu}{\eta} \right] + \frac{1}{G_o^2} - \frac{1}{G^2} = 0. \quad (2.23)$$

Being interested in small variations around G_o^2 (that correspond to the linear limit $Y = |\bar{a}|^2 \rightarrow 0$), we write $G^2 = G_o^2 + \delta G_o^2$ with $|\delta G_o^2/G_o^2| \ll 1$. In this manner, $1/G_o^2 - 1/G^2 = \delta G_o^2/G_o^4 + h.o.t.$,

eventually leading to

$$\delta G_o^2 = -2G_o^3 \Re \left[\frac{|\bar{a}|^2(\mu + \nu)}{\eta} \right] + h.o.t. \quad (2.24)$$

We recognise at leading-order equation (2.21) where $(\delta L)\hat{\mathbf{u}}_o = -|\bar{a}|^2[2C(\hat{\mathbf{u}}_o, \mathbf{u}_{2,0}) + 2C(\hat{\mathbf{u}}_o^*, \hat{\mathbf{u}}_{2,2})]$. Thus, in the small gain variation limit, the WNNh model both contains the sensitivity formula of the harmonic gain to the base flow static perturbation $|\bar{a}|^2 \mathbf{u}_{2,0}$, and embeds the effect of the second harmonic $\hat{\mathbf{u}}_{2,2}$ as well.

2.4.2 Applying the WNNh model to the Navier–Stokes equations.

The incompressible Navier–Stokes equations are written after linearising around the equilibrium velocity field \mathbf{U}_e ,

$$B \frac{d\mathbf{q}}{dt} = L\mathbf{q} + \mathbf{d}, \quad (2.25)$$

with the state vector $\mathbf{q} = [\mathbf{u}, p]^T$, the forcing $\mathbf{d} = [\mathbf{f}, 0]^T$, the singular mass matrix

$$B = \begin{bmatrix} I & 0 \\ 0 & 0 \end{bmatrix},$$

and the linearised Navier–Stokes operator

$$L = \begin{bmatrix} -(\mathbf{U}_e \cdot \nabla) * -(* \cdot \nabla) \mathbf{U}_e + Re^{-1} \Delta(*) & \nabla(*) \\ \nabla \cdot (*) & 0 \end{bmatrix}.$$

Several subtleties arise from the peculiarity of the pressure variable, that ensure the instantaneous satisfaction of the incompressibility condition: (i) the absence of time derivative of the pressure results in a singular mass matrix, (ii) forcing terms remain restricted to the momentum equations as we choose to have no source/sink of mass and (iii) the pressure is not included in the energy norm of the response. This complicates slightly the practical computation of the gain. For the harmonic response model, the resolvent operator is generalised as $R(i\omega_o) = (i\omega_o B - L)^{-1}$, and the gain is measured according to

$$G^2(i\omega_o) = \frac{\langle \hat{\mathbf{q}}, \hat{\mathbf{q}} \rangle_B}{\langle \hat{\mathbf{d}}, \hat{\mathbf{d}} \rangle},$$

where we used the following scalar products

$$\begin{aligned} \langle \hat{\mathbf{q}}_a, \hat{\mathbf{q}}_b \rangle_B &= \int_{\Omega} \left(\hat{u}_{a,x}^* \hat{u}_{b,x} + \hat{u}_{a,y}^* \hat{u}_{b,y} + \hat{u}_{a,z}^* \hat{u}_{b,z} \right) d\Omega, \quad \text{and} \\ \langle \hat{\mathbf{q}}_a, \hat{\mathbf{q}}_b \rangle &= \int_{\Omega} \left(\hat{u}_{a,x}^* \hat{u}_{b,x} + \hat{u}_{a,y}^* \hat{u}_{b,y} + \hat{u}_{a,z}^* \hat{u}_{b,z} + \hat{p}_a^* \hat{p}_b \right) d\Omega. \end{aligned}$$

The B -scalar product excludes pressure, such that the pseudonorm $\langle \hat{\mathbf{q}}, \hat{\mathbf{q}} \rangle_B = \|\hat{\mathbf{q}}\|_B^2$ is the total kinetic energy of the response. The scalar product at the denominator includes pressure, although this will not change the norm of $\hat{\mathbf{d}}$, namely $\langle \hat{\mathbf{d}}, \hat{\mathbf{d}} \rangle = \|\hat{\mathbf{d}}\|^2$, since we have no source/sink of mass. The weakly nonlinear coefficients must be considered under these scalar products. Let $\hat{\mathbf{q}}_o = [\hat{\mathbf{u}}_o, p_o]^T$ with $\|\hat{\mathbf{q}}_o\|_B = 1$, $\hat{\mathbf{d}}_o = [\hat{\mathbf{f}}_o, 0]^T$ with $\|\hat{\mathbf{d}}_o\| = 1$, and $\hat{\mathbf{d}}_h = [\hat{\mathbf{f}}_h, 0]^T$ with $\|\hat{\mathbf{d}}_h\| = 1$, then

$$\begin{aligned} \gamma &= \langle \hat{\mathbf{d}}_o, \hat{\mathbf{d}}_h \rangle, \quad 1/\eta = \langle \hat{\mathbf{d}}_o, B\hat{\mathbf{q}}_o \rangle = \langle \hat{\mathbf{d}}_o, \hat{\mathbf{q}}_o \rangle_B, \\ \mu/\eta &= \langle \hat{\mathbf{d}}_o, \hat{\mathbf{d}}_{3,1}^{(3)} \rangle, \quad \nu/\eta = \langle \hat{\mathbf{d}}_o, \hat{\mathbf{d}}_{3,1}^{(4)} \rangle, \end{aligned}$$

where $\hat{\mathbf{d}}_{3,1}^{(3)} = [\hat{\mathbf{f}}_{3,1}^{(3)}, 0]^T$, $\hat{\mathbf{d}}_{3,1}^{(4)} = [\hat{\mathbf{f}}_{3,1}^{(4)}, 0]^T$, $\hat{\mathbf{f}}_{3,1}^{(3)} = 2C(\hat{\mathbf{u}}_o, \mathbf{u}_{2,0})$ and $\hat{\mathbf{f}}_{3,1}^{(4)} = 2C(\hat{\mathbf{u}}_o^*, \hat{\mathbf{u}}_{2,2})$. The pressure field does not influence the weakly nonlinear coefficients. For instance

$$\begin{aligned} 1/\eta &= \int_{\Omega} \left(\hat{f}_{o,x}^* \hat{u}_{o,x} + \hat{f}_{o,y}^* \hat{u}_{o,y} + \hat{f}_{o,z}^* \hat{u}_{o,z} \right) d\Omega, \quad \text{and} \\ \mu/\eta &= \int_{\Omega} \left(\hat{f}_{o,x}^* \hat{f}_{(3,1),x}^{(3)} + \hat{f}_{o,y}^* \hat{f}_{(3,1),y}^{(3)} + \hat{f}_{o,z}^* \hat{f}_{(3,1),z}^{(3)} \right) d\Omega. \end{aligned}$$

The linear and nonlinear Navier-Stokes equations are solved for (u_x, u_y, p) employing the Finite Element Method with Taylor-Hood (P2, P2, P1) elements, respectively, after implementation of the weak form in the software FreeFem++. The steady solutions of the Navier-Stokes equations are solved using the iterative Newton–Raphson method, and the linear operators are built thanks to a sparse solver implemented in FreeFem++. The singular-value decomposition is performed in Matlab following directly Garnaud et al. (2013b). Finally, DNS are performed by applying a time scheme based on the characteristic–Galerkin method as described in Benitez and Bermudez (2011).

For the two-dimensional flow past a BFS presented in §2.2.1, we refer to Mantič-Lugo and Gallaire (2016b) for the validation of the codes with existing literature and the mesh convergence, since the same codes have been used. The length of the outlet channel is chosen as $L_{out} = 50$ for $Re \leq 500$ (Mantič-Lugo & Gallaire, 2016b), $L_{out} = 65$ for $Re = 600$, and $L_{out} = 80$ for $Re = 700$. This ensures the convergence of the linear gain and weakly nonlinear coefficients. For the plane Poiseuille studied in §2.2.2, the validation is proposed in the main text.

2.4.3 Higher-order corrections of the WNNh equation.

Recall (2.11) obtained at order $\sqrt{\epsilon_o}^3$:

$$\Phi \bar{\mathbf{u}}_{3,1} = -A|A|^2 \left[2C(\hat{\mathbf{u}}_o, \mathbf{u}_{2,0}) + 2C(\hat{\mathbf{u}}_o^*, \hat{\mathbf{u}}_{2,2}) \right] - \hat{\mathbf{u}}_o \frac{dA}{dT} - A\hat{\mathbf{f}}_o + \phi\hat{\mathbf{f}}_h, \quad (2.26)$$

After the imposition of the Fredholm alternative, leading to (2.12) for dA/dT , the relation (2.26) becomes

$$\begin{aligned} \Phi \bar{\mathbf{u}}_{3,1} = & A|A|^2 [-2C(\hat{\mathbf{u}}_o, \mathbf{u}_{2,0}) - 2C(\hat{\mathbf{u}}_o^*, \hat{\mathbf{u}}_{2,2}) + \zeta \hat{\mathbf{u}}_o] \\ & + A(-\hat{\mathbf{f}}_o + \eta \hat{\mathbf{u}}_o) + \phi(\hat{\mathbf{f}}_h - \eta\gamma \hat{\mathbf{u}}_o) \end{aligned} \quad (2.27)$$

where $\zeta = (\mu + \nu)$. For higher-order corrections of the WNNh model, the field $\bar{\mathbf{u}}_{3,1}$ is needed and is solution of (2.27) where the operator Φ is singular since $\hat{\mathbf{u}}_o \neq \mathbf{0}$ belongs to its kernel. Since by construction $\hat{\mathbf{f}}_o = \epsilon_o R(i\omega_o)^\dagger \hat{\mathbf{u}}_o$, it follows immediately that $\langle \text{RHS}, \hat{\mathbf{f}}_o \rangle = \epsilon_o \langle R(i\omega_o) \text{RHS}, \hat{\mathbf{u}}_o \rangle$. Thus, thanks to the (imposed) orthogonality of the RHS with $\hat{\mathbf{f}}_o$ ($\langle \text{RHS}, \hat{\mathbf{f}}_o \rangle = 0$), solving the equation replacing Φ by $(i\omega_o I - L)$ leads directly to $\bar{\mathbf{u}}_{3,1}$ being orthogonal to $\hat{\mathbf{u}}_o$. Therefore, $P\bar{\mathbf{u}}_{3,1} = 0$ and $(i\omega_o I - L)\bar{\mathbf{u}}_{3,1} = \Phi \bar{\mathbf{u}}_{3,1}$, which implies that the field $\bar{\mathbf{u}}_{3,1}$ computed with $(i\omega_o I - L)$ instead of Φ is directly the particular solution of (2.27). Note that $\bar{\mathbf{u}}_{3,1}$ appears as a true correction to $\hat{\mathbf{u}}_o$ in the sense of the scalar product. This property has the striking and important consequence that the operator Φ never needs to be constructed explicitly, whatever the order of the amplitude equation. The homogeneous part of the solution of (2.27) is arbitrarily proportional to $\hat{\mathbf{u}}_o$. It can be ignored without loss of generality Fujimura (1991). Eventually, the term $P\bar{\mathbf{u}}_{j,1} e^{i\omega_o t} + c.c$ collected at order $O(\sqrt{\epsilon_o}^{j+2})$ disappears if $j \geq 2$. This is due to the nullity of $\bar{\mathbf{u}}_{j,1}$ for even j , and to the nullity of $P\bar{\mathbf{u}}_{j,1}$ for odd j . Overall, the particular solution at order $\sqrt{\epsilon_o}^3$ is written

$$\mathbf{u}_3(t, T) = \left(\phi \hat{\mathbf{u}}_{3,1}^{(a)} + A \hat{\mathbf{u}}_{3,1}^{(b)} + A|A|^2 \hat{\mathbf{u}}_{3,1}^{(c)} \right) e^{i\omega_o t} + A^3 e^{3i\omega_o t} \hat{\mathbf{u}}_{3,3} + c.c, \quad (2.28)$$

where

$$\begin{aligned} (i\omega_o I - L) \hat{\mathbf{u}}_{3,1}^{(a)} &= \hat{\mathbf{f}}_h - \eta\gamma \hat{\mathbf{u}}_o, \\ (i\omega_o I - L) \hat{\mathbf{u}}_{3,1}^{(b)} &= -\hat{\mathbf{f}}_o + \eta \hat{\mathbf{u}}_o, \\ (i\omega_o I - L) \hat{\mathbf{u}}_{3,1}^{(c)} &= -2C(\hat{\mathbf{u}}_o, \mathbf{u}_{2,0}) - 2C(\hat{\mathbf{u}}_o^*, \hat{\mathbf{u}}_{2,2}) + \zeta \hat{\mathbf{u}}_o \\ (3i\omega_o I - L) \hat{\mathbf{u}}_{3,3} &= -2C(\hat{\mathbf{u}}_o, \hat{\mathbf{u}}_{2,2}) \end{aligned} \quad (2.29)$$

The equation at order ϵ_o^2 is assembled as

$$(\Phi \bar{\mathbf{u}}_{4,1} e^{i\omega_o t} + c.c) + \mathbf{s}_4 = -2C(\mathbf{u}_1, \mathbf{u}_3) - C(\mathbf{u}_2, \mathbf{u}_2) - \partial_T \mathbf{u}_2 + (P\bar{\mathbf{u}}_{2,1} e^{i\omega_o t} + c.c) \quad (2.30)$$

As mentioned, $P\bar{\mathbf{u}}_{2,1} = \mathbf{0}$ since $\bar{\mathbf{u}}_{2,1} = \mathbf{0}$, and the forcing terms are $-2C(\mathbf{u}_1, \mathbf{u}_3)$, $-C(\mathbf{u}_2, \mathbf{u}_2)$ and $-\partial_T \mathbf{u}_2$. We first develop $C(\mathbf{u}_1, \mathbf{u}_3)$ as

$$\begin{aligned} C(\mathbf{u}_1, \mathbf{u}_3) &= \phi AC(\hat{\mathbf{u}}_o, \hat{\mathbf{u}}_{3,1}^{(a)*}) + |A|^2 C(\hat{\mathbf{u}}_o, \hat{\mathbf{u}}_{3,1}^{(b)*}) + |A|^4 C(\hat{\mathbf{u}}_o, \hat{\mathbf{u}}_{3,1}^{(c)*}) \\ &+ \left[\phi AC(\hat{\mathbf{u}}_o, \hat{\mathbf{u}}_{3,1}^{(a)}) + A^2 C(\hat{\mathbf{u}}_o, \hat{\mathbf{u}}_{3,1}^{(b)}) + A^2 |A|^2 \left[C(\hat{\mathbf{u}}_o, \hat{\mathbf{u}}_{3,1}^{(c)}) + C(\hat{\mathbf{u}}_o^*, \hat{\mathbf{u}}_{33}) \right] \right] e^{2i\omega_o t} \\ &+ A^4 e^{4i\omega_o t} C(\hat{\mathbf{u}}_o, \hat{\mathbf{u}}_{33}) + c.c, \end{aligned}$$

then $C(\mathbf{u}_2, \mathbf{u}_2)$ as

$$\begin{aligned} C(\mathbf{u}_2, \mathbf{u}_2) &= |A|^4 [C(\hat{\mathbf{u}}_{2,2}, \hat{\mathbf{u}}_{2,2}^*) + c.c.] + |A|^4 C(\mathbf{u}_{2,0}, \mathbf{u}_{2,0}) \\ &+ \left[2A^2 |A|^2 e^{2i\omega_o t} C(\mathbf{u}_{2,0}, \hat{\mathbf{u}}_{2,2}) + c.c. \right] + \left[A^4 e^{4i\omega_o t} C(\hat{\mathbf{u}}_{2,2}, \hat{\mathbf{u}}_{2,2}) + c.c. \right]. \end{aligned}$$

In addition,

$$\begin{aligned} \partial_T |A|^2 &= A^* \partial_T A + A \partial_T A^* = A^* (\phi\eta - \eta A - \zeta A |A|^2) + A (\phi\eta^* - \eta^* A^* - \zeta^* A^* |A|^2) \\ &= \phi\eta A^* + \phi\eta^* A - (\eta + \eta^*) |A|^2 - (\zeta + \zeta^*) |A|^4, \end{aligned}$$

and

$$\partial_T A^2 = 2A \partial_T A = 2\phi\eta A - 2\eta A^2 - 2\zeta A^2 |A|^2,$$

such that

$$\begin{aligned} \partial_T \mathbf{u}_2 &= \partial_T (|A|^2 \mathbf{u}_{2,0} + A^2 e^{2i\omega_o t} \hat{\mathbf{u}}_{2,2} + A^{*2} e^{-2i\omega_o t} \hat{\mathbf{u}}_{2,2}^*) \\ &= (\phi\eta^* A \mathbf{u}_{2,0} + c.c.) - (\zeta + \zeta^*) |A|^4 \mathbf{u}_{2,0} - (\eta + \eta^*) |A|^2 \mathbf{u}_{2,0} \\ &+ [(2\phi\eta A \hat{\mathbf{u}}_{2,2} - 2\eta A^2 \hat{\mathbf{u}}_{2,2} - 2\zeta A^2 |A|^2 \hat{\mathbf{u}}_{2,2}) e^{2i\omega_o t} + c.c.]. \end{aligned}$$

Eventually, collecting all terms leads to the following particular solution for \mathbf{u}_4

$$\begin{aligned} \mathbf{u}_4 &= [\phi A \hat{\mathbf{u}}_{4,0}^{(a)} + c.c.] + |A|^2 \mathbf{u}_{4,0}^{(b)} + |A|^4 \mathbf{u}_{4,0}^{(c)} + \dots \\ &+ [(\phi A \hat{\mathbf{u}}_{4,2}^{(a)} + A^2 \hat{\mathbf{u}}_{4,2}^{(b)} + A^2 |A|^2 \hat{\mathbf{u}}_{4,2}^{(c)}) e^{2i\omega_o t} + c.c.] + [A^4 e^{4i\omega_o t} \hat{\mathbf{u}}_{4,4} + c.c.], \end{aligned}$$

with

$$\begin{aligned} -L \hat{\mathbf{u}}_{4,0}^{(a)} &= -\eta^* \mathbf{u}_{2,0} - 2C(\hat{\mathbf{u}}_o, \hat{\mathbf{u}}_{3,1}^{(a)*}), \\ -L \mathbf{u}_{4,0}^{(b)} &= \mathbf{u}_{2,0} (\eta + \eta^*) - [2C(\hat{\mathbf{u}}_o, \hat{\mathbf{u}}_{3,1}^{(b)*}) + c.c.], \\ -L \mathbf{u}_{4,0}^{(c)} &= \mathbf{u}_{2,0} (\zeta + \zeta^*) - C(\mathbf{u}_{2,0}, \mathbf{u}_{2,0}) - [C(\hat{\mathbf{u}}_{2,2}, \hat{\mathbf{u}}_{2,2}^*) + c.c.] - [2C(\hat{\mathbf{u}}_o, \hat{\mathbf{u}}_{3,1}^{(c)*}) + c.c.], \\ (2i\omega_o I - L) \hat{\mathbf{u}}_{4,2}^{(a)} &= -2\eta \hat{\mathbf{u}}_{2,2} - 2C(\hat{\mathbf{u}}_o, \hat{\mathbf{u}}_{3,1}^{(a)}), \\ (2i\omega_o I - L) \hat{\mathbf{u}}_{4,2}^{(b)} &= 2\eta \hat{\mathbf{u}}_{2,2} - 2C(\hat{\mathbf{u}}_o, \hat{\mathbf{u}}_{3,1}^{(b)}), \\ (2i\omega_o I - L) \hat{\mathbf{u}}_{4,2}^{(c)} &= 2\zeta \hat{\mathbf{u}}_{2,2} - 2C(\mathbf{u}_{2,0}, \hat{\mathbf{u}}_{2,2}) - 2C(\hat{\mathbf{u}}_o, \hat{\mathbf{u}}_{3,1}^{(c)}) - 2C(\hat{\mathbf{u}}_o^*, \hat{\mathbf{u}}_{3,3}), \\ (4i\omega_o I - L) \hat{\mathbf{u}}_{4,4} &= -C(\hat{\mathbf{u}}_{2,2}, \hat{\mathbf{u}}_{2,2}) - 2C(\hat{\mathbf{u}}_o, \hat{\mathbf{u}}_{3,3}). \end{aligned}$$

The norms of the particular solutions at successive orders ϵ_o , $\sqrt{\epsilon_o^3}$ and ϵ_o^2 are outlined in table 2.3 for the plane Poiseuille flow at $(Re, k_x, k_z) = (3000, 1.2, 0)$ considered in §2.2.2 and forced at $\omega_o = 0.3810$. Despite a large harmonic gain for $\omega = 0$ as visible in figure 2.7, the stationary field $\mathbf{u}_{2,0}$ remains of reasonable amplitude as the associated Reynolds stress forcing $C(\hat{\mathbf{u}}_o, \hat{\mathbf{u}}_o^*)$ projects poorly on the most amplified singular mode for $\omega = 0$. However, the same does not hold for the stationary fields $\hat{\mathbf{u}}_{4,0}^{(a,b,c)}$ at order ϵ_o^2 , all of significantly large amplitudes. This implies that the asymptotic hierarchy is only maintained until order $\sqrt{\epsilon_o^3}$. Indeed, if it

		$\ \mathbf{u}_{2,0}\ $		$\ \hat{\mathbf{u}}_{2,2}\ $	
		11.5		2.07	
		$\ \hat{\mathbf{u}}_{3,1}^{(a)}\ $	$\ \hat{\mathbf{u}}_{3,1}^{(b)}\ $	$\ \hat{\mathbf{u}}_{3,1}^{(c)}\ $	$\ \hat{\mathbf{u}}_{3,3}\ $
		10.6	10.6	21.7	11.4
$\ \hat{\mathbf{u}}_{4,0}^{(a)}\ $	$\ \mathbf{u}_{4,0}^{(b)}\ $	$\ \mathbf{u}_{4,0}^{(c)}\ $	$\ \hat{\mathbf{u}}_{4,2}^{(a)}\ $	$\ \hat{\mathbf{u}}_{4,2}^{(b)}\ $	$\ \hat{\mathbf{u}}_{4,2}^{(c)}\ $
$10.5 \cdot 10^4$	$4.2 \cdot 10^4$	$5.3 \cdot 10^4$	$1.6 \cdot 10^2$	$4.0 \cdot 10^2$	$1.6 \cdot 10^2$

Table 2.3: Norms of the particular solutions at $O(\epsilon_o)$, $O(\sqrt{\epsilon_o^3})$ and $O(\epsilon_o^2)$ for the plane Poiseuille flow at $(Re, k_x, k_z) = (3000, 1.2, 0)$ considered in §2.2.2, and forced at $\omega_o = 0.3810$

holds that

$$\sqrt{\epsilon_o} \gg \epsilon_o (\|\mathbf{u}_{2,0}\|, \|\hat{\mathbf{u}}_{2,2}\|) \gg \sqrt{\epsilon_o^3} (\|\hat{\mathbf{u}}_{3,1}^{(a)}\|, \|\hat{\mathbf{u}}_{3,1}^{(b)}\|, \|\hat{\mathbf{u}}_{3,1}^{(c)}\|, \|\hat{\mathbf{u}}_{3,3}\|)$$

such that, until order $\sqrt{\epsilon_o^3}$, each order appears as a true correction of the previous one, this does not hold for order ϵ_o^2 . As $\epsilon_o^2 \|\hat{\mathbf{u}}_{4,0}^{(a)}\|$ is of order unity, it cannot be considered as a correction of the order $\sqrt{\epsilon_o^3}$ but appears directly at the base flow level, which is asymptotically ill posed.

2.4.4 Modal amplitude equation for harmonic forcing.

The dominant eigenmode $\hat{\mathbf{q}}_1$ satisfies $L\hat{\mathbf{q}}_1 = \sigma_1\hat{\mathbf{q}}_1$. Let its small damping rate $\sigma_{1,r}$ (i.e. the real part of σ_1), be scaled in terms of ϵ_o as $\sigma_{1,r} = \theta\epsilon_o$, where $\theta = O(1)$ (and $\theta \leq 0$). The forcing frequency ω_o is detuned around the natural one, i.e. $\omega_o = \omega_1 + \beta\epsilon_o$ where ω_1 is the imaginary part of σ_1 and $\beta = O(1)$. The shift-operator procedure introduced in Meliga et al. (2009, 2012) is adopted thereafter, in order to apply the classical weakly nonlinear formalism. Namely, we perturb L as $L = \bar{L} + \epsilon_o S$ where S satisfies $S\hat{\mathbf{q}}_1 = \theta\hat{\mathbf{q}}_1$ and is such that all the other eigenvectors of L constitute its kernel (i.e. $S\hat{\mathbf{q}}_i = \mathbf{0}$ for $i = 2, 3, \dots$). In this way, the perturbed operator \bar{L} possesses the same eigenvector as L , only the eigenvalue σ_1 associated with $\hat{\mathbf{q}}_1$ is shifted of $-\sigma_{1,r}$ such as to be truly neutral: $\bar{L}\hat{\mathbf{q}}_1 = (L - \epsilon_o S)\hat{\mathbf{q}}_1 = L\hat{\mathbf{q}}_1 - \sigma_{1,r}\hat{\mathbf{q}}_1 = i\omega_1\hat{\mathbf{q}}_1$. The asymptotic multiple-scale expansion of the forced Navier-Stokes equations is expressed

$$\begin{aligned} & \sqrt{\epsilon_o} \left[(\partial_t - \bar{L})\mathbf{u}_1 \right] + \epsilon_o \left[(\partial_t - \bar{L})\mathbf{u}_2 + C(\mathbf{u}_1, \mathbf{u}_1) \right] + \dots \\ & + \sqrt{\epsilon_o^3} \left[(\partial_t - \bar{L})\mathbf{u}_3 + 2C(\mathbf{u}_1, \mathbf{u}_2) + \partial_T \mathbf{u}_1 - S\mathbf{u}_1 \right] + O(\epsilon_o^2) = \phi \sqrt{\epsilon_o^3} e^{i\omega_o t} \hat{\mathbf{f}}_o + c.c. \end{aligned} \quad (2.31)$$

The equation at order $\sqrt{\epsilon_o}$ reads

$$(\partial_t - \bar{L})\mathbf{u}_1 = 0,$$

which leads to the solution $\mathbf{u}_1 = A(T)\hat{\mathbf{q}}_1 e^{i\omega_1 t} + c.c.$ At order ϵ_o , we obtain for \mathbf{u}_2 the equation

$$\begin{aligned} (\partial_t - \bar{L})\mathbf{u}_2 &= -C(\mathbf{u}_1, \mathbf{u}_1) \\ &= -2|A|^2 C(\hat{\mathbf{q}}_1, \hat{\mathbf{q}}_1^*) - \left[A^2 C(\hat{\mathbf{q}}_1, \hat{\mathbf{q}}_1) e^{i2\omega_1 t} + c.c. \right], \end{aligned}$$

whose solution is $\mathbf{u}_2 = |A|^2 \mathbf{q}_{2,0} + [A^2 e^{2i\omega_o t} \hat{\mathbf{q}}_{2,2} + c.c.]$, where

$$\begin{aligned} -\bar{L}\mathbf{q}_{2,0} &= -2C(\hat{\mathbf{q}}_1, \hat{\mathbf{q}}_1^*), \\ (2i\omega_o I - \bar{L})\hat{\mathbf{q}}_{2,2} &= -C(\hat{\mathbf{q}}_1, \hat{\mathbf{q}}_1). \end{aligned}$$

At order $\sqrt{\epsilon_o^3}$ is assembled

$$\begin{aligned} (\partial_t - \bar{L})\mathbf{u}_3 &= -2C(\mathbf{u}_1, \mathbf{u}_2) + S\mathbf{u}_1 - \partial_T \mathbf{u}_1 + \phi(e^{i\beta T + i\omega_1 t} \hat{\mathbf{f}}_o + c.c) \\ &= \left[-2A|A|^2 [C(\hat{\mathbf{q}}_{2,2}, \hat{\mathbf{q}}_1^*) + C(\mathbf{q}_{2,0}, \hat{\mathbf{q}}_1)] + \theta A \hat{\mathbf{q}}_1 - \hat{\mathbf{q}}_1 \frac{dA}{dT} + \phi e^{i\beta T} \hat{\mathbf{f}}_o \right] e^{i\omega_1 t} \\ &\quad + c.c + \text{non-resonant terms} \end{aligned}$$

where we used that $S\mathbf{u}_1 = \theta A \hat{\mathbf{q}}_1 e^{i\omega_1 t} + c.c.$ Cancelling the projection of the resonant part of the forcing term (inside the brackets) on the adjoint $\hat{\mathbf{a}}_1$, results in an equation for A :

$$\frac{dA}{dT} = \theta A - A|A|^2 \frac{\langle 2C(\hat{\mathbf{q}}_{2,2}, \hat{\mathbf{q}}_1^*) + 2C(\mathbf{q}_{2,0}, \hat{\mathbf{q}}_1), \hat{\mathbf{a}}_1 \rangle}{\langle \hat{\mathbf{q}}_1, \hat{\mathbf{a}}_1 \rangle} + \phi e^{i\beta T} \frac{\langle \hat{\mathbf{f}}_o, \hat{\mathbf{a}}_1 \rangle}{\langle \hat{\mathbf{q}}_1, \hat{\mathbf{a}}_1 \rangle}.$$

Note that, for $\omega_o = \omega_1$ (i.e, the detuning parameter $\beta = 0$), the amplitude in the linear regime, A_l , reads

$$0 = \theta A + \phi \frac{\langle \hat{\mathbf{f}}_o, \hat{\mathbf{a}}_1 \rangle}{\langle \hat{\mathbf{q}}_1, \hat{\mathbf{a}}_1 \rangle} \Leftrightarrow A_l = -\phi \frac{\langle \hat{\mathbf{f}}_o, \hat{\mathbf{a}}_1 \rangle}{\langle \hat{\mathbf{q}}_1, \hat{\mathbf{a}}_1 \rangle} \theta^{-1},$$

which corresponds to the following linear harmonic gain:

$$G = \frac{\sqrt{\epsilon_o} |A_l|}{\phi \sqrt{\epsilon_o^3}} = \frac{1}{\epsilon_o} \left| \frac{\langle \hat{\mathbf{f}}_o, \hat{\mathbf{a}}_1 \rangle}{\langle \hat{\mathbf{q}}_1, \hat{\mathbf{a}}_1 \rangle} \right| \frac{\epsilon_o}{|\sigma_{1,r}|} = \left| \frac{\langle \hat{\mathbf{f}}_o, \hat{\mathbf{a}}_1 \rangle}{\langle \hat{\mathbf{q}}_1, \hat{\mathbf{a}}_1 \rangle} \right| \frac{1}{|\sigma_{1,r}|},$$

which is different from the norm of the resolvent operator, i.e, $1/\epsilon_o$. Thus, even the matching with the linear regime is not guaranteed with this classical, modal approach.

2.4.5 Uniqueness of the operator perturbation

A sort of "proof by contradiction" is proposed : we will perturb $R(i\omega_o)^{-1}$ with an operator of size larger than its minimum value ϵ_o and show that the subsequent amplitude equation leads to an inconsistent result.

It follows from $R(i\omega_o)^{-1}\hat{\mathbf{u}}_o = \epsilon_o\hat{\mathbf{f}}_o$ in (2.4) that

$$\left[R(i\omega_o)^{-1} - \frac{\epsilon_o}{\langle \hat{\mathbf{g}} | \hat{\mathbf{u}}_o \rangle} \hat{\mathbf{f}}_o \langle \hat{\mathbf{g}} | * \rangle \right] \hat{\mathbf{u}}_o = \mathbf{0} \quad (2.32)$$

holds for all the possible choices of $\hat{\mathbf{g}}$ (in the main text we chose $\hat{\mathbf{g}} = \hat{\mathbf{u}}_o$). Without loss of generality we impose $\|\hat{\mathbf{g}}\|^2 = 1$. Let us write $\langle \hat{\mathbf{g}} | \hat{\mathbf{u}}_o \rangle = |\langle \hat{\mathbf{g}} | \hat{\mathbf{u}}_o \rangle| e^{i\alpha}$ and define $\varepsilon \doteq \epsilon_o / |\langle \hat{\mathbf{g}} | \hat{\mathbf{u}}_o \rangle| \geq \epsilon_o$, which is necessarily larger than or equal to ϵ_o . We pick a $\hat{\mathbf{g}}$ such that $\varepsilon \ll 1$, and select ε as our new small parameter. We can define the singular operator as

$$\Phi \doteq R(i\omega_o)^{-1} - \varepsilon P, \quad \text{where } P = e^{-i\alpha} \hat{\mathbf{f}}_o \langle \hat{\mathbf{g}} | * \rangle, \quad (2.33)$$

(implying $\|P\| = 1$). We clearly still have $\Phi \hat{\mathbf{u}}_o = \mathbf{0}$, and we can show that $\Phi^\dagger \hat{\mathbf{a}} = \mathbf{0}$ with $\hat{\mathbf{a}} \doteq R(i\omega_o)^\dagger \hat{\mathbf{g}}$ (indeed if $\hat{\mathbf{g}} = \hat{\mathbf{u}}_o$, we have $\hat{\mathbf{a}} = \hat{\mathbf{f}}_o$). We can perform the exact same asymptotic expansion as in the main text, replacing the small parameter ϵ_o by ε everywhere. In particular, the NSEs are forced by $\mathbf{F} = \sqrt{\varepsilon^3} \hat{\mathbf{f}}_h e^{i\omega_o t} + c.c.$ The amplitude equation that we would eventually obtain is

$$\frac{1}{\eta} \frac{dA}{dT} = \phi \langle \hat{\mathbf{a}} | \hat{\mathbf{f}}_h \rangle - |\langle \hat{\mathbf{g}} | \hat{\mathbf{u}}_o \rangle| \langle \hat{\mathbf{a}} | \hat{\mathbf{f}}_o \rangle A - \frac{\mu + \nu}{\eta} A |A|^2, \quad (2.34)$$

with the coefficients

$$\eta = \frac{1}{\langle \hat{\mathbf{a}} | \hat{\mathbf{u}}_o \rangle}, \quad \frac{\mu}{\eta} = \langle \hat{\mathbf{a}} | 2C(\hat{\mathbf{u}}_o, \mathbf{u}_{2,0}) \rangle, \quad \frac{\nu}{\eta} = \langle \hat{\mathbf{a}} | 2C(\hat{\mathbf{u}}_o^*, \hat{\mathbf{u}}_{2,2}) \rangle \quad (2.35)$$

In the linear regime, the equilibrium solution of this amplitude equation is

$$A = \phi \langle \hat{\mathbf{a}} | \hat{\mathbf{f}}_h \rangle / (|\langle \hat{\mathbf{g}} | \hat{\mathbf{u}}_o \rangle| \langle \hat{\mathbf{a}} | \hat{\mathbf{f}}_o \rangle), \quad (2.36)$$

which leads to a linear gain of

$$G = \frac{\|\sqrt{\varepsilon} A \hat{\mathbf{u}}_o\|}{\|\phi \sqrt{\varepsilon^3} \hat{\mathbf{f}}_h\|} = \frac{1}{\varepsilon} \frac{|\langle \hat{\mathbf{a}} | \hat{\mathbf{f}}_h \rangle|}{|\langle \hat{\mathbf{g}} | \hat{\mathbf{u}}_o \rangle| |\langle \hat{\mathbf{a}} | \hat{\mathbf{f}}_o \rangle|} = \frac{1}{\varepsilon_o} \frac{|\langle \hat{\mathbf{a}} | \hat{\mathbf{f}}_h \rangle|}{|\langle \hat{\mathbf{a}} | \hat{\mathbf{f}}_o \rangle|} \quad (2.37)$$

If we force the flow with the optimal forcing structure $\hat{\mathbf{f}}_h = \hat{\mathbf{f}}_o$, we indeed recover the linear gain $G = 1/\varepsilon_o$. However, the contradiction lies in the fact if we choose to force with $\hat{\mathbf{f}}_h = \hat{\mathbf{a}}$ instead, the linear gain becomes $G = (1/\varepsilon_o) / |\langle \hat{\mathbf{a}} | \hat{\mathbf{f}}_o \rangle| \geq 1/\varepsilon_o$, meaning that we found a forcing structure that led to a larger gain than $\hat{\mathbf{f}}_o$, which is by definition impossible. To guarantee the consistency of our amplitude equation (which must predict the correct linear gain), we must have $\hat{\mathbf{a}} = \hat{\mathbf{f}}_o$, which implies directly $\hat{\mathbf{g}} = \hat{\mathbf{u}}_o$ and $\varepsilon = \varepsilon_o$. As a corollary, $\hat{\mathbf{a}} = \hat{\mathbf{f}}_o$ is also the only choice that guarantees the consistency between the amplitude equation and the sensitivity formula shown in Appendix 2.4.1.

Response to a stochastic forcing **Part II**

3 A non-modal weakly nonlinear amplitude equation for the variance maintained by a stochastic forcing

3.1 Introduction

Some flows experience a transition from laminar to turbulent far below the threshold predicted by linear stability theory, which relies on the eigenvalues of the linearised Navier-Stokes operator. In addition, the value of the bifurcation parameter at the transition strongly depends on the level of external noise. Among them are the canonical Couette and Poiseuille parallel shear flows, as detailed in Schmid and Henningson (2001). Non-parallel flows such as jets and the backward-facing step (BFS) flow, studied for instance in Garnaud et al. (2013a) and Blackburn et al. (2008), should also be mentioned. The transition scenario advanced in Trefethen et al. (1993) relies on the non-normality property of the linearised Navier-Stokes operator. The latter implies that a linearly stable flow can nevertheless strongly amplify a small initial structure or a sustained forcing term through non-modal mechanisms (see Schmid (2007) for a review). Thereby, the response may be carried into a regime where nonlinearities set in and the flow escapes from its linearly stable solution.

In this perspective, numerous studies have computed the small-amplitude structures that are the *most amplified* by the flow: initial conditions, harmonic forcing or stochastic forcing, resulting, respectively, in the optimal transient growth, harmonic gain and stochastic gain. Formally, such studies generally consist in finding the singular mode of a specific linear operator, which can be very different from the eigenmodes of the linearised Navier-Stokes operator. For the harmonic forcing problem, one could for instance refer to the work of Schmid and Henningson (2001) and Jovanović and Bamieh (2005) on the parallel plane Couette and Poiseuille flows. The problem of the flow response to a stochastic forcing, studied in the rest of this chapter, mimics more realistic situations. Indeed, unpredictable noise may arise from

different sources in Nature such as residual turbulence, variation of atmospheric conditions, acoustic disturbances, geometrical defects, and many others. The response to white noise has for instance been considered for the plane Couette and Poiseuille flow in Farrell and Ioannou (1993), and in Boujo and Gallaire (2015), Dergham et al. (2013), and Mantič-Lugo and Gallaire (2016a) for the backward-facing step (BFS) flow. Owing to the non-normality of the linearised operator, all these flows can sustain a large variance even if the noise intensity is comparatively weak.

In the linear paradigm, however, amplifications do not depend on the amplitude of the initial condition or forcing. The latter are assumed arbitrarily small, such that nonlinear terms are negligible. Therefore, the nonlinear interactions involved in the subcritical transition or in the saturation process cannot be captured by definition. For this reason, more elaborate models accounting for a nonlinear coupling between the mean flow and the linear perturbation have been proposed. For instance, Marston et al. (2008) considered a barotropic flow on a rotating sphere, and performed a cumulant expansion of the vorticity statistics that was closed by neglecting the third and higher cumulants; this amounts to neglecting the fluctuation-fluctuation interactions while retaining the fluctuation-mean flow interactions. By comparison with statistics accumulated directly in the direct numerical simulations (DNS), Marston et al. (2008) showed that this truncation was well justified in certain regimes (see their fig. 5 and 6), for instance when the relaxation time towards a zonal jet was short, in which case the fluctuations were suppressed by the strong coupling to the jet.

Instead of being neglected, the fluctuation-fluctuation interactions are sometimes replaced by a stochastic parametrisation, for instance white noise, as originally done in Farrell and Ioannou (2003). This led to the stochastic structural stability theory (S3T or SSST), which was, for instance, able to describe sustained coherent structures appearing during the transition to turbulence in two-dimensional atmospheric flows, as well as in three-dimensional parallel Couette flow (Farrell & Ioannou, 2012). In these shear flows, the success of the SSST theory, despite the fact that modelling the fluctuation-fluctuation interactions as white noise seems to be an oversimplification, is explained as follows in Farrell and Ioannou (2019):

"In the case of homogeneous isotropic turbulence the stochastic excitation must be very carefully fashioned in order to obtain approximately valid statistics using a stochastic closure [...] while in shear flow the form of the stochastic excitation is not crucial. The reason is that in shear flow the [Navier-Stokes] operator [linearized around the mean flow] is non-normal and a restricted set of perturbations participate strongly in the interaction with the mean flow. As a result the statistical state of the turbulence is primarily determined by the quasilinear interaction between the mean and these perturbations rather than by nonlinear interaction among the perturbations".

This "quasi-linear" approach, which consists in allowing fluctuations-mean flow interactions and either neglecting or modelling other interactions, has been extended to a resolvent-based approach applied to a turbulent pipe flow in McKeon and Sharma (2010). The Navier-Stokes

equations (NSE) were re-formulated as a nonlinear equation for the mean velocity, and an input-output equation for the fluctuation, where the latter is the linear response to a forcing term modelling the nonlinear fluctuating term through the resolvent operator around the mean velocity. The closure problem for the mean flow equation is avoided by knowing *a priori* the mean profile from experimental data. Following an argument essentially similar to the one quoted above from Farrell and Ioannou (2019), when the resolvent operator is low-rank, in the sense that there exists a small set of forcing-response pairs of modes associated with gains much larger than all the others, the fluctuation can be well approximated as a combination of these leading response modes.

This type of mean flow-resolvent analysis has been performed by numerous authors since then and has often proven successful in reproducing the main features of self-sustained turbulence. This was the case for the turbulent jet studied in Pickering et al. (2020), where the resolvent mode around a mean-flow eddy-viscosity model projected well on the spectral proper orthogonal decomposition (SPOD) modes that optimally describe the turbulent flow statistics from large eddy simulation (LES) data. Note that, because of the non-normality of the resolvent operator, strong amplification may occur even in the absence of a dominant eigenvalue in the (eigen)spectrum of the linearised Navier-Stokes operator around the mean flow; for this reason, the question of the relevance of a stability analysis around the mean flow is discussed in Symon et al. (2018). Recently, a resolvent-based approach was also adopted in Rosenberg and McKeon (2019) to compute traveling waves in Couette and Poiseuille flow. Instead of assuming the mean flow to be known *a priori*, the coupled system was solved iteratively, requiring only the knowledge of the traveling wave speed and amplitude. Note that the latter approach is conceptually very similar to that adopted in Mantič-Lugo et al. (2014). The only difference lies in the fact that fluctuations-fluctuations interactions are neglected in the equation for the fluctuation in Mantič-Lugo et al., 2014, whereas they are treated as a forcing term whose response is solely along the leading resolvent mode in Rosenberg and McKeon (2019).

The quasi-linear assumption that the dominant nonlinear mechanism is the Reynolds stress feedback onto the mean flow excludes, for instance, systems with strong harmonic generation and subharmonic excitation, as illustrated in Meliga (2017). It has also proven to be in default in Tobias and Marston (2013) in the case of turbulent zonal jets that are driven too far from equilibrium (for which the rates of forcing and dissipation go to zero). A generalisation has been proposed in Marston et al. (2016), leading to a system constituted of a nonlinear equation for the slowly varying part of the velocity field (instead of just the mean flow), and a linear equation for the rapidly varying part (instead of the entire fluctuations); in this manner, the small scales can exchange energy with each other, through their interaction with the large scales. With a sufficiently large number of modes included in the slowly varying, this generalised model converges and improves the predictions, at an increased numerical cost.

Amplitude equations for the response of nonlinear systems to stochastic forcing constitute another class of modelling techniques, in principle restricted to the weakly nonlinear regime,

but much cheaper to implement. The technique was developed for instance in Rajan and Davies (1988) and Nayfeh and Serhan (1990) using the method of multiple scales and/or stochastic averaging on the Duffing and Duffing-Rayleigh oscillators, respectively. Similar to their deterministic counterparts, however, the possibility to construct these simplified equations relies on the existence of a resonant frequency, as they describe the slowly varying modulation of the associated eigenmode.

In chapter 2, we derived an amplitude equation to extend the linear harmonic gain curve in a weakly nonlinear regime by increasing the forcing amplitude. The method does not rely on modal quantities, in contrast to classical techniques, and the present chapter aims at generalising this method to the response to stochastic forcing. Namely, by assuming the linearized system to exhibit a large response-to-forcing variance gain, we derive an equation for its weakly nonlinear evolution as we increase the variance of the stochastic forcing. This amounts to adapting the method proposed in chapter 2 to a slightly more general inner product.

No assumptions will be made on the dominant nonlinear interaction mechanisms, and the Fourier (frequency) components of the linear response can be arbitrarily different from eigenmodes as long as the linear operator is sufficiently non-normal. The weakly nonlinear evolution of the variance of the flow response to stochastic forcing can be determined at a numerical cost considerably lower than that of a direct numerical simulation (DNS).

3.2 Linear regime

Let us first characterize the stochastic response of the flow in the linear regime, whose weakly nonlinear continuation will be studied subsequently. A perturbative flow velocity field \mathbf{u} , around a fixed point \mathbf{U}_e , forced also at perturbative level by \mathbf{f} , is governed by the linear equation

$$\partial_t \mathbf{u} = L\mathbf{u} + \mathbf{f}, \quad (3.1)$$

where L results from the linearisation of the Navier-Stokes equations around \mathbf{U}_e . Specifically, $L\mathbf{u} = -(\mathbf{U}_e \cdot \nabla)\mathbf{u} - (\mathbf{u} \cdot \nabla)\mathbf{U}_e + Re^{-1}\Delta\mathbf{u} - \nabla p(\mathbf{u})$, where Re is the Reynolds number, and where the pressure field p is such that the velocity field \mathbf{u} is divergence-free. Note that both fields are linked through a linear Poisson equation. In practice, p is included in the state variable, resulting in a singular mass matrix, omitted here for the sake of clarity.

The specific form $\mathbf{f}(\mathbf{x}, t; \theta) = \mathbf{f}_s(\mathbf{x})\xi(t; \theta)$ is chosen for the stochastic forcing, where $\mathbf{f}_s(\mathbf{x})$ is the forcing spatial structure and $\xi(t; \theta)$ a scalar random process. The symbol θ designates a random variable, following a certain probability law. Two different values taken by the random variable θ correspond to two different realisations of the random process. The process $\xi(t; \theta)$ may be a delta-correlated white noise, but is not necessarily.

We insist that the form of stochastic forcing $\mathbf{f}(\mathbf{x}, t; \theta) = \mathbf{f}_s(\mathbf{x})\xi(t; \theta)$, considered here, describes a very specific excitation with typically a strong spatial correlation, and there exist more general modelisations. For instance, a more complete description of an actual stochastic forcing could be obtained by summing $\mathbf{f}(\mathbf{x}, t; \theta) = \sum_j \mathbf{f}_{s,j}(\mathbf{x})\xi_j(t; \theta_j)$ together with spatio-temporal covariance matrices.

We introduce the Fourier transform $\mathcal{F}(\bullet)$ of a temporal signal of length $[0, T]$ with $T \rightarrow \infty$, and its inverse $\mathcal{F}^{-1}(\bullet)$, as

$$\hat{\mathbf{u}}(\omega) = \mathcal{F}(\mathbf{u}(t)) = \frac{1}{\sqrt{T}} \int_0^T \mathbf{u}(t) e^{-i\omega t} dt, \quad \mathbf{u}(t) = \mathcal{F}^{-1}(\hat{\mathbf{u}}(\omega)) = \frac{\sqrt{T}}{2\pi} \int_{-\infty}^{\infty} \hat{\mathbf{u}}(\omega) e^{i\omega t} d\omega, \quad (3.2)$$

respectively. By computing

$$\begin{aligned} \mathcal{F}^{-1}(\mathcal{F}(\mathbf{u}(t))) &= \frac{\sqrt{T}}{2\pi} \int_{-\infty}^{\infty} \frac{1}{\sqrt{T}} \int_0^T \mathbf{u}(b) e^{-i\omega b} db e^{i\omega t} d\omega \\ &= \frac{1}{2\pi} \int_{-\infty}^{\infty} \int_0^T \mathbf{u}(b) e^{i\omega(t-b)} db d\omega \\ &= \frac{1}{2\pi} \int_0^T \mathbf{u}(b) \int_{-\infty}^{\infty} e^{i\omega(t-b)} d\omega db, \end{aligned} \quad (3.3)$$

we verify that $\mathcal{F}^{-1}(\mathcal{F}(\mathbf{u}(t))) = \mathbf{u}(t)$ if and only if we adopt the following interpretation of the Dirac impulse δ

$$\int_{-\infty}^{\infty} e^{i\omega(t-b)} d\omega = 2\pi \delta(t-b), \quad (3.4)$$

where $\delta(t-b)$ has an infinite amplitude if $t=b$, and is null otherwise. This way,

$$\mathcal{F}^{-1}(\mathcal{F}(\mathbf{u}(t))) = \int_0^T \mathbf{u}(b) \delta(t-b) db = \mathbf{u}(t). \quad (3.5)$$

We assume the stochastic process $\xi(t; \theta)$ to be statistically steady, such that we can characterize it in the Fourier domain as

$$\{|\hat{\xi}(\omega; \theta)|^2\} = g(\omega), \quad (3.6)$$

where $\{\bullet\}$ denotes the ensemble average over the different realisations, and where $g(\omega)$ is the given power spectral density (PSD) of the process $\xi(t; \theta)$. We show in Appendix 3.6.1 that (3.6) is equivalent in the temporal domain to

$$\{\overline{\xi(t; \theta)\xi(t+s; \theta)}\} = \frac{1}{2\pi} \int_{-\infty}^{\infty} g(\omega) e^{i\omega s} d\omega, \quad (3.7)$$

where the overbar denotes the temporal ensemble average, i.e.

$$\bar{\bullet} = \frac{1}{T} \int_0^T \bullet dt. \quad (3.8)$$

In the following, we denote by $\|\cdot\|$ the L^2 norm induced by the Hermitian inner product $\langle \hat{\mathbf{u}}_a | \hat{\mathbf{u}}_b \rangle = \int_{\Omega} \hat{\mathbf{u}}_a^H \hat{\mathbf{u}}_b d\Omega$ (the superscript H denotes the Hermitian transpose). A relevant measure of input-output gain of the system (3.1) under stochastic forcing, is the ratio of the mean square (that we call "variance" in the following by abuse of language) of the statistically steady response, $\{\overline{\|\mathbf{u}(t;\theta)\|^2}\}$, over that of the forcing, $\{\overline{\|\mathbf{f}_s \xi(t;\theta)\|^2}\}$. Importantly, the variance can also be seen as the norm induced by the inner product measuring the resemblance between two stochastic fields $\mathbf{h}(t;\theta)$ and $\mathbf{g}(t;\theta)$ as

$$\begin{aligned} \overline{\langle \mathbf{h}(t;\theta) | \mathbf{g}(t;\theta) \rangle} &= \left\{ \frac{1}{T} \int_0^T \int_{\Omega} \mathbf{h}(t;\theta)^H \mathbf{g}(t;\theta) d\Omega dt \right\} \\ &= \left\{ \frac{1}{2\pi} \int_{-\infty}^{\infty} \int_{\Omega} \hat{\mathbf{h}}(\omega;\theta)^H \hat{\mathbf{g}}(\omega;\theta) d\Omega d\omega \right\} \\ &= \{ [\langle \hat{\mathbf{h}}(\omega;\theta) | \hat{\mathbf{g}}(\omega;\theta) \rangle] \}, \end{aligned} \quad (3.9)$$

where we have introduced the operation $[\bullet]$, a normalized integration over the frequencies as

$$[\bullet] = \frac{1}{2\pi} \int_{-\infty}^{\infty} \bullet d\omega. \quad (3.10)$$

The transformation from integrating over time to integrating over the frequencies, used in (3.9), is demonstrated in Appendix 3.6.2 and ensues from the definition of the Fourier transforms (Parseval's theorem).

Optimising over the forcing structure \mathbf{f}_s , the maximum variance amplification attainable by the system reads

$$G = \max_{\mathbf{f}_s} \frac{\overline{\|\mathbf{u}(t;\theta)\|^2}}{\overline{\|\mathbf{f}_s \xi(t;\theta)\|^2}} = \max_{\mathbf{f}_s} \frac{\{[\|\hat{\mathbf{u}}(\omega;\theta)\|^2]\}}{\{[\|\mathbf{f}_s \hat{\xi}(\omega;\theta)\|^2]\}} = \frac{1}{\epsilon_o^2}, \quad (3.11)$$

where we defined ϵ_o as the inverse of the square root of the maximum stochastic gain G . Furthermore, in the statistically steady regime, (3.1) can be solved in the Fourier domain as $\hat{\mathbf{u}}(\omega;\theta) = \hat{\xi}(\omega;\theta) R(\omega) \mathbf{f}_s$, where

$$R(\omega) \doteq (i\omega I - L)^{-1} \quad (3.12)$$

is the resolvent operator. The gain (3.11) can be re-expressed

$$G = \max_{\mathbf{f}_s} \frac{\{[\langle \mathbf{f}_s | \hat{\xi}(\omega;\theta)^2 R(\omega)^\dagger R(\omega) \mathbf{f}_s \rangle]\}}{\{[\langle \mathbf{f}_s | \hat{\xi}(\omega;\theta)^2 \mathbf{f}_s \rangle]\}} = \frac{1}{[g(\omega)]} \max_{\mathbf{f}_s} \frac{\langle \mathbf{f}_s | B^\infty \mathbf{f}_s \rangle}{\|\mathbf{f}_s\|^2}, \quad (3.13)$$

where we have defined the operator

$$B^\infty = \frac{1}{2\pi} \int_{-\infty}^{\infty} g(\omega) R(\omega)^\dagger R(\omega) d\omega = [g(\omega) R(\omega)^\dagger R(\omega)]. \quad (3.14)$$

The operator $R(\omega)^\dagger$ denotes the adjoint of $R(\omega)$ under the L^2 inner product, such that $\langle R(\omega) \hat{\mathbf{u}}_a | \hat{\mathbf{u}}_b \rangle = \langle \hat{\mathbf{u}}_a | R(\omega)^\dagger \hat{\mathbf{u}}_b \rangle$ for all $\hat{\mathbf{u}}_a, \hat{\mathbf{u}}_b$ in the domains of $R(\omega)$ and $R(\omega)^\dagger$, respectively. The operator B^∞ is positive definite, Hermitian with positive and real eigenvalues associated with mutually orthogonal eigenvectors.

The maximum gain (3.13) is the largest eigenvalue of B^∞ divided by $[g(\omega)]$. The associated eigenvector, denoted \mathbf{f}_o and normalised as

$$\langle \mathbf{f}_o | [g(\omega)] \mathbf{f}_o \rangle = \|\mathbf{f}_o\|^2 [g(\omega)] = 1, \quad (3.15)$$

is the optimal forcing structure (hence the subscript "o"), i.e. the forcing structure that leads to the largest stochastically variance amplification. In other terms,

$$B^\infty \mathbf{f}_o = G[g(\omega)] \mathbf{f}_o = \frac{[g(\omega)]}{\epsilon_o^2} \mathbf{f}_o, \quad \text{implying} \quad \langle \mathbf{f}_o | B^\infty \mathbf{f}_o \rangle = \frac{1}{\epsilon_o^2}. \quad (3.16)$$

We further assume that the largest eigenvalue of B^∞ is much larger than all the others, which corresponds to sub-optimal gains. In this manner, if the actual (unknown) forcing of the system does not promote a particular sub-optimal eigenmode of B^∞ , but projects comparably on all of them, then the response to the actual forcing is expected to be dominated by the response to the optimal forcing \mathbf{f}_o . This was demonstrated in (1.59) in the introductory part of this thesis. This low-rank approximation is commonly done and well justified for strongly non-normal operators (Symon et al., 2018), and explains why we restrict our analysis to the response to $\xi(t; \theta) \mathbf{f}_o$ and do not include additional forcing modes.

By linearity, forcing the system (3.1) with $\mathbf{f}(t; \theta) = \epsilon_o \xi(t; \theta) \mathbf{f}_o$, where we recall that we have defined $\epsilon_o \doteq 1/\sqrt{G}$, leads to a response $\mathbf{l}(t; \theta)$ of unit variance, i.e.

$$\overline{\|\mathbf{l}(t; \theta)\|^2} = \{ \overline{\|\hat{\mathbf{l}}(\omega; \theta)\|^2} \} = \epsilon_o^2 \langle \mathbf{f}_o | B^\infty \mathbf{f}_o \rangle = 1, \quad (3.17)$$

where we used the expression of the linear response in the Fourier domain,

$$\hat{\mathbf{l}}(\omega; \theta) = \epsilon_o \hat{\xi}(\omega; \theta) R(\omega) \mathbf{f}_o, \quad \text{or, equivalently,} \quad R(\omega)^{-1} \hat{\mathbf{l}}(\omega; \theta) = \epsilon_o \hat{\xi}(\omega; \theta) \mathbf{f}_o. \quad (3.18)$$

Since L is strongly non-normal, as assumed in the rest of the present study, none of ϵ_o or \mathbf{f}_o are immediately determined from its spectral (modal) properties; furthermore, strong non-normality typically implies $\epsilon_o \ll 1$ (Farrell & Ioannou, 1993).

It follows from the second equation in (3.18) that the inverse resolvent maps a field of unit norm (induced by the inner product (3.9)), according to (3.17), on a field of norm ϵ_o , according to (3.15). Since ϵ_o is by assumption very small, this suggests that the inverse resolvent is close to

Chapter 3 A non-modal amplitude equation for the variance of the stochastic response

being singular, if "close" refers to the induced norm in question. Thereby, it is mathematically justified to construct a singular operator $\Phi(\omega; \theta)$ as a perturbation of the inverse resolvent, expressing

$$\begin{aligned}\Phi(\omega; \theta)(\bullet) &= R(\omega)^{-1} \bullet - \epsilon_o P(\omega; \theta)(\bullet), \quad \text{where} \\ P(\omega; \theta)(\bullet) &= \hat{\xi}(\omega; \theta) \mathbf{f}_o \{ \{ \langle \hat{\mathbf{l}}(\omega; \theta) | \bullet \rangle \} \},\end{aligned}\tag{3.19}$$

where $\Phi(\omega; \theta)(\bullet)$ simply means that the operator $\Phi(\omega; \theta)$ is applied on some field \bullet . The parenthesis are included to highlight the fact that, for some scalar $A(\omega; \theta)$ and some field $\hat{\mathbf{g}}(\omega; \theta)$

$$\Phi(\omega; \theta)(A(\omega; \theta) \hat{\mathbf{g}}(\omega; \theta)) \neq A(\omega; \theta) \Phi(\omega; \theta)(\hat{\mathbf{g}}(\omega; \theta)),\tag{3.20}$$

for the application of $\Phi(\omega; \theta)$ involves an integration over the frequencies and an ensemble average. Only if A is a deterministic scalar that does not depend on the frequency, can we write

$$\Phi(\omega; \theta)(A \hat{\mathbf{g}}(\omega; \theta)) = A \Phi(\omega; \theta)(\hat{\mathbf{g}}(\omega; \theta)),\tag{3.21}$$

(and same for $P(\omega; \theta)(\bullet)$). The linear operator $P(\omega; \theta)(\bullet)$ is such that

$$P(\omega; \theta)(\hat{\mathbf{l}}(\omega; \theta)) = \hat{\xi}(\omega; \theta) \mathbf{f}_o \underbrace{\{ \{ \langle \hat{\mathbf{l}}(\omega; \theta) | \hat{\mathbf{l}}(\omega; \theta) \rangle \} \}}_{=1 \text{ by (3.17)}} = \hat{\xi}(\omega; \theta) \mathbf{f}_o.\tag{3.22}$$

Therefore,

$$\Phi(\omega; \theta)(\hat{\mathbf{l}}(\omega; \theta)) = R(\omega)^{-1} \hat{\mathbf{l}}(\omega; \theta) - \epsilon_o P(\omega; \theta)(\hat{\mathbf{l}}(\omega; \theta)) = R(\omega)^{-1} \hat{\mathbf{l}}(\omega; \theta) - \hat{\xi}(\omega; \theta) \mathbf{f}_o = \mathbf{0}.\tag{3.23}$$

In other words, $\Phi(\omega; \theta)$ is a singular operator with $\hat{\mathbf{l}}(\omega; \theta)$ as a non-trivial kernel. Its adjoint operator $\Phi(\omega; \theta)^\dagger(\bullet)$, under the inner product (3.9), is such that

$$\{ \{ \langle \Phi(\omega; \theta)(\hat{\mathbf{g}}(\omega; \theta)) | \hat{\mathbf{h}}(\omega; \theta) \rangle \} \} = \{ \{ \langle \hat{\mathbf{g}}(\omega; \theta) | \Phi(\omega; \theta)^\dagger(\hat{\mathbf{h}}(\omega; \theta)) \rangle \} \}, \forall \hat{\mathbf{g}} \in \mathcal{D}(\Phi), \hat{\mathbf{h}} \in \mathcal{D}(\Phi^\dagger).\tag{3.24}$$

It is written

$$\begin{aligned}\Phi(\omega; \theta)^\dagger(\bullet) &= (R(\omega)^{-1})^\dagger \bullet - \epsilon_o P(\omega; \theta)^\dagger(\bullet) \quad \text{where} \\ P(\omega; \theta)^\dagger(\bullet) &= \hat{\mathbf{l}}(\omega; \theta) \{ \{ \langle \hat{\xi}(\omega; \theta) \mathbf{f}_o | \bullet \rangle \} \}.\end{aligned}\tag{3.25}$$

Furthermore, we show in appendix 3.6.4 that the stochastic field

$$\hat{\mathbf{a}}(\omega; \theta) = \epsilon_o R(\omega)^\dagger \hat{\mathbf{l}}(\omega; \theta), \quad \text{is such that} \quad \Phi(\omega; \theta)^\dagger(\hat{\mathbf{a}}(\omega; \theta)) = \mathbf{0}.\tag{3.26}$$

In other terms, $\hat{\mathbf{a}}(\omega; \theta)$ is the non-trivial kernel of the adjoint operator $\Phi(\omega; \theta)^\dagger(\bullet)$.

Expansion (3.19) is *a priori* justified in the sense that the induced-norm of the operator P is $\{ \{ \|P\|^2 \} \} = 1$ (shown in Appendix 3.6.3), and thus the operator perturbation (3.19) is of size ϵ_o ,

indeed small by assumption.

Note that perturbation (3.19) is essence similar to that in (2.5), extended to a more general inner product, involving an integration over the frequencies and an ensemble average in addition to integrating over space. Consequently, the computations proposed in the next section, in the weakly nonlinear regime, are close to those outlined in chapter 2.

3.3 Weakly nonlinear regime

In this section, we suggest a procedure to derive a weakly nonlinear equation for the amplitude of the linear stochastic response. We illustrate the method directly on the incompressible Navier-Stokes equations, which we recall to be

$$\partial_t \mathbf{U} = -C(\mathbf{U}, \mathbf{U}) - \nabla p + \text{Re}^{-1} \Delta \mathbf{U} + F \xi(t; \theta) \mathbf{f}_h, \quad (3.27)$$

with the nonlinear, bilinear operator

$$C(\mathbf{x}, \mathbf{y}) = \frac{1}{2} ((\mathbf{x} \cdot \nabla) \mathbf{y} + (\mathbf{y} \cdot \nabla) \mathbf{x}). \quad (3.28)$$

The stochastic forcing is such that $\xi(t; \theta) \mathbf{f}_h$ has a unit variance, i.e.

$$\overline{\|\xi(t; \theta) \mathbf{f}_h\|^2} = \{ \|\hat{\xi}(\omega; \theta) \mathbf{f}_h\|^2 \} = \|\mathbf{f}_h\|^2 [g(\omega)] = 1. \quad (3.29)$$

This way, the variance of the stochastic forcing $F \xi(t; \theta) \mathbf{f}_h$ is directly given by F^2 . The forcing structure \mathbf{f}_h is for now unspecified. In what follows, we assume F to be small, which is quantified by scaling

$$F = \phi \sqrt{\epsilon_o^3}, \quad (3.30)$$

where the prefactor $\phi = O(1)$ sets the forcing variance. Thereby we seek a solution for the response in the statistically steady regime under the form of the following multiple-scale asymptotic expansion,

$$\begin{aligned} \mathbf{U}(t, T_2, T_3; \theta) = & \mathbf{U}_b + \sqrt{\epsilon_o} \mathbf{u}_1(t, T_2, T_3; \theta) + \epsilon_o \mathbf{u}_2(t, T_2, T_3; \theta) \\ & + \sqrt{\epsilon_o^3} \mathbf{u}_3(t, T_2, T_3; \theta) + O(\epsilon_o^2). \end{aligned} \quad (3.31)$$

where we introduced the slow time scales $T_2 = \sqrt{\epsilon_o} t$ and $T_3 = \epsilon_o t$ and where \mathbf{U}_b is a stable fixed point of the Navier-Stokes equations. We inject both (3.30) and (3.31) in the Navier-Stokes equations (3.27), and take the Fourier transform (with respect to t) of the resulting expansion,

leading to

$$\begin{aligned} & \sqrt{\epsilon_o} (R^{-1} \hat{\mathbf{u}}_1) + \\ & \epsilon_o (R^{-1} \hat{\mathbf{u}}_2 + \partial_{T_2} \hat{\mathbf{u}}_1 + \mathcal{F}(C(\mathbf{u}_1, \mathbf{u}_1))) + \\ & \sqrt{\epsilon_o^3} (R^{-1} \hat{\mathbf{u}}_3 + \partial_{T_3} \hat{\mathbf{u}}_1 + \partial_{T_2} \hat{\mathbf{u}}_2 + 2\mathcal{F}(C(\mathbf{u}_2, \mathbf{u}_1)) - \phi \hat{\xi} \mathbf{f}_h) + O(\epsilon_o^2) = \mathbf{0}. \end{aligned} \quad (3.32)$$

By perturbing the inverse resolvent operator as in (3.19), expansion (3.32) becomes

$$\begin{aligned} & \sqrt{\epsilon_o} (\Phi(\hat{\mathbf{u}}_1)) + \\ & \epsilon_o (\Phi(\hat{\mathbf{u}}_2) + \partial_{T_2} \hat{\mathbf{u}}_1 + \mathcal{F}(C(\mathbf{u}_1, \mathbf{u}_1))) + \\ & \sqrt{\epsilon_o^3} (\Phi(\hat{\mathbf{u}}_3) + \partial_{T_3} \hat{\mathbf{u}}_1 + \partial_{T_2} \hat{\mathbf{u}}_2 + 2\mathcal{F}(C(\mathbf{u}_2, \mathbf{u}_1)) + P(\hat{\mathbf{u}}_1) - \phi \hat{\xi} \mathbf{f}_h) + O(\epsilon_o^2) = \mathbf{0}. \end{aligned} \quad (3.33)$$

At order $\sqrt{\epsilon_o}$ in (3.33), the following homogeneous equation as to be satisfied

$$\Phi(\omega; \theta) (\hat{\mathbf{u}}_1(\omega, T_2, T_3; \theta)) = \mathbf{0}. \quad (3.34)$$

Its general solution consists of an arbitrary component on the kernel of Φ , i.e.

$$\begin{aligned} \hat{\mathbf{u}}_1(\omega, T_2, T_3; \theta) &= A(T_2, T_3) \hat{\mathbf{l}}(\omega; \theta), \quad \text{writing in the temporal domain,} \\ \mathbf{u}_1(t, T_2, T_3; \theta) &= A(T_2, T_3) \mathbf{l}(t; \theta), \end{aligned} \quad (3.35)$$

where $A(T_2, T_3)$ is an arbitrary scalar that solely depends on the slow times scales. It is important to notice that A can't depend on the stochastic argument θ , for $A(T_2, T_3; \theta) \hat{\mathbf{l}}(\omega; \theta)$ does not belong to the kernel of Φ for the reason evoked when describing (3.20).

Pursuing the development up to $O(\epsilon_o)$ leads to solving

$$\Phi(\hat{\mathbf{u}}_2) = -\partial_{T_2} \hat{\mathbf{u}}_1 - \mathcal{F}(C(\mathbf{u}_1, \mathbf{u}_1)) = -\hat{\mathbf{l}} \partial_{T_2} A - A^2 \mathcal{F}(C(\mathbf{l}, \mathbf{l})). \quad (3.36)$$

For $\hat{\mathbf{u}}_2$ to yield a non-diverging particular solution, the right-hand side in (3.36) must be orthogonal to the kernel of the adjoint operator Φ^\dagger . This orthogonality must hold under the inner product (3.9), for it is under this inner product that Φ^\dagger was constructed in (3.24). This leads to an equation for the partial derivative of A with respect to T_2

$$\eta \frac{\partial A}{\partial T_2} = \mu_2 A^2, \quad (3.37)$$

where we have defined the (deterministic) coefficients η and μ_2 as

$$\eta = \{ \{ \langle \hat{\mathbf{a}}(\omega; \theta) | \hat{\mathbf{l}}(\omega; \theta) \rangle \} \} \quad (3.38)$$

and

$$\begin{aligned}
 \mu_2 &= -\left\{ \left\langle \hat{\mathbf{u}}(\omega; \theta) \middle| \mathcal{F}(C(\mathbf{l}, \mathbf{l}))(\omega; \theta) \right\rangle \right\} \\
 &= \left\{ \left\langle \hat{\mathbf{l}}(\omega; \theta) \middle| \hat{\mathbf{u}}_2^{A^2}(\omega; \theta) \right\rangle \right\} \\
 &= \left\langle \mathbf{l}(t; \theta) \middle| \mathbf{u}_2^{A^2}(t; \theta) \right\rangle.
 \end{aligned} \tag{3.39}$$

In (3.39), we have introduced the field

$$\hat{\mathbf{u}}_2^{A^2}(\omega; \theta) = -\epsilon_o R(\omega) \mathcal{F}(C(\mathbf{l}, \mathbf{l}))(\omega; \theta), \tag{3.40}$$

which amounts to solving in the temporal domain

$$\partial_t \mathbf{u}_2^{A^2} = L \mathbf{u}_2^{A^2} - \epsilon_o C(\mathbf{l}, \mathbf{l}). \tag{3.41}$$

Injecting (3.37) in (3.36) leads to the new system

$$\Phi(\hat{\mathbf{u}}_2)(\omega; \theta) = A^2 \underbrace{\left(-\hat{\mathbf{l}}(\omega; \theta) \frac{\mu_2}{\eta} - \mathcal{F}(C(\mathbf{l}, \mathbf{l}))(\omega; \theta) \right)}_{=\hat{\mathbf{f}}_{2,\perp}^{A^2}} = A^2 \hat{\mathbf{f}}_{2,\perp}^{A^2}(\omega; \theta) \tag{3.42}$$

where the forcing term $\hat{\mathbf{f}}_{2,\perp}^{A^2}$ is by construction orthogonal to the adjoint

$$\begin{aligned}
 \left\{ \left\langle \hat{\mathbf{u}}(\omega; \theta) \middle| \hat{\mathbf{f}}_{2,\perp}^{A^2}(\omega; \theta) \right\rangle \right\} &= 0 \Leftrightarrow \\
 \left\{ \left\langle \hat{\mathbf{l}}(\omega; \theta) \middle| R(\omega) \hat{\mathbf{f}}_{2,\perp}^{A^2}(\omega; \theta) \right\rangle \right\} &= 0 \Leftrightarrow \\
 \left\{ \left\langle \hat{\mathbf{l}}(\omega; \theta) \middle| \hat{\mathbf{u}}_{2,\perp}^{A^2}(\omega; \theta) \right\rangle \right\} &= 0.
 \end{aligned} \tag{3.43}$$

where we have introduced the field $\hat{\mathbf{u}}_{2,\perp}^{A^2} = R \hat{\mathbf{f}}_{2,\perp}^{A^2}$. The particular solution to the second-order equation (3.42) is directly given by $A^2 \hat{\mathbf{u}}_{2,\perp}^{A^2}$, since

$$\begin{aligned}
 \Phi(\omega; \theta) \left(A^2 \hat{\mathbf{u}}_{2,\perp}^{A^2}(\omega; \theta) \right) &= A^2 R(\omega)^{-1} \hat{\mathbf{u}}_{2,\perp}^{A^2}(\omega; \theta) - A^2 \hat{\xi}(\omega; \theta) \mathbf{f}_o \underbrace{\left\{ \left\langle \hat{\mathbf{l}}(\omega; \theta) \middle| \hat{\mathbf{u}}_{2,\perp}^{A^2}(\omega; \theta) \right\rangle \right\}}_{=0 \text{ by (3.43)}} \\
 &= A^2 \hat{\mathbf{f}}_{2,\perp}^{A^2}(\omega; \theta),
 \end{aligned} \tag{3.44}$$

which solves (3.42) indeed. Eventually, the general solution at $O(\epsilon_o)$ writes in the Fourier domain

$$\hat{\mathbf{u}}_2(\omega, T_2, T_3; \theta) = A(T_2, T_3)^2 \hat{\mathbf{u}}_{2,\perp}^{A^2}(\omega; \theta) + A_2(T_2, T_3) \hat{\mathbf{l}}(\omega; \theta), \tag{3.45}$$

where A_2 is another arbitrary amplitude.

Chapter 3 A non-modal amplitude equation for the variance of the stochastic response

At order $\sqrt{\epsilon_o^3}$, the equation

$$\Phi(\hat{\mathbf{u}}_3) = -\partial_{T_3}\hat{\mathbf{u}}_1 - \partial_{T_2}\hat{\mathbf{u}}_2 - 2\mathcal{F}(C(\mathbf{u}_2, \mathbf{u}_1)) + \phi\hat{\xi}\mathbf{f}_h - P(\hat{\mathbf{u}}_1) = \hat{\mathbf{f}}_3, \quad (3.46)$$

is unraveled, where the field $\hat{\mathbf{f}}_3$ was introduced. Thenceforth, we successively compute

$$\begin{aligned} \frac{\partial\hat{\mathbf{u}}_2}{\partial T_2} &= \hat{\mathbf{u}}_{2,\perp}^{A^2} 2A \frac{\partial A}{\partial T_2} + \hat{\mathbf{l}} \frac{\partial A_2}{\partial T_2} \\ &= \hat{\mathbf{u}}_{2,\perp}^{A^2} \frac{2\mu_2}{\eta} A^3 + \hat{\mathbf{l}} \frac{\partial A_2}{\partial T_2}, \end{aligned} \quad (3.47)$$

as well as

$$2\mathcal{F}(C(\mathbf{u}_2, \mathbf{u}_1)) = 2A^3 \mathcal{F}\left(C\left(\mathbf{u}_{2,\perp}^{A^2}, \mathbf{l}\right)\right) + 2AA_2 \mathcal{F}(C(\mathbf{l}, \mathbf{l})), \quad (3.48)$$

and eventually

$$P(\hat{\mathbf{u}}_1) = AP(\hat{\mathbf{l}}) = A\xi\mathbf{f}_o. \quad (3.49)$$

Using these results, the right-hand side $\hat{\mathbf{f}}_3$ in (3.46) is written

$$\hat{\mathbf{f}}_3 = -\left(\frac{\partial A_2}{\partial T_2} + \frac{\partial A}{\partial T_3}\right)\hat{\mathbf{l}} - A^3\left(2\mathcal{F}\left(C\left(\mathbf{u}_{2,\perp}^{A^2}, \mathbf{l}\right)\right) + \hat{\mathbf{u}}_{2,\perp}^{A^2} \frac{2\mu_2}{\eta}\right) - AA_2 2\mathcal{F}(C(\mathbf{l}, \mathbf{l})) + (\phi - A)\hat{\xi}\mathbf{f}_o. \quad (3.50)$$

Once again, it must be imposed that the latter is orthogonal to $\hat{\mathbf{a}}$ under the inner product (3.9)

$$\{[\langle \hat{\mathbf{a}} | \hat{\mathbf{f}}_3 \rangle]\} = 0 \Leftrightarrow \eta \left(\frac{\partial A_2}{\partial T_2} + \frac{\partial A}{\partial T_3} \right) = \gamma\phi - A + 2\mu_2 AA_2 + \mu_3 A^3. \quad (3.51)$$

The coefficient γ is given by the expression

$$\begin{aligned} \gamma &= \{[\langle \hat{\mathbf{a}} | \hat{\xi}\mathbf{f}_h \rangle]\} = \epsilon_o \left\{ \left[\langle R^\dagger \hat{\mathbf{l}} | \hat{\xi}\mathbf{f}_h \rangle \right] \right\} = \epsilon_o^2 \left\{ \left[\langle |\hat{\xi}|^2 R^\dagger R \mathbf{f}_o | \mathbf{f}_h \rangle \right] \right\} \\ &= \epsilon_o^2 \langle B^\infty \mathbf{f}_o | \mathbf{f}_h \rangle = [g] \langle \mathbf{f}_o | \mathbf{f}_h \rangle, \end{aligned} \quad (3.52)$$

which, if \mathbf{f}_h is chosen as being the optimal structure \mathbf{f}_o , reduces to

$$\gamma = \{[\langle \hat{\mathbf{a}} | \hat{\xi}\mathbf{f}_o \rangle]\} = [g] \langle \mathbf{f}_o | \mathbf{f}_o \rangle = 1, \quad (3.53)$$

in virtue of (3.15). The coefficient μ_3 is computed as

$$\begin{aligned} \mu_3 &= -\left\{ \left[\left\langle \hat{\mathbf{a}} \left| \left(\mathcal{F}\left(2C\left(\mathbf{u}_{2,\perp}^{A^2}, \mathbf{l}\right)\right) + \hat{\mathbf{u}}_{2,\perp}^{A^2} \frac{2\mu_2}{\eta} \right) \right\rangle \right] \right\} \\ &= -\left\{ \left[\left\langle \hat{\mathbf{l}} \left| \epsilon_o R \left(\mathcal{F}\left(2C\left(\mathbf{u}_{2,\perp}^{A^2}, \mathbf{l}\right)\right) + \hat{\mathbf{u}}_{2,\perp}^{A^2} \frac{2\mu_2}{\eta} \right) \right\rangle \right] \right\} \\ &= \left\{ \left[\left\langle \hat{\mathbf{l}} \left| \hat{\mathbf{u}}_3^{A^3} \right\rangle \right] \right\} \\ &= \left\{ \left[\langle \mathbf{l} | \mathbf{u}_3^{A^3} \rangle \right] \right\}, \end{aligned} \quad (3.54)$$

where we have defined the third-order field in the Fourier domain

$$\hat{\mathbf{u}}_3^{A^3} = -\epsilon_o R \left(\mathcal{F} \left(2C \left(\mathbf{u}_{2,\perp}^{A^2}, \mathbf{l} \right) \right) + \hat{\mathbf{u}}_{2,\perp}^{A^2} \frac{2\mu_2}{\eta} \right), \quad (3.55)$$

which solves in the temporal domain the following evolution equation

$$\partial_t \mathbf{u}_3^{A^3} = L \mathbf{u}_3^{A^3} - \epsilon_o 2C \left(\mathbf{u}_{2,\perp}^{A^2}, \mathbf{l} \right) - \epsilon_o \mathbf{u}_{2,\perp}^{A^2} \frac{2\mu_2}{\eta}. \quad (3.56)$$

By using (3.35) and (3.45), the overall component along the homogeneous solution $\hat{\mathbf{l}}$ is assembled as

$$\tilde{A}(T_2, T_3) = A(T_2, T_3) + \sqrt{\epsilon_o} A_2(T_2, T_3) + O(\epsilon_o). \quad (3.57)$$

The total derivative of \tilde{A} with respect to the actual time t is expressed

$$\begin{aligned} \frac{d\tilde{A}}{dt} &= \cancel{\frac{\partial \tilde{A}}{\partial t}} + \frac{\partial T_2}{\partial t} \frac{\partial \tilde{A}}{\partial T_2} + \frac{\partial T_3}{\partial t} \frac{\partial \tilde{A}}{\partial T_3} \\ &= \sqrt{\epsilon_o} \frac{\partial A}{\partial T_2} + \epsilon_o \left(\frac{\partial A_2}{\partial T_2} + \frac{\partial A}{\partial T_3} \right) + O(\sqrt{\epsilon_o^3}) \\ &= \sqrt{\epsilon_o} \frac{\mu_2}{\eta} A^2 + \frac{\epsilon_o}{\eta} (\gamma\phi - A + 2\mu_2 A A_2 + \mu_3 A^3) + O(\sqrt{\epsilon_o^3}) \\ &= \sqrt{\epsilon_o} \frac{\mu_2}{\eta} \tilde{A}^2 + \frac{\epsilon_o}{\eta} (\gamma\phi - \tilde{A} + \mu_3 \tilde{A}^3) + O(\sqrt{\epsilon_o^3}). \end{aligned} \quad (3.58)$$

By introducing the rescaled amplitude $a = \sqrt{\epsilon_o} \tilde{A} = O(\sqrt{\epsilon_o})$, this becomes

$$\eta \frac{da}{dt} = \gamma F - \epsilon_o a + \mu_2 a^2 + \mu_3 a^3 + O(\epsilon_o^2). \quad (3.59)$$

The equilibrium solution to (3.59), denoted \bar{a} , characterizes the statistically steady regime of the perturbation response, in which the expansion (3.31) becomes

$$\mathbf{U}(t; \theta) - \mathbf{U}_b = \bar{a} \mathbf{l}(t; \theta) + \bar{a}^2 \mathbf{u}_{2,\perp}^{A^2}(t; \theta) + O(\sqrt{\epsilon_o^3}). \quad (3.60)$$

The associated response-to-forcing perturbation variance gain is computed as

$$\begin{aligned} \frac{\overline{\|\mathbf{U}(t; \theta) - \mathbf{U}_b\|^2}}{\overline{\|F\xi(t; \theta) \mathbf{f}_h\|^2}} &= \frac{\bar{a}^2 + \bar{a}^4 \overline{\|\mathbf{u}_{2,\perp}^{A^2}(t; \theta)\|^2}}{F^2} + O(\sqrt{\epsilon_o^5}) \\ &= \frac{\bar{a}^2 + O(\epsilon_o^2)}{F^2}, \end{aligned} \quad (3.61)$$

where we have used $\overline{\|\mathbf{l}\|^2} = 1$ and $\overline{\langle \mathbf{l} | \mathbf{u}_{2,\perp}^{A^2} \rangle} = 0$, in virtue of (3.17) and (3.43), respectively.

Thereby, we define the leading-order stochastic gain as

$$G_{\text{WNN}} = \frac{\bar{a}^2}{F^2}, \quad (3.62)$$

the subscript "WNN" for Weakly Nonlinear Non-normal.

In the linear regime when F vanishes in (3.59), the equilibrium solution tends to $\bar{a} = \gamma F / \epsilon_o$, corresponding to a gain

$$\lim_{F \rightarrow 0} G_{\text{WNN}} = \frac{\gamma^2 F^2}{\epsilon_o^2 F^2} = \frac{\gamma^2}{\epsilon_o^2} = \gamma^2 G = \left\{ \overline{\langle \mathbf{u}_h(t; \theta) | \mathbf{l}(t; \theta) \rangle} \right\}^2. \quad (3.63)$$

where the last equality is demonstrated in appendix 3.6.5, the field \mathbf{u}_h having been defined as the linear response to $\xi \mathbf{f}_h$. This limit is consistent with the linear regime: if the forcing structure \mathbf{f}_h is chosen as being the optimal one \mathbf{f}_o , then we have $\gamma = 1$ and the weakly nonlinear gain reduces to the linear one G (defined in 3.11). On the contrary, if \mathbf{f}_h is chosen as being orthogonal to \mathbf{f}_o , the associated linear response \mathbf{u}_h is orthogonal to \mathbf{l} and the linear gain is null. That is precisely because the variance gain G_{WNN} inherently describes that of \mathbf{l} , and if the linear flow is forced along \mathbf{f}_h with $\langle \mathbf{f}_h | \mathbf{f}_o \rangle = 0$, no component of the response along \mathbf{l} is created under the inner product (3.9).

In the following section, for a selected application case, we compare the predictions of the weakly nonlinear stochastic gain (3.62) with fully nonlinear simulations as we increase the forcing strength F .

3.4 Application to the backward-facing step flow

We consider as an application case the nonlinear evolution of the stochastic gain in the two-dimensional backward-facing step (BFS) flow at $\text{Re} = 500$. As mentioned in chapter 2, streamwise non-normality mechanisms make this flow particularly receptive to external excitations (Blackburn et al., 2008). A Poiseuille profile of unit centreline velocity is imposed at the inlet.

The stochastic process $\xi(t; \theta)$ is chosen as a Gaussian-distributed, zero-average white noise of unit intensity, and band-limited with a cut-off frequency $\omega_c = \pi$. This corresponds to the particular case where

$$\{|\hat{\xi}(\omega; \theta)|^2\} = g(\omega) = 1, \quad |\omega| \leq \omega_c = \pi, \quad (3.64)$$

and $|\hat{\xi}(\omega; \theta)| = 0$ otherwise, implying

$$[g(\omega)] = \frac{1}{2\pi} \int_{-\omega_c=-\pi}^{\omega_c=\pi} g(\omega) = 1, \quad (3.65)$$

The probability density function of the noise is a Gaussian centered around 0, thus $\{\xi\} = 0$.

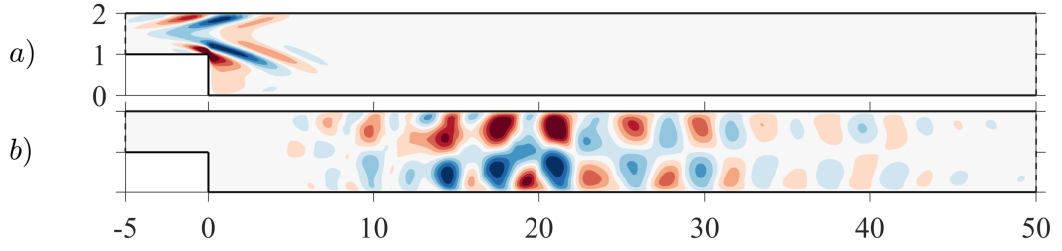


Figure 3.1: **(a)** Streamwise component of the optimal stochastic forcing \mathbf{f}_o in the BFS flow, $Re = 500$. **(b)** DNS snapshot of the associated streamwise velocity response (perturbation around the base flow) to $F\xi(t;\theta)\mathbf{f}_o$ with $F = 0.00025$.

Furthermore, the flow is forced with its optimal forcing structure, i.e. $\mathbf{f}_h = \mathbf{f}_o$, such that $\gamma = 1$.

The nonlinear and linearised NSE are solved with the Finite Element Method (see details in Appendix 3.6.6). Figure 3.1(a) shows the optimal stochastic forcing \mathbf{f}_o , which is remarkably similar to the optimal harmonic forcing structure at the most amplified frequency $\omega = 0.47$, as determined via a resolvent analysis and shown in figure 2.4(a). The harmonic gain being relatively selective in frequencies and being maximal at $\omega = 0.47$, the associated forcing structure is naturally favored when maximising the present stochastic gain, since the selected noise excites all frequencies with the same intensity. Figure 3.1(b) shows a DNS snapshot of the flow response to $F\xi(t;\theta)\mathbf{f}_o$ for $F = 0.00025$.

The linear problems and the coefficients μ_2 and μ_3 are computed in the frequency domain, where the frequencies have been discretised in N uniformly distributed values $\omega \in [0, \omega_c]$ with $\omega_c = \pi$. The coefficient μ_2 in front of the quadratic term in (3.59) is found to vanish after performing the ensemble average. That is because the probability density function of the noise, denoted $P(\xi)$, is a Gaussian centered around zero, and thus it is even, such that $P(-\xi) = P(\xi)$. On the other hand, the coefficient μ_2 in (3.39) can be re-expressed as

$$\mu_2 = -\epsilon_o^4 \left\{ \left\langle \left\langle R^\dagger R \mathbf{f}_o \hat{\xi} \left| \mathcal{F} \left(C \left(\mathcal{F}^{-1} (R \mathbf{f}_o \hat{\xi}), \mathcal{F}^{-1} (R \mathbf{f}_o \hat{\xi}) \right) \right) \right\rangle \right\rangle \right\} = \{\tilde{\mu}_2\} \quad (3.66)$$

Due to the linearity of the Fourier transform, the function inside the ensemble average in (3.66), which we have defined as $\tilde{\mu}_2$, is an odd function of ξ , i.e., $\tilde{\mu}_2(-\xi) = -\tilde{\mu}_2(\xi)$. Thereby, its ensemble average (or expected value) writes

$$\mu_2 = \{\tilde{\mu}_2\} = \int \tilde{\mu}_2(\xi) P(\xi) d\xi = 0, \quad (3.67)$$

since the integrand is odd. The nullity of μ_2 greatly simplifies the ensuing calculations, and the coefficient μ_3 is found upon implementing the following algorithm.

-
1. Choose the values for N and ω_c , which sets the discretisation of the frequency interval.

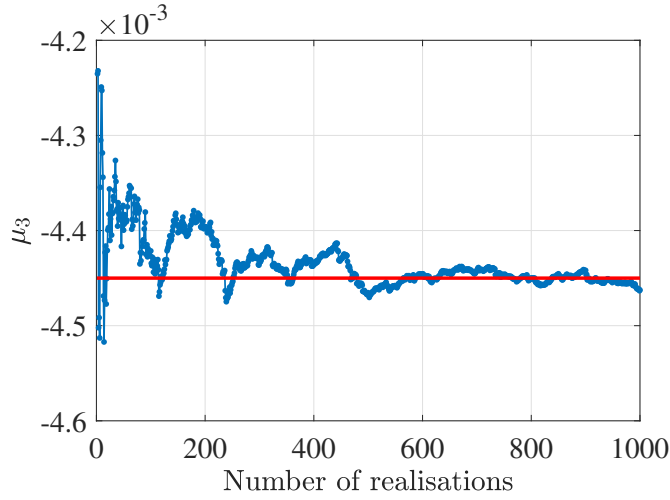


Figure 3.2: Evolution of the coefficient μ_3 as a function of the number of realisations included in the ensemble average. Each realisation results from a different, randomly drawn, white noise process.

2. Over the discrete set of frequencies, pre-compute once for all the deterministic scalar ϵ_o and fields \mathbf{f}_o and $R\mathbf{f}_o$.
3. Draw randomly a band-limited white noise $\hat{\xi}$ and deduce $\hat{\mathbf{l}} = \epsilon_o \hat{\xi} R\mathbf{f}_o$.
4. Compute $\mathbf{l} = \mathcal{F}^{-1}(\hat{\mathbf{l}})$ then $\hat{\mathbf{u}}_{2,\perp}^{A^2} = -R\mathcal{F}(C(\mathbf{l}, \mathbf{l}))$.
5. Compute $\mathbf{u}_{2,\perp}^{A^2} = \mathcal{F}^{-1}(\hat{\mathbf{u}}_{2,\perp}^{A^2})$ then $\hat{\mathbf{u}}_3^{A^3} = -\epsilon_o R\mathcal{F}(2C(\mathbf{u}_{2,\perp}^{A^2}, \mathbf{l}))$.
6. Compute $\tilde{\mu}_3 = \langle \hat{\mathbf{l}} | \hat{\mathbf{u}}_3^{A^3} \rangle$ and store its value.
7. Update $\mu_3 = \{\tilde{\mu}_3\}$ and return to (3) until convergence of μ_3 .

The algorithm is found to converge to the value

$$\mu_3 = -4.45 \times 10^{-3}, \quad (3.68)$$

after 10^3 different realisations of the white noise (see convergence curve in figure 3.2, and a frequency domain $\omega \in [0, \omega_c]$ discretized in $N = 2^7 + 1$ points. The coefficient η is not needed in determining the equilibrium solutions of (3.59), therefore is not calculated.

The weakly nonlinear gain defined in (3.62) is compared with the fully nonlinear gain extracted from a DNS of (3.27), and defined hereafter as

$$G_{\text{DNS}} \doteq \frac{\overline{\|\mathbf{u}_p(t)\|^2}}{F^2} = \frac{\{ \|\hat{\mathbf{u}}_p\|^2 \}}{F^2}, \quad \text{with } \mathbf{u}_p(t) = \mathbf{U}(t) - \bar{\mathbf{U}}. \quad (3.69)$$

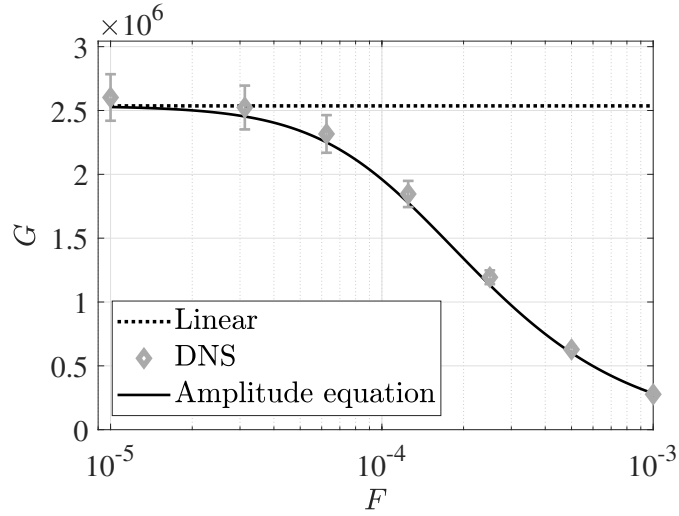


Figure 3.3: Weakly and fully nonlinear stochastic gains (defined respectively in (3.62) and (3.69)) for the BFS flow at $\text{Re} = 500$. Error bars around DNS points show plus or minus one standard deviation.

Contrarily to the weakly nonlinear calculations, the DNS are performed in the time domain, with duration $T = 2049$ units of times after the transients fade away, sampled at $\Delta t = \pi/\omega_c = 1$ and ensemble-averaged over 10 realisations of the white noise (this lower number of realisations is the consequence of each one being numerically costly).

The weakly nonlinear gain as defined in (3.62), with \bar{a} the root of the polynomial at the right-hand side of (3.59) (with $\mu_2 = 0$ for this particular Gaussian noise case) is represented in figure 3.3 as a function of F . The evolution of the fully nonlinear gain, as defined in (3.69) is also added, as well as the linear gain in (3.11). The comparison of the weakly nonlinear gain with the DNS data shows good agreement: the amplitude equation (3.59) captures well the monotonous decay of the gain with increasing F . For small F close to the linear regime, DNS and weakly nonlinear (which collapse to the linear) approach differ slightly, which is believed to be due to an imperfect convergence of the DNS data, due to the large standard deviation at small F and the poor number of realisations.

Note that such good agreement in figure 3.3 is probably made possible by the frequency selectivity of the BFS flow. Specifically, as apparent in figure 3.4 that, for a given noise realisation, the L^2 norm of the leading order field $\|\hat{\mathbf{u}}\|^2 = \|\hat{\xi}\epsilon_o R \mathbf{f}_o\|^2$ is localized around $\omega \approx 0.47$, due to the selectivity of the forcing structure \mathbf{f}_o . The quadratic nature of the nonlinearity implies that the L^2 norm of the second-order field $\|\hat{\mathbf{u}}_{2,\perp}^{A^2}\|^2$ is localized around $\omega = 0$ and $\omega = 2 \times 0.47$. In turns, the L^2 norm of the third-order field $\|\hat{\mathbf{u}}_3^{A^3}\|^2$ again is localized around the frequency $\omega \approx 0.47$. As a consequence, the first and third-order fields have a very similar energy distribution as a function of the frequency in figure 3.4, which makes the coefficient μ_3 in (3.54) non-negligible. Such resemblance between the leading and third-order fields justifies all the more enforcing their orthogonality in the sense of the inner product (3.9) (which also integrates over the

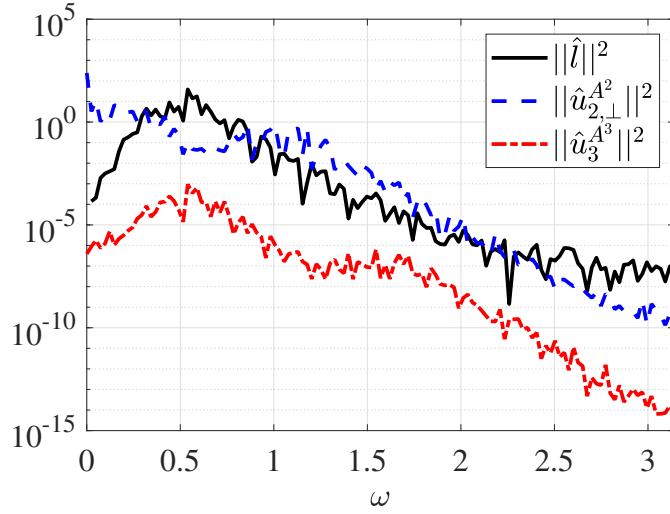


Figure 3.4: For a given noise realisation ξ , are shown the L^2 norm of the leading order field $\hat{\boldsymbol{l}} = \epsilon_o \xi R \boldsymbol{f}_o$, of the second-order particular solution $\hat{\boldsymbol{u}}_{2,\perp}^{A^2} = R \boldsymbol{f}_{2,\perp}^{A^2}$ and of the third order field $\hat{\boldsymbol{u}}_3^{A^3}$ given by (3.55).

frequency) such as to preserve the asymptotic hierarchy. This presumably is why the results ensuing this orthogonality condition are so effective in capturing fully nonlinear results. Nevertheless, the performances of the amplitude equation (3.59) are expected to be perhaps less impressive in a configuration where $\|\hat{\boldsymbol{l}}\|^2$ is less localized in frequency, but exhibits large values over a wide range of frequencies.

3.5 Conclusion

In this chapter, we have shown that the methodology outlined in chapter 2 for the response to a harmonic forcing can be extended to the response to a (specific) stochastic forcing, by selecting a more general inner product in (3.9), involving an integration over space, time (or frequencies) and an ensemble average. The linear system experiences a large response-to-forcing amplification of the norm induced by such an inner product. Consequently, the resolvent operator is close to being singular and exactly is by perturbing it with a small operator perturbation. Accordingly, the adjective "small" refers to the norm induced by the generalized inner product. The ensuing amplitude equation predicted well the weakly nonlinear evolution of the gain for the BFS flow at $\text{Re} = 500$ as the induced norm of the stochastic forcing was increased. This good performance remains to be established in more complicated flows, less selective in frequency.

Note that the approach could easily be extended to cases where the flow is subject to several

(say N) stochastic forcings, i.e. to

$$\mathbf{f}(t; \boldsymbol{\theta}) = \sum_{j=1}^N \mathbf{f}_j \xi_j(t; \theta_j), \quad (3.70)$$

as long as the forcing processes $\mathbf{f}_j \xi_j(t; \theta_j)$ are orthonormal under the inner product (3.9), i.e., as long as

$$\left\{ \left\langle \mathbf{f}_j \hat{\xi}_j(\omega; \theta_j) \middle| \mathbf{f}_n \hat{\xi}_n(\omega; \theta_n) \right\rangle \right\} = \delta_{jn}. \quad (3.71)$$

Indeed, in the latter case, the operator perturbation (3.19) can be straightforwardly completed as

$$\begin{aligned} \Phi(\omega; \boldsymbol{\theta})(\bullet) &= R(\omega)^{-1} \bullet - \sum_{j=1}^N \epsilon_j P_j(\omega; \theta_j)(\bullet), \quad \text{with} \\ P_j(\omega; \theta_j)(\bullet) &= \hat{\xi}_j(\omega; \theta_j) \mathbf{f}_j \left\{ \left\langle \hat{\mathbf{l}}_j(\omega; \theta_j) \middle| \bullet \right\rangle \right\}, \end{aligned} \quad (3.72)$$

and where

$$\hat{\mathbf{l}}_j(\omega; \theta) = \epsilon_j \hat{\xi}_j(\omega; \theta_j) R(\omega) \mathbf{f}_j, \quad \text{and } \epsilon_j \text{ is such that } \left\{ \left\| \hat{\mathbf{l}}_j(\omega; \theta) \right\|^2 \right\} = 1. \quad (3.73)$$

Precisely due to the orthonormality property in (3.71), the operator Φ is such that

$$\Phi(\omega; \boldsymbol{\theta})(\hat{\mathbf{l}}_j(\omega; \theta)) = \mathbf{0} \quad \text{for each } j = 1, 2, \dots \quad (3.74)$$

Thenceforth, one can proceed with the nonlinear expansion to eventually obtain a system of N nonlinear coupled amplitude equations.

Nevertheless, coming back to the simplest case where $N = 1$ was detailed in this chapter, the amplitude equation is limited to the description of the variance, a simple integrated measure of the flow response. Corollary, because the inner product selected in (3.9) is integrating over space, frequency, and taking the expected value, the amplitude is condemned to be a deterministic scalar that does not depend on the frequency.

For this reason, in the next chapter we consider the same problem but, for the perturbation of the inverse resolvent, return to the simple L^2 inner product considered in chapter 2. This will have the consequence that the amplitude for the stochastic response will generically depend on the frequency and will also be stochastic. At the cost of an operator perturbation less well justified and analytical developments becoming substantially more complex, the weakly nonlinear evolution of the whole Fourier spectrum of the linear response can be captured.

3.6 Appendix

3.6.1 Link between the PSD and the auto-correlation function

Upon taking the inverse Fourier transform of (3.6), we obtain

$$\begin{aligned}
 \mathcal{F}^{-1}(\{|\hat{\xi}(\omega; \theta)|^2\}) &= \mathcal{F}^{-1}(g(\omega)) \Leftrightarrow, \\
 \frac{\sqrt{T}}{2\pi} \frac{1}{T} \int_0^T \int_0^T \{\xi(t; \theta)\xi(b; \theta)\} \int_{-\infty}^{\infty} e^{i\omega(t-b+s)} d\omega dt db &= \frac{\sqrt{T}}{2\pi} \int_{-\infty}^{\infty} g(\omega) e^{ist} d\omega \Leftrightarrow, \\
 \frac{1}{\sqrt{T}} \int_0^T \int_0^T \{\xi(t; \theta)\xi(b; \theta)\} \delta(t-b+s) dt db &= \frac{\sqrt{T}}{2\pi} \int_{-\infty}^{\infty} g(\omega) e^{ist} d\omega \Leftrightarrow, \\
 \frac{1}{T} \int_0^T \{\xi(t; \theta)\xi(t+s; \theta)\} dt &= \frac{1}{2\pi} \int_{-\infty}^{\infty} g(\omega) e^{ist} d\omega \Leftrightarrow, \\
 \overline{\{\xi(t; \theta)\xi(t+s; \theta)\}} &= \frac{1}{2\pi} \int_{-\infty}^{\infty} g(\omega) e^{ist} d\omega.
 \end{aligned} \tag{3.75}$$

3.6.2 Norm in the frequency domain

$$\begin{aligned}
 \overline{\langle \mathbf{h}(t; \theta) | \mathbf{g}(t; \theta) \rangle} &= \frac{1}{T} \int_0^T \frac{T}{4\pi^2} \int_{-\infty}^{\infty} \int_{-\infty}^{\infty} \langle \hat{\mathbf{h}}(\omega; \theta) | \hat{\mathbf{g}}(s; \theta) \rangle e^{it(s-\omega)} d\omega ds dt \\
 &= \frac{1}{2\pi} \int_{-\infty}^{\infty} \int_{-\infty}^{\infty} \langle \hat{\mathbf{h}}(\omega; \theta) | \hat{\mathbf{g}}(s; \theta) \rangle \delta(s-\omega) d\omega ds \\
 &= \frac{1}{2\pi} \int_{-\infty}^{\infty} \langle \hat{\mathbf{h}}(\omega; \theta) | \hat{\mathbf{g}}(\omega; \theta) \rangle d\omega \\
 &= [\langle \hat{\mathbf{h}}(\omega; \theta) | \hat{\mathbf{g}}(\omega; \theta) \rangle].
 \end{aligned} \tag{3.76}$$

3.6.3 Norm of the perturbation operator

$$\begin{aligned}
 \{[\|P(\omega; \theta)(\bullet)\|^2]\} &= \max_{\hat{\mathbf{g}}} \frac{\{[\|P(\omega; \theta)(\hat{\mathbf{g}}(\omega; \theta))\|^2]\}}{\{[\|\hat{\mathbf{g}}(\omega; \theta)\|^2]\}} \\
 &= \max_{\hat{\mathbf{g}}} \frac{\{[\|\hat{\xi}(\omega; \theta) \mathbf{f}_o \{[\langle \hat{\mathbf{l}}(\omega; \theta) | \hat{\mathbf{g}}(\omega; \theta) \rangle]\} \|^2]\}}{\{[\|\hat{\mathbf{g}}(\omega; \theta)\|^2]\}} \\
 &= \underbrace{\{[\|\hat{\xi}(\omega; \theta) \mathbf{f}_o\|^2]\}}_{=1 \text{ by (3.15)}} \max_{\hat{\mathbf{g}}} \frac{|\{[\langle \hat{\mathbf{l}}(\omega; \theta) | \hat{\mathbf{g}}(\omega; \theta) \rangle]\}|^2}{\{[\|\hat{\mathbf{g}}(\omega; \theta)\|^2]\}} \\
 &= 1,
 \end{aligned} \tag{3.77}$$

where selecting $\hat{\mathbf{g}}(\omega; \theta) = \hat{\mathbf{l}}(\omega; \theta)$ leads to the largest possible amplification.

3.6.4 Kernel of the adjoint operator

$$\begin{aligned}
\Phi(\omega; \theta)^\dagger (\hat{\mathbf{a}}(\omega; \theta)) &= (R(\omega)^{-1})^\dagger \hat{\mathbf{a}}(\omega; \theta) - \epsilon_o P(\omega)^\dagger (\hat{\mathbf{a}}(\omega; \theta)) \\
&= \epsilon_o (R(\omega)^{-1})^\dagger R(\omega)^\dagger \hat{\mathbf{l}}(\omega; \theta) - \epsilon_o^2 P(\omega)^\dagger (R(\omega)^\dagger \hat{\mathbf{l}}(\omega; \theta)) \\
&= \epsilon_o (R(\omega)^\dagger)^{-1} R(\omega)^\dagger \hat{\mathbf{l}}(\omega; \theta) - \epsilon_o^2 \hat{\mathbf{l}}(\omega; \theta) \left\{ \left[\langle \hat{\xi}(\omega; \theta) \mathbf{f}_o \mid R(\omega)^\dagger \hat{\mathbf{l}}(\omega; \theta) \rangle \right] \right\} \quad (3.78) \\
&= \epsilon_o \hat{\mathbf{l}}(\omega; \theta) - \epsilon_o \hat{\mathbf{l}}(\omega; \theta) \underbrace{\left\{ \left[\langle \hat{\mathbf{l}}(\omega; \theta) \mid \hat{\mathbf{l}}(\omega; \theta) \rangle \right] \right\}}_{=1 \text{ by (3.17)}} \\
&= \mathbf{0},
\end{aligned}$$

where we used that the inverse of the adjoint is the adjoint of the inverse.

3.6.5 Linear gain for a generic forcing structure

Let us denote by $\mathbf{u}_h(t; \theta)$ the response to the stochastic forcing $\xi(t; \theta) \mathbf{f}_h$, i.e. $\hat{\mathbf{u}}_h(\omega; \theta) = \hat{\xi}(\omega; \theta) R(\omega) \mathbf{f}_h$. The projection of $\hat{\mathbf{u}}_h(\omega; \theta)$ onto $\hat{\mathbf{l}}(\omega; \theta)$ under the inner product (3.9) reads

$$\begin{aligned}
\left\{ \left[\langle \hat{\mathbf{u}}_h(\omega; \theta) \mid \hat{\mathbf{l}}(\omega; \theta) \rangle \right] \right\} &= \epsilon_o \left\{ \left[\langle \mathbf{f}_h \mid |\hat{\xi}(\omega; \theta)|^2 R(\omega)^\dagger R(\omega) \mathbf{f}_o \rangle \right] \right\} \\
&= \epsilon_o \langle \mathbf{f}_h \mid B^\infty \mathbf{f}_o \rangle \\
&= [g(\omega)] \langle \mathbf{f}_h \mid \mathbf{f}_o \rangle \sqrt{G} \\
&= \gamma \sqrt{G}.
\end{aligned} \quad (3.79)$$

3.6.6 Numerical implementation

The linear and nonlinear NSE are solved for (u_x, u_y, p) employing the Finite Element Method with Taylor-Hood (P2, P2, P1) elements, respectively, after implementation of their weak form in the software FreeFem++. The steady solution of the nonlinear NSE is found using the iterative Newton–Raphson method, and the linear operators are built thanks to a sparse solver available in FreeFem++. The optimal forcing structure \mathbf{f}_o is found on the software MATLAB after discretizing the integral expression for B^∞ and performing the lower-upper (LU) decomposition of the resolvent operators to speed up their application. Finally, DNS are performed in FreeFem++ by applying a time scheme based on the characteristic–Galerkin method. We refer to Mantič-Lugo and Gallaire, 2016b for the validation of the codes with existing literature when possible and for the mesh convergence analysis since the same codes have been used.

4 Weakly nonlinear evolution of stochastically driven non-normal systems

Remark: This chapter is largely inspired by the article Ducimetière et al. (2022c), in collaboration with Edouard Boujo and François Gallaire.

4.1 Introduction

In this chapter, we also propose a theoretical approach to derive an amplitude equation governing the weakly nonlinear evolution of non-normal systems subject to stochastic forcing. As in the previous chapter, the approach does not rely on the presence of an eigenvalue close to the neutral axis, applying instead to any sufficiently non-normal operator, and the Fourier components of the response are allowed to be arbitrarily different from any eigenmode.

Nevertheless, the approach followed in the present chapter differs from that proposed in the previous one, in that the amplitude equation now depends on the frequency. In that, it can be seen as a "spectral envelope" of the Fourier spectrum of the linear response.

The methodology is outlined for a generic nonlinear dynamical system, and the application case highlights a common non-normal mechanism in hydrodynamics: convective non-normal amplification in the flow past a backward-facing step.

4.2 Linear regime

A generic nonlinear dynamical system is considered,

$$\partial_t \mathbf{U} = N(\mathbf{U}) + \mathbf{F}, \tag{4.1}$$

where $N(\cdot)$ is a nonlinear operator and \mathbf{F} a forcing term. The first step of our analysis is to linearise (4.1) around an unforced equilibrium \mathbf{U}_e solution of $N(\mathbf{U}_e) = \mathbf{0}$. Small-amplitude forcing and perturbations, $\epsilon \mathbf{f}$ and $\epsilon \mathbf{u}$ ($\epsilon \ll 1$), are considered around \mathbf{U}_e . An asymptotic expansion of (4.1) in terms of ϵ can thus be performed. At order ϵ , the fields \mathbf{u} and \mathbf{f} are linked through the linear relation

$$\partial_t \mathbf{u} = L\mathbf{u} + \mathbf{f}, \quad (4.2)$$

where L results from the linearisation of N around \mathbf{U}_e . For fluid flows governed by the incompressible Navier-Stokes equations, we recall $L\mathbf{u} = -(\mathbf{U}_e \cdot \nabla)\mathbf{u} - (\mathbf{u} \cdot \nabla)\mathbf{U}_e + Re^{-1}\Delta\mathbf{u} - \nabla p(\mathbf{u})$, where Re is the Reynolds number, and where the pressure field p is such that the velocity field \mathbf{u} is divergence-free.

Exactly as in the previous chapter, the specific form $\mathbf{f}(\mathbf{x}, t) = \mathbf{f}_s(\mathbf{x})\xi(t)$ is chosen for the stochastic forcing. The field $\mathbf{f}_s(\mathbf{x})$ is the forcing spatial structure and $\xi(t)$ a Gaussian band-limited white noise process with unit intensity, zero mean, and a cut-off frequency at $\omega_c = \pi$, i.e.

$$\{|\hat{\xi}(\omega)|^2\} = 1, \quad |\omega| \leq \omega_c = \pi, \quad \{\xi(t)\} = 0, \quad (4.3)$$

and the cut-off frequency is such that the noise has a variance

$$\begin{aligned} \{\overline{\xi(t)^2}\} &= \left\{ \frac{T}{4\pi^2} \int_{-\infty}^{\infty} \int_{-\infty}^{\infty} \hat{\xi}(\omega)^* \hat{\xi}(s) e^{it(s-\omega)} d\omega ds \right\} \\ &= \left\{ \frac{T}{4\pi^2} \int_{-\infty}^{\infty} \int_{-\infty}^{\infty} \hat{\xi}(\omega)^* \hat{\xi}(s) \overline{e^{it(s-\omega)}} d\omega ds \right\} \\ &= \frac{1}{2\pi} \int_{-\infty}^{\infty} \int_{-\infty}^{\infty} \{\hat{\xi}(\omega)^* \hat{\xi}(s)\} \delta(s-\omega) d\omega ds \\ &= \frac{1}{2\pi} \int_{-\infty}^{\infty} \{|\hat{\xi}(\omega)|^2\} d\omega \\ &= \frac{1}{2\pi} \int_{-\omega_c=\pi}^{\omega_c=\pi} 1 d\omega \\ &= 1. \end{aligned} \quad (4.4)$$

where we have used the interpretation of the Dirac impulse in (3.4). Note that the variance (4.4) diverges in case of an actual white noise with $\omega_c \rightarrow \infty$. Thereby, setting a finite cutoff frequency ω_c guarantees the noise to have a finite variance.

The white noise $\xi(t)$ is the only source of randomness of the system. In this chapter, we omit the dependency on the stochastic argument, to lighten the formalism.

As we saw in the previous chapter, a relevant measure of input-output gain of the system (4.2) is the ratio of the statistically steady variance maintained by the stochastic forcing, $\{\overline{\|\mathbf{u}(t)\|^2}\}$,

divided by that of the forcing

$$\left\{ \overline{\|\xi(t)\mathbf{f}_h\|^2} \right\} = \underbrace{\left\{ \overline{\xi(t)^2} \right\}}_{=1 \text{ by (4.4)}} \|\mathbf{f}_h\|^2 = \|\mathbf{f}_h\|^2 \quad (4.5)$$

Optimising over the forcing structure, as in (3.13) the maximum attainable gain is

$$G = \max_{\mathbf{f}_s} \frac{\left\{ \overline{\|\mathbf{u}(t)\|^2} \right\}}{\|\mathbf{f}_s\|^2} \doteq \frac{1}{\epsilon_o^2}. \quad (4.6)$$

We have seen that, using the inverse Fourier transform of $\mathbf{u}(t)$, we can write

$$\left\{ \overline{\|\mathbf{u}(t)\|^2} \right\} = \langle \mathbf{f}_s | B^\infty \mathbf{f}_s \rangle, \quad (4.7)$$

with B^∞ given in (3.14), which in this particular case reduces to

$$B^\infty = \frac{1}{2\pi} \int_{-\pi}^{\pi} R(\omega)^\dagger R(\omega) d\omega = \left[g(\omega) R(\omega)^\dagger R(\omega) \right]. \quad (4.8)$$

We recall the operator B^∞ to be positive definite Hermitian with positive and real eigenvalues associated with mutually orthogonal eigenvectors. The maximum gain (4.6) is the largest eigenvalue of B^∞ . The associated eigenvector, denoted \mathbf{f}_o and normalised as $\langle \mathbf{f}_o | \mathbf{f}_o \rangle = \|\mathbf{f}_o\|^2 = 1$, is the optimal forcing structure (hence the subscript "o"), i.e the forcing structure that leads to the largest stochastically maintained variance amplification. As we said, if in addition the largest eigenvalue of B^∞ is much larger than all the others, which correspond to suboptimal gains, and if the actual (unknown) forcing of the system does not trigger a particular suboptimal eigenvector of B^∞ but projects comparably on all the eigenvectors, then the response to the actual forcing is expected to be dominated by the response to the optimal forcing \mathbf{f}_o , regardless of the specific shape of the actual forcing. This low-rank approximation explains why we restrict our analysis to the response to $\xi(t)\mathbf{f}_o$ and do not include additional forcing modes.

By linearity, forcing the system (4.2) with $\mathbf{f} = \epsilon_o \xi(t)\mathbf{f}_o$, where we defined $\epsilon_o^2 \doteq 1/G$, leads to a response $\mathbf{l}(t)$ of unit variance, $\left\{ \overline{\|\mathbf{l}(t)\|^2} \right\} = \epsilon_o^2 \langle \mathbf{f}_o | B^\infty \mathbf{f}_o \rangle = 1$, and zero mean, $\{\mathbf{l}(t)\} = 0$. In the Fourier domain, $\hat{\mathbf{l}}(\omega) = \epsilon_o \hat{\xi}(\omega) R(\omega) \mathbf{f}_o = \hat{\xi}(\omega) \hat{\mathbf{q}}(\omega)$ where we introduced the deterministic field $\hat{\mathbf{q}}(\omega) \doteq \epsilon_o R(\omega) \mathbf{f}_o$, or

$$R(\omega)^{-1} \hat{\mathbf{q}}(\omega) = \epsilon_o \mathbf{f}_o. \quad (4.9)$$

Since L is strongly non-normal, as assumed in the rest of the present study, neither of ϵ_o or \mathbf{f}_o are immediately determined from its spectral (modal) properties; furthermore, strong non-normality implies $\epsilon_o \ll 1$ (Farrell & Ioannou, 1993). It follows from (4.9) that we can

perturb the inverse resolvent as

$$\bar{\Phi}(\omega) \doteq R(\omega)^{-1} - \epsilon_o P(\omega), \quad \text{where} \quad P(\omega) = \mathbf{f}_o \frac{\langle \hat{\mathbf{q}}(\omega) | \cdot \rangle}{\|\hat{\mathbf{q}}(\omega)\|^2}, \quad (4.10)$$

i.e. the linear operator $P(\omega)$ is such that $P(\omega)\hat{\mathbf{g}}(\omega) = \mathbf{f}_o \langle \hat{\mathbf{q}}(\omega) | \hat{\mathbf{g}}(\omega) \rangle \|\hat{\mathbf{q}}(\omega)\|^{-2}$, for any field $\hat{\mathbf{g}}(\omega)$. This leads to $\bar{\Phi}(\omega)\hat{\mathbf{q}}(\omega) = \mathbf{0}$, for all ω , such that $\bar{\Phi}(\omega)$ is a singular operator for each frequency and $\hat{\mathbf{q}}(\omega)$ its non-trivial kernel.

Crucially, note that the perturbation of the inverse resolvent in (4.10) is different from that in (3.19), in that the perturbation operator now only involves integration over space. That is also why the division by $\|\hat{\mathbf{q}}(\omega)\|^2$ is required in (4.10), because the linear response $\hat{\mathbf{l}}(\omega)$ only is of unit norm when the integration of the frequencies and the ensemble average are included. Consequently, the well posedness of the perturbation (4.10) is less clear than the one (3.19), for it is not true that $\|P(\omega)\| = 1$. Typically, for the frequencies where $\|\hat{\mathbf{q}}(\omega)\| \ll 1$, expansion (4.10) is ill-posed.

Expansion (4.10) is justified *a priori* only over the range of frequencies for which

$$\|R(\omega)^{-1}\| \gg \epsilon_o \|P(\omega)\| = \|R(\omega)\mathbf{f}_o\|^{-1}, \quad (4.11)$$

where we have used that $\|P(\omega)\| = \|\hat{\mathbf{q}}(\omega)\|^{-1}$. Since $\|R(\omega)^{-1}\|$ is equal to the inverse of the smallest singular value of $R(\omega)$, the inequality (4.11) can be re-expressed as

$$\|R(\omega)\mathbf{f}_o\| \gg \min_{\|f\|=1} \|R(\omega)\mathbf{f}\| \quad (4.12)$$

In other words, the expansion is justified for all frequencies that amplify the optimal forcing structure \mathbf{f}_o much more than the least amplified structure, which can be seen as a condition of large “spectral” gap in the singular-values.

Note also that, contrarily to (3.19), both $P(\omega)$ and $\bar{\Phi}(\omega)$ are currently deterministic operators.

Using that

$$P(\omega)^\dagger = \hat{\mathbf{q}}(\omega) \frac{\langle \mathbf{f}_o | \cdot \rangle}{\|\hat{\mathbf{q}}(\omega)\|^2}, \quad (4.13)$$

we can show that the non-trivial kernel of the adjoint operator $\bar{\Phi}(\omega)^\dagger$ is

$$\hat{\mathbf{a}}(\omega) \doteq R(\omega)^\dagger \hat{\mathbf{q}}(\omega), \quad (4.14)$$

such that $\bar{\Phi}(\omega)^\dagger \hat{\mathbf{a}}(\omega) = \mathbf{0}$.

4.3 Weakly nonlinear regime

We now develop a method to derive an amplitude equation for the weakly nonlinear amplification of a stochastic forcing.

4.3.1 Generic nonlinear system and application to a toy model

The method is based on a multiple-scale asymptotic expansion, for which the gain inverse $\epsilon_o \ll 1$ constitutes a natural choice of small parameter. The system (4.1) is weakly forced by

$$F = \phi \epsilon_o^2 \mathbf{f}_h \xi(t). \quad (4.15)$$

In general, the spatial forcing structure \mathbf{f}_h need not be chosen as the optimal one \mathbf{f}_o . We impose $\|\mathbf{f}_h\|^2 = 1$ such that the prefactor $\phi = O(1)$ sets the forcing effective value

$$F \doteq \sqrt{\{|\phi \epsilon_o^2 \mathbf{f}_h \xi(t)|^2\}} = \phi \epsilon_o^2 \|\mathbf{f}_h\| = \phi \epsilon_o^2. \quad (4.16)$$

A separation of time scales is assumed for the response, with the slow time scale $\tau_1 \doteq \epsilon_o t$ aiming at capturing slow variations of the response

$$\mathbf{U}(t, \tau_1) = \mathbf{U}_e + \epsilon_o \mathbf{u}_1(t, \tau_1) + \epsilon_o^2 \mathbf{u}_2(t, \tau_1) + O(\epsilon_o^3) \quad (4.17)$$

around the statistically steady regime. Introducing the expansion (4.17) into (4.1), isolating the Fourier component at ω and perturbing $R(\omega)^{-1}$ according to (4.10) yields

$$\epsilon_o [\Phi \hat{\mathbf{u}}_1] + \epsilon_o^2 [\Phi \hat{\mathbf{u}}_2 + \mathbf{d}_{\tau_1} \hat{\mathbf{u}}_1 - \mathcal{F}(N_2(\mathbf{u}_1)) - \phi \mathbf{f}_h \hat{\xi} + P \hat{\mathbf{u}}_1] + O(\epsilon_o^3) = \mathbf{0}, \quad (4.18)$$

where

$$N(\mathbf{U}) = N(\mathbf{U}_e) + \epsilon_o L \mathbf{u}_1 + \epsilon_o^2 [L \mathbf{u}_2 + N_2(\mathbf{u}_1)] + O(\epsilon_o^3) \quad (4.19)$$

and with $\hat{\mathbf{u}}_i = \hat{\mathbf{u}}_i(\tau_1; \omega)$ for $i = 1, 2, \dots$

At $O(\epsilon_o)$ of the expansion (4.18), we obtain

$$\Phi(\omega) \hat{\mathbf{u}}_1(\tau_1; \omega) = \mathbf{0} \quad (4.20)$$

Since by construction $\hat{\mathbf{q}}(\omega)$ is the non-trivial kernel of $\Phi(\omega)$, the general solution is

$$\hat{\mathbf{u}}_1(\tau_1; \omega) = \hat{B}(\tau_1; \omega) \hat{\mathbf{q}}(\omega), \quad (4.21)$$

with \hat{B} a slowly varying complex scalar amplitude to be determined.

At $O(\epsilon_o^2)$, we assemble

$$\Phi \hat{\mathbf{u}}_2 = -\hat{\mathbf{q}} d_{\tau_1} \hat{B} + \hat{\mathbf{g}}_2[\hat{B}] + \phi \mathbf{f}_h \hat{\xi} - \mathbf{f}_o \hat{B}, \quad (4.22)$$

for which we used that $P\hat{B}\hat{\mathbf{q}} = \hat{B}\mathbf{f}_o$ and defined

$$\hat{\mathbf{g}}_2[\hat{B}] \doteq \mathcal{F} \left(N_2(\mathcal{F}^{-1}(\hat{B}\hat{\mathbf{q}})) \right). \quad (4.23)$$

Note that because the slow time scales as ϵ_o , the term $\hat{\mathbf{q}} d_{\tau_1} \hat{B}$ and the term $\hat{\mathbf{g}}_2[\hat{B}]$, which compute the nonlinear interaction of the $O(\epsilon_o)$ solution with itself, appear at the same order in (4.22). Therefore, the slow time scale can be physically interpreted as the time scale at which the (weak) nonlinearities are influential.

The operator Φ being singular, the only way for (4.22) to yield a non-diverging solution and thus preserve the asymptotic hierarchy is if the right-hand side is orthogonal to $\hat{\mathbf{a}}$, the kernel of Φ^\dagger . This solvability condition (or Fredholm alternative) yields an amplitude equation for $d_{\tau_1} \hat{B}$,

$$\langle \hat{\mathbf{a}} | \hat{\mathbf{q}} \rangle d_{\tau_1} \hat{B} = \hat{\mathbf{g}}_2[\hat{B}] + \langle \hat{\mathbf{a}} | \mathbf{f}_h \rangle \phi \hat{\xi} - \langle \hat{\mathbf{a}} | \mathbf{f}_o \rangle \hat{B}, \quad (4.24)$$

where we have defined the functional

$$\hat{\mathbf{g}}_2[\hat{B}] \doteq \langle \hat{\mathbf{a}} | \hat{\mathbf{g}}_2[\hat{B}] \rangle. \quad (4.25)$$

If $\hat{\mathbf{f}}_2$ designates the right-hand side of (4.22), the solvability condition

$$0 = \langle \hat{\mathbf{f}}_2 | \hat{\mathbf{a}} \rangle = \langle R\hat{\mathbf{f}}_2 | \hat{\mathbf{q}} \rangle \quad (4.26)$$

implies $\hat{\mathbf{u}}_2 = R\hat{\mathbf{f}}_2$ to be directly the particular solution. By defining $\mathbf{u}_2(t) \doteq \mathcal{F}^{-1}(\hat{\mathbf{u}}_2)$, one can easily show that the solvability condition also implies that

$$\overline{\langle \mathbf{u}_2(t) | \mathbf{l}(t-\tau) \rangle} = \frac{1}{2\pi} \int_{-\infty}^{\infty} \hat{\xi} \langle \hat{\mathbf{f}}_2 | \hat{\mathbf{a}} \rangle e^{-i\tau\omega} d\omega = 0, \quad \forall \tau. \quad (4.27)$$

In words, a physical implication of the solvability condition is that, on average in the temporal domain, the second-order field must not project on the optimal response (which exhibits the largest possible maintained variance) or on any of its time-shifted versions. This preserves the asymptotic hierarchy thereby guaranteeing that the expansion is well-posed.

We will refer to (4.24) as the Weakly Nonlinear Non-normal stochastic (WNNs) model. Depending, for instance, on the nature of the nonlinearity, it may already capture dominant weakly nonlinear effects, without the need for higher-order correction. This will be the case of our first application case, and in this scenario, an equilibrium solution is found by solving (4.24) for a statistically steady regime $d_{\tau_1} \hat{B} = 0$. In any case, and by definition, an equilibrium solution $\hat{B}(\omega)$ does not depend on the slow time scale(s) and is associated with the weakly

nonlinear stochastic gain

$$\begin{aligned}
G_{\text{WNNs}} &= \frac{\overline{\{\|\epsilon_o \mathbf{u}_1(t)\|^2\}}}{F^2} = \frac{\overline{\{\|\epsilon_o \hat{\mathbf{u}}_1(\omega)\|^2\}}}{F^2} = \frac{\epsilon_o^2 \overline{\{\langle \hat{B}(\omega) \hat{\mathbf{q}}(\omega) | \hat{B}(\omega) \hat{\mathbf{q}}(\omega) \rangle\}}}{F^2} \\
&= \frac{\epsilon_o^2 \overline{\{\|\hat{B}(\omega)\|^2\}} \overline{\langle \hat{\mathbf{q}}(\omega) | \hat{\mathbf{q}}(\omega) \rangle}}{F^2} \\
&= \frac{1}{2\pi \epsilon_o^2 \phi^2} \int_{-\infty}^{\infty} \{\|\hat{B}(\omega)\|^2\} \|\hat{\mathbf{q}}(\omega)\|^2 d\omega.
\end{aligned} \tag{4.28}$$

since $F^2 = \phi^2 \epsilon_o^4$.

Note that, in the time-independent case $d_{\tau_1} \hat{B} = 0$, the method presented in this chapter is in a certain sense more general than the method of harmonic balance, but in another sense more restricted. More general because the nonlinear evolution captured by the amplitude equation does not rely on the assumption that the dominant nonlinear mechanism is the Reynolds stress feedback onto the mean flow, thus does not neglect the nonlinearity arising from the cross-coupling between different frequencies. These cross-couplings are fully embedded in the term $\hat{g}_2[\hat{B}]$. More restricted, however, because our method explicitly relies on an asymptotic expansion, which makes it simpler to implement but in principle also limits its validity to weak forcing. This is not the case for the harmonic balance technique, which has been shown to work also in the strongly nonlinear regime, where the spatial structure of the saturated response differs considerably from that of the linear regime (Mantič-Lugo & Gallaire, 2016b). Specifically, the harmonic balance technique typically retains the spatial degrees of freedom, whereas the space-independent amplitude equation condemns the response to be structurally close to the linear one.

In the linear regime $\phi \rightarrow 0$, the equilibrium solution of (4.24) is simply

$$\hat{B} = \phi \hat{\xi} \frac{\langle \hat{\mathbf{a}} | \mathbf{f}_h \rangle}{\langle \hat{\mathbf{a}} | \mathbf{f}_o \rangle}, \tag{4.29}$$

implying

$$\{\langle \mathbf{u}_1(t) | \mathbf{l}(t) \rangle\} = \phi \epsilon_o^2 \langle \mathbf{f}_h | B^\infty \mathbf{f}_o \rangle = \phi \langle \mathbf{f}_h | \mathbf{f}_o \rangle. \tag{4.30}$$

Therefore if the applied forcing is orthogonal to \mathbf{f}_o , the response to the former will be *in average* orthogonal to the response of the latter, which is consistent. Conversely, if the optimal forcing is applied, the linear solution is $\hat{B} = \phi \hat{\xi}$ and leads to the expected gain $G = 1/\epsilon_o^2$. In the rest of the chapter, we choose $\mathbf{f}_h = \mathbf{f}_o$ for the sake of simplicity.

The weakly nonlinear gain defined in (4.28) will be compared with the fully nonlinear gain extracted from a DNS of (4.1), and repeated hereafter as being

$$G_{\text{DNS}} \doteq \frac{\overline{\{\|\mathbf{u}_p(t)\|^2\}}}{F^2} = \frac{1}{2\pi F^2} \int_{-\infty}^{\infty} \|\hat{\mathbf{u}}_p(\omega)\|^2 d\omega, \quad \text{with} \quad \mathbf{u}_p(t) = \mathbf{U}(t) - \bar{\mathbf{U}}. \tag{4.31}$$

In contrast to the WNNs approach, the DNS are performed in the time domain for $t \in [0, T]$.

We first discuss the performance of the WNNs model on a toy model, for which our results should be easily reproducible. We consider the 2×2 system

$$\frac{d\mathbf{U}}{dt} = L\mathbf{U} + \|\mathbf{U}\|M\mathbf{U} + F\xi(t)\mathbf{f}_o, \quad \text{with } L = \begin{bmatrix} -1/Re & 1 \\ 0 & -2/Re \end{bmatrix}, M = \begin{bmatrix} 0 & -1 \\ -1 & 0 \end{bmatrix}, \quad (4.32)$$

thus the nonlinear operator in (4.1) is $N(\mathbf{U}) = L\mathbf{U} + \|\mathbf{U}\|M\mathbf{U}$. This system is a slightly modified version of that in Trefethen et al. (1993) (where $M_{21} = 1$), such that its only stable equilibrium solution is $\mathbf{U}_e = \mathbf{0}$ (two other equilibria exist but are unstable).

Provided $Re \gg 1$, the matrix L is strongly non-normal and amplifies energy transiently, although its two eigenvalues $-1/Re$ and $-2/Re$ are strictly stable. For $Re = 160$ we compute $\mathbf{f}_o = [0.0125, 0.9999]^T$ associated with the gain $1/\epsilon_o^2 = 3.4143 \times 10^5$. We solve the WNNs model numerically, with the amplitude equation (4.24) for $d_{\tau_1} \hat{B} = 0$ uniformly discretised with N frequencies $\omega \in [0, \omega_c]$ where $\omega_c = \pi$. More details are provided in the Appendix 4.5.1.

In figure 4.2, predictions from the WNNs model are compared with fully nonlinear gains, where $\mathbf{U}(t)$ is extracted from a DNS of (4.32), for $t \in [0, T]$ with $T = 6.6 \cdot 10^5$ simulated and sampled at $\Delta t = \pi/\omega_c \approx 5$. For both the WNNs and the DNS approaches, the results have been ensemble-averaged over 10^4 realisations of the white noise. The agreement is remarkable for all the considered forcing amplitudes, thus we need not correct the amplitude equation with $O(\epsilon_o^3)$ terms. The WNNs model correctly predicts the monotonic decrease of the gain with the forcing amplitude (Fig. 4.2a) and the modification of the frequency distribution (Fig. 4.2b), in particular the significant increase of the most amplified frequency. We propose a tentative explanation for the shift of the response peak to higher frequencies as follows

In figure 4.2b, the peak of the linear response in $\omega = 0$ is due to the presence of both eigenvalues on the imaginary axis (although their location alone is insufficient to deduce the stochastic gain, due to the non-normality of the operator). We explain the shift of the peak to higher frequencies with increasing nonlinearities as follows. The equilibrium solution ($d_{\tau_1} \hat{B} = 0$) of the amplitude equation (4.24) reads

$$\hat{B} = \frac{\epsilon_o}{\|\hat{\mathbf{q}}\|^2} \hat{g}_2[\hat{B}] + \phi \hat{\xi}, \quad (4.33)$$

where we used that $\langle \hat{\mathbf{a}} | \mathbf{f}_o \rangle = \langle \hat{\mathbf{q}} | \hat{\mathbf{q}} \rangle / \epsilon_o = \|\hat{\mathbf{q}}\|^2 / \epsilon_o$. We plot in figure 4.1 the ensemble average of the absolute value of

1. the solution : $\{|\hat{B}|\}$,
2. the nonlinear term : $\epsilon_o \|\hat{\mathbf{q}}\|^{-2} \{|\hat{g}_2[\hat{B}]\}$,
3. the same nonlinear term but replacing \hat{B} by its solution in the linear regime $\phi \hat{\xi}$: $\epsilon_o \|\hat{\mathbf{q}}\|^{-2} \{|\hat{g}_2[\phi \hat{\xi}]\}$,

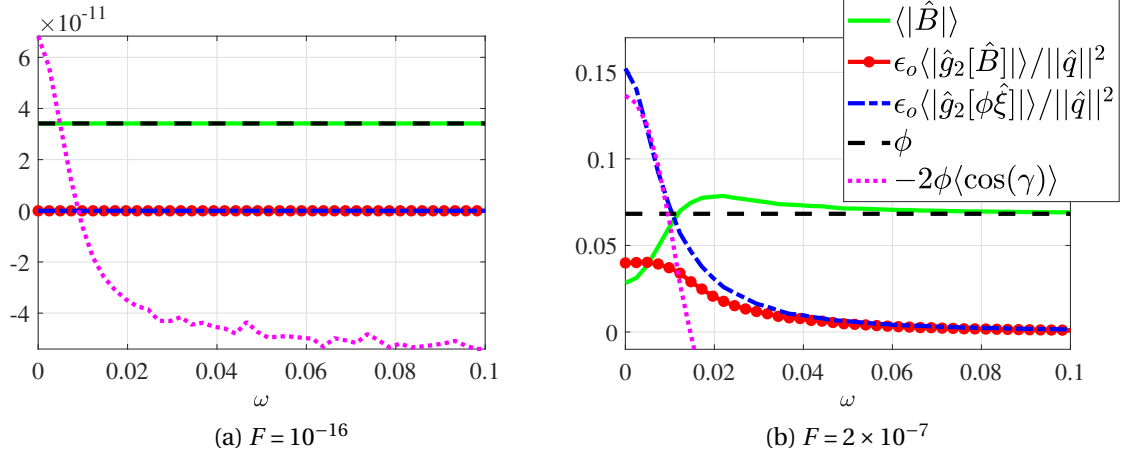


Figure 4.1

4. the linear stochastic forcing term : $\{\phi \hat{\xi}\} = \phi$.

In the linear regime for $F = 10^{-16}$ ($\phi \rightarrow 0$) in fig. 4.1a, $\hat{B} = \phi \hat{\xi}$ is solution, for the nonlinear term \hat{g}_2 is virtually zero. However when we increase the forcing up to $F = 2 \times 10^{-7}$ in fig. 4.1b, the nonlinear interaction of the linear (optimal) response $\phi \hat{\xi} \hat{q}$ with itself is no more negligible and creates a strong response peaked around $\omega = 0$, which projects back on the optimal response (see dash-dotted blue line in fig. 4.1b). Thereby, $\hat{B} = \phi \hat{\xi}$ cannot be solution anymore, and \hat{B} must adapt around $\omega = 0$ such as to enforce the solvability condition. In more physical terms, \hat{B} must adapt around $\omega = 0$ such that the nonlinear interaction of $\hat{B} \hat{q}$ with itself is less amplified around $\omega = 0$ than the one of $\phi \hat{\xi} \hat{q}$, thus preserving the asymptotic hierarchy. This is indeed what we observe in fig. 4.1b, where the red curve (with the bullet markers) is significantly less amplified than the dashed-blue one. Whether this new \hat{B} must have a larger or lower amplitude than its linear value ϕ is given by the phase difference, that we call γ , between the nonlinear and the forcing terms in (4.33). It is easy to show that $|\hat{B}| \leq \phi$ if and only if

$$-2\phi \cos(\gamma) \geq \epsilon_o \|\hat{q}\|^{-2} |\hat{g}_2[\hat{B}]| \quad (4.34)$$

For this reason we show $-2\phi \langle \cos(\gamma) \rangle$ in fig. 4.1b (see the magenta dotted line). In the range $0 \leq \omega \leq 0.012$, $\langle \cos(\gamma) \rangle$ decreases monotonically from -1 in $\omega = 0$ (the forcing and the nonlinear terms are in anti-phase) to -0.2 in $\omega = 0.012$; in addition the magenta dotted line is above the red one, thus $|\hat{B}| \leq \phi$ and the nonlinearities are saturating in the sense that the weakly nonlinear response is of lower amplitude than the linear one. On the contrary, for $\omega \geq 0.012$ the phase difference between the forcing and the nonlinear terms is such that $|\hat{B}| \geq \phi$ and the nonlinearities are desaturating. Therefore the maximum of $\|\hat{B} \hat{q}\|$ is now increased to $\omega = 0.005$. This tendency is conserved for all the considered F .

We have also verified that the predictions for the stochastic gain (see inset in Fig. 4.2a) and the Fourier spectra (not shown) remain very good for different values of the small parameter ϵ_o ,

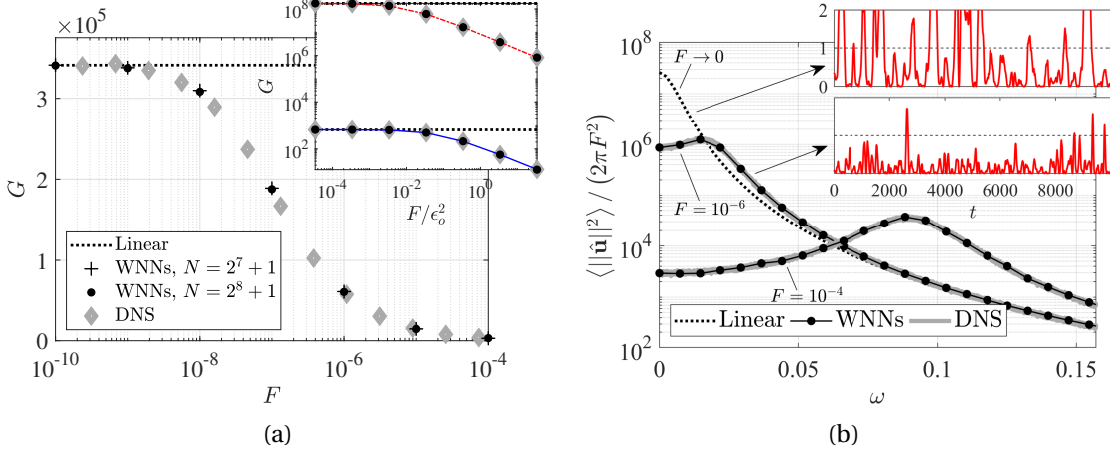


Figure 4.2: **(a)** Weakly and fully nonlinear stochastic gains (defined respectively in (4.28) and (4.31)) for the toy model (4.32), $Re = 160$. Inset: same for $Re = 20$ (continuous blue line) and $Re = 1280$ (dash-dotted red line), but in log-log scale with the x -axis rescaled by the linear gain. **(b)** For the case $Re = 160$, associated ensemble-averaged Fourier spectra of the response $\hat{\mathbf{u}}$ (where $\epsilon_o \hat{\mathbf{u}}_1 = \epsilon_o \hat{\mathbf{B}} \hat{\mathbf{q}}$ in the WNNs approach and $\hat{\mathbf{u}}_p$ in the DNS), normalised such that G is twice the area under the curve. Insets: single realisations of $\epsilon_o^2 \|\mathbf{u}_p(t)\|^2 / F^2$ as a function of time in the statistically steady regime (red solid line), and ensemble average in the linear regime (black dashed line).

namely for $Re = 20$ and $Re = 1280$.

4.3.2 Bilinear system and application to the backward-facing step flow

The weakly nonlinear evolution of the stochastic gain is now sought for the incompressible Navier-Stokes equations (NSE). The nonlinear term $C(\mathbf{U}, \mathbf{U})$, where $C(\mathbf{a}, \mathbf{b}) \doteq ((\mathbf{b} \cdot \nabla) \mathbf{a} + (\mathbf{a} \cdot \nabla) \mathbf{b})/2$, is bilinear. Therefore, we expect essential nonlinear interactions to arise at third order in the expansion parameter, which we want to account for in the amplitude equation. Although it is certainly possible to correct (4.24) at order $O(\epsilon_o^3)$ after introducing a slower time scale τ_2 , it is simpler to rescale the forcing and the linear term such that they appear directly at the third order. In this manner, we avoid a response at second order, which would interact at the next order and obscure the amplitude equation unnecessarily. We propose the rescaled multiple-scale expansion

$$\mathbf{U}(t, \tau_1, \tau_2) = \mathbf{U}_e + \sqrt{\epsilon_o} \mathbf{u}_1(t, \tau_1, \tau_2) + \epsilon_o \mathbf{u}_2(t, \tau_1, \tau_2) + \sqrt{\epsilon_o^3} \mathbf{u}_3(t, \tau_1, \tau_2) + O(\epsilon_o^2), \quad (4.35)$$

where $\tau_1 = \sqrt{\epsilon_o} t$ and $\tau_2 = \epsilon_o t$. The flow is weakly forced by

$$\mathbf{F} = \phi \sqrt{\epsilon_o^3} \mathbf{f}_o \xi(t) \quad (4.36)$$

(a second advantage of the rescaling is that the forcing amplitude

$$F = \phi \sqrt{\epsilon_o^3} \quad (4.37)$$

can be larger than that previously defined by a factor $1/\sqrt{\epsilon_o}$. Following the method outlined in the previous section, we introduce (4.35) in the NSE, take the Fourier component at ω and perturb the inverse resolvent according to (4.10). The solution at $O(\sqrt{\epsilon_o})$ is again

$$\hat{\mathbf{u}}_1(\tau_1, \tau_2; \omega) = \hat{\mathbf{B}}(\tau_1, \tau_2; \omega) \hat{\mathbf{q}}(\omega). \quad (4.38)$$

At $O(\epsilon_o)$ we unravel

$$\Phi \hat{\mathbf{u}}_2 = -\hat{\mathbf{q}} \partial_{\tau_1} \hat{\mathbf{B}} + \hat{\mathbf{g}}_2[\hat{\mathbf{B}}], \quad (4.39)$$

with

$$\hat{\mathbf{g}}_2[\hat{\mathbf{B}}] = -\mathcal{F} \left(C(\mathcal{F}^{-1}(\hat{\mathbf{B}}\hat{\mathbf{q}}), \mathcal{F}^{-1}(\hat{\mathbf{B}}\hat{\mathbf{q}})) \right). \quad (4.40)$$

Imposing the Fredholm alternative such that the right-hand side ($\doteq \hat{\mathbf{f}}_2$) of (4.39) is orthogonal to $\hat{\mathbf{a}}$ yields

$$\langle \hat{\mathbf{a}} | \hat{\mathbf{q}} \rangle \partial_{\tau_1} \hat{\mathbf{B}} = \langle \hat{\mathbf{a}} | \hat{\mathbf{g}}_2[\hat{\mathbf{B}}] \rangle = \hat{\mathbf{g}}_2[\hat{\mathbf{B}}]. \quad (4.41)$$

The field $\hat{\mathbf{u}}_2^\perp \doteq R \hat{\mathbf{f}}_2$ is such that

$$\langle \hat{\mathbf{u}}_2^\perp | \hat{\mathbf{q}} \rangle = \langle \hat{\mathbf{f}}_2 | \hat{\mathbf{a}} \rangle = 0. \quad (4.42)$$

thus $\Phi \hat{\mathbf{u}}_2^\perp = R^{-1} \hat{\mathbf{u}}_2^\perp$ and $\hat{\mathbf{u}}_2^\perp$ constitutes the particular solution of (4.39). The general solution can be written as $\hat{\mathbf{u}}_2 = \hat{\mathbf{u}}_2^\perp + \hat{\mathbf{B}}_2 \hat{\mathbf{q}}$, with an arbitrary component $\hat{\mathbf{B}}_2 \hat{\mathbf{q}}$ on the kernel. We set $\hat{\mathbf{B}}_2 = 0$ in the following, such that the component on $\hat{\mathbf{q}}$ of the overall response is fully embedded in $\hat{\mathbf{B}}$, which can be corrected at higher order thanks to its dependence on slower time scales. Consequently,

$$\hat{\mathbf{u}}_2[\hat{\mathbf{B}}] = \hat{\mathbf{u}}_2^\perp[\hat{\mathbf{B}}] = R \left(\hat{\mathbf{g}}_2[\hat{\mathbf{B}}] - \langle \hat{\mathbf{a}} | \hat{\mathbf{q}} \rangle^{-1} \hat{\mathbf{g}}_2[\hat{\mathbf{B}}] \hat{\mathbf{q}} \right). \quad (4.43)$$

Collecting terms at $O(\sqrt{\epsilon_o^3})$, injecting the expressions for $\hat{\mathbf{u}}_1$ and $\hat{\mathbf{u}}_2$ and using the Fredholm alternative leads to an expression for $\partial_{\tau_2} \hat{\mathbf{B}}$,

$$\langle \hat{\mathbf{a}} | \hat{\mathbf{q}} \rangle \partial_{\tau_2} \hat{\mathbf{B}} = \langle \hat{\mathbf{a}} | \mathbf{f}_o \rangle (\phi \hat{\xi} - \hat{\mathbf{B}}) - \langle \hat{\mathbf{a}} | \partial_{\tau_1} \hat{\mathbf{u}}_2[\hat{\mathbf{B}}] \rangle + \hat{\mathbf{g}}_3[\hat{\mathbf{B}}], \quad (4.44)$$

with the functional

$$\hat{\mathbf{g}}_3[\hat{\mathbf{B}}] = -\langle \hat{\mathbf{a}} | \mathcal{F} \left(2C(\mathcal{F}^{-1}(\hat{\mathbf{B}}\hat{\mathbf{q}}), \mathcal{F}^{-1}(\hat{\mathbf{u}}_2[\hat{\mathbf{B}}])) \right) \rangle. \quad (4.45)$$

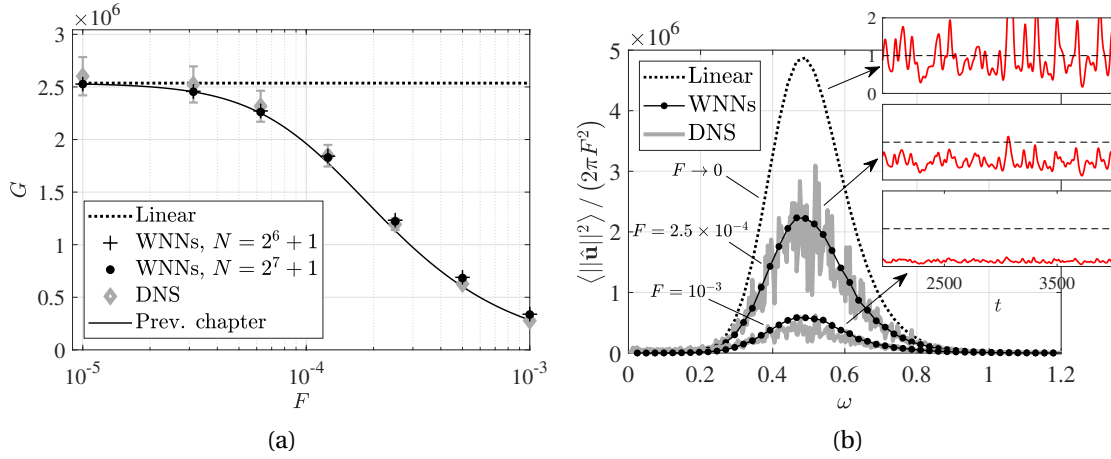


Figure 4.3: Same as Fig. 4.2 for the BFS flow, $Re = 500$. Error bars around DNS points show plus or minus one standard deviation. In (a) we also reproduce as the continuous black line the results from the equilibrium solution amplitude equation (3.59), derived in the previous chapter, and already shown in figure 3.3.

The total slow temporal evolution of \hat{B} for a given frequency is found by combining partial derivatives with respect to the slow time scales (Orchini et al., 2016) as

$$\frac{d\hat{B}}{d\tau_1} = \frac{\partial \hat{B}}{\partial \tau_1} + \frac{\partial_{\tau_1}}{\partial \tau_2} \frac{\partial \hat{B}}{\partial \tau_2} = \frac{\partial \hat{B}}{\partial \tau_1} + \sqrt{\epsilon_o} \frac{\partial \hat{B}}{\partial \tau_2}. \quad (4.46)$$

Eventually, it leads to an ordinary differential equation for \hat{B} (remember that $\mathbf{f}_h = \mathbf{f}_o$):

$$\langle \hat{\mathbf{a}} | \hat{\mathbf{q}} \rangle d_{\tau_1} \hat{B} = \hat{g}_2[\hat{B}] + \sqrt{\epsilon_o} [\langle \hat{\mathbf{a}} | \mathbf{f}_o \rangle (\phi \hat{\xi} - \hat{B}) + \hat{g}_3[\hat{B}] - \partial_{\tau_1} \langle \hat{\mathbf{a}} | \hat{\mathbf{u}}_2[\hat{B}] \rangle]. \quad (4.47)$$

An equilibrium solution $\hat{B}(\omega)$ of (4.47) is sought for given choices of ϕ and phase distribution for $\hat{\xi}$. It is associated with the statistically steady stochastic gain (4.28). In the linear regime, $\phi \rightarrow 0$ and $\hat{B} \rightarrow \phi \hat{\xi}$, so the gain reduces to $G = 1/\epsilon_o^2$ as expected. All the nonlinear terms such as $\hat{g}_2[\hat{B}]$, $\hat{g}_3[\hat{B}]$ and $\partial_{\tau_1} \langle \hat{\mathbf{a}} | \hat{\mathbf{u}}_2[\hat{B}] \rangle$ are convolution integrals accounting for the nonlinear interactions between the Fourier modes. They can be discretised in the frequency domain as quadratic or cubic products of the Fourier components of $\hat{B}(\omega)$. Detailed expressions are given in Appendix 4.5.2, together with an algorithm to solve for the equilibrium solution.

We now consider the weakly nonlinear evolution of the stochastic gain in the two-dimensional backward-facing step (BFS) flow at $Re = 500$, the same as in the previous chapter. As mentioned, the nonlinear and linearised NSE are solved with the finite element method. Figure 3.1(a) shows the optimal stochastic forcing \mathbf{f}_o and a DNS snapshot of the flow response to $F\hat{\xi}(t)\mathbf{f}_o$ for $F = 0.00025$.

The results of the WNNs model are reported in Fig. 4.3, where the amplitude equation (4.47) for $d_{\tau_1} \hat{B} = 0$ was uniformly discretised with N frequencies $\omega \in [0, \omega_c]$ with $\omega_c = \pi$, and the results were ensemble-averaged over 500 realisations of the white noise. Predictions from

the DNS are also shown, resulting from simulations of duration $T = 2049$ after the transients fade away, sampled at $\Delta t = \pi/\omega_c = 1$ and ensemble-averaged over 10 realisations of the white noise (this lower number of realisations is the consequence of each one being numerically costly). Unlike the toy model of section 4.3.1, the amplitude equation built from a forcing introduced at second order and stopped at second order did not capture significant nonlinear effects (not shown). Introducing instead the forcing at third order, as described above, the comparison with DNS data is conclusive: the stochastic gains experience a monotonic decay with increasing F , also associated with a decreasing standard deviation for the DNS data.

We now emphasise that the fully nonlinear stochastic gain in (4.31) considers perturbation around the *temporal mean* flow, and not around the *base* flow \mathbf{U}_e . This distinction was unimportant in the previous application case since the nonlinearity did not generate a temporal mean. The creation of non-zero temporal mean ($\overline{\mathbf{U}(t)} \neq 0$) is associated with a diverging behaviour of the Fourier component at $\omega = 0$, as the normalisation in (3.2) directly implies $\hat{\mathbf{U}}(0) = \overline{\mathbf{U}(t)}\sqrt{T} \rightarrow \infty$. Since this divergence is unlikely to be captured by $\hat{B}(0)$, we omitted its contribution in the gain calculation, but noted that this did not change the gain. However, the WNNs model certainly takes into account the effects of temporal mean flow corrections on $\hat{\mathbf{u}}_1(\omega)$, as such steady corrections are created at the next order and embedded in $\mathbf{u}_2(t)$.

For small F close to the linear regime, DNS and WNNs show some discrepancies (Fig. 4.3a) that are believed to be due to an imperfect convergence of the DNS data, because of the large standard deviation at small F and the limited number of realisations. The limit of large F is also associated with a slight departure of the (well-converged) DNS data from the WNNs predictions, although it is believed this time to be due solely to increasingly strong nonlinearities. In fig.4.3b, the Fourier spectra reveal that increasing F conserves the most amplified frequency, which may be due to the fact that the forcing structure is fixed to \mathbf{f}_o , extremely similar to the optimal harmonic forcing for $\omega = 0.47$. In the inset, from the temporal evolution of the signal $\propto \|\mathbf{u}(t)\|^2$ we recover that, for this particular flow, nonlinearities not only saturate the average level of energy of the response, but also significantly reduce the amplitude of the oscillations (i.e, the standard deviation).

In figure 4.3a, we also reproduce as the continuous black line the results from the equilibrium solution amplitude equation (3.59) derived in the previous chapter, and already shown in figure 3.3. Results are remarkably similar with the current WNNs approach. This is particularly interesting by recalling that in (3.59), the quadratic term vanished (i.e. $\mu_2 = 0$) due to the nature of the considered noise. Thereby, if the WNNs results were obtained by including quadratic nonlinearities embedded in the convolution \hat{g}_2 , their effects vanish upon taking the ensemble average.

If interested solely in the gain variation, the agreement between both weakly nonlinear approaches clearly advocate in favor of (3.59), considering its simplicity with respect to the WNNs equation. Equation (3.59), however, would not predict well the weakly nonlinear evolution of the response at each frequency in figure 4.3b, for it possesses only one degree of

freedom and does not depend on the frequency. In other terms, it can only rescale the linear spectrum in figure 4.3b, without modifying its shape. Yet, as we said, if it is inherently unable to describe the details of the Fourier spectrum variation at each frequency, it predicts very well the evolution of its integral, i.e. the stochastic gain.

Finally, note that the asymptotic expansions (4.17) and (4.35) have been scaled differently in order for the linear ($\propto \hat{B}$) and forcing ($\propto \phi \hat{\xi}$) terms to appear at the last considered order. This raises the question of how to know *a priori*, and for a given nonlinearity, the minimal order that should be considered. Although a "trial and error" process is always arguably acceptable, we postulate that it is the earliest order where the nonlinear term generates a component oscillating at ω_o , in the limit where the linear response \hat{q} is monochromatic and oscillating at ω_o . Indeed, if we impose the solvability condition solely at the order(s) before, \hat{B} will conserve its linear value, for the nonlinear term will naturally yield a null scalar product with the adjoint for all frequencies (both fields being non-zero at different frequencies). This scenario, which we want to avoid, does not occur in the opposite limit where the frequency spectrum of \hat{q} is flat. Of course, the linear optimal response has generally no reason to be monochromatic, but might still show a maximum in energy at selective frequencies, as was the case in Fig. 4.2b and Fig. 4.3b. If we express $\mathbf{u}_1 = \hat{B} \hat{q} e^{i\omega_o t} + c.c.$, the nonlinearity of the toy system at second order (i.e. $\|\mathbf{u}_1\| M \mathbf{u}_1$) already generates terms oscillating at ω_o ; therefore it was sufficient to consider only up to this second order to see an improvement over the linear prediction. For the NSE, however, one needs to go to the third order to recover terms in ω_o (specifically $\hat{B} |\hat{B}|^2 e^{i\omega_o t}$, as well known for classical weakly nonlinear equations for an eigenmode amplitude).

4.4 Conclusions

By generalising the method proposed in chapter 2 to include several frequencies in the leading order response instead of only one, we have derived an amplitude equation describing the weakly nonlinear, statistically steady response to stochastic forcing in arbitrarily stable yet non-normal systems.

Contrarily to the paradigm proposed in chapter 3, the inner product involved in the perturbation operator remains purely over spatial dimensions despite the fact that the linear response varies continuously over the frequencies. This has the consequence that the operator perturbation is less well posed than that proposed in chapter 3. Indeed, in the previous chapter, the operator perturbation was such that

$$\{ \|\epsilon_o P(\omega; \theta)\| \} = \epsilon_o \ll 1, \quad (4.48)$$

whereas in the current chapter we have

$$\|\epsilon_o P(\omega)\| = \frac{\epsilon_o}{\|\hat{q}(\omega)\|}, \quad (4.49)$$

which may be very large. This results the fact that the norm induced by the L^2 inner produced

is not the one associated with a large amplification $1/\epsilon_o$, the latter having also involved integration over frequencies. Thereby, (4.49) can't lead a unit perturbation of size ϵ_o for each frequency. The perturbation is only valid over a certain range of frequencies, the one leading to the largest amplification of the \mathbf{f}_o through application of the resolvent operator (i.e., around the peak of the linear transfer function $\|R(\omega)\mathbf{f}_o\|$).

Nevertheless, relaxing the inner product to be solely over space gives the possibility for the amplitude to vary over the frequencies. Thereby the amplitude equation can describe the weakly nonlinear evolution of the Fourier spectrum of linear response over a continuous range of frequency. This constitutes an amelioration over the equation derived in chapter 3, which predicted the evolution of the integral of the Fourier spectrum (i.e., the stochastic gain). However, such amelioration is at the cost of making the computations, and the final amplitude equation to be solved for, considerably more complex as nonlinear interactions between frequencies are accounted for through convolution products. One is then left to the choice between the amplitude (3.59) whose equilibrium solution simply is the root of a third-order polynomial but describing only an integrated quantity, and a much more complicated but for informative amplitude equation.

The amplitude equation derived in this chapter may still save a significant amount of computational resources compared to fully nonlinear simulations, where long simulated times and/or many realisations are needed to ensure statistical convergence, which becomes rapidly impracticable for large systems like fluid flows. The amplitude equation has been successfully compared to fully nonlinear numerical simulations, and predicts well the variation of both the stochastic gain and the Fourier spectrum with the forcing amplitude.

Future research may include applying the methods developed in the previous and current chapter to realistic flows (e.g. atmospheric flows subject to weak forcing, such as zonal jets in barotropic flows (Bouchet et al., 2013)), and developing extensions towards systems with multiple attractors and noise-induced transitions.

The latter subject is considered in the next chapter. Specifically, we consider a stochastically forced fluid flow past the onset of a supercritical pitchfork bifurcation, where two attractors exist. The dynamics is reduced to a stochastically forced modal amplitude equation, from which the statistics of the noise-induced transitions between the two attractors can be predicted. This will serve as a building block for the ultimate chapter of this second part, coupling a modal stochastic response which transits between attractors, and a non-normal one.

4.5 Appendix

4.5.1 discretisation of the amplitude equation in the frequency domain

We recall from the main text (Eq.(3.5) for $\mathbf{f}_h = \mathbf{f}_o$) that we seek the equilibrium solution of the amplitude equation

$$\langle \hat{\mathbf{a}} | \hat{\mathbf{q}} \rangle \frac{d\hat{B}}{d\tau_1} = \hat{g}_2[\hat{B}] + \langle \hat{\mathbf{a}} | \mathbf{f}_o \rangle (\phi \hat{\xi} - \hat{B}) = 0. \quad (4.50)$$

The first step is to discretize it, in the frequency domain. For this purpose, let ω_s designates the sampling frequency of the corresponding temporal signals, that are discretized using $2(N-1)$ (a power of two) uniformly distributed points between $t = 0$ and $t = T$. In this manner, we have in practice $-\omega_c \leq \omega \leq \omega_c$ where $\omega_c = \omega_s/2$, and the positive part of this frequency interval is discretized with N uniformly distributed points between $\omega = 0$ and $\omega = \omega_c$. Namely, the discrete set of positive frequencies writes $\omega_n = (n-1)\Delta\omega$ for $n = 1, 2, \dots, N$ and $\Delta\omega = \omega_c/(N-1)$. The discrete Fourier transforms varying over this interval are real-valued in $\omega_1 = 0$ and $\omega_N = \omega_c$, but generally complex everywhere else; for instance, $\hat{B}(\omega)$ is discretized as $[B_{r,1}, B_{r,2} + iB_{i,2}, \dots, B_{r,N-1} + iB_{i,N-1}, B_{r,N}]$ which amounts to $2(N-2) + 2 = 2(N-1)$ independent components in total. Only the variation over the set of positive frequencies is needed, as the Fourier component of a real-valued signal at a negative frequency is the complex conjugate of the one at the opposite frequency: $\hat{B}(-\omega) = \hat{B}(\omega)^*$. With (4.50) discretized, the following simple procedure is implemented in MATLAB:

Algorithm :

1. Choose the values for N and ω_c , which sets the discretisation of the frequencies.
2. Over the discrete set of frequencies, pre-compute once for all the *deterministic* fields \mathbf{f}_o , $\hat{\mathbf{q}}$, $\hat{\mathbf{a}}$.
3. Choose a value for ϕ (which sets the forcing amplitude).
4. Draw a white noise ($|\hat{\xi}(\omega)| = 1 \forall \omega$, but random phases uniformly distributed between 0 and 2π), for instance with the commands `xi = exp(1i*2*pi*rand(1,N))`, then `xi(1)=real(xi(1))/abs(real(xi(1)))` and `xi(N)=real(xi(N))/abs(real(xi(N)))`.
5. Find the \hat{B} that solves $r(\hat{B}; \phi, \hat{\xi}) = 0$ where $r(\hat{B}; \phi, \hat{\xi}) \doteq \hat{g}_2[\hat{B}] + \langle \hat{\mathbf{a}} | \mathbf{f}_o \rangle (\phi \hat{\xi} - \hat{B})$, using the nonlinear solver "fsolve"; the functional $\hat{g}_2[\hat{B}]$ is evaluated using the commands "ifft" and "fft".
6. Update the statistics on \hat{B} , for instance its ensemble average, and, if not converged go back to (4).

Of course the convergence in terms of N and ω_c must be ensured.

4.5.2 The particular case of the NSE: discretisation of the amplitude equation in the frequency domain

We recall from the main text that

$$\begin{aligned} \langle \hat{\mathbf{a}} | \hat{\mathbf{q}} \rangle \frac{\partial \hat{B}}{\partial \tau_1} &= \hat{g}_2[\hat{B}], \quad \text{and} \\ \langle \hat{\mathbf{a}} | \hat{\mathbf{q}} \rangle \frac{\partial \hat{B}}{\partial \tau_2} &= \langle \hat{\mathbf{a}} | \mathbf{f}_o \rangle (\phi \hat{\xi} - \hat{B}) + \hat{g}_3[\hat{B}] - \frac{\partial \langle \hat{\mathbf{a}} | \hat{\mathbf{u}}_2[\hat{B}] \rangle}{\partial \tau_1}. \end{aligned} \quad (4.51)$$

The equilibrium solution(s) of the assembled amplitude equation solves :

$$\begin{aligned} \frac{d\hat{B}}{d\tau_1} &= \frac{\partial \hat{B}}{\partial \tau_1} + \sqrt{\epsilon_o} \frac{\partial \hat{B}}{\partial \tau_1} = 0 \Leftrightarrow \\ \hat{g}_2[\hat{B}] + \sqrt{\epsilon_o} \left[\langle \hat{\mathbf{a}} | \mathbf{f}_o \rangle (\phi \hat{\xi} - \hat{B}) + \hat{g}_3[\hat{B}] - \frac{\partial \langle \hat{\mathbf{a}} | \hat{\mathbf{u}}_2[\hat{B}] \rangle}{\partial \tau_1} \right] &= 0. \end{aligned} \quad (4.52)$$

In the following, after re-expressing the nonlinear terms $\hat{g}_2[\hat{B}]$, $\hat{g}_3[\hat{B}]$ and $\partial_{\tau_1} \langle \hat{\mathbf{a}} | \hat{\mathbf{u}}_2[\hat{B}] \rangle$ in (4.52) as convolution integrals, we discretize them in the frequency domain. In this manner, we make their dependency on the discrete set of \hat{B}_i ($i = 1, 2, \dots, N$) as explicit as possible. All the other, linear, terms are simple to discretize.

Derivation of the convolution integral

We first develop:

$$\begin{aligned} 2C(\mathcal{F}^{-1}(\hat{\mathbf{u}}_a), \mathcal{F}^{-1}(\hat{\mathbf{u}}_b)) &= \nabla \mathcal{F}^{-1}(\hat{\mathbf{u}}_a) \mathcal{F}^{-1}(\hat{\mathbf{u}}_b) + \nabla \mathcal{F}^{-1}(\hat{\mathbf{u}}_b) \mathcal{F}^{-1}(\hat{\mathbf{u}}_a) \\ &= \frac{T}{4\pi^2} \int_{-\infty}^{\infty} \nabla \hat{\mathbf{u}}_a(p) e^{ipt} dp \int_{-\infty}^{\infty} \hat{\mathbf{u}}_b(s) e^{ist} ds + \frac{T}{4\pi^2} \int_{-\infty}^{\infty} \nabla \hat{\mathbf{u}}_b(s) e^{ist} ds \int_{-\infty}^{\infty} \hat{\mathbf{u}}_a(p) e^{ipt} dp \\ &= \frac{T}{4\pi^2} \iint_{-\infty}^{\infty} 2C(\hat{\mathbf{u}}_a(p), \hat{\mathbf{u}}_b(s)) e^{i(p+s)t} dp ds \\ &= \frac{T}{4\pi^2} \iint_{-\infty}^{\infty} 2C(\hat{\mathbf{u}}_a(\omega - s), \hat{\mathbf{u}}_b(s)) e^{i\omega t} d\omega ds \\ &= \mathcal{F}^{-1} \left(\frac{\sqrt{T}}{2\pi} \int_{-\infty}^{\infty} 2C(\hat{\mathbf{u}}_a(\omega - s), \hat{\mathbf{u}}_b(s)) ds \right), \end{aligned} \quad (4.53)$$

from which it comes immediately that :

$$\mathcal{F}(C(\mathcal{F}^{-1}(\hat{\mathbf{u}}_a), \mathcal{F}^{-1}(\hat{\mathbf{u}}_b))) = \frac{\sqrt{T}}{2\pi} \int_{-\infty}^{\infty} C(\hat{\mathbf{u}}_a(\omega - s), \hat{\mathbf{u}}_b(s)) ds. \quad (4.54)$$

Discretisation of the convolution integral

Let ω_s designates the sampling frequency of the temporal signals, such that we have in practice $-\omega_c \leq \omega \leq \omega_c$ where $\omega_c = \omega_s/2$. Over this set of frequencies, the integrand in (4.54) is defined if and only if we have both $-\omega_c \leq s \leq \omega_c$ and $\omega - \omega_c \leq s \leq \omega + \omega_c$. From now on considering only positive frequencies, i.e $0 \leq \omega \leq \omega_c$, the integrand is then defined if and only if

$$\omega - \omega_c \leq s \leq \omega_c. \quad (4.55)$$

Thereby

$$\begin{aligned} \int_{-\infty}^{\infty} C(\hat{\mathbf{u}}_a(\omega - s), \hat{\mathbf{u}}_b(s)) ds &\approx \int_{\omega - \omega_c}^{\omega_c} C(\hat{\mathbf{u}}_a(\omega - s), \hat{\mathbf{u}}_b(s)) ds \\ &= \int_{\omega - \omega_c}^0 C(\hat{\mathbf{u}}_a(\omega - s), \hat{\mathbf{u}}_b(s)) ds + \int_0^{\omega_c} C(\hat{\mathbf{u}}_a(\omega - s), \hat{\mathbf{u}}_b(s)) ds. \end{aligned} \quad (4.56)$$

The first of the two terms of the sum in (4.56) is transformed as

$$\begin{aligned} \int_{\omega - \omega_c}^0 C(\hat{\mathbf{u}}_a(\omega - s), \hat{\mathbf{u}}_b(s)) ds &= \int_0^{\omega_c - \omega} C(\hat{\mathbf{u}}_a(\omega + s), \hat{\mathbf{u}}_b(-s)) ds \\ &= \int_0^{\omega_c - \omega} C(\hat{\mathbf{u}}_a(\omega + s), \hat{\mathbf{u}}_b^*(s)) ds, \end{aligned} \quad (4.57)$$

where we used that $\hat{\mathbf{u}}_b(-s) = \hat{\mathbf{u}}_b^*(s)$ arising from the fact that all temporal signals are real-valued. The second of the two terms of the sum in (4.56) is transformed according to

$$\begin{aligned} &\int_0^{\omega_c} C(\hat{\mathbf{u}}_a(\omega - s), \hat{\mathbf{u}}_b(s)) ds \\ &= \int_0^{\omega} C(\hat{\mathbf{u}}_a(\omega - s), \hat{\mathbf{u}}_b(s)) ds + \int_{\omega}^{\omega_c} C(\hat{\mathbf{u}}_a(\omega - s), \hat{\mathbf{u}}_b(s)) ds \\ &= \int_0^{\omega} C(\hat{\mathbf{u}}_a(\omega - s), \hat{\mathbf{u}}_b(s)) ds + \int_{\omega}^{\omega_c} C(\hat{\mathbf{u}}_a^*(s - \omega), \hat{\mathbf{u}}_b(s)) ds \\ &= \int_0^{\omega} C(\hat{\mathbf{u}}_a(\omega - s), \hat{\mathbf{u}}_b(s)) ds + \int_0^{\omega_c - \omega} C(\hat{\mathbf{u}}_a^*(s), \hat{\mathbf{u}}_b(s + \omega)) ds. \end{aligned} \quad (4.58)$$

In this manner, only the knowledge of $\hat{\mathbf{u}}_a$ and $\hat{\mathbf{u}}_b$ over positives frequencies is required. Overall,

$$\begin{aligned} &\int_{\omega - \omega_c}^{\omega_c} C(\hat{\mathbf{u}}_a(\omega - s), \hat{\mathbf{u}}_b(s)) ds = \\ &\int_0^{\omega} C(\hat{\mathbf{u}}_a(\omega - s), \hat{\mathbf{u}}_b(s)) ds + \int_0^{\omega_c - \omega} C(\hat{\mathbf{u}}_a(\omega + s), \hat{\mathbf{u}}_b^*(s)) + C(\hat{\mathbf{u}}_a^*(s), \hat{\mathbf{u}}_b(s + \omega)) ds. \end{aligned} \quad (4.59)$$

Let us now discretize (4.59). As said in the previous section, positive frequencies are discretized using N uniformly distributed points between $\omega = 0$ and $\omega = \omega_c$ (ω_c the cut-off frequency). Namely, the discrete set of positive frequencies writes $\omega_n = (n-1)\Delta\omega$ for $n = 1, 2, \dots, N$ and $\Delta\omega = \omega_c/(N-1)$. Eventually, the discrete version of expression (4.54) reads

$$\mathcal{F}(C(\mathcal{F}^{-1}(\hat{\mathbf{u}}_a), \mathcal{F}^{-1}(\hat{\mathbf{u}}_b))) \approx \frac{\sqrt{T}}{2\pi} \left[\sum_{k=1}^n \delta_k^n C(\hat{\mathbf{u}}_{a,n-k+1}, \hat{\mathbf{u}}_{b,k}) + \sum_{k=1}^{N+1-n} \delta_k^{N+1-n} \left[C(\hat{\mathbf{u}}_{a,k}^*, \hat{\mathbf{u}}_{b,n+k-1}) + C(\hat{\mathbf{u}}_{a,n+k-1}, \hat{\mathbf{u}}_{b,k}^*) \right] \right], \quad (4.60)$$

where we used for instance $\hat{\mathbf{u}}_a(\omega_n - s_k) = \hat{\mathbf{u}}_a(\Delta\omega(n-1-k+1)) = \hat{\mathbf{u}}_{a,n-k+1}$. The scalar δ_i^j is a quadrature coefficient where $i \in [1, j]$ is a running index. In our computations, we used the trapezoidal method such that

$$\delta_1^1 = 0, \quad \text{and} \quad \delta_i^j = \begin{cases} \omega_c/(2(N-1)) & \text{if } i = 1 \\ \omega_c/(N-1) & \text{if } 1 < i < j, \text{ for } j > 1. \\ \omega_c/(2(N-1)) & \text{if } i = j \end{cases} \quad (4.61)$$

Discretisation of the amplitude equation

Discretisation of $\hat{g}_2[\hat{B}]$:

Using (4.60), the functional $\hat{g}_2[\hat{B}] = -\langle \hat{\mathbf{a}} | \mathcal{F}(C(\mathcal{F}^{-1}(\hat{\mathbf{u}}_1), \mathcal{F}^{-1}(\hat{\mathbf{u}}_1))) \rangle$ with $\hat{\mathbf{u}}_1 = \hat{B}\hat{\mathbf{q}}$ is discretized as:

$$\hat{g}_{2,n} = \sum_{k=1}^n \hat{B}_{n-k+1} \hat{B}_k \Theta_{nk} + \sum_{k=1}^{N+1-n} \hat{B}_{n+k-1} \hat{B}_k^* \Xi_{nk}, \quad (4.62)$$

with

$$\begin{aligned} \Theta_{nk} &= -\frac{\sqrt{T}}{2\pi} \delta_k^n \langle \hat{\mathbf{a}}_n | C(\hat{\mathbf{q}}_{n-k+1}, \hat{\mathbf{q}}_k) \rangle, \quad 1 \leq k \leq n, \\ \Xi_{nk} &= -\frac{\sqrt{T}}{\pi} \delta_k^{N+1-n} \langle \hat{\mathbf{a}}_n | C(\hat{\mathbf{q}}_{n+k-1}, \hat{\mathbf{q}}_k^*) \rangle, \quad 1 \leq k \leq N+1-n. \end{aligned} \quad (4.63)$$

The sums in (4.62) can also be written in matrix form:

$$\hat{g}_2[\hat{B}] = \begin{bmatrix} \Theta_{11}\hat{B}_1 & & \mathbf{0} \\ \vdots & \ddots & \\ \Theta_{1N}\hat{B}_N & \dots & \Theta_{NN}\hat{B}_1 \end{bmatrix} \begin{bmatrix} \hat{B}_1 \\ \vdots \\ \hat{B}_N \end{bmatrix} + \begin{bmatrix} \Xi_{11}\hat{B}_1 & \dots & \Xi_{1N}\hat{B}_N \\ \vdots & \ddots & \\ \Xi_{N1}\hat{B}_N & & \mathbf{0} \end{bmatrix} \begin{bmatrix} \hat{B}_1^* \\ \vdots \\ \hat{B}_N^* \end{bmatrix} \quad (4.64)$$

Discretisation of $\partial_{\tau_1} \langle \hat{\mathbf{a}} | \hat{\mathbf{u}}_2[\hat{B}] \rangle = \langle \hat{\mathbf{a}} | \partial_{\tau_1} \hat{\mathbf{u}}_2[\hat{B}] \rangle$:

Since

$$\hat{\mathbf{u}}_2[\hat{B}] = R \left(\hat{\mathbf{g}}_2[\hat{B}] - \frac{\langle \hat{\mathbf{a}} | \hat{\mathbf{g}}_2[\hat{B}] \rangle}{\langle \hat{\mathbf{a}} | \hat{\mathbf{q}} \rangle} \hat{\mathbf{q}} \right), \quad (4.65)$$

where we recall that $\langle \hat{\mathbf{a}} | \hat{\mathbf{g}}_2[\hat{B}] \rangle = \hat{g}_2[\hat{B}]$, expression (4.62) results in the following discretisation for the field $\hat{\mathbf{u}}_2[\hat{B}]$:

$$\hat{\mathbf{u}}_{2,m} = \sum_{j=1}^m \hat{B}_{m-j+1} \hat{B}_j \hat{\mathbf{d}}_{mj} + \sum_{j=1}^{N+1-m} \hat{B}_{m+j-1} \hat{B}_j^* \hat{\mathbf{h}}_{mj}, \quad (4.66)$$

with

$$\begin{aligned} \hat{\mathbf{d}}_{mj} &= R_m \left[-\frac{\sqrt{T}}{2\pi} \delta_j^m C(\hat{\mathbf{q}}_{m-j+1}, \hat{\mathbf{q}}_j) - \alpha_{mj} \hat{\mathbf{q}}_m \right], \\ \hat{\mathbf{h}}_{mj} &= R_m \left[-\frac{\sqrt{T}}{\pi} \delta_j^{N+1-m} C(\hat{\mathbf{q}}_{m+j-1}, \hat{\mathbf{q}}_j^*) - \beta_{mj} \hat{\mathbf{q}}_m \right], \end{aligned} \quad (4.67)$$

and where we defined $\alpha_{mj} = \Theta_{mj} / \langle \hat{\mathbf{a}}_m | \hat{\mathbf{q}}_m \rangle$ and $\beta_{mj} = \Xi_{mj} / \langle \hat{\mathbf{a}}_m | \hat{\mathbf{q}}_m \rangle$. The fields $\hat{\mathbf{d}}_{mj}$ and $\hat{\mathbf{h}}_{mj}$ verify $\langle \hat{\mathbf{q}}_m | \hat{\mathbf{d}}_{mj} \rangle = \langle \hat{\mathbf{q}}_m | \hat{\mathbf{h}}_{mj} \rangle = 0$, implying $\langle \hat{\mathbf{q}}_m | \hat{\mathbf{u}}_{2,m} \rangle = 0$; therefore, each Fourier component generated at second order (i.e $O\epsilon_o$) is orthogonal to the Fourier component of the optimal linear solution at the same frequency. The partial derivative of $\hat{\mathbf{u}}_{2,m}$ with respect to τ_1 follows directly from (4.66):

$$\begin{aligned} \partial_{\tau_1} \hat{\mathbf{u}}_{2,n} &= \sum_{k=1}^n (\partial_{\tau_1} \hat{B}_{n-k+1}) \hat{B}_k \hat{\mathbf{d}}_{nk} + \sum_{k=1}^n \hat{B}_{n-k+1} (\partial_{\tau_1} \hat{B}_k) \hat{\mathbf{d}}_{nk} \\ &+ \sum_{k=1}^{N+1-n} (\partial_{\tau_1} \hat{B}_{n+k-1}) \hat{B}_k^* \hat{\mathbf{h}}_{nk} + \sum_{k=1}^{N+1-n} \hat{B}_{n+k-1} (\partial_{\tau_1} \hat{B}_k^*) \hat{\mathbf{h}}_{nk}. \end{aligned} \quad (4.68)$$

Since $\partial_{\tau_1} \hat{B} = \hat{g}_2[\hat{B}] / \langle \hat{\mathbf{a}} | \hat{\mathbf{q}} \rangle$, we can again use (4.62) and

$$\partial_{\tau_1} \hat{B}_m = \sum_{j=1}^m \hat{B}_{m-j+1} \hat{B}_j \alpha_{mj} + \sum_{j=1}^{N+1-m} \hat{B}_{m+j-1} \hat{B}_j^* \beta_{mj}. \quad (4.69)$$

Evaluating (4.69) in $m = n - k + 1$, $m = n + k - 1$ and $m = k$ yields, respectively:

$$\partial_{\tau_1} \hat{B}_{n-k+1} = \sum_{j=1}^{n-k+1} \hat{B}_{n-k-j+2} \hat{B}_j \alpha_{n-k+1,j} + \sum_{j=1}^{N-n+k} \hat{B}_{n-k+j} \hat{B}_j^* \beta_{n-k+1,j}, \quad (4.70)$$

$$\partial_{\tau_1} \hat{B}_{n+k-1} = \sum_{j=1}^{n+k-1} \hat{B}_{n+k-j} \hat{B}_j \alpha_{n+k-1,j} + \sum_{j=1}^{N-n-k+2} \hat{B}_{n+k+j-2} \hat{B}_j^* \beta_{n+k-1,j}, \quad (4.71)$$

and

$$\partial_{\tau_1} \hat{B}_k^* = \sum_{j=1}^k \hat{B}_{k-j+1}^* \hat{B}_j^* \alpha_{kj}^* + \sum_{j=1}^{N+1-k} \hat{B}_{k+j-1}^* \hat{B}_j^* \beta_{kj}^*. \quad (4.72)$$

After injecting (4.70), (4.71) and (4.72) in (4.68), and projecting on the adjoint, we end up on

$$\begin{aligned} \langle \hat{\mathbf{a}}_n | \partial_{\tau_1} \hat{\mathbf{u}}_{2,n} \rangle &= \sum_{k=1}^n \hat{B}_k \left(\sum_{j=1}^{n-k+1} \hat{B}_{n-k-j+2} \hat{B}_j \mathcal{G}_{nkj} + \sum_{j=1}^{N-n+k} \hat{B}_{n-k+j} \hat{B}_j^* \mathcal{H}_{nkj} \right) \\ &+ \sum_{k=1}^n \hat{B}_{n-k+1} \left(\sum_{j=1}^k \hat{B}_{k-j+1} \hat{B}_j \mathcal{I}_{nkj} + \sum_{j=1}^{N+1-k} \hat{B}_{k+j-1} \hat{B}_j^* \mathcal{J}_{nkj} \right) \\ &+ \sum_{k=1}^{N+1-n} \hat{B}_k^* \left(\sum_{j=1}^{n+k-1} \hat{B}_{n+k-j} \hat{B}_j \mathcal{K}_{nkj} + \sum_{j=1}^{N-n-k+2} \hat{B}_{n+k+j-2} \hat{B}_j^* \mathcal{L}_{nkj} \right) \\ &+ \sum_{k=1}^{N+1-n} \hat{B}_{n+k-1} \left(\sum_{j=1}^k \hat{B}_{k-j+1}^* \hat{B}_j^* \mathcal{M}_{nkj} + \sum_{j=1}^{N+1-k} \hat{B}_{k+j-1}^* \hat{B}_j^* \mathcal{N}_{nkj} \right), \end{aligned} \quad (4.73)$$

where we defined the following third-order tensors

$$\begin{aligned} \mathcal{G}_{nkj} &= \alpha_{n-k+1,j} \langle \hat{\mathbf{a}}_n | \hat{\mathbf{d}}_{n,k} \rangle, \quad 1 \leq j \leq n-k+1, \quad 1 \leq k \leq n \\ \mathcal{H}_{nkj} &= \beta_{n-k+1,j} \langle \hat{\mathbf{a}}_n | \hat{\mathbf{d}}_{n,k} \rangle, \quad 1 \leq j \leq N-n+k, \quad 1 \leq k \leq n \\ \mathcal{I}_{nkj} &= \alpha_{kj} \langle \hat{\mathbf{a}}_n | \hat{\mathbf{d}}_{n,k} \rangle, \quad 1 \leq j \leq k, \quad 1 \leq k \leq n \\ \mathcal{J}_{nkj} &= \beta_{kj} \langle \hat{\mathbf{a}}_n | \hat{\mathbf{d}}_{n,k} \rangle, \quad 1 \leq j \leq N+1-k, \quad 1 \leq k \leq n \\ \mathcal{K}_{nkj} &= \alpha_{n+k-1,j} \langle \hat{\mathbf{a}}_n | \hat{\mathbf{h}}_{n,k} \rangle, \quad 1 \leq j \leq n+k-1, \quad 1 \leq k \leq N+1-n \\ \mathcal{L}_{nkj} &= \beta_{n+k-1,j} \langle \hat{\mathbf{a}}_n | \hat{\mathbf{h}}_{n,k} \rangle, \quad 1 \leq j \leq N-n-k+2, \quad 1 \leq k \leq N+1-n \\ \mathcal{M}_{nkj} &= \alpha_{kj}^* \langle \hat{\mathbf{a}}_n | \hat{\mathbf{h}}_{n,k} \rangle, \quad 1 \leq j \leq k, \quad 1 \leq k \leq N+1-n \\ \mathcal{N}_{nkj} &= \beta_{kj}^* \langle \hat{\mathbf{a}}_n | \hat{\mathbf{h}}_{n,k} \rangle, \quad 1 \leq j \leq N+1-k, \quad 1 \leq k \leq N+1-n. \end{aligned} \quad (4.74)$$

Discretisation of $\hat{g}_3[\hat{B}]$:

We recall that

$$\hat{g}_3[B] = -\langle \hat{\mathbf{a}} | \mathcal{F} (2C(\mathcal{F}^{-1}(\hat{\mathbf{u}}_1), \mathcal{F}^{-1}(\hat{\mathbf{u}}_2))) \rangle. \quad (4.75)$$

Using again (4.60) leads to the following discretisation

$$\begin{aligned} &(\mathcal{F} (2C(\mathcal{F}^{-1}(\hat{\mathbf{u}}_1), \mathcal{F}^{-1}(\hat{\mathbf{u}}_2))))_n = \\ &\frac{\sqrt{T}}{\pi} \left[\sum_{k=1}^n \delta_k^n C(\hat{\mathbf{u}}_{1,n-k+1}, \hat{\mathbf{u}}_{2,k}) + \sum_{k=1}^{N+1-n} \delta_k^{N+1-n} \left[C(\hat{\mathbf{u}}_{1,k}^*, \hat{\mathbf{u}}_{2,n+k-1}) + C(\hat{\mathbf{u}}_{1,n+k-1}, \hat{\mathbf{u}}_{2,k}^*) \right] \right]. \end{aligned} \quad (4.76)$$

In addition, using (4.66) and $\hat{\mathbf{u}}_{1,i} = \hat{B}_i \hat{\mathbf{q}}_i$, we can further express

$$\begin{aligned} C(\hat{\mathbf{u}}_{1,n-k+1}, \hat{\mathbf{u}}_{2,k}) &= C \left(\hat{B}_{n-k+1} \hat{\mathbf{q}}_{n-k+1}, \sum_{j=1}^k \hat{B}_{k-j+1} \hat{B}_j \hat{\mathbf{d}}_{kj} + \sum_{j=1}^{N+1-k} \hat{B}_{k+j-1} \hat{B}_j^* \hat{\mathbf{h}}_{kj} \right) \\ &= \hat{B}_{n-k+1} \left[\sum_{j=1}^k \hat{B}_{k-j+1} \hat{B}_j C(\hat{\mathbf{q}}_{n-k+1}, \hat{\mathbf{d}}_{kj}) + \sum_{j=1}^{N+1-k} \hat{B}_{k+j-1} \hat{B}_j^* C(\hat{\mathbf{q}}_{n-k+1}, \hat{\mathbf{h}}_{kj}) \right], \end{aligned} \quad (4.77)$$

as well as

$$\begin{aligned} C(\hat{\mathbf{u}}_{1,k}^*, \hat{\mathbf{u}}_{2,n+k-1}) &= C \left(\hat{B}_k^* \hat{\mathbf{q}}_k^*, \sum_{j=1}^{n+k-1} \hat{B}_{n+k-j} \hat{B}_j \hat{\mathbf{d}}_{n+k-1,j} + \sum_{j=1}^{N-n-k+2} \hat{B}_{n+k+j-2} \hat{B}_j^* \hat{\mathbf{h}}_{n+k-1,j} \right) \\ &= \hat{B}_k^* \left[\sum_{j=1}^{n+k-1} \hat{B}_{n+k-j} \hat{B}_j C(\hat{\mathbf{q}}_k^*, \hat{\mathbf{d}}_{n+k-1,j}) + \sum_{j=1}^{N-n-k+2} \hat{B}_{n+k+j-2} \hat{B}_j^* C(\hat{\mathbf{q}}_k^*, \hat{\mathbf{h}}_{n+k-1,j}) \right], \end{aligned} \quad (4.78)$$

and eventually

$$\begin{aligned} C(\hat{\mathbf{u}}_{1,n+k-1}, \hat{\mathbf{u}}_{2,k}^*) &= C \left(\hat{B}_{n+k-1} \hat{\mathbf{q}}_{n+k-1}, \sum_{j=1}^k \hat{B}_{k-j+1}^* \hat{B}_j \hat{\mathbf{d}}_{kj}^* + \sum_{j=1}^{N+1-k} \hat{B}_{k+j-1}^* \hat{B}_j \hat{\mathbf{h}}_{kj}^* \right) \\ &= \hat{B}_{n+k-1} \left[\sum_{j=1}^k \hat{B}_{k-j+1}^* \hat{B}_j C(\hat{\mathbf{q}}_{n+k-1}, \hat{\mathbf{d}}_{kj}^*) + \sum_{j=1}^{N+1-k} \hat{B}_{k+j-1}^* \hat{B}_j C(\hat{\mathbf{q}}_{n+k-1}, \hat{\mathbf{h}}_{kj}^*) \right]. \end{aligned} \quad (4.79)$$

This results in the following discretisation for $\hat{g}_3[B]$:

$$\begin{aligned} \hat{g}_{3,n} &= \sum_{k=1}^n \hat{B}_{n-k+1} \left[\sum_{j=1}^k \hat{B}_{k-j+1} \hat{B}_j \mathcal{A}_{nkj} + \sum_{j=1}^{N+1-k} \hat{B}_{k+j-1} \hat{B}_j^* \mathcal{B}_{nkj} \right] \\ &+ \sum_{k=1}^{N+1-n} \hat{B}_k^* \left[\sum_{j=1}^{n+k-1} \hat{B}_{n+k-j} \hat{B}_j \mathcal{C}_{nkj} + \sum_{j=1}^{N-n-k+2} \hat{B}_{n+k+j-2} \hat{B}_j^* \mathcal{D}_{nkj} \right] \\ &+ \sum_{k=1}^{N+1-n} \hat{B}_{n+k-1} \left[\sum_{j=1}^k \hat{B}_{k-j+1}^* \hat{B}_j \mathcal{E}_{nkj} + \sum_{j=1}^{N+1-k} \hat{B}_{k+j-1}^* \hat{B}_j \mathcal{F}_{nkj} \right], \end{aligned} \quad (4.80)$$

where we defined the following third-order tensors

$$\begin{aligned}
\mathcal{A}_{nkj} &= -\frac{\sqrt{T}}{\pi} \delta_k^n \langle \hat{\mathbf{a}}_n | C(\hat{\mathbf{q}}_{n-k+1}, \hat{\mathbf{d}}_{kj}) \rangle, \quad 1 \leq j \leq k, \quad 1 \leq k \leq n \\
\mathcal{B}_{nkj} &= -\frac{\sqrt{T}}{\pi} \delta_k^n \langle \hat{\mathbf{a}}_n | C(\hat{\mathbf{q}}_{n-k+1}, \hat{\mathbf{h}}_{kj}) \rangle, \quad 1 \leq j \leq N+1-k, \quad 1 \leq k \leq n \\
\mathcal{C}_{nkj} &= -\frac{\sqrt{T}}{\pi} \delta_k^{N+1-n} \langle \hat{\mathbf{a}}_n | C(\hat{\mathbf{q}}_k^*, \hat{\mathbf{d}}_{n+k-1,j}) \rangle, \quad 1 \leq j \leq n+k-1, \quad 1 \leq k \leq N+1-n \\
\mathcal{D}_{nkj} &= -\frac{\sqrt{T}}{\pi} \delta_k^{N+1-n} \langle \hat{\mathbf{a}}_n | C(\hat{\mathbf{q}}_k^*, \hat{\mathbf{h}}_{n+k-1,j}) \rangle, \quad 1 \leq j \leq N-n-k+2, \quad 1 \leq k \leq N+1-n \\
\mathcal{E}_{nkj} &= -\frac{\sqrt{T}}{\pi} \delta_k^{N+1-n} \langle \hat{\mathbf{a}}_n | C(\hat{\mathbf{q}}_{n+k-1}, \hat{\mathbf{d}}_{kj}^*) \rangle, \quad 1 \leq j \leq k, \quad 1 \leq k \leq N+1-n \\
\mathcal{F}_{nkj} &= -\frac{\sqrt{T}}{\pi} \delta_k^{N+1-n} \langle \hat{\mathbf{a}}_n | C(\hat{\mathbf{q}}_{n+k-1}, \hat{\mathbf{h}}_{kj}^*) \rangle, \quad 1 \leq j \leq N+1-k, \quad 1 \leq k \leq N+1-n.
\end{aligned} \tag{4.81}$$

As a summary, upon the choice of ϕ and $\hat{\xi}$ we are led to solve

$$\begin{aligned}
r(\hat{B}; \phi, \hat{\xi}) &= 0, \quad \text{with} \\
r(\hat{B}; \phi, \hat{\xi}) &\doteq \hat{g}_2[\hat{B}] + \sqrt{\epsilon_o} [\gamma(\phi \hat{\xi} - \hat{B}) + \hat{g}_3[\hat{B}] - \langle \hat{\mathbf{a}} | \partial_{\tau_1} \hat{\mathbf{u}}_2 \rangle],
\end{aligned} \tag{4.82}$$

where we defined $\gamma = \langle \hat{\mathbf{a}} | \mathbf{f}_o \rangle$. At the discrete level, this amounts to solving for a system of N nonlinearly coupled equations for the N unknowns \hat{B}_n ($n = 1, 2, \dots, N$):

$$r_n = \hat{g}_{2,n} + \sqrt{\epsilon_o} [\gamma_n(\phi \hat{\xi}_n - \hat{B}_n) + \hat{g}_{3,n} - \langle \hat{\mathbf{a}}_n | \partial_{\tau_1} \hat{\mathbf{u}}_{2,n} \rangle] = 0, \quad n = 1, 2, \dots, N, \tag{4.83}$$

where $\hat{g}_{2,n}$, $\hat{g}_{3,n}$ and $\langle \hat{\mathbf{a}}_n | \partial_{\tau_1} \hat{\mathbf{u}}_{2,n} \rangle$ are evaluated using respectively the simple sum (4.62) and the double sums (4.80) and (4.73). This suggests the following procedure:

Algorithm :

1. Choose the values for N and ω_c , which sets the discretisation of the frequencies.
2. Over the discrete set of frequencies, pre-compute once for all the *deterministic* fields \mathbf{f}_o , $\hat{\mathbf{q}}$, $\hat{\mathbf{a}}$, the scalar γ , and the tensors $\Theta, \Xi, \mathcal{A}, \mathcal{B}, \mathcal{C}, \mathcal{D}, \mathcal{E}, \mathcal{F}, \mathcal{G}, \mathcal{H}, \mathcal{I}, \mathcal{J}, \mathcal{K}, \mathcal{L}, \mathcal{M}, \mathcal{N}$.
3. Choose a value for ϕ (which sets the forcing amplitude).
4. Draw randomly a white noise ($|\hat{\xi}(\omega)| = 1 \forall \omega$, but random phases uniformly distributed between 0 and 2π).
5. Solve the system (4.83) by means of a nonlinear solver, for instance `fsolve` on MATLAB.
6. Update the statistics on \hat{B} , for instance its ensemble average, and, if not converged go back to (4).

Of course the convergence in terms of N and ω_c must be ensured.

5 Noise-induced transitions past the onset of a steady symmetry-breaking bifurcation: the case of the sudden expansion

Remark: This chapter is largely inspired by the submitted manuscript Ducimetière et al. (2024), in collaboration with Edouard Boujo and François Gallaire.

5.1 Introduction

Fluid flows, governed by the Navier-Stokes equations, are known to exhibit an extremely rich phenomenology, including pattern formation, spatio-temporal chaos, turbulence, etc... Specifically, some fluid flows can reach an attracting coherent structure (e.g. fixed point) where they appear to be locally stationary for possibly extremely long times, but, from time to time, because of a rare fluctuation, exit the basin attraction of such coherent structure and transit towards another one. Although possibly restricted to some specific regimes in the parameter space, rare transitions are observed in completely different contexts. These include three- or two-dimensional experimental turbulent flows (Sommeria, 1986), for instance, wakes behind an Ahmed body (a simplified car model) (Grandemange et al., 2013) or an axisymmetric (Brackston et al., 2016; Callahan et al., 2022) bluff body. Other examples are found in magneto-hydrodynamics experiments (Berhanu et al., 2007), two-dimensional numerical turbulent flows (Bouchet & Simonnet, 2009; Bouchet et al., 2019; Dallas et al., 2020) and atmospheric flows (Schmeits & Dijkstra, 2001; Weeks et al., 1997).

In the framework of equilibrium statistical mechanics, steady states of the system minimize a potential. Thenceforth, some laws describing the probability of rare transitions can be analytically derived. The Arrhenius law, in particular, considers a bi-stable overdamped system driven by a stochastic noise $\xi(t)$ at temperature T_e , $d_t x = -d_x V(x) + \sqrt{2k_B T_e} \xi(t)$,

with V a double-well potential of potential barrier ΔV . The law predicts the expected time $\{\Delta T\}$ between two transitions to scale like the exponential of minus the potential barrier separating two attractors, divided by the square of the fluctuations intensity, i.e. $\{\Delta T\} \propto \exp(-\Delta V/(k_B \Gamma_e))$.

However, fluid flows are mostly out-of-equilibrium systems, for energy is constantly injected (typically at boundaries) and dissipated by viscosity. In addition, Navier-Stokes equations have a continuously infinite number of degrees of freedom, which, after discretization, translates into thousands or millions of degrees of freedom, depending on the flow complexity. Therefore, characterizing rare transitions from one basin of attraction of the Navier-Stokes equations to another is a current scientific challenge.

There exist some specific numerical approaches in considering these transition events. All are motivated by the fact that a direct numerical simulation of the system is inappropriate in the statistical study of transition events, both because they occur over possibly extremely long time scales, and because the large number of degrees of freedom makes the numerical simulations of the Navier-Stokes equations unreasonably slow and energetically costly. Instead, the used numerical techniques incorporate some elements of the large deviation theory (Freidlin & Wentzell, 1998), which considers non-equilibrium dynamical systems in the limit where they are forced by weak noise (consistent with the fact that transitions are rare). The general idea is to compute the most likely trajectory that links two given stable and distinct states. This specific trajectory is called an *instanton*, and was shown in Freidlin and Wentzell (1998) to minimize an action in the path integral representation of the system. The probability of the transition along the instanton can also be computed and used to estimate the expected time between two transition events.

The instanton was numerically computed in different fluid flow modelizations, from two-dimensional geophysical turbulence (Bouchet & Simonnet, 2009; Bouchet et al., 2011) to one-dimensional Burgers turbulence (Grafke et al., 2013), to the transition between the plane Poiseuille flow and a traveling wave solution in a two-dimensional periodic domain (Wan et al., 2015). More recently, Schorlepp et al. (2022) considered the three-dimensional stochastically forced Navier–Stokes equations, and obtained the most likely configurations for extreme vorticity and strain events as the numerical solutions of the instanton problem. A more indirect manner to determine the instanton is by using the adaptive multilevel splitting algorithm (C erou & Guyader, 2007), which is a rare event algorithm whose effect is to magnify the number of transition events. Thereby, very large statistics of transition paths can be produced, which are expected to concentrate around and reveal the instanton. Recently, this method was successfully employed in Bouchet et al. (2019) for the turbulent flow obtained from a simplified model of Jupiter troposphere’s dynamics. The work presented in Lestang et al. (2020), concerned about extreme mechanical forces exerted by a turbulent flow impinging on a bluff body, constitutes another example. It was also shown in a recent work Lecoanet and Kerswell (2018) that the computation of the instanton trajectory could be linked to a more basic nonlinear maximization problem of the flow kinetic energy (Pringle & Kerswell, 2010).

To the knowledge of the authors, all the works mentioned so far relied on numerical tools. In the present chapter, we shall employ a different strategy, expected to be valid at least in some simplified situations. In the spirit of Cates and Nardini (2023), who focused on the extension of the classical nucleation theory to an active phase-separating system, we first aim at analytically reducing the dimensionality of a flow forced by a weak and slowly varying stochastic noise. Then, analytical tools from statistical mechanics such as the Fokker-Planck equation will be deployed to compute the statistics of the reduced-order system, which is substantially easier to study and physically interpret than the original equation.

A general method for reducing the dimensionality of a nonlinear system was developed in dynamical system theory, and is valid asymptotically close to a bifurcation point in the parameter space, where an eigenmode of the linearized operator becomes unstable and grows exponentially. The idea is to derive an equation for the amplitude(s) of the bifurcating eigenmode(s). Such an equation is of minimal dimension (and nonlinear order) yet extracts the core of the nonlinear behavior of the original equation in the vicinity of a bifurcation point (Guckenheimer & Holmes, 1983). Its derivation relies on a clear multiple-scale asymptotic expansion procedure, and its first use in fluid mechanics dates back to Gor'kov (1957) in the context of thermal convection. It was used in numerous studies since then and still is nowadays, for instance in (Buza et al., 2022; Kerswell et al., 2004; Ohm & Shelley, 2022; Shukla & Alam, 2011; Sipp & Lebedev, 2007; Zampogna & Boujo, 2023) to cite only a few.

Of particular interest here, the analyses in Camarri and Mengali (2019), Hawa and Rusak (2001), and Rusak and Hawa (1999) derive a Stuart-Landau weakly nonlinear amplitude equation, for the steady symmetry-breaking eigenmode in the flow past a two-dimensional plane sudden expansion. Thereby, the two asymmetric attractors of the flow after the bifurcation could be approached as the equilibrium solutions of a single-degree-of-freedom equation, with good accuracy for Reynolds numbers asymptotically close to its critical value at the bifurcation. Note that a substantial body of work is devoted to the sudden expansion flow, due to its common appearance in the industrial or academic context. In addition to the ones already presented, could also be mentioned the studies in Lanzerstorfer and Kuhlmann (2012) and Debuysschère et al. (2021), concerned with the stability of the two-dimensional plane sudden expansion for different geometries, and inlet velocity profiles, respectively.

The construction of amplitude equations can be generalized to nonlinear dynamical systems subject to a stochastic forcing, as shown in Rajan and Davies (1988) and Rong et al. (1998) and Nayfeh and Serhan (1990) for the Duffing and Duffing-Rayleigh oscillators, respectively. The inclusion of a noise term in an amplitude equation would have the effect of making its solution transit from one of its equilibrium solutions to another, for instance when the latter equation describes a supercritical or subcritical pitchfork or a subcritical Hopf bifurcation. The statistics of these transitions could be obtained with low computational efforts, yet in principle apply to the original equation, under the simplifying hypothesis made for the derivation of the amplitude equation.

However, if stochastic amplitude equations were found to be accurate models for some specific flows indeed (Brackston et al., 2016; Callaham et al., 2022; Pétrélis et al., 2009), the noise term systematically resulted from an *ad-hoc* addition. In other words, the rigorous method deployed for the Duffing oscillators in Rajan and Davies (1988) and Rong et al. (1998) and Nayfeh and Serhan (1990) to recover a noise term at the level of the amplitude equation directly from the stochastically forced original equation, does not seem to have been yet applied to the Navier-Stokes equations. Therefore, this will be the primary focus of the present chapter.

For this purpose, we will consider a flow experiencing a supercritical pitchfork bifurcation, such that our method is a generalization of that outlined in Camarri and Mengali (2019) and will result in a stochastically forced Stuart-Landau equation. Yet, the proposed method is expected to be adaptable to other fluid flows subject to multi-stability, thus to noise-induced transitions, closely after a bifurcation. Such situations include other flows experiencing a supercritical pitchfork bifurcation, such as the one in a pipe junction for some junction angles (Chen et al., 2017) or between a co-rotating disk pair for some gap ratio (Randriamampianina et al., 2001). Supercritical pitchfork bifurcations also occur in laminar (or turbulent) three-dimensional wakes of rectangular prisms for some aspect ratios (Zampogna & Boujo, 2023), in the granular plane Couette flow for some parameters (Shukla & Alam, 2011), in active suspensions of elongated swimming particles (immotile shakers or motile pullers/pushers) for some swimming speed (Ohm & Shelley, 2022), in the two-dimensional flow past an inverted flag if the aspect ratio is large enough and the mass ratio small enough (Tavallaeinejad et al., 2020), etc. The method could also be extended to flows subject to a subcritical Hopf or subcritical pitchfork bifurcation. In the latter case, three stable equilibria exist, and some examples are found in the infinitely diverging channel (Jeffery-Hamel flow) (Kerswell et al., 2004), in active suspensions (Ohm & Shelley, 2022), in an axisymmetric liquid bridge subjected to axial flow (Lowry & Steen, 1997) and many others.

The method to derive a stochastically forced Stuart-Landau equation directly from the stochastically forced Navier-Stokes equations is outlined in § 5.3. The probability density function of its solution, as well as the statistics of the transition time between its two deterministic attractors, will then be computed by means of the Fokker-Planck equation. The results are reported and compared with direct numerical simulations in § 5.4.

5.2 Problem definition

We consider fluid flows governed by the incompressible Navier-Stokes equations (NSE)

$$\begin{aligned}\partial_t \mathbf{U} &= -C[\mathbf{U}, \mathbf{U}] - \nabla P + \text{Re}^{-1} \Delta \mathbf{U} + F\xi(\alpha \epsilon t) \mathbf{f} \\ 0 &= \nabla \cdot \mathbf{U},\end{aligned}\tag{5.1}$$

where \mathbf{U} is the velocity field, P is the pressure field ensuring \mathbf{U} to be divergence-free, and Re is the Reynolds number. The nonlinear advection operator $C[\mathbf{a}, \mathbf{b}] \doteq ((\nabla \mathbf{a}) \mathbf{b} + (\nabla \mathbf{b}) \mathbf{a})/2$ has been defined. We will restrict the analysis to Re numbers asymptotically close to a critical value Re_c ,

where the flow experiences a steady and supercritical symmetry-breaking bifurcation, also called supercritical “pitchfork” bifurcation. Note that in the rest of the chapter, the use of the term “symmetry” will always refer to a discrete symmetry. Specifically, we will consider cases where a distance to criticality, defined as

$$\epsilon \doteq \text{Re}_c^{-1} - \text{Re}^{-1}, \quad \text{is such that} \quad 0 < \epsilon \ll 1, \quad (5.2)$$

in accordance with Camarri and Mengali (2019) and Sipp and Lebedev (2007). In other terms, the symmetric flow at $\text{Re} > \text{Re}_c$ possesses a steady symmetry-breaking eigenmode unstable with a growth rate of $O(\epsilon)$. In the linear regime, this mode thus grows exponentially until nonlinearities have an effect after a long time of $O(\epsilon^{-1})$, implying its amplitude to be both linearly and nonlinearly modulated over a slow time scale $\tau \doteq \epsilon t$.

In addition, the flow is stochastically forced with $F\xi(\alpha\epsilon t)\mathbf{f}$, where $\mathbf{f} = \mathbf{f}(\mathbf{x})$ is the forcing spatial structure. The term $\xi(\alpha\epsilon t)$, with $\alpha > 0$ and $\alpha = O(1)$, is a random signal with zero mean. Since ϵ is by assumption very small, this signal varies slowly as compared to $\xi(t)$, and according to the same slow time τ as that of the symmetry-breaking eigenmode. The signal $\xi(t)$ is a Gaussian sampling-limited white noise signal. The latter has a typically large band-limiting frequency ω_d , given by the sampling time step Δt as $\omega_d = \pi / \Delta t$.

In order to characterize these random processes, we introduce the Fourier transform $\mathcal{F}(\ast)$ of a temporal signal of length $[0, T]$ with $T \rightarrow \infty$, and its inverse $\mathcal{F}^{-1}(\ast)$ as

$$\hat{\mathbf{u}}(\omega) = \mathcal{F}(\mathbf{u}(t)) = \frac{1}{\sqrt{T}} \int_0^T \mathbf{u}(t) e^{-i\omega t} dt, \quad \mathbf{u}(t) = \mathcal{F}^{-1}(\hat{\mathbf{u}}(\omega)) = \frac{\sqrt{T}}{2\pi} \int_{-\infty}^{\infty} \hat{\mathbf{u}}(\omega) e^{i\omega t} d\omega. \quad (5.3)$$

In the Fourier domain, the random signal $\hat{\xi}(\omega) = \mathcal{F}(\xi(t))$ is constructed as

$$|\hat{\xi}(\omega)| = \alpha\sqrt{\epsilon}, \quad \text{for } |\omega| \leq \omega_d, \quad \text{and } |\hat{\xi}(\omega)| = 0 \quad \text{elsewhere.} \quad (5.4)$$

Note that $\alpha\sqrt{\epsilon}$ does not depend on the frequency. The choice of this specific value for the intensity of $\xi(t)$ is made purposely so that the Fourier transform of the noise $\xi(\alpha\epsilon t)$, when taken over the slow time $\tau = \epsilon t$, yields a unit intensity. Since α is not included in the definition of the slow time τ , its square root is not taken in (5.4), whereas that of ϵ is. The calculations will be provided in the next section. For each ω , the phase of $\hat{\xi}(\omega)$ is random and drawn according to a uniformly distributed law between 0 and 2π .

We emphasize that the stochastic forcing considered in the present chapter is not general but specific for at least two reasons. The first is that it consists of a scalar noise process depending solely on time, multiplying a structure that is frozen in space. The second is that the (sampling-limited) white noise defined in (5.4) has a constant value for $|\hat{\xi}(\omega)|$, whereas it would be more generally characterized by a constant value for $\{|\hat{\xi}(\omega)|^2\}$, if $\{\ast\}$ denotes the ensemble average. This generalisation matters in the cases where T is finite and/or if the noise is not an ergodic process.

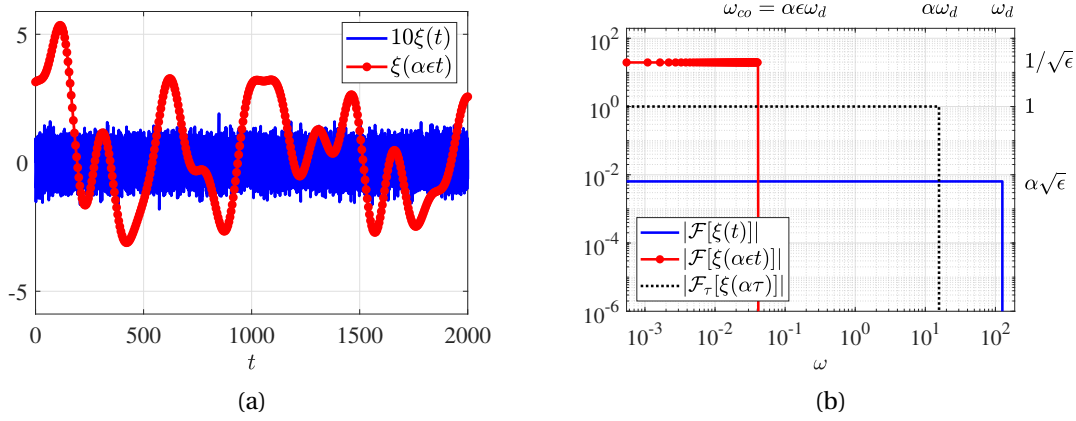


Figure 5.1: (a) Example of random signals as a function of time. The blue continuous line is a sampling-limited white noise $\xi(t)$ (multiplied by a factor 10 for better visualization), whereas the blue continuous line with bullets is the slowly varying version $\xi(\alpha\epsilon t)$. (b) Module of the Fourier transforms of the signals shown in (a). The specific values $\epsilon = 0.0026$, $\alpha = 1/8$ and a sampling time step $\Delta t = 0.025$ have been selected; this sets $\omega_d = 125.7$ and $\omega_{co} = 0.04$.

From the definition (5.3), it follows that

$$\mathcal{F}(\xi(\alpha\epsilon t)) = \frac{1}{\sqrt{T}} \int_0^T \xi(\alpha\epsilon t) e^{-i\omega t} dt = \frac{1}{\alpha\epsilon\sqrt{T}} \int_0^{\alpha\epsilon T} \xi(s) e^{-is\omega/(\alpha\epsilon)} ds = \frac{1}{\alpha\epsilon} \hat{\xi}\left(\frac{\omega}{\alpha\epsilon}\right), \quad (5.5)$$

(which is a well-known property of the Fourier transform) therefore,

$$|\mathcal{F}(\xi(\alpha\epsilon t))| = \frac{1}{\sqrt{\epsilon}} \text{ for } |\omega| \leq \omega_{co}, \quad (5.6)$$

where we have defined

$$\omega_{co} \doteq \alpha\epsilon\omega_d, \quad \text{and where we recall that } \alpha = O(1). \quad (5.7)$$

Therefore, the frequency ω_{co} is the cut-off frequency (hence the subscript “co”) of the slowly varying noise $\xi(\alpha\epsilon t)$. Although it was implicit, in (5.5) we have also used the fact that, since we take the limit of infinitely large T and $\alpha, \epsilon > 0$, integrating between 0 and T or between 0 and $\alpha\epsilon T$ leads to the same result. The small parameter ϵ being set by the Re number, the parameter α gives the freedom to change ω_{co} as long as α is of order unity. Accordingly, the small parameter $\alpha\epsilon = \omega_{co}/\omega_d = O(\epsilon) \ll 1$ takes the immediate meaning of the ratio between the shortest measurable time scale (i.e., the sampling one = π/ω_d), and the shortest time scale excited by $\xi(\alpha\epsilon t)$.

Some random signals $\xi(t)$ and $\xi(\alpha\epsilon t)$ are shown in figure 5.1 in both the temporal and Fourier domains. We stress that, as long as the slow noise is band-limited with a cut-off frequency around ω_{co} , the results are not expected to depend on the specific shape of its spectrum (see also a more detailed discussion in section IV.D.)

Table 5.1: Characterization of the dimensionless parameters

Parameter	Mathematical constraint	Permit to fix independently ...
ϵ	$\ll 1$... the Re number, according to (5.2)
α	$O(1)$... the noise cut-off frequency ω_c , according to (5.7)
ϕ	$O(1)$... the noise intensity F , according to (5.9)

We also introduce the Hermitian inner products

$$\langle \mathbf{u}_a | \mathbf{u}_b \rangle \doteq \int_{\Omega} \mathbf{u}_a^H \mathbf{u}_b d\Omega \quad \text{and} \quad \left\langle \begin{bmatrix} \mathbf{u}_a \\ p_a \end{bmatrix} \middle| \begin{bmatrix} \mathbf{u}_b \\ p_b \end{bmatrix} \right\rangle_p \doteq \int_{\Omega} \mathbf{u}_a^H \mathbf{u}_b + p_a^H p_b d\Omega, \quad (5.8)$$

where the superscript H denotes the Hermitian transpose and the symbol Ω the spatial domain. In (5.8) the second inner product includes the pressure (hence the subscript p) whereas the first doesn't. In the following, $\| * \|$ designates the norm induced by the first scalar product in (5.8). The spatial structure of the forcing in velocity \mathbf{f} has a unitary norm, i.e. $\|\mathbf{f}\| = 1$, and we scale the forcing amplitude F as

$$F \doteq \phi \sqrt{\epsilon^3} \ll 1 \quad \text{with} \quad \phi = O(1). \quad (5.9)$$

The characterization of the parameters ϵ , α , and ϕ is summarized in table 5.1. Their respective presence gives sufficient freedom for the Re number, the slow noise cut-off frequency ω_{co} , and the forcing amplitude F , to be chosen independently of each other. For instance, a noise with the same intensity and cut-off frequency could force flows with two different Re numbers; in the latter case, the parameter ϵ would be different between the two flows but α and ϕ could be adapted to conserve ω_{co} and F .

5.3 Weakly nonlinear expansion

We now derive an equation for the amplitude of the bifurcated steady mode, in the presence of a weak and slowly-varying noise. In the absence of this stochastic forcing, the calculations would be similar in all respects to those of Camarri and Mengali (2019). Moreover, the derivation of an amplitude equation for the Duffing oscillator subject to a narrow-band noise was proposed already in Nayfeh and Serhan (1990), Rajan and Davies (1988), and Rong et al. (1998), among others. The rigorous procedure outlined in these latter works to include a noise term in an amplitude equation is applied to the Navier-Stokes equation thereafter.

As already mentioned, since we consider Re numbers close to a critical value for a steady bifurcation, as expressed in (5.2), the temporal variations of the flow perturbation around the neutral equilibrium are assumed to occur over the slow time scale $\tau = \epsilon t$. This assumption and the ensuing scaling are consistent with the fact that the flow is forced by the slow noise

$\xi(\alpha\epsilon t) = \xi(\alpha\tau)$. The flow field is approached by the following expansions

$$\begin{aligned} \mathbf{U} &= \mathbf{U}_c + \sqrt{\epsilon}\mathbf{u}_1(\tau) + \epsilon\mathbf{u}_2(\tau) + \sqrt{\epsilon^3}\mathbf{u}_3(\tau) + O(\epsilon^2), \text{ and} \\ P &= P_c + \sqrt{\epsilon}p_1(\tau) + \epsilon p_2(\tau) + \sqrt{\epsilon^3}p_3(\tau) + O(\epsilon^2), \end{aligned} \quad (5.10)$$

where $\mathbf{U}_c(\mathbf{x})$ is a velocity field in a neutral equilibrium at Re_c , symmetric in space around a generic plane for three-dimensional flows, or around a generic axis for two-dimensional flows. Considering a two-dimensional flow with a symmetry axis located at $y = y_s$, the symmetry assumption of \mathbf{U}_c implies

$$\mathbf{U}_c(\mathbf{x}) = \begin{bmatrix} U_c(x, y) \\ V_c(x, y) \end{bmatrix} = \begin{bmatrix} U_c(x, 2y_s - y) \\ -V_c(x, 2y_s - y) \end{bmatrix}. \quad (5.11)$$

By increasing the Re number above Re_c , the flow \mathbf{U}_c is subject to a steady bifurcation which breaks the symmetry of the overall flow.

Introducing the expansions (5.2) and (5.10) into (5.1) leads to a cascade of linear problems to be solved successively. At order $O(\sqrt{\epsilon})$, we collect

$$\begin{bmatrix} \mathbf{0} \\ 0 \end{bmatrix} = L \begin{bmatrix} \mathbf{u}_1 \\ p_1 \end{bmatrix} \text{ with } L \doteq \begin{bmatrix} -2C[\mathbf{U}_c, *] + Re_c^{-1}\Delta & -\nabla \\ \nabla \cdot & 0 \end{bmatrix}, \text{ therefore } \begin{bmatrix} \mathbf{u}_1(\tau, \mathbf{x}) \\ p_1(\tau, \mathbf{x}) \end{bmatrix} = A(\tau) \begin{bmatrix} \mathbf{q}(\mathbf{x}) \\ p_{\mathbf{q}}(\mathbf{x}) \end{bmatrix}, \quad (5.12)$$

where $[\mathbf{q}(\mathbf{x}), p_{\mathbf{q}}]^T$ is the eigenmode of the linear operator L that is associated with a null eigenvalue. We normalize it such that $\|\mathbf{q}\| = 1$. Note that \mathbf{q} is also the non-trivial kernel of L . In addition, the eigenmode \mathbf{q} is anti-symmetric: therefore, again considering a two-dimensional flow and a symmetry axis at $y = y_s$, the velocity field \mathbf{q} satisfies

$$\mathbf{q}(\mathbf{x}) = \begin{bmatrix} q_x(x, y) \\ q_y(x, y) \end{bmatrix} = \begin{bmatrix} -q_x(x, 2y_s - y) \\ q_y(x, 2y_s - y) \end{bmatrix}. \quad (5.13)$$

In the following, the adjoint mode associated with $[\mathbf{q}, p_{\mathbf{q}}]^T$ will be denoted by $[\mathbf{q}^\dagger, p_{\mathbf{q}}^\dagger]^T$. In other terms, it corresponds to the eigenmode associated with the null eigenvalue of the operator L^\dagger , adjoint to L under the second scalar product in (5.8). The slowly varying and real scalar amplitude $A(\tau)$ in (5.12) is for now arbitrary.

At $O(\epsilon)$ we obtain the solution $\mathbf{u}_2(\tau, \mathbf{x}) = A(\tau)^2 \mathbf{u}_2^{A^2}(\mathbf{x}) + \mathbf{u}_2^\Delta(\mathbf{x})$, where

$$-L \begin{bmatrix} \mathbf{u}_2^{A^2} \\ p_2^{A^2} \end{bmatrix} = \begin{bmatrix} -C[\mathbf{q}, \mathbf{q}] \\ 0 \end{bmatrix}, \text{ and } -L \begin{bmatrix} \mathbf{u}_2^\Delta \\ p_2^\Delta \end{bmatrix} = \begin{bmatrix} -\Delta \mathbf{U}_c \\ 0 \end{bmatrix}. \quad (5.14)$$

The operator L being singular, the compatibility condition needs to be verified for the particular solutions to the systems in (5.14) to be non-diverging. The latter condition requires the right-hand side to be orthogonal to the kernel of the adjoint of L , i.e. orthogonal to $[\mathbf{q}^\dagger, p_{\mathbf{q}}^\dagger]$.

The symmetric fields $C[\mathbf{q}, \mathbf{q}]$ and $\Delta\mathbf{U}_c$ yielding a null inner product with the anti-symmetric one \mathbf{q}^\dagger , this condition is naturally satisfied and the two systems can directly be solved for. In practice, this can for instance be done with a pseudo-inverse algorithm. The component of $\mathbf{u}_2^{A^2}$ and \mathbf{u}_2^Δ on the kernel \mathbf{q} that stems from the homogeneous part of the solution is set to zero according to $\langle \mathbf{q}^\dagger | \mathbf{u}_2^{A^2} \rangle = \langle \mathbf{q}^\dagger | \mathbf{u}_2^\Delta \rangle = 0$. Indeed, accounting for a non-zero homogeneous solution was shown in Camarri and Mengali (2019) to have no consequences on the coefficients of the final amplitude equation.

At $O(\sqrt{\epsilon^3})$ we assemble the system

$$-L \begin{bmatrix} \mathbf{u}_3 \\ p_3 \end{bmatrix} = -A \begin{bmatrix} 2C[\mathbf{q}, \mathbf{u}_2^\Delta] + \Delta\mathbf{q} \\ 0 \end{bmatrix} - A^3 \begin{bmatrix} 2C[\mathbf{q}, \mathbf{u}_2^{A^2}] \\ 0 \end{bmatrix} - \frac{dA}{d\tau} \begin{bmatrix} \mathbf{q} \\ 0 \end{bmatrix} + \phi\xi(\alpha\tau) \begin{bmatrix} \mathbf{f} \\ 0 \end{bmatrix}. \quad (5.15)$$

This time, the compatibility condition is not naturally satisfied but leads to an equation for $A(\tau)$

$$\frac{dA}{d\tau} = \lambda A(\tau) + \mu A(\tau)^3 + \eta\phi\xi(\alpha\tau) = -\frac{dV}{dA} + \eta\phi\xi(\alpha\tau), \quad (5.16)$$

with the coefficients

$$\lambda = -\frac{\langle \mathbf{q}^\dagger | 2C[\mathbf{q}, \mathbf{u}_2^\Delta] + \Delta\mathbf{q} \rangle}{\langle \mathbf{q}^\dagger | \mathbf{q} \rangle}, \quad \mu = -\frac{\langle \mathbf{q}^\dagger | 2C[\mathbf{q}, \mathbf{u}_2^{A^2}] \rangle}{\langle \mathbf{q}^\dagger | \mathbf{q} \rangle} \quad \text{and} \quad \eta = \frac{\langle \mathbf{q}^\dagger | \mathbf{f} \rangle}{\langle \mathbf{q}^\dagger | \mathbf{q} \rangle}. \quad (5.17)$$

In addition, the double-well potential

$$V = V[A] \doteq -\frac{\lambda A^2}{2} - \frac{\mu A^4}{4} \quad (5.18)$$

has been defined. Equation (5.16), for the amplitude of the anti-symmetric bifurcated mode, is the classic Stuart-Landau equation for a real-valued amplitude, with the difference that it is now stochastically forced. The stochastic term was not an *ad hoc* addition to a pre-existing amplitude equation, but was derived rigorously from the forced Navier-Stokes equations (5.1). The explicit formulas for the coefficients in (5.17) can be directly evaluated numerically and do not require any *a posteriori* fitting. Indeed, they involve scalar products of fields that are all known: the eigenmode \mathbf{q} , the adjoint mode \mathbf{q}^\dagger , the second-order fields \mathbf{u}_2^Δ and $\mathbf{u}_2^{A^2}$, all defined at $\text{Re} = \text{Re}_c$, as well as the forcing structure \mathbf{f} .

The Fourier transform over the slow time scale, noted $\mathcal{F}_\tau(*)$, of the noise $\xi(\alpha\tau)$ reads

$$\begin{aligned} \mathcal{F}_\tau(\xi(\alpha\tau)) &= \frac{1}{\sqrt{\epsilon T}} \int_0^{\epsilon T} \xi(\alpha\tau) e^{-i\omega\tau} d\tau = \frac{\sqrt{\epsilon}}{\sqrt{T}} \int_0^T \xi(\alpha\epsilon t) e^{-i\omega\epsilon t} dt \\ &= \frac{1}{\alpha\sqrt{\epsilon}\sqrt{T}} \int_0^{\alpha\epsilon T} \xi(s) e^{-i\omega s/\alpha} ds \\ &= \frac{1}{\alpha\sqrt{\epsilon}} \hat{\xi}\left(\frac{\omega}{\alpha}\right), \end{aligned} \quad (5.19)$$

therefore, following (5.4), we have that

$$|\mathcal{F}_\tau(\xi(\alpha\tau))| = 1 \quad \text{for} \quad |\omega| \leq \alpha\omega_d, \quad (5.20)$$

and $|\mathcal{F}_\tau(\xi(\alpha\tau))| = 0$ everywhere else. This profile is illustrated by the black dotted line in figure 5.1b. It is important to notice that $\mathcal{F}_\tau(\xi(\alpha\tau))$ is independent of the small parameter ϵ , which was done intentionally and explains the peculiar choice of intensity in (5.4). In this manner, the amplitude equation (5.16) does not depend on ϵ and the ensuing results need not be re-computed for each Re considered, if everything else is fixed.

Let us briefly discuss the deterministic regime where $\phi = 0$. The coefficient λ contains the sensitivity of the null eigenvalue to a base flow modification $+\epsilon\mathbf{u}_2^\Delta$ induced by the fact that we consider a $\text{Re} > \text{Re}_c$. Therefore, $\epsilon\lambda$ is directly the growth rate of the bifurcated steady mode and is positive. Accordingly, the equilibrium solution $\bar{A}_0 = 0$ of (5.16), corresponding to a symmetric flow, is unstable. The coefficient μ contains the sensitivity of the null eigenvalue to a base flow modification $+\epsilon A^2 \mathbf{u}_2^{A^2}$, non-linearly induced by the Reynolds stress of the perturbation $\sqrt{\epsilon} A \mathbf{q}$. If μ is negative, then nonlinearities have a stabilizing effect that counteracts linear instability. Therefore two additional equilibrium solutions $\pm \bar{A}$, with $\bar{A} \doteq \sqrt{-\lambda/\mu} > 0$, exist and are stable. They are the two minima of the potential V . On the contrary, if μ is positive, nonlinearities included in (5.16) have a destabilizing effect and no stable equilibrium exists at that order: the bifurcation is subcritical and the expansion must be pursued at higher orders. This latter case will not be treated in what follows.

In the stochastically forced regime where $\phi \neq 0$, the amplitude A may randomly switch back and forth between the two attractors \bar{A} and $-\bar{A}$ after unpredictable and possibly long times. Therefore, we are particularly interested in the probability distribution of A . The probability density function (PDF) P of the amplitude A can be computed directly by means of the Fokker-Planck equation (Risken, 1996). For this, the state space needs to be augmented in order to account for the fact that $\xi(\alpha\tau)$ is a band-limited white noise because of the presence of the constant α in the argument. Following Risken (1996) (Appendix A1 and Supplement S.10), $\xi(\alpha\tau)$ is treated as a system variable resulting from low-pass filtering, at a cut-off frequency of $\alpha\omega_d$, of a white noise (on the slow time scale) $\chi(\tau)$ whose band-limiting frequency is the largest achievable by the system, ω_d . We insist that ω_d is chosen sufficiently large for none of the results presented in this chapter to depend on it. For the sake of simplicity, a first-order low-pass filter of cut-off frequency $\alpha\omega_d$ is chosen and thus $\xi(\alpha\tau)$ is approached by the solution of the first order stochastic differential equation

$$\frac{d\xi}{d\tau} + \alpha\omega_d \xi = \alpha\omega_d \chi, \quad (5.21)$$

where $\chi(\tau)$ is a white noise such that $|\mathcal{F}_\tau(\chi)| = 1$ for $|\omega| \leq \omega_d$. Equation (5.21) leads to $|\mathcal{F}_\tau(\xi)|^2 = 1/(1 + \omega^2/(\alpha\omega_d)^2)$, which is a rather coarse approximation of (5.20). This matters little, however, since as mentioned, the results aren't expected to depend too much on the exact shape of the noise as long as they conserve the cut-off frequency. Again following Risken

(1996) (Chapter 4.7), the Fokker-Planck equation associated with the system consisting of the equations (5.16) and (5.21) writes

$$\frac{\partial P}{\partial \tau} = -\frac{\partial}{\partial A} [(\lambda A + \mu A^3 + \eta \phi \xi) P] + \alpha \omega_d \frac{\partial (\xi P)}{\partial \xi} + \frac{(\alpha \omega_d)^2}{2} \frac{\partial^2 P}{\partial \xi^2}, \quad (5.22)$$

where $P = P[A, \xi, \tau]$ vanishes for $|A|, |\xi| \rightarrow \infty$. By definition of a probability density function, P has a unitary area: $\iint_{-\infty}^{\infty} P dA d\xi = 1, \forall \tau$. We introduce $\bar{P} = \bar{P}[A]$ the PDF of only A in a stationary regime, reached after infinitely long τ , such that

$$\bar{P} \doteq \int_{-\infty}^{\infty} \left(\lim_{\tau \rightarrow \infty} P[A, \xi, \tau] \right) d\xi. \quad (5.23)$$

We also define \bar{P}^w to be \bar{P} in the “pure” white noise limit where $\alpha \omega_d \rightarrow \infty$, which possesses the analytical expression

$$\bar{P}^w \doteq \lim_{\alpha \omega_d \rightarrow \infty} \bar{P} = \frac{1}{Z} \exp\left(-\frac{2V}{(\phi \eta)^2}\right), \quad Z \text{ a normalization constant.} \quad (5.24)$$

In the next section, the stochastically forced weakly nonlinear (WNL) amplitude A , its probability density function \bar{P} , and the statistics of the escape time ΔT of A between its two attractors $\pm \bar{A}$ will be computed for a selected flow geometry. Furthermore, results will be compared to direct numerical simulations (DNS).

5.4 Application case: the flow past a sudden expansion

The application case is chosen as the two-dimensional plane flow past a sudden expansion (see the non-dimensional geometry in figure 5.2a). The Reynolds number is defined as $Re = hU_\infty/\nu$, where h is the inlet channel height, U_∞ the centreline (maximum) velocity of the inlet parabolic velocity profile and ν the kinematic viscosity. The inlet is located at the streamwise coordinate $x = -5$ (made non-dimensional by h). At $x = 0$, the flow goes through a sudden expansion of expansion ratio $ER = 3$, and the outlet of the expansion is situated further downstream at $x = L = 40$, where the flow re-parallelized.

The linear and nonlinear Navier–Stokes equations are solved for the velocity field $\mathbf{U} = [U, V]^T$ and the pressure by means of the finite element method with Taylor–Hood (P2, P2, P1) elements, respectively, after implementation of the weak form in the software FreeFem++. The steady solutions of the Navier–Stokes equations are solved using the iterative Newton–Raphson method, and the linear operators are built thanks to a sparse solver UMFPACK implemented in FreeFem++. The mesh is constituted of approximately 4×10^4 triangular elements, whose edge size varies between a minimum value of 0.015 near the expansion corners and a maximal value of 0.15 farther upstream and downstream, leading to about 2×10^5 degrees of freedom for the global flow field (velocity and pressure).

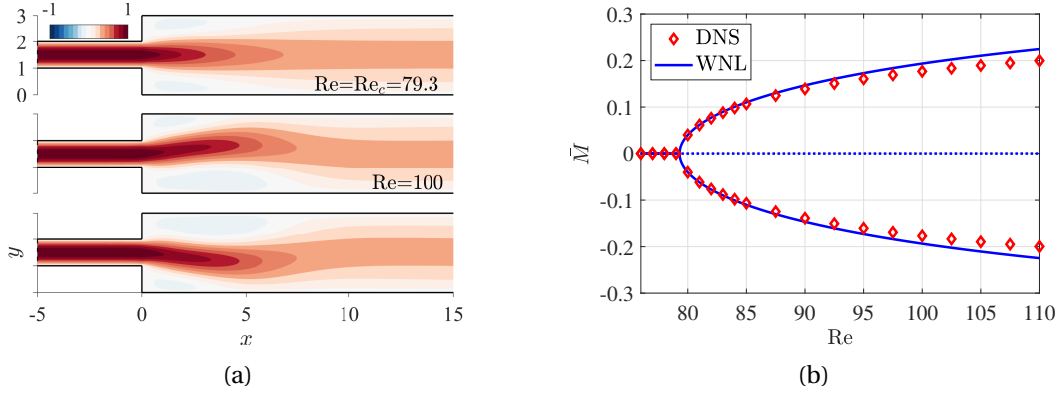


Figure 5.2: Deterministic case $\phi = 0$. (a) Snapshots of the streamwise velocity of the stable steady solution(s) obtained by DNS at $Re = Re_c = 79.3$ (top) and at $Re = 100 > 79.3$ (center & bottom); in the latter case, two equilibrium solutions are found. (b) Measure M that quantifies the asymmetry of the flow, as defined in (5.25), and computed in the steady regime for both WNL and DNS approaches. The continuous blue line is associated with the stable equilibrium solutions predicted by the deterministic amplitude equation $\pm \bar{M}$ with $\bar{M} = \sqrt{\bar{\epsilon}} \beta \bar{A}$, whereas the dotted line corresponds to the unstable equilibrium.

5.4.1 Deterministic regime

The critical Re number before the steady bifurcation is numerically found to be $Re_c = 79.3$, which compares relatively well with the value $Re_c = 81.4$ reported in Camarri and Mengali (2019). As we checked the convergence of Re_c with respect to the spatial discretization, the slight difference is rather explained by the fact that our entrance length is half of the one considered in Camarri and Mengali (2019). For $Re \leq Re_c$, the flow is symmetric in the sense of (5.11) around the centerline axis at $y = y_s = 1.5$, as can be seen in the uppermost snapshot in figure 5.2a.

For $Re > Re_c$, the symmetry of the flow is broken, as we can observe on the snapshots at the center and the bottom of figure 5.2a. The degree of asymmetry is quantified according to a scalar measure that we call M , and whose definition is always arguably arbitrary. Nevertheless, we propose it to be the signed L^2 -norm of the cross-wise velocity component evaluated along the symmetry axis (located at $y = y_s = 1.5$). The sign is chosen as being that of the cross-wise velocity along the symmetry axis and at $x = 2$, for it is where the cross-wise velocity component q_y of the anti-symmetric eigenmode $\mathbf{q} = [q_x, q_y]^T$ (with $\|\mathbf{q}\| = 1$) reaches its (chosen positive) maximum. In other terms, $q_y(x = 2, y_s) = \max_x [q_y(x, y_s)] = 0.136$. Eventually, M reads

$$M \doteq \text{sgn}[V(x = 2, y_s)] \sqrt{\int_0^L V(x, y_s)^2 dx}. \quad (5.25)$$

The WNL approximation of M is given by evaluating $V(x, y_s)$ according to the expansion (5.10), then using that $V_c(x, y_s) = v_2(x, y_s) = 0$, $\forall x$ (V_c the cross-wise velocity of the base flow and v_2

that of the second order field \mathbf{u}_2) for a symmetry reason, leading to

$$\begin{aligned}
 M &= \operatorname{sgn}[\underbrace{\sqrt{\epsilon} q_y(2, y_s)}_{>0} A + O(\sqrt{\epsilon^3})] \sqrt{\int_0^L (\sqrt{\epsilon} A q_y(x, y_s) + O(\sqrt{\epsilon^3}))^2 dx} \\
 &= \operatorname{sgn}(A) \sqrt{\epsilon} |A| \sqrt{\int_0^L q_y(x, y_s)^2 dx} + O(\sqrt{\epsilon^3}) \\
 &= \sqrt{\epsilon} \beta A + O(\sqrt{\epsilon^3}),
 \end{aligned} \tag{5.26}$$

with $\beta = \sqrt{\int_0^L q_y(x, y_s)^2 dx} = 0.266$ a proportionality constant.

The coefficients in (5.17) are found as $\lambda = 5.984$ and $\mu = -0.02962$, leading to $\bar{A} = \sqrt{-\lambda/\mu} = 14.21$. We stress that the coefficients are evaluated from known fields, without any fitting parameters. For a given Re number (setting ϵ), the equilibrium amplitudes $\pm \bar{A}$ are associated with the equilibrium asymmetry measures $\pm \bar{M}$ with $\bar{M} = \sqrt{\epsilon} \beta \bar{A}$. The slope of the red dashed line in figure 4b of Camarri and Mengali (2019) corresponds to our definition of λ . By visual inspection, we estimate for the former a value of ≈ 5.8 which indeed agrees well with our λ ; no numerical value is given for μ in Camarri and Mengali (2019).

In the deterministic case where $\phi = 0$, the DNS and WNL steady solutions are compared under the measure M in figure 5.2b as a function of the Re number. Close the threshold value Re_c , both approaches are in excellent agreement, thus validating the well-posedness of the weakly nonlinear expansion (5.10). Note that, interestingly, the latter implies the scaling $M \propto \sqrt{1/\operatorname{Re}_c - 1/\operatorname{Re}}$ when Re is asymptotically close to Re_c . The agreement between both approaches progressively degrades as we increase Re, presumably due to higher-order nonlinearities neglected in the expansion. Nevertheless, the relative error remains reasonable for the considered range of Re, with a maximum value of $\approx 11\%$ for $\operatorname{Re} = 110$. Overall, the agreement between both approaches is comparable with the one already reported (with a different measure) in figure 5 of Hawa and Rusak (2001).

In the rest of the study, we will fix the Re number to $\operatorname{Re} = 100$.

5.4.2 Stochastic regime: amplitude statistics

Let us now activate the stochastic forcing ($\phi \neq 0$). We choose the forcing structure to be $\mathbf{f} = \mathbf{q}^\dagger$, which maximizes the absolute value of η in (5.17), thus the impact of the forcing. We numerically find $\eta = 1.492$. For $\operatorname{Re} = 100$, we show in figure 5.3 some temporal signals of M for four gradually increasing forcing amplitudes ϕ , of the same given noise realization $\xi(\alpha \epsilon t)$. The cut-off frequency ω_{co} of the slowly-varying noise is set at $\omega_{co} = 0.04$. Due to the non-normality of the operator L , this specific choice is not arbitrary and will be detailed in the last section of the chapter. The WNL predictions and the DNS data are compared directly, as they are forced by the exact same noise. For both signals, under the stochastic forcing, M

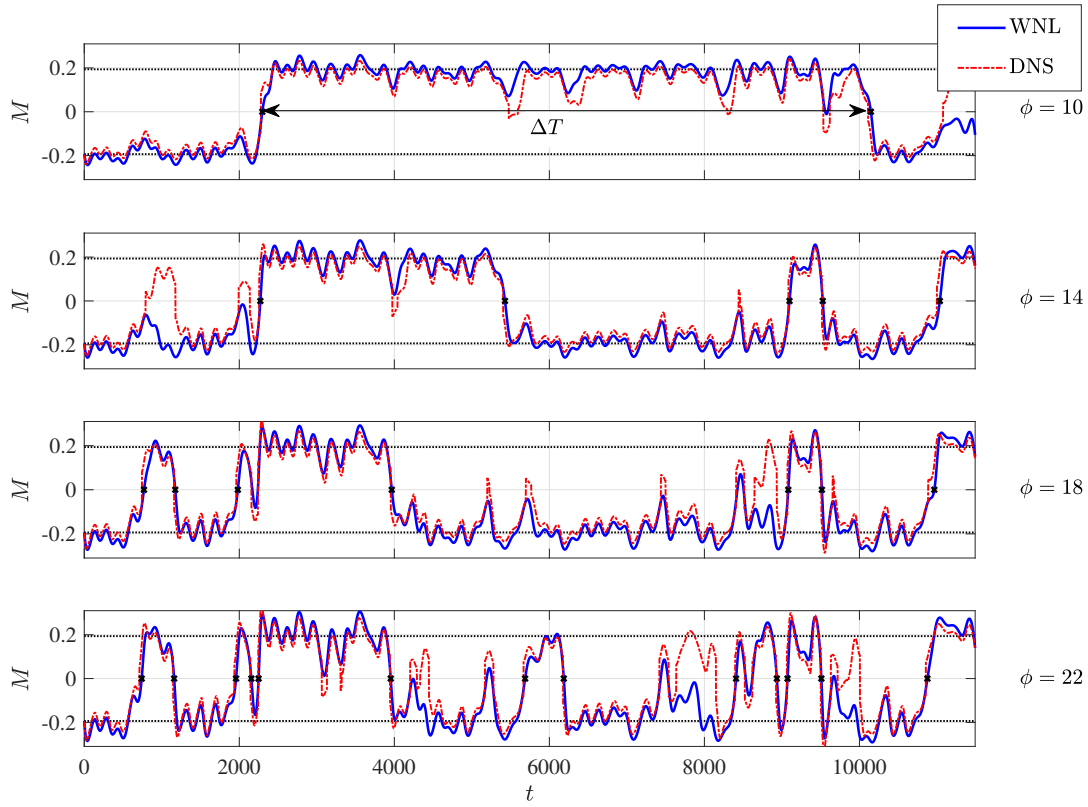


Figure 5.3: Temporal signal of M in a stochastically forced regime, with forcing amplitudes $\phi \in [10, 14, 18, 22]$. The noise realization $\xi(\alpha \epsilon t)$ is the same for all the results shown. A Re number of $\text{Re} = 100$ is chosen, implying $\epsilon = 0.0026$. A time step $\Delta t = 0.025$ was found sufficient for the convergence of the results, which sets $\omega_d = 125.7$. We further choose $\omega_{co} = 0.04$, which determines $\alpha = 1/8$ that we check to be $O(1)$ indeed. The two deterministic attractors $\pm \bar{M}$ with $\bar{M} = \sqrt{\epsilon} \beta \bar{A} = 0.1935$ are highlighted by horizontal black dotted lines. The small crosses highlight a “transition” (see definition in text) of the WNL signal from the neighborhood of one attractor to the neighborhood of the other.

experiences some random oscillations in the neighborhood of one of the two attractors. After some time, these oscillations may by chance become sufficiently strong such that M transits to the neighborhood of the other attractor, as it overcame the potential barrier separating the two. This scenario is increasingly likely with the forcing amplitude. With the exception of some relatively short episodes, the agreement between WNL and DNS signals is visually excellent in figure 5.3, at least for the considered noise realization. A small but systematic overestimation of the WNL prediction is to be noticed though, already present at the deterministic level and observable in figure 5.2b for $Re = 100$. Some discontinuities can also be noticed in the DNS signal, due to the multiplication with the sgn function in the definition of M .

A more quantitative and systematic comparison of both approaches is performed by running, for a given forcing amplitude, nine additional simulations to that of in figure 5.3, each corresponding to a different random noise realization. This generated a sufficient amount of data for convergence of the PDF of $|M|$, shown in figure 5.4 for $\phi \in [10, 14, 18, 22]$. We also show \bar{P} , the PDF associated with the steady solution of the Fokker-Planck equation (5.22), defined in (5.23). Its asymptotic shape in the limit where $\alpha\omega_d$ tends to infinity, \bar{P}^w defined in (5.24), is also visible. First, we observe that \bar{P} agrees poorly with \bar{P}^w , from which we conclude that accounting for a filtered noise in the Fokker-Planck model, at a cut-off frequency $\alpha\omega_d$ (over the slow time, thus $\epsilon\alpha\omega_d$ over the fast), has a significant effect. The probability density function \bar{P} is more localized than \bar{P}^w around \bar{M} , presumably because the noise corresponding to the former is filtered and thereby has a lower root-mean-square (by Parseval's theorem) than the noise of the latter, thus is less efficient in dislodging M from one of its attractors.

On the other hand, from the excellent agreement between \bar{P} and the PDF obtained from direct simulations of the amplitude equation (5.16), we also conclude that the results are robust to the order of the filter that generates the slow noise; indeed, \bar{P} is associated with a first-order filtered noise whereas the noise in (5.16) is infinite-order filtered (square signal in the frequency domain). Therefore, one does not need to be too careful in the way the slow noise is constructed.

The agreement between \bar{P} and the PDF reconstructed from the DNS is globally satisfactory when plotted over $|M|/\bar{M}$. When plotted over $|M|$ (see inset of figure 5.5a), both PDFs are slightly offset due to the difference between deterministic attractors. In addition, the agreement seems to degrade for $|M| \rightarrow 0$. This is explained by the fact that M , due to its definition as a L^2 norm of the cross-wise velocity (5.25), is null if and only if the cross-wise velocity is strictly null everywhere along the symmetry axis; because, for instance, of higher-order nonlinear terms neglected in the expansion, this condition is very unlikely to be met in the DNS. This effect is all the more pronounced by increasing ϕ .

5.4.3 Stochastic regime: escape time statistics

By considering the absolute value $|M|$, the transition events from the neighborhood of one attractor to the other were not considered. However, as developed in the introduction, they are

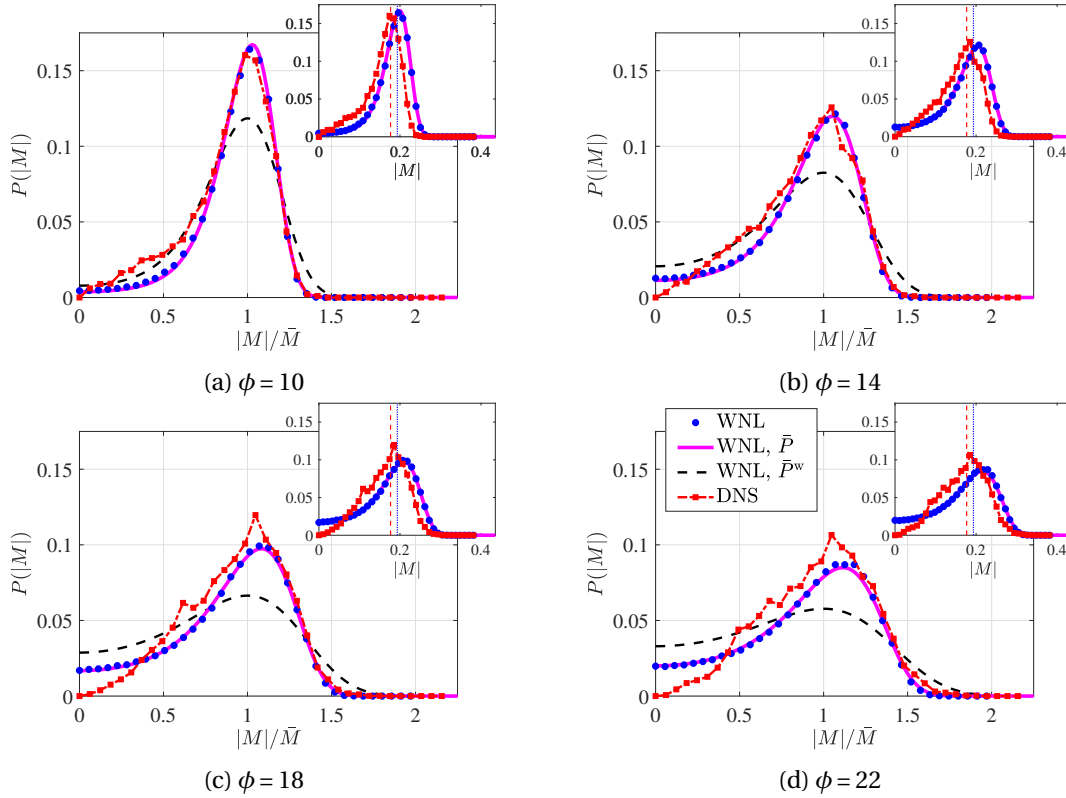


Figure 5.4: Probability density function of $|M|$ for the four different forcing amplitudes considered in figure 5.3. The external parameters are also the same as for figure 5.3. For the blue dots “WNL” and the red dashed-dotted line with the square markers “DNS”, ten simulations, each corresponding to a different noise realization and long of $t = 1.1 \times 10^4$ units of times, were performed and post-treated. The magenta line “WNL, \bar{P} ”, defined in (5.23), is the steady solution of the Fokker-Planck equation (5.22). The black dashed line “WNL, \bar{P}^w ”, defined in (5.24), also corresponds to the steady solution of the Fokker-Planck equation but in a case of “pure” white noise where $\alpha\omega_d \rightarrow \infty$. The insets show to the same data as the main figures, but as a function of $|M|$ instead of $|M|/\bar{M}$. The vertical red dashed line is the deterministic attractor \bar{M} of the DNS whereas the vertical, dotted, blue line is the one from the WNL approach (see figure 5.2b)

of great interest in practice and thus are studied thereafter. Let us first put a formal definition of what we mean by “transition”. A “transition” from the neighborhood of one attractor to the other is decreed whenever the following scenario occurs: at some t_1 , M goes above $-c\bar{M} < 0$ (resp. below $c\bar{M} > 0$), and doesn’t go below (resp. above) this same threshold again before going above (resp. below) the opposite one $c\bar{M}$ (resp. $-c\bar{M}$) at some t_3 , where the constant $c > 0$ is chosen, perhaps arbitrarily, as $c = 0.8$; then a transition has occurred at the largest of all time(s) in the interval $[t_1, t_3]$ for which M is null. Under this definition, the transitions are highlighted for the WNL signal by the black crosses in figure 5.3. For $\phi = 10$ the time interval ΔT separating two transitions, shown with an arrow in figure 5.3, sometimes called an “escape time” or “first passage time”, seems to be on average extremely long. This also underlines the importance of using a reduced-order model. In a simulation long of $\tau = 30$

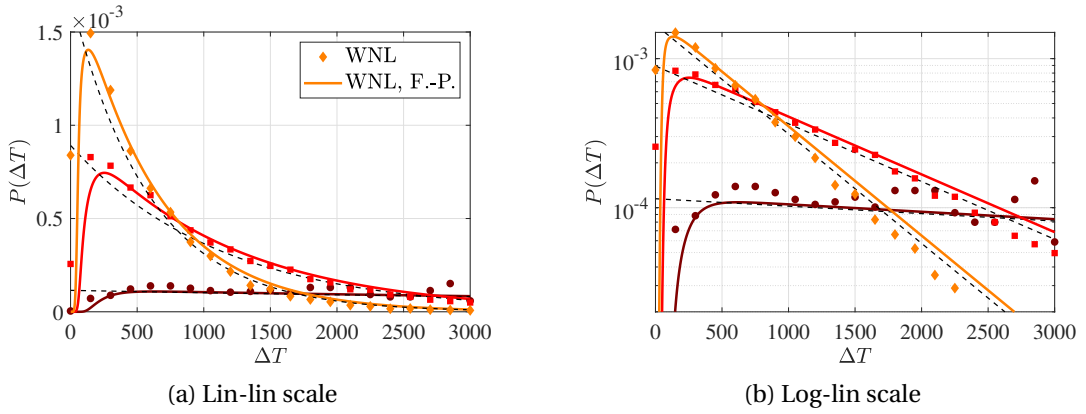


Figure 5.5: Probability density function of the escape time ΔT between two transition events from the neighborhood of one attractor to the neighborhood of the other. Lighter colors correspond to larger forcing amplitude ϕ where $\phi \in [10, 18, 26]$. The parameters are the same as for figure 5.3, specifically $Re = 100$ and $\omega_{co} = 0.04$. For the markers “WNL” (dots for $\phi = 10$, squares for $\phi = 18$ and diamonds for $\phi = 26$), ten direct simulations of (5.16), each corresponding to a different noise realization and long of $t = 1.1 \times 10^6$ units of times, were performed and post-treated. The continuous lines “WNL, F.-P.” (F.-P. for Fokker-Planck), are obtained by marching in time the Fokker-Planck equation (5.22) with appropriate initial/boundary conditions (see main text). Subfigures (a) and (b) show the same data, (a) in linear-linear scale and (b) in log-linear scale. The thin black dashed- lines are exponential laws $b \exp(-b\Delta T)$, where $b = b(\phi)$ is a fitted parameter.

(corresponding to $t = \tau/\epsilon = 1.1 \times 10^4$) units of times, only two transitions could be captured, at a large computational cost for the DNS. By increasing ϕ to $\phi = 22$, the oscillations of M around $\pm \bar{M}$ are more intense, and the transitions are more frequent (thirteen transitions could be captured).

In order to approximate the PDF of the escape time ΔT between two transitions, a sufficiently large number of these transition events has to be reported, and the simulations have to be sufficiently long to also capture very large ΔT , constituting the tail of its PDF. For this reason, for each of the considered forcing amplitude, ten simulations of the amplitude equation (5.16) to an extremely large final time of $\tau = 3000$ (corresponding to $t = \tau/\epsilon = 1.1 \times 10^6$), were performed. Each of these simulations corresponds to a different realization of the slow noise. Some PDF of ΔT reconstructed by post-processing the so-generated data are proposed in figure 5.5 (lin-lin scale in figure 5.5a, and log-lin scale in figure 5.5b).

Alternatively, the PDF of ΔT can be computed by marching in time the Fokker-Planck equation (5.22) with appropriate boundary and initial conditions (Bonciolini et al., 2018). The initial condition is set as

$$P[A, \xi, \tau = 0] = \delta(A - \bar{A}) \frac{\exp\left(-\frac{\xi^2}{2\sigma^2}\right)}{\sigma\sqrt{2\pi}}, \quad (5.27)$$

which translates the fact that trajectories are systematically started at the attractor \bar{A} , whereas the initial condition for the noise is random and follows a centered normal distribution of standard deviation σ , i.e. $\xi(t=0) \sim \mathcal{N}(0, \sigma^2)$. Precisely because the noise has zero mean, the variance σ^2 is equal to the root mean square of the signal, which is expressed by Parseval's theorem

$$\sigma^2 \stackrel{\{\xi\}=0}{=} \frac{1}{T} \int_0^T \xi(\alpha \epsilon t)^2 dt = \frac{1}{2\pi} \int_{-\infty}^{\infty} |\mathcal{F}(\xi(\alpha \epsilon t))|^2 d\omega = \frac{2\omega_{co}}{\epsilon 2\pi} = \frac{\alpha \omega_d}{\pi} = \frac{\alpha}{\Delta t} \quad (5.28)$$

(i.e. two times the area below the red or black curve in figure 5.1, divided by 2π). For the boundary condition, $P = 0$ for $|\xi|$, $A \rightarrow \infty$ is maintained, but instead of also imposing $P = 0$ for $A \rightarrow -\infty$, we set $P[-c\bar{A}, \xi, \tau] = 0, \forall \xi, \tau$. As expressed in Bonciolini et al. (2018): “*this boundary condition is a probability sink, which leads to a monotonic decay in time of the integral* [$\iint P[A, \xi, \tau] dA d\xi$, which] *represents the probability of not having crossed the threshold* $[-c\bar{A}]$ *before time* t . Consequently the PDF of the escape time is the temporal derivative of $1 - \iint P[A, \xi, \tau] dA d\xi$, for the latter expression is the probability of having escaped to the neighborhood of the attractor $-c\bar{A}$, while (5.27) guarantees that all trajectories initially were at the other attractor \bar{A} .

The PDFs resulting from this approach are included in figure 5.5 and compared with those obtained by post-processing the data generated from direct simulation of (5.16). The agreement between both approaches is globally good. Moreover, it is observed in figure 5.5b that the PDF of the escape time decays exponentially for sufficiently large ΔT ; thereby it can be thought of as following an exponential law, reading $b e^{-b \Delta T}$. The parameter b is fitted on the PDF obtained with the Fokker-Planck equation, and gives a fair approximation, particularly for the lowest ϕ considered in the figure. It is also clear that increasing the forcing amplitude implies a faster exponential decay of the PDF. Indeed, by increasing the intensity of the external excitation, crossing the potential barrier between the two attractors is made easier, thus large escape times are less and less likely.

The mean escape time $\{\Delta T\}$ and its standard deviation $\text{std}(\Delta T)$ associated with the PDFs in figure 5.5 and those for others forcing amplitudes are shown in figure 5.6 as a function of the forcing amplitude. The agreement between the results from the Fokker-Planck equation and from direct simulations of the amplitude equation is good for the mean escape time. They also collide on the value $1/b$ predicted by the exponential law. Although the differences are barely visible in figure 5.6a, the value $1/b$ is all the closer to $\{\Delta T\}$ obtained from Fokker-Planck than ϕ is small; in other words, the PDF of ΔT tends towards an exponential law in the limit where $\phi \rightarrow 0$. This result is well-known from the large deviation theory.

In the “pure” white noise limit where $\alpha \omega_d \rightarrow \infty$, and for vanishing forcing amplitude, the mean escape time is given by the Eyring-Kramers formula (sometimes also called Kramer's escape rate) according to

$$\lim_{\phi \rightarrow 0} \lim_{\alpha \omega_d \rightarrow \infty} \{\Delta T\} = \frac{1}{\epsilon} \frac{\sqrt{V''(\bar{A})|V''(0)|}}{2\pi} \exp\left[-\frac{2\Delta V}{(\eta\phi)^2}\right], \quad (5.29)$$

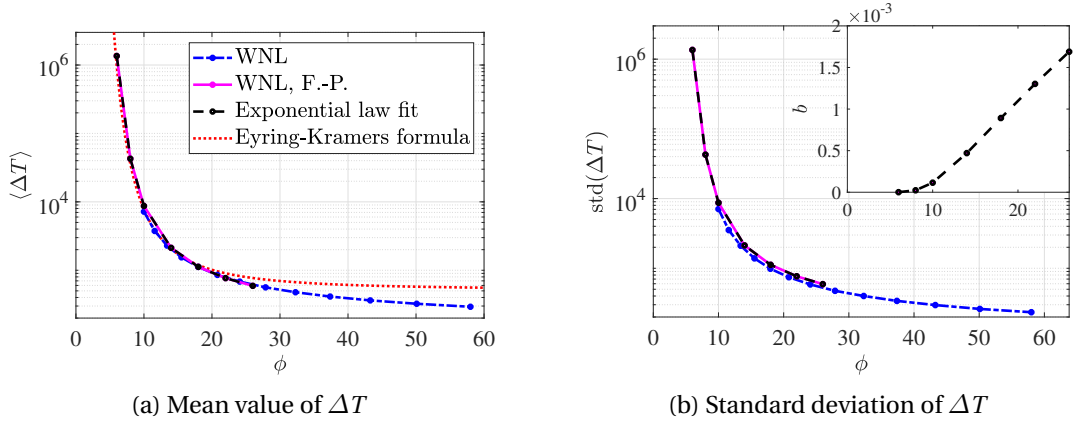


Figure 5.6: Mean value and standard deviation of ΔT . The parameters are the same as for figure 5.3, specifically $Re = 100$ and $\omega_{co} = 0.04$. The blue dash-dotted line is obtained as follows: for each forcing amplitude ten direct simulations of (5.16), each corresponding to a different noise realization and long of $t = 1.1 \times 10^6$ units of times, were performed and post-treated. The continuous magenta line “WNL, F.-P.” (F.-P. for Fokker-Planck), is obtained by marching in time the Fokker-Planck equation (5.22) with appropriate initial/boundary conditions. In the subfigure (b) the inset shows the fitted parameter b of the exponential law writing $b \exp(-b\Delta T)$. The mean value and the standard deviation reconstructed from this exponential law, both equal to $1/b$, are shown by means of the blacked dashed line. The red dotted line is the Eyring-Kramers formula as given in (5.29).

where

$$\Delta V \doteq V(\bar{A}) - V(0) = \frac{\lambda^2}{4\mu}, \quad V''(\bar{A}) = 2\lambda, \quad \text{and} \quad V''(0) = -\lambda \quad (5.30)$$

Expression (5.29) can be found in Risken (1996), Chapter 5.10, formula (5.111). Without the pre-factor multiplying the exponential, (5.29) is referred to as the Arrhenius law in thermodynamics. The relevance of the Eyring-Kramers formula here might appear surprising given the out-of-equilibrium nature of the system (5.1). Nevertheless, it stems from the fact that, in the specific situation considered in this chapter, the Navier-Stokes equation could be reduced to a one-dimensional noisy dynamic, with the deterministic part deriving from a potential. Note that the factor $1/\epsilon$ in (5.29) accounts for the fact that the amplitude equation is written over the slow time scale $\tau = \epsilon t$. The Eyring-Kramers formula (5.29) is drawn as the red-dotted line in figure 5.6a, and appears accurate until relatively large $\phi \approx 15$. Above this value, it is interesting to notice that the parameter b increases rather linearly with ϕ , such that the mean escape time decreases as a rational function, thus faster than (5.29).

The evolution of the standard deviation of ΔT with ϕ , shown in figure 5.6b, is quantitatively and qualitatively similar to the one of $\{\Delta T\}$.

Note that the statistics of the escape time ΔT shown in figure 5.5 and figure 5.6 have not been directly compared with those from DNS. That is because, as said, they have been produced

over simulations long of $t = 1.1 \times 10^6$ units of time, deliberately extremely long to capture large ΔT . We could not afford DNS of such extreme length, and this is precisely what motivated the approach proposed in this chapter. If, as mentioned in the introduction, specific algorithms exist in computing the escape time directly from the fully nonlinear Navier-Stokes equation in (5.1), their implementation is out of the scope of this chapter. Note, however, that a complete comparison between fully and weakly nonlinear escape time statistics would be necessary, since a good agreement between the steady statistics in figure 5.4 generically does not imply a good agreement between dynamical quantities such as ΔT . Results shown in figure 5.3, however, suggest that such a comparison would be successful.

5.4.4 Stochastic regime: choice of the cut-off frequency

Let us now say a word about the choice of the cut-off frequency ω_{co} . First, it is important to notice that the band-limiting frequency $\omega_d = \pi / \Delta t$ can be chosen, in theory, to be arbitrarily large. Therefore, $\omega_{co} = \epsilon \alpha \omega_d$, ϵ being set by the Re number and $\alpha = O(1)$, could also be arbitrarily large (as long as it is much smaller than ω_d). However, if the linearized operator L , defined in (5.12), is non-normal, there is a specific value of ω_{co} above which we expect the predictions from the amplitude equation to become inaccurate. To determine it, we consider the response of the flow linearized around the neutral, symmetric equilibrium at Re_c , \mathbf{U}_c , to a stochastic forcing $\mathbf{f}\xi(t)$, where $\|\mathbf{f}\| = 1$ and $\xi(t)$ is a white noise such that $|\hat{\xi}(\omega)| = 1$, $\forall \omega$. In the linear paradigm, the amplitude of the forcing term is irrelevant and is set to one for the rest of the reasoning. In the Fourier domain, valid in the limit of large times after the transients fade away, the response writes $\hat{\mathbf{u}}(\omega) = R(\omega)\mathbf{f}\hat{\xi}(\omega)$, the operator $R(\omega) \doteq (i\omega I - L)^{-1}$ being called the resolvent operator. By decomposition on the basis of eigenmodes of L , the resolvent operator has a dyadic representation (Luchini & Bottaro, 2014; Schmid & Brandt, 2014b)

$$R(\omega) = \sum_{j=1}^{\infty} \frac{1}{i\omega - \gamma_j} \frac{\mathbf{q}_j \langle \mathbf{q}_j^\dagger | * \rangle}{\langle \mathbf{q}_j^\dagger | \mathbf{q}_j \rangle}, \quad (5.31)$$

where \mathbf{q}_j (with $\|\mathbf{q}_j\| = 1$), \mathbf{q}_j^\dagger (with $\|\mathbf{q}_j^\dagger\| = 1$) and γ_j are the j th eigenmode, associated adjoint mode and eigenvalue of L , respectively. Eigenvalues are ordered such that $\Re(\gamma_1) \geq \Re(\gamma_2) \geq \dots$, implying $\gamma_1 = 0$, $\mathbf{q}_1 = \mathbf{q}$ and $\mathbf{q}_1^\dagger = \mathbf{q}^\dagger$. The forcing structure considered in the chapter was chosen to be $\mathbf{f} = \mathbf{q}^\dagger$, which generates

$$R(\omega)\mathbf{q}^\dagger = \frac{1}{i\omega} \frac{\mathbf{q}}{\langle \mathbf{q}^\dagger | \mathbf{q} \rangle} + \sum_{j=2}^{\infty} \frac{1}{i\omega - \gamma_j} \frac{\mathbf{q}_j \langle \mathbf{q}_j^\dagger | \mathbf{q}^\dagger \rangle}{\langle \mathbf{q}_j^\dagger | \mathbf{q}_j \rangle}. \quad (5.32)$$

Had the operator L been normal, both the direct modes and the adjoint modes would form an orthonormal basis and all the inner products $\langle \mathbf{q}_j^\dagger | \mathbf{q}^\dagger \rangle$ for $j \geq 2$ would be identically null. This way, the transfer function $\|R(\omega)\mathbf{q}^\dagger \hat{\xi}(\omega)\| / \|\mathbf{q}^\dagger \hat{\xi}(\omega)\| = \|R(\omega)\mathbf{q}^\dagger\|$ reduces to a classical

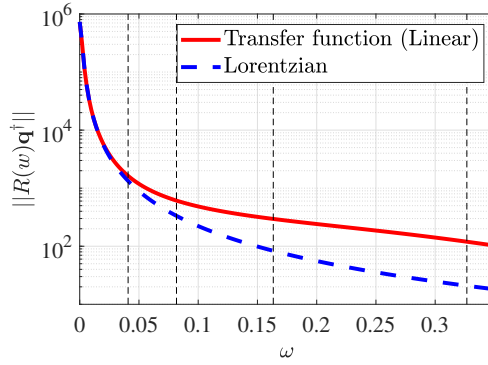


Figure 5.7: The red continuous line is the (linear) transfer function $\|R(\omega)\mathbf{q}^\dagger\|$ (norm of the expression (5.32)) with $\mathbf{f} = \mathbf{q}^\dagger$ of the sudden expansion flow linearized around its symmetric neutral equilibrium at $\text{Re} = \text{Re}_c$. The blue dashed line is the Lorentzian function (5.33) only accounting for the response of the virtually neutral mode \mathbf{q} , resonant at $\omega = 0$. Both curves would collide exactly if L was a normal operator, for \mathbf{q}^\dagger would then excite only \mathbf{q} . Four horizontal black dashed-lines are drawn at $\omega \in [4, 8, 16, 32] \times 10^{-2}$.

Lorentzian (resonant) response peaked around the resonant frequency $\omega = 0$

$$\|R(\omega)\mathbf{q}^\dagger\|^2 = \frac{1}{\omega^2 \langle \mathbf{q} | \mathbf{q}^\dagger \rangle^2}. \quad (5.33)$$

However, L is generally non-normal due to the linearization of the advection term, and neither the direct eigenmodes nor the adjoint ones constitute an orthonormal basis. Therefore the sum in (5.32) does not vanish, and the Lorentzian (5.33) is only accurate in the limit $|\omega| \rightarrow 0$, where the term in $1/(i\omega)$ in (5.32) dominates the sum.

To illustrate this, we compare in figure 5.7 the transfer function $\|R(\omega)\mathbf{q}^\dagger\|$ of the sudden expansion (at $\text{Re} = \text{Re}_c$), with the Lorentzian response (5.33). As expected, both curves coincide in the limit $|\omega| \rightarrow 0$, where the virtually neutral eigenmode enters in resonance and thus dominates the flow response. Nevertheless, by increasing the frequency above $\omega = 0.04$, both curves depart from each other and the Lorentzian significantly underestimates the response. This is the consequence of the non-normality of the operator L , which implies that \mathbf{q}^\dagger has a non-null projection over all the other adjoint modes, thus exciting in the response all the associated direct modes; far from the resonant frequency, the eigenmode \mathbf{q} has no reason to dominate over this response. Consequently, if the noise term contains frequency above $\omega_{co} = 0.04$, reducing the first-order dynamics of the system on the single mode \mathbf{q} , which was the case in the weakly nonlinear expansion, see (5.12), might be a poor approximation.

This is exemplified in figure 5.8, where we show the probability density function of $|M|$, similarly as in figure 5.4, but for a fixed forcing amplitude $\phi = 12$ and four increasing values of the cut-off frequency, $\omega_{co} \in [0.04, 0.08, 0.16, 0.32]$. The agreement between the PDF obtained from the WNL approach (direct simulation or Fokker-Planck), and the one extracted from DNS, seems to progressively degrade by increasing ω_{co} . This is particularly true for M close to

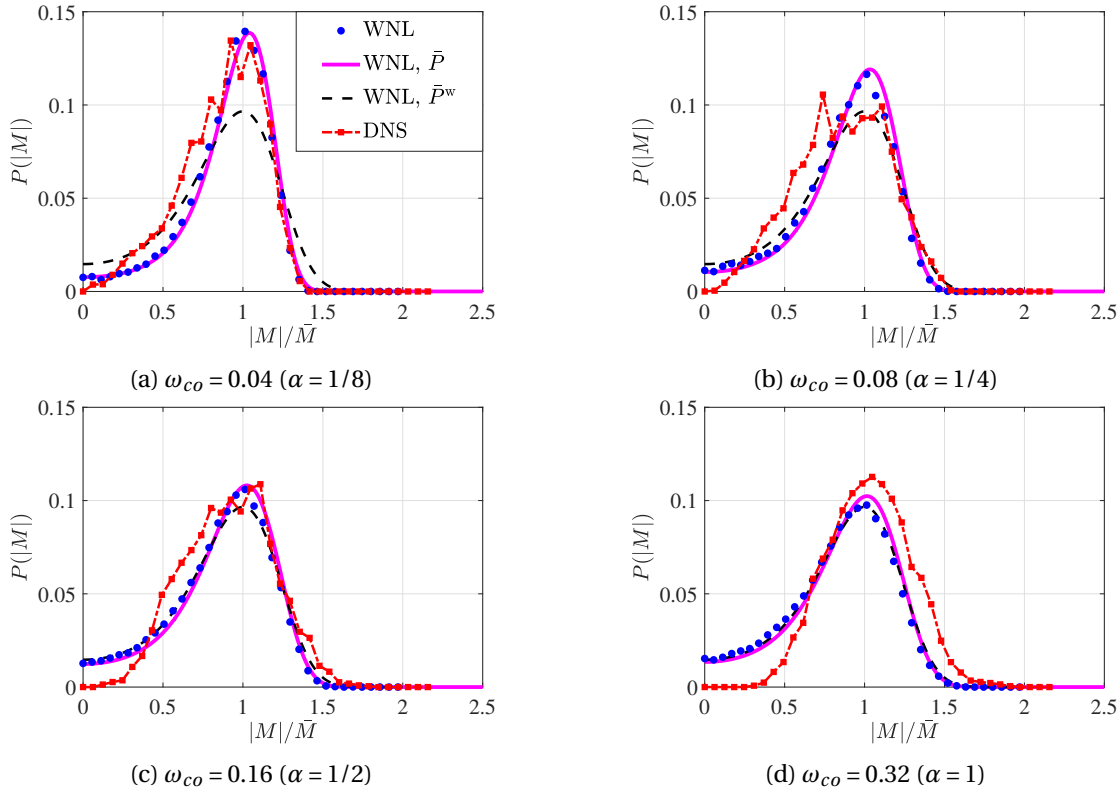


Figure 5.8: Probability density function of $|M|$, similarly as in figure 5.4 but for a fixed $\phi = 12$; to save some computational time, the ten simulations, each corresponding to a different noise realization have been shortened to $t = 1.1 \times 10^3$ units of times with respect to the computations shown in figure 5.4. The data are shown for four different values of the cut-off frequency $\omega_{co} \in [4, 8, 16, 32] \times 10^{-2}$. These four specific frequencies are highlighted with vertical black dashed lines in figure 5.7.

zero where the weakly nonlinear PDF largely overestimates the nonlinear one. As explained previously, that is because for too large ω_{co} the eigenmode \mathbf{q} , which is the only one described by the amplitude equation, does not dominate the flow response anymore, and other modes reveal themselves. Due to the activity of these auxiliary modes, the probability of having a null or very low cross-wise velocity along the symmetry axis is reduced, and it becomes more and more unlikely for $|M|$ to take null or small values. Presumably for the same reasons, it appears in figure 5.8d that for the largest considered $\omega_{co} = 0.32$, on the contrary, large values of $|M|$ become more likely in the DNS than in the WNL method. As a side comment, note also that increasing ω_{co} incidentally makes \bar{P} converge towards \bar{P}^w , as expected.

5.5 Summary and perspectives

In summary, based on the existing literature we have proposed a method to derive a stochastically forced equation for the amplitude of the slowly varying dominant eigenmode, after

a steady symmetry-breaking bifurcation. To this purpose, the noise too was assumed to be slowly varying, in other words, filtered at a certain cut-off frequency much slower than the band-limiting frequency of the overall system. We gave a precise manner to evaluate *a priori* the cut-off frequency for which the weakly nonlinear expansion, that reduces the linear dynamics to a single eigenmode, is justified. It is the frequency above which the transfer function of the linearized flow departs from a Lorentzian, that only encompasses the dominant mode. We also showed that the order of the filter, generating the slow noise from a classical white noise, mattered little.

The probability density function of the mode amplitude obtained from the amplitude equation, either by direct simulations or by solving the related Fokker-Planck equation, compared well with the stochastically forced direct numerical simulations. Unsurprisingly, this is particularly true for small forcing amplitude, as increasing the latter increases the relative importance of higher-order nonlinear terms that have been neglected in the weakly nonlinear expansion, and renders small values of the asymmetry measure M unlikely.

The amplitude equation has reduced the dynamics of the flow to a single coordinate whose dynamics derive from a potential. This is particularly convenient when it comes to computing escape time statistics. Indeed, for vanishing forcing amplitude, the waiting time between two events where the solution transits from the neighborhood of one attractor to the other, was found to increase as the exponential of the inverse of the forcing intensity squared. Clearly, this precludes the utilization of direct numerical simulations. On the other hand, as a reduced-order model, the amplitude equation can make predictions at a low numerical cost.

Nevertheless, even in different cases where the obtained amplitude equation will contain more than one degree of freedom, therefore where generically no potential function exists, the method proposed in this chapter can be seen as bridging a system of very high dimension, governed by the Navier-Stokes equation, with the large deviation theory and/or the Fokker-Planck equation that are very effective in systems of low dimension. In this manner, predictions about rare transition statistics could be made without relying on intensive numerical techniques.

For future research, the method outlined in this chapter shall be extended to more general stochastic forcings than a single spatial structure multiplied by a slow noise. Instead, one could consider forcing the flow as in Farrell and Ioannou (1993) with a sum of orthonormal forcing spatial structures, multiplied by uncorrelated white noise processes. As in Farrell and Ioannou (1993), this orthonormal family of forcing structures can be sorted in descending order from largest to smallest maintained variance of the linear response. Because of the non-normality of the linearized operator, it is possible that only a few of the leading forcings contribute to most of the total variance and thus need to be included. The leading (also called "optimal") forcing structure will be the adjoint mode, as considered in this chapter, for the associated modal response is resonant in $\omega = 0$ thus its variance (proportional to the integral of (5.33) over the frequencies) diverges. The sub-optimal forcing structures, however, will be orthogonal to the adjoint and trigger streamwise convective non-normal amplification in the flow at non-zero

frequencies. At a nonlinear level, the modal and non-normal responses will interact with each other, which is not taken into account in the present analysis, and knowing the role played by the non-normal response at non-zero frequencies over the noise-induced transitions would be of great interest. For this purpose, the method proposed in Ducimetière et al. (2022b, 2022c) to derive amplitude equations for non-normal responses, could be coupled with that proposed in the present chapter for the modal one. In considering noises that are not slowly varying, one could think of splitting slowly and rapidly varying parts and consider the linear response to the rapidly varying part in the Fourier domain at third-order.

Eventually, we believe that, although concerned with the rather specific configurations of laminar flows past a supercritical bifurcation and subject to external stochastic forcing, the present study could be seen as part of a more general and fundamental study on out-of-equilibrium systems with infinitely many degrees of freedoms. This includes fluid flows in a turbulent regime, where rare transitions are observed in numerous situations, as presented in the introduction. It could be interesting to extend the method proposed here to transitions between turbulent large-scale coherent structures, where the stochastic driving is endogenous and results from nonlinear interactions of the fluctuations. For instance, the construction of a stochastically forced amplitude equation could be done on a turbulent mean flow obtained *a priori* with a quasi-linear analysis as developed in Farrell and Ioannou (2012). Indeed, such turbulent mean flows are also subject to bifurcations and multi-stability, as clearly shown in Constantinou et al. (2014), Farrell and Ioannou (2012), and Parker and Krommes (2013) and many others.

The scope also covers other physical systems governed by other stochastic ordinary or partial differential equations. This includes active matter, population dynamics, adaptive networks, microbiological systems, climate science, and many others. As an example, it could be interesting to apply the present method in the spatiotemporal system of bacteria considered in Grafke et al. (2017) and subject to a subcritical pitchfork bifurcation above a critical mean bacterial density. Consequently, a stable solution made of a dense bacterial colony appearing at one boundary of the domain co-exists with another symmetrically placed at the other boundary of the domain. It was shown in Grafke et al. (2017) that, in certain regimes, the introduction of noise triggers rare and aperiodic transitions between these two solutions.

6 Coupling modal and non-modal stochastic responses past the onset of a steady symmetry-breaking bifurcation

6.1 Introduction

The present chapter aims at generalizing the developments made in the previous one, in that, here, the noise process in the stochastic forcing term is not *a priori* assumed to vary over a slow time scale. In other terms, the noise is not filtered at a very small cut-off frequency. Yet, we show that it is still possible to formally reduce the dynamics of the bifurcated mode to a stochastically forced amplitude equation.

As shown in the previous chapter, this is at the cost of taking into account the possibly substantial response of the system at larger frequencies and resulting from the non-normality of the linearized operator. That is because the forcing structure, even if purely along the adjoint of the neutral, resonant mode at the null frequency, still yields a non-zero projection on the adjoint of all the other eigenmodes, thus making these latter contribute to the response. This specific contribution, which decomposes in all the eigenmodes but the neutral one (in the sense that it is triggered by the part of the forcing that is orthogonal to the adjoint of the neutral mode), is called the "non-normal response" in the rest of this chapter. It can become substantial if non-modal mechanisms are active. For instance, at larger frequencies, the Kelvin-Helmholtz (convective shear instability) mechanism around $\omega = 0.3$ was important in the sudden expansion flow at $Re = 100$ considered in the previous chapter. If this non-normal amplification is so large that the response-to-forcing amplification can be scaled in terms of the inverse of the weakly nonlinear expansion parameter, the non-normal response threatens the asymptotic hierarchy and has to be taken into account.

This is formally done in this chapter by proposing an operator perturbation of the inverse

resolvent, in line with the techniques proposed in chapters 2, 3 and 4. The relevant non-normal amplification is here sought and assumed to be very large in terms of the inner product inducing the mean square norm, which we also call "variance" in what follows. Therefore, it is this specific inner product that is used in the inverse resolvent perturbation, to incorporate the non-normal response in its kernel, as done in section 6.2. Accordingly, it is under this specific inner product that the adjoint of this singular operator is constructed. The singular operator then contains two elements in its kernel: (i) the non-normal response by construction via the operator perturbation, and (ii) the neutral mode, naturally present and left untouched by the operator perturbation. As shown in section 6.3, the operator perturbation can be encompassed in a classical weakly nonlinear expansion, closed by the Fredholm alternative. The latter consists here in imposing orthogonality of the higher-order forcing terms with both the adjoint eigenmode and the adjoint of the non-normal response, under the spatiotemporal inner product. Eventually, this leads to a system of coupled equations for the amplitude of the bifurcated mode and the non-normal response, respectively.

We purposely do not include the ensemble average in the inner product, since, from the results of chapter 3, we anticipate that this would preclude the amplitudes to depending on the stochastic argument (i.e., they would be deterministic) whereas these precisely are the stochastic oscillations of the amplitudes that are sought here.

In section 6.4, the method is tested on a toy model past the onset of a supercritical pitchfork bifurcation. The linearized model at neutrality is constructed in such a way as to show a substantial non-normal response at larger frequencies, in addition to the resonance at zero frequency. The probability density function of the bifurcated mode amplitude, as predicted by the system of amplitude equations, is compared to those resulting from fully nonlinear simulations and for increasing forcing amplitudes. The agreement is conclusive and reveals the nonlinear coupling between the modal and the non-modal response to be an essential ingredient.

6.2 Problem definition and linear regime

Let us consider the specific nonlinear dynamical system

$$\partial_t \mathbf{U} = -C(\mathbf{U}, \mathbf{U}) + (\tilde{L} + \epsilon^2 \delta L) \mathbf{U} + \mathbf{F}, \quad (6.1)$$

where $C(\mathbf{U}, \mathbf{U})$ is a bi-linear, nonlinear operator whereas both \tilde{L} and δL are linear ones with $0 \leq \epsilon^2 \ll 1$ an external parameter. The term \mathbf{F} denotes a body force. For $\epsilon = 0$, the system (6.1) possesses an unforced equilibrium denoted $\mathbf{U}_{e,c}$, satisfying

$$\mathbf{0} = -C(\mathbf{U}_{e,c}, \mathbf{U}_{e,c}) + \tilde{L} \mathbf{U}_{e,c}. \quad (6.2)$$

By considering asymptotically small perturbation \mathbf{u} around $\mathbf{U}_{e,c}$ and \mathbf{F} to also be asymptotically small and equal to \mathbf{f} , follows the linear equation

$$\partial_t \mathbf{u} = L_n \mathbf{u} + \mathbf{f}, \quad (6.3)$$

where $L_n \mathbf{u} = -C(\mathbf{U}_{e,c}, \mathbf{u}) - C(\mathbf{u}, \mathbf{U}_{e,c}) + \tilde{L}\mathbf{u}$. We assume L_n to be a neutral, singular operator with a null eigenvalue and denote by \mathbf{q} , normalized as $\|\mathbf{q}\| = 1$, the steady, real, and neutral eigenmode of L_n . In other terms, \mathbf{q} is such that $L_n \mathbf{q} = 0$ and $\mathbf{q} = \mathbf{0}$. We also define its adjoint mode \mathbf{q}^\dagger , such that $L_n^\dagger \mathbf{q}^\dagger = \mathbf{0}$. In what follows, the adjoint eigenmode is normalized such that

$$\langle \mathbf{q}^\dagger | \mathbf{q} \rangle = 1, \quad (6.4)$$

which generically implies $\|\mathbf{q}^\dagger\| \neq 1$.

We also assume the system to bifurcate to a steady, symmetry-breaking (pitchfork) bifurcation as soon as $\epsilon^2 > 0$. As an example, in the case of the previous chapter, we identify $\epsilon^2 = \text{Re}_c^{-1} - \text{Re}^{-1}$ and $\delta L = -\Delta$ (with Δ the Laplacian appearing in the Navier-Stokes equations).

Exactly as in chapter 3 and chapter 4, the specific form

$$\mathbf{f}(\mathbf{x}, t) = \mathbf{f}_s(\mathbf{x})\xi(t) \quad (6.5)$$

is chosen for the stochastic forcing. The field $\mathbf{f}_s(\mathbf{x})$ is the forcing spatial structure and $\xi(t)$ a Gaussian band-limited white noise process with unit intensity, zero mean, and a cut-off frequency $\omega_c = \pi$. It is expressed in the Fourier domain as

$$|\hat{\xi}(\omega)|^2 = 1, \quad |\omega| \leq \omega_c = \pi, \quad \text{as well as} \quad \overline{\hat{\xi}(t)} = 0. \quad (6.6)$$

Note that the definition of the noise above is not equivalent to that proposed in chapters 3 and 4 in (4.3), but is more restrictive, for it characterizes directly $|\hat{\xi}(\omega)|^2$ and not its ensemble average. As said in the introduction, in deriving the amplitude equations, the ensemble average is not taken in this chapter since we are interested in how the amplitude of the bifurcated eigenmode varies over time and transits from one attractor to the other. This information is lost (integrated) upon performing the ensemble average.

The value of the cut-off frequency guarantees the noise to have a unitary variance. By "variance" of a signal, we mean its mean square, and not its mean square deviation (the mean value is not subtracted). We also insist that, in the rest of this chapter, the term "variance" does not involve an ensemble average, as was the case in chapters 3 and 4. Instead, is meant here that

$$\overline{\xi(t)^2} = \frac{1}{2\pi} \int_{-\infty}^{\infty} |\hat{\xi}(\omega)|^2 d\omega = \frac{1}{2\pi} \int_{-\pi}^{\pi} 1 d\omega = 1. \quad (6.7)$$

It is again possible to optimize the stochastic gain of the system at neutrality given in (6.3),

over the forcing structure \mathbf{f}_s . It amounts to solving

$$G = \max_{\mathbf{f}_s} \frac{\overline{\|\mathbf{u}(t)\|^2}}{\overline{\|\xi(t)\mathbf{f}_s\|^2}} = \max_{\mathbf{f}_s} \frac{[\langle \hat{\mathbf{u}}(\omega) | \hat{\mathbf{u}}(\omega) \rangle]}{\xi(\omega)^2 \|\mathbf{f}_s\|^2} = \max_{\mathbf{f}_s} \frac{\langle \mathbf{f}_s | B^\infty \mathbf{f}_s \rangle}{\|\mathbf{f}_s\|^2}. \quad (6.8)$$

where we recall the operation $[\bullet]$ to denote

$$[\bullet] = \frac{1}{2\pi} \int_{-\infty}^{\infty} \bullet \, d\omega, \quad (6.9)$$

and where, in the context,

$$B^\infty = \frac{1}{2\pi} \int_{-\omega_c=-\pi}^{\omega_c=\pi} |\hat{\xi}(\omega)|^2 R(\omega)^\dagger R(\omega) \, d\omega = \frac{1}{2\pi} \int_{-\pi}^{\pi} R(\omega)^\dagger R(\omega) \, d\omega, \quad (6.10)$$

with

$$R(\omega) = (i\omega I - L_n)^{-1}. \quad (6.11)$$

In the definition (6.8) of the stochastic gain, the selected inner product also does not involve an ensemble average. The associated optimal forcing structure, denoted \mathbf{f}_o with $\|\mathbf{f}_o\| = 1$, is the leading eigenmode of B^∞ . The optimal forcing structure \mathbf{f}_o can be shown to be along the adjoint eigenmode \mathbf{q}^\dagger (i.e. $\mathbf{f}_o \propto \mathbf{q}^\dagger$). Indeed, let us say that \mathbf{q} and \mathbf{q}^\dagger are associated with the real eigenvalue δ with $\delta \rightarrow 0$. Then, using the dyadic representation of the resolvent operator, its application on some field \mathbf{f}_s reads

$$R(\omega)\mathbf{f}_s = \sum_j \mathbf{q}_j \frac{\langle \mathbf{q}_j^\dagger | \mathbf{f}_s \rangle}{(i\omega - \sigma_j) \langle \mathbf{q}_j^\dagger | \mathbf{q}_j \rangle} \quad (6.12)$$

implying in turn,

$$R(\omega)^\dagger R(\omega)\mathbf{f}_s = \sum_k \sum_j \mathbf{q}_k^\dagger \frac{\langle \mathbf{q}_k | \mathbf{q}_j \rangle \langle \mathbf{q}_j^\dagger | \mathbf{f}_s \rangle}{(i\omega - \sigma_j)(-i\omega - \sigma_k^*) \langle \mathbf{q}_j^\dagger | \mathbf{q}_j \rangle \langle \mathbf{q}_k | \mathbf{q}_k \rangle}. \quad (6.13)$$

Thereby, the application of B^∞ on \mathbf{f}_s is dominated in the limit $\delta \rightarrow 0$ by

$$B^\infty \mathbf{f}_s = \frac{1}{\pi} \int_0^\pi R(\omega)^\dagger R(\omega)\mathbf{f}_s \, d\omega \xrightarrow{\delta \rightarrow 0} \mathbf{q}^\dagger \frac{\langle \mathbf{q}^\dagger | \mathbf{f}_s \rangle}{\langle \mathbf{q}^\dagger | \mathbf{q} \rangle^2} \frac{1}{\pi\delta} \arctan\left(\frac{\pi}{\delta}\right) \quad (6.14)$$

From (6.14), it is clear that the structure that maximizes the gain (6.8) is along \mathbf{q}^\dagger , and that is associated with an diverging gain $\lim_{\delta \rightarrow 0} G = \infty$. This is simply due to the resonant nature of the system in $\omega = 0$, making the integral over the frequencies diverge.

Let us now come back to the case where $\delta = 0$. By using once again the dyadic representation

of the resolvent operator, the linear response to $\mathbf{f}_o \xi(t)$ reads in the Fourier domain,

$$\hat{\mathbf{u}}(\omega) = R(\omega) \mathbf{f}_o \hat{\xi}(\omega) = \mathbf{q} \frac{\hat{\xi}(\omega) \langle \mathbf{q}^\dagger | \mathbf{f}_o \rangle}{i\omega \langle \mathbf{q}^\dagger | \mathbf{q} \rangle} + \sum_{j \geq 2} \mathbf{q}_j \frac{\hat{\xi}(\omega) \langle \mathbf{q}_j^\dagger | \mathbf{f}_o \rangle}{(i\omega - \sigma_j) \langle \mathbf{q}_j^\dagger | \mathbf{q}_j \rangle} = \hat{\mathbf{u}}_L(\omega) + \hat{\mathbf{u}}^\perp(\omega). \quad (6.15)$$

where $\sigma_1 = 0$ and all σ_j , $j \geq 2$ have a strictly negative real part (i.e. are linearly stable). In (6.15) we have defined

$$\hat{\mathbf{u}}_L(\omega) = \mathbf{q} \frac{\hat{\xi}(\omega) \langle \mathbf{q}^\dagger | \mathbf{f}_o \rangle}{i\omega \langle \mathbf{q}^\dagger | \mathbf{q} \rangle} \quad (6.16)$$

as the Lorentzian part of the response, triggered by the fact that $\langle \mathbf{q}^\dagger | \mathbf{f}_o \rangle \neq 0$ (i.e. the Fredholm alternative is not satisfied) and being solely along the neutral, resonant mode \mathbf{q} . The Lorentzian is associated with an infinite gain, for the integral of $(i\omega)^{-1}$ over the frequencies does not converge (remember that $|\hat{\xi}(\omega)| = 1$ for $|\omega| < \omega_c$).

We have also defined

$$\hat{\mathbf{u}}^\perp(\omega) = \sum_{j \geq 2} \mathbf{q}_j \frac{\hat{\xi}(\omega) \langle \mathbf{q}_j^\dagger | \mathbf{f}_o \rangle}{(i\omega - \sigma_j) \langle \mathbf{q}_j^\dagger | \mathbf{q}_j \rangle}, \quad (6.17)$$

the superscript " \perp " highlighting $\langle \mathbf{q}^\dagger | \hat{\mathbf{u}}^\perp(\omega) \rangle = 0$ for all ω , as the part of the response that is induced by the non-normality of the operator L_n , in the sense that this part would be identically null if L_n was normal. Indeed, \mathbf{f}_o is along \mathbf{q}^\dagger by construction, and $\langle \mathbf{q}_j^\dagger | \mathbf{q}^\dagger \rangle$ for $j \geq 2$ is zero if and only if L_n is normal since the adjoint modes constitute then an orthogonal family. But it is not the case if L_n is non-normal, as considered here, and forcing the system solely along the adjoint of one of the eigenmodes also excites all the others, which contribute to the linear response.

In the previous chapter, $\hat{\mathbf{u}}^\perp(\omega)$, which describes the non-normality-induced departure of the linear response from a Lorentzian, was undesired, for the amplitude equation we have derived could only describe a Lorentzian along the neutral mode \mathbf{q} . Thereby, the noise $\hat{\xi}(\omega)$ was filtered accordingly and $\hat{\mathbf{u}}^\perp(\omega)$ became negligible. The latter approach was arguably artificial, and the present chapter aims at more generality. In particular, both the Lorentzian response and the non-normal one will be considered. The former will be associated with a modal amplitude equation as in chapter 5, and the latter with a non-modal amplitude equation for the variance as in chapter 3. Both equations will be nonlinearly coupled.

For this purpose, the first step is to decompose the forcing structure \mathbf{f}_o into the sum of two terms: the first, $\propto \mathbf{q}$, generates solely the Lorentzian response $\hat{\mathbf{u}}_L(\omega)$, the second, denoted \mathbf{f}_o^\perp ,

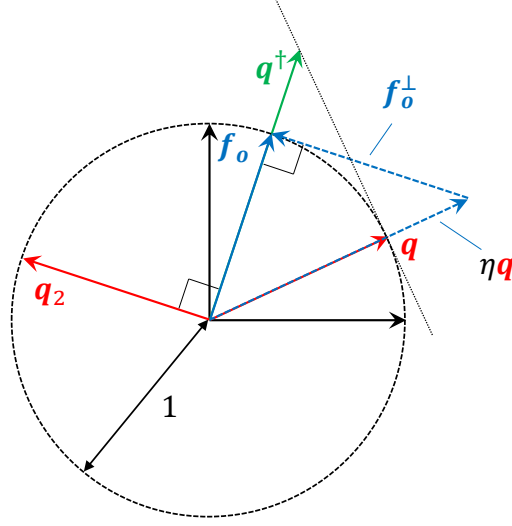


Figure 6.1: Schematic representation in the Euclidian space of the decomposition of the forcing structure $\mathbf{f}_o = \eta\mathbf{q} + \mathbf{f}_o^\perp$ according to (6.18). Note that, by construction $\langle \mathbf{q}^\dagger | \mathbf{f}_o^\perp \rangle = 0$, $\mathbf{f}_o \propto \mathbf{q}^\dagger$, $\|\mathbf{f}_o\| = 1$ and $\langle \mathbf{q}^\dagger | \mathbf{q} \rangle = 1$.

solely the non-normal response $\hat{\mathbf{u}}^\perp(\omega)$. It is easily shown that this decomposition writes

$$\mathbf{f}_o = \underbrace{\mathbf{q} \frac{\langle \mathbf{q}^\dagger | \mathbf{f}_o \rangle}{\langle \mathbf{q}^\dagger | \mathbf{q} \rangle}}_{\doteq \eta} + \underbrace{\left(\mathbf{f}_o - \mathbf{q} \frac{\langle \mathbf{q}^\dagger | \mathbf{f}_o \rangle}{\langle \mathbf{q}^\dagger | \mathbf{q} \rangle} \right)}_{\mathbf{f}_o^\perp} = \eta\mathbf{q} + \mathbf{f}_o^\perp, \quad (6.18)$$

where the superscript " \perp " again highlights the fact that $\langle \mathbf{q}^\dagger | \mathbf{f}_o^\perp \rangle = 0$. We check that

$$\begin{aligned} R(\omega)\eta\mathbf{q} &= \eta\mathbf{q} \frac{\hat{\xi}(\omega) \langle \mathbf{q}^\dagger | \mathbf{q} \rangle}{i\omega \langle \mathbf{q}^\dagger | \mathbf{q} \rangle} + \eta \sum_{j \geq 2} \mathbf{q}_j \frac{\hat{\xi}(\omega) \overbrace{\langle \mathbf{q}_j^\dagger | \mathbf{q} \rangle}^{=0}}{(i\omega - \sigma_j) \langle \mathbf{q}_j^\dagger | \mathbf{q}_j \rangle} \\ &= \eta\mathbf{q} \frac{\hat{\xi}(\omega)}{i\omega} = \mathbf{q} \frac{\langle \mathbf{q}^\dagger | \mathbf{f}_o \rangle}{\langle \mathbf{q}^\dagger | \mathbf{q} \rangle} \frac{\hat{\xi}(\omega)}{i\omega} = \hat{\mathbf{u}}_L(\omega), \end{aligned} \quad (6.19)$$

owing to the bi-orthogonality of the direct and adjoint eigenmode families. In addition,

$$R(\omega)\mathbf{f}_o^\perp = \sum_{j \geq 2} \mathbf{q}_j \frac{\hat{\xi}(\omega) \overbrace{\langle \mathbf{q}_j^\dagger | \mathbf{f}_o^\perp \rangle}^{= \langle \mathbf{q}_j^\dagger | \mathbf{f}_o \rangle}}{(i\omega - \sigma_j) \langle \mathbf{q}_j^\dagger | \mathbf{q}_j \rangle} = \hat{\mathbf{u}}^\perp(\omega), \quad (6.20)$$

where $\langle \mathbf{q}_j^\dagger | \mathbf{f}_o^\perp \rangle = \langle \mathbf{q}_j^\dagger | \mathbf{f}_o \rangle$ for $j \geq 2$ is a consequence of the fact that \mathbf{f}_o^\perp is orthogonal to \mathbf{q}^\dagger .

The decomposition (6.18) of the forcing \mathbf{f}_o is sketched in dimension two in figure 6.1.

The "non-normal response" $\hat{\mathbf{u}}^\perp(\omega) = \hat{\xi}(\omega)R(\omega)\mathbf{f}_o^\perp$, although non-normality is also involved in the Lorentzian response through the denominator $\langle \mathbf{q}^\dagger | \mathbf{q} \rangle$, is associated with a finite gain which can be very large. It is computed as the ratio between the variance of the non-normal response $\mathbf{u}^\perp(t)$ (the inverse Fourier transform of $\hat{\mathbf{u}}^\perp(\omega)$), and the part of the forcing triggering it, i.e. $\xi(t)\mathbf{f}_o^\perp$

$$\frac{\overline{\|\mathbf{u}^\perp(t)\|^2}}{\overline{\|\xi(t)\mathbf{f}_o^\perp\|^2}} = \frac{\overline{\|\hat{\xi}(\omega)R(\omega)\mathbf{f}_o^\perp\|^2}}{\overline{\|\mathbf{f}_o^\perp\|^2}} = \frac{\langle \mathbf{f}_o^\perp | B^\infty \mathbf{f}_o^\perp \rangle}{\overline{\|\mathbf{f}_o^\perp\|^2}} = \frac{1}{\epsilon_o^2}, \quad (6.21)$$

where ϵ_o has been introduced. In the following, we assume the non-normal gain in (6.21) to be very large, such that $\epsilon_o \ll 1$ can be scaled in terms of the small parameter ϵ according to

$$\epsilon_o = \theta \epsilon^2, \quad \text{with } \theta = O(1). \quad (6.22)$$

In agreement with the line of thought proposed in chapter 2 and chapter 3, a large response-over-forcing amplification under the inner product

$$\overline{\langle \mathbf{x}(t) | \mathbf{y}(t) \rangle} = [\langle \hat{\mathbf{x}}(\omega) | \hat{\mathbf{y}}(\omega) \rangle], \quad (6.23)$$

used in (6.21) and inducing the variance norm, implies that a small perturbation ("small" referring to the same norm) suffices to make the inverse resolvent singular. Indeed, let us define the normalized non-normal response $\mathbf{l}^\perp(t)$ as

$$\mathbf{l}^\perp(t) = \frac{\epsilon_o}{\overline{\|\mathbf{f}_o^\perp\|}} \mathbf{u}^\perp(t). \quad (6.24)$$

In this way,

$$(\partial_t - L_n)\mathbf{u}^\perp(t) = \xi(t)\mathbf{f}_o^\perp \Rightarrow (\partial_t - L_n)\mathbf{l}^\perp(t) = \frac{\epsilon_o}{\overline{\|\mathbf{f}_o^\perp\|}} \xi(t)\mathbf{f}_o^\perp, \quad (6.25)$$

implying $\mathbf{l}^\perp(t)$ to have a unit variance since

$$\overline{\langle \mathbf{l}^\perp(t) | \mathbf{l}^\perp(t) \rangle} = \frac{\epsilon_o^2}{\overline{\|\mathbf{f}_o^\perp\|^2}} \overline{\langle \mathbf{u}^\perp(t) | \mathbf{u}^\perp(t) \rangle} = 1 \quad (6.26)$$

according to the definition (6.21) of ϵ_o .

Crucially, (6.25) indicates that the spatiotemporal operator $(\partial_t - L_n)$ is close to possessing a second non-trivial element in its kernel (the first being \mathbf{q}), in the sense that it maps the response $\mathbf{l}^\perp(t)$, of unitary spatiotemporal (variance) norm, onto the field $\epsilon_o \xi(t)\mathbf{f}_o^\perp / \overline{\|\mathbf{f}_o^\perp\|}^{-1}$, of spatiotemporal norm $\epsilon_o \ll 1$, very small by assumption. Therefore, we can perturb $(\partial_t - L_n)$ according to

$$\Gamma(t)(\bullet) = (\partial_t - L_n)\bullet - \epsilon_o P(t)(\bullet), \quad \text{with } P(t) = \frac{\xi(t)\mathbf{f}_o^\perp}{\overline{\|\mathbf{f}_o^\perp\|}} \overline{\langle \mathbf{l}^\perp(t) | \bullet \rangle}, \quad (6.27)$$

where the induced norm of the perturbation operator is unitary, i.e.

$$\overline{\|P(t)\|^2} = \max_{\mathbf{y}} \frac{\overline{\|P(t)(\mathbf{y}(t))\|^2}}{\overline{\|\mathbf{y}(t)\|^2}} = 1, \quad (6.28)$$

achieved for $\mathbf{y}(t) = \mathbf{l}^\perp(t)$. The operator Γ indeed possesses the non-normal response as a non-trivial element in its kernel since

$$\begin{aligned} \Gamma(t)(\mathbf{l}^\perp(t)) &= (\partial_t - L_n)\mathbf{l}^\perp(t) - P(t)(\mathbf{l}^\perp(t)) \\ &= \frac{\epsilon_o}{\|\mathbf{f}_o^\perp\|} (\partial_t - L_n)\mathbf{u}^\perp(t) - \frac{\epsilon_o}{\|\mathbf{f}_o^\perp\|} \xi(t)\mathbf{f}_o^\perp \\ &= \mathbf{0} \end{aligned} \quad (6.29)$$

by definition. Furthermore, the eigenmode \mathbf{q} , in the kernel of $(\partial_t - L_n)$, also is in the kernel of Γ since

$$\begin{aligned} \Gamma(t)(\mathbf{q}) &= \underbrace{\partial_t \mathbf{q}}_{=\mathbf{0}} - \underbrace{L_n \mathbf{q}}_{=\mathbf{0}} - \epsilon_o \frac{\xi(t)\mathbf{f}_o^\perp}{\|\mathbf{f}_o^\perp\|} \overline{\langle \mathbf{l}^\perp(t) | \mathbf{q} \rangle} \\ &= -\epsilon_o \frac{\xi(t)\mathbf{f}_o^\perp}{\|\mathbf{f}_o^\perp\|} \left\langle \underbrace{\mathbf{l}^\perp(t)}_{=\mathbf{0}} \middle| \mathbf{q} \right\rangle, \\ &= \mathbf{0} \end{aligned} \quad (6.30)$$

where we have used that the non-normal response ξ yields a null temporal average, i.e.

$$\overline{\mathbf{l}^\perp(t)} = \mathbf{0} \quad (6.31)$$

since it is the linear response of a noise chosen to also have a zero average in (6.6). Thereby, we insist that the non-trivial kernel of the operator $\Gamma(t)(\bullet)$ contains two elements: $\mathbf{l}^\perp(t)$ and \mathbf{q} .

The operator perturbation was performed in the temporal domain in (6.27), but, in the statistically steady regime, it is strictly equivalent to perturbing the inverse resolvent (in the Fourier domain) as

$$\Phi(\omega)(\bullet) = R(\omega)^{-1} \bullet - \epsilon_o P(\omega)(\bullet), \quad \text{with} \quad P(\omega) = \frac{\hat{\xi}(\omega)\mathbf{f}_o^\perp}{\|\mathbf{f}_o^\perp\|} \left[\left\langle \hat{\mathbf{l}}^\perp(\omega) \middle| \bullet \right\rangle \right], \quad (6.32)$$

whose non-trivial kernel is composed of $\hat{\mathbf{l}}^\perp(\omega)$ as well as

$$\mathcal{F}(\mathbf{q}) = \frac{1}{\sqrt{T}} \int_0^T \mathbf{q} e^{-i\omega t} dt = \frac{2\pi\delta(\omega)}{\sqrt{T}} \mathbf{q}. \quad (6.33)$$

Nevertheless, computations shall be made in the temporal domain in this chapter to avoid carrying the term $2\pi\delta(\omega)/\sqrt{T}$ all along the calculations, and thus lighten the formalism.

The adjoint operator of I under the inner product (6.23), writes

$$I^\dagger(t) = (\partial_t - L_n)^\dagger - \epsilon_o \underbrace{\frac{\mathbf{l}^\perp(t)}{\|\mathbf{f}_o^\perp\|} \overline{\langle \xi(t) \mathbf{f}_o^\perp | \bullet \rangle}}_{\doteq P^\dagger(\bullet)} = -\partial_t - L_n^\dagger - \epsilon_o \frac{\mathbf{l}^\perp(t)}{\|\mathbf{f}_o^\perp\|} \overline{\langle \xi(t) \mathbf{f}_o^\perp | \bullet \rangle}, \quad (6.34)$$

where $(\partial_t - L_n)^\dagger$ denotes the adjoint operator of $(\partial_t - L_n)$ under the spatiotemporal inner product (6.23), i.e.

$$\overline{\langle (\partial_t - L_n) \mathbf{g} | \mathbf{h} \rangle} = \overline{\langle \mathbf{g} | (\partial_t - L_n)^\dagger \mathbf{h} \rangle}, \quad \forall \mathbf{g} \in \mathcal{D}((\partial_t - L_n)), \mathbf{h} \in \mathcal{D}((\partial_t - L_n)^\dagger) \quad (6.35)$$

Its non-trivial kernel is constituted of \mathbf{q}^\dagger , together with

$$\mathbf{a}(t) = \chi ((\partial_t - L_n)^{-1})^\dagger \mathbf{l}^\perp(t), \quad (6.36)$$

with χ a normalization constant, or equivalently,

$$\mathbf{a}(t) = \mathcal{F}^{-1}(\hat{\mathbf{a}}(\omega)), \quad \text{with} \quad \hat{\mathbf{a}}(\omega) = \chi R(\omega)^\dagger \hat{\mathbf{l}}^\perp(\omega). \quad (6.37)$$

Indeed, it is easily checked that

$$\begin{aligned} I^\dagger(t)(\mathbf{a}(t)) &= \chi (\partial_t - L_n)^\dagger ((\partial_t - L_n)^{-1})^\dagger \mathbf{l}^\perp(t) - \chi \epsilon_o \frac{\mathbf{l}^\perp(t)}{\|\mathbf{f}_o^\perp\|} \overline{\langle \xi(t) \mathbf{f}_o^\perp | ((\partial_t - L_n)^{-1})^\dagger \mathbf{l}^\perp(t) \rangle} \\ &= \chi \underbrace{(\partial_t - L_n)^\dagger ((\partial_t - L_n)^\dagger)^{-1}}_{=I} \mathbf{l}^\perp(t) - \chi \epsilon_o \frac{\mathbf{l}^\perp(t)}{\|\mathbf{f}_o^\perp\|} \overline{\langle \underbrace{(\partial_t - L_n)^{-1} \xi(t) \mathbf{f}_o^\perp}_{\mathbf{u}^\perp(t)} | \mathbf{l}^\perp(t) \rangle} \\ &= \chi \mathbf{l}^\perp(t) - \chi \mathbf{l}^\perp(t) \overline{\langle \mathbf{l}^\perp(t) | \mathbf{l}^\perp(t) \rangle} \\ &= \mathbf{0}, \end{aligned} \quad (6.38)$$

where we have used that the adjoint of the inverse is the inverse of the adjoint. The scalar χ is chosen such that

$$\overline{\langle \mathbf{a}(t) | \mathbf{l}^\perp(t) \rangle} = 1 \Leftrightarrow \chi = \left(\overline{\langle \mathbf{l}^\perp(t) | (\partial_t - L_n)^{-1} \mathbf{l}^\perp(t) \rangle} \right)^{-1} \quad (6.39)$$

The kernel of I^\dagger also contains the adjoint eigenmode \mathbf{q}^\dagger

$$I^\dagger(t)(\mathbf{q}^\dagger) = \underbrace{-\partial_t \mathbf{q}^\dagger}_{=0} - \underbrace{L_n^\dagger \mathbf{q}^\dagger}_{=0} - \epsilon_o \frac{\mathbf{l}^\perp(t)}{\|\mathbf{f}_o^\perp\|} \overline{\langle \xi(t) \mathbf{f}_o^\perp | \mathbf{q}^\dagger \rangle} = -\epsilon_o \frac{\mathbf{l}^\perp(t)}{\|\mathbf{f}_o^\perp\|} \overline{\langle \underbrace{\xi(t) \mathbf{f}_o^\perp}_{=0} | \mathbf{q}^\dagger \rangle} = \mathbf{0}. \quad (6.40)$$

In the next section, a weakly nonlinear expansion is proposed for the system, which we recall

to be past the onset of a pitchfork bifurcation for $0 < \epsilon \ll 1$ and subject to stochastic forcing. The expansion will result in a system of two non-linearly coupled equations: one for the bifurcated, symmetry-breaking eigenmode \mathbf{q} , the other for the variance of $\mathbf{l}^\perp(t)$, the part of the stochastic response constituted of all the other eigenmodes (i.e. the non-normality induced part of the response). For this purpose, we are equipped with the forcing decomposition in (6.18), followed by the operator perturbation in (6.27) to fill the kernel with the non-normality induced part of the response.

6.3 Weakly nonlinear expansion

The nonlinear system (6.1) is weakly stochastically forced by

$$\mathbf{F}(\mathbf{x}, t) = F\xi(t)\mathbf{f}_o(\mathbf{x}), \quad \text{with } F \ll 1, \quad \text{scaled as } F = \phi\epsilon^3. \quad (6.41)$$

We recall $\epsilon^2 \ll 1$ to also be a small parameter measuring the distance to the critical point in the parameter space, where the system succumbs to a supercritical pitchfork bifurcation.

The process $\xi(t)$ was characterized in the previous section, and we repeat that the structure $\mathbf{f}_o \propto \mathbf{q}^\dagger$ is normalized as $\|\mathbf{f}_o\| = 1$. The prefactor $\phi = O(1)$ directly sets the variance F^2 of the stochastic forcing.

The weak forcing variance suggests the solution to (6.1) to be sought in terms of a multiple-scale asymptotic expansion in terms of the power of ϵ as

$$\mathbf{U} = \mathbf{U}_e + \epsilon\mathbf{u}_1(t, \tau_1, \tau_2) + \epsilon^2\mathbf{u}_2(t, \tau_1, \tau_2) + \epsilon^3\mathbf{u}_3(t, \tau_1, \tau_2) + O(\epsilon^4), \quad (6.42)$$

with the independent variables τ_1 and τ_2 evaluated as $\tau_1 = \epsilon t$ and $\tau_2 = \epsilon^2 t$, thus corresponding to slow times. Injecting (6.42) in (6.1) leads to the expansion

$$\begin{aligned} & \epsilon(\partial_t \mathbf{u}_1 - L_n \mathbf{u}_1) + \\ & \epsilon^2(\partial_t \mathbf{u}_2 - L_n \mathbf{u}_2 + \partial_{\tau_1} \mathbf{u}_1 - \delta L \mathbf{U}_e + C(\mathbf{u}_1, \mathbf{u}_1)) + \\ & \epsilon^3(\partial_t \mathbf{u}_3 - L_n \mathbf{u}_3 + \partial_{\tau_1} \mathbf{u}_2 + \partial_{\tau_2} \mathbf{u}_1 - \delta L \mathbf{u}_1 + 2C(\mathbf{u}_1, \mathbf{u}_2) - \phi \mathbf{f}_o \xi) + O(\epsilon^4) = \mathbf{0}, \end{aligned} \quad (6.43)$$

The operator $(\partial_t - L_n)$ is then perturbed according to (6.27), and the small parameter ϵ_o linked to the expansion parameter as in (6.22) (i.e. $\epsilon_o = \theta\epsilon^2$ with $\theta = O(1)$), eventually leading to the expansion

$$\begin{aligned} & \epsilon(\Gamma(\mathbf{u}_1)) + \\ & \epsilon^2(\Gamma(\mathbf{u}_2) + \partial_{\tau_1} \mathbf{u}_1 - \delta L \mathbf{U}_e + C(\mathbf{u}_1, \mathbf{u}_1)) + \\ & \epsilon^3(\Gamma(\mathbf{u}_3) + \partial_{\tau_1} \mathbf{u}_2 + \partial_{\tau_2} \mathbf{u}_1 - \delta L \mathbf{u}_1 + 2C(\mathbf{u}_1, \mathbf{u}_2) - \phi \mathbf{f}_o \xi + \theta P(\mathbf{u}_1)) + O(\epsilon^4) = \mathbf{0}. \end{aligned} \quad (6.44)$$

The equation to be satisfied at $O(\epsilon)$ reads

$$\Gamma(\mathbf{u}_1) = \mathbf{0}, \quad (6.45)$$

whose general solution is

$$\mathbf{u}_1(t, \tau_1, \tau_2) = A(\tau_1, \tau_2)\mathbf{q} + B(\tau_1, \tau_2)\mathbf{l}^\perp(t), \quad (6.46)$$

where A and B are undetermined scalars that depend solely on the variables τ_1 and τ_2 , independent of t , such that A and B can be taken out of the temporal average operation and

$$\Gamma(A\mathbf{q} + B\mathbf{l}^\perp) = \underbrace{A\Gamma(\mathbf{q})}_{=\mathbf{0}} + \underbrace{B\Gamma(\mathbf{l}^\perp)}_{=\mathbf{0}} = \mathbf{0} \quad (6.47)$$

holds indeed. Contrarily to the developments in chapter 3, the amplitudes here are stochastic quantities. That is made possible by the fact that the operator perturbation purposely does not involve an ensemble average, only a temporal one. Thereby, even if stochastic, A and B can be taken out of the inner product, leading to (6.47).

At $O(\epsilon^2)$,

$$\begin{aligned} \Gamma(\mathbf{u}_2) &= -\mathbf{q} \frac{\partial A}{\partial \tau_1} - \mathbf{l}^\perp \frac{\partial B}{\partial \tau_1} - A^2 C(\mathbf{q}, \mathbf{q}) - 2ABC(\mathbf{q}, \mathbf{l}^\perp) - B^2 C(\mathbf{l}^\perp, \mathbf{l}^\perp) + \delta L \mathbf{U}_e \\ &= \mathbf{f}_2 \end{aligned} \quad (6.48)$$

must be satisfied. For this equation to yield a non-diverging particular solution, the right-hand side must be orthogonal to the kernel of Γ^\dagger under the inner product (6.23). Specifically,

$$\overline{\langle \mathbf{q}^\dagger | \mathbf{f}_2(t) \rangle} = \langle \mathbf{q}^\dagger | \overline{\mathbf{f}_2(t)} \rangle = 0, \quad (6.49)$$

as well as

$$\overline{\langle \mathbf{a}(t) | \mathbf{f}_2(t) \rangle} = 0, \quad (6.50)$$

must both be enforced. In Appendix 6.6.1, we show that (6.49) leads to

$$\frac{\partial A}{\partial \tau_1} = \alpha_1 B^2, \quad \text{with} \quad \alpha_1 = -\langle \mathbf{q}^\dagger | \overline{C(\mathbf{l}^\perp, \mathbf{l}^\perp)} \rangle, \quad (6.51)$$

then that (6.50) leads to

$$\frac{\partial B}{\partial \tau_1} = \beta_1 AB, \quad \text{with} \quad \beta_1 = -\overline{\langle \mathbf{a} | 2C(\mathbf{q}, \mathbf{l}^\perp) \rangle}. \quad (6.52)$$

Injecting (6.51) and (6.52) back in (6.48) yields

$$\begin{aligned}\Gamma(\mathbf{u}_2) &= -A^2 C(\mathbf{q}, \mathbf{q}) - AB(2C(\mathbf{q}, \mathbf{l}^\perp) + \mathbf{l}^\perp \beta_1) - B^2(C(\mathbf{l}^\perp, \mathbf{l}^\perp) + \alpha_1 \mathbf{q}) + \delta L \mathbf{U}_e \\ &= A^2 \mathbf{f}_2^{A^2} + AB \mathbf{f}_2^{AB} + B^2 \mathbf{f}_2^{B^2} + \mathbf{f}_2^\delta,\end{aligned}\quad (6.53)$$

whose particular solution reads

$$\mathbf{u}_2 = A^2 \mathbf{u}_2^{A^2} + AB \mathbf{u}_2^{AB} + B^2 \mathbf{u}_2^{B^2} + \mathbf{u}_2^\delta, \quad (6.54)$$

with

$$\begin{aligned}(\partial_t - L_n) \mathbf{u}_2^{A^2} &= \mathbf{f}_2^{A^2} = -C(\mathbf{q}, \mathbf{q}) \\ (\partial_t - L_n) \mathbf{u}_2^{AB} &= \mathbf{f}_2^{AB} = -2C(\mathbf{q}, \mathbf{l}^\perp) - \mathbf{l}^\perp \beta_1 \\ (\partial_t - L_n) \mathbf{u}_2^{B^2} &= \mathbf{f}_2^{B^2} = -C(\mathbf{l}^\perp, \mathbf{l}^\perp) - \alpha_1 \mathbf{q} \\ (\partial_t - L_n) \mathbf{u}_2^\delta &= \mathbf{f}_2^\delta = \delta L \mathbf{U}_e.\end{aligned}\quad (6.55)$$

Indeed,

$$0 = \overline{\langle \mathbf{a} | \mathbf{f}_2^{A^2} \rangle} = \overline{\langle \mathbf{l}^\perp(t) | (\partial_t - L_n)^{-1} \mathbf{f}_2^{A^2} \rangle} = \overline{\langle \mathbf{l}^\perp(t) | \mathbf{u}_2^{A^2} \rangle}, \quad (6.56)$$

implying

$$\Gamma(\mathbf{u}_2^{A^2}) = (\partial_t - L_n) \mathbf{u}_2^{A^2} = \mathbf{f}_2^{A^2} \quad (6.57)$$

indeed, and the same reasoning applies to all the other components of the particular solution. Crucially, note that both fields $\mathbf{u}_2^{A^2}$ and \mathbf{u}_2^δ tend toward a constant value, and that the field \mathbf{u}_2^{AB} yields a null temporal average (i.e. $\overline{\mathbf{u}_2^{AB}} = 0$) since it is the linear response of a forcing term with a null temporal average. The homogeneous solution is ignored in (6.54), presumably without loss of generality.

The equation to be solved at $O(\epsilon^3)$ is written

$$\begin{aligned}\Gamma(\mathbf{u}_3) &= -\mathbf{q} \frac{\partial A}{\partial \tau_2} - \mathbf{l}^\perp \frac{\partial B}{\partial \tau_2} + A \delta L \mathbf{q} + B \delta L \mathbf{l}^\perp - \partial_{\tau_1} \mathbf{u}_2 - 2C(\mathbf{u}_1, \mathbf{u}_2) + \phi \mathbf{f}_o \xi - \theta P(\mathbf{u}_1) \\ &= \mathbf{f}_3.\end{aligned}\quad (6.58)$$

We make explicit

$$\partial_{\tau_1} \mathbf{u}_2 = 2\alpha_1 AB^2 \mathbf{u}_2^{A^2} + (\alpha_1 B^3 + \beta_1 A^2 B) \mathbf{u}_2^{AB} + 2\beta_1 AB^2 \mathbf{u}_2^{B^2}, \quad (6.59)$$

followed by

$$\begin{aligned}C(\mathbf{u}_1, \mathbf{u}_2) &= AC(\mathbf{q}, \mathbf{u}_2^\delta) + BC(\mathbf{l}^\perp, \mathbf{u}_2^\delta) + A^3 C(\mathbf{q}, \mathbf{u}_2^{A^2}) + B^3 C(\mathbf{l}^\perp, \mathbf{u}_2^{B^2}) \\ &\quad + A^2 B (C(\mathbf{q}, \mathbf{u}_2^{AB}) + C(\mathbf{l}^\perp, \mathbf{u}_2^{A^2})) + AB^2 (C(\mathbf{q}, \mathbf{u}_2^{B^2}) + C(\mathbf{l}^\perp, \mathbf{u}_2^{AB})),\end{aligned}\quad (6.60)$$

as well as

$$\begin{aligned}
P(\mathbf{u}_1) &= \frac{\xi(t) \mathbf{f}_o^\perp}{\|\mathbf{f}_o^\perp\|} \overline{\langle \mathbf{l}^\perp(t) | A\mathbf{q} + B\mathbf{l}^\perp(t) \rangle} = A \frac{\xi(t) \mathbf{f}_o^\perp}{\|\mathbf{f}_o^\perp\|} \underbrace{\left\langle \mathbf{l}^\perp(t) \middle| \mathbf{q} \right\rangle}_{=0} + B \frac{\xi(t) \mathbf{f}_o^\perp}{\|\mathbf{f}_o^\perp\|} \underbrace{\langle \mathbf{l}^\perp(t) | \mathbf{l}^\perp(t) \rangle}_{=1} \\
&= B \frac{\xi(t) \mathbf{f}_o^\perp}{\|\mathbf{f}_o^\perp\|}.
\end{aligned} \tag{6.61}$$

Furthermore, in (6.58), the stochastic forcing term $\xi(t) \mathbf{f}_o$ requires a special treatment. First, we recall the latter to be decomposed as

$$\mathbf{f}_o \xi(t) = \eta \mathbf{q} \xi(t) + \mathbf{f}_o^\perp \zeta(t), \tag{6.62}$$

where, by construction, the first term at the right-hand side only excites the neutral, steady, eigenmode \mathbf{q} and thus generates a Lorentzian transfer function peaked around $\omega = 0$. The second term excites all the other eigenmodes by non-normality. Then, let us introduce the noise process $\zeta(t)$, defined from $\xi(t)$ in the Fourier domain as

$$\begin{aligned}
\mathcal{F}(\zeta(t))(s) &= \epsilon^2 \mathcal{F}(\xi(t))(\omega)|_{\omega=\epsilon^2 s}, \quad |s| \leq \frac{\omega_c}{\epsilon^2}, \quad \text{or, equivalently,} \\
\hat{\zeta}(s) &= \epsilon^2 \hat{\xi}(\epsilon^2 s), \quad |s| \leq \frac{\omega_c}{\epsilon^2}.
\end{aligned} \tag{6.63}$$

On the other hand, it was shown in (5.5) using the definition of the Fourier transform and performing a change of variable, that

$$\mathcal{F}(\zeta(\epsilon^2 t))(\omega) = \frac{1}{\epsilon^2} \mathcal{F}(\zeta(t))(s)|_{s=\omega/\epsilon^2}. \tag{6.64}$$

As a consequence, defining $\zeta(t)$ as in (6.63) guarantees that

$$\begin{aligned}
\mathcal{F}(\zeta(\epsilon^2 t))(\omega) &= \epsilon^2 \frac{1}{\epsilon^2} \mathcal{F}(\xi(t))(\omega)|_{\omega=\epsilon^2 s=\epsilon^2 \omega/\epsilon^2} = \mathcal{F}(\xi(t))(\omega) \Leftrightarrow \\
\zeta(\epsilon^2 t) &= \xi(t), \quad \forall t.
\end{aligned} \tag{6.65}$$

In words, we constructed a new stochastic process $\zeta(t)$ which varies much faster than $\xi(t)$, in such a manner that taking its slow variations $\zeta(\epsilon^2 t)$ directly is equal to $\xi(t)$. This construction is convenient, in that $\zeta(\epsilon^2 t) = \zeta(\tau_2)$ varies over the slow time scale τ_2 , thereby can be included as stochastic forcing term directly at the amplitude equation level.

This construction could have been made in the previous chapter but would have been useless since the noise ξ naturally depended on the slow time scale, due to the necessity to select a very small cut-off frequency to neutralize the non-normal response \mathbf{l}^\perp . Here, the cut-off frequency $\omega_c = \pi$ can't be scaled in terms of the small parameter, and $\xi(t)$ itself does not naturally depend on a slow time scale as $\zeta(\epsilon^2 t)$ does.

In (6.62), the relation $\xi(t) = \zeta(\epsilon^2 t) = \zeta(\tau_2)$ is used solely in the first term $\eta \mathbf{q} \xi(t)$ in the right-hand side, whereas $\xi(t)$ is kept as is when multiplying \mathbf{f}_o^\perp in the second term in the right-hand side,

i.e.

$$\mathbf{f}_o \xi(t) = \eta \mathbf{q} \zeta(\tau_2) + \mathbf{f}_o^\perp \xi(t). \quad (6.66)$$

This way, the first term will act as a source of stochastic excitation in the equation for A , therefore the Lorentzian part of the linear response will be carried by the amplitude A , which must be since the latter multiplies the constant mode \mathbf{q} . On the other hand, the amplitude B should not be stochastically forced in the linear regime, but, on the contrary, should be a deterministic constant. That is because B multiplies \mathbf{l}^\perp which already encompasses the full spectrum of the non-normal linear response.

Injecting (6.66) back in (6.58), we show in Appendix 6.6.2 that imposing

$$\overline{\langle \mathbf{q}^\dagger | \mathbf{f}_3(t) \rangle} = \langle \mathbf{q}^\dagger | \overline{\mathbf{f}_3(t)} \rangle = 0 \quad (6.67)$$

yields

$$\frac{\partial A}{\partial \tau_2} = \alpha_2 A + \alpha_3 A^3 + \alpha_4 A B^2 + \phi \eta \zeta, \quad (6.68)$$

with

$$\begin{aligned} \alpha_2 &= -\langle \mathbf{q}^\dagger | -\delta L \mathbf{q} + 2C(\mathbf{q}, \mathbf{u}_2^\delta) \rangle, \\ \alpha_3 &= -\langle \mathbf{q}^\dagger | 2C(\mathbf{q}, \mathbf{u}_2^{A^2}) \rangle, \quad \text{and eventually} \\ \alpha_4 &= -\langle \mathbf{q}^\dagger | 2\beta_1 \overline{\mathbf{u}_2^{B^2}} + 2C(\mathbf{q}, \overline{\mathbf{u}_2^{B^2}}) + \overline{2C(\mathbf{l}^\perp, \mathbf{u}_2^{AB})} \rangle. \end{aligned} \quad (6.69)$$

Then, is shown that imposing

$$\overline{\langle \mathbf{a}(t) | \mathbf{f}_3(t) \rangle} = 0 \quad (6.70)$$

leads to

$$\frac{\partial B}{\partial \tau_2} = \phi \|\mathbf{f}_o^\perp\| - \theta B + \beta_2 B + \beta_3 B^3 + \beta_4 A^2 B \quad (6.71)$$

with

$$\begin{aligned} \beta_2 &= -\overline{\langle \mathbf{a} | -\delta L \mathbf{l}^\perp + 2C(\mathbf{l}^\perp, \mathbf{u}_2^\delta) \rangle} \\ \beta_3 &= -\overline{\langle \mathbf{a} | \alpha_1 \mathbf{u}_2^{AB} + 2C(\mathbf{l}^\perp, \mathbf{u}_2^{B^2}) \rangle}, \quad \text{and eventually} \\ \beta_4 &= -\overline{\langle \mathbf{a} | \beta_1 \mathbf{u}_2^{AB} + 2C(\mathbf{q}, \mathbf{u}_2^{AB}) + 2C(\mathbf{l}^\perp, \mathbf{u}_2^{A^2}) \rangle}. \end{aligned} \quad (6.72)$$

The total derivatives of the re-scaled amplitudes $a = \epsilon A$ and $b = \epsilon B$ with respect to the time t is

written

$$\begin{aligned}\frac{da}{dt} &= \epsilon \left(\frac{\partial \tau_1}{\partial t} \frac{\partial A}{\partial \tau_1} + \frac{\partial \tau_2}{\partial t} \frac{\partial A}{\partial \tau_2} \right) \Big|_{(\tau_1, \tau_2) = (\epsilon t, \epsilon^2 t)} \\ &= \left(\epsilon^2 \frac{\partial A}{\partial \tau_1} + \epsilon^3 \frac{\partial A}{\partial \tau_2} \right) \Big|_{(\tau_1, \tau_2) = (\epsilon t, \epsilon^2 t)}\end{aligned}\quad (6.73)$$

and similarly for b , which eventually leads to the system of amplitude equations

$$\begin{aligned}\frac{da}{dt} &= \epsilon^2 \alpha_2 a + \alpha_1 b^2 + \alpha_3 a^3 + \alpha_4 a b^2 + F \eta \xi(t) \\ \frac{db}{dt} &= \epsilon^2 \beta_2 b + F \|\mathbf{f}_o^\perp\| - \epsilon_o b + \beta_1 a b + \beta_3 b^3 + \beta_4 a^2 b\end{aligned}\quad (6.74)$$

where the definitions $\zeta(\epsilon^2 t) = \xi(t)$, $F = \phi \epsilon^3$ and $\theta \epsilon^2 = \epsilon_o$ have been taken into account.

In the linear limit $F \rightarrow 0$ the system decouples, and if further evaluated at neutrality where $\epsilon = 0$, reduces to

$$\frac{da}{dt} = F \eta \xi(t) \Rightarrow \hat{a}(\omega) = F \eta \frac{\hat{\xi}(\omega)}{i\omega}, \quad \text{and} \quad b \rightarrow \bar{b} = \frac{F \|\mathbf{f}_o^\perp\|}{\epsilon_o} = c s t, \quad (6.75)$$

thereby the linear response to $F \xi(t) \mathbf{f}_o$ reads in the Fourier domain

$$\hat{a}(\omega) \mathbf{q} + \bar{b} \hat{\mathbf{l}}^\perp(\omega) = F \eta \frac{\hat{\xi}(\omega)}{i\omega} \mathbf{q} + F \frac{\|\mathbf{f}_o^\perp\|}{\epsilon_o} \hat{\mathbf{l}}^\perp(\omega) = F \left(\mathbf{q} \frac{\langle \mathbf{q} | \mathbf{f}_o \rangle}{\langle \mathbf{q}^\dagger | \mathbf{q} \rangle} \frac{\hat{\xi}(\omega)}{i\omega} + \hat{\mathbf{u}}^\perp(\omega) \right) \quad (6.76)$$

which is exactly as computed in (6.15) (multiplied by F by linearity since the forcing also is multiplied by F). Thereby, the system of amplitude equation is exact in the linear regime and recovers the response to be the sum of a Lorentzian rescaled by F (captured by $a(t)$) and a non-normal response whose entire spectrum is rescaled by F (captured by \bar{b}).

Note that the coefficients in (6.74) can be physically interpreted.

- The coefficients $\epsilon^2 \alpha_2$ and $\epsilon^2 \beta_2$ are the sensitivity of the neutral eigenvalue and linear non-normal gain, respectively, to the $+\epsilon^2 \delta L$ modification of the linear operator. Thereby, they multiply a term linear a and b , respectively.
- The coefficient α_1 takes into account the fact that the nonlinear interaction of the non-normal response with itself ($\propto b^2$) yields a non-zero temporal average value which may project on \mathbf{q} thus acts as a source of a . Note that this coefficient is identically null here since $\mathbf{f}_o \propto \mathbf{q}^\dagger$ has the same spatial symmetry as \mathbf{q}^\dagger , therefore $\overline{C(\mathbf{l}^\perp, \mathbf{l}^\perp)}$ has the opposite symmetry and their spatial inner product is null.
- The coefficient β_1 is the sensibility of the non-normal linear gain to a $+a\mathbf{q}$ modification of the base flow, thus it multiplies a term $\propto ba$. This coefficient also is identically null here since \mathbf{f}_o had the same spatial symmetry as \mathbf{q}^\dagger .

- The coefficients α_3 (resp. β_3) contain the retro-action of the nonlinear interaction of the neutral mode (resp. non-normal response) with itself, on itself.
- The coefficient α_4 contains the sensibility of the neutral eigenvalue to the fact that the mean flow has been distorted by the nonlinear interaction of the non-normal response with itself $\propto b^2$ (i.e., it contains the sensibility to a $+b^2 \overline{\mathbf{u}_2^{B^2}}$ modification of the base flow into a mean flow). Thereby, it multiplies a cubic coupling term in ab^2 . This coefficient also contains the fact that the second-order field, created by the nonlinear interaction of the non-normal response with the mode, has a nonlinear retroaction on the non-normal response which creates a non-zero temporal average, and projects on \mathbf{q}^\dagger to act as a source of a .
- The coefficient β_4 contains the sensibility of the non-normal response amplitude to the nonlinear distortion of the base flow resulting from the nonlinear interaction of the mode with itself. In other words, it contains the sensitivity of the non-normal response to a $+a^2 \mathbf{u}_2^{A^2}$ modification of the base flow, hence multiplying a cubic coupling term in ba^2 . It also contains the effect of the nonlinear interaction, with the mode, of the second-order field ensuing from the nonlinear interaction of the non-normal response with the mode.

The same system as (6.74) would be obtained in the configuration where \mathbf{f}_o was not purely along the adjoint mode (that is why we did not replace $\mathbf{f}_o = \mathbf{q}^\dagger$ and did not cancel α_1 and β_1 in the developments). In the latter case, b would be non-null even if L_n was a normal operator.

In the next section, we test the performances of the system (6.74) in a weakly nonlinear regime and for a toy model. Of particular importance, is the question of the improvement of the predicted statistics of a by the coupling with the nonlinear response b , as compared to a configuration where the non-normal response is ignored and a considered independently (as a traditional weakly nonlinear approach would consider).

6.4 Application to a toy model

The method outlined in the previous section is applied to the specific stochastically forced nonlinear system writing

$$\frac{d\mathbf{U}}{dt} = \underbrace{(L_n + \epsilon^2 \delta L)}_{=L} \mathbf{U} + \|\mathbf{U}\|^2 B \mathbf{U} + \epsilon^3 \phi \xi \mathbf{f}_o, \quad (6.77)$$

with

$$L_n = \begin{bmatrix} 0 & c & c \\ 0 & -2\eta_s \omega_s & -\omega_s^2 \\ 0 & 1 & 0 \end{bmatrix}, \quad \delta L = \begin{bmatrix} 1 & 1 & 1 \\ 0 & 1 & 1 \\ 0 & 1 & 1 \end{bmatrix}, \quad \text{and} \quad B = -10^{-1} \delta L. \quad (6.78)$$

The symbols $c > 0$, $\omega_s > 0$ and $1 \gg \eta_s > 0$ denote free parameters, and the matrix L_n possesses the eigenvalues

$$\sigma_1 = 0, \quad \sigma_2 = -\eta_s \omega_s + i\omega_s \sqrt{1 - \eta_s^2}, \quad \text{and} \quad \sigma_3 = -\eta_s \omega_s - i\omega_s \sqrt{1 - \eta_s^2}. \quad (6.79)$$

Thereby, L_n is linearly neutral and singular, σ_1 being null and σ_2 and σ_3 being damped. These latter eigenvalues have an eigenfrequency close to ω_s and a damping rate equal to $\eta_s \omega_s$. The parameter c is a coupling constant that controls the degree of non-normality of the system but doesn't affect the eigenvalues. The steady, neutral eigenmode \mathbf{q} associated with σ_1 reads

$$\mathbf{q} = \begin{bmatrix} 1 \\ 0 \\ 0 \end{bmatrix}, \quad \text{and its adjoint} \quad \mathbf{q}^\dagger = \begin{bmatrix} 1 \\ \frac{c}{\omega_s} \\ \frac{c(2\eta_s - \omega_s)}{\omega_s} \end{bmatrix} \quad (6.80)$$

normalized as $\|\mathbf{q}\|^2 = \langle \mathbf{q} | \mathbf{q} \rangle = 1$ and $\langle \mathbf{q}^\dagger | \mathbf{q} \rangle = 1$, respectively. In the context, $\langle \bullet | \bullet \rangle$ denotes simply $\langle \mathbf{a} | \mathbf{b} \rangle = \mathbf{a}^H \mathbf{b}$.

The unforced system (6.77) is subject to a supercritical pitchfork bifurcation at $\epsilon = 0$, where the unique equilibrium solution is $\mathbf{U}_{e,c} = \mathbf{0}$ yields a linearized operator L_n which is linearly neutral along the eigenmode (6.80). For $\epsilon > 0$, the equilibrium $\mathbf{U}_e = \mathbf{0}$ still exists but is unstable and the system possesses two additional stable equilibria

$$\mathbf{U}_e = \begin{bmatrix} \pm \epsilon \sqrt{10} \\ 0 \\ 0 \end{bmatrix}. \quad (6.81)$$

In the rest of this section, we set rather arbitrarily

$$\omega_s = 0.2, \quad \eta_s = 0.01, \quad \text{and} \quad c = 10. \quad (6.82)$$

In figure 6.2, we show in the Fourier domain the norm squared of the linear response to $\mathbf{f}_o \xi(t)$ of the system (6.77) for $\epsilon = 0$, reading

$$\|\hat{\mathbf{u}}(\omega)\| = \|R(\omega) \mathbf{f}_o \hat{\xi}(\omega)\| = \|R(\omega) \mathbf{f}_o\|, \quad |\omega| \leq \omega_c = \pi \quad (6.83)$$

where we used that $|\hat{\xi}(\omega)| = 1$ for $|\omega| \leq \omega_c$. We recall that $R(\omega) = (i\omega I - L_n)^{-1}$, and that $\mathbf{f}_o \propto \mathbf{q}^\dagger$ with $\|\mathbf{f}_o\| = 1$. The decomposition (6.15) of the linear response into the sum of a Lorentzian $\hat{\mathbf{u}}_L(\omega)$ around $\omega = 0$ and a rest $\hat{\mathbf{u}}^\perp(\omega)$ generated by non-normality, is also illustrated by adding $\|\hat{\mathbf{u}}_L(\omega)\|^2$ and $\|\hat{\mathbf{u}}^\perp(\omega)\|^2$ to the figure. Even though the forcing structure \mathbf{f}_o is purely along the adjoint of the neutral mode at $\omega = 0$, non-normality of the matrix L_n in (6.78) implies that $\mathbf{f}_o \xi(t)$ also excites the two other eigenmodes of L_n . Consequently, we observe in figure 6.2 that the system also responds substantially around $\omega_s = 0.2$ and $\hat{\mathbf{u}}^\perp(\omega)$ is dominant there, whereas negligible around $\omega = 0$ since the Lorentzian is diverging in the latter region.

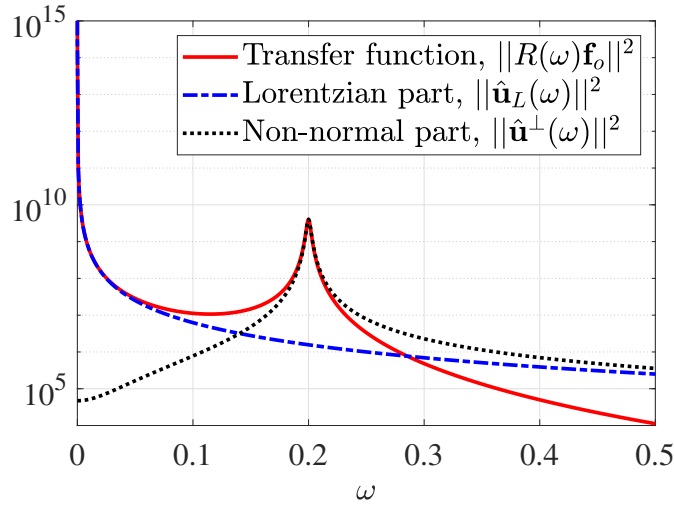


Figure 6.2: Norm squared of the linear response $\|\hat{\mathbf{u}}(\omega)\|^2 = \|R(\omega)\mathbf{f}_o\|^2 = \|\hat{\mathbf{u}}_L(\omega) + \hat{\mathbf{u}}^\perp(\omega)\|^2$ as a function of the frequency, together with the squared norm of its components, $\|\hat{\mathbf{u}}_L(\omega)\|^2$ and $\|\hat{\mathbf{u}}^\perp(\omega)\|^2$. Note that the equality $\|\hat{\mathbf{u}}_L(\omega) + \hat{\mathbf{u}}^\perp(\omega)\|^2 = \|\hat{\mathbf{u}}_L(\omega)\|^2 + \|\hat{\mathbf{u}}^\perp(\omega)\|^2$ generically does not hold.

The non-normal response far from $\omega = 0$ being significant, we expect the latter to have an influence on the nonlinear dynamics of the bifurcated mode \mathbf{q} for $\epsilon > 0$, which we aim at capturing in the weakly nonlinear regime by postulating the expansion

$$\mathbf{U} = \underbrace{\mathbf{U}_{e,c}}_{=\mathbf{0}} + \epsilon \mathbf{u}_1(t, \tau_1, \tau_2) + \epsilon^2 \mathbf{u}_2(t, \tau_1, \tau_2) + \epsilon^3 \mathbf{u}_3(t, \tau_1, \tau_2) + O(\epsilon^4), \quad (6.84)$$

The nonlinear operator $N(\mathbf{U}) = \|\mathbf{U}\|^2 B\mathbf{U}$ is expanded around $\mathbf{U}_{e,c} = \mathbf{0}$ as

$$N(\mathbf{0} + \epsilon \mathbf{u}_1 + \epsilon^2 \mathbf{u}_2 + \epsilon^3 \mathbf{u}_3) = \epsilon^3 \|\mathbf{u}_1\|^2 B\mathbf{u}_1 + O(\epsilon^4) = \epsilon^3 N_3(\mathbf{u}_1, \mathbf{u}_1) + O(\epsilon^4), \quad (6.85)$$

with

$$N_3(\mathbf{a}, \mathbf{b}) = \frac{1}{3} (\langle \mathbf{a} | \mathbf{b} \rangle B\mathbf{a} + \langle \mathbf{b} | \mathbf{a} \rangle B\mathbf{a} + \|\mathbf{a}\|^2 B\mathbf{b}) \neq N_3(\mathbf{b}, \mathbf{a}). \quad (6.86)$$

The nonlinear operator yields no contributions at $O(\epsilon^2)$ and the ensuing second-order coefficients appearing in (6.51) and (6.52) also vanish. This implies that the amplitudes A and B do not depend on τ_1 . The second-order particular solution \mathbf{u}_2 is also null, and we easily obtain the following system of coupled amplitude equations by closing the expansion at third-order

$$\begin{aligned} \frac{dA}{d\tau_2} &= \alpha_2 A + \alpha_3 A^3 + \alpha_4 AB^2 + \phi\eta\zeta, \\ \frac{dB}{d\tau_2} &= \phi\|\mathbf{f}_o^\perp\| - \theta B + \beta_2 B + \beta_3 B^3 + \beta_4 A^2 B, \end{aligned} \quad (6.87)$$

with the slightly modified coefficients

$$\begin{aligned}\alpha_2 &= \langle \mathbf{q}^\dagger | \delta L \mathbf{q} \rangle, \\ \alpha_3 &= \langle \mathbf{q}^\dagger | N_3(\mathbf{q}, \mathbf{q}) \rangle, \\ \alpha_4 &= \langle \mathbf{q}^\dagger | 3\overline{N_3(\mathbf{l}^\perp, \mathbf{q})} \rangle,\end{aligned}\tag{6.88}$$

as well as

$$\begin{aligned}\beta_2 &= \overline{\langle \mathbf{a} | \delta L \mathbf{l}^\perp \rangle} \\ \beta_3 &= \overline{\langle \mathbf{a} | N_3(\mathbf{l}^\perp, \mathbf{l}^\perp) \rangle}, \quad \text{and eventually} \\ \beta_4 &= \overline{\langle \mathbf{a} | 3N_3(\mathbf{q}, \mathbf{l}^\perp) \rangle}.\end{aligned}\tag{6.89}$$

The re-scaled amplitudes $a = \epsilon A$ and $b = \epsilon B$ obey the equations

$$\begin{aligned}\frac{da}{dt} &= \epsilon^2 \alpha_2 a + \alpha_3 a^3 + \alpha_4 a b^2 + F \eta \xi, \\ \frac{db}{dt} &= F \| \mathbf{f}_o^\perp \| - \epsilon_o b + \epsilon^2 \beta_2 b + \beta_3 b^3 + \beta_4 b a^2.\end{aligned}\tag{6.90}$$

Again, in the system (6.90), the coefficients $\epsilon^2 \alpha_2$ and $\epsilon^2 \beta_2$ are the sensitivities of the neutral eigenvalue and the linear non-normal response amplitude, respectively, to a $+\epsilon^2 \delta L$ perturbation of the operator L_n . The coefficients α_3 and β_3 multiply cubic terms arising from the nonlinear interaction of the eigenmode, respectively the linear non-normal response, with itself and retro-acting on itself. The coefficient α_4 multiplies a cubic coupling term stemming from the fact that the bifurcated mode evolves on a mean flow that has been distorted under the action of the nonlinear interaction $\propto b^2$ of the non-normal response with itself. Similarly, the coefficient β_4 takes into account the mirror effect that the non-normal response evolves over a base flow that has been distorted by the nonlinear interaction $\propto a^2$ of the bifurcated eigenmode with itself.

For a given F (F^2 being the variance of stochastic forcing) and a given ϵ , both amplitudes are determined by integrating the system (6.90) numerically with a time step $\Delta t = 10^{-1}$. This way, the largest frequency captured by the numerical solution (i.e. the Nyquist frequency) $\omega_d = \pi / \Delta t$, is ten times larger than the cut-off frequency of the noise. Each simulation lasts 10^8 units of time, which was found largely sufficient for the convergence of all temporal averages, in particular for the coefficients.

The accuracy of the leading order description (6.91), denoted with the acronym "WNL" in what follows, is compared with direct, fully nonlinear simulations ("DNS") of the original system (6.77). Fully nonlinear simulations are also performed with a time step of $\Delta t = 10^{-1}$ until a final time $T = 10^8$.

We recall that the amplitudes a and b are associated with the leading order description of the

system

$$\mathbf{U}(t) = a(\epsilon^2 t)\mathbf{q} + b(\epsilon^2 t)\mathbf{l}^\perp(t) + O(\epsilon^3), \quad (6.91)$$

with $a, b = O(\epsilon)$. Thereby, the first measure of comparison between both WNL and DNS approaches is simply chosen as the root mean square \sqrt{E} of the respective signals

$$\sqrt{E} = \sqrt{\|\mathbf{y}\|^2}, \quad \text{where } \mathbf{y} = \begin{cases} a\mathbf{q} + b\mathbf{l}^\perp & \text{for the WNL approach} \\ \mathbf{U} & \text{for the DNS approach.} \end{cases} \quad (6.92)$$

The results are proposed in figure 6.3 as a function of F , and for

$$\epsilon^2 = \epsilon_o = 3.52 \times 10^{-4}, \quad (6.93)$$

corresponding to $\theta = 1$ (which is a way to ensure that $\theta = O(1)$ indeed). For comparison, we also show some WNL results obtained after having artificially decoupled the equation for a and b by setting to zero α_4 and β_4 in (6.90)

$$\begin{aligned} \frac{da}{dt} &= \epsilon^2 \alpha_2 a + \alpha_3 a^3 + \cancel{\alpha_4 a b^2} + F\eta\xi, \\ \frac{db}{dt} &= F\|\mathbf{f}_o^\perp\| - \epsilon_o b + \epsilon^2 \beta_2 b + \beta_3 b^3 + \cancel{\beta_4 b a^2}. \end{aligned} \quad (6.94)$$

Still in figure 6.3, are also included some results where the amplitude b was artificially set to zero, such that we only simulated

$$\frac{da}{dt} = \epsilon^2 \alpha_2 a + \alpha_3 a^3 + F\eta\xi, \quad (6.95)$$

as a classical (modal) amplitude equation would result in.

In the limit $F \rightarrow 0$ where the system is unforced in figure 6.3, the r.m.s from the DNS converges to that of the equilibrium solutions $\sqrt{E} = \epsilon\sqrt{10} = \sqrt{3.52 \times 10^{-4} \times 10} = 0.06$. The WNL also converges toward this exact value since $b \rightarrow 0$ and the equilibrium solution for a , denoted \bar{a} , reads

$$\bar{a} = \sqrt{\frac{-\alpha_2}{\alpha_3}}\epsilon = \sqrt{10}\epsilon, \quad (6.96)$$

which occurs to be the exact solution. This is inherent to the chosen toy system and is not expected to be generically true. By increasing the forcing amplitude F , the r.m.s of the DNS response first slightly decreases, then substantially increases. In doing so, the WNL is revealed to be an accurate model. Most importantly, the inclusion of the non-normal response (with amplitude b) and its coupling with the modal one (with amplitude a) improves the agreement with the DNS as compared to the classical (modal) case where only the amplitude equation for a is considered. That is because the non-normal response is largely amplified by the system, thus feeding back on the mean flow over which the bifurcated mode is evolving. From a

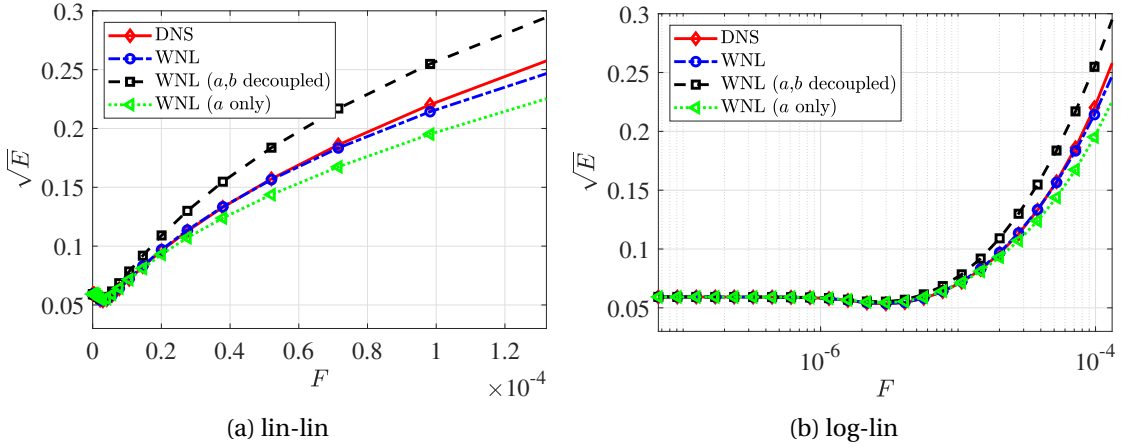


Figure 6.3: Root mean square defined in (6.92) of the stochastic response of the toy system (6.77), as (i) extracted from a DNS (continuous line with diamond markers) (ii) approached by the weakly nonlinear system of amplitude equations (6.90) (dash-dotted line with circle markers) (iii) approached by the weakly nonlinear system of amplitude equations in which the coupling terms have been artificially suppressed (6.94) (dashed line with square markers) and (iv) approached by the weakly nonlinear amplitude equation for a only and where b not considered (6.95) (dotted line with triangle markers), as would be the case in a classical, modal approach. We recall that $\epsilon^2 = \epsilon_o = 3.52 \times 10^{-4}$, value at which the system possesses two equilibria solution at $[\pm 0.06, 0, 0]^T$ both with a root mean square $\sqrt{E} = 0.06$. In frame (a) the results are shown in lin-lin scale, whereas they are shown in log-lin in frame (b).

mathematical perspective, the classical modal approach cannot capture this coupling, for the non-normal response cannot be incorporated in the non-resonance condition; in other terms, in a classical approach, the non-normal response is thought of as remaining at third-order, whereas it is shown here that, precisely because it is largely amplified, it must feed back at leading order to yield a system of coupled amplitude equation.

The improvement induced by accounting for the modal and non-modal coupling is also clear in figure 6.4, where we compare the density probability function (PDF) of a , denoted $P[a]$, with that where a is extracted from the DNS, $P[a^{\text{DNS}}]$ with

$$a^{\text{DNS}}(t) = \frac{\langle \mathbf{q}^\dagger | \mathbf{U}(t) \rangle}{\langle \mathbf{q}^\dagger | \mathbf{q} \rangle} = \langle \mathbf{q}^\dagger | \mathbf{U}(t) \rangle. \quad (6.97)$$

The coupled system of amplitude equations shows a significantly better agreement with the fully nonlinear probability density function than the decoupled one. In particular, from $F = 2.01 \times 10^{-5}$ onward, the coupled system can capture that the PDF is no longer bi-modal, presumably because the mean flow distortion by the non-normal response had restored $\mathbf{0}$ as being the unique and stable equilibrium of the system. The decoupled system lacks the term in ab^2 and thus can't capture the restoration of the symmetry by increasing b (ensuing from the increase of F) and remains bi-modal for all considered forcing amplitudes.

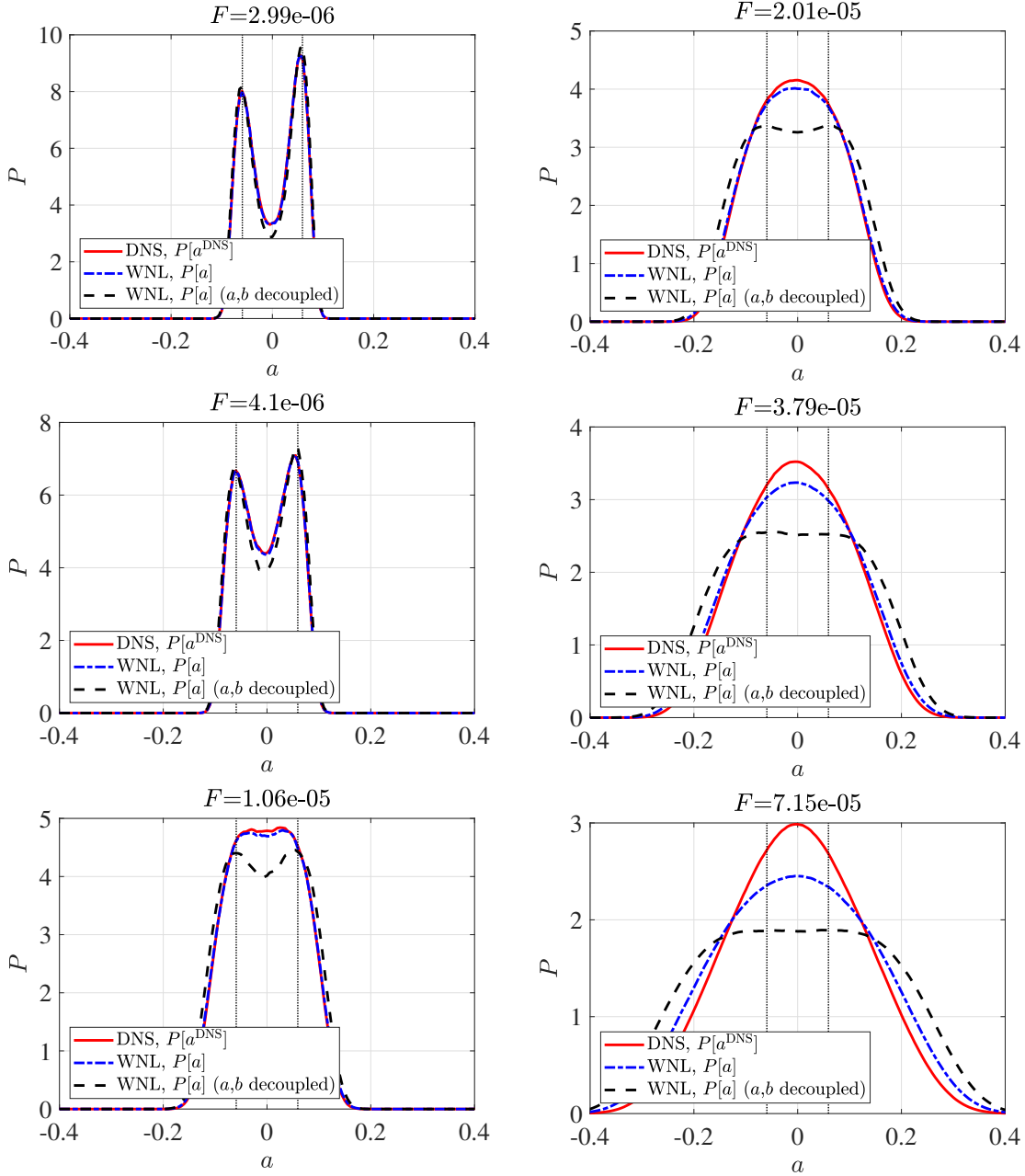


Figure 6.4: Probability density function of the amplitude a of the bifurcated mode \mathbf{q} , where a is either extracted from a DNS according to (6.97) (continuous line), or a solution of the weakly nonlinear system of amplitude equation (6.90) (dash-dotted line), or a solution of the weakly nonlinear system of amplitude equations where a and b have been artificially decoupled (6.94) (dashed line). The thin vertical lines highlight the two deterministic attractors at ± 0.06 .

6.5 Conclusions and perspectives

In this chapter, we have decomposed the linear response to a stochastic forcing into the sum of (i) a modal, Lorentzian response along a neutral mode, and (ii) a response along all

the other eigenmodes, ensuing from the non-normality of the linearized operator. The non-normal response was assumed to experience a large response-to-forcing gain, as measured by the mean square norm induced under the spatiotemporal inner product. Thereby, in the lineament of the ideas advanced in the previous chapters, a perturbation operator involving the spatiotemporal inner product was sufficient to make singular the inverse resolvent or its equivalent in the temporal domain. The singular operator thus constructed contained both (i) the neutral mode and (ii) the non-normal response.

A weakly nonlinear expansion encompassing the inverse resolvent perturbation led to a system of nonlinearly coupled equations for the amplitude of the mode and the non-normal response, respectively. These equations have been obtained by satisfying at each order the Fredholm alternative generalized to the spatiotemporal inner product, for it is under this inner product that the adjoint of the singular operator had to be constructed. Enforcing a spatiotemporal orthogonality with the adjoint of the neutral mode is equivalent to saying that the temporal mean of the forcing term must be orthogonal to the adjoint under the spatial inner product. This is an intuitive condition that would also be found with a classical weakly nonlinear expansion. The originality of the method lies in the fact that an amplitude equation for the non-normal response is also derived, by enforcing a spatiotemporal orthogonality of the forcing term with the adjoint of the non-normal response. These two orthogonality conditions preserve the asymptotic hierarchy. The first one because it prevents resonance from occurring at higher orders, the second because it prevents the forcing terms from being largely amplified by non-normality, and thus emerging at leading order since the non-normal gain scales as the inverse of the square of the small parameter.

The system of amplitude equations is exact in the linear regime. There, the stochastically forced amplitude for the mode shows an inherent Lorentzian response, and the amplitude for the non-normal response reduces to a deterministic constant which was the proper re-scaling of the normalized non-normal response. The system of amplitude equation captures the leading order nonlinear interaction between the modal and the non-modal responses, and the coupling terms made intuitive physical senses.

The method has then been tested on a relatively caricatural toy model and has shown promising results. Specifically, the prediction of the probability density function of the mode amplitude in a weakly nonlinear regime was greatly improved by the coupling with the non-normal response, which can't be taken into account by a classical weakly nonlinear expansion. The coupled system of amplitude equations successfully predicted the restoration of the equilibrium symmetry by increasing the forcing amplitude, thereby the strength of the non-normal response, implying the density probability function to recover a unique global maximum at $a = 0$ after some threshold F .

The method remains to be applied to the Navier-Stokes equations. For this, the sudden expansion flow considered in the previous chapter, for $Re = 100$ past a supercritical pitchfork bifurcation at $Re_c = 79.3$, has also been considered as an application case here. However,

this corresponds to $\epsilon^2 = \text{Re}_c^{-1} - \text{Re}^{-1} = 0.0026$, whereas the inverse of the square root of the non-normal gain at Re_c , ϵ_o , was found to be rather weak $\epsilon_o = 0.12$. Consequently, the scaling (6.22) does not hold, for we can't say anymore that $\theta = O(1)$. Instead, it is the scaling

$$\epsilon_o = \theta \epsilon, \quad \text{with } \theta = O(1), \quad (6.98)$$

which is the proper one. This does not pose fundamental analytical problems, and the weakly nonlinear expansion can be adapted to this new scaling. However, the computations are rendered far more complex and the expressions of the coefficients are considerably heavier, to the point where physical interpretations are obscured.

As a potential application case, one could think of selecting a sudden expansion with a smaller aspect ratio, which is known to increase the critical Reynolds number Re_c at which the bifurcation occurs (Lanzerstorfer & Kuhlmann, 2012). Thereby, since the non-normal gain (at Re_c) is expected to increase with Re_c , there may exist an aspect ratio below which the scaling (6.22) holds and the ensuing system of amplitude equation (6.74) is directly applicable.

6.6 Appendix

6.6.1 Fredholm alternative imposed at second order

In deriving (6.51) from (6.49), we have used that

$$\begin{aligned}
\langle \mathbf{q}^\dagger | \overline{C(\mathbf{q}, \mathbf{q})} \rangle &= \langle \mathbf{q}^\dagger | C(\mathbf{q}, \mathbf{q}) \rangle = 0 \quad \text{and} \\
\langle \mathbf{q}^\dagger | \overline{\delta L \mathbf{U}_e} \rangle &= \langle \mathbf{q}^\dagger | \delta L \mathbf{U}_e \rangle = 0 \quad \text{for symmetry reasons, as well as} \\
\langle \mathbf{q}^\dagger | \overline{C(\mathbf{q}, \mathbf{l}^\perp)} \rangle &= \langle \mathbf{q}^\dagger | C(\mathbf{q}, \overline{\mathbf{l}^\perp}) \rangle = 0 \quad \text{and} \\
\langle \mathbf{q}^\dagger | \overline{\mathbf{l}^\perp} \rangle &= 0, \quad \text{since by construction } \overline{\mathbf{l}^\perp} = \mathbf{0}.
\end{aligned} \tag{6.99}$$

Then, in deriving (6.52) from (6.50) we have used that, since by construction the adjoint $\mathbf{a}(t)$ as a zero average, i.e., $\overline{\mathbf{a}} = \mathbf{0}$, the following terms cancel naturally

$$\begin{aligned}
\overline{\langle \mathbf{a} | C(\mathbf{q}, \mathbf{q}) \rangle} &= \langle \overline{\mathbf{a}} | C(\mathbf{q}, \mathbf{q}) \rangle = 0, \\
\overline{\langle \mathbf{a} | \delta L_n \mathbf{U}_e \rangle} &= \langle \overline{\mathbf{a}} | \delta L_n \mathbf{U}_e \rangle = 0 \quad \text{and} \\
\overline{\langle \mathbf{a} | \mathbf{q} \rangle} &= \langle \overline{\mathbf{a}} | \mathbf{q} \rangle = 0.
\end{aligned} \tag{6.100}$$

In addition, the scalar

$$\tilde{\beta} = -\langle \mathbf{a}(t) | C(\mathbf{l}^\perp(t), \mathbf{l}^\perp(t)) \rangle = -\chi \left\langle \left((\partial_t - L_n)^{-1} \right)^\dagger \mathbf{l}^\perp(t) \middle| C(\mathbf{l}^\perp(t), \mathbf{l}^\perp(t)) \right\rangle \tag{6.101}$$

is an odd function of \mathbf{l}^\perp , such that

$$\tilde{\beta}(-\mathbf{l}^\perp(t)) = -\tilde{\beta}(\mathbf{l}^\perp(t)). \tag{6.102}$$

By assuming that $\tilde{\beta}$ is an ergodic process, its temporal average is equal to its ensemble average. But the ensemble average of an odd function of \mathbf{l}^\perp must vanish since \mathbf{l}^\perp is the linear response of a process with a Gaussian distribution, thereby it must also have a Gaussian distribution. Consequently, under the ergodic hypothesis for $\tilde{\beta}$, the amplitude equation (6.52) does not contain a term in B^2 .

6.6.2 Fredholm alternative imposed at third order

In the derivation of (6.68) from (6.67), we have used successively

$$\begin{aligned}
\overline{\langle \mathbf{q}^\dagger | \mathbf{l}^\perp \rangle} &= \langle \mathbf{q}^\dagger | \overline{\mathbf{l}^\perp} \rangle = 0, \\
\overline{\langle \mathbf{q}^\dagger | \mathbf{u}_2^{AB} \rangle} &= \langle \mathbf{q}^\dagger | \overline{\mathbf{u}_2^{AB}} \rangle = 0, \\
\overline{\langle \mathbf{q}^\dagger | C(\mathbf{l}^\perp, \mathbf{u}_2^\delta) \rangle} &= \langle \mathbf{q}^\dagger | C(\overline{\mathbf{l}^\perp}, \mathbf{u}_2^\delta) \rangle = 0, \\
\overline{\langle \mathbf{q}^\dagger | (C(\mathbf{q}, \mathbf{u}_2^{AB}) + C(\mathbf{l}^\perp, \mathbf{u}_2^{A^2})) \rangle} &= \langle \mathbf{q}^\dagger | (C(\mathbf{q}, \overline{\mathbf{u}_2^{AB}}) + C(\overline{\mathbf{l}^\perp}, \mathbf{u}_2^{A^2})) \rangle = 0, \\
\overline{\langle \mathbf{q}^\dagger | \xi \mathbf{f}_o^\perp \rangle} &= \langle \mathbf{q}^\dagger | \overline{\xi \mathbf{f}_o^\perp} \rangle = 0
\end{aligned} \tag{6.103}$$

In virtue of $\overline{\mathbf{l}^\perp} = \overline{\mathbf{u}_2^{AB}} = \mathbf{0}$, $\overline{\xi} = 0$, and that $\mathbf{u}_2^{A^2}$ and \mathbf{u}_2^δ are constant. We have also used that $\langle \mathbf{q}^\dagger | 2\alpha_1 \mathbf{u}_2^{A^2} \rangle$ by symmetry, and that

$$\frac{\overline{\langle \mathbf{q}^\dagger | \eta \mathbf{q} \zeta(\tau_2) \rangle}}{\overline{\langle \mathbf{q}^\dagger | \mathbf{q} \rangle}} = \eta \zeta(\tau_2) \frac{\langle \mathbf{q}^\dagger | \mathbf{q} \rangle}{\langle \mathbf{q}^\dagger | \mathbf{q} \rangle} = \eta \zeta(\tau_2), \tag{6.104}$$

and that the coefficient

$$-2 \overline{\langle \mathbf{q}^\dagger | C(\mathbf{l}^\perp, \mathbf{u}_2^{B^2}) \rangle} = -2 \langle \mathbf{q}^\dagger | \overline{C(\mathbf{l}^\perp, \mathbf{u}_2^{B^2})} \rangle \tag{6.105}$$

vanishes under the ergodic hypothesis since $C(\mathbf{l}^\perp, \mathbf{u}_2^{B^2})$ is an odd function of \mathbf{l}^\perp .

In the derivation of (6.71) from (6.70), we have used successively

$$\begin{aligned}
\overline{\langle \mathbf{a} | \mathbf{q} \rangle} &= \langle \overline{\mathbf{a}} | \mathbf{q} \rangle = 0, \\
\overline{\langle \mathbf{a} | \mathbf{u}_2^{A^2} \rangle} &= \langle \overline{\mathbf{a}} | \mathbf{u}_2^{A^2} \rangle = 0, \\
\overline{\langle \mathbf{a} | C(\mathbf{q}, \mathbf{u}_2^\delta) \rangle} &= \langle \overline{\mathbf{a}} | C(\mathbf{q}, \mathbf{u}_2^\delta) \rangle = 0, \\
\overline{\langle \mathbf{a} | C(\mathbf{q}, \mathbf{u}_2^{A^2}) \rangle} &= \langle \overline{\mathbf{a}} | C(\mathbf{q}, \mathbf{u}_2^{A^2}) \rangle = 0
\end{aligned} \tag{6.106}$$

since $\overline{\mathbf{a}} = \mathbf{0}$. In addition

$$\begin{aligned}
\overline{\langle \mathbf{a} | \xi \mathbf{f}_o^\perp \rangle} &= \epsilon_o \overline{\langle ((\partial_t - L_n)^{-1})^\dagger \mathbf{l}^\perp | \xi \mathbf{f}_o^\perp \rangle} \\
&= \epsilon_o \overline{\langle \mathbf{l}^\perp | (\partial_t - L_n)^{-1} \xi \mathbf{f}_o^\perp \rangle} \\
&= \epsilon_o \overline{\langle \mathbf{l}^\perp | \mathbf{u}^\perp \rangle} \\
&= \epsilon_o \frac{\|\mathbf{f}_o^\perp\|}{\epsilon_o} \overline{\langle \mathbf{l}^\perp | \mathbf{l}^\perp \rangle} \\
&= \|\mathbf{f}_o^\perp\|.
\end{aligned} \tag{6.107}$$

Eventually, the term

$$-\overline{\langle \mathbf{a} | 2\beta_1 \mathbf{u}_2^{B^2} + 2C(\mathbf{q}, \mathbf{u}_2^{B^2}) + 2C(\mathbf{l}^\perp, \mathbf{u}_2^{AB}) \rangle} \quad (6.108)$$

is odd in \mathbf{l}^\perp thereby vanishes under the ergodic assumption.

Response to an initial perturbation **Part III**

7 A non-modal weakly nonlinear amplitude equation for the transient response

Remark: This chapter is largely inspired by the second half of the article Ducimetière et al. (2022a), in collaboration with Edouard Boujo and François Gallaire.

7.1 Introduction

Some flows experience a transition from laminar to turbulent far below the threshold predicted by the linear stability theory which relies on eigenvalues. Sometimes, such thresholds do not even exist. In addition, the value of the external parameter at which the flow transits strongly depends on the level of external noise. Among them are the canonical Couette and Poiseuille parallel shear flows, as comprehensively reported in Schmid and Henningson (2001). Non-parallel flows such as jets and the backward-facing step flow, documented respectively in Garnaud et al. (2013a) and Barkley et al. (2000), could also be mentioned.

The transition scenario advanced in Trefethen et al. (1993) relies on the non-normality property of the linearized Navier-Stokes operator. The linear response of a non-normal operator generally results from an intricate cooperation between a large amount of eigenmodes. The leading, i.e. least stable or most unstable eigenvalue solely provides the asymptotic (long-time) linear behavior of the energy of the unforced system. At finite time, restriction to the leading eigenmode is generally irrelevant. In particular, a negative growth rate for all eigenvalues is not a guarantee that the energy decays monotonically for all initial conditions. That is because eigenmodes of a non-normal operator are not orthogonal under the inner product that induces the energy norm. Consequently, some small-amplitude perturbations may experience a large transient amplification (figure 7.1). Through these non-modal mechanisms, the response may be carried in a regime where nonlinearities set in and the flow escapes from its linearly stable solution (figure 7.1).

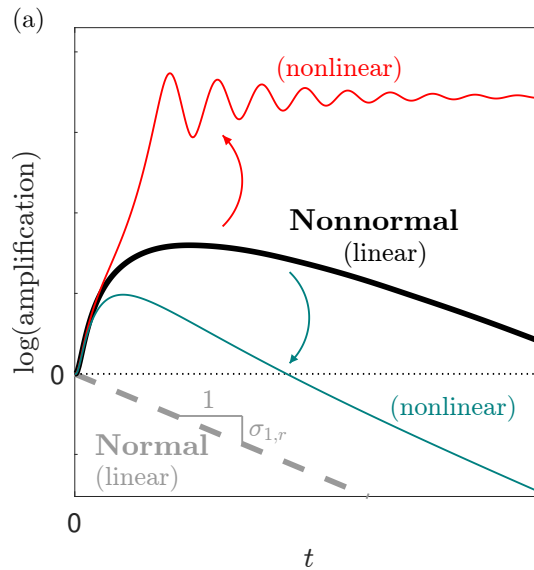


Figure 7.1: Cartoon representation of nonlinearity and non-normality, illustrated in the time domain (see figure 2.1 for an illustration in the frequency domain), for a linearly stable system. In the linear regime, the amplitude of the perturbations eventually decays like $\exp(\sigma_{1,r} t)$. non-normal systems can experience a very large transient growth. Nonlinearity may be stabilising or destabilising.

In this perspective, numerous studies computed the initial condition structures that are the most amplified by flow, i.e., leading to the optimal transient growth gain. Formally, such studies generally consist of finding the singular mode of the propagator for a given temporal horizon, and the eigenmodes of the linearized Navier-Stokes operator are mainly irrelevant. For the transient growth problem, one could for instance refer to

In the linear paradigm adopted in all these works, quantities do not depend on the amplitude of the initial condition. The latter is assumed arbitrarily small such that the nonlinear terms are negligible. Thus the nonlinear interactions involved in the subcritical transition, or in the saturation process, can't be captured by definition.

In the vein of previous chapters concerned with responses to forcings, the current one advances a method to derive an amplitude equation for the linearly most amplified transient response. The amplitude equation makes possible the prolongation of the transient gain, at a selected time $t = t_o$ in a weakly nonlinear regime. Specifically, at a very low numerical cost, we predict the transient gain of the response as we increase the amplitude of the linearly optimal initial condition (§7.2). Once again, the method does not rely on the presence of an eigenvalue close to the neutral axis.

The analysis proposed in the present chapter can be seen as another extension of that in chapter 2. However, in contrast with chapter 3, the extension does not consist of generalizing the inner product operated by the operator perturbation of the inverse resolvent. While keeping

the same L^2 inner product as in chapter 2, it consists of perturbing the inverse propagator operator instead of the inverse resolvent one. This is a consequence of the nature of the problem considered here. The resolvent operator does not appear naturally because it characterizes response to forcing in a time-asymptotic, statistically steady regime. The propagator, on the contrary, naturally appears in the current problem of an unforced, finite-time response. It is the application of the propagator operator that leads to a strong amplification, thereby, it is the application of the inverse propagator that leads to a strong reduction. Consistently with the logic unfolded throughout this thesis, it is then the latter operator that should be perturbed.

The method is illustrated with two flows, the nonparallel flow past a backward-facing step (sketched in figure 7.2a) and the parallel plane Poiseuille flow (figure 7.2b). These two non-normal flows exhibit large gains, both in the context of harmonic forcing, as we studied in chapter 2, and transient growth (§7.2.1-7.2.2).

Let us first consider a generic nonlinear dynamical system,

$$\partial_t \mathbf{U} = N(\mathbf{U}) + \mathbf{F}, \quad \mathbf{U}(0) = \mathbf{U}_0, \quad (7.1)$$

where $N(*)$ is a nonlinear operator and \mathbf{F} is a forcing term. An appropriate and common step to begin the analysis of (7.1) is to linearise it around an unforced equilibrium. The latter is denoted \mathbf{U}_e and satisfies $N(\mathbf{U}_e) = \mathbf{0}$. Around this equilibrium are considered small-amplitude perturbations in velocity $\epsilon \mathbf{u}$, forcing $\epsilon \mathbf{f}$, and initial condition $\epsilon \mathbf{u}_0$, where $\epsilon \ll 1$. An asymptotic expansion of (7.1) in terms of ϵ can thus be performed, transforming the nonlinear equation into a series of linear ones. The fields \mathbf{u} , \mathbf{f} and \mathbf{u}_0 are recovered at order ϵ and linked through the linear relation

$$\partial_t \mathbf{u} = L\mathbf{u} + \mathbf{f}, \quad \mathbf{u}(0) = \mathbf{u}_0, \quad (7.2)$$

where L results from the linearisation of N around \mathbf{U}_e . For fluid flows governed by the incompressible Navier-Stokes equations, $L\mathbf{u} = -(\mathbf{U}_e \cdot \nabla)\mathbf{u} - (\mathbf{u} \cdot \nabla)\mathbf{U}_e + Re^{-1} \Delta \mathbf{u} - \nabla p(\mathbf{u})$, where the pressure field p is such that the velocity field \mathbf{u} is divergence-free. Both fields are linked through a linear Poisson equation. In practice, pressure is included in the state variable, resulting in a singular mass matrix; it is omitted here, for the sake of clarity.

7.2 Transient Growth

Next, we derive an amplitude equation for the weakly nonlinear transient growth in an unforced ($\mathbf{f} = \mathbf{0}$) system, without restriction on its linear stability. The solution to the linearised equation (7.2) is $\mathbf{u}(t) = e^{Lt} \mathbf{u}(0)$, where e^{Lt} is the operator exponential of Lt . In an unforced context, the propagator e^{Lt} maps an initial structure at time $t = 0$ onto its evolution at $t \geq 0$. The largest linear amplification at $t_o > 0$ (subscript o for “optimal”) is

$$G(t_o) = \max_{\mathbf{u}(0)} \frac{\|\mathbf{u}(t_o)\|}{\|\mathbf{u}(0)\|} = \|e^{Lt_o}\| \doteq \frac{1}{\epsilon_o}. \quad (7.3)$$

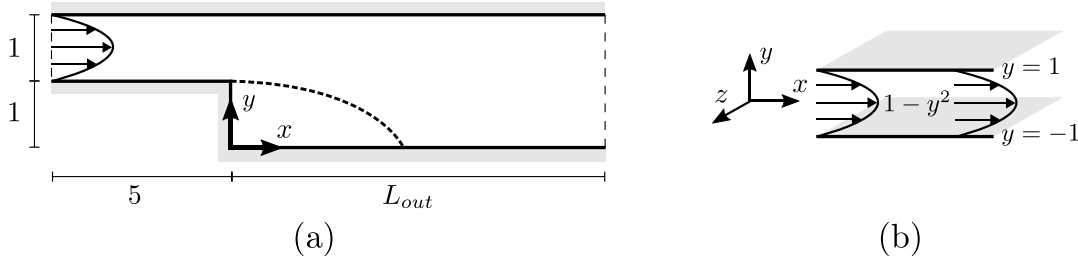


Figure 7.2: Sketch of the flow configurations. **(a)** Two-dimensional flow over a backward-facing step, with fully developed parabolic profile of unit maximum centerline velocity at the inlet. **(b)** Three-dimensional plane Poiseuille flow, confined between two solid walls at $y = \pm 1$, and invariant in the x (streamwise) and z (spanwise) directions

The singular-value decomposition of the propagator e^{Lt_0} provides the transient gain $G(t_0)$ as the largest singular value of e^{Lt_0} , as well as the left and right singular pair \mathbf{v}_o and \mathbf{u}_o , respectively,

$$e^{-Lt_0} \mathbf{v}_o = \epsilon_o \mathbf{u}_o, \quad \left[(e^{Lt_0})^\dagger \right]^{-1} \mathbf{u}_o = \epsilon_o \mathbf{v}_o, \quad (7.4)$$

where $\|\mathbf{v}_o\| = \|\mathbf{u}_o\| = 1$. The field \mathbf{u}_o is the optimal initial structure for the propagation time $t = t_0$, and \mathbf{v}_o is its normalised evolution at t_0 . The corresponding amplification is $1/\epsilon_o$, as defined in (7.3). Smaller singular values are sub-optimal gains, associated with orthogonal sub-optimal initial conditions. Their orthogonality is ensured by the fact that singular vectors of the operator e^{Lt_0} also are the eigenvectors of the symmetric operator $(e^{Lt_0})^\dagger e^{Lt_0}$, the singular values of the former being the square root of the eigenvalues of the latter. Of all the t_0 , the time leading to the largest optimal gain will be highlighted with the subscript m (for “maximum”) such that $\max_{t_0 > 0} G(t_0) = G(t_{0,m})$.

By construction, the linear gain is independent of the amplitude of the initial condition $\mathbf{u}(0)$. As this amplitude increases, however, nonlinearities may come into play and the nonlinear gain may depart from the linear gain G . Similar to the previous section on harmonic gain, we propose a method for capturing the effect of weak nonlinearities on the transient gain.

Due to the assumed non-normality of L , the inverse gain is small, $\epsilon_o \ll 1$. While the previous section focused on the inverse resolvent, it is now the inverse propagator e^{-Lt_0} that appears close to singular. The first equality of (7.4) can be rewritten as $(e^{-Lt_0} - \epsilon_o \mathbf{u}_o \langle \mathbf{v}_o, * \rangle) \mathbf{v}_o = \mathbf{0}$, which shows that the operator $(e^{-Lt_0} - \epsilon_o \mathbf{u}_o \langle \mathbf{v}_o, * \rangle)$ is singular since $\mathbf{v}_o \neq \mathbf{0}$ belongs to its kernel. Mirroring our previous reasoning for the WNNh model, we now wish to construct a perturbed inverse propagator whose kernel is the linear trajectory

$$\mathbf{l}(t) \doteq \epsilon_o e^{Lt} \mathbf{u}_o \quad (7.5)$$

seeded by the optimal initial condition \mathbf{u}_o and of unit norm in $t = t_0$ since $\mathbf{l}(t_0) = \mathbf{v}_o$. One conceptual difficulty lies in the fact that the linear response is not a fixed vector field, but a

time-dependent trajectory; therefore, the perturbed inverse propagator too should depend on time. We propose to perturb the inverse propagator for all $t \geq 0$ as

$$\bar{\Phi}(t) = e^{-Lt} - \epsilon_o P(t), \quad \text{where} \quad P(t) \doteq H(t) \frac{\mathbf{u}_o \langle \mathbf{l}(t), * \rangle}{\|\mathbf{l}(t)\|^2}, \quad (7.6)$$

and where the Heaviside distribution $H(t)$ satisfies $H(0) = 0$ and $H(t > 0) = 1$. As the time $t \rightarrow t_o$, the perturbation operator $P \rightarrow \mathbf{u}_o \langle \mathbf{v}_o, * \rangle$ such that $\|P\| \rightarrow 1$ and the expansion (7.6) is certainly justified. The non-trivial kernel of $\bar{\Phi}(t)$ is $\mathbf{l}(t)$ for all $t > 0$; the kernel reduces to $\mathbf{0}$ at $t = 0$ since $\bar{\Phi}(0) = I$. We show in addition that, for $t > 0$, the non-trivial kernel of the adjoint operator $\bar{\Phi}(t)^\dagger$ is

$$\mathbf{a}(t) \doteq (e^{Lt})^\dagger \mathbf{l}(t). \quad (7.7)$$

Indeed, using that $P^\dagger = \mathbf{l}(t) \langle \mathbf{u}_o, * \rangle / \langle \mathbf{l}(t), \mathbf{l}(t) \rangle$ for $t > 0$, we have

$$\begin{aligned} \bar{\Phi}(t)^\dagger \mathbf{a}(t) &= (e^{-Lt})^\dagger \mathbf{a}(t) - \epsilon_o \mathbf{l}(t) \frac{\langle \mathbf{u}_o, \mathbf{a}(t) \rangle}{\langle \mathbf{l}(t), \mathbf{l}(t) \rangle} \\ &= (e^{-Lt})^\dagger \mathbf{a}(t) - \epsilon_o \mathbf{l}(t) \frac{\langle e^{Lt} \mathbf{u}_o, \mathbf{l}(t) \rangle}{\langle \mathbf{l}(t), \mathbf{l}(t) \rangle} \\ &= (e^{-Lt})^\dagger \mathbf{a}(t) - \mathbf{l}(t) \\ &= \left[(e^{Lt})^\dagger \right]^{-1} \mathbf{a}(t) - \mathbf{l}(t) \\ &= \mathbf{0}. \end{aligned}$$

As an illustration of the singularisation of e^{-Lt_o} , parts of the spectra of e^{-Lt_o} and $\bar{\Phi}(t_o)$ are shown in figure 7.3 for the plane Poiseuille flow sketched in figure 7.2. The red dot at the origin is the null singular eigenvalue of $\bar{\Phi}(t_o)$ associated with $\mathbf{l}(t_o)$. Since $\|P(t_o)\| = 1$, this singular eigenvalue lies on the ϵ_o -pseudospectrum of e^{-Lt_o} , meaning that a perturbation of amplitude ϵ_o is sufficient to make the inverse propagator singular.

Recalling that L is assumed strongly non-normal, we choose $\epsilon_o \ll 1$ as expansion parameter, introduce the slow time scale $T = \epsilon_o t$ and propose the multiple-scale expansion

$$\mathbf{U}(t, T) = \mathbf{U}_e + \epsilon_o \mathbf{u}_1(t, T) + \epsilon_o^2 \mathbf{u}_2(t, T) + O(\epsilon_o^3). \quad (7.8)$$

The square root scaling of the previous section is not made here, as resonance at second order cannot be excluded *a priori*. The flow is initialised with $\mathbf{U}(0) = \alpha \epsilon_o^2 \mathbf{u}_o$, where $\alpha = O(1)$ is a prefactor. After injecting this expansion in the unforced Navier-Stokes equations, we obtain

$$\epsilon_o (\partial_t - L) \mathbf{u}_1 + \epsilon_o^2 [(\partial_t - L) \mathbf{u}_2 + C(\mathbf{u}_1, \mathbf{u}_1) + \partial_T \mathbf{u}_1] + O(\epsilon_o^3) = \mathbf{0}, \quad (7.9)$$

subject to $\mathbf{u}_2(0) = \alpha \mathbf{u}_o$, and $\mathbf{u}_i(0) = \mathbf{0}$ for $i \neq 2$. In its primary quality of inverse propagator, the following property holds for e^{-Lt} : $\partial_t(e^{-Lt}) = -e^{-Lt}L$, where the commutation of e^{-Lt}

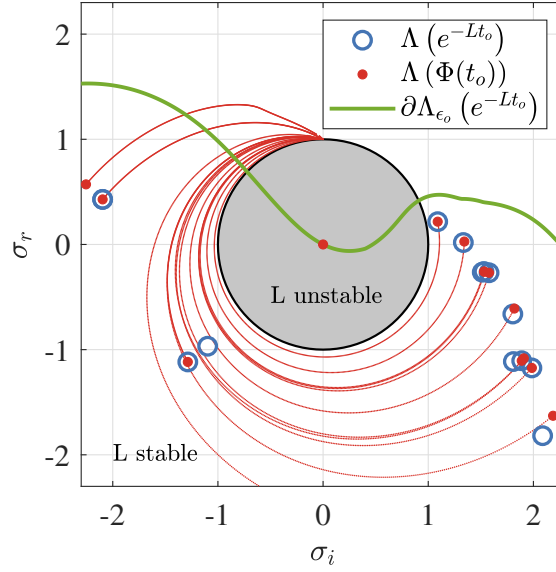


Figure 7.3: Restricted spectra (fifteen least stable eigenvalues) of the natural and perturbed inverse propagators of the plane Poiseuille flow (sketched in figure 7.2b) for $t = t_o = 10$ and $(Re, k_x, k_z) = (3000, 0.5, 2)$ (purely one-dimensional computations using the code of Schmid and Henningson (2001) based on a Fourier expansion of wavenumbers k_x and k_z in x and z , respectively). Blue circles: eigenvalues of e^{-Lt_o} . Red dots: eigenvalues of $\Phi(t_o)$. By construction, one eigenvalue of $\Phi(t)$ lies at the origin. Thin red lines: full locus of the eigenvalues of $\Phi(t)$ for $t \leq t_o$. Green line: ϵ_o -pseudospectrum of e^{-Lt_o} , such that $\|(e^{-Lt_o} - zI)^{-1}\| = 1/\epsilon_o$.

and L has not been used. Thanks to this relation, we write $(\partial_t - L)\mathbf{u}_i = e^{Lt}\partial_t(e^{-Lt}\mathbf{u}_i)$. As a result, L disappears from the asymptotic expansion but e^{-Lt} appears. The latter is perturbed according to (7.6), leading to $e^{Lt}\partial_t(e^{-Lt}\mathbf{u}_i) = e^{Lt}\partial_t(\Phi(t)\mathbf{u}_i) + \epsilon_o e^{Lt}\partial_t(P(t)\mathbf{u}_i)$ for $i = 1, 2, \dots$. The asymptotic expansion (7.9) becomes

$$\epsilon_o e^{Lt}\partial_t(\Phi\mathbf{u}_1) + \epsilon_o^2 \left[e^{Lt}\partial_t(\Phi\mathbf{u}_2) + C(\mathbf{u}_1, \mathbf{u}_1) + \partial_T\mathbf{u}_1 + e^{Lt}\partial_t(P(t)\mathbf{u}_1) \right] + O(\epsilon_o^3) = \mathbf{0}. \quad (7.10)$$

Note that the transformation performed from (7.9) to (7.10) is not restricted to time-independent base flows, as the property $\partial_t(\Psi(t)^{-1}) = -\Psi(t)^{-1}L(t)$ holds for a time-varying operator $L(t)$ and the associated propagator $\Psi(t)$. This can be shown easily by taking the time derivative of $\Psi(t)^{-1}\mathbf{u}(t) = \mathbf{u}(0)$. Terms of (7.10) are then collected at each order in ϵ_o , leading to a succession of linear problems, detailed hereafter.

At order ϵ_o , we collect $\partial_t(\Phi\mathbf{u}_1) = \mathbf{0}$, subject to $\mathbf{u}_1(0) = \mathbf{0}$. We obtain $\Phi\mathbf{u}_1 = \Phi(0)\mathbf{u}_1(0) = \mathbf{0}$, therefore $\mathbf{u}_1(t, T)$ is proportional to the kernel of $\Phi(t)$ for all $t \geq 0$. We choose the non-trivial solution

$$\mathbf{u}_1(t, T) = A(T)H(t)\mathbf{l}(t), \quad (7.11)$$

where the initial condition $\mathbf{u}_1(0) = \mathbf{0}$ is enforced by $H(t)$, while the slowly varying scalar amplitude $A(T)$ is continuous in T and modulates the linear trajectory. This choice is motivated by

the observation that, since A must be constant in time in the linear regime, we expect it to be weakly time-dependent in the weakly nonlinear regime. We stress that $A(T)$ does not depend explicitly on t , such that $\partial_t A = 0$. Note that the choice $\mathbf{u}_1(t) = A(t)H(t)\mathbf{l}(t)$ would also have been possible, and the assumption of the amplitude depending on a slow time scale is made solely to simplify the ensuing calculations.

At order ϵ_o^2 , we collect

$$\partial_t(\Phi \mathbf{u}_2) + A^2 H e^{-Lt} C(\mathbf{l}, \mathbf{l}) + H \frac{dA}{dT} e^{-Lt} \mathbf{l} + \text{Ad}_t(H P \mathbf{l}) = \mathbf{0}, \quad (7.12)$$

subject to $\mathbf{u}_2(0) = \alpha \mathbf{u}_o$. We have used the property $H(t)^2 = H(t)$, which will henceforth be understood. The particular solution of (7.12) yields

$$\mathbf{u}_2(t, T) = \mathbf{u}_2^{(a)}(t) + A(T)^2 \mathbf{u}_2^{(b)}(t) + \frac{dA(T)}{dT} \mathbf{u}_2^{(c)}(t) + A(T) \mathbf{u}_2^{(d)}(t), \quad (7.13)$$

where

$$\begin{aligned} d_t(\Phi \mathbf{u}_2^{(a)}) &= \mathbf{0}, & d_t(\Phi \mathbf{u}_2^{(b)}) &= -H e^{-Lt} C(\mathbf{l}, \mathbf{l}), \\ d_t(\Phi \mathbf{u}_2^{(c)}) &= -H e^{-Lt} \mathbf{l}, & \text{and } d_t(\Phi \mathbf{u}_2^{(d)}) &= -d_t(H P \mathbf{l}), \end{aligned}$$

subject to the initial conditions $\mathbf{u}_2^{(a)}(0) = \alpha \mathbf{u}_o$ and $\mathbf{u}_2^{(b)}(0) = \mathbf{u}_2^{(c)}(0) = \mathbf{u}_2^{(d)}(0) = \mathbf{0}$. Time integration can now be performed without ambiguity as all the partial derivatives ($\partial_t \dots$) have been replaced by total derivatives ($d_t \dots$). After time integration between $t = 0$ and $t > 0$, we obtain a series of problems for $\mathbf{u}_2^{(a)}$, $\mathbf{u}_2^{(b)}$, $\mathbf{u}_2^{(c)}$ and $\mathbf{u}_2^{(d)}$:

$$\Phi(t) \mathbf{u}_2^{(a)}(t) = \Phi(0) \mathbf{u}_2^{(a)}(0) = \alpha \mathbf{u}_o,$$

since $\Phi(0) = I$;

$$\Phi(t) \mathbf{u}_2^{(b)}(t) = - \int_0^t H(s) e^{-Ls} C[\mathbf{l}(s), \mathbf{l}(s)] ds = e^{-Lt} \tilde{\mathbf{u}}_2(t),$$

where

$$\frac{d\tilde{\mathbf{u}}_2}{dt} = L \tilde{\mathbf{u}}_2 - C(\mathbf{l}, \mathbf{l}), \quad \tilde{\mathbf{u}}_2(0) = \mathbf{0}, \quad (7.14)$$

and where we used that the general solution of $d_t \mathbf{x} = L \mathbf{x} + \mathbf{F}$ is $\mathbf{x}(t) = e^{Lt} [\mathbf{x}(0) + \int_0^t e^{-Ls} \mathbf{F}(s) ds]$;

$$\begin{aligned} \Phi(t) \mathbf{u}_2^{(c)}(t) &= - \int_0^t H(s) e^{-Ls} \mathbf{l}(s) ds \\ &= - \int_0^t H(s) \epsilon_o \mathbf{u}_o ds = -\epsilon_o \mathbf{u}_o t, \end{aligned}$$

since $e^{-Lt}\mathbf{l}(t) = \epsilon_o\mathbf{u}_o$ holds by construction; and

$$\Phi(t)\mathbf{u}_2^{(d)}(t) = -[H(t)P(t)\mathbf{l}(t) - H(0)P(0)\mathbf{l}(0)] = -\mathbf{u}_o,$$

since, by construction, $H(t)P(t)\mathbf{l}(t) = H(t)\mathbf{u}_o$. Note that the presence of the Heaviside distribution inside the integral is unimportant. Eventually,

$$\Phi\mathbf{u}_2 = \alpha\mathbf{u}_o + A^2 e^{-Lt}\tilde{\mathbf{u}}_2 - \epsilon_o t \frac{dA}{dT}\mathbf{u}_o - A\mathbf{u}_o, \quad t > 0. \quad (7.15)$$

Invoking again the Fredholm alternative, (7.15) admits a non-diverging particular solution if and only if its right-hand side is orthogonal to $\mathbf{a}(t)$ for all $t > 0$. This leads to

$$\langle \mathbf{u}_o, \mathbf{a}(t) \rangle (\alpha - A) + A^2 \langle e^{-Lt}\tilde{\mathbf{u}}_2(t), \mathbf{a}(t) \rangle - \epsilon_o t \frac{dA}{dT} \langle \mathbf{u}_o, \mathbf{a}(t) \rangle = 0, \quad t > 0. \quad (7.16)$$

Dividing (7.16) by $\langle \mathbf{u}_o, \mathbf{a}(t) \rangle$ leads to

$$(\alpha - A) + \epsilon_o A^2 \mu_2(t) - \epsilon_o t \frac{dA}{dT} = 0, \quad t > 0, \quad (7.17)$$

where

$$\mu_2(t) = \epsilon_o^{-1} \frac{\langle e^{-Lt}\tilde{\mathbf{u}}_2(t), \mathbf{a}(t) \rangle}{\langle \mathbf{u}_o, \mathbf{a}(t) \rangle} = \frac{\langle \tilde{\mathbf{u}}_2(t), \mathbf{l}(t) \rangle}{\langle \mathbf{l}(t), \mathbf{l}(t) \rangle}. \quad (7.18)$$

Equation (7.17) is re-expressed as $E(t, T) = 0$ for $t > 0$, where $E(t, T) = (\alpha - A) + \epsilon_o A^2 \mu_2(t) - \epsilon_o t d_T A$. Since $\int_{t \rightarrow 0}^t \partial_s E(s, T) ds = E(t, T) - E(t \rightarrow 0, T)$, solving $E(t, T) = 0$ is equivalent to solving $\partial_t E(t, T) = 0$ for $t > 0$ subject to $E(t \rightarrow 0, T) = 0$. Thereby, the partial derivative of (7.17) with respect to the short time scale t is taken, leading to

$$\epsilon_o A^2 \frac{d\mu_2(t)}{dt} - \epsilon_o \frac{dA}{dT} = 0, \quad 0 < t, \quad (7.19)$$

where we have used that $\partial_t A = 0$ by construction since $A = A(T)$ does not explicitly depend on t . Furthermore, the relation (7.19) is subject to $E(t \rightarrow 0, T) = \lim_{t \rightarrow 0} (\alpha - A) = 0$ where we have used that $\tilde{\mathbf{u}}_2(t \rightarrow 0) = \tilde{\mathbf{u}}_2(0) = 0$. To be meaningful, equation (7.19) and its initial condition must be re-written solely in terms of t , which is done by evaluating T along $T = \epsilon_o t$. The total derivative of A , denoted $d_t A$, is now needed, as it takes into account the implicit dependence of A on t . By definition, $d_t A = \partial_t A + \epsilon_o \partial_T A = \epsilon_o d_T A$, such that the final amplitude equation reads

$$\frac{dA}{dt} = \epsilon_o A^2 \frac{d\mu_2(t)}{dt}, \quad \text{with } A(0) = \alpha, \quad (7.20)$$

as $\lim_{t \rightarrow 0} (\alpha - A(\epsilon_o t)) = 0$ implies $A(t \rightarrow 0) = \alpha$, and the amplitude A is extended by continuity in $t = 0$ so as to eventually impose $A(0) = \alpha$. Note that the evaluation in $T = \epsilon_o t$ and the passage to the total derivative would lead to indeterminacy in its solution if performed directly in

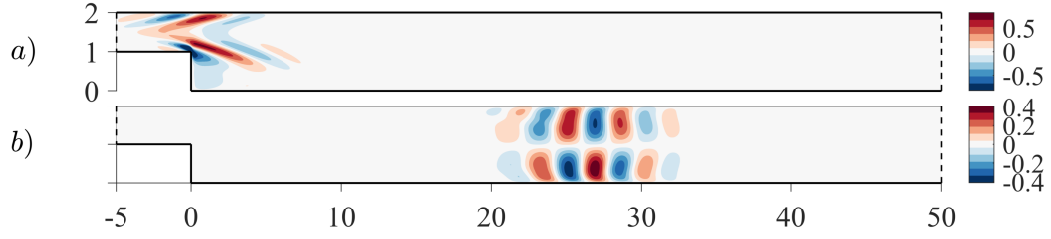


Figure 7.4: **(a)** Streamwise (x) component of the optimal initial condition \mathbf{u}_o for the BFS (sketched in figure 7.2a) at $Re = 500$ and at $t_o = t_{o,m} = 58$. **(b)** Streamwise component of the evolution \mathbf{v}_o at $t = t_o$. Both structures are normalised as $\|\mathbf{u}_o\| = \|\mathbf{v}_o\| = 1$.

(7.17), since that equation is not subject to any initial condition. Indeed, at linear level for instance, it would yield $d_t A = (\alpha - A)/t$, which admits the family of solutions $A(t) = \alpha + Ct$, with C an undetermined constant.

We stress that the inverse propagator is not needed to solve the amplitude equation (7.20). Just like the original problem considered in this section, (7.20) is unforced and has a non-zero initial condition. In the linear regime, $A = \alpha$ for all times, and the linear gain is $\|\epsilon_o \alpha \mathbf{I}(t)\| / \|\alpha \epsilon_o^2\| = \|\mathbf{I}(t)\| / \epsilon_o$. At $t = t_o$, in particular, we recover that it is equal to $1/\epsilon_o$ since $\|\mathbf{I}(t_o)\| = \|\mathbf{v}_o\| = 1$.

In the following, we call equation (7.20) the Weakly Nonlinear non-normal transient (WNNt) model. It can be corrected with higher-order terms, which requires solving the linear singular system (7.15), as detailed in Appendix 7.4.2. We show in particular that singular higher-order solutions are orthogonal to the first order order solution $\mathbf{I}(t)$, and that the action of Φ need not be computed explicitly but can in practice be replaced by the action of e^{-Lt} .

7.2.1 Application case: the flow past a backward-facing step

The WNNt model is applied to the backward-facing step flow for $Re = 500$ and $t_o = t_{o,m} = 58$. See Appendix 7.4.1 for details about the numerical method. For these parameters, the linear optimal structures (fig. 7.4) and gain are validated with the results presented in Blackburn et al. (2008). The quadratic term in (7.20), although asymptotically correct, happens to be insufficient to capture the nonlinear saturation of the transient gain for this particular flow, in particular because of the weak value of the coefficient $\mu_2(t)$. Indeed, $\mathbf{I}(t_o) = \mathbf{v}_o$ appears to be dominated by a specific spatial wavenumber (see figure 7.4b), thus the field $\tilde{\mathbf{u}}_2$, being generated by the nonlinear interaction of $\mathbf{I}(t)$ with itself, is dominated by spatial harmonics and its projection on $\mathbf{I}(t)$ is close to zero. For this flow the WNNt model therefore needs to be extended to order ϵ_o^3 (see Appendix 7.4.2), yielding

$$\frac{dA}{dt} = \epsilon_o A^2 \frac{d\mu_2}{dt} + \epsilon_o^2 A^3 \frac{d\mu_3}{dt}, \quad A(0) = \alpha, \quad (7.21)$$

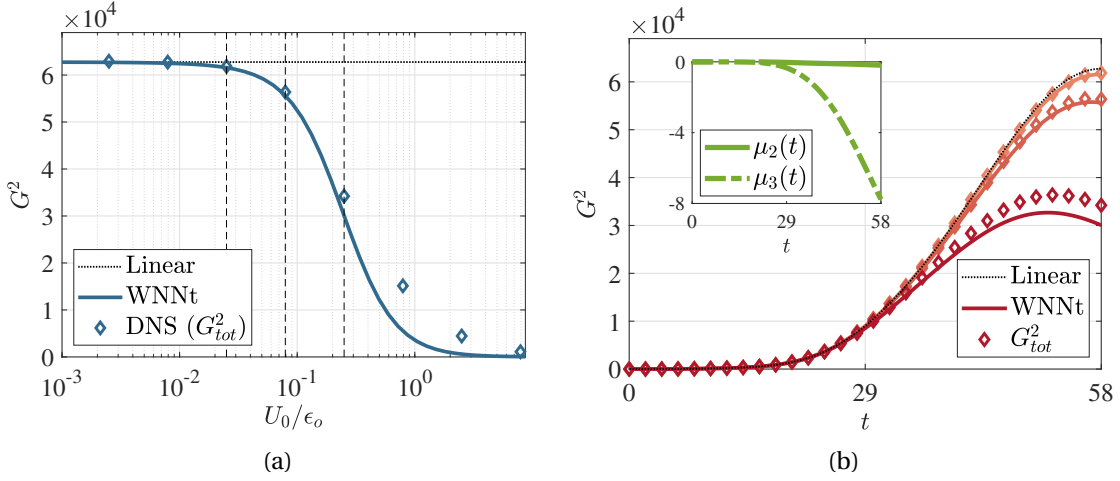


Figure 7.5: Transient gain in the flow past a BFS (sketched in figure 7.2a) for $Re = 500$. **(a)** Gain squared $G(t_o)^2$ for $t_o = t_{o,m} = 58$ as a function of the amplitude of the initial condition. **(b)** History of the gain squared for $0 \leq t \leq t_{o,m}$ and for three amplitudes of initial condition, $U_0/\epsilon_o = [0.025, 0.08, 0.25]$ (vertical dashed lines in (a)); larger amplitudes darker. Inset: weakly nonlinear coefficients $\mu_2(t)$ (continuous line) and $\mu_3(t)$ (dashed-dotted line) as a function of time.

where

$$\mu_3(t) \doteq \frac{\langle \tilde{\mathbf{u}}_3(t), \mathbf{l}(t) \rangle}{\langle \mathbf{l}(t), \mathbf{l}(t) \rangle}, \quad (7.22)$$

and

$$\frac{d\tilde{\mathbf{u}}_3}{dt} = L\tilde{\mathbf{u}}_3 - 2[C(\mathbf{l}, \tilde{\mathbf{u}}_2) - \mu_2 C(\mathbf{l}, \mathbf{l}) + \dot{\mu}_2(\tilde{\mathbf{u}}_2 - \mu_2 \mathbf{l})], \quad \tilde{\mathbf{u}}_3(0) = \mathbf{0}.$$

Equation (7.21) is similar to (7.20), although corrected by a cubic term. We formulate the amplitude equation (7.21) in terms of the rescaled quantities $a = \epsilon_o A$ and the amplitude of the initial condition $U_0 = \|\mathbf{U}(0)\| = \alpha \epsilon_o^2$:

$$\frac{da}{dt} = a^2 \frac{d\mu_2}{dt} + a^3 \frac{d\mu_3}{dt}, \quad a(0) = \frac{U_0}{\epsilon_o}. \quad (7.23)$$

In this manner, the weakly nonlinear transient gain becomes $G(t_o) = a(t_o)/U_0$. Note that in (7.23) the amplitude $a(t)$ does not depend on U_0 nor on ϵ_o independently, but on their ratio U_0/ϵ_o . Thus, as expected, increasingly nonlinear regimes are found when the amplitude of the initial condition increases with respect to the linear gain.

Predictions from equation (7.23) are shown in figure 7.5 together with the linear and fully nonlinear DNS gain evaluated as $G_{tot}(t) = \|\mathbf{U}(t) - \mathbf{U}_e\|/U_0$. In figure 7.5a, the WNNt model extended to $O(\epsilon_o^3)$ appears to capture the weakly evolution of the transient gain with satisfactory precision. When the amplitude of the initial condition is too large, the higher-order

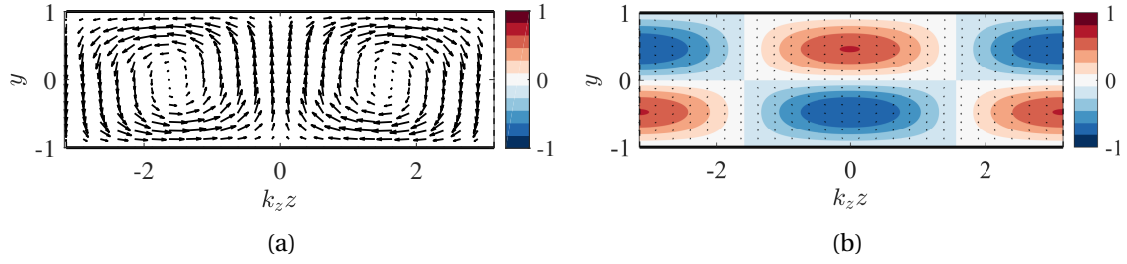


Figure 7.6: **(a)** Optimal initial condition \mathbf{u}_o for the plane Poiseuille flow (sketched in figure 7.2b) for $(Re, k_x, k_z) = (3000, 0, 2)$ and $t_o = t_{o,m} = 230$. Arrows: cross-sectional velocity field $(u_{o,z}, u_{o,y})$. Contours: streamwise component $u_{o,x}$. **(b)** Evolution \mathbf{v}_o at $t = t_o$. Both fields are normalised as $\|\mathbf{u}_o\| = \|\mathbf{v}_o\| = 1$. Initial vortices have a null streamwise component $u_{o,x}$, and streaks at $t = t_o$ have negligible cross-sectional components $(v_{o,z}, v_{o,y})$. Only one wavelength $-\pi \leq k_z z \leq \pi$ is shown.

fields $\tilde{\mathbf{u}}_2, \tilde{\mathbf{u}}_3, \dots$ are expected to have a significant amplitude, and thus the WNNt prediction deteriorates since it is based on an asymptotic hierarchy. In figure 7.5b, the gain history of $G_{tot}(t)$ for all times $0 \leq t \leq t_o$ is successfully compared to $a(t)\|\mathbf{l}(t)\|/U_0$. The coefficient $\mu_3(t)$ is much larger than $\mu_2(t)$ (inset), and is largely dominated by the part of $\tilde{\mathbf{u}}_3$ generated by the forcing term $C(\mathbf{l}, \tilde{\mathbf{u}}_2)$. Since $\mu_3(t)$ is monotonically decreasing toward $\mu_3(t_o) = -7.77$, larger times are subject to a stronger saturation. This leads to a decrease of the time for which the specific initial condition \mathbf{u}_o leads to a maximum transient gain, consistently with the DNS results.

7.2.2 Application case: lift-up in the plane Poiseuille flow

The WNNt is now applied to the plane Poiseuille flow. The set of parameters $(Re, k_x, k_z, t_o) = (3000, 0, 2, t_{o,m} = 230)$ is selected. In both the linear and nonlinear computations, the wavenumber $k_x = 0$ is maintained such that the fields are constant in x , and only the dependence in y and z is computed. Contrarily to the application case in chapter 2, perturbations can now be fully three-dimensional (i.e. $\mathbf{u} = (u_x(y, z), u_y(y, z), u_z(y, z))$). The computations are performed in the spanwise-periodic box $(y, z) \in [-1, 1] \times [-\pi/2, \pi/2] \equiv \Omega$. All the scalar products are taken upon integration inside this periodic box, in particular for the normalisation $\langle \mathbf{u}_o, \mathbf{u}_o \rangle = \langle \mathbf{v}_o, \mathbf{v}_o \rangle = 1$, and for the evaluation of the weakly nonlinear coefficients. The linear optimal gain is validated with the result of Schmid and Henningson (2001); the associated optimal initial condition and its evolution at $t = t_o$ are shown in figures 7.6a and 7.6b, respectively. The optimal initial condition consists of vortices aligned in the streamwise direction; as these streamwise vortices are superimposed on the parabolic base flow, they bring low-velocity fluid from the wall towards the channel centre and high-velocity fluid from the centre of the channel towards the walls, thus generating alternated streamwise streaks. Due to the spanwise periodicity of the optimal initial condition \mathbf{u}_o , all the solutions at even orders ϵ_o^{2n} ($n = 1, 2, 3, \dots$) only yield even spatial harmonics in k_z and are orthogonal to $\mathbf{l}(t)$, such that the coefficient

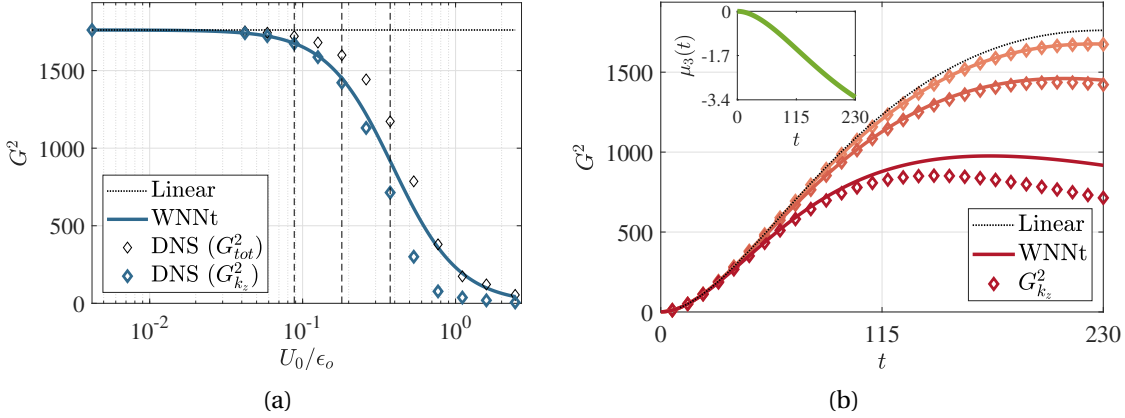


Figure 7.7: Transient gain in the plane Poiseuille flow (sketched in figure 7.2b) for $(Re, k_x, k_z) = (3000, 0, 2)$. **(a)** Gain squared $G(t_o)^2$ for $t_o = t_{o,m} = 230$ as a function of the amplitude of the initial condition. Streamwise invariance $k_x = 0$ is enforced in the DNS as well. **(b)** History of the gain squared for $0 \leq t \leq t_{o,m}$ and for three amplitudes of initial condition, $U_0/\epsilon_0 = [0.088, 0.18, 0.37]$ (vertical dashed lines in (a)); larger amplitudes darker. Inset: weakly nonlinear coefficient $\mu_3(t)$ as a function of time.

$\mu_2(t)$ defined in (7.18) is null at all times. Therefore, (7.23) reduces to

$$\frac{da}{dt} = a^3 \frac{d\mu_3}{dt}, \quad a(0) = \frac{U_0}{\epsilon_0}, \quad (7.24)$$

and $\tilde{\mathbf{u}}_3$ solves the simplified equation

$$\frac{d\tilde{\mathbf{u}}_3}{dt} = L\tilde{\mathbf{u}}_3 - 2C(\tilde{\mathbf{u}}_2, \mathbf{l}), \quad \tilde{\mathbf{u}}_3(0) = \mathbf{0}. \quad (7.25)$$

The analytical solution of (7.24) is written

$$a(t) = \frac{U_0}{\epsilon_0} \left[1 - \left(\frac{U_0}{\epsilon_0} \right)^2 2\mu_3(t) \right]^{-1/2}. \quad (7.26)$$

We show in Appendix 7.4.3 that, at first order in the gain variation, (7.26) reduces to the sensitivity of the transient gain to the base flow modification $(U_0/\epsilon_0)^2 \tilde{\mathbf{u}}_2(t)$.

Predictions from equation (7.26) are shown in figure 7.7 together with the linear and fully nonlinear DNS gains. These DNS gains are evaluated in two ways: using either the total perturbation around the base flow, for G_{tot} (already defined), or using only the part of the perturbation fluctuating at k_z along z , for G_{k_z} (in the same manner that we considered only the component oscillating at ω_o in the computation of the gain in the harmonic forcing part). Indeed, $a(t)$ multiplies the linear trajectory field $\mathbf{l}(t)$ that is purely fluctuating at k_z along z . The WNNt model predicts G_{k_z} accurately in the weakly nonlinear regime for $t = t_{o,m}$, which supports our approach (figure 7.7a). In the strongly nonlinear regime, beyond $U_0/\epsilon_0 \approx 0.4$, the model overestimates G_{k_z} . This can be interpreted by noting that G_{tot} is twice as large as G_{k_z} ,

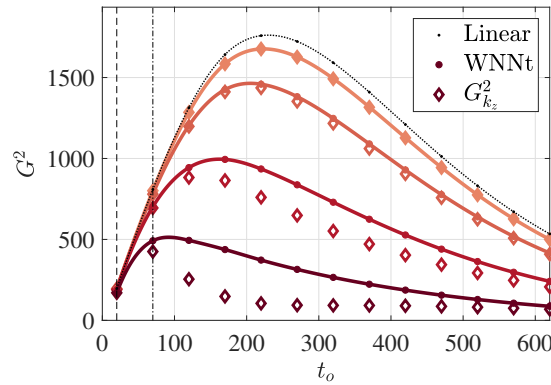


Figure 7.8: Gain envelope in the plane Poiseuille flow for $Re = 3000$ and $k_x = 0$ (maintained in the DNS as well); the numerical box has a length of π and periodic boundary conditions in the spanwise (z) direction, so the optimisation algorithm automatically select the most amplified wavenumber among all harmonics $k_z = 2n$ with $n = 1, 2, \dots$. Optimisation times are $t_o = 20, 70, 120, \dots, 620$: the times $t_o = 20$ (horizontal dashed line), $t_o = 70$ (horizontal dashed-dotted line) and $t_o \geq 120$ correspond respectively to $k_z = 6$, $k_z = 4$ and $k_z = 2$. Four amplitudes of initial condition, $U_0/\epsilon_{o,m} = [0.088, 0.18, 0.37, 0.77]$ are selected, the larger amplitudes are darker.

i.e. more energy is contained in the higher-order terms generated by the linear response than in the linear response itself. Therefore, this is not the amplitude equation (7.26) that breaks down, but the very idea of an asymptotic expansion. Whether higher-order terms remain smaller than the fundamental is certainly flow dependent, and the WNNt model is expected to be even more accurate when this is the case, as shown in §7.2.1 for the flow past a BFS, which generated rather weak higher-order fields.

Figure 7.7b compares for $t \leq t_o$ the history of the approximated gain $a(t)||\mathbf{l}(t)||/U_0$ with that of the DNS gain G_{k_z} , and shows a convincing overall agreement. The coefficient $\mu_3(t)$ is negative and decays monotonically with time until $\mu_3(t_o) = -3.30$ (inset), enhancing the saturation. This results in a reduction of the approximated optimal time with the amplitude of the initial condition, as also observed in the DNS.

The impact of the optimisation time t_o (and therefore the one of ϵ_o) on the WNNt predictions is studied in Fig.7.8. The weakly nonlinear evolution of the gain envelope for an increasing amplitude of the initial condition is reported together with DNS data. For each optimisation time, the (linear) corresponding optimal initial condition is applied. The agreement between WNNt and DNS is satisfactory over the whole range of optimisation times t_o , particularly those associated with lower linear gain as they require higher U_0 to reach a fully nonlinear regime; on the contrary optimisation times for which the linear gains are large are subject to a more pronounced degradation of the predictions in the considered range of U_0 . However, the decrease of both the maximum gain and the time for which it is reached is well captured by the WNNt model.

7.3 Conclusions

In summary, we have derived an amplitude equation for non-normal systems, describing the transient response to a linearly optimal initial condition, in a weakly nonlinear regime. We shall highlight once again that, in the derivation of the amplitude equation, the presence of a neutral or weakly damped mode was not assumed. In analogy with the approach proposed in chapter 2, the procedure is based on the fact that the propagator operator can be made singular by perturbing it slightly, which can be encompassed in a multiple scale asymptotic expansion closed by a classical compatibility condition.

Predictions of the amplitude equation have been compared with fully nonlinear simulations, both in parallel and non-parallel two-dimensional flows. In all cases, they predict accurately the supercritical nonlinear evolution of the response as the amplitude of the initial condition is increased.

The method presents numerous possibilities for extension. (i) Multiple trajectories could be encompassed in the weakly nonlinear expansion, resulting in a system of coupled amplitude equations. The nonlinear interactions of transient responses are particularly relevant when distinct structures lead to comparable gains, for instance, optimal and sub-optimal initial conditions (Blackburn et al., 2008; Butler and Farrell, 1992). (ii) The assumption of a time-independent state operator and the associated operator exponential formalism is unnecessary, and the developments can be adapted to time-varying base flows. (iii) Since the amplitude equation characterizes the transient gain in a weakly nonlinear regime, it can be accounted for to yield a slightly more general optimisation problem than that in (7.3). For a given amplitude of the initial condition, this generalized optimisation problem would result in the maximum gain attainable in the weakly nonlinear regime (at least under the approximation of the amplitude equation). Only in the limit where the initial amplitude vanishes should the problem be equivalent to (7.3). The ensuing structures would constitute weakly nonlinear optimal structures, which could be compared with fully nonlinear ones Pringle and Kerswell (2010).

Extensions (ii) will be treated in the next chapter, chapter 8, where we adapt the method to characterize the transient response over the diffusing (time-varying) Lamb-Oseen vortex flow. This particular flow was also selected as it is notoriously known to experience a bypass transition. In other terms, nonlinearities have an "anti-saturating" role, in contrast with that considered in this chapter, in figure 7.5a and figure 7.7a, and the relevance of the amplitude equation in such case will be studied in details.

Extension (iii) will be realized in chapter 9. For a given pair of wavenumbers, the distortion of the optimal initial condition as we account for weak nonlinearities and increase the initial amplitude will be illustrated on the three-dimensional plane Poiseuille flow. The question of whether this weakly nonlinear optimal is more relevant than the linear ones to trigger turbulence will be discussed.

Finally, it should be noted that the proposed method is not restricted to the Navier-Stokes equations, but applies to all nonlinear systems whose linearised operator exhibits strong non-normality (see Trefethen and Embree, 2005 §55-60 for a comprehensive discussion, as well as the situations discussed in the introduction). For instance in ecological models describing the temporal evolution of a population, such as the canonical Lotka-Volterra predator-prey equations, the so-called resilience of a community (spectral abscissa of the Jacobian of the system) is known to be sometimes a misleading or incomplete measure (Neubert & Caswell, 1997). The conjunction of non-normality and nonlinearity is then key to predicting a population's extinction/survival.

7.4 Appendix

7.4.1 Applying the WNNt model to the Navier–Stokes equations.

For the transient growth model, the linearised problem writes

$$B \frac{d\mathbf{q}}{dt} = L\mathbf{q} \quad \text{subject to} \quad \mathbf{q}(0) = \begin{bmatrix} \mathbf{u}(0) \\ 0 \end{bmatrix}, \quad (7.27)$$

with the state vector $\mathbf{q} = [\mathbf{u}, p]^T$, the singular mass matrix

$$B = \begin{bmatrix} I & 0 \\ 0 & 0 \end{bmatrix},$$

and the linearised Navier–Stokes operator

$$L = \begin{bmatrix} -(\mathbf{U}_e \cdot \nabla) * -(* \cdot \nabla) \mathbf{U}_e + Re^{-1} \Delta(*) & \nabla(*) \\ \nabla \cdot (*) & 0 \end{bmatrix}.$$

Several subtleties arise from the peculiarity of the pressure variable, that ensures the instantaneous satisfaction of the incompressibility condition: (i) the absence of time-derivative of the pressure results in a singular mass matrix, (ii) forcing terms remain restricted to the momentum equations as we choose to have no source/sink of mass and (iii) the pressure is not included in the energy norm of the response.

The gain is measured as

$$G(t_0)^2 = \frac{\langle \mathbf{q}(t_0), \mathbf{q}(t_0) \rangle_B}{\langle \mathbf{q}(0), \mathbf{q}(0) \rangle_B}, \quad (7.28)$$

where the pressure component of the initial condition can be chosen as $p(0) = 0$. We used the following scalar product

$$\langle \hat{\mathbf{q}}_a, \hat{\mathbf{q}}_b \rangle_B = \int_{\Omega} \left(\hat{u}_{a,x}^* \hat{u}_{b,x} + \hat{u}_{a,y}^* \hat{u}_{b,y} + \hat{u}_{a,z}^* \hat{u}_{b,z} \right) d\Omega, \quad \text{where}$$

the B -scalar product excludes pressure, such that the pseudonorm $\langle \hat{\mathbf{q}}, \hat{\mathbf{q}} \rangle_B = \|\hat{\mathbf{q}}\|_B^2$ is the kinetic energy.

The orthogonality properties holds under the B -scalar product, and the weakly nonlinear coefficient $\mu_2(t)$ writes

$$\mu_2(t) = \epsilon_o \frac{\langle \tilde{\mathbf{q}}_2(t), \mathbf{q}_1(t) \rangle_B}{\langle \mathbf{q}_1(t), \mathbf{q}_1(t) \rangle_B}, \quad (7.29)$$

where $\mathbf{q}_1(t) = [\mathbf{l}(t), p_1(t)]^T$, and where $\tilde{\mathbf{q}}_2 = [\tilde{\mathbf{u}}_2(t), \tilde{p}_2(t)]^T$ is solution of

$${}_B \frac{d\tilde{\mathbf{q}}_2}{dt} = L\tilde{\mathbf{q}}_2 - \begin{bmatrix} C(\mathbf{l}, \mathbf{l}) \\ 0 \end{bmatrix}, \quad \tilde{\mathbf{q}}_2(0) = \mathbf{0}. \quad (7.30)$$

Again, pressure does not influence the weakly nonlinear coefficient since only velocity fields are involved in the scalar product. In particular at $t = t_o$, $\mathbf{q}_1(t_o) = [\mathbf{v}_o, p_1(t_o)]^T$ thus

$$\langle \mathbf{q}_1(t_o), \mathbf{q}_1(t_o) \rangle_B = 1 \quad (7.31)$$

by construction, and

$$\mu_2(t_o) = \epsilon_o \int_{\Omega} \tilde{u}_{2,x} v_{o,x} + \tilde{u}_{2,y} v_{o,y} + \tilde{u}_{2,z} v_{o,z} d\Omega. \quad (7.32)$$

The software FreeFem++ is again used to solve for the velocity and pressure by means of the Finite Element Method with Taylor-Hood elements, (P2 for velocity and P1 for pressure). The practical computation of the gain (7.28) proposed in Garnaud et al. (2013a) is followed. The application of the propagator e^{Lt} (resp. its adjoint $(e^{Lt})^\dagger$) are performed by integrating in time the linearised problem (7.27) (resp. the adjoint problem) with the Crank-Nicolson method. The application of the inverse propagator e^{-Lt} is never needed.

For the transient growth past the backward-facing step studied in §7.2.1, our linear optimisation codes are validated upon comparison with the results of Blackburn et al. (2008). For $(Re, t_o) = (500, 58)$, we obtained $G(t_o)^2 = 62.8 \times 10^3$, against $G(t_o)^2 = 63.1 \times 10^3$ in Blackburn et al. (2008). The $\approx 0.5\%$ relative error could be explained by the fact that our entrance length is $L_i = 5$, against $L_i = 10$ in Blackburn et al. (2008). For the plane Poiseuille flow analysed in §7.2.2, the validation was performed thanks to the open-source results of Schmid and Henningson (2001), obtained with a Chebyshev polynomial discretisation, and where the singular value decomposition of the matrix exponential e^{Lt} is performed directly. For the chosen set of parameters $(Re, k_x, k_z, t_o) = (3000, 0, 2, 230)$, convergence was achieved for a squared linear gain of $G(t_o)^2 = 1761.8$, against $G(t_o)^2 = 1761.9$ in Schmid and Henningson (2001).

7.4.2 Higher-order corrections of the WNNt equation.

Recall the equation (7.15) obtained at order ϵ_0^2 :

$$\Phi \mathbf{u}_2 = \alpha \mathbf{u}_0 + A^2 e^{-Lt} \tilde{\mathbf{u}}_2 - \frac{dA}{dT} \epsilon_0 \mathbf{u}_0 t - A \mathbf{u}_0.$$

After satisfaction of the Fredholm alternative, which leads to an equation for the amplitude A , the relation (7.15) can be re-expressed as

$$\Phi \mathbf{u}_2 = A^2 (e^{-Lt} \tilde{\mathbf{u}}_2 - \epsilon_0 \mu_2 \mathbf{u}_0) \quad \text{for } t > 0, \quad (7.33)$$

where the orthogonality of the right-hand side (RHS) with $\mathbf{a}(t)$ is ensured by construction of $\mu_2(t) = \langle \tilde{\mathbf{u}}_2(t), \mathbf{l}(t) \rangle / \langle \mathbf{l}(t), \mathbf{l}(t) \rangle$ in (7.18). The general solution to (7.33) reads $\mathbf{u}_2 = \mathbf{u}_2^{(\perp L)} + A_2 \mathbf{l}(t)$. The particular solution of the system, $\mathbf{u}_2^{(\perp L)}$, is obtained by solving (7.33) after replacing $\Phi(t)$ by e^{-Lt} . Indeed, such $\mathbf{u}_2^{(\perp L)}$ must be orthogonal to $\mathbf{l}(t)$, since $0 = \langle \text{RHS}, \mathbf{a}(t) \rangle = \langle e^{Lt} (\text{RHS}), \mathbf{l}(t) \rangle = \langle \mathbf{u}_2^{(\perp L)}, \mathbf{l}(t) \rangle$. On the other hand, the term $A_2 \mathbf{l}(t)$ constitutes the homogeneous part of the solution, where A_2 is a scalar amplitude. It can be kept in further calculations, provided it is included in the final amplitude for $\mathbf{l}(t)$, which would then become $\epsilon_0 A + \epsilon_0^2 A_2 + O(\epsilon_0^3)$. Instead, and without loss of generality (Fujimura (1991)), we propose to set $A_2 = 0$ such that

$$\mathbf{u}_2 = \mathbf{u}_2^{(\perp L)} = A^2 (\tilde{\mathbf{u}}_2 - \mu_2 \mathbf{l}) \quad \text{for } t > 0. \quad (7.34)$$

In particular, this implies that the term $\partial_t(P\mathbf{u}_2)$ that appears at order $O(\epsilon_0^3)$ actually vanishes since $P\mathbf{u}_2 = P\mathbf{u}_2^{(\perp L)} = \mathbf{0}$. If this is performed at each order $j \geq 3$, all the terms $\partial_t(P\mathbf{u}_j)$ vanish. In this way, the "retroaction" forcing due to the operator perturbation only appears at $O(\epsilon_0^2)$.

Deriving a higher-order amplitude equation for transient growth requires introducing a very long time scale $\tau = \epsilon_0^2 t$, such that $A = A(T, \tau)$. The total derivative in T should then be replaced as partial derivative, and the amplitude equation derived at order ϵ_0^2 writes $\partial_T A = A^2 \dot{\mu}_2$ subject to $\lim_{t \rightarrow 0} (\alpha - A) = 0$. One gathers at order ϵ_0^3 for $t > 0$:

$$\begin{aligned} \partial_t(\Phi \mathbf{u}_3) &= -2A^3 e^{-Lt} C(\mathbf{l}, \mathbf{u}_2) - e^{-Lt} \partial_T \mathbf{u}_2 - e^{-Lt} \partial_\tau \mathbf{u}_1 - \partial_t(P\mathbf{u}_2) \\ &= -2A^3 H e^{-Lt} [C(\mathbf{l}, \tilde{\mathbf{u}}_2) - \mu_2 C(\mathbf{l}, \mathbf{l})] - 2A(\partial_T A) (e^{-Lt} \tilde{\mathbf{u}}_2 - \epsilon_0 \mu_2 \mathbf{u}_0) - \epsilon_0 \mathbf{u}_0 \partial_\tau A \\ &= -2A^3 e^{-Lt} [C(\mathbf{l}, \tilde{\mathbf{u}}_2) - \mu_2 C(\mathbf{l}, \mathbf{l}) + \dot{\mu}_2 (\tilde{\mathbf{u}}_2 - \mu_2 \mathbf{l})] - \epsilon_0 \mathbf{u}_0 \partial_\tau A, \end{aligned} \quad (7.35)$$

since (i) $\partial_T \mathbf{u}_2 = 2A(\partial_T A) (\tilde{\mathbf{u}}_2 - \mu_2 \mathbf{l})$, (ii) $P\mathbf{u}_2 = \mathbf{0}$, and (iii) $e^{-Lt} \partial_\tau \mathbf{u}_1 = H e^{-Lt} \mathbf{l} \partial_\tau A = H \epsilon_0 \mathbf{u}_0 \partial_\tau A$. Equation (7.35) is subject to $\mathbf{u}_3(0) = \mathbf{0}$. Its particular solution yields

$$\mathbf{u}_3(t, T, \tau) = A(T, \tau)^3 \mathbf{u}_3^{(a)}(t) + \frac{\partial A(T, \tau)}{\partial \tau} \mathbf{u}_3^{(b)}(t), \quad (7.36)$$

where

$$\begin{aligned} d_t \left[\Phi \mathbf{u}_3^{(a)} \right] &= -2e^{-Lt} \left[C(\mathbf{l}, \tilde{\mathbf{u}}_2) - \mu_2 C(\mathbf{l}, \mathbf{l}) + \dot{\mu}_2 (\tilde{\mathbf{u}}_2 - \mu_2 \mathbf{l}) \right], \quad \text{and} \\ d_t \left[\Phi \mathbf{u}_3^{(b)} \right] &= -\epsilon_o \mathbf{u}_o, \end{aligned}$$

subject to the initial conditions $\mathbf{u}_3^{(a)}(0) = \mathbf{u}_3^{(b)}(0) = \mathbf{0}$. After time integration, we obtain

$$\Phi \mathbf{u}_3 = A^3 e^{-Lt} \tilde{\mathbf{u}}_3 - \epsilon_o \mathbf{u}_o t \partial_\tau A, \quad t > 0, \quad (7.37)$$

where $\tilde{\mathbf{u}}_3$ is solution of

$$\frac{d\tilde{\mathbf{u}}_3}{dt} = L\tilde{\mathbf{u}}_3 - 2 \left[C(\mathbf{l}, \tilde{\mathbf{u}}_2) - \mu_2 C(\mathbf{l}, \mathbf{l}) + \dot{\mu}_2 (\tilde{\mathbf{u}}_2 - \mu_2 \mathbf{l}) \right], \quad \tilde{\mathbf{u}}_3(0) = \mathbf{0}.$$

Canceling the projection of the RHS of (7.37) on $\mathbf{a}(t)$, dividing the ensuing relation by $\langle \mathbf{a}(t), \mathbf{u}_o \rangle$, and taking the partial derivative with respect to t leads to

$$\epsilon_o A^3 \frac{d\mu_3}{dt} = \epsilon_o \frac{\partial A}{\partial t}, \quad t > 0, \quad (7.38)$$

where

$$\mu_3(t) = \epsilon_o^{-1} \frac{\langle e^{-Lt} \tilde{\mathbf{u}}_3(t), \mathbf{a}(t) \rangle}{\langle \mathbf{u}_o, \mathbf{a}(t) \rangle} = \frac{\langle \tilde{\mathbf{u}}_3(t), \mathbf{l}(t) \rangle}{\langle \mathbf{l}(t), \mathbf{l}(t) \rangle}.$$

To be meaningful, equation (7.38) and its initial condition must be re-written solely in terms of t , which is done by evaluating $T = \epsilon_o t$ and $\tau = \epsilon_o^2 t$. The *total* derivative of A , denoted $d_t A$, is now needed, as it takes into account the *implicit* dependence of A ; it reads $d_t A = \partial_t A + \epsilon_o \partial_T A + \epsilon_o^2 \partial_\tau A = \epsilon_o \partial_T A + \epsilon_o^2 \partial_\tau A$, such that

$$\epsilon_o A^2 \frac{d\mu_2(t)}{dt} + \epsilon_o^2 A^3 \frac{d\mu_3(t)}{dt} = \frac{dA}{dt}, \quad t > 0,$$

subject to $\lim_{t \rightarrow 0} (\alpha - A(\epsilon_o t, \epsilon_o^2 t)) = 0$ so $A(t \rightarrow 0) = \alpha$ and the amplitude A is extended by continuity in $t = 0$ so as to impose $A(0) = \alpha$.

7.4.3 Transient gain sensitivity and comparison with the WNNt model.

We consider a linear system $\partial_t \mathbf{u} = L\mathbf{u}$ subject to the initial condition $\mathbf{u}(0)$ with $\|\mathbf{u}(0)\| = 1$. The linear transient gain at $t = t_o$ writes $G_o = \|\mathbf{u}(t_o)\|$. A variational method is used to derive the variation of the optimal transient gain induced by a small perturbation δL of operator. Let us introduce the Lagrangian

$$\mathcal{L} = G_o^2 - \int_0^{t_o} \langle \partial_t \mathbf{u} - L\mathbf{u}, \mathbf{u}^\dagger \rangle dt - \beta (1 - \|\mathbf{u}(0)\|^2),$$

where the Lagrange multipliers \mathbf{u}^\dagger and β enforce the constraints on the state equation and on the norm of the initial condition, respectively. Imposing $\langle \partial_{\mathbf{u}} \mathcal{L}, \delta \mathbf{u} \rangle = 0$ for all $\delta \mathbf{u}$ leads to the adjoint equation $\partial_t \mathbf{u}^\dagger = -L^\dagger \mathbf{u}^\dagger$, to be integrated backward in time from the terminal condition $\mathbf{u}^\dagger(t_o) = 2\mathbf{u}(t_o)$. Eventually, the gain variation induced by δL is

$$\delta(G_o^2) = \left\langle \frac{\partial \mathcal{L}}{\partial L}, \delta L \right\rangle = \int_0^{t_o} \langle (\delta L) \mathbf{u}, \mathbf{u}^\dagger \rangle dt. \quad (7.39)$$

(Note that formula (7.39) was also derived in Meliga (2018) although using a different approach). On the other hand, we derived in the main text for the WNNt model:

$$a(t) = \frac{U_0}{\epsilon_o} \left[1 - \left(\frac{U_0}{\epsilon_o} \right)^2 2\mu_3(t) \right]^{-1/2}. \quad (7.40)$$

The weakly-nonlinear transient gain squared can be expressed as $G(t_o)^2 = (a(t_o)/U_0)^2$, while the linear gain squared is $G_o^2 = (1/\epsilon_o)^2$, such that

$$\frac{1}{G(t_o)^2} - \frac{1}{G_o^2} = -U_0^2 2\mu_3(t_o).$$

We are interested in small variations around G_o^2 , thus we write $G(t_o)^2 = G_o^2 + \delta G_o^2$ with $|\delta G_o^2/G_o^2| \ll 1$. In this manner, $1/G_o^2 - 1/G(t_o)^2 = \delta(G_o^2)/G_o^4 + h.o.t$, eventually leading to

$$\delta(G_o^2) = 2\mu_3(t_o) \frac{U_0^2}{\epsilon_o^4}.$$

In addition,

$$\mu_3(t_o) = \epsilon_o^{-1} \frac{\langle e^{-Lt_o} \tilde{\mathbf{u}}_3(t_o), \mathbf{a}(t_o) \rangle}{\langle \mathbf{u}_o, \mathbf{a}(t_o) \rangle},$$

with $\tilde{\mathbf{u}}_3(t) = -e^{Lt} \int_0^t 2e^{-Ls} C[\tilde{\mathbf{u}}_2(s), \mathbf{l}(s)] ds$. Therefore

$$\begin{aligned} \mu_3(t_o) &= -\epsilon_o^{-1} \frac{\langle \int_0^{t_o} 2e^{-Ls} C[\tilde{\mathbf{u}}_2(s), \mathbf{l}(s)] ds, \mathbf{a}(t_o) \rangle}{\langle \mathbf{u}_o, \mathbf{a}(t_o) \rangle} \\ &= -\epsilon_o^{-1} \frac{\int_0^{t_o} \langle 2e^{-Ls} C[\tilde{\mathbf{u}}_2(s), \mathbf{l}(s)], \mathbf{a}(t_o) \rangle ds}{\langle \mathbf{u}_o, \mathbf{a}(t_o) \rangle}. \end{aligned}$$

By definition, $\mathbf{a}(t_o) = (e^{Lt_o})^\dagger \mathbf{l}(t_o)$ and $\langle \mathbf{u}_o, \mathbf{a}(t_o) \rangle = \langle e^{Lt_o} \mathbf{u}_o, \mathbf{l}(t_o) \rangle = 1/\epsilon_o$. In addition, $(e^{-Ls})^\dagger (e^{Lt_o})^\dagger = (e^{Lt_o} e^{-Ls})^\dagger = (e^{-L(s-t_o)})^\dagger$, such that

$$\mu_3(t_o) = - \int_0^{t_o} \langle 2C[\tilde{\mathbf{u}}_2(s), \mathbf{l}(s)], (e^{-L(s-t_o)})^\dagger \mathbf{l}(t_o) \rangle ds.$$

In terms of our previous notations, we have the direct correspondence $\mathbf{u}(t) = \mathbf{l}(t)/\epsilon_o$ and $\mathbf{u}^\dagger(s) = (e^{-L(s-t_o)})^\dagger 2\mathbf{u}(t_o)$, so we can write

$$\begin{aligned} \delta(G_o^2) &= \left(\frac{2U_o^2}{\epsilon_o^4} \right) \left(-\frac{\epsilon_o^2}{2} \int_0^{t_o} \langle 2C[\tilde{\mathbf{u}}_2(s), \mathbf{u}(s)], (e^{-L(s-t_o)})^\dagger 2\mathbf{u}(t_o) \rangle ds \right) \\ &= - \int_0^{t_o} \langle 2C[(U_o/\epsilon_o)^2 \tilde{\mathbf{u}}_2(s), \mathbf{u}(s)], \mathbf{u}^\dagger(s) \rangle ds. \end{aligned}$$

The sensitivity relation (7.39) is immediately recognised, where δL is here induced by the addition of $(U_o/\epsilon_o)^2 \tilde{\mathbf{u}}_2$ to the base flow. Indeed, $U_o/\epsilon_o = a_{lin}$ is the linear solution of (7.40) corresponding the limit $U_o \rightarrow 0$, such that the flow field is described in this limit by $\mathbf{U}(t) = \mathbf{U}_e + a_{lin}\mathbf{l}(t) + a_{lin}^2 \tilde{\mathbf{u}}_2(t) + O(\epsilon_o^3)$.

8 A weakly nonlinear amplitude equation approach to the bypass transition in the two-dimensional Lamb–Oseen vortex

Remark: This chapter constitutes the article Ducimetière and Gallaire (2023).

8.1 Introduction

The two-dimensional axisymmetric Lamb–Oseen (Gaussian) vortex flow, the vorticity of which is a strictly decreasing radial function, is linearly stable: the eigenvalues of L , the linearized Navier–Stokes operator around this flow, all possess a positive or null damping rate. In fact, even in the absence of viscosity where all damping rates are null, linear perturbations experience an inviscid exponential decay; this phenomenon, called “Landau damping”, was observed and interpreted for instance in Schecter et al. (2000). In particular, it was analytically derived that the Landau damping rate can be related to the vorticity gradient, at the specific radius where the angular velocity associated with the dominant Landau pole is equal to that of the base flow.

The Landau damping can be interpreted in mathematical terms. In an inviscid framework, Schecter et al. (2000) consider at first a “top-hat” base vortex, for which the vorticity decreases slowly then rapidly drops to exactly zero for $r \geq r_v$. This vortex supports a continuum of modes whose critical layers are located at some $r \leq r_v$, where they are singular since the base vorticity gradient is non-zero there; it also supports a discrete (“Kelvin”, according to the terminology of, for instance, Balmforth et al. (2001)) mode whose critical layer is located at $r_c \geq r_v$ where the base vorticity gradient is exactly zero: for this reason, the discrete mode is smooth, regular and can be interpreted as a classical eigenmode. Secondly, Schecter et al. (2000) consider a base vortex that is equivalent to the first, with the addition of a low-vorticity

“skirt” that extends radially to a new, larger, $r_v \geq r_c$. This introduces a non-zero base vorticity gradient at r_c which ruins the regularity of the previously discrete mode. However, Schecter et al. (2000) argue that symptoms of the original discrete mode remain; some of the continuum modes closely resemble the latter in terms of structure and frequency and combine to form what Schecter et al. (2000) call a “quasi-mode”. Therefore, if the discrete mode is used as an initial condition, it will excite the continuum following a Lorentzian distribution that is peaked around the discrete mode frequency (see figure 3 in Schecter et al. (2000)). As time evolves, the continuum modes disperse, and their superposition behaves like an exponentially damped version of the original discrete mode (hence the appellation “quasi-mode”).

Schecter et al. (2000) also consider the response of a Gaussian vortex, such as the one considered here, to a generic external impulse. Although the response does not behave as a single damped wave but projects well on a very large number of structurally different modes, the Landau damping is still found to be relevant and to dominate the initial decay of the perturbation.

Nevertheless, Rossi et al. (1997) evidenced that the Gaussian vortex flow, despite its linear stability, could relax to a new non-axisymmetric, called “tripolar”, state when subject to an arbitrary perturbation of sufficiently large amplitude. Such phenomenology is symptomatic of a subcritical bifurcation. This tripolar structure is well described for instance in Nolan and Farrell (1999) as a vortex for “*which the low vorticity of the moat pools into two satellites of an elliptically deformed central vortex, with the whole structure rotating cyclonically*”. It has been observed in the laboratory experiments of Denoix et al. (1994) as well as in Kloosterziel and van Heijst (1991), Van Heijst and Kloosterziel (1989), and Van Heijst et al. (1991), and described in this last article as being “*a very stable structure, even persisting in a highly sheared fluid environment*”.

This corroborates its importance in geophysical contexts, where tropical cyclones sometimes show rotating elliptical eyes, as was reported for instance by Kuo et al. (1999) for Typhoon Herb, which occurred in Taiwan in 1996. A radar located on the Wu-Feng mountain could measure the horizontal distribution of maximum reflectivity for the Typhoon, from which we observe an elliptical eye (see their figures 1 and 2). The eye was rotating cyclonically with a period of 144 min. Concerned with Hurricane Olivia, which was part of the 1994 Pacific hurricane season, the work of Reasor et al. (2000) also documented an elliptical eye (see their figure 16). The ratio of minor to major axis was approximately 0.7, and the period of (cyclonic) rotation was found to be around 50 min.

A substantial body of theoretical work has therefore been devoted to the apparition and persistence of the tripolar state. Some of them reflect on the problem in terms of the Landau damping, for instance, Balmforth et al. (2001), Le Dizès (2000), Schecter et al. (2000), Turner and Gilbert (2007), and Turner et al. (2008). Common to all these latter works is the following idea: if the perturbation is large enough to nonlinearly feedback on the mean vorticity (averaged in the azimuthal direction), in such a way that the mean vorticity gradient vanishes

near the radius where the angular velocity associated with the dominant Landau pole equates to that of the base flow, then the Landau damping is deactivated. Indeed, it was shown in Schecter et al. (2000), Turner and Gilbert (2007), and Turner et al. (2008) that such cancelling of the Landau damping goes with the appearance of an undamped Kelvin mode. The effects of flattening the mean vorticity distribution have been thoroughly studied in Schecter et al. (2000) and Turner et al. (2008), although it was introduced rather artificially to *a posteriori* mimic nonlinear effects. It has, however, been rigorously quantified using a matched asymptotic expansion in Balmforth et al. (2001), the small parameter being directly linked to the amount of vorticity near the critical radius r_c of the neutral Kelvin mode of a compact vortex, whose vorticity there would be zero otherwise. The developments result in an amplitude equation for the weakly nonlinear quasi-mode, that can predict a secondary instability for a sufficiently strong disturbance amplitude.

Under certain conditions, the vorticity tripole has also been shown to be the nonlinear fate of a shear instability (also sometimes called “barotropic” instability, in opposition to “baroclinic” instability, this latter requiring density stratification). This was illustrated clearly for instance in Carnevale and Kloosterziel (1994), Carton and Legras (1994), Carton et al. (1989), and Kossin et al. (2000), and many other works. If the mean vorticity profile (averaged along the azimuthal direction) presents a local extremum at some radius, a necessary condition for shear instability is satisfied according to a generalization of the Rayleigh theorem of inflectional point by Billant and Gallaire (2005). This is, for instance, the case of the family of shielded monopoles, where the vortex core of positive vorticity is surrounded by a ring of negative vorticity. By increasing the intensity of the shear, the shielded vortex becomes unstable with a maximum growth rate for perturbations of azimuthal wavenumber $m = 2$; by increasing the shear further, $m = 3$ becomes even more unstable (see figure 7 in Carnevale and Kloosterziel (1994)). Inspired by velocity measurements of Hurricane Gilbert that occurred in 1988, Kossin et al. (2000) considered the vorticity of a piecewise-constant vorticity profile. The latter is constituted of four distinct regions of vorticity: an inner region of very high vorticity, a moat region of relatively low vorticity, an annular ring of positive vorticity, and an irrotational far field. Kossin et al. (2000) then show that, by narrowing the moat, a shear instability appears with a maximum growth rate at a wavenumber $m = 2$ (see their figure A1). This shear instability can be conceptualized as resulting from a wave interaction across the moat, between two Rossby waves riding respectively the inner edge of the annular ring, and the outer edge of the central vortex. Note that what we designate here as a “Rossby” wave, according to the terminology of Kossin et al. (2000), is similar to the “Kelvin” mode discussed until now. Nonlinear simulations have then shown this instability to saturate into a tripolar state.

Furthermore, an important ingredient to the subcritical transition towards the tripolar state was found to be the non-normality of the linear operator L . An operator is non-normal if it does not commute with its adjoint, the expression of the latter being relative to the choice of an inner product. The eigenvectors of a non-normal operator do not form an orthogonal basis under this inner product, thus a negative growth rate for all eigenvalues is not a guarantee for the associated norm to decay monotonically. In fact, some small-amplitude perturbations

may experience a large transient amplification. In particular, the linear transient growth analyses conducted for instance in Antkowiak (2005), Antkowiak and Brancher (2004), Heaton and Peake (2007), Mao and Sherwin (2012), and Pradeep and Hussain (2006), have revealed the Lamb-Oseen (and Batchelor) vortex flow to support such strong transient energy growth. Therefore, perturbations to the base flow field, such as free-stream turbulence or acoustic disturbances, can be amplified strongly enough through non-normal, linear, mechanisms to lead to a regime where nonlinearities come into play; the flow may then escape from its linearly stable solution. This conjunction of non-normality then nonlinearity corresponds to the “by-pass” scenario proposed in (Trefethen et al., 1993) and contextualized to the Lamb-Oseen vortex flow in Antkowiak (2005). Recently, the transient growth analysis of the Lamb-Oseen vortex has been numerically extended in the fully nonlinear regime via a Lagrangian optimization in Navrose et al. (2018).

The present work aims at reconciling the simplicity of a weakly nonlinear model (such as in Balmforth et al. (2001) and Sipp (2000)), in the sense that it is easier to solve and interpret than the original equation, with non-normality. Specifically, the objective is to construct an amplitude equation that is not restricted to the description of close-to-neutral modes or quasi-modes, but that extends to responses associated with optimal transient growth.

The amplitude equation analytically derived in this chapter will not restrict the shape of the base flow in order for the latter to support a close-to-neutral mode or a quasi-mode, and will tolerate arbitrary temporal dependence of this base flow; this is precisely because these complexities are already incorporated in the optimal transient growth analysis of which we study the weakly nonlinear continuation. This makes possible the weakly nonlinear analysis of optimal responses on vortices with more realistic vorticity profiles from field measurements. For instance, this could be applied to the profile reported in figure 1 of Kossin et al. (2000), from flight-level radar measurement of Hurricane Gilbert.

The derivation of a weakly nonlinear reduced-order model will make it possible to distinguish the regimes where weak nonlinearities reinforce the transient gain, from the regimes where they cause it to decrease. It will also provide a rough criterion for the minimum amplitude of the initial condition required to trigger a bypass transition away from the axisymmetric state. It will also help us quantify the importance of the distortion of the flow averaged in the azimuthal direction, called “mean flow”, with respect to the importance of the second harmonic in nonlinear effects at stake.

After a brief derivation on the linear formulation in §8.2, the method advanced to derive the amplitude equation is outlined in §8.3; specifically, we vary the amplitude of a given initial condition and predict, at low numerical cost, the gain of the response at a selected time $t = t_o$. The (general) method is then illustrated with the two-dimensional Lamb-Oseen vortex flow with azimuthal wavenumber $m = 2$ in §8.5, exhibiting large gain and subcritical bifurcation.

8.2 Linear formulation

In the following subsection, the formulation of the linear transient growth problem is briefly recalled. In the rest of the chapter, we shall consider a purely two-dimensional flow, invariant and with zero velocity in the axial direction. This two-dimensionality implicitly assumes the flow not to be subject to any three-dimensional instabilities, or any kind of spontaneous axial variations. This assumption is often made in considering vortex flows, and will not be discussed further in the present chapter. Note that the restriction to a two-dimensional flow is not intrinsic to the analytical development proposed in the following, but is simply made to ease the computations thus concentrating our efforts on the analysis of the subcritical transition toward the tripolar state.

Let $\mathbf{U}_b(r, t) = [0, U_{b,\theta}]^T(r, t)$ denote a reference vortex flow, satisfying the Navier-Stokes equations exactly (without body force) and supporting a small-amplitude perturbation field of the form

$$\begin{bmatrix} \mathbf{u} \\ p \end{bmatrix}(r, \theta, t) = \begin{bmatrix} \hat{\mathbf{u}} \\ \hat{p} \end{bmatrix}(r, t)e^{im\theta} + \text{c.c.} \quad (8.1)$$

and $\hat{\mathbf{u}}(r, t) = [\hat{u}_r, \hat{u}_\theta]^T(r, t)$. The invariance of the base flow along the azimuthal (θ) coordinate justifies the Fourier mode expansion of the perturbation in this direction; $m \in \mathbb{Z}$ denotes the wavenumber in the azimuthal direction. Linearizing the Navier-Stokes equations around $\mathbf{U}_b(r, t)$ leads to an equation for the temporal evolution of the velocity field $\hat{\mathbf{u}}(r, t)$

$$\begin{aligned} \partial_t \hat{\mathbf{u}} = & \underbrace{\begin{bmatrix} (\Delta_m - 1/r^2)/Re - im\Omega & -2im/(r^2 Re) + 2\Omega \\ 2im/(r^2 Re) - W_z & (\Delta_m - 1/r^2)/Re - im\Omega \end{bmatrix}}_{\doteq A_m(t)} \hat{\mathbf{u}} - \hat{\nabla}_m \hat{p}(\hat{\mathbf{u}}) \\ & \doteq L_m(t) \hat{\mathbf{u}} \end{aligned} \quad (8.2)$$

where $\hat{\nabla}_m \doteq [\partial_r, im/r]^T$ and

$$\Omega \doteq U_{b,\theta}/r, \quad W_z \doteq \Omega + \partial_r U_{b,\theta}, \quad \Delta_m \doteq \partial_{rr} + (1/r)\partial_r - m^2/r^2. \quad (8.3)$$

The letter Ω denotes the angular velocity of the base flow, where W_z is its vorticity along the z -axis. The operator $im\Omega$ is the advection by the base flow, and Δ_m is the Laplacian associated with viscous diffusion: it is therefore systematically multiplied by $1/Re$. The presence of the pressure term in (8.2) ensures the velocity field $\hat{\mathbf{u}}$ to be divergence free for all times. Indeed, the pressure is linearly linked to the velocity field according to the Poisson equation

$$\Delta_m \hat{p}(\mathbf{u}) = -2i(m\partial_r U_{b,\theta}/r) \hat{u}_r + 2(\partial_r + 1/r)(\Omega \hat{u}_\theta), \quad (8.4)$$

obtained by taking the divergence of the momentum equations, then enforcing the continuity $(\partial_r + 1/r)\hat{u}_r + im\hat{u}_\theta/r = 0$. The perturbation fields are subject to the following boundary

conditions over $r \in [0; +\infty[$, valid for all times

$$\begin{cases} \hat{u}_r|_{r=0} = \hat{u}_\theta|_{r=0} = 0 \\ \partial_r \hat{p}|_{r=0} = 0 \end{cases} \quad \text{for } m \text{ even, and} \quad \begin{cases} \partial_r \hat{u}_r|_{r=0} = \partial_r \hat{u}_\theta|_{r=0} = 0 \\ \hat{p}|_{r=0} = 0 \end{cases} \quad \text{for } m \text{ odd,} \quad (8.5)$$

as well as $\lim_{r \rightarrow \infty} \hat{\mathbf{u}} = \mathbf{0}$. As shown in the appendix of Kerswell and Davey (1996), by imposing the parity conditions (8.5), “*the correct axial behaviour automatically follows without need to explicitly impose the regularity conditions*”.

Only the temporal dependence of the operators will be made explicit in the rest of the chapter; for instance, $L_m(t)$, whose temporal dependence is inherited from the base flow, is actually $L_m(t) = L_m(r, t; \text{Re})$. Precisely due to the fact that it depends on time, the operator exponential formalism cannot be used to solve (8.2). Instead, and given the value of the perturbation field at a time t_i , its temporal evolution at a further time t according to (8.2) formally reads $\hat{\mathbf{u}}(t) = \Psi(t, t_i) \hat{\mathbf{u}}(t_i)$. The operator $\Psi(t, t_i)$ is traditionally named the propagator, for its action directly maps $\hat{\mathbf{u}}(t_i)$ onto $\hat{\mathbf{u}}(t)$ (Farrell & Ioannou, 1996). If $t_i = 0$ in particular,

$$\hat{\mathbf{u}}(t) = \Psi(t, 0) \hat{\mathbf{u}}(0). \quad (8.6)$$

The propagator responds to the semigroup properties

$$\Psi(t, t_i) = \Psi(t, s) \Psi(s, t_i), \quad (8.7)$$

and $\Psi(t_i, t_i) = \mathbf{I}$ (the identity operator). Injecting $\hat{\mathbf{u}}(t) = \Psi(t, t_i) \hat{\mathbf{u}}(t_i)$ in (8.2), and enforcing the equation to be satisfied for all $\hat{\mathbf{u}}(t_i)$ leads to an evolution equation for the propagator

$$\partial_t \Psi(t, t_i) = L_m(t) \Psi(t, t_i). \quad (8.8)$$

By evaluating (8.7) at $t = t_i$ and $s = t$, it follows that

$$\mathbf{I} = \Psi(t_i, t) \Psi(t, t_i) \quad \text{thereby} \quad [\Psi(t, t_i)]^{-1} = \Psi(t_i, t). \quad (8.9)$$

Eventually, taking the temporal derivative of the first equation in (8.9) results in an evolution equation for the inverse propagator

$$\partial_t \Psi(t_i, t) = -\Psi(t_i, t) L_m(t). \quad (8.10)$$

Note that in presence of a forcing term $\hat{\mathbf{f}}(t)$ at the right-hand side of the system (8.2), its solution (8.6) generalizes into

$$\hat{\mathbf{u}}(t) = \Psi(t, 0) \hat{\mathbf{u}}(0) + \Psi(t, 0) \int_0^t \Psi(0, s) \hat{\mathbf{f}}(s) ds. \quad (8.11)$$

This formula will turn out to be useful in a moment.

The transient growth analysis amounts to constructing an orthonormal basis for the initial

flow field, with the particular feature that elements of this basis are ranked according to how much they are amplified at a given temporal horizon $t_o > 0$. The first element of this basis is the initial condition that is most amplified at $t = t_o$, the second is the most amplified under the constraint that it must be orthogonal to the first, *etc* ... Due to the non-normality of $L_m(t)$, the first few elements often lead to amplifications that are much larger than all the others. In the case where the initial condition projects equivalently on each element of the basis, the flow response at $t = t_o$ is dominated by those stemming from the few first elements of the basis only. In other terms, the key idea behind a transient growth (and/or a resolvent) analysis is that the response of a system to external perturbations is intrinsic to the operator, thus the precise form of these external perturbations matters little.

The first step is to define according to which measure the amplification is sought for. In the following, we choose the norm induced by the Hermitian inner product

$$\langle \hat{\mathbf{u}}_a | \hat{\mathbf{u}}_b \rangle \doteq \int_0^\infty \hat{\mathbf{u}}_a^H \hat{\mathbf{u}}_b r dr, \quad (8.12)$$

the superscript 'H' denoting the Hermitian transpose. Note that $\langle \hat{\mathbf{u}} | \hat{\mathbf{u}} \rangle = \|\hat{\mathbf{u}}\|^2$ is directly the kinetic energy of the perturbation. The largest linear amplification (or "gain") between an initial flow structure and its evolution at $t = t_o > 0$ (subscript *o* for 'optimal') reads

$$G_o(t_o) \doteq \max_{\hat{\mathbf{u}}(0)} \frac{\|\hat{\mathbf{u}}(t_o)\|}{\|\hat{\mathbf{u}}(0)\|} \doteq \frac{1}{\epsilon_o}. \quad (8.13)$$

The optimal gain does not depend on the time itself, but only on the temporal horizon t_o . In the following, G_o alone implies $G_o(t_o)$. The propagator formalism (8.6) is used to re-write the maximization problem (8.13) as an eigenvalue problem

$$\begin{aligned} G_o^2 &= \max_{\hat{\mathbf{u}}(0)} \frac{\langle \hat{\mathbf{u}}(t_o) | \hat{\mathbf{u}}(t_o) \rangle}{\langle \hat{\mathbf{u}}(0) | \hat{\mathbf{u}}(0) \rangle} = \max_{\hat{\mathbf{u}}(0)} \frac{\langle \Psi(t_o, 0) \hat{\mathbf{u}}(0) | \Psi(t_o, 0) \hat{\mathbf{u}}(0) \rangle}{\langle \hat{\mathbf{u}}(0) | \hat{\mathbf{u}}(0) \rangle} \\ &= \max_{\hat{\mathbf{u}}(0)} \frac{\langle \hat{\mathbf{u}}(0) | \Psi(t_o, 0)^\dagger \Psi(t_o, 0) \hat{\mathbf{u}}(0) \rangle}{\langle \hat{\mathbf{u}}(0) | \hat{\mathbf{u}}(0) \rangle}, \end{aligned} \quad (8.14)$$

where the operator $\Psi(t_o, 0)^\dagger$ denotes the adjoint of $\Psi(t_o, 0)$ under the inner product (8.12). From (8.14), it is clear that G_o^2 is also the largest (necessary real) eigenvalue of the self-adjoint operator $\Psi(t_o, 0)^\dagger \Psi(t_o, 0)$, and the associated eigenvector, named $\hat{\mathbf{u}}_o$ in what follows, is the optimal initial condition. The latter is normalized such that $\langle \hat{\mathbf{u}}_o | \hat{\mathbf{u}}_o \rangle = 1$. Smaller eigenvalues and corresponding eigenmodes constitute sub-optimal gains and initial conditions, and the family of eigenvectors is orthonormal. Let $\hat{\mathbf{l}}_o$ be the unit-norm response to the optimal initial condition $\hat{\mathbf{u}}_o$ at $t = t_o$, such that $\hat{\mathbf{l}}_o \doteq \Psi(t_o, 0) \hat{\mathbf{u}}_o / G_o$ and $\langle \hat{\mathbf{l}}_o | \hat{\mathbf{l}}_o \rangle = 1$. From this definition, and using that $\Psi(t_o, 0)^\dagger \Psi(t_o, 0) \hat{\mathbf{u}}_o = G_o^2 \hat{\mathbf{u}}_o$ and that the inverse of the adjoint is the adjoint of the inverse, two relations follow

$$\Psi(0, t_o) \hat{\mathbf{l}}_o = \epsilon_o \hat{\mathbf{u}}_o, \quad \text{and} \quad \Psi(0, t_o)^\dagger \hat{\mathbf{u}}_o = \epsilon_o \hat{\mathbf{l}}_o \quad (8.15)$$

where we recall that ϵ_o is the inverse of the optimal gain. Note that these two last relations also indicate the optimal initial condition and its associated response to be respectively the right and left singular vectors of $\Psi(t_o, 0)$, associated with its largest singular value. Since the operator $L_m(t)$ is assumed in the rest of the study to be strongly non-normal, the structures $\hat{\mathbf{u}}_o$ and $\hat{\mathbf{l}}_o$ generally project poorly each of its direct and adjoint eigenmodes (except in the limit $t_o \rightarrow \infty$).

The full linear response seeded by $\epsilon_o \hat{\mathbf{u}}_o$ and such that $\hat{\mathbf{l}}(t_o) = \hat{\mathbf{l}}_o$ reads $\hat{\mathbf{l}}(t) = \epsilon_o \Psi(t, 0) \hat{\mathbf{u}}_o$, or $\Psi(0, t) \hat{\mathbf{l}}(t) = \epsilon_o \hat{\mathbf{u}}_o$. The gain associated with this full linear response reads

$$G(t; t_o) \doteq \frac{\|\hat{\mathbf{l}}(t)\|}{\|\epsilon_o \hat{\mathbf{u}}_o\|} = \frac{\|\hat{\mathbf{l}}(t)\|}{\epsilon_o} = \|\Psi(t, 0) \hat{\mathbf{u}}_o\|, \quad (8.16)$$

where the parameter t_o after the semi-colon in $G(t; t_o)$ highlights that this gain was optimized for the time t_o specifically. Therefore, the gain (8.16) evaluated in $t = t_o$ equals to that defined in (8.13), i.e., $G(t_o; t_o) = G_o(t_o)$. Nevertheless, we insist that the gain (8.16) depends on the time t and is parameterized by the temporal horizon t_o , whereas the optimal gain (8.13) depends only on the temporal horizon t_o . In the following, the shortened notation $G(t)$ will systematically imply $G(t; t_o)$, and will be sometimes used to lighten the writing.

Of all the temporal horizons t_o , the one leading to the largest optimal gain will be highlighted with the subscript ‘max’ such that

$$\max_{t_o > 0} G_o(t_o) = G_o(t_{o,\max}) \doteq \frac{1}{\epsilon_{o,\max}}. \quad (8.17)$$

8.3 Weakly nonlinear formulation

In the linear paradigm, the gain is independent of $\|\hat{\mathbf{u}}(0)\|$, for the latter is assumed to be arbitrarily small. In reality, $\|\hat{\mathbf{u}}(0)\|$ may be sufficiently large for the nonlinear corrections to the response not to be negligible anymore, thus for the transient gain to depart from its linear prediction. Building on our previous work (Ducimetière et al., 2022a), we propose thereafter a method for capturing weakly nonlinear effects on the transient gain over a time-varying base flow.

In the rest of the present study, we subject the two-dimensional, unforced, Navier-Stokes equations governing the flow field $\mathbf{U}(t)$ to a small-amplitude initial perturbation around the reference vortex flow $\mathbf{U}_b(t)$. The initial perturbation has an azimuthal wavenumber m and its radial structure $\hat{\mathbf{u}}_h$, with $\|\hat{\mathbf{u}}_h\| = 1$, is for now arbitrary. The strong non-normality assumption justifies further assuming the transient gain to be large, that is to say, $\epsilon_o \ll 1$, such that ϵ_o constitutes a natural choice of small parameter with which to scale the amplitude of the initial perturbation. Specifically,

$$\mathbf{U}(0) - \mathbf{U}_b(0) = \alpha \sqrt{\epsilon_o^{-3}} (\hat{\mathbf{u}}_h e^{im\theta} + \text{c.c.}) = U_0 (\hat{\mathbf{u}}_h e^{im\theta} + \text{c.c.}), \quad (8.18)$$

where the amplitude of the initial condition, $U_0 \doteq \alpha \sqrt{\epsilon_0}^{-3}$, can vary through the real prefactor $\alpha = O(1)$. We intend at capturing the variation of the transient gain by increasing U_0 .

For this purpose, the total flow field \mathbf{U} is developed as a multiple-scale asymptotic expansion in terms of powers of $\sqrt{\epsilon_0}$ around the reference vortex flow $\mathbf{U}_b(t)$

$$\mathbf{U}(t, T) = \mathbf{U}_b(t) + \sqrt{\epsilon_0} \mathbf{u}_1(t, T) + \epsilon_0 \mathbf{u}_2(t, T) + \sqrt{\epsilon_0}^3 \mathbf{u}_3(t, T) + O(\epsilon_0^2). \quad (8.19)$$

The slow time scale $T \doteq \epsilon_0 t$ was introduced, aiming at capturing the slow modulation of the linear trajectory as nonlinearities progressively set in. The reason for which the expansion and the scaling of the initial condition are made in terms of powers of $\sqrt{\epsilon_0}$ shall be specified later. Injecting (8.19) in the Navier-Stokes equations, then expanding each \mathbf{u}_j as a Fourier series in space according to

$$\mathbf{u}_j(t, T) = \bar{\mathbf{u}}_j^{(0)}(t, T) + \sum_n (\bar{\mathbf{u}}_j^{(n)}(t, T) e^{inm\theta} + \text{c.c.}) \quad (8.20)$$

with $n = 1, 2, 3, \dots$, yields

$$\begin{aligned} & \sqrt{\epsilon_0} \left[\left[(\partial_t - L_m(t)) \bar{\mathbf{u}}_1^{(1)} e^{im\theta} + \text{c.c.} \right] + \bar{\mathbf{s}}_1 \right] + \\ & \epsilon_0 \left[\left[(\partial_t - L_m(t)) \bar{\mathbf{u}}_2^{(1)} e^{im\theta} + \text{c.c.} \right] + \bar{\mathbf{s}}_2 + C[\mathbf{u}_1, \mathbf{u}_1] \right] + \\ & \sqrt{\epsilon_0}^3 \left[\left[(\partial_t - L_m(t)) \bar{\mathbf{u}}_3^{(1)} e^{im\theta} + \text{c.c.} \right] + \bar{\mathbf{s}}_3 + \partial_T \mathbf{u}_1 + C[\mathbf{u}_1, \mathbf{u}_2] + C[\mathbf{u}_2, \mathbf{u}_1] \right] + \\ & O(\epsilon_0^2) = \mathbf{0}, \end{aligned} \quad (8.21)$$

where the nonlinear advection operator

$$C[\mathbf{x}, \mathbf{y}] \doteq (\mathbf{x} \cdot \nabla) \mathbf{y} + r^{-1} [-x_\theta y_\theta, (x_\theta y_r + x_r y_\theta)/2]^T, \quad \nabla = [\partial_r, r^{-1} \partial_\theta], \quad (8.22)$$

has been defined. The fundamental field, corresponding to $n = 1$, has been isolated at each order in (8.21), and the harmonics have been incorporated in $\bar{\mathbf{s}}_j$ with

$$\bar{\mathbf{s}}_j = (\partial_t - L_0(t)) \bar{\mathbf{u}}_j^{(0)} + \sum_n \left[(\partial_t - L_{nm}(t)) \bar{\mathbf{u}}_j^{(n)} e^{inm\theta} + \text{c.c.} \right] \quad (8.23)$$

for $n = 2, 3, \dots$. From (8.18), the only field with a non-zero initial condition is the fundamental one appearing at third order, specifically, $\bar{\mathbf{u}}_3^{(1)}|_{t=0} = \alpha \hat{\mathbf{u}}_h$. On the other hand, the relation

$$(\partial_t - L_m(t)) \bar{\mathbf{u}}_j^{(1)} = \Psi(t, 0) \partial_t \left(\Psi(0, t) \bar{\mathbf{u}}_j^{(1)} \right) \quad (8.24)$$

can be established using (8.10). Further injecting (8.24) in (8.21) leads to

$$\begin{aligned}
& \sqrt{\epsilon_o} \left[\left[\Psi(t, 0) \partial_t \left(\Psi(0, t) \bar{\mathbf{u}}_1^{(1)} \right) e^{im\theta} + \text{c.c.} \right] + \bar{\mathbf{s}}_1 \right] + \\
& \epsilon_o \left[\left[\Psi(t, 0) \partial_t \left(\Psi(0, t) \bar{\mathbf{u}}_2^{(1)} \right) e^{im\theta} + \text{c.c.} \right] + \bar{\mathbf{s}}_2 + C[\mathbf{u}_1, \mathbf{u}_1] \right] + \\
& \sqrt{\epsilon_o^3} \left[\left[\Psi(t, 0) \partial_t \left(\Psi(0, t) \bar{\mathbf{u}}_3^{(1)} \right) e^{im\theta} + \text{c.c.} \right] + \bar{\mathbf{s}}_3 + \partial_T \mathbf{u}_1 + C[\mathbf{u}_1, \mathbf{u}_2] + C[\mathbf{u}_2, \mathbf{u}_1] \right] + \\
& O(\epsilon_o^2) = \mathbf{0},
\end{aligned} \tag{8.25}$$

We recall that the application of the operator $\Psi(0, t)$ is equivalent to integrating the system backward from t to 0, and that it maps the optimal response $\hat{\mathbf{l}}_o$ on a field of very small amplitude $\epsilon_o \ll 1$ (by assumption) in (8.15). The main idea behind our method is to take advantage of this by perturbing the operator $\Psi(0, t)$ for all $t \geq 0$ according to

$$\Phi(0, t) \doteq \Psi(0, t) - \epsilon_o P(t), \quad \text{with} \quad P(t) \doteq H(t) \frac{\hat{\mathbf{u}}_o \langle \hat{\mathbf{l}}(t) | * \rangle}{\|\hat{\mathbf{l}}(t)\|^2}, \tag{8.26}$$

and where the Heaviside distribution $H(t)$ is defined as $H(0) = 0$ and $H(t > 0) = 1$. The operator $\langle \hat{\mathbf{l}}(t) | * \rangle$ applied to any field $\hat{\mathbf{g}}$ simply results in $\langle \hat{\mathbf{l}}(t) | \hat{\mathbf{g}} \rangle$. The operator $\Phi(0, t)$ satisfies $\Phi(0, 0) = \mathbf{I}$ and $\Phi(0, t) \hat{\mathbf{l}}(t) = \mathbf{0}$ for $t > 0$, and therefore is singular for all strictly positive times; the linear trajectory $\hat{\mathbf{l}}(t)$ constitutes its non-trivial (time-evolving) kernel. We further show in Appendix 8.7.1 that the non-trivial kernel $\hat{\mathbf{b}}(t)$ of the adjoint operator $\Phi(0, t)^\dagger$ for $t > 0$, such that $\Phi(0, t)^\dagger \hat{\mathbf{b}}(t) = \mathbf{0}$, reads $\hat{\mathbf{b}}(t) = \Psi(t, 0)^\dagger \hat{\mathbf{l}}(t)$.

Note that

$$\Phi(0, t) = \Psi(0, t) \left(\mathbf{I} - \hat{\mathbf{l}}(t) \frac{\langle \hat{\mathbf{l}}(t) | * \rangle}{\|\hat{\mathbf{l}}(t)\|^2} \right), \tag{8.27}$$

where the term in parenthesis is an orthogonal projection operator: it is self-adjoint, linear, idempotent, and its application projects into the subspace that is complementary to $\hat{\mathbf{l}}(t)$. Therefore (8.26), by stating that $\Psi(0, t) \approx \Phi(0, t)$, implies that applying $\Psi(0, t)$, or applying $\Phi(0, t)$ that first removes the component on $\hat{\mathbf{l}}(t)$ then applies $\Psi(0, t)$, both lead to very similar initial states. That is precisely because $\Psi(0, t)$ maps $\hat{\mathbf{l}}(t)$ on $\epsilon_o \hat{\mathbf{u}}_o$ of very small amplitude $\epsilon_o \ll 1$.

In principle, expansion (8.26) requires

$$\|\Psi(0, t)\| \gg \epsilon_o \|P(t)\| = \frac{\epsilon_o}{\|\hat{\mathbf{l}}(t)\|} = \frac{1}{\|\Psi(t, 0) \hat{\mathbf{u}}_o\|}. \tag{8.28}$$

By using that the norm of the inverse of an operator is the inverse of its minimum singular value

$$\|\Psi(0, t)\| = \left(\min_{\hat{\mathbf{u}}(0), \|\hat{\mathbf{u}}(0)\|=1} \|\Psi(t, 0) \hat{\mathbf{u}}(0)\| \right)^{-1}, \tag{8.29}$$

the condition above is equivalent to

$$\min_{\hat{\mathbf{u}}(0), \|\hat{\mathbf{u}}(0)\|=1} \|\Psi(t, 0)\hat{\mathbf{u}}(0)\| \ll \|\Psi(t, 0)\hat{\mathbf{u}}_o\|. \quad (8.30)$$

In other terms, the operator perturbation *a priori* holds for the times t such that the response to the initial condition that is the least amplified at t , is much smaller than the response to $\hat{\mathbf{u}}_o$ that is the most amplified at t_o . This is certainly verified for times around $t = t_o$, which is appropriate, for the response $\hat{\mathbf{l}}(t)$ is expected to be nonlinearly modified at first at these times.

By then perturbing the operator $\Psi(0, t)$ in (8.25) according to (8.26), we are left with

$$\begin{aligned} & \sqrt{\epsilon_o} \left[\left[\Psi(t, 0)\partial_t \left(\Phi(0, t)\bar{\mathbf{u}}_1^{(1)} \right) e^{im\theta} + \text{c.c.} \right] + \bar{\mathbf{s}}_1 \right] + \\ & \epsilon_o \left[\left[\Psi(t, 0)\partial_t \left(\Phi(0, t)\bar{\mathbf{u}}_2^{(1)} \right) e^{im\theta} + \text{c.c.} \right] + \bar{\mathbf{s}}_2 + C[\mathbf{u}_1, \mathbf{u}_1] \right] + \\ & \sqrt{\epsilon_o^3} \left[\left[\Psi(t, 0)\partial_t \left(\Phi(0, t)\bar{\mathbf{u}}_3^{(1)} \right) e^{im\theta} + \text{c.c.} \right] + \bar{\mathbf{s}}_3 + \partial_T \mathbf{u}_1 + C[\mathbf{u}_1, \mathbf{u}_2] + C[\mathbf{u}_2, \mathbf{u}_1] + \right. \\ & \left. \left[\Psi(t, 0)\partial_t \left(P(t)\bar{\mathbf{u}}_1^{(1)} \right) e^{im\theta} + \text{c.c.} \right] \right] + O(\epsilon_o^2) = \mathbf{0}. \end{aligned} \quad (8.31)$$

Note that the perturbation operator $\epsilon_o P(t)$, modifying $\Psi(0, t)$ in $\Phi(0, t)$ at leading order $O(\sqrt{\epsilon_o})$, is compensated for at third order $O(\sqrt{\epsilon_o^3})$ specifically. This was made purposely and explains *a posteriori* why the asymptotic expansion was outlined in terms of integer powers of $\sqrt{\epsilon_o}$, instead of being for instance in terms of integer powers of ϵ_o . More precisely, we anticipated the forcing term $C[\mathbf{u}_1, \mathbf{u}_2] + C[\mathbf{u}_2, \mathbf{u}_1]$ appearing at third order, to have a non-zero component on the fundamental wavenumber m , due to the bi-linearity of the operator $C[* , *]$; therefore, making the term in $P(t)$ appear at third order as well, was a way of putting all forcing terms oscillating at m at the same order.

Note also that only the propagator associated with the wavenumber m was perturbed, although harmonics may equally lead to significant transient gains. This selective perturbation is justified *a priori* by the fact these harmonics are not externally excited like the fundamental pair is through the initial condition, but are only generated nonlinearly at higher orders. If, however, the harmonic responses are *a posteriori* found to endanger the asymptotic hierarchy, they can always be included in the kernel of their associated propagators in the manner of (8.26).

Terms in (8.31) are collected at each order in $\sqrt{\epsilon_o}$, yielding a cascade of linear problems. At order $\sqrt{\epsilon_o}$ we assemble $(\partial_t - L_{nm}(t))\bar{\mathbf{u}}_1^{(n)} = \mathbf{0}$ with $\bar{\mathbf{u}}_1^{(n)}|_{t=0} = \mathbf{0}$ for $n = 0, 2, 3, \dots$ and

$$\Psi(t, 0)\partial_t \left(\Phi(0, t)\bar{\mathbf{u}}_1^{(1)} \right) = \mathbf{0} \quad \text{with} \quad \bar{\mathbf{u}}_1^{(1)}|_{t=0} = \mathbf{0}. \quad (8.32)$$

This leads to $\bar{\mathbf{u}}_1^{(n)} = \mathbf{0}$ for all times and $n \neq 1$. In addition, multiplying (8.32) by $\Psi(0, t)$, then integrating in time and using $\Phi(0, 0) = \mathbf{I}$, gives $\Phi(0, t)\bar{\mathbf{u}}_1^{(1)} = \mathbf{0}$. The kernel of $\Phi(0, t)$ being equal

to $H(t)\hat{\mathbf{l}}(t)$ for $t \geq 0$, the solution for $\bar{\mathbf{u}}_1^{(1)}$ reads

$$\bar{\mathbf{u}}_1^{(1)}(t, T) = A(T)H(t)\hat{\mathbf{l}}(t) \quad \text{for } t \geq 0, \quad (8.33)$$

where $A(T) \in \mathbb{C}$ is a slowly varying scalar amplitude verifying $\partial_t A = 0$. Eventually, the general solution at $\sqrt{\epsilon_o}$ is written

$$\mathbf{u}_1(t, T) = A(T)H(t)\hat{\mathbf{l}}(t)e^{im\theta} + \text{c.c.} \quad \text{for } t \geq 0. \quad (8.34)$$

In the linear regime, A would be constant over time; therefore, by continuity, we expect its variation to be small in the weakly nonlinear regime. This is what is implied in the fact that A depends on the slow time T , since $d_t A = \partial_t A + (\partial_t T)\partial_T A = \epsilon_o \partial_T A = O(\epsilon_o) \ll 1$.

At order ϵ_o , the solution is

$$\mathbf{u}_2(t, T) = |A(T)|^2 \mathbf{u}_2^{(0)}(t) + \left(A(T)^2 \hat{\mathbf{u}}_2^{(2)}(t) e^{i2m\theta} + \text{c.c.} \right) \quad (8.35)$$

for $t \geq 0$, where

$$\begin{aligned} (\partial_t - L_0(t))\mathbf{u}_2^{(0)} &= -C_m [\hat{\mathbf{l}}^*, \hat{\mathbf{l}}] + \text{c.c.}, \quad \mathbf{u}_2^{(0)}(0) = \mathbf{0}, \quad \text{and} \\ (\partial_t - L_{2m}(t))\hat{\mathbf{u}}_2^{(2)} &= -C_m [\hat{\mathbf{l}}, \hat{\mathbf{l}}], \quad \hat{\mathbf{u}}_2^{(2)}(0) = \mathbf{0}. \end{aligned} \quad (8.36)$$

The advection operator in the Fourier space $C_m [\hat{\mathbf{x}}, \hat{\mathbf{y}}]$ is as (8.22), excepted that ∇ is replaced by $\hat{\nabla}_m$; it computes the transport, by the field $\hat{\mathbf{x}}$, of the field $\hat{\mathbf{y}}$ oscillating at m . In principle, the Heaviside distribution $H(t)$ multiplies the forcing terms in (8.36). However, it can be ignored here without loss of generality, for the forcing terms appear inside an integral between 0 and t in the formal expression of the solution, where the presence of a Heaviside distribution is unimportant. In (8.35), the homogeneous solution $A_2(T)H(t)\hat{\mathbf{l}}(t)$, solving the system $\Phi(0, t)\bar{\mathbf{u}}_2^{(1)} = \mathbf{0}$ for $t \geq 0$, was ignored. In this manner, the component of the overall solution on $\hat{\mathbf{l}}(t)$ is fully embedded in A , without needing to be corrected.

At order $\sqrt{\epsilon_o}^3$ in (8.31) are gathered two equations: the first yields the Fourier component of the solution oscillating at m

$$\Psi(t, 0)\partial_t \left(\Phi(0, t)\bar{\mathbf{u}}_3^{(1)} \right) = -A|A|^2 H\tilde{\mathbf{f}} - (d_T A)H\hat{\mathbf{l}} - A\Psi(t, 0)\partial_t (P(t)H\hat{\mathbf{l}}), \quad (8.37)$$

subject to $\bar{\mathbf{u}}_3^{(1)}|_{t=0} = \alpha\hat{\mathbf{u}}_h$ and where we defined

$$\tilde{\mathbf{f}} \doteq C_{2m} [\hat{\mathbf{l}}^*, \hat{\mathbf{u}}_2^{(2)}] + C_{-m} [\hat{\mathbf{u}}_2^{(2)}, \hat{\mathbf{l}}^*] + C_0 [\hat{\mathbf{l}}, \mathbf{u}_2^{(0)}] + C_m [\mathbf{u}_2^{(0)}, \hat{\mathbf{l}}], \quad (8.38)$$

depending only on the fast time scale t . The second equation governs the Fourier component oscillating at $3m$

$$(\partial_t - L_{3m}(t))\bar{\mathbf{u}}_3^{(3)} = -A^3 \left(C_{2m} [\hat{\mathbf{l}}, \hat{\mathbf{u}}_2^{(2)}] + C_m [\hat{\mathbf{u}}_2^{(2)}, \hat{\mathbf{l}}] \right), \quad (8.39)$$

subject to $\bar{\mathbf{u}}_3^{(3)}|_{t=0} = \mathbf{0}$. Noticing that $P(t)H\hat{\mathbf{l}} = H^2\hat{\mathbf{u}}_o = H\hat{\mathbf{u}}_o$, that $\Psi(0, t)\hat{\mathbf{l}} = \epsilon_o\hat{\mathbf{u}}_o$ (by definition) and multiplying (8.37) by $\Psi(0, t)$ results in

$$\partial_t \left(\Phi(0, t) \bar{\mathbf{u}}_3^{(1)} \right) = -A|A|^2 H\Psi(0, t) \tilde{\mathbf{f}} - (d_T A) H\epsilon_o \hat{\mathbf{u}}_o - A\partial_t (H\hat{\mathbf{u}}_o). \quad (8.40)$$

Integration over the time t , detailed in Appendix 8.7.2, leads to

$$\Phi(0, t) \bar{\mathbf{u}}_3^{(1)} = \alpha \hat{\mathbf{u}}_h + A|A|^2 \Psi(0, t) \tilde{\mathbf{u}} - (d_T A) \epsilon_o t \hat{\mathbf{u}}_o - AH\hat{\mathbf{u}}_o, \quad (8.41)$$

where

$$(\partial_t - L_m(t)) \tilde{\mathbf{u}} = -\tilde{\mathbf{f}}, \text{ subject to } \tilde{\mathbf{u}}(0) = \mathbf{0}. \quad (8.42)$$

Evaluating (8.41) in $t=0$ in particular, we check that $\bar{\mathbf{u}}_3^{(1)}|_{t=0} = \alpha \hat{\mathbf{u}}_h$ indeed. The operator $\Phi(0, t)$ being singular for strictly positive time, (8.41) admits a non-diverging particular solution if and only if its right-hand side is orthogonal to $\hat{\mathbf{b}}(t)$ for all $t > 0$ (Fredholm alternative). This condition results in

$$\epsilon_o t \frac{dA}{dT} = \alpha \frac{\langle \hat{\mathbf{b}} | \hat{\mathbf{u}}_h \rangle}{\langle \hat{\mathbf{b}} | \hat{\mathbf{u}}_o \rangle} - A + A|A|^2 \frac{\langle \hat{\mathbf{b}} | \Psi(0, t) \tilde{\mathbf{u}} \rangle}{\langle \hat{\mathbf{b}} | \hat{\mathbf{u}}_o \rangle} \quad (8.43)$$

for $t > 0$. The adjoint field $\hat{\mathbf{b}}(t) = \Psi(t, 0)^\dagger \hat{\mathbf{l}}(t)$ tends towards $\hat{\mathbf{b}}(0) = \hat{\mathbf{l}}(0) = \epsilon_o \hat{\mathbf{u}}_o$ when t tends towards 0. Therefore, in this limit, (8.43) reduces to

$$\lim_{t \rightarrow 0} A = \alpha \langle \hat{\mathbf{u}}_o | \hat{\mathbf{u}}_h \rangle, \quad (8.44)$$

where we also used that the limits of both the left-hand side and the nonlinear term in (8.43) are 0 when t goes to 0; the former because of the presence of the factor t , and the latter because $\tilde{\mathbf{u}}(0) = \mathbf{0}$. Solving (8.43) is equivalent to solving its partial derivative with respect to the fast time scale t , reading

$$\epsilon_o \frac{dA}{dT} = \alpha \frac{d}{dt} \left(\frac{\langle \hat{\mathbf{b}} | \hat{\mathbf{u}}_h \rangle}{\langle \hat{\mathbf{b}} | \hat{\mathbf{u}}_o \rangle} \right) + A|A|^2 \frac{d}{dt} \left(\frac{\langle \hat{\mathbf{b}} | \Psi(0, t) \tilde{\mathbf{u}} \rangle}{\langle \hat{\mathbf{b}} | \hat{\mathbf{u}}_o \rangle} \right), \quad (8.45)$$

subject to the initial condition (8.44). The system is written solely in terms of t by evaluating (8.44) and (8.45) at $T = \epsilon_o t$, and remembering that $d_t A = \epsilon_o d_T A|_{T=\epsilon_o t}$, leading to

$$\frac{dA}{dt} = \alpha \frac{d}{dt} \left(\frac{\langle \hat{\mathbf{b}} | \hat{\mathbf{u}}_h \rangle}{\langle \hat{\mathbf{b}} | \hat{\mathbf{u}}_o \rangle} \right) + A|A|^2 \frac{d}{dt} \left(\frac{\langle \hat{\mathbf{b}} | \Psi(0, t) \tilde{\mathbf{u}} \rangle}{\langle \hat{\mathbf{b}} | \hat{\mathbf{u}}_o \rangle} \right), \text{ with } A(0) = \alpha \langle \hat{\mathbf{u}}_o | \hat{\mathbf{u}}_h \rangle. \quad (8.46)$$

The amplitude A , previously undefined at $t=0$, was prolonged by continuity there by stating $A(0) = \lim_{t \rightarrow 0} A(t)$. Note that such rewriting of the amplitude equation in terms of t was not done directly for (8.43), since it would have given an ode without an initial condition, (8.44) being intrinsically satisfied.

Introducing the rescaled amplitude $a \doteq \sqrt{\epsilon_o} A$ and remembering the amplitude of the initial

condition to be $U_0 = \alpha \sqrt{\epsilon_o^{-3}}$, equation (8.46) writes

$$\frac{da}{dt} = \frac{U_0}{\epsilon_o} \frac{d}{dt} \left(\frac{\langle \hat{\mathbf{b}} | \hat{\mathbf{u}}_h \rangle}{\langle \hat{\mathbf{b}} | \hat{\mathbf{u}}_o \rangle} \right) + a |a|^2 \frac{d\mu}{dt}, \quad \text{with } a(0) = \frac{U_0}{\epsilon_o} \langle \hat{\mathbf{u}}_o | \hat{\mathbf{u}}_h \rangle, \quad (8.47)$$

and where we defined the nonlinear coefficient

$$\mu(t) \doteq \frac{1}{\epsilon_o} \frac{\langle \hat{\mathbf{b}}(t) | \Psi(0, t) \tilde{\mathbf{u}}(t) \rangle}{\langle \hat{\mathbf{b}}(t) | \hat{\mathbf{u}}_o \rangle} = \frac{1}{\epsilon_o} \frac{\langle \Psi(t, 0)^\dagger \hat{\mathbf{l}}(t) | \Psi(0, t) \tilde{\mathbf{u}}(t) \rangle}{\langle \Psi(t, 0)^\dagger \hat{\mathbf{l}}(t) | \hat{\mathbf{u}}_o \rangle} = \frac{\langle \hat{\mathbf{l}}(t) | \tilde{\mathbf{u}}(t) \rangle}{\|\hat{\mathbf{l}}(t)\|^2}. \quad (8.48)$$

From here, the weakly nonlinear transient gain corresponding to the wavenumber m for $t > 0$ is simply

$$G_w(t; t_o) = \frac{\|\sqrt{\epsilon_o} \tilde{\mathbf{u}}_1^{(1)}(t)\|}{\|U_0 \hat{\mathbf{u}}_h\|} = \frac{|a(t)| \|\hat{\mathbf{l}}(t)\|}{U_0}. \quad (8.49)$$

The parameter t_o after the semi-colon in $G_w(t; t_o)$ underlines that it is the weakly nonlinear prolongation of a gain that was linearly optimized for $t = t_o$. Again, in what follows, the shortened notation $G_w(t)$ will systematically imply $G_w(t; t_o)$. Note that $G_w(t_o) = |a(t_o)|/U_0$.

The linear regime corresponds to the limit $U_0/\epsilon_o \rightarrow 0$, or simply $U_0 \rightarrow 0$, since if the amplitude of the initial condition is much smaller than the linear gain, then the amplitude of its response is much smaller than one. In this limit, the nonlinear terms in (8.47) becomes negligible, and the solution tends towards

$$a(t) = \frac{U_0}{\epsilon_o} \frac{\langle \hat{\mathbf{b}}(t) | \hat{\mathbf{u}}_h \rangle}{\langle \hat{\mathbf{b}}(t) | \hat{\mathbf{u}}_o \rangle} = \frac{\langle \hat{\mathbf{l}}(t) | U_0 \Psi(t, 0) \hat{\mathbf{u}}_h \rangle}{\|\hat{\mathbf{l}}(t)\|^2}, \quad (8.50)$$

which is the properly normalized projection on $\hat{\mathbf{l}}(t)$ of the response to the initial condition $U_0 \hat{\mathbf{u}}_h$, as expected at a linear level since $a(t)$ is the amplitude along $\hat{\mathbf{l}}(t)$.

Note that in (8.26) any other perturbation operator of the form $P = H \hat{\mathbf{u}}_o \langle \hat{\mathbf{x}} | * \rangle / \langle \hat{\mathbf{x}} | \hat{\mathbf{l}} \rangle$, with $\hat{\mathbf{x}}$ any trajectory, would also have led to a singular operator with $\hat{\mathbf{l}}$ as a non-trivial kernel, but with $\hat{\mathbf{b}} = \Psi(t, 0)^\dagger \hat{\mathbf{x}}$ as a non-trivial kernel of its adjoint. Choosing $\hat{\mathbf{x}} = \hat{\mathbf{l}}$ implying $\hat{\mathbf{b}} = \Psi(t, 0)^\dagger \hat{\mathbf{l}}$, as was done so far, is the only choice leading to a coherent result in (8.50), thereby guaranteeing the uniqueness of P in (8.26); as a side comment, it should be noted that among all $\hat{\mathbf{x}}$, $\hat{\mathbf{x}} = \hat{\mathbf{l}}$ also leads to the P of the smallest possible norm.

For the gain at $t = t_o$, (8.50) corresponds to

$$\lim_{U_0 \rightarrow 0} G_w(t_o) = \frac{1}{\epsilon_o} \frac{|\langle \hat{\mathbf{b}}(t_o) | \hat{\mathbf{u}}_h \rangle|}{|\langle \hat{\mathbf{b}}(t_o) | \hat{\mathbf{u}}_o \rangle|} = \frac{1}{\epsilon_o} |\langle \hat{\mathbf{u}}_o | \hat{\mathbf{u}}_h \rangle|, \quad (8.51)$$

since $\hat{\mathbf{b}}(t_o) = \epsilon_o \Psi(t_o, 0)^\dagger \Psi(t_o, 0) \hat{\mathbf{u}}_o = \hat{\mathbf{u}}_o$. The result (8.51) also is as expected from the linear prediction. In particular, we recover $\lim_{U_0 \rightarrow 0} G_w(t_o) = 1/\epsilon_o = G_o$ when the optimal initial condition is applied ($\hat{\mathbf{u}}_h = \hat{\mathbf{u}}_o$). It also predicts the gain to be null when $\hat{\mathbf{u}}_h$ is orthogonal to $\hat{\mathbf{u}}_o$,

indicating the linear response at $t = t_o$ to be orthogonal to $\hat{\boldsymbol{l}}_o$ without taking into account the gains associated with sub-optimal forcings. Therefore, these latter should be $O(1/\sqrt{\epsilon_o})$ to be mathematically consistent.

For the rest of the chapter, we set $\hat{\boldsymbol{u}}_h = \hat{\boldsymbol{u}}_o$. In physical terms, this choice, although very specific, is found to be the most natural in the absence of information regarding the structure of the actual initial condition $\hat{\boldsymbol{u}}_h$. Note, however, that $\hat{\boldsymbol{u}}_h$ might project very poorly on $\hat{\boldsymbol{u}}_o$, and in the latter case reducing the dynamics to the response to $\hat{\boldsymbol{u}}_o$ would give inaccurate results.

Further expressing $a(t)$ in terms of an amplitude $|a(t)| \in \mathbb{R}^+$ and a phase $\phi(t) \in \mathbb{R}$ such that $a(t) \doteq |a(t)|e^{i\phi(t)}$, the amplitude equation (8.47) becomes

$$\begin{aligned} \frac{d|a|}{dt} &= |a|^3 \frac{d\mu_r}{dt}, \text{ with } |a(0)| = \frac{U_0}{\epsilon_o}, \text{ and} \\ \frac{d\phi}{dt} &= |a|^2 \frac{d\mu_i}{dt}, \text{ with } \phi(0) = 0. \end{aligned} \quad (8.52)$$

the subscripts “ r ” and “ i ” denoting the real and imaginary parts, respectively. The equation for $|a|$, in particular, bears the following analytical solution

$$|a(t)| = \frac{U_0}{\epsilon_o} \frac{1}{\sqrt{1 - 2\left(\frac{U_0}{\epsilon_o}\right)^2 \mu_r(t)}}, \text{ thus } G_w(t) = \frac{G(t)}{\sqrt{1 - 2\left(\frac{U_0}{\epsilon_o}\right)^2 \mu_r(t)}}. \quad (8.53)$$

For any time t , the gain decreases strictly monotonically with U_0 if $\mu_r(t) < 0$, thus is maximum in the linear regime. Moreover, the gain stays constant with U_0 if $\mu_r(t) = 0$, and increases strictly monotonically if $\mu_r(t) > 0$. In the latter case, by increasing U_0 the gain eventually becomes singular (tending towards $+\infty$ at time t) for

$$U_0 = \frac{\epsilon_o}{\sqrt{2\mu_r(t)}}, \text{ defined if } \mu_r(t) > 0. \quad (8.54)$$

In the following, we call (8.53) the Weakly Nonlinear Non-normal transient (WNNt) model. In Appendix 8.7.3 we show that at first order in the gain variation, (8.53) partly reduces to the sensitivity of the gain $G(t)$ to the axisymmetric base flow modification $+a_l^2 \boldsymbol{u}_2^{(0)}(t)$, where $a_l \doteq (U_0/\epsilon_o)$ is the amplitude of the response in the linear regime. In this sense, our model states that small gain modifications by increasing U_0 , are partly due to the fact that the perturbation now evolves over a base flow that is distorted through the action of the Reynolds stress forcing $-C_m [a_l \hat{\boldsymbol{l}}^*, a_l \hat{\boldsymbol{l}}] + \text{c.c.}$ of this very same perturbation (nonlinear feedback). In addition, (8.53) also includes the effects of the second harmonic oscillating at $2m$.

In Appendix 8.7.4, a second method that is more immediate, although perhaps less rigorous, is proposed to derive the amplitude equation (8.43). This method does not rely on the singularization of the propagator, and was named the “pseudo-forcing method”.

8.4 Linear and fully nonlinear transient growth in the diffusing, two-dimensional, Lamb-Oseen vortex

Equation (8.53) is employed thereafter for the analysis of the transient gain experienced by a two-dimensional Gaussian vortex in a weakly nonlinear regime.

8.4.1 Flow geometry

Vortices are flows combining rotation and shear, and the majority of them possess a localized distribution of vorticity. The Lamb-Oseen vortex is perhaps the simpler solution of the Navier-Stokes equation containing these ingredients, thus is adopted in the rest of this chapter. It expresses

$$U_{b,r}(r, t) = 0, \quad U_{b,\theta}(r, t) = \frac{1 - e^{-r^2/(1+4t/\text{Re})}}{r}. \quad (8.55)$$

The associated vorticity field, W_z , has a Gaussian radial profile

$$W_z(r, t) = \frac{U_{b,\theta}}{r} + \frac{\partial U_{b,\theta}}{\partial r} = \frac{2}{1+4t/\text{Re}} e^{-r^2/(1+4t/\text{Re})}, \quad (8.56)$$

that diffuses with time for finite Re values. For the linear velocity perturbation, we select the azimuthal wavenumber $m = 2$, since it is the wavenumber associated with the subcritical bifurcation towards the tripolar state described in the introduction (see for instance Rossi et al. (1997)). Only the response to an initial condition with $m = 2$ will be considered in this chapter.

8.4.2 Numerical methods

In practice, the Poisson equation (8.4) for the pressure is never solved directly, the latter being included in the state space instead:

$$M \partial_t \begin{bmatrix} \hat{\mathbf{u}} \\ \hat{p} \end{bmatrix} = \begin{bmatrix} A_m(t) & -\hat{\mathbf{V}}_m \\ \hat{\mathbf{V}}_m & 0 \end{bmatrix} \begin{bmatrix} \hat{\mathbf{u}} \\ \hat{p} \end{bmatrix} \doteq B_m(t) \begin{bmatrix} \hat{\mathbf{u}} \\ \hat{p} \end{bmatrix}, \quad \text{with} \quad M \doteq \begin{bmatrix} \mathbf{I} & 0 \\ 0 & 0 \end{bmatrix}. \quad (8.57)$$

Systems (8.57) and (8.2) lead to the same solution for the velocity field, and (8.2) was selected for the analytical development only because it does not contain the singular mass matrix, which lightens the writing. To produce the linear and weakly nonlinear results, (8.57) is discretized on Matlab by means of the pseudospectral Chebyshev collocation method. Specifically, the variables are collocated at the N Gauss-Lobatto nodes $s = \cos(j\pi/(N-1))$, with $j = 0, 1, \dots, N-1$, which includes the endpoints $s = -1$ and $s = 1$. This grid is mapped on the physical domain $0 \leq r \leq R_{max}$ using an algebraic mapping with domain truncation $r = L(1+s)/(s_{max}-s)$, where L is a mapping parameter to cluster the points close to the origin, and is set equal to 3. The parameter s_{max} is defined as $s_{max} \doteq (2L+R_{max})/R_{max}$ (see Canuto et al. (2007) and Viola et al. (2016)). In the present work, $R_{max} = 50$ and $N = 300$ proved to be

sufficient for the convergence of all results. The lines corresponding to $r = 0$ and $r = R_{max}$ in the discretized version of (8.57) are replaced by those enforcing the boundary conditions there; this also avoids the problem of the singularity in $r = 0$.

The action of the propagator $\Psi(t, 0)$ is computed in practice by marching (8.57) in time using a Crank-Nicholson scheme. Specifically, if the pressure and the velocity field are known and equal to $[\hat{\mathbf{u}}^{(n)}, \hat{p}^{(n)}]^T$ at a time t_n , their values at $t_{n+1} = t_n + \Delta t$ are obtained upon inverting the system

$$\left(\frac{M}{\Delta t} - \frac{1}{2} B_m(t_{n+1}) \right) \begin{bmatrix} \hat{\mathbf{u}}^{(n+1)} \\ \hat{p}^{(n+1)} \end{bmatrix} = \left(\frac{M}{\Delta t} + \frac{1}{2} B_m(t_n) \right) \begin{bmatrix} \hat{\mathbf{u}}^{(n)} \\ \hat{p}^{(n)} \end{bmatrix}, \quad (8.58)$$

which is done employing the command backslash on Matlab. The solutions to the other linear time-dependent systems at higher orders are also approximated upon discretizing in time with a Crank-Nicholson scheme. The adjoint system to (8.57) reads

$$-M \partial_t \begin{bmatrix} \hat{\mathbf{u}}^\dagger \\ \hat{p}^\dagger \end{bmatrix} = B_m(t)^\dagger \begin{bmatrix} \hat{\mathbf{u}}^\dagger \\ \hat{p}^\dagger \end{bmatrix}, \quad (8.59)$$

where we used $M^\dagger = M$, and where the expression of $B_m(t)^\dagger$ and the boundary conditions for the adjoint field are derived in Appendix 8.7.5. The action of the adjoint propagator $\Psi(t, 0)^\dagger$, necessary for the linear optimization, is determined by time marching (8.59) backward. That is, from known adjoint velocity and pressure fields at a time t_{n+1} , their evolution at $t_n = t_{n+1} - \Delta t$ are obtained by solving

$$\left(\frac{M}{\Delta t} - \frac{1}{2} B_m^\dagger(t_n) \right) \begin{bmatrix} \hat{\mathbf{u}}^{\dagger, (n)} \\ \hat{p}^{\dagger, (n)} \end{bmatrix} = \left(\frac{M}{\Delta t} + \frac{1}{2} B_m^\dagger(t_{n+1}) \right) \begin{bmatrix} \hat{\mathbf{u}}^{\dagger, (n+1)} \\ \hat{p}^{\dagger, (n+1)} \end{bmatrix}. \quad (8.60)$$

A time step of $\Delta t = 0.02$ was selected and was found sufficient to guarantee convergence of the results.

The fully nonlinear simulations (DNS) were performed using the spectral element solver Nek5000. A two-dimensional square grid $(x, y) \in [-R_{max}, R_{max}] \times [-R_{max}, R_{max}]$ was used, with a particularly high density of elements near the vortex core region where the flow gradients are intense. Convergence of the results by refining the mesh and extending the size of the computational domain has been checked.

8.4.3 Linear results

The results of the linear transient growth analysis for $m = 2$ and varying $\text{Re} \in [1.25, 2.5, 5, 10] \times 10^3$ are presented below. The optimal gain $G_o(t_o)$ defined in (8.13), also called ‘‘envelope’’, is shown as a function of t_o in figure 8.1a and for different Re . For all considered Re values, $G_o(t_o)$ reaches a clear maximum at relatively small t_o , before decreasing and plateauing by further increasing t_o . The values $G_o(t_{o, \max})$ of these maxima, and of the corresponding temporal

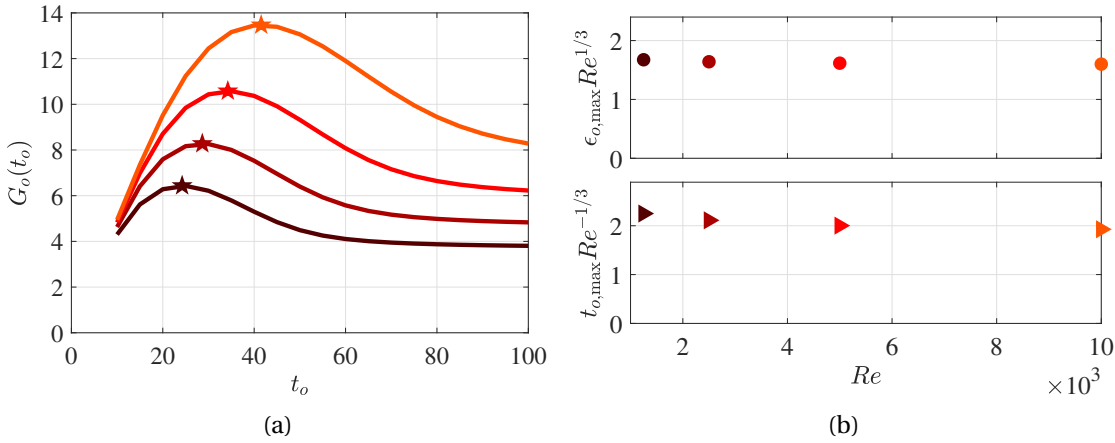


Figure 8.1: Linear transient growth in the two-dimensional, time-dependent Lamb-Oseen vortex flow for varying Re number $\in [1.25, 2.5, 5, 10] \times 10^3$, larger Re corresponding to lighter colours. The perturbation has wavenumber $m = 2$. (a) Optimal gain as defined in (8.13) as a function of the temporal horizon t_o . The star marker corresponds to its maximum value over t_o and for a given Re, that is, to $G_o(t_{o,\max}) = 1/\epsilon_{o,\max}$. (b) Top panel: $\epsilon_{o,\max}$ multiplied by $Re^{1/3}$ and plotted as a function of Re; bottom panel: $t_{o,\max}$ multiplied by $Re^{-1/3}$ and shown as a function of Re.

horizons $t_{o,\max}$, seem to increase monotonically with the Re number.

The type of dependence is made explicit in figure 8.1b, where we propose in the top panel to plot $\epsilon_{o,\max}$ multiplied by $Re^{1/3}$ as a function of Re, demonstrating that $G_o(t_{o,\max}) \propto Re^{1/3}$. In the bottom panel, $t_{o,\max}$ multiplied by $Re^{-1/3}$ is also shown as a function of Re: while the data align slightly less well on a constant line, the agreement remains correct and stating $t_{o,\max} \propto Re^{1/3}$ is a fair approximation. All these results are in excellent agreement with those presented in chapter 3 of Antkowiak (2005). In particular, the power-law dependencies of both $G_o(t_{o,\max})$ and $t_{o,\max}$ have already been observed and interpreted physically, and discussed next.

In figure 8.2, by fixing $Re = 5000$, the optimal gain $G_o(t_o)$ over t_o is reproduced from figure 8.1, as well as the gain $G(t)$ associated with the linear trajectory optimized for $t_o = t_{o,\max} = 35$ specifically. We check that $G(0) = 1$, that $G(35) = G_o(35)$ and that G is below G_o everywhere else. At the times corresponding to the black dots, the axial vorticity structure, expressed as

$$\hat{\omega} = (1/r + \partial_r)\hat{u}_\theta - (im/r)\hat{u}_r, \quad (8.61)$$

is shown in figure 8.3. For the panel in the top-left corner, we observe that the optimal initial condition consists of an arrangement of vorticity sheets, or “spirals”, orientated in counter-shear with respect to the base flow. As time increases, the sheets unfold under the effect of advection by the base flow, in analogy with the Orr mechanism. Antkowiak and Brancher (2004) and Antkowiak (2005) also argue that a Kelvin wave (corresponding to a core mode) is transiently excited in the heart of the vortex, by induction of the vorticity spirals.

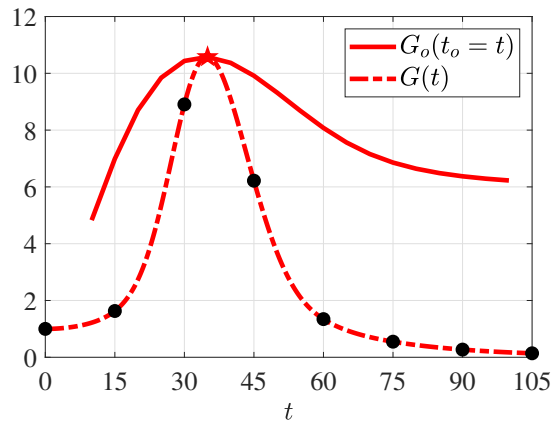


Figure 8.2: The continuous line is the reproduction of the envelope shown in figure 8.1a for $\text{Re} = 5000$. The dash-dotted line is the gain $G(t)$ associated with the linear trajectory optimized for $t_o = t_{o,\text{max}} = 35$, defined in (8.16). By definition, both curves collapse at $t = 35$. The black dots correspond to $t = 0, 15, 30, \dots, 105$, for which the corresponding vorticity structures are shown in figure 8.3.

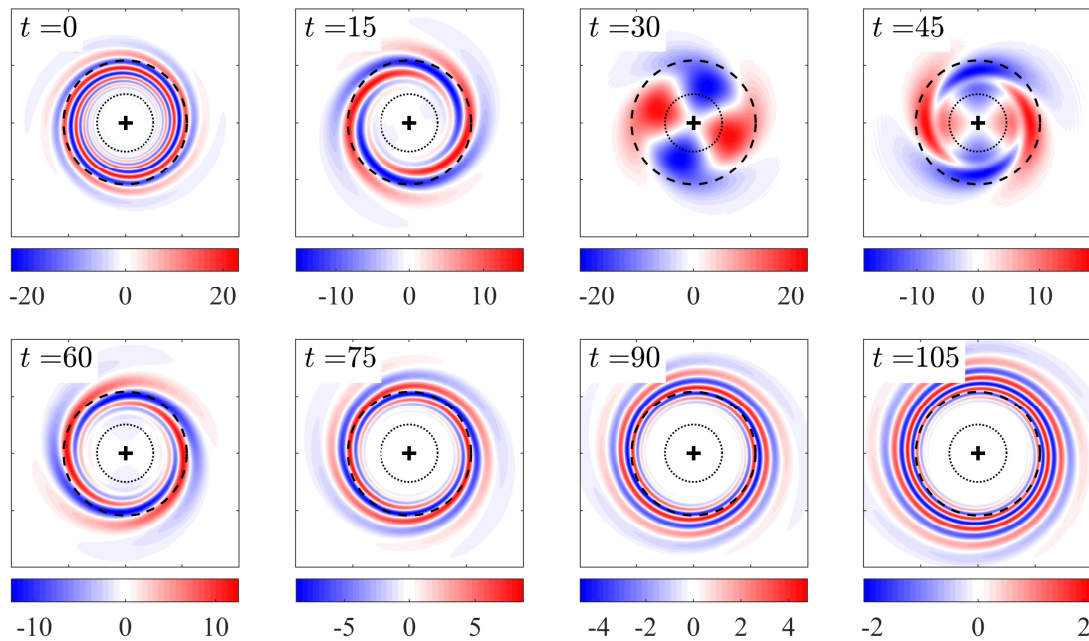


Figure 8.3: Temporal evolution of the vorticity structure $\hat{w}(r, t)$ of the optimal linear response, shown at the specific times corresponding to by the black dots in figure 8.2. Each subfigure shows only $[x, y] \in [-4, 4] \times [-4, 4]$. The plus sign denotes the origin, the dotted circle is the unit circle, and the dashed circle highlights the radius r_q as defined in (8.63).

By “induction” is meant that a radial velocity perturbation is induced in the heart of the vortex as the spirals unfold, and advects the base vorticity which is large here, thus acting as a source for the vorticity perturbation. The core mode is particularly visible in the heart of the vortex in the top-right panel corresponding to $t = 45$. However, it quickly disappears

for later times, as the vorticity spirals roll up in the other direction, this time in line with the base advection (see the panel for $t = 60$). Doing so, the vorticity perturbation decays with time due to a shear-diffusion averaging mechanism studied by Rhines and Young (1983) for a passive scalar and in Lundgren (1982) for vorticity. In particular, Lundgren (1982) concludes that, as long as the vorticity perturbations are rapidly radially varying, the shear-diffusion homogenization mechanism is qualitatively identical to the passive scalar case. This was confirmed numerically a few years later in Bernoff and Lingeitch (1994), where it is further demonstrated that the decay of the perturbation vorticity spirals acts on a $\text{Re}^{1/3}$ time scale. From here, Antkowiak (2005) argues that, in the limit of vanishing viscosity, the evolution equation for the perturbation vorticity $\hat{\omega}$ becomes time reversible; therefore the unfolding (Orr) amplification mechanism can be seen as the “mirror” of the shear diffusion, a damping one. Indeed, the curve for $G(t)$ is fairly symmetric around $t = t_o$ in figure 8.2, and would be even more so for larger Re values. In this sense, the Orr mechanism has an “anti-mixing” effect. This explains why the temporal horizon leading to the largest amplification is also in $\text{Re}^{1/3}$, because it is the “natural” amplification time scale of the vortex. It should be noted that this conception of the Orr and shear-diffusion mechanism as “mirroring” each other was already present in Farrell (1987) in the context of plane shear flows. As a side comment, Antkowiak (2005) also derives the $\text{Re}^{1/3}$ dependence of $t_{o,\text{max}}$ by simply balancing the unfolding and the diffusion (in the radial direction) time scales.

We insist that, apart from a tenuous transient excitation of a core mode by vortex induction, the amplification mechanism of the perturbation is essentially the Orr mechanism. Farrell and Ioannou (1993) have shown that this mechanism was associated with the scaling law $G_o(t_o) \propto t_o$ (note that the gain defined in Farrell and Ioannou (1993) is the square of the gain presently defined). From here, the scaling law $G_o(t_{o,\text{max}}) \propto \text{Re}^{1/3}$ follows immediately.

The shear-diffusion (thus the Orr) mechanism is in essence non-viscous. The only role played by viscosity is to select the radial length scale of the initial vorticity structure (which would tend to be infinitely thin in the absence of viscosity, and the optimal gain and associated temporal horizon follow). Indeed, vorticity sheets that are too thin will be smoothed out by viscosity. If both the optimal gain and the decay *time* are $\propto \text{Re}^{1/3}$, then the decay *rate* is independent of Re . In fact, the decay of the vorticity moments associated with the structures observable in figure 8.3 after $t = 35$, can also be interpreted in terms of the Landau damping phenomenon, which is purely inviscid (Schechter et al., 2000), as developed in the introduction.

More precisely, the exponential decay rate of the vorticity moments can be obtained from a Landau pole of the vortex base profile, as first demonstrated in Briggs et al. (1970). For this, one first needs to define the m -th multipole moment of the vorticity perturbation as

$$Q^{(m)}(t) = \int_0^\infty r^{m+1} \hat{\omega}(r, t) dr = [r^{m+1} (\hat{u}_\theta - i \hat{u}_r)]_{r \rightarrow \infty}. \quad (8.62)$$

Then, to quote Schechter et al. (2000), “A Landau pole is a complex frequency $\omega_q - i\gamma$ at which the Laplace transform of $Q^{(m)}(t)$ is singular [...]. A Landau pole contributes a term to $Q^{(m)}(t)$ of

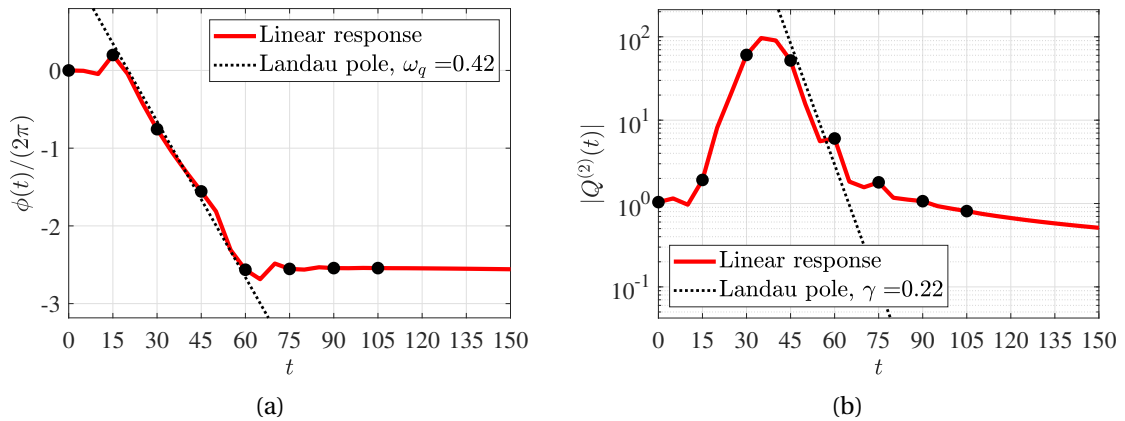


Figure 8.4: Temporal evolution of the vorticity moment $Q^{(2)}(t)$ corresponding to the linear response shown in figure 8.2 and figure 8.3; the black dots again denote the specific times where the vorticity field is shown in figure 8.3. (a) Phase $\phi(t)$ divided by 2π . (b) Amplitude $|Q^{(2)}(t)|$. The black dashed lines correspond to a pure Landau damping $Q^{(2)}(t) = e^{-i\omega_q t - \gamma t}$, where we use fitted values for ω_q and γ .

the form $e^{-\gamma t - i\omega_q t}$. A Landau pole, like an eigenvalue, is a property of some specific linear operator acting on a perturbation and, in this sense, depends on the base profile and the wavenumber of the perturbation, but not on the specific radial shape of the latter. A Landau pole is generally not unique, and its calculation amounts to solving an eigenvalue problem along a radial contour that was deformed in the complex plane (see the appendix in Schecter et al. (2000)); however, one can reasonably expect one of these potentially multiple Landau poles to dominate over the others.

In considering the response of an inviscid Gaussian vortex to a generic external impulse with $m = 2$, Schecter et al. (2000) indeed find that the quadrupole moment $Q^{(2)}(t)$ of the vorticity perturbation “decays exponentially, and the decay rate is given by a Landau pole”. In addition, is also mentioned that “the vorticity perturbation [...] is poorly described by a single damped wave [...] Rather, the vorticity perturbation is rapidly dominated by spiral filament”. This is also the structure observed from $t = 60$ in figure 8.3, which closely resembles the figure 9 in Schecter et al. (2000). In other terms, the response excites a very large number of structurally different eigenmodes, yet it does not invalidate the relevance of the dominant Landau pole.

By writing the quadrupole in terms of amplitude and phase, $Q^{(2)}(t) = |Q^{(2)}(t)|e^{i\phi(t)}$, we display in figure 8.4a the temporal evolution of the phase $\phi(t)$ normalized by 2π and corresponding to the response shown in figure 8.3. The amplitude $|Q^{(2)}(t)|$ is also shown in figure 8.4b. The best fit of the form of a pure Landau damping $Q^{(2)}(t) = e^{-i\omega_q t - \gamma t}$ is also proposed. Clearly, the phase changes at a constant rate in figure 8.4a for $15 \leq t \leq 65$, and $|Q^{(2)}(t)|$ decays exponentially in figure 8.4b for $40 \leq t \leq 65$. Therefore, we confirm that the quadrupole moment $Q^{(2)}(t)$, associated with the linear response in figure 8.3, is well approximated by a Landau pole in its decaying part, although we consider a viscous flow over a time-dependent base vortex, which is not the case in Schecter et al. (2000). The Reynolds number $Re = 5000$, however, seems

sufficiently large for the conclusions drawn in Schechter et al. (2000) to also hold here. In the following, reference will be made to the Landau pole to qualitatively interpret the nonlinear effects, even if the fact that Re is finite possibly makes it less rigorous. The precise value of γ in figure 8.4b is unimportant, for the comparison with any analytical prediction of the Landau pole is outside the scope of this chapter. Note that the exponential decay is followed by an algebraic one for large times, which is also observed in Schechter et al. (2000). The fitted value $\omega_q = 0.42$ in figure 8.4a is, however, important, for it gives the location r_q of the radius where the angular velocity ω_q/m associated with the Landau pole is equal to that of the base flow

$$m\Omega(r_q(t), t) = \omega_q. \quad (8.63)$$

The radius solving (8.63) at each time is highlighted by a dashed circle in figure 8.3. It takes the value $r_q \approx 2.16$, very weakly dependent on time.

It can be shown that the decay rate of the Landau pole is linked to the radial derivative of the base vorticity at r_q specifically. In fact, as demonstrated in Schechter et al. (2000), Turner and Gilbert (2007), and Turner et al. (2008), the exponential damping mechanism can be removed from any vortex, in particular a Gaussian one, by cancelling such derivative at r_q .

The poor modal description of a perturbation evolution over a Gaussian vortex, mentioned in Schechter et al. (2000) and confirmed in figure 8.3, is the reason for which non-modal analytical tools are deployed in the present study, in particular for studying nonlinear effects. We address these latter now.

8.4.4 Fully nonlinear results

We introduce the fully nonlinear results obtained from DNS in the present section. Let us define \mathbf{u}_p as being the perturbation between the fully nonlinear solution \mathbf{U} obtained from a DNS, and the reference Lamb-Oseen solution \mathbf{U}_b in (8.55); in other terms, $\mathbf{u}_p \doteq \mathbf{U} - \mathbf{U}_b$. We recall that this perturbation is initialized along the wavenumber $m = 2$ with the linear optimal initial condition with an amplitude U_0 , such that

$$\mathbf{u}_p|_{t=0} = U_0 \hat{\mathbf{u}}_o e^{im\theta} + \text{c.c.} \quad (8.64)$$

Owing to nonlinear effects, \mathbf{u}_p generally does not oscillate purely along m for strictly positive times. For this reason we need to further extract $\hat{\mathbf{u}}_p^{(1)}$, the component of \mathbf{u}_p oscillating at the fundamental wavenumber m , hence the superscript '(1)'. For this, a Fourier series is naturally used as

$$\begin{aligned} \hat{\mathbf{u}}_p^{(1)}(r) &\doteq \frac{1}{2\pi} \int_0^{2\pi} \mathbf{u}_p(r, \theta) \cos(m\theta) d\theta - \frac{i}{2\pi} \int_0^{2\pi} \mathbf{u}_p(r, \theta) \sin(m\theta) d\theta, \quad \text{such that} \\ \mathbf{u}_p^{(1)}(r, \theta) &\doteq \hat{\mathbf{u}}_p^{(1)}(r) e^{im\theta} + \text{c.c.} \end{aligned} \quad (8.65)$$

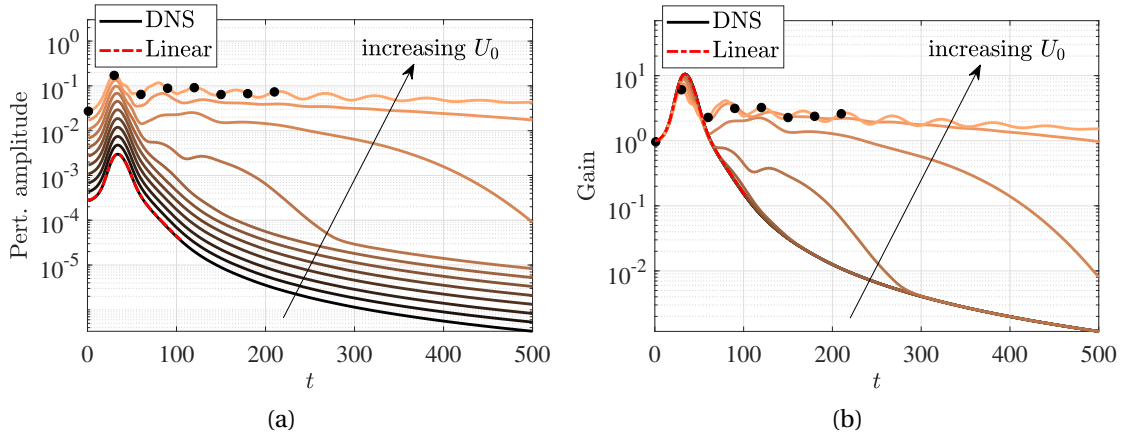


Figure 8.5: (a) Amplitude of the fully nonlinear fundamental perturbation $\hat{\mathbf{u}}_p^{(1)}$ as defined in (8.65), initialized with the linear optimal condition for $(\text{Re}, m, t_o) = (5000, 2, 35)$. Larger U_0 values correspond to lighter colours. (b) The same data are divided by their corresponding U_0 , yielding the nonlinear gains as defined in (8.66). For the largest considered $U_0 = 2.82 \times 10^{-2}$, black dots are located at $t = 0, 30, 60, \dots, 210$, for which the corresponding vorticity structures are shown in figure 8.6.

From here, the fully nonlinear gain (associated with the fundamental pair) is immediately defined as

$$G_{\text{DNS}} \doteq \frac{\|\hat{\mathbf{u}}_p^{(1)}\|}{U_0}. \quad (8.66)$$

By fixing $\text{Re} = 5000$ and $t_o = 35$, we report in figure 8.5a the fully nonlinear evolution of the perturbation amplitude $\|\hat{\mathbf{u}}_p^{(1)}\|$, for different amplitudes of the initial condition U_0 . The associated gain, that is, the same data divided by the corresponding U_0 , is shown in figure 8.5b.

Figure 8.5a illustrates well a bypass transition, also called ‘‘bootstrapping effect’’ in Trefethen et al. (1993), where linear transient growth and nonlinear mechanisms interact to bring about a transition to a new state, distinct from the reference one. Indeed, as we increase the amplitude of the initial condition (linearly in log scale), the transient growth of the perturbation, initiated by the linear Orr mechanism as we have seen, becomes sufficient to trigger nonlinear terms; for the two largest considered U_0 , this prevents the flow to re-axisymmetrize to the Lamb-Oseen vortex. Interestingly, for the third and fourth largest considered U_0 , the flow seems to temporarily approach a new state but nevertheless relaxes towards the reference one.

For the largest considered $U_0 = 2.82 \times 10^{-2}$ and the set of times highlighted by the black dots, we report in figure 8.6 the structure of the vorticity perturbation. From $t = 60$, the flow has reached a new nonlinear quasi-equilibrium state, that diffuses very slowly due to viscous effects, and rotates counterclockwise with a period of approximately 45 units of times. The corresponding total vorticity field, which is obtained by adding to figure 8.6 the Gaussian

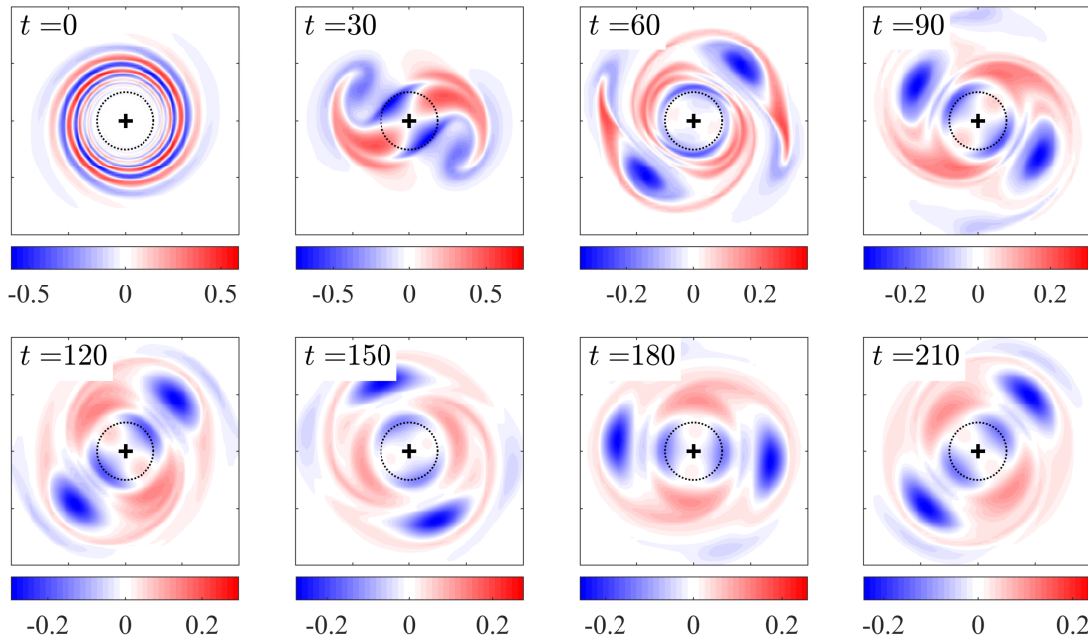


Figure 8.6: Temporal evolution of the vorticity structure of the fully nonlinear perturbation for $U_0 = 2.82 \times 10^{-2}$, shown at the specific times highlighted by the black dots in figure 8.5. Each panel shows only $[x, y] \in [-4, 4] \times [-4, 4]$, the plus sign denotes the origin, and the dashed line is the unit circle.

reference vorticity (8.56), takes a tripolar shape. This is shown in figure 8.7 for $t \geq 120$, where the heart of the vortex takes an elliptical shape that is surrounded by two satellite vortices of low and negative vorticities (corresponding to the two blues spots in figure 8.6 from $t = 60$). As developed in the introduction, this tripolar state was already largely reported in a variety of contexts. In particular, its spatial structure compares well with the one reported in figure 2 of Antkowiak and Brancher (2007) for $\text{Re} = 1000$, or with the experimental visualization in Kloosterziel and van Heijst (1991).

In terms of the gain in figure 8.5b, we notice that all the curves corresponding to different U_0 collapse for small times, confirming the linearity of the initial growth mechanism. However, they significantly depart from each other at larger times. If nonlinearities seem to saturate the gain for times around $t_o = 35$, they clearly increase the latter up to three orders of magnitude for large times; as said, that is because the flow bifurcated to another state, thereby the perturbation that is measured around the reference vortex remains large.

The weakly nonlinear model is now employed to assess the gain evolution with U_0 shown in figure 8.5b.

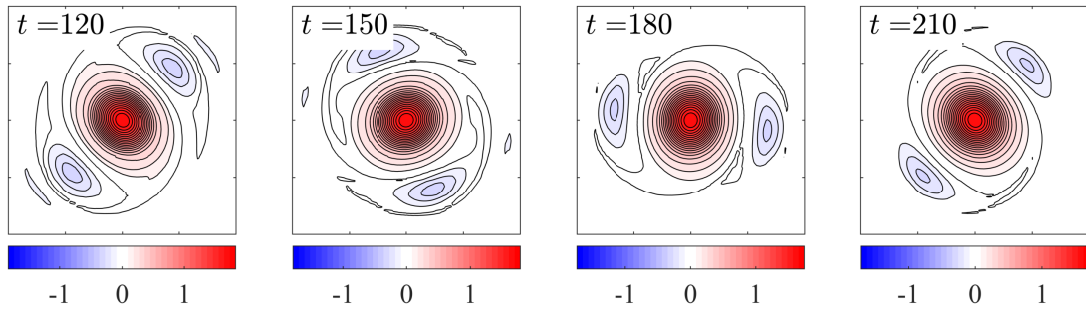


Figure 8.7: Same as in figure 8.6 but the reference vorticity field (8.56) has been added, so as to visualize the total, fully nonlinear, vorticity field; some isolines are also shown to better expose the elliptical deformation of the vortex core.

8.5 Weakly nonlinear transient growth in the diffusing Lamb-Oseen vortex in dimension two

In the weakly nonlinear paradigm, the perturbation field \mathbf{u}_p is approached by $\mathbf{u}_p = \sqrt{\epsilon_o} \mathbf{u}_1 + \epsilon_o \mathbf{u}_2 + \sqrt{\epsilon_o^3} \mathbf{u}_3 + O(\epsilon_o^2)$, as can be seen in (8.19). Consequently $\hat{\mathbf{u}}_p^{(1)}$ is approximated by $\sqrt{\epsilon_o} \bar{\mathbf{u}}_1^{(1)} + \sqrt{\epsilon_o^3} \bar{\mathbf{u}}_3^{(1)} + O(\sqrt{\epsilon_o^5})$, therefore the fully nonlinear gain G_{DNS} defined in (8.66) is expected to reduce to the weakly nonlinear one G_w defined in (8.49), since $\epsilon_o \ll 1$. These two quantities are compared in this section. Note that we checked that for all considered Re values the first sub-optimal transient gain was $O(1/\sqrt{\epsilon_o})$, in contrast to $1/\epsilon_o$ for the optimal one, which mathematically justifies focusing on the response to $\hat{\mathbf{u}}_o$ only.

8.5.1 Transient change from nonlinear saturation to nonlinear amplification

The real part of the weakly nonlinear coefficient, defined in (8.48), is shown in figure 8.8a for $\text{Re} = 5000$ and $t_o = t_{o,\text{max}} = 35$. It is further split into the sum of a mean flow distortion contribution, $\mu_r^{(0)}$, arising from $\mathbf{u}_2^{(0)}$ only, and second harmonic contribution, $\mu_r^{(2)}$, arising from $\hat{\mathbf{u}}_2^{(2)}$ only. In this manner, $\mu_r = \mu_r^{(0)} + \mu_r^{(2)}$.

Remarkably, after having significantly decreased until reaching a minimum at $t = 59$, the coefficient μ_r increases again and changes sign at $t = 87$. It then reaches its maximum at $t = 107$, and decreases again until plateauing around zero for $t \geq 150$. A change of sign in μ_r brings diversity to the behaviours reported in Ducimetière et al. (2022a), concerning transient growths in the streamwise-invariant Poiseuille flow, and in the flow past a backward-facing step. There, only negative coefficients, corresponding to saturating nonlinearities, were observed. In the present work, however, nonlinearities appear to reinforce the gain for some time. When it is negative, the behaviour of μ_r seems largely dominated by the contribution from the mean flow distortion $\mu_r^{(0)}$. When the former is positive, however, $\mu_r^{(0)}$ is reduced and the second harmonics appear to contribute as much to the sum.

Upon taking the derivative of the square the weakly nonlinear gain in (8.53) with respect to

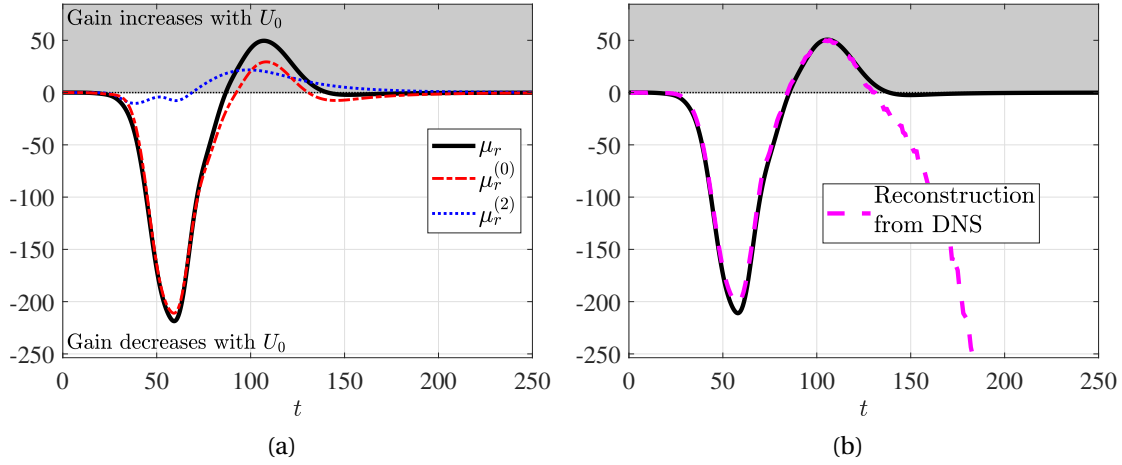


Figure 8.8: (a) Real part of the weakly nonlinear coefficient μ defined in (8.48) (black continuous line). It is further split as the sum of a contribution from a mean flow distortion (red dash-dotted line), plus a contribution from the second harmonic (blue dotted line). In the grey zone, the weakly nonlinear gain G_w defined in (8.49) increases monotonically with U_0 , since $\mu_r > 0$. In the white zone, it decreases monotonically. (b) The coefficient μ_r is compared with its reconstruction from DNS data (magenta dashed line) according to (8.68).

U_0^2 , we obtain

$$\frac{\partial(G_w^2)}{\partial(U_0^2)} = \frac{2\mu_r}{\epsilon_o^2 - 2U_0^2\mu_r} G_w^2. \quad (8.67)$$

Therefore, the coefficient μ_r relates directly to the rate of change of G_w^2 with respect to U_0^2 in the limit where U_0 tends towards zero as

$$\mu_r = \frac{\epsilon_o^2}{2} \left(\lim_{U_0 \rightarrow 0} \frac{1}{G_w^2} \frac{\partial(G_w^2)}{\partial(U_0^2)} \right). \quad (8.68)$$

By using (8.68), the coefficient μ_r can be reconstructed directly from DNS data. For this, the derivative in (8.68) is estimated by using a first-order finite difference approximation between DNS data for the gain squared, corresponding to the two lowest considered $U_0 = 2.26 \times 10^{-4}$ and $U_0 = 2.82 \times 10^{-4}$. The result is shown as the magenta dotted line in 8.8b, and compared with the actual μ_r . The good agreement between both curves for $t \leq 130$ *a posteriori* validates for these times our weakly nonlinear expansion, at least in the limit of small U_0 . However, both curves depart significantly after $t = 130$, presumably due to the violation of the condition (8.30) ensuring that the asymptotic expansion is well posed. Indeed, the response to the initial condition optimized for $t = t_o = 35$ was shown to rapidly decay in amplitude for larger times in figure 8.2; therefore the norm of the perturbation operator, $\|P(t)\| = 1/\|\hat{l}(t)\|$, increases accordingly.

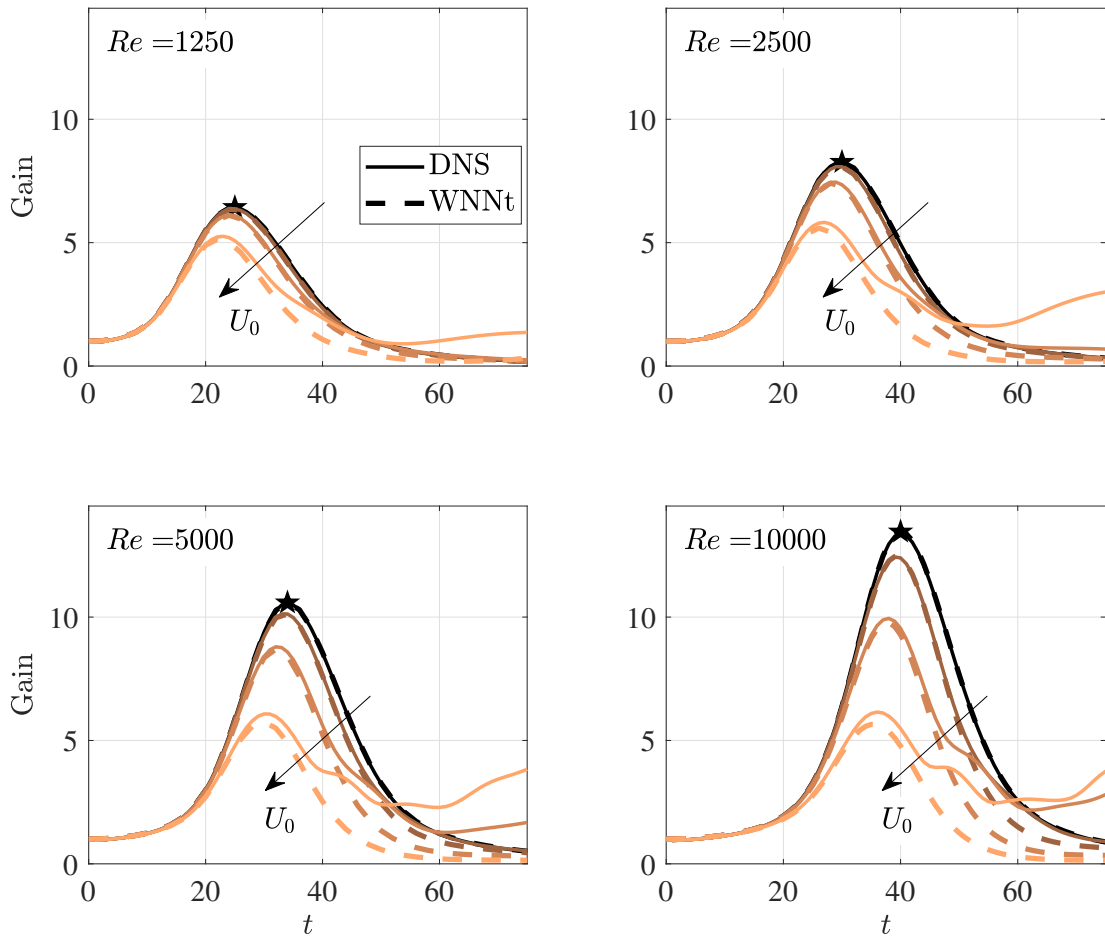


Figure 8.9: Weakly and fully nonlinear gains as defined in (8.49) and (8.66), respectively. Larger $U_0 \in [0.03, 0.45, 1.12, 2.82] \times 10^{-2}$ correspond to lighter colours (direction of increasing U_0 is also indicated by the arrow). The continuous line stands for DNS data whereas the dash-dotted is for the weakly nonlinear model. Temporal horizons are $t_o = t_{o,\max} = [25, 30, 35, 40]$ (times at which a black star is shown) for $Re = [1.25, 2.5, 5, 10] \times 10^3$, respectively.

8.5.2 Comparison of fully and weakly nonlinear gains

In figure 8.9 the weakly nonlinear gain, associated with the coefficient in figure 8.8, is compared with the fully nonlinear one. For the moment, only short times where the gains are large are shown. The later evolution, being associated with orders of magnitude smaller gains, will be considered in figure 8.10 in log scale. On the time interval chosen for figure 8.9, the coefficient μ_r is negative, thereby the model predicts the gain to decrease monotonically with U_0 . For values of U_0 small enough so that the linear gain (black curves in 8.9) is only slightly modulated, the agreement with DNS data is excellent. By increasing U_0 , the agreement degrades only slowly and remains very good for these relatively small times, for instance over $0 \leq t \leq 40$ in the panel corresponding to $Re = 10^4$. This corresponds to times when the nonlinear structure remains symptomatic of the linear one, in the sense that the flow has not yet reached the

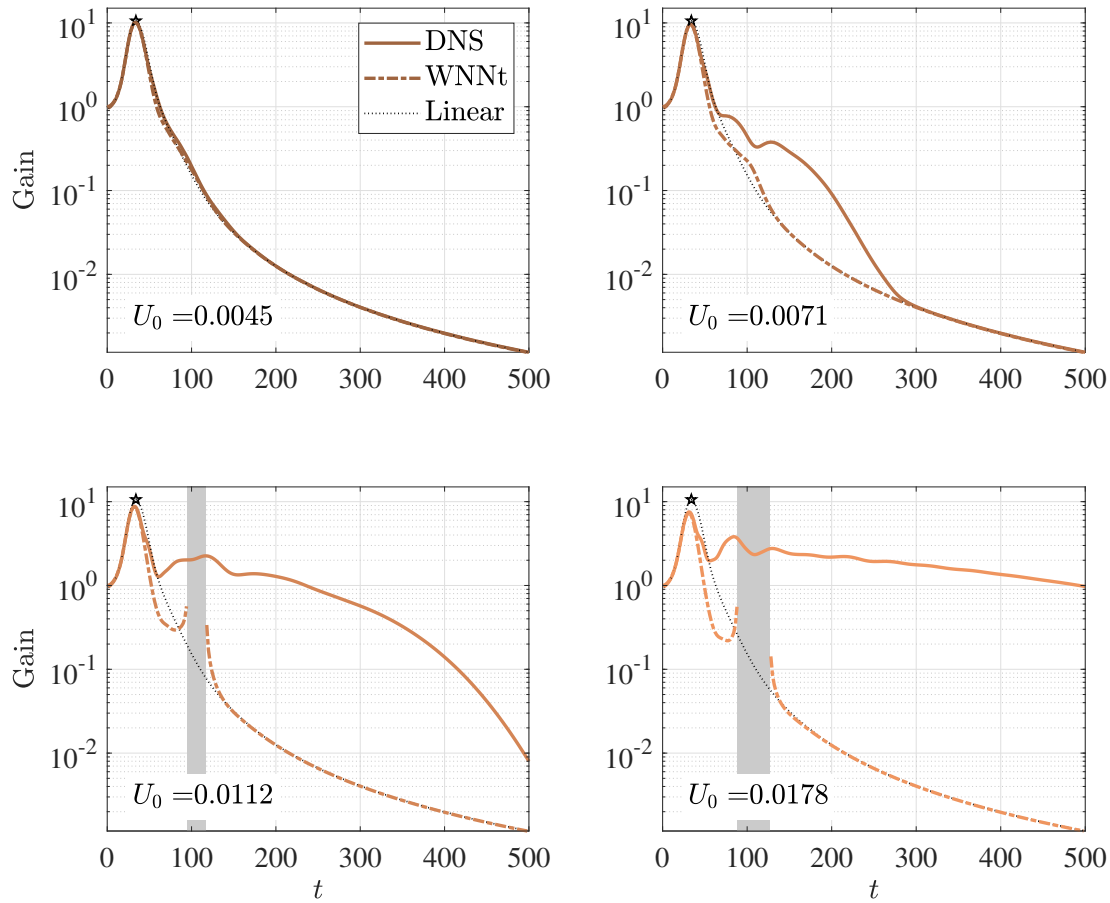


Figure 8.10: Weakly and fully nonlinear gains for $\text{Re} = 5000$ and increasing amplitude of the initial condition $U_0 \in [4.5, 7.1, 11.2, 17.8] \times 10^{-3}$. Each panel corresponds to a different U_0 . The grey box denotes the time interval (8.69) over which the weakly nonlinear gain is undefined. The latter is singular at the boundaries of this interval.

tripolar state (temporarily or not, as shown in figure 8.5). Indeed, the amplitude equation (8.52) is independent of space, which condemns the response to be structurally close to the linear one. For later times and large U_0 , as soon as the fully nonlinear gain begins to oscillate and to bear a non-monotonic behaviour, the agreement with our weakly nonlinear model rapidly degrades. The reason is precisely that, the response whose nonlinear evolution is approached by our model, is not selected by the flow anymore, which has reached another state, temporarily or not, and that is structurally completely different; about this new state, the amplitude equation has no information.

Nevertheless, while the proposed amplitude equation fails to predict the gain and the structure of the flow when at the tripolar state, it does predict a bifurcation threshold. This is illustrated in figure 8.10, where the same data as in figure 8.9 for $\text{Re} = 5000$ is shown, although the time interval is extended until $t = 150$ to include the time interval where the real part of the weakly nonlinear coefficient becomes positive, indicating “anti-saturation”. The weakly nonlinear

gain is undefined on the time interval where

$$\mu_r(t) \geq \frac{1}{2} \left(\frac{\epsilon_o}{U_0} \right)^2 > 0, \quad (8.69)$$

which widens by increasing U_0 . The gain is singular (tends to infinity) at the times corresponding to the boundaries of this interval. The latter is highlighted by the grey zones in figure 8.10.

8.5.3 Bifurcation thresholds

By looking at the panels corresponding to $U_0 = 1.12 \times 10^{-2}$ and $U_0 = 1.78 \times 10^{-2}$, we observe that over the time interval where the equation has no solution, i.e. the grey zone, the fully nonlinear simulation seems to have reached the tripolar state (although for $U_0 = 1.12 \times 10^{-2}$ it is only temporary as it eventually relaxes towards the reference state). In this sense, a loss of solution in the amplitude equation could indicate that the DNS has left the state around which the weakly nonlinear expansion was constructed. The minimum U_0 for which the weakly nonlinear gain becomes singular may then be considered as an approximation of the actual bifurcation threshold. Such minimal U_0 , named U_0^s is what follows, reads

$$U_0^s = \frac{\epsilon_o}{\sqrt{2\mu_r(t_s)}}, \quad \text{where } \mu_r(t_s) = \max_t \mu_r(t), \quad (8.70)$$

and is defined if and only if $\mu_r(t_s) > 0$.

A bifurcation threshold in the DNS solutions must also be defined and compared directly with (8.70). To the knowledge of the authors, there is no clear and universal subcritical bifurcation criterion, and the choice made is always arguably arbitrary. Nevertheless, we will opt for the criterion proposed in Antkowiak (2005), based on the observation that the tripolar state is characterized by a deformed, non-axisymmetric, heart. Therefore a characteristic aspect ratio λ of the heart is established as

$$\lambda^2 \doteq \frac{J+R}{J-R}, \quad \text{with } J = (J_{20} + J_{02}), \quad R = \sqrt{(J_{20} - J_{02})^2 + 4J_{11}^2} \quad \text{and} \quad (8.71)$$

$J_{mn} \doteq \int_{\Omega} x^m y^n \hat{\omega}(x, y) dx dy$ a vorticity moment. A characteristic eccentricity is further defined as $e \doteq \sqrt{1 - 1/\lambda^2}$. From here, Antkowiak (2005) computes the typical half-life time (that is where the criterion is rather arbitrary) of the heart deformation as

$$\tau, \quad \text{such that } \int_0^\tau e(t) dt = \frac{1}{2} \int_0^{t_f} e(t) dt, \quad (8.72)$$

where $t_f = 500$ is the final time of the fully nonlinear simulations.

We report the half-life time as a function of U_0 and for different Re values in figure 8.11a. For each Re number, we also highlight an inflection point in τ at a certain U_0 , and we declare the

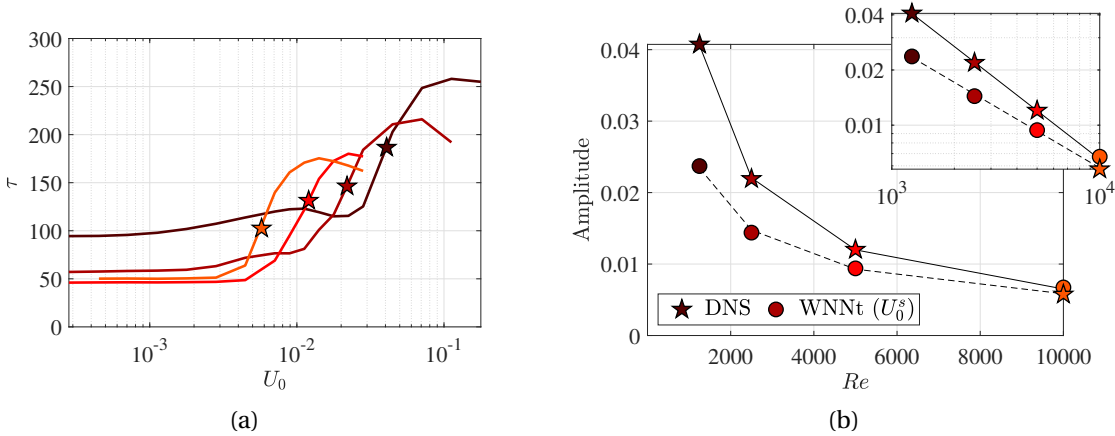


Figure 8.11: (a) Typical half-life time of the heart deformation defined in (8.72), as a function of the amplitude of the initial condition U_0 . Larger $Re = [1.25, 2.5, 5, 10] \times 10^3$ correspond to lighter colours. A star highlights an inflection point, for which the corresponding U_0 is declared as being the threshold amplitude for the subcritical bifurcation. Such thresholds U_0 are reported in (b) as a function of Re (also with a star symbol). The prediction from the weakly nonlinear model, U_0^s defined in (8.70) is also shown. The thin continuous line is a power law fitted on the DNS data for the first three considered Re , with $\propto Re^{-0.88}$, whereas the thin dashed line is fitted on the weakly nonlinear data with $\propto Re^{-0.66}$. The inset shows the same in log-log scale.

latter as being the subcritical bifurcation threshold. It is reported directly as a function of Re in figure 8.11b, and compared with the weakly nonlinear prediction U_0^s , in both linear and log scales. Both approaches clearly highlight a decreasing power-law dependence of the subcritical bifurcation threshold with the Re number. For the fully nonlinear data, the fitted exponent -0.88 found in the present study, agrees relatively well with the one reported in Antkowiak and Brancher (2007), which is -0.8 . However, since little information is given regarding how the threshold amplitude was computed in Antkowiak and Brancher (2007), the agreement with our results is perhaps fortunate. In any case, the negative power-law dependence with Re implies that the threshold amplitude above which the flow goes into the basin of attraction of the tripolar state, and in the direction given by the linear optimal, vanishes for increasing Re . This may explain the formation and persistence of elliptical vortex eyewalls in some tropical cyclones (Kuo et al., 1999; Reasor et al., 2000). We insist that we only consider perturbations in the direction of the linear optimal, whereas nonlinear optimal perturbations can also be found by relying on the techniques presented in Pringle and Kerswell (2010). The latter would be associated with a threshold amplitude U_0 for a subcritical bifurcation even smaller than the one shown in figure 8.11. The fitted exponent for the weakly nonlinear model is found as being -0.66 , thereby the threshold amplitudes between both models differ significantly by decreasing Re in figure 8.11b.

This discrepancy between exponents may be explained as follows. For the DNS, our bifurcation criterion aims at computing the threshold above which the flow has definitely bifurcated, whereas the loss of solution in the amplitude equation refers to a specific time interval. The

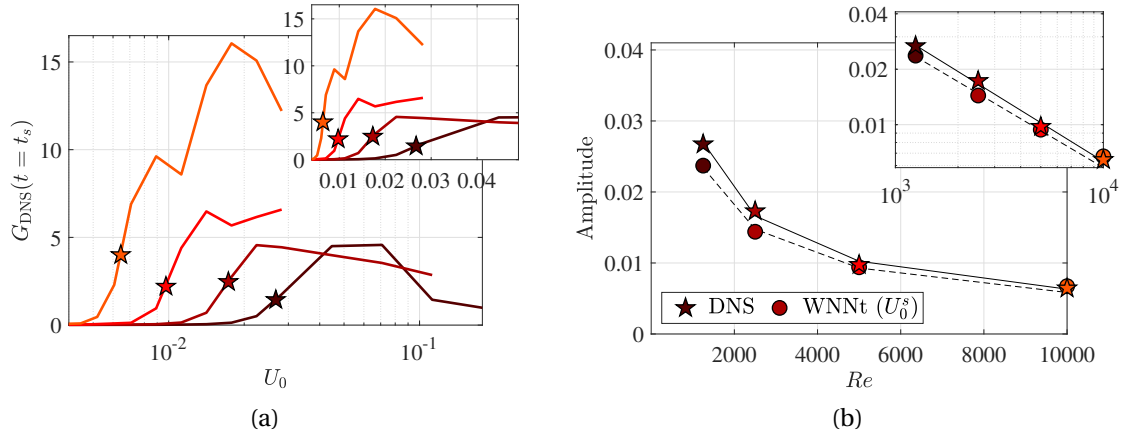


Figure 8.12: Same as in figure 8.11, although the inflection point is sought in $G_{\text{DNS}}(t = t_s)$, where t_s , defined in (8.70), is the first time for which the amplitude equation predicts a loss of solution. In (a), the inset shows the same data in linear scale. In (b), the thin continuous line is a power law fitted on the DNS data with $\propto Re^{-0.69}$, whereas the thin dashed line $\propto Re^{-0.66}$ is similar to figure 8.11.

importance of this conceptual difference is well illustrated in the bottom-left panel in figure 8.10 for $U_0 = 1.12 \times 10^{-2}$. Here, the amplitude equation predicts that no solution exists over some time interval; thus, according to the criterion (8.70), the flow has bifurcated. However, if the DNS data seem indeed to have reached the tripolar state over this time interval, it relaxes to the reference state at longer times; thus, the criterion based on τ concludes that the flow has not yet bifurcated.

For this reason, we propose another criterion, rather artificial, for which both “bifurcation” refer to the same specific time t_s , the first time for which the amplitude equation predicts a loss of solution (see (8.70)). The threshold U_0 in the DNS is decreed as being the one corresponding to an inflection point in $G_{\text{DNS}}(t = t_s)$, as shown in figure 8.12a despite a quite coarse resolution. The agreement with U_0^s improves significantly in figure 8.12b (as compared with figure 8.11b). Note that, for both models, the power-law dependence of the threshold amplitude cannot be only explained by the power-law dependence of the linear optimal transient gain, for the latter was shown to be in $-1/3$.

8.5.4 Physical interpretation of the nonlinear “anti-saturation”: mean flow distortion and inversion of the vorticity gradient

We now propose to interpret physically the behaviour of the coefficient associated with the (azimuthal) mean flow distortion, $\mu_r^{(0)}$ shown in figure 8.8, and attempt to discuss the reason why it changes sign and leads to the subcritical behaviour discussed above. In the following discussion, we will focus on the case $Re = 5000$. First, the energy of the mean flow distortion $\mathbf{u}_2^{(0)}$ is shown as the red curve in figure 8.13a.

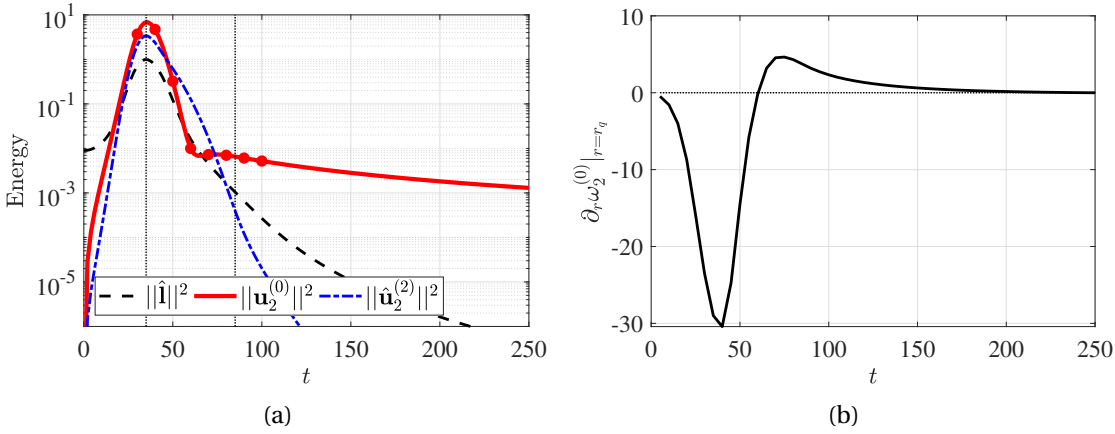


Figure 8.13: (a) For $\text{Re} = 5000$, the evolution of the energy $\|\cdot\|^2$ of the linear response $\hat{\mathbf{l}}$ (black dashed line), of the second harmonic $\hat{\mathbf{u}}_2^{(2)}$ (blue dashed-dotted line) and, mainly, of the mean flow distortion $\mathbf{u}_2^{(0)}$ (red continuous line). The red dots correspond to the specific times $t = 30, 40, \dots, 100$, for which the vorticity structure of $\mathbf{u}_2^{(0)}$ is reported in figure 8.14. Two horizontal dotted lines are drawn at $t = 35$ and $t = 85$. (b) Slope of the vorticity at the radius r_q , i.e. $\partial_r \omega_2^{(0)}|_{r=r_q}$, as a function of time.

For comparison, the energies of the linear response and of the second harmonic are also shown. As written in (8.36), the mean flow distortion is forced by

$$\mathbf{f}_2^{(0)} = -C_m \left[\hat{\mathbf{l}}^*, \hat{\mathbf{l}} \right] + \text{c.c.}, \quad (8.73)$$

which is the Reynolds stress of the linear response. Under its action, the energy of $\mathbf{u}_2^{(0)}$ increases until reaching a maximum around $t = t_o = 35$, before decaying until $t = 65$. From here, the energy rebounds very slightly, then decays extremely slowly for $t \geq 85$. It is striking to notice in figure 8.13a that $\mathbf{u}_2^{(0)}$ can persist for extremely long times, even when the linear response, whose nonlinear interactions force $\mathbf{u}_2^{(0)}$, has vanished. This suggests that $\mathbf{u}_2^{(0)}$ can persist even in the absence of sustained forcing. This is also illustrated in figure 8.14, where we show $\omega_2^{(0)}$, the vorticity structure associated with $\mathbf{u}_2^{(0)}$, for the different times highlighted by the red dots in figure 8.13a. If we observe a transient regime until the panel for $t = 70$, the vorticity field does not seem to evolve afterward, except by slow diffusion.

It will simplify the rest of the analysis to notice that $\mathbf{u}_2^{(0)}$ only possesses an azimuthal component, i.e. $\mathbf{u}_2^{(0)} = u_{2,\theta}^{(0)} \mathbf{e}_\theta$. That is because $\mathbf{u}_2^{(0)}$ is associated with the wavenumber $m = 0$, for which the equation for the radial perturbation is $\partial_r (r u_{2,r}^{(0)}) = 0$ from the continuity. This leads to $u_{2,r}^{(0)} = 0$ and a forced diffusion equation for $u_{2,\theta}^{(0)}$, reading

$$\partial_t u_{2,\theta}^{(0)} = \text{Re}^{-1} (\Delta_0 - 1/r^2) u_{2,\theta}^{(0)} + f_{2,\theta}^{(0)}. \quad (8.74)$$

The panels in the first row in figure 8.15 show the evolution of $f_{2,\theta}^{(0)}$ (left) and $u_{2,\theta}^{(0)}$ (right) over

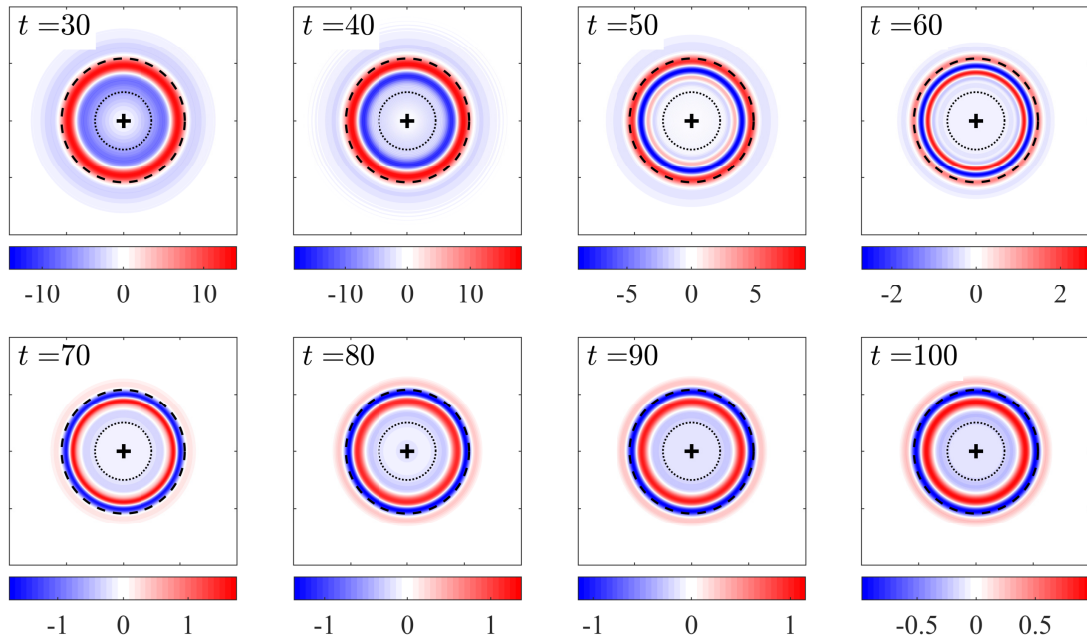


Figure 8.14: Temporal evolution of $\omega_2^{(0)}$, the vorticity structure of $\mathbf{u}_2^{(0)}$, the mean flow distortion induced by the Reynolds stress of the linear response shown at the specific times corresponding to the red dots in figure 8.13a. Each panel shows only $[x, y] \in [-4, 4] \times [-4, 4]$. The plus sign denotes the origin, the dotted circle is the unit circle, and the dashed circle highlights the radius r_q solving (8.63) with $\omega_q = 0.42$.

$0 \leq t \leq 35$. The Reynolds stress forcing $f_{2,\theta}^{(0)}$ grows in amplitude (since $\hat{\mathbf{l}}$ does) while roughly conserving its shape, which $u_{2,\theta}^{(0)}$ seems to imitate closely, although logically with some delay. This direct structural link between the forcing and the response is certainly due to the absence of an advection term in (8.74).

The panels in the second row in figure 8.15 show the evolution over the times $35 \leq t \leq 85$. Notice that the forcing $f_{2,\theta}^{(0)}$ has shapes at $t = 30$ and $t = 40$ that are similar but have opposite signs. As developed in section 8.4.3, this is because the spiral structures in $\hat{\mathbf{l}}$, that unroll in one direction until $t = 35$, roll up symmetrically in the other direction afterward. Under the action of this forcing that is now adverse, the velocity $u_{2,\theta}^{(0)}$ tends to invert in the bottom-right panel of figure 8.15, which implies its momentary flattening, therefore $u_{2,\theta}^{(0)}$ rapidly loses energy. This energy would have grown again (which it does shortly after $t = 65$ in figure 8.13a) if the forcing could maintain its intensity, but the latter decays rapidly with the one of $\hat{\mathbf{l}}$.

After $t = 85$ the velocity $u_{2,\theta}^{(0)}$ evolves freely, for $f_{2,\theta}^{(0)}$ is negligible. The persistence of $u_{2,\theta}^{(0)}$ is then easily understood once it is realized that the diffusion operator in (8.74) possesses a continuum of orthogonal Bessel eigenfunctions (the domain is infinite). They are associated with eigenvalues spanning the strictly negative part of the imaginary axis. Accordingly, after discretization, we found an extremely dense packing of eigenvalues all along the negative part of the imaginary axis, increasingly dense with the number of discretization points. The

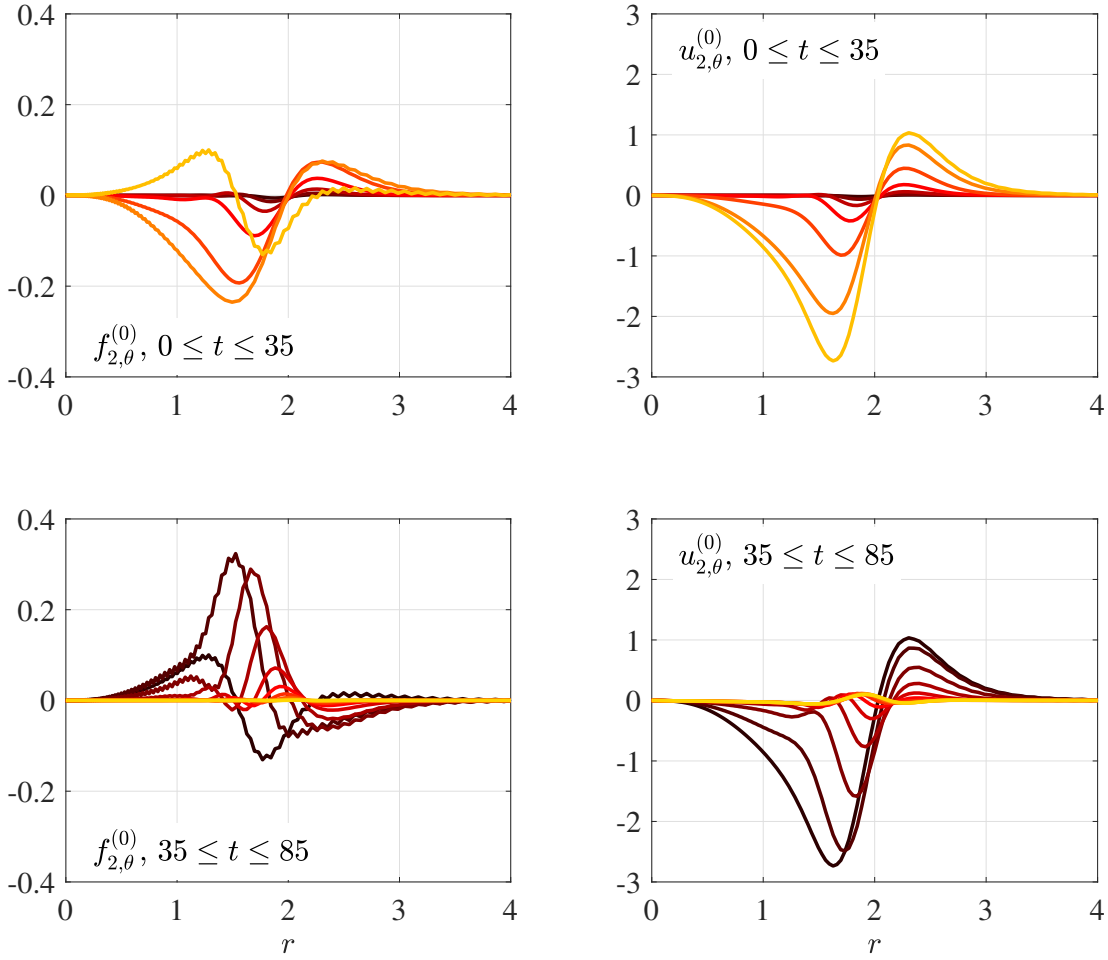


Figure 8.15: Temporal evolution of the forcing $f_{2,\theta}^{(0)}$ (panels at the left) and of the velocity response $u_{2,\theta}^{(0)}$ (panels at the right). Panels at the top and the bottom lines correspond to two different and successive time intervals. The top line is for $t = 0, 5, \dots, 35$ (on the left of the first vertical line in figure 8.13a) and the second for $t = 35, 40, \dots, 85$ (between the two vertical lines in figure 8.13a). Larger times correspond to lighter colours.

velocity structure left by the forcing that has vanished at $t = 85$, projects over a significant number of these Bessel eigenfunctions, including some with very low damping rates of the order of 10^{-4} . It is therefore not surprising to see this structure subject to very slow diffusion in figure 8.13a and figure 8.14.

After having proposed some elements to understand the evolution of $u_{2,\theta}^{(0)}$, let us study now how it feeds back on the response. We show in figure 8.13b the slope of $\omega_2^{(0)}$ at the specific radius r_q where the angular velocity ω_q/m associated with the Landau pole is equal to that of the base flow. We recall this specific radius to be found by solving (8.63) with the fit value $\omega_q = 0.42$, resulting in $r_q \approx 2.16$, very weakly time dependent.

The slope is negative until $t = 60$, where it changes sign. As a consequence, from $t = 60$ onward,

the addition of $\omega_2^{(0)}$ to the reference vorticity has a positive contribution to the total vorticity slope at r_q . In parallel, we recall that $\mu_r^{(0)}$ can be directly interpreted as the sensibility at a time t of the transient gain to the addition of $u_{2,\theta}^{(0)}$ to the reference flow. For this, $\mu_r^{(0)}$ computes the integrated effect of this addition between 0 and t (see formula 8.94). Therefore, the decreasing tendency of $\mu_r^{(0)}$ until $t = 60$ in figure 8.8, results from the negativity of the slope of $\omega_2^{(0)}$ at r_q , which enhances the Landau damping rate of the response, whose integrated effect is to reduce the gain. Such an effect of the mean vorticity slope at r_q on the Landau damping was reported in Schecter et al. (2000), Turner and Gilbert (2007), and Turner et al. (2008). On the contrary, from $t = 60$ onward the coefficient $\mu_r^{(0)}$ increases, for the presence of $\omega_2^{(0)}$ now reduces the Landau damping rate; the integrated effect of such mitigation of the Landau damping rate over time leads to a coefficient that becomes positive, traducing a weakly nonlinear gain larger than the linear one. In other words, we interpret the subcritical behaviour of our amplitude equation as being partially because the mean flow distortion reminiscence, shown in figure 8.14 for large time, tends to erase the vorticity slope at the specific radius r_q , therefore letting the perturbation persist. This conclusion is comparable to the one drawn in Balmforth et al. (2001). In addition, the present amplitude equation leads to the conclusion that, when μ_r is at its maximum, the effect of the second harmonic is just as important as the one of the mean flow, although it is harder to interpret.

We insist that the conclusions drawn below relate only to predictions of the amplitude equation, thereby possibly explaining DNS behaviour only when both approaches agree. However, precisely because they do not at large U_0 and after increasingly short times in figures 8.9 and 8.10, the departure between weakly and fully nonlinear responses there remains to be interpreted. This can still be done by using the amplitude equation, although in an indirect manner.

In figure 8.16, we compare the linear stability to $m = 2$ perturbations of the (azimuthal) mean flow extracted from the DNS, and the one predicted by the weakly nonlinear approach. This is done for $U_0 = 2.82 \times 10^{-2}$, the largest considered initial condition amplitude in figure 8.9. The weakly nonlinear mean flow is simply obtained by evaluating the weakly nonlinear expansion as $U_{b,\theta} + a^2 u_{2,\theta}^{(0)}$, where a solves the amplitude equation. The linear stability is assessed by replacing the reference flow by the mean one in (8.2), then assuming a temporal dependence as $\hat{\mathbf{u}}(r, t) \doteq \tilde{\mathbf{u}}(r) e^{\sigma t}$, and solving the subsequent eigenvalue problem. The azimuthal mean is linearly unstable if and only if there exists an eigenvalue σ such that $\text{Re}(\sigma) = \sigma_r > 0$, and the corresponding eigenmode grows exponentially to the extent that the growth rate is much smaller than the rate of change of the base flow. The mean vorticity profiles are also shown in figure 8.17.

For $10 \leq t \leq 20$ in figure 8.16, both DNS and weakly nonlinear mean flows appear unstable, with an excellent agreement between the growth rates, and between the corresponding vorticity profiles in figure 8.17. For $t = 15$ and $t = 20$ in figure 8.17, these profiles consist of a central region of large vorticity, surrounded by a ring of locally enhanced but relatively smaller vorticity.

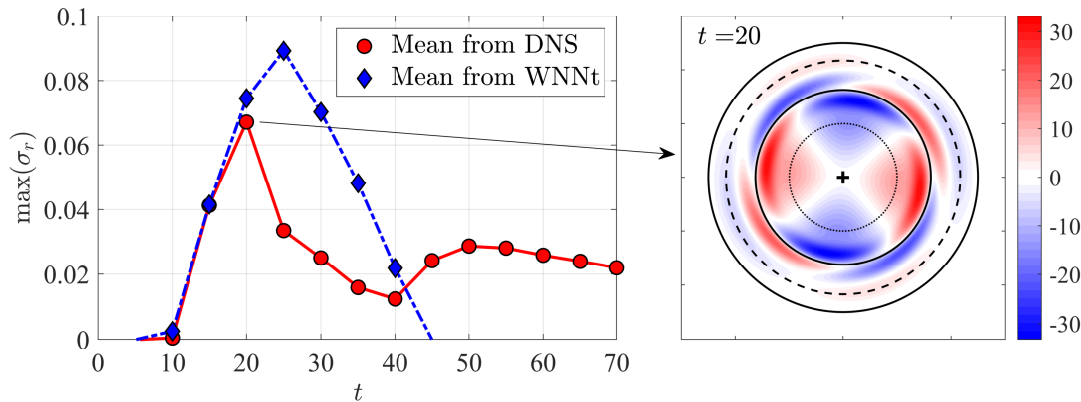


Figure 8.16: Left: maximum growth rate of the eigenvalues of the Navier-Stokes operator at $Re = 5000$ and linearized around the (azimuthal) mean flow, in order to describe $m = 2$ perturbations. Mean flows corresponding to $U_0 = 2.82 \times 10^{-2}$ are obtained either from DNS data (continuous line linking red dots) or by evaluating the weakly nonlinear expansion (dash-dotted line linking blue diamonds). Positive growth rate values imply linear instability. At the right, is shown the eigenmode corresponding to the most unstable eigenvalue of the operator linearized around the DNS mean flow, at $t = 20$. The radius of the dotted circle is equal to one, the radius of the dashed circle is equal to r_q , and the radii of the continuous-line circle highlight the extrema of the mean vorticity profile. The color scale is arbitrary.

A local minimum is to be noticed at $r = 1.6$ between these two regions, as well as a second one a little further at $r = 2.5$. Note the qualitative resemblance with the profiles considered in Kossin et al. (2000) (see their figures 1 and 12). The structure of the most unstable eigenmode supported by the DNS mean vorticity profile at $t = 20$ is shown at the right of figure 8.16. It bears several characteristics of a shear instability. Specifically, its phase velocity is very close to the angular velocity of the mean flow at the radius of the vorticity extremum (see the largest dot in figure 8.17). This radius, highlighted by the first black continuous circle in figure 8.16, is also the zero amplitude isoline of the eigenmode structure. Tightly around, the eigenmode reaches its largest amplitude under the form of four external lobes, rotated of $\approx \pi/2$ in the anticlockwise direction with respect to four internal ones. This structure is similar to the one shown in figure 2 of Carton and Legras (1994), who interpret it under the Rossby-wave interaction paradigm. In words, the mean vorticity profile can be thought of as supporting Rossby (vorticity) waves at the “edges” (sharp slope) at one side and the other of the local minima. These two vorticity waves are precisely the internal and external series of lobes of the eigenmode structures. The velocity perturbation induced by a vorticity wave has a phase lag of $\pi/2$ with respect to the latter. Therefore, since the lobe series are also rotated of $\approx \pi/2$ with respect to each other, the velocity perturbation induced by one is in phase with the vorticity perturbation of the other, thus reinforcing its growth. In addition, Carton and Legras (1994) mentions that both waves interact in such a way as to travel with the same phase speed, thus the reinforcement of the one by the other is preserved in time, eventually leading to instability.

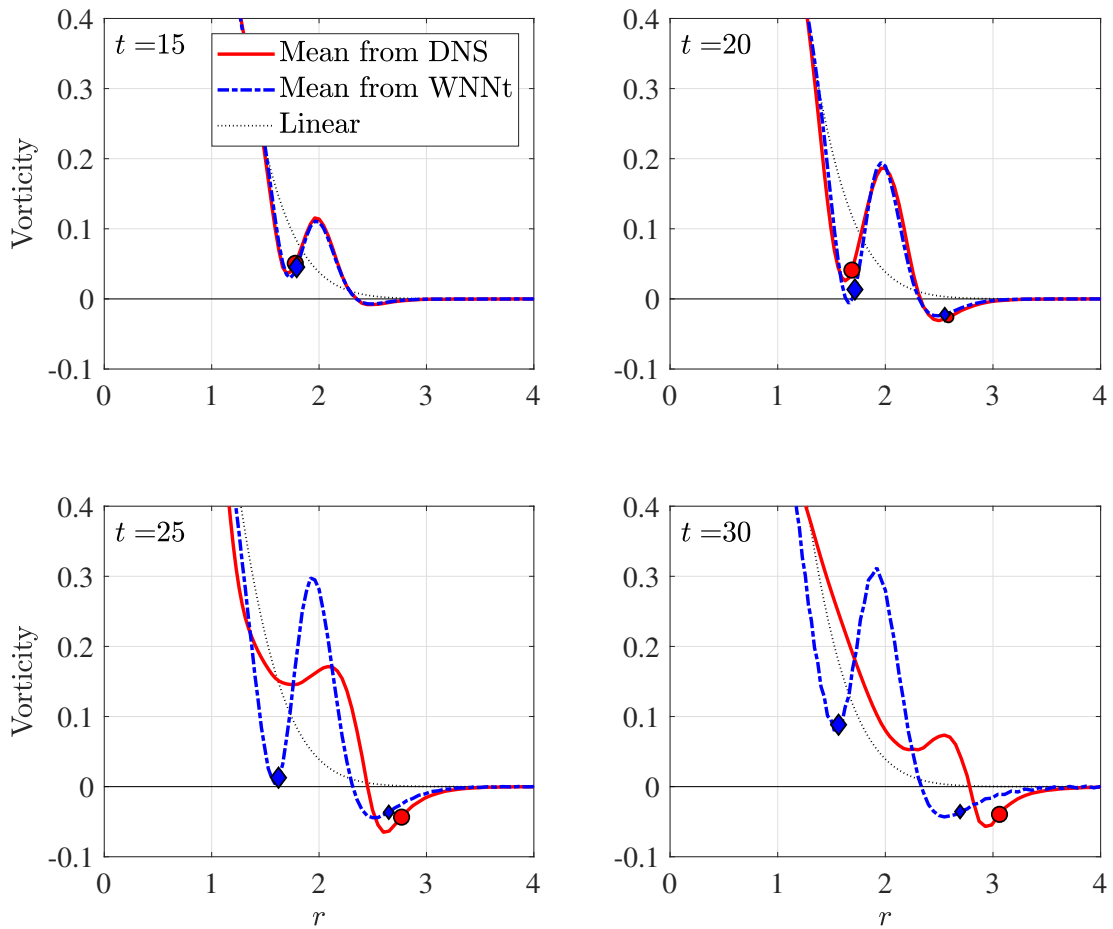


Figure 8.17: Mean (axisymmetric) vorticity profiles corresponding to $U_0 = 2.82 \times 10^{-2}$, extracted from DNS data (red continuous) and reconstituted from the weakly nonlinear expansion as $W_z + a^2 \omega_2^{(0)}$, where a solves the amplitude equation (blue dashed-dotted line). The largest dot (respectively diamond) is located at the radius for which $-m\Omega = \sigma_i$ where σ_i is the imaginary part of the most unstable eigenvalue of the DNS (respectively weakly nonlinear) profile. This also corresponds to the critical radius of the most unstable mode. The respectively smaller dot or diamond (if exists) stands for the second most unstable mode.

From $20 \leq t$ in figure 8.16, growth rates determined with both approaches depart significantly from each other, and so do the mean vorticities profiles in figure 8.17. This is because the unstable mode grows and evolves in the DNS and feeds back on the mean flow, whereas in our weakly nonlinear approach, the structure of the mean flow distortion is fully determined by the Reynolds stress of the linear response.

Overall, it is plausible to think of the departure of the fully nonlinear solution from the weakly nonlinear one, observable in figure 8.9 for large U_0 , as resulting from a shear instability. This instability reaches its maximum growth rate around $t = 20$, and requires some time for the unstable mode to gain in amplitude and for its nonlinear evolution, taking a tripolar shape, to dominate the energy of the response from $t = 40$ and for $U_0 = 2.82 \times 10^{-2}$ in figure 8.9. This goes

in the sense of Carton and Legras (1994) and Kossin et al. (2000), who have also shown shear instability modes to saturate into a tripolar state. The weakly nonlinear expansion does not predict an amplitude for the unstable mode, for the latter only declares as a “secondary” mode, on the top of the optimal response. Therefore the predictions from the amplitude equation, for the optimal response, depart from DNS results after the time needed for the shear-driven unstable mode to become dominant.

8.6 Summary and perspectives

In conclusion, we believe our work to have brought a twofold generalization to existing literature. The first lies on a purely methodological level. We have derived an amplitude equation for non-normal systems, describing the transient response to an initial condition, in a weakly nonlinear regime. Unlike in Ducimetière et al. (2022a), the reference state of these systems can now depend arbitrarily on times, owing to the propagator formalism, without the need for this latter to take its particular operator exponential shape. This offers numerous possibilities of applications, and weak nonlinearities could be modelled, for instance, in pulsating pipe flows, which play a key role in the hemodynamic system of many species (Pier & Schmid, 2017, 2021); it could also be applied to time-dependent stratified shear flows, which have revealed to support strong transient growth, for instance in Arratia et al. (2013) and Parker et al. (2021). Not only could the weakly nonlinear evolution of the gain associated with the linear optimal perturbation be captured, but the amplitude equation could also be included in a Lagrangian optimization problem whose stationary conditions would constitute a weakly nonlinear optimal, parameterized by the amplitude of the initial condition.

The method does not rely on any modal (“eigenmodal”) quantities, therefore the existence of a continuous spectrum and/or the absence of discrete eigenmode is not problematic. Corollary, the shape of the reference flow is not constrained, apart from the fact that it should lead to strong energy growth at some finite time. The equation is derived for the amplitude of the time-dependent (linear) optimal response, whose computation already encompassed the entirety of the spectrum, regardless of its precise nature. This was particularly convenient when applied to the two-dimensional Lamb-Oseen (Gaussian) vortex flow, the linear optimal response of which is characterized by vorticity filaments under constant shear by the reference flow. The work of Schechter et al. (2000) has shown this response to project well onto a very large number of eigenmodes constituting the continuum, all with different shapes and frequencies. Therefore it was extremely poorly described as a single eigenmode, which invalidates the use of classical weakly nonlinear methods.

Instead, by using the amplitude equation (8.52), we could correctly predict for different Re values the nonlinear evolution of the response for $0 \leq t \leq 130$, and for small amplitudes of the initial condition. In this specific regime, at $Re = 5000$ as an example, nonlinearities have been found to reduce the transient gain for $0 \leq t \leq 87$, but to enhance it for $87 \leq t \leq 130$, as confirmed by DNS. Owing to the simplicity of the amplitude equation and its link to the

sensitivity formula, this could be further related to the creation of an azimuthal mean flow distortion from the Reynolds stress of the linear response, which affects the Landau damping controlling the non-viscous dissipation of the response. The second harmonic effect has also been found to be important over the time interval where nonlinearities reinforce the gain.

However, for relatively large amplitudes of the initial condition, the predictions of the amplitude equation are found to remain accurate at small times only. After a well-captured episode of diminution of the gain, the DNS simulations with the largest considered initial condition amplitudes depart from the weakly nonlinear prediction and evidence a bifurcation towards a tripolar state. By performing a mean flow stability analysis, this departure can be related to the emergence of a shear instability. Specifically, the mean flow distortion by the Reynolds stress of the linear response, at the same time that it enhances the Landau damping by its effect at the radius r_q , generates a vorticity ring closely around the central part of the vortex. A shear instability results from an interaction between the inner "edge" (sharp slope) of this annular ring and the outer edge of the central region. The weakly nonlinear approach does not predict an equation for the unstable mode that emerges on the mean flow. Therefore, as soon as the unstable mode dominates the response, around $t = 40$ for the largest considered $U_0 = 2.82 \times 10^{-2}$ and $Re = 5000$, the weakly nonlinear description rapidly degrades in terms of both energy and structure.

Nevertheless, at larger times, the amplitude equation can still give indirect information about the fully nonlinear response. Specifically, for $Re = 5000$, for a given and above a certain value for the amplitude of the initial condition, the amplitude equation has no solution over a finite time interval contained in $87 \leq t \leq 130$, where the coefficient μ_r is positive. The non-existence of any solution over a time interval may imply that, at least over the same time interval, the fully nonlinear solution must have reached another nonlinear state. This seems confirmed by the DNS. In this sense, the threshold initial condition amplitude predicted by the amplitude equation could be a reasonable approximation of the fully nonlinear one, even if a direct comparison between the former and the latter is found to be delicate.

For future research, the nonlinear self-sustaining mechanism(s) of the tripolar state remain to be clarified. In this perspective, a semi-linear approach such as the one deployed in Yim et al. (2020) could be appropriate. This approach relies on the assumption that the dominant nonlinear mechanism is the Reynolds stress feedback onto the mean flow, thus neglecting the nonlinearity arising from the cross-coupling between different frequencies. In this sense, it is less rigorous than the weakly nonlinear expansion proposed here. Nevertheless, the semi-linear model does not assume the fluctuation over the mean flow to be small and typically retains its spatial degrees of freedom. Therefore the nonlinear structure it predicts is possibly considerably different from that of the linear regime and could evolve towards a tripole.

Eventually, we believe that the fact that the proposed method does not make assumptions on the shape of the base profile, nor on the values of external parameters, only that the reference flow should lead to some energy growth, could be exploited further. For instance, the proposed

amplitude equation could be employed to assess and interpret weakly nonlinear effects on the optimal response on vorticity profiles from actual field measurements such as those reported in Kossin and Schubert (2001), Kossin et al. (2000), Kuo et al. (1999), and Reasor et al. (2000). Indeed, the mean vorticity profile predicted in figure 8.17 of this work is qualitatively very similar to the one of Hurricane Gilbert shown in figure 1 of Kossin et al. (2000). This raises the question of the relevance of non-normal mechanisms combined with nonlinear effects in tropical cyclones.

8.7 Appendix

8.7.1 Kernel of the adjoint of the perturbed inverse propagator

We demonstrate in the following that the non-trivial kernel $\hat{\mathbf{b}}(t)$ of the adjoint operator $\Phi(0, t)^\dagger$ for $t > 0$ reads $\hat{\mathbf{b}}(t) = \Psi(t, 0)^\dagger \hat{\mathbf{l}}(t)$.

$$\begin{aligned}
\Phi(0, t)^\dagger \hat{\mathbf{b}}(t) &= \left[\Psi(0, t) \left(\mathbf{I} - \hat{\mathbf{l}}(t) \frac{\langle \hat{\mathbf{l}}(t) | * \rangle}{\|\hat{\mathbf{l}}(t)\|^2} \right) \right]^\dagger \hat{\mathbf{b}}(t) \\
&= \left(\mathbf{I} - \hat{\mathbf{l}}(t) \frac{\langle \hat{\mathbf{l}}(t) | * \rangle}{\|\hat{\mathbf{l}}(t)\|^2} \right) \Psi(0, t)^\dagger \hat{\mathbf{b}}(t) \\
&= \left(\mathbf{I} - \hat{\mathbf{l}}(t) \frac{\langle \hat{\mathbf{l}}(t) | * \rangle}{\|\hat{\mathbf{l}}(t)\|^2} \right) [\Psi(t, 0) \Psi(0, t)]^\dagger \hat{\mathbf{l}}(t) \\
&= \left(\mathbf{I} - \hat{\mathbf{l}}(t) \frac{\langle \hat{\mathbf{l}}(t) | * \rangle}{\|\hat{\mathbf{l}}(t)\|^2} \right) \hat{\mathbf{l}}(t) \\
&= \mathbf{0}.
\end{aligned} \tag{8.75}$$

8.7.2 Temporal integration of the third-order equation.

From (8.40) The particular solution for $\bar{\mathbf{u}}_3^{(1)}$ reads

$$\bar{\mathbf{u}}_3^{(1)}(t, T) = \hat{\mathbf{u}}_{3a}^{(1)}(t) + A(T)|A(T)|^2 \hat{\mathbf{u}}_{3b}^{(1)}(t) + (\mathbf{d}_T A(T)) \hat{\mathbf{u}}_{3c}^{(1)}(t) + A(T) \hat{\mathbf{u}}_{3d}^{(1)}(t) \tag{8.76}$$

where

$$\begin{aligned}
\partial_t \left(\Phi(0, t) \hat{\mathbf{u}}_{3a}^{(1)} \right) &= \mathbf{0} \quad \text{with} \quad \hat{\mathbf{u}}_{3a}^{(1)}(0) = \alpha \hat{\mathbf{u}}_h, \\
\partial_t \left(\Phi(0, t) \hat{\mathbf{u}}_{3b}^{(1)} \right) &= -H \Psi(0, t) \tilde{\mathbf{f}} \quad \text{with} \quad \hat{\mathbf{u}}_{3b}^{(1)}(0) = \mathbf{0}, \\
\partial_t \left(\Phi(0, t) \hat{\mathbf{u}}_{3c}^{(1)} \right) &= -H \epsilon_o \hat{\mathbf{u}}_o \quad \text{with} \quad \hat{\mathbf{u}}_{3c}^{(1)}(0) = \mathbf{0}, \\
\partial_t \left(\Phi(0, t) \hat{\mathbf{u}}_{3d}^{(1)} \right) &= -\partial_t (H \hat{\mathbf{u}}_o) \quad \text{with} \quad \hat{\mathbf{u}}_{3d}^{(1)}(0) = \mathbf{0},
\end{aligned} \tag{8.77}$$

Integrating in time the first equation in (8.77) and using $\bar{\Phi}(0, 0) = \mathbf{I}$ yields

$$\bar{\Phi}(0, t) \hat{\mathbf{u}}_{3a}^{(1)}(t) = \bar{\Phi}(0, 0) \hat{\mathbf{u}}_{3a}^{(1)}(0) = \alpha \hat{\mathbf{u}}_h. \quad (8.78)$$

Integrating the second gives

$$\bar{\Phi}(0, t) \hat{\mathbf{u}}_{3b}^{(1)}(t) = - \int_0^t H(s) \Psi(0, s) \tilde{\mathbf{f}}(s) ds = - \int_0^t \Psi(0, s) \tilde{\mathbf{f}}(s) ds = \Psi(0, t) \tilde{\mathbf{u}}(t) \quad (8.79)$$

where we have defined

$$\tilde{\mathbf{u}}(t) \doteq -\Psi(t, 0) \int_0^t \Psi(0, s) \tilde{\mathbf{f}}(s) ds, \quad (8.80)$$

or, equivalently using (8.11), $\tilde{\mathbf{u}}$ solves

$$(\partial_t - L_m(t)) \tilde{\mathbf{u}} = -\tilde{\mathbf{f}}, \text{ subject to } \tilde{\mathbf{u}}(0) = \mathbf{0}. \quad (8.81)$$

By integrating the third

$$\begin{aligned} \bar{\Phi}(0, t) \hat{\mathbf{u}}_{3c}^{(1)}(t) &= - \int_0^t H(s) \epsilon_o \hat{\mathbf{u}}_o ds = - [H(s) \epsilon_o s \hat{\mathbf{u}}_o]_{s=0}^{s=t} + \int_0^t \delta(s) \epsilon_o s \hat{\mathbf{u}}_o ds \\ &= -\epsilon_o t \hat{\mathbf{u}}_o, \end{aligned} \quad (8.82)$$

and eventually the fourth

$$\bar{\Phi}(0, t) \hat{\mathbf{u}}_{3d}^{(1)}(t) = -H(t) \hat{\mathbf{u}}_o. \quad (8.83)$$

Injecting these four solutions in (8.76) and combining it with (8.40) leads to

$$\bar{\Phi}(0, t) \bar{\mathbf{u}}_3^{(1)} = \alpha \hat{\mathbf{u}}_h + A|A|^2 \Psi(0, t) \tilde{\mathbf{u}} - (d_T A) \epsilon_o t \hat{\mathbf{u}}_o - AH \hat{\mathbf{u}}_o. \quad (8.84)$$

8.7.3 Transient gain sensitivity in time-varying base flow and comparison with the amplitude equation.

We recall that the gain squared associated with the linear trajectory optimized for $t = t_o$, through the choice of the initial condition $\hat{\mathbf{u}}_o$, reads

$$G(t; t_o)^2 = \|\Psi(t, 0) \hat{\mathbf{u}}_o\|^2 = \left\langle \hat{\mathbf{u}}_o \left| \Psi(t, 0)^\dagger \Psi(t, 0) \hat{\mathbf{u}}_o \right. \right\rangle. \quad (8.85)$$

Note that, by definition, $G(t_o; t_o) = G_o(t_o) = 1/\epsilon_o$ as defined in (8.13). We recall as well that $G(t)$ is used as a shortened notation for $G(t; t_o)$. We derive thereafter the variation $\delta(G(t)^2)$ of this

linear gain induced by a variation $\delta L_m(t)$ of the operator $L_m(t)$. We first compute

$$\begin{aligned}
\delta(G(t)^2) &= \left\langle \hat{\mathbf{u}}_o \left| \delta(\Psi(t,0)^\dagger \Psi(t,0)) \hat{\mathbf{u}}_o \right. \right\rangle \\
&= \left\langle \hat{\mathbf{u}}_o \left| \delta(\Psi(t,0)^\dagger) \Psi(t,0) \hat{\mathbf{u}}_o + \Psi(t,0)^\dagger \delta \Psi(t,0) \hat{\mathbf{u}}_o \right. \right\rangle \\
&= \langle \delta \Psi(t,0) \hat{\mathbf{u}}_o | \Psi(t,0) \hat{\mathbf{u}}_o \rangle + \langle \Psi(t,0) \hat{\mathbf{u}}_o | \delta \Psi(t,0) \hat{\mathbf{u}}_o \rangle \\
&= 2\Re(\langle \Psi(t,0) \hat{\mathbf{u}}_o | \delta \Psi(t,0) \hat{\mathbf{u}}_o \rangle) \\
&= 2\epsilon_o^{-1} \Re(\langle \hat{\mathbf{l}}(t) | \delta \Psi(t,0) \hat{\mathbf{u}}_o \rangle),
\end{aligned} \tag{8.86}$$

where we used that $\delta(\Psi(t,0)^\dagger) = (\delta \Psi(t,0))^\dagger$: the variation of the adjoint is the adjoint of the variation, as easily shown by using the definition of the adjoint operator. Next, we link $\delta \Psi(t,0)$ with $\delta L_m(t)$ by taking the variation of (8.8), which leads to

$$\partial_t(\delta \Psi(t,0)) = (\delta L_m(t))\Psi(t,0) + L_m(t)\delta \Psi(t,0). \tag{8.87}$$

Multiplying (8.87) by $\Psi(0,t)$ and using (8.10), stating that $L_m(t) = -\Psi(t,0)\partial_t\Psi(0,t)$, leads to

$$\begin{aligned}
\Psi(0,t)\partial_t(\delta \Psi(t,0)) &= \Psi(0,t)(\delta L_m(t))\Psi(t,0) - (\partial_t\Psi(0,t))\delta \Psi(t,0), \text{ thus} \\
\partial_t(\Psi(0,t)\delta \Psi(t,0)) &= \Psi(0,t)(\delta L_m(t))\Psi(t,0).
\end{aligned} \tag{8.88}$$

Integrating (8.88) in time and imposing $\delta \Psi(0,0)$ to be null results in

$$\begin{aligned}
\delta \Psi(t,0) &= \Psi(0,t) \int_0^t \Psi(0,s)(\delta L_m(s))\Psi(s,0)ds \\
&= \int_0^t \Psi(0,t)\Psi(0,s)(\delta L_m(s))\Psi(s,0)ds.
\end{aligned} \tag{8.89}$$

In the particular case where L_m does not depend on time the propagator writes $\Psi(t,0) = e^{L_m t}$, and relation (8.89) reduces to the formula (6) at p.175 of Bellman (1997). By injecting (8.89) in (8.86) we obtain

$$\begin{aligned}
\delta(G(t)^2) &= 2\epsilon_o^{-1} \Re \left(\left\langle \hat{\mathbf{l}}(t) \left| \int_0^t \Psi(0,t)\Psi(0,s)(\delta L_m(s))\Psi(s,0) \hat{\mathbf{u}}_o ds \right. \right\rangle \right) \\
&= 2\epsilon_o^{-2} \Re \left(\int_0^t \left\langle \Psi(0,t)\Psi(0,s)^\dagger \hat{\mathbf{l}}(t) \left| \delta L_m(s) \hat{\mathbf{l}}(s) \right. \right\rangle ds \right).
\end{aligned} \tag{8.90}$$

On the other hand, by re-formulating (8.53), the weakly nonlinear gain G_w is found to satisfy

$$1 - \frac{G(t)^2}{G_w(t)^2} = 2 \left(\frac{U_0}{\epsilon_o} \right)^2 \mu_r(t). \tag{8.91}$$

Considering small variations around the linear gain $G_w(t)^2 = G(t)^2 + \delta(G(t)^2)$ with $\delta(G(t)^2)/G(t)^2 \ll 1$, (8.91) reduces to

$$\delta(G(t)^2) = 2G(t)^2 \left(\frac{U_0}{\epsilon_o} \right)^2 \mu_r(t), \tag{8.92}$$

but

$$\begin{aligned}\mu(t) &= \frac{\langle \hat{\mathbf{l}}(t) | \tilde{\mathbf{u}}(t) \rangle}{\|\hat{\mathbf{l}}(t)\|^2} = -\frac{\langle \hat{\mathbf{l}}(t) | \Psi(t, 0) \int_0^t \Psi(0, s) \tilde{\mathbf{f}}(s) ds \rangle}{\|\hat{\mathbf{l}}(t)\|^2} \\ &= -\frac{\int_0^t \langle \Psi(t, s)^\dagger \hat{\mathbf{l}}(t) | \tilde{\mathbf{f}}(s) \rangle ds}{\|\hat{\mathbf{l}}(t)\|^2} \\ &= -\frac{1}{(\epsilon_o G(t))^2} \int_0^t \langle \Psi(t, s)^\dagger \hat{\mathbf{l}}(t) | \tilde{\mathbf{f}}(s) \rangle ds.\end{aligned}\quad (8.93)$$

Combining (8.92) with (8.93) results in

$$\delta(G(t)^2) = -2\epsilon_o^{-2} \left(\frac{U_0}{\epsilon_o} \right)^2 \operatorname{Re} \left(\int_0^t \langle \Psi(t, s)^\dagger \hat{\mathbf{l}}(t) | \tilde{\mathbf{f}}(s) \rangle ds \right). \quad (8.94)$$

Identifying (8.90) with (8.94) leads us to conclude that the small variation of the weakly nonlinear gain around the linear one, as predicted by our model, reduces to the sensitivity of this linear gain to a perturbation $\delta L_m(t)$ satisfying

$$\delta L_m(t) \hat{\mathbf{l}}(t) = -\left(\frac{U_0}{\epsilon_o} \right)^2 \tilde{\mathbf{f}}(t). \quad (8.95)$$

From the definition of $\tilde{\mathbf{f}}(t)$ in (8.38), such δL_m corresponds to an axisymmetric perturbation of the base flow from \mathbf{U}_b to $\mathbf{U}_b + (U_0/\epsilon_o)^2 \mathbf{u}_2^{(0)}$, and also embeds the effect of the second harmonics $\hat{\mathbf{u}}_2^{(2)}$. Note that (U_0/ϵ_o) is the amplitude of the response in the linear regime.

8.7.4 The pseudo-forcing method

We add to the asymptotic expansion (8.21) the trivial equality

$$\mathbf{0} = \left[\sqrt{\epsilon_o} (\epsilon_o A(T) \delta(t) \hat{\mathbf{u}}_o) - \sqrt{\epsilon_o}^3 (A(T) \delta(t) \hat{\mathbf{u}}_o) \right] e^{im\theta} + \text{c.c.} \quad (8.96)$$

where $\delta(t) = dH(t)/dt$ such that $\int_0^{t>0} \delta(t) dt = H(t > 0) - H(0) = 1$. The terms are then directly collected at each order without ever perturbing the propagator. According to (8.96), the term $\epsilon_o A(T) \delta(t) \hat{\mathbf{u}}_o$ will act as a forcing at order $\sqrt{\epsilon_o}$, whereas the term $-A(T) \delta(t) \hat{\mathbf{u}}_o$ will act as a forcing at order $\sqrt{\epsilon_o}^3$.

The equation assembled at $\sqrt{\epsilon_o}$ is therefore

$$(\partial_t - L_m(t)) \bar{\mathbf{u}}_1^{(1)} = A \delta \epsilon_o \hat{\mathbf{u}}_o, \quad \text{with } \bar{\mathbf{u}}_1^{(1)}|_{t=0} = \mathbf{0}. \quad (8.97)$$

By postulating $\bar{\mathbf{u}}_1^{(1)}(t, T) = A(T) \hat{\mathbf{u}}_1^{(1)}(t)$, the field $\hat{\mathbf{u}}_1^{(1)}$ solves

$$\hat{\mathbf{u}}_1^{(1)}(t) = \Psi(t, 0) \int_0^t \Psi(0, s) \delta(s) \epsilon_o \hat{\mathbf{u}}_o ds = \begin{cases} \mathbf{0} & \text{if } t = 0 \\ \Psi(t, 0) \epsilon_o \hat{\mathbf{u}}_o = \hat{\mathbf{l}}(t) & \text{if } t > 0, \end{cases} \quad (8.98)$$

thereby $\hat{\mathbf{u}}_1^{(1)}(t) = H(t)\hat{\mathbf{l}}(t)$ and $\bar{\mathbf{u}}_1^{(1)}(t, T) = A(T)H(t)\hat{\mathbf{l}}(t)$ for $t \geq 0$ exactly as in (8.33). The equations and their solutions at order ϵ_o are the same as in the main text. At order $\sqrt{\epsilon_o^3}$, the equation for the Fourier component at (m) reads

$$(\partial_t - L_m(t))\bar{\mathbf{u}}_3^{(1)} = -A|A|^2 H\tilde{\mathbf{f}} - (d_T A)H\hat{\mathbf{l}} - A\delta\hat{\mathbf{u}}_o, \text{ with } \bar{\mathbf{u}}_3^{(1)}|_{t=0} = \alpha\hat{\mathbf{u}}_h, \quad (8.99)$$

where A is still undetermined. The Fredholm alternative cannot be invoked since (8.99) is directly solvable, but is replaced by an asymptotic-preserving argument of the same nature. As $\bar{\mathbf{u}}_3^{(1)}$ oscillates at m and is subject to a non-zero initial condition, it is susceptible to be amplified of a factor $1/\epsilon_o$ at $t = t_o$, thus conveying the response at order $\sqrt{\epsilon_o}$; to avoid this scenario ruining the asymptotic hierarchy, we impose the orthogonality of $\bar{\mathbf{u}}_3^{(1)}$ with the linear response that is the most amplified at $t = t_o$, that is $\hat{\mathbf{l}}(t)$, which closes the system. Is it easily shown that the solution to (8.99) reads

$$\bar{\mathbf{u}}_3^{(1)} = \Psi(t, 0)\alpha\hat{\mathbf{u}}_h + A|A|^2\tilde{\mathbf{u}} - t(d_T A)\hat{\mathbf{l}} - \epsilon_o^{-1}AH\hat{\mathbf{l}} \quad (8.100)$$

whose condition of orthogonality with $\hat{\mathbf{l}}(t)$ for all $t > 0$ results in

$$\langle \hat{\mathbf{l}} | \bar{\mathbf{u}}_3^{(1)} \rangle = \alpha \langle \hat{\mathbf{l}} | \Psi(t, 0)\hat{\mathbf{u}}_h \rangle + A|A|^2 \langle \hat{\mathbf{l}} | \tilde{\mathbf{u}} \rangle - t(d_T A) \|\hat{\mathbf{l}}\|^2 - \epsilon_o^{-1} AH \|\hat{\mathbf{l}}\|^2 = 0. \quad (8.101)$$

Multiplying (8.101) by $\epsilon_o / \|\hat{\mathbf{l}}\|^2 = 1 / \langle \hat{\mathbf{b}} | \hat{\mathbf{u}}_o \rangle$ gives eventually

$$\epsilon_o t \frac{dA}{dT} = \alpha \frac{\langle \hat{\mathbf{b}} | \hat{\mathbf{u}}_h \rangle}{\langle \hat{\mathbf{b}} | \hat{\mathbf{u}}_o \rangle} + A|A|^2 \frac{\langle \hat{\mathbf{b}} | \Psi(0, t)\tilde{\mathbf{u}} \rangle}{\langle \hat{\mathbf{b}} | \hat{\mathbf{u}}_o \rangle} - A. \quad (8.102)$$

which is exactly the amplitude equation (8.43) derived in the main text by perturbing the propagator.

As a side comment, note that $\bar{\mathbf{u}}_3^{(1)}$ in (8.100) is also the particular solution of (8.41). Indeed, the orthogonality condition guarantees $\langle \hat{\mathbf{l}} | \bar{\mathbf{u}}_3^{(1)} \rangle = 0$ such that $\Phi(0, t)\bar{\mathbf{u}}_3^{(1)} = \Psi(0, t)\bar{\mathbf{u}}_3^{(1)}$ and (8.41) is automatically satisfied. Therefore, not only are the amplitude equations the same for both methods, but also the higher-order terms of the development, requiring knowledge of the field $\bar{\mathbf{u}}_3^{(1)}$. This holds as long as the homogeneous solution on $\bar{\mathbf{u}}_3^{(1)}$, not necessarily null for the method of the singularization of the propagator, is ignored.

8.7.5 Expression of the adjoint operator

The adjoint of the operator $B_m(t)$ under the scalar product defined in (8.12) is such that $\langle B_m \hat{\mathbf{q}}_a | \hat{\mathbf{q}}_b \rangle = \langle \hat{\mathbf{q}}_a | B_m^\dagger \hat{\mathbf{q}}_b \rangle$ for any $\hat{\mathbf{q}}_a \doteq [\hat{\mathbf{u}}_a, \hat{p}_a]$ and $\hat{\mathbf{q}}_b \doteq [\hat{\mathbf{u}}_b, \hat{p}_b]$. By performing integrations by parts, the following relations are easily demonstrated

$$\begin{aligned} \langle \partial_r \hat{\mathbf{u}}_a | \hat{\mathbf{u}}_b \rangle &= (r \hat{\mathbf{u}}_a^H \hat{\mathbf{u}}_b) |_{r \rightarrow \infty} - \langle \hat{\mathbf{u}}_a | (\partial_r + 1/r) \hat{\mathbf{u}}_b \rangle, \\ \langle \Delta_m \hat{\mathbf{u}}_a | \hat{\mathbf{u}}_b \rangle &= [(\partial_r \hat{\mathbf{u}}_a^H) \hat{\mathbf{u}}_b r - \hat{\mathbf{u}}_a^H (r \partial_r \hat{\mathbf{u}}_b)] |_{r \rightarrow \infty} + \langle \hat{\mathbf{u}}_a | \Delta_m \hat{\mathbf{u}}_b \rangle. \end{aligned} \quad (8.103)$$

From here, the explicit expression of $B_m(t)$ is derived immediately as being

$$B_m(t)^\dagger = \begin{bmatrix} (\Delta_m - 1/r^2)/\text{Re} + im\Omega & -2im/(r^2\text{Re}) - W_z & -\partial_r \\ 2im/(r^2\text{Re}) + 2\Omega & (\Delta_m - 1/r^2)/\text{Re} + im\Omega & -im/r \\ \partial_r + 1/r & im/r & 0 \end{bmatrix} \quad (8.104)$$

and the cancellation of the boundary terms resulting from the integration by part imposes

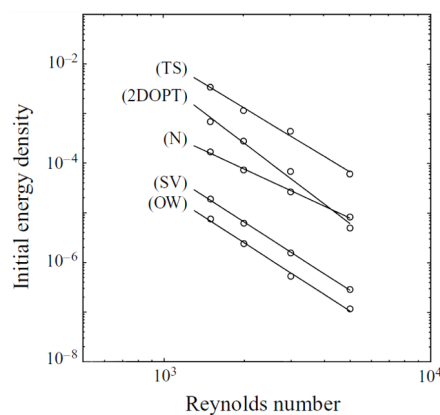
$$-(r\hat{p}^*\hat{u}^\dagger) + (r\hat{u}^*\hat{p}^\dagger) + r(\hat{u}^\dagger\partial_r\hat{u}^* - \hat{u}^*\partial_r\hat{u}^\dagger) + r(\hat{v}^\dagger\partial_r\hat{v}^* - \hat{v}^*\partial_r\hat{v}^\dagger) = 0 \quad (8.105)$$

to hold at $r \rightarrow \infty$. Using the far-field condition on the direct field, stating $\hat{\mathbf{u}}|_{r \rightarrow \infty} = \mathbf{0}$, condition (8.105) implies the adjoint velocity field to also vanish at infinity, i.e., $\hat{\mathbf{u}}^\dagger|_{r \rightarrow \infty} = \mathbf{0}$.

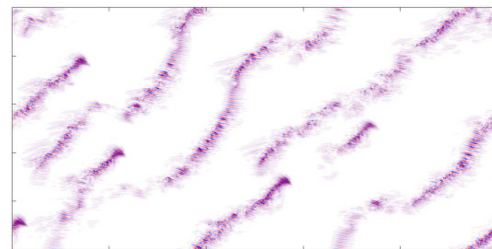
9 Weakly nonlinear optimization

9.1 Introduction

The work of Reddy et al. (1998) numerically considered the response of the three-dimensional plane Poiseuille flow, to different initial perturbations. They found that streamwise vortices and oblique wave initial perturbations require less energy density to induce a transition to turbulence than random noise, or than the linearly unstable mode (known as the "Tollmien-Schlichting" wave). This result is reproduced in Fig. 9.1a.



(a) From Reddy et al. (1998)



(b) From Shimizu and Manneville (2019)

Figure 9.1: (a) Threshold initial perturbation energy density, for the transition to turbulence in the three-dimensional plane Poiseuille flow. Initial perturbations take the form of Tollmien-Schlichting waves (TS), random three-dimensional noise (N), streamwise vortices (SV) and oblique waves (OW). The circles correspond to data from simulations. (b) One-sided Laminar-Turbulent" regime in Poiseuille flow at $Re = 850$.

The irrelevance of the linearly most unstable mode, in this specific context, motivated instead linear transient growth analyses which identified streamwise vortices as being the initial perturbation leading to the largest energy growth. In this, transient growth analyses led to a

more realistic prediction than the linear stability analysis, as can be deduced by comparing the curves for (TS) and (SV) in Fig. 9.1a).

However, Reddy et al. (1998) identified oblique waves as requiring slightly less energy than streamwise vortices to initiate the transition, which was not captured by the linear transient growth analyses. This was later confirmed by the computations of the nonlinear optimal perturbations Farano et al. (2015), as well as by many fully nonlinear simulations performed in very large channels, which uncovered oblique turbulent bands in the transitional flow regime (see Fig. 9.1b for an example). These results suggested that both non-normality and nonlinearity were necessary ingredients to capture the spontaneous oblique patterns. They all were, however, obtained at a substantial numerical cost.

In the previous chapters of this part, chapter 7 and chapter 8, we have suggested a method to reconcile non-normality, at the origin of the non-normal transient response, with nonlinearity. This was done at a low computational cost, by restricting the analysis to a weakly nonlinear regime. It resulted in a scalar equation that could account for the influence of leading order nonlinearities on the amplitude of the linearly optimal structure.

The objective of the present chapter is to compute, for the plane Poiseuille flow, initial perturbation structures that lead to the largest possible energy growth in the weakly nonlinear regime. We hope that such weakly nonlinear optimal structures will be more efficient than the linear ones also in triggering turbulence, although there are *a priori* no mathematical reasons for that. In other terms, by accounting for leading order nonlinearities only, we aim to approach the minimal seed structures (Kerswell, 2018; Pringle & Kerswell, 2010; Pringle et al., 2012) at a low numerical cost. Indeed, minimal seed structures also ensue from maximizing the kinetic energy of the flow in a fully nonlinear regime, and for a sufficiently large temporal horizon. The latter aspect is important since, as seen, perturbation over a stable base flow can yield a very large transient growth in energy at finite times, and yet decay afterward. In the case where the flow has only one global attractor, the maximal transient gain at a certain temporal horizon can only vanish by increasing the temporal horizon, since perturbations must decay asymptotically with time. If, however, the flow possesses another attracting state (e.g. a turbulent attractor) the transient gain does not vanish with the temporal horizon if the perturbed flow has transited toward this other state. That is because the perturbation is taken as the difference between the current flow and its initial attractor. Therefore, in maximizing the transient gain for a sufficiently large temporal horizon, the scenario where the initial perturbation leads to a transition (thus a finite transient gain due to a persistent perturbation) is logically favored over the scenario that leads to a re-laminarisation towards the base state (thus a vanishing transient gain).

After having briefly introduced the flow configuration and recalled the weakly nonlinear amplitude equation in section 9.2, we outline an optimisation algorithm in section 9.3. The latter results from the cancellation of the first-order variations of a Lagrangian, where the amplitude equation has been included under the form of a constraint. This requires also including as

constraints the linear equations governing the higher-order fields, involved in the inner product for the coefficient of the amplitude equation. In section 9.4, we implement the algorithm to compute the weakly nonlinear initial condition that yields the largest energy growth in the plane Poiseuille flow, for a given streamwise-spanwise wavenumbers pair, temporal horizon, and initial amplitude. We then compare the efficiency of the weakly nonlinear optimal initial conditions with that of the linear ones, in triggering turbulence.

9.2 Flow configuration and governing equations

Let $\mathbf{U}_b(y, t) = [U_b(y, t), 0, 0]^T(r, t)$ denotes a three-dimensional plane channel base flow, bounded in the y (crosswise) direction but invariant in the x (streamwise) and z (spanwise) ones. We refer for instance to the Poiseuille flow sketched in figure 2.2, and satisfying the Navier-Stokes equations (NSE) subject to a constant pressure gradient. It supports an infinitesimal perturbation field of the form

$$\tilde{\mathbf{u}}_1(x, y, z, t) = \hat{\mathbf{u}}_1(y, t)e^{i(\alpha x + \beta z)} + \text{c.c.} \quad (9.1)$$

The invariance of the base flow along the x and z coordinates justifies the Fourier mode expansion of the perturbation in these two directions. Linearizing the Navier-Stokes equations around $\mathbf{U}_b(y, t)$ leads to a linear equation for the temporal evolution of the perturbation field $\hat{\mathbf{u}}_1$, written as

$$\partial_t \hat{\mathbf{u}}_1 = L \hat{\mathbf{u}}_1, \quad \text{or, equivalently,} \quad \hat{\mathbf{u}}_1(t) = \Psi(t, 0) \hat{\mathbf{u}}_1(0). \quad (9.2)$$

The operator $\Psi(t, 0)$ is called the "propagator", associated with the linearized Navier-Stokes operator L . It maps the field at time 0 onto that at t . Without loss of generality, the initial condition for the perturbation is normalized as $\|\hat{\mathbf{u}}_1(0)\| = 1$. The linear trajectory is associated with a transient gain

$$G(t) = \frac{\|\hat{\mathbf{u}}_1(t)\|}{\|\hat{\mathbf{u}}_1(0)\|} = \|\hat{\mathbf{u}}_1(t)\|, \quad (9.3)$$

where $\|\bullet\|$ here denotes norm induced by the L^2 inner product over y

$$\|\hat{\mathbf{u}}_1\|^2 = \langle \hat{\mathbf{u}}_1 | \hat{\mathbf{u}}_1 \rangle = \int_{-1}^1 |\hat{u}_{1,x}|^2 + |\hat{u}_{1,y}|^2 + |\hat{u}_{1,z}|^2 dy. \quad (9.4)$$

In the previous chapter, we studied the effect of perturbing the NSE initially with the same initial condition $\hat{\mathbf{u}}_1(0)$, but multiplied by an amplitude U_0 which is small but non-vanishing. We have shown analytically that the linear gain could be prolonged in a weakly nonlinear regime, such as to take into account leading-orders nonlinearities affecting the response. Specifically, upon proposing an asymptotic expansion of the flow in terms of powers of

$G(t_o)^{-1/2}$, t_o being the temporal horizon of interest, we have derived

$$G_w(t) = \frac{B(t) \|\hat{\mathbf{u}}_1(t)\|}{U_0}, \quad (9.5)$$

where $B(t)$ is a scalar given by

$$B(t) = U_0 \frac{1}{\sqrt{1 - 2U_0^2 \bar{\mu}_r(t)}}. \quad (9.6)$$

The time-varying coefficient $\bar{\mu}_r$ that appears in (9.6) is the real part of

$$\bar{\mu} = \frac{\langle \hat{\mathbf{u}}_1(t) | \hat{\mathbf{u}}_3(t) \rangle}{\langle \hat{\mathbf{u}}_1(t) | \hat{\mathbf{u}}_1(t) \rangle}, \quad (9.7)$$

where the field $\hat{\mathbf{u}}_3$ is induced by linear interactions stemming from $\hat{\mathbf{u}}_1$. It is found by solving successively (9.2) for $\hat{\mathbf{u}}_1$, followed by

$$\begin{aligned} \partial_t \hat{\mathbf{u}}_2^{(2)} &= L^{(2)} \hat{\mathbf{u}}_2^{(2)} - C[\hat{\mathbf{u}}_1, \hat{\mathbf{u}}_1], \quad \text{with } \hat{\mathbf{u}}_2^{(2)}(0) = \mathbf{0}, \\ \partial_t \mathbf{u}_2^{(0)} &= L^{(0)} \mathbf{u}_2^{(0)} - 2C[\hat{\mathbf{u}}_1^*, \hat{\mathbf{u}}_1], \quad \text{with } \mathbf{u}_2^{(0)}(0) = \mathbf{0} \\ \partial_t \hat{\mathbf{u}}_3 &= L \hat{\mathbf{u}}_3 - 2C[\hat{\mathbf{u}}_1^*, \hat{\mathbf{u}}_2^{(2)}] - 2C[\hat{\mathbf{u}}_1, \mathbf{u}_2^{(0)}], \quad \text{with } \hat{\mathbf{u}}_3(0) = \mathbf{0}. \end{aligned} \quad (9.8)$$

The superscript "*" denotes complex conjugation and C is the nonlinear, bilinear advection operator. It describes the transport by some field $\hat{\mathbf{g}}$, associated with the wavenumber pair $(m\alpha, m\beta)$, of some other field $\hat{\mathbf{h}}$, associated with the wavenumber pair $(n\alpha, n\beta)$, such that

$$C[\hat{\mathbf{g}}, \hat{\mathbf{h}}] \doteq \frac{1}{2} ((\hat{\mathbf{g}} \cdot \tilde{\nabla}_n) \hat{\mathbf{h}} + (\hat{\mathbf{h}} \cdot \tilde{\nabla}_m) \hat{\mathbf{g}}), \quad \text{with } \tilde{\nabla}_p = [ip\alpha, \partial_y, ip\beta], \quad (9.9)$$

In (9.8) the field $\hat{\mathbf{u}}_2^{(2)}$ is the second harmonic associated with the wavenumbers pair $(2\alpha, 2\beta)$. By the application of spatial derivatives, the linearized Navier-Stokes operators depend on the wavenumber pairs and $L^{(2)}$, associated with $(2\alpha, 2\beta)$, governs the dynamics of $\hat{\mathbf{u}}_2^{(2)}$. The field $\mathbf{u}_2^{(0)}$ is the mean flow correction associated with a non-oscillating field in space with wavenumbers pair $(0, 0)$ (hence its designation of "mean flow") and whose dynamics is governed by the operator $L^{(0)}$. The field $\hat{\mathbf{u}}_3$ is associated with the same wavenumbers pair (α, β) as $\hat{\mathbf{u}}_1$, and the weakly nonlinear behavior is determined by their normalized inner product in (9.7).

In the linear limit where $U_0 \rightarrow 0$, the amplitude B in (9.6) tends towards U_0 and the gain G_w in (9.5) reduces indeed to the linear one G in (9.3). By selecting the specific trajectory $\hat{\mathbf{u}}_1(t) = \hat{\mathbf{l}}(t)/\epsilon_o = \Psi(t, 0) \hat{\mathbf{u}}_o$, where the initial condition $\hat{\mathbf{u}}_o$ leads to the largest possible gain at t_o , $G(t_o)$, and where $\epsilon_o = 1/G(t_o)$, results of the previous chapter are recovered exactly.

Crucially, note that any other choices of trajectory presumably degrade the prediction stemming from the asymptotic expansion in terms of $G(t_o)^{-1/2}$, precisely because the truncation errors of the expansion scale in terms of some power of $G(t_o)^{-1/2}$. In particular, the perturba-

tion making the inverse propagator singular along a generic trajectory is written

$$\bar{\Psi}(0, t) - \bar{P}(t), \quad \text{with} \quad \bar{P}(t) = H(t) \frac{\hat{\mathbf{u}}_1(0) \langle \hat{\mathbf{u}}_1(t) | * \rangle}{\langle \hat{\mathbf{u}}_1(t) | \hat{\mathbf{u}}_1(t) \rangle}. \quad (9.10)$$

For a given temporal horizon t_o , the perturbation operator \bar{P} has a norm

$$\|\bar{P}(t_o)\| = \frac{1}{\|\hat{\mathbf{u}}(t_o)\|} = \frac{1}{G(t_o)}, \quad (9.11)$$

which is minimized by selecting $\hat{\mathbf{u}}_1(0) = \hat{\mathbf{u}}_o$. Trajectories seeded by any other initial conditions lead to a larger perturbation operator size $\|\bar{P}(t_o)\|$, possibly to the point of making the expansion (9.10) questionable.

In the next section, we propose a variational approach to maximize the weakly nonlinear gain G_w in (9.5), for a given initial amplitude U_0 , and by acting on the structure of the initial condition.

9.3 Weakly nonlinear Lagrangian optimization

In the linear regime, maximising the gain (9.3) at some temporal horizon t_o , or its square G^2 , amounts to canceling the first-order variations of the Lagrangian

$$\mathcal{L} = G^2 - I_1, \quad (9.12)$$

where I_1 enforces the constraints that $\hat{\mathbf{u}}_1$ must solve the linear evolution equation (9.2), with a unit-norm initial condition. Specifically,

$$I_1 = I_1[\hat{\mathbf{u}}_1, \hat{\mathbf{u}}_1^\dagger, \alpha; t_o] = \int_0^{t_o} \langle \partial_t \hat{\mathbf{u}}_1 - L \hat{\mathbf{u}}_1 | \hat{\mathbf{u}}_1^\dagger \rangle dt + \alpha (1 - \|\hat{\mathbf{u}}_1(0)\|^2) + \text{c.c.}, \quad (9.13)$$

the field $\hat{\mathbf{u}}_1^\dagger$ being Lagrange multiplier. In the weakly nonlinear regime, the Lagrangian (9.12) is augmented as

$$\mathcal{L} = G_w^2 - I_1 - I_2^{(2)} - I_2^{(0)} - I_3 - \gamma f, \quad (9.14)$$

where

$$G_w^2 = G_w[B, \hat{\mathbf{u}}_1; t_o, U_0]^2 = \frac{B(t_o)^2 \|\hat{\mathbf{u}}_1(t_o)\|^2}{U_0^2} \quad (9.15)$$

is the gain (squared) at $t = t_o$, to be maximized. Note that including nonlinear effects implies a parametric dependency of the gain in the amplitude of the initial condition U_0 . Expression (9.6) evaluated at $t = t_o$ gives $B(t_o)$, the weakly nonlinear amplitude of the response at time t_o , and is included as a constraint in the Lagrangian through the term $-\gamma f$. Indeed, the scalar γ is

a Lagrange multiplier enforcing the equation $f = 0$, where

$$f = f[B, \hat{\mathbf{u}}_1, \hat{\mathbf{u}}_3; t_o, U_0] = \frac{1}{2} \left(\frac{1}{U_0^2} - \frac{1}{B(t_o)^2} \right) - \bar{\mu}_r [\hat{\mathbf{u}}_1(t_o), \hat{\mathbf{u}}_3(t_o)] \quad (9.16)$$

so that $f = 0$ is equivalent to (9.6). Through the coefficient $\bar{\mu}_r$, the amplitude $B(t_o)$ requires the knowledge of the field $\hat{\mathbf{u}}_3$, which itself depends on $\hat{\mathbf{u}}_2^{(2)}$ and $\mathbf{u}_2^{(0)}$. Thereby their evolution equations (9.8) also must be included as constraints in the Lagrangian, which is done according to the terms

$$I_2^{(2)} = \int_0^{t_o} \left\langle \partial_t \hat{\mathbf{u}}_2^{(2)} - L^{(2)} \hat{\mathbf{u}}_2^{(2)} + C[\hat{\mathbf{u}}_1, \hat{\mathbf{u}}_1] \Big| \hat{\mathbf{u}}_2^{(2),\dagger} \right\rangle dt + \text{c.c.} \quad (9.17)$$

for $\hat{\mathbf{u}}_2^{(2)}$ associated with the Lagrange multiplier $\hat{\mathbf{u}}_2^{(2),\dagger}$,

$$I_2^{(0)} = \int_0^{t_o} \left\langle \partial_t \mathbf{u}_2^{(0)} - L^{(0)} \mathbf{u}_2^{(0)} + 2C[\hat{\mathbf{u}}_1^*, \hat{\mathbf{u}}_1] \Big| \mathbf{u}_2^{(0),\dagger} \right\rangle dt \quad (9.18)$$

for $\mathbf{u}_2^{(0)}$ associated with the Lagrange multiplier $\mathbf{u}_2^{(0),\dagger}$ and eventually

$$I_3 = \int_0^{t_o} \left\langle \partial_t \hat{\mathbf{u}}_3 - L \hat{\mathbf{u}}_3 + 2C[\hat{\mathbf{u}}_1^*, \hat{\mathbf{u}}_2^{(2)}] + 2C[\hat{\mathbf{u}}_1, \mathbf{u}_2^{(0)}] \Big| \hat{\mathbf{u}}_3^\dagger \right\rangle dt + \text{c.c.} \quad (9.19)$$

for $\hat{\mathbf{u}}_3$ associated with the Lagrange multiplier $\hat{\mathbf{u}}_3^\dagger$. The dependencies of the Lagrangian (9.14) are made explicit as

$$\mathcal{L} = \mathcal{L} \left[B, \hat{\mathbf{u}}_1, \hat{\mathbf{u}}_1^\dagger, \alpha, \hat{\mathbf{u}}_2^{(2)}, \hat{\mathbf{u}}_2^{(2),\dagger}, \mathbf{u}_2^{(0)}, \mathbf{u}_2^{(0),\dagger}, \hat{\mathbf{u}}_3, \hat{\mathbf{u}}_3^\dagger, \gamma; t_o, U_0 \right]. \quad (9.20)$$

Optimality conditions are classically found by canceling all first-order variations of the Lagrangian. If \mathcal{L} depends on some function $\hat{\mathbf{g}}$ appearing inside a spatiotemporal inner product, the first-order variation of \mathcal{L} with respect to $\hat{\mathbf{g}}$ reads

$$\int_0^{t_o} \left\langle \frac{\delta \mathcal{L}}{\delta \hat{\mathbf{g}}} \Big| \hat{\mathbf{g}} \right\rangle dt = \lim_{\epsilon \rightarrow 0} \frac{\mathcal{L}(\dots, \hat{\mathbf{g}} + \epsilon \tilde{\mathbf{g}}, \dots) - \mathcal{L}(\dots, \hat{\mathbf{g}}, \dots)}{\epsilon} \quad (9.21)$$

(where the dots imply the other functions to remain unperturbed, as for a partial derivative).

By computing the variation of \mathcal{L} with respect to the Lagrange multipliers $\hat{\mathbf{u}}_1^\dagger$, α , $\hat{\mathbf{u}}_2^{(2),\dagger}$, $\mathbf{u}_2^{(0),\dagger}$, $\hat{\mathbf{u}}_3^\dagger$ and γ , the respective corresponding constraint equations are recovered. Canceling the variations with respect to B , $\hat{\mathbf{u}}_1$, $\hat{\mathbf{u}}_2^{(2)}$, $\mathbf{u}_2^{(0)}$ and $\hat{\mathbf{u}}_3$, in contrast, leads to non-trivial equations for the Lagrange multipliers. We first compute

$$\frac{\delta \mathcal{L}}{\delta B} \tilde{B} = \frac{\delta G_w^2}{\delta B} \tilde{B} - \gamma \frac{\delta f}{\delta B} \tilde{B} = 2B \tilde{B} \frac{\|\hat{\mathbf{u}}_1(t_o)\|^2}{U_0^2} - \gamma \frac{\tilde{B}}{B^3} \quad (9.22)$$

(where B is evaluated at $t = t_o$). Thereby, imposing

$$\frac{\delta \mathcal{L}}{\delta B} \tilde{B} = 0, \forall \tilde{B} \quad \text{implies} \quad \boxed{\gamma = \frac{2B(t_o)^4 \|\hat{\mathbf{u}}_1(t_o)\|^2}{U_0^2}}, \quad (9.23)$$

which determines the Lagrange multiplier γ . Then,

$$\begin{aligned} \int_0^{t_o} \left\langle \frac{\delta \mathcal{L}}{\delta \hat{\mathbf{u}}_1} \Big| \tilde{\mathbf{u}}_1 \right\rangle dt = & \left\langle \frac{\delta G_w^2}{\delta \hat{\mathbf{u}}_1} \Big| \tilde{\mathbf{u}}_1 \right\rangle \Big|_{t=t_o} - \int_0^{t_o} \left\langle \frac{\delta I_1}{\delta \hat{\mathbf{u}}_1} \Big| \tilde{\mathbf{u}}_1 \right\rangle dt - \int_0^{t_o} \left\langle \frac{\delta I_2^{(2)}}{\delta \hat{\mathbf{u}}_1} \Big| \tilde{\mathbf{u}}_1 \right\rangle dt \\ & - \int_0^{t_o} \left\langle \frac{\delta I_2^{(0)}}{\delta \hat{\mathbf{u}}_1} \Big| \tilde{\mathbf{u}}_1 \right\rangle dt - \int_0^{t_o} \left\langle \frac{\delta I_3}{\delta \hat{\mathbf{u}}_1} \Big| \tilde{\mathbf{u}}_1 \right\rangle dt + \gamma \left\langle \frac{\delta \bar{\mu}_r}{\delta \hat{\mathbf{u}}_1} \Big| \tilde{\mathbf{u}}_1 \right\rangle \Big|_{t=t_o}. \end{aligned} \quad (9.24)$$

All the variations with respect to $\hat{\mathbf{u}}_1$ involved in (9.24) are computed explicitly in Appendix 9.6.1, from which we can show that

$$\begin{aligned} \int_0^{t_o} \left\langle \frac{\delta \mathcal{L}}{\delta \hat{\mathbf{u}}_1} \Big| \tilde{\mathbf{u}}_1 \right\rangle dt = 0, \quad \forall \tilde{\mathbf{u}}_1 \Rightarrow \\ \frac{B(t_o)^2}{U_0^2} \langle \tilde{\mathbf{u}}_1(t_o) | \hat{\mathbf{u}}_1(t_o) \rangle - \langle \tilde{\mathbf{u}}_1(t_o) | \hat{\mathbf{u}}_1^\dagger(t_o) \rangle + \langle \tilde{\mathbf{u}}_1(0) | \hat{\mathbf{u}}_1^\dagger(0) + \alpha \hat{\mathbf{u}}_1(0) \rangle \\ + \int_0^{t_o} \langle \tilde{\mathbf{u}}_1 | \partial_t \hat{\mathbf{u}}_1^\dagger + L^\dagger \hat{\mathbf{u}}_1^\dagger \rangle dt - \int_0^{t_o} \langle \tilde{\mathbf{u}}_1 | 2C^\dagger [\hat{\mathbf{u}}_1, \hat{\mathbf{u}}_2^{(2),\dagger}] \rangle dt \\ - \int_0^{t_o} \langle \tilde{\mathbf{u}}_1 | 2C^\dagger [\hat{\mathbf{u}}_1^*, \mathbf{u}_2^{(0),\dagger}] \rangle dt - \int_0^{t_o} \langle \tilde{\mathbf{u}}_1 | 2C^\dagger [\hat{\mathbf{u}}_2^{(2),*}, \hat{\mathbf{u}}_3^{\dagger,*}] + 2C^\dagger [\mathbf{u}_2^{(0)}, \hat{\mathbf{u}}_3^\dagger] \rangle dt \\ + \frac{\gamma}{2} \langle \tilde{\mathbf{u}}_1(t_o) | F(\hat{\mathbf{u}}_1(t_o), \hat{\mathbf{u}}_3(t_o)) \rangle + \text{c.c.} = 0, \quad \forall \tilde{\mathbf{u}}_1. \end{aligned} \quad (9.25)$$

This leads to three equations, one valid at $t = t_o$,

$$\begin{aligned} \frac{B(t_o)^2}{U_0^2} \hat{\mathbf{u}}_1(t_o) - \hat{\mathbf{u}}_1^\dagger(t_o) + \frac{\gamma}{2} F(\hat{\mathbf{u}}_1(t_o), \hat{\mathbf{u}}_3(t_o)) = 0 \Rightarrow \\ \boxed{\hat{\mathbf{u}}_1(t_o)^\dagger = \frac{B(t_o)^2}{U_0^2} \hat{\mathbf{u}}_1(t_o) + \frac{\gamma}{2} F(\hat{\mathbf{u}}_1(t_o), \hat{\mathbf{u}}_3(t_o))}, \end{aligned} \quad (9.26)$$

another valid at $t = 0$,

$$\hat{\mathbf{u}}_1^\dagger(0) + \alpha \hat{\mathbf{u}}_1(0) = 0 \stackrel{\|\hat{\mathbf{u}}_1(0)\|=1}{\Rightarrow} \boxed{\hat{\mathbf{u}}_1(0) = \frac{\hat{\mathbf{u}}_1^\dagger(0)}{\|\hat{\mathbf{u}}_1^\dagger(0)\|^2}} \quad (9.27)$$

and, eventually, a third one valid for all times between 0 and t_o ,

$$\boxed{\partial_t \hat{\mathbf{u}}_1^\dagger = -L^\dagger \hat{\mathbf{u}}_1^\dagger + 2C^\dagger [\hat{\mathbf{u}}_1, \hat{\mathbf{u}}_2^{(2),\dagger}] + 2C^\dagger [\hat{\mathbf{u}}_1^*, \mathbf{u}_2^{(0),\dagger}] + 2C^\dagger [\hat{\mathbf{u}}_2^{(2),*}, \hat{\mathbf{u}}_3^{\dagger,*}] + 2C^\dagger [\mathbf{u}_2^{(0)}, \hat{\mathbf{u}}_3^\dagger]} \quad (9.28)$$

The latter evolution equation needs to be integrated backward from the knowledge of $\hat{\mathbf{u}}_1^\dagger(t_o)$.

We proceed with the calculations by imposing that the variation of \mathcal{L} with respect to $\hat{\mathbf{u}}_2^{(2)}$ must also be null at optimality. In mathematical terms,

$$\begin{aligned} \int_0^{t_0} \left\langle \frac{\delta \mathcal{L}}{\delta \hat{\mathbf{u}}_2^{(2)}} \middle| \tilde{\mathbf{u}}_2^{(2)} \right\rangle dt &= - \int_0^{t_0} \left\langle \frac{\delta I_2^{(2)}}{\delta \hat{\mathbf{u}}_2^{(2)}} \middle| \tilde{\mathbf{u}}_2^{(2)} \right\rangle dt - \int_0^{t_0} \left\langle \frac{\delta I_3}{\delta \hat{\mathbf{u}}_2^{(2)}} \middle| \tilde{\mathbf{u}}_2^{(2)} \right\rangle dt = 0, \quad \forall \tilde{\mathbf{u}}_2^{(2)} \Rightarrow \\ &- \left\langle \tilde{\mathbf{u}}_2^{(2)}(t_0) \middle| \hat{\mathbf{u}}_2^{(2),\dagger}(t_0) \right\rangle \\ &+ \int_0^{t_0} \left\langle \tilde{\mathbf{u}}_2^{(2)} \middle| \partial_t \hat{\mathbf{u}}_2^{(2),\dagger} + L^{(2),\dagger} \hat{\mathbf{u}}_2^{(2),\dagger} - 2C^\dagger [\hat{\mathbf{u}}_1^*, \hat{\mathbf{u}}_3^\dagger] \right\rangle dt + \text{c.c.} = 0, \quad \forall \tilde{\mathbf{u}}_2^{(2)} \end{aligned} \quad (9.29)$$

where results from Appendix 9.6.2 have been utilized. This leads to two new equations, the first being valid at $t = t_0$,

$$\boxed{\hat{\mathbf{u}}_2^{(2),\dagger}(t_0) = \mathbf{0}}, \quad (9.30)$$

and the second for all times between 0 and t_0 ,

$$\boxed{\partial_t \hat{\mathbf{u}}_2^{(2),\dagger} = -L^{(2),\dagger} \hat{\mathbf{u}}_2^{(2),\dagger} + 2C^\dagger [\hat{\mathbf{u}}_1^*, \hat{\mathbf{u}}_3^\dagger]}, \quad (9.31)$$

to be integrated backward from the knowledge of $\hat{\mathbf{u}}_2^{(2),\dagger}(t_0)$. Similarly,

$$\begin{aligned} \int_0^{t_0} \left\langle \frac{\delta \mathcal{L}}{\delta \mathbf{u}_2^{(0)}} \middle| \tilde{\mathbf{u}}_2^{(0)} \right\rangle dt &= - \int_0^{t_0} \left\langle \frac{\delta I_2^{(0)}}{\delta \mathbf{u}_2^{(0)}} \middle| \tilde{\mathbf{u}}_2^{(0)} \right\rangle dt - \int_0^{t_0} \left\langle \frac{\delta I_3}{\delta \mathbf{u}_2^{(0)}} \middle| \tilde{\mathbf{u}}_2^{(0)} \right\rangle dt = 0, \quad \forall \tilde{\mathbf{u}}_2^{(0)} \Rightarrow \\ &- \left\langle \tilde{\mathbf{u}}_2^{(0)}(t_0) \middle| \mathbf{u}_2^{(0),\dagger}(t_0) \right\rangle \\ &+ \int_0^{t_0} \left\langle \tilde{\mathbf{u}}_2^{(0)} \middle| \partial_t \mathbf{u}_2^{(0),\dagger} + L^{(0),\dagger} \mathbf{u}_2^{(0),\dagger} - 2C^\dagger [\hat{\mathbf{u}}_1, \hat{\mathbf{u}}_3^\dagger] - 2C^\dagger [\hat{\mathbf{u}}_1^*, \hat{\mathbf{u}}_3^{\dagger,*}] \right\rangle dt = 0, \quad \forall \tilde{\mathbf{u}}_2^{(0)} \end{aligned} \quad (9.32)$$

using the developments in Appendix 9.6.2. This implies directly

$$\boxed{\mathbf{u}_2^{(0),\dagger}(t_0) = \mathbf{0}}, \quad (9.33)$$

as well as

$$\boxed{\partial_t \mathbf{u}_2^{(0),\dagger} = -L^{(0),\dagger} \mathbf{u}_2^{(0),\dagger} + 2C^\dagger [\hat{\mathbf{u}}_1, \hat{\mathbf{u}}_3^\dagger] + 2C^\dagger [\hat{\mathbf{u}}_1^*, \hat{\mathbf{u}}_3^{\dagger,*}]}, \quad (9.34)$$

to be integrated backward from $\mathbf{u}_2^{(0),\dagger}(t_0)$. Eventually,

$$\begin{aligned} \int_0^{t_0} \left\langle \frac{\delta \mathcal{L}}{\delta \hat{\mathbf{u}}_3} \middle| \tilde{\mathbf{u}}_3 \right\rangle dt &= - \int_0^{t_0} \left\langle \frac{\delta I_3}{\delta \hat{\mathbf{u}}_3} \middle| \tilde{\mathbf{u}}_3 \right\rangle dt + \gamma \left\langle \frac{\delta \bar{\mu}_r}{\delta \hat{\mathbf{u}}_3} \middle| \tilde{\mathbf{u}}_3 \right\rangle \bigg|_{t=t_0} = 0, \quad \forall \tilde{\mathbf{u}}_3 \Rightarrow \\ &- \left\langle \tilde{\mathbf{u}}_3(t_0) \middle| \hat{\mathbf{u}}_3^\dagger(t_0) \right\rangle + \int_0^{t_0} \left\langle \tilde{\mathbf{u}}_3 \middle| \partial_t \hat{\mathbf{u}}_3^\dagger + L^\dagger \hat{\mathbf{u}}_3^\dagger \right\rangle dt \\ &+ \frac{\gamma}{2} \frac{\langle \tilde{\mathbf{u}}_3(t_0) | \hat{\mathbf{u}}_1(t_0) \rangle}{\langle \hat{\mathbf{u}}_1(t_0) | \hat{\mathbf{u}}_1(t_0) \rangle} + \text{c.c.} = 0, \quad \forall \tilde{\mathbf{u}}_3 \end{aligned} \quad (9.35)$$

from Appendix 9.6.4, implying

$$\hat{\mathbf{u}}_3^\dagger(t_o) = \frac{\gamma}{2} \frac{\hat{\mathbf{u}}_1(t_o)}{\langle \hat{\mathbf{u}}_1(t_o) | \hat{\mathbf{u}}_1(t_o) \rangle}, \quad (9.36)$$

as well as

$$\partial_t \hat{\mathbf{u}}_3^\dagger = -L^\dagger \hat{\mathbf{u}}_3 \quad (9.37)$$

for $0 \leq t \leq t_o$, to be integrated backward from $\hat{\mathbf{u}}_3^\dagger(t_o)$. All the computations done so far can be assembled into the following optimization algorithm,

1. Choose a temporal horizon t_o and an initial amplitude U_0 .
2. Pick an initial guess for $\hat{\mathbf{u}}_1(0)$ (for instance, the linear optimal corresponding to that t_o).
3. From the knowledge of $\hat{\mathbf{u}}_1(0)$, integrate the evolution equations (9.2) and (9.8) from $t = 0$ to $t = t_o$ to obtain the fields $\hat{\mathbf{u}}_1(t)$, $\hat{\mathbf{u}}_2^{(2)}(t)$, $\mathbf{u}_2^{(0)}(t)$ and $\hat{\mathbf{u}}_3(t)$ over $t \in [0, t_o]$.
4. From the knowledge of $\hat{\mathbf{u}}_1(t_o)$ and $\hat{\mathbf{u}}_3(t_o)$, compute the weakly nonlinear amplitude $B(t_o)$ with (9.6), and evaluate the associated weakly nonlinear gain according to (9.15).
5. From the knowledge of $\hat{\mathbf{u}}_1(t_o)$ and $B(t_o)$, compute the Lagrange multiplier γ using (9.23).
6. Compute $\hat{\mathbf{u}}_3^\dagger(t)$ over $t \in [0, t_o]$ by integrating (9.37) backward from its condition at $t = t_o$ given in (9.36) (and which requires the knowledge of γ).
7. From the knowledge $\hat{\mathbf{u}}_3^\dagger(t)$, compute $\hat{\mathbf{u}}_2^{(2),\dagger}(t)$ and $\mathbf{u}_2^{(0),\dagger}(t)$ over $t \in [0, t_o]$ by integrating (9.31) and (9.34) backward from their conditions at $t = t_o$, given (9.30) and (9.33), respectively.
8. From the knowledge $\hat{\mathbf{u}}_3^\dagger(t)$, $\hat{\mathbf{u}}_2^{(2),\dagger}(t)$ and $\mathbf{u}_2^{(0),\dagger}(t)$ compute $\hat{\mathbf{u}}_1^\dagger(t)$ over $t \in [0, t_o]$ by integrating (9.28) backward from its condition at $t = t_o$ given in (9.26).
9. From the knowledge of $\hat{\mathbf{u}}_1^\dagger(t_o)$, choose the new initial condition $\hat{\mathbf{u}}_1(0)$ according to (9.27), possibly with some relaxation factors, and go back to step 3 until convergence of the weakly nonlinear gain.
10. To check for other existing maxima, it is appropriate to restart the algorithm with a completely different initial guess for $\hat{\mathbf{u}}_1(0)$.

The algorithm proposed above is implemented for the plan Poiseuille flow in the following section.

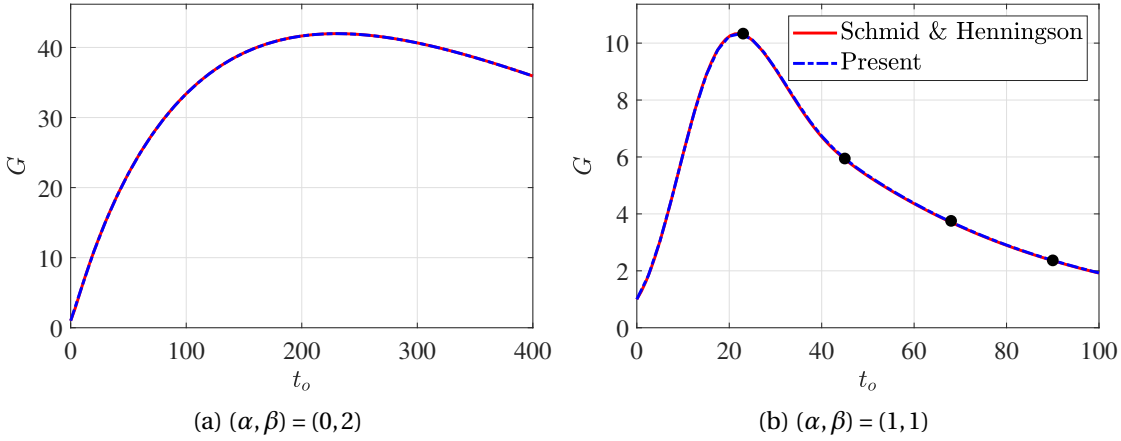


Figure 9.2: Optimal linear transient gain as a function of the temporal horizon t_o , for the plane Poiseuille flow shown in figure 2.2 and for $\text{Re} = 3000$. Two different pairs of wavenumbers (α, β) are considered. Optimal transient gains produced by the open source codes given in Schmid (2007) are also shown. The black bullets for $t_o \in [22, 45, 68, 90]$ highlight the temporal horizons that will be further studied.

9.4 Application case: the plane Poiseuille flow

In this section, initial perturbations along a given wavenumber pair that are optimal in the sense of the weakly nonlinear amplitude equation, are computed for the three-dimensional plane Poiseuille flow. Their relevance in a fully nonlinear regime, as compared with the linearly optimal ones, is then studied.

In the linear regime, the perturbation possesses a single wavenumbers pair (α, β) , thereby is periodic in x and z with a wavelength $2\pi/\alpha$ and $2\pi/\beta$, respectively, and no harmonics are generated. In the fully nonlinear regime, simulations are performed inside the three-dimensional domain with coordinates

$$x \in [0, 2\pi/\alpha], \quad y \in [-1, 1], \quad z \in [-\pi/\beta, \pi/\beta], \quad (9.38)$$

with periodic boundary conditions in x and z . This makes possible the nonlinear production of harmonics $(n\alpha, p\beta)$, $n = 0, 1, 2, \dots$ and, independently, $p = 0, 1, 2, \dots$

In figure 9.2, we show the maximal linear transient gain for the plane Poiseuille flow at $\text{Re} = 3000$ as a function of the temporal horizon t_o , and for two different wavenumbers pairs. Results from the Schmid and Henningson (2001) are recovered. Motivated by the work of Reddy et al. (1998), showing that oblique perturbations are more efficient than streamwise ones in triggering turbulence in the plane Poiseuille flow, in what follows, we will restrict the analysis to the case $(\alpha, \beta) = (1, 1)$ shown in figure 9.2b. In addition, the temporal horizons $t_o \in [22, 45, 68, 90]$ (black bullets in figure 9.2b) are selected for a more detailed study.

Let $\mathbf{U}(x, y, z, t)$ be a fully nonlinear solution, obtained from a DNS in the x -and- z periodic

three-dimensional domain (9.38). This solution can be decomposed as the sum of perturbation $\mathbf{u}_p(x, y, z, t)$ plus a mean flow (over space) $\bar{\mathbf{U}}(y, t)$. The latter and the former field are extracted according to

$$\begin{aligned} \bar{\mathbf{U}}(y, t) &= \frac{\alpha}{2\pi} \frac{\beta}{2\pi} \int_0^{2\pi/\alpha} \int_{-\pi/\beta}^{\pi/\beta} \mathbf{U}(x, y, z, t) dz dx, \quad \text{then} \\ \mathbf{u}_p(x, y, z, t) &= \mathbf{U}(x, y, z, t) - \bar{\mathbf{U}}(y, t). \end{aligned} \quad (9.39)$$

In all generalities, the perturbation does not oscillate purely along the pair (α, β) but contains harmonics. Thereby, the component of the perturbation along (α, β) , denoted $\mathbf{u}_{\alpha, \beta}$, needs to be extracted as

$$\begin{aligned} \mathbf{u}_{\alpha, \beta}(x, y, z, t) &= \hat{\mathbf{u}}_{\alpha, \beta}(y) e^{i(\alpha x + \beta z)} + \text{c.c.}, \quad \text{with} \\ \hat{\mathbf{u}}_{\alpha, \beta}(y, t) &= \frac{\alpha\beta}{4\pi^2} \int_0^{2\pi/\alpha} \int_{-\pi/\beta}^{\pi/\beta} \mathbf{u}_p \cos(\alpha x + \beta z) dz dx \\ &\quad - i \frac{\alpha\beta}{4\pi^2} \int_0^{2\pi/\alpha} \int_{-\pi/\beta}^{\pi/\beta} \mathbf{u}_p \sin(\alpha x + \beta z) dz dx. \end{aligned} \quad (9.40)$$

(Note that, in the linear regime no harmonics exist and \mathbf{u}_p reduces to $\mathbf{u}_{\alpha, \beta}$). The perturbation \mathbf{u}_p is associated with an energy E_p , computed as

$$E_p = \frac{\alpha\beta}{8\pi^2} \int_{-\pi/\beta}^{\pi/\beta} \int_{-1}^1 \int_0^{2\pi/\alpha} \mathbf{u}_{p,x}^2 + \mathbf{u}_{p,y}^2 + \mathbf{u}_{p,z}^2 dx dy dz. \quad (9.41)$$

The normalization prefactor in front of the integral guarantees the consistency with the induced norm $\|\bullet\|^2$ introduced in (9.4) and used in the previous section. Indeed, the energy of $\mathbf{u}_{\alpha, \beta}$ is computed as

$$\begin{aligned} E_{\alpha, \beta} &= \frac{\alpha\beta}{8\pi^2} \int_{-\pi/\beta}^{\pi/\beta} \int_{-1}^1 \int_0^{2\pi/\alpha} \mathbf{u}_{\alpha, \beta, x}^2 + \mathbf{u}_{\alpha, \beta, y}^2 + \mathbf{u}_{\alpha, \beta, z}^2 dx dy dz, \\ &= \frac{\alpha\beta}{8\pi^2} \int_{-\pi/\beta}^{\pi/\beta} \int_{-1}^1 \int_0^{2\pi/\alpha} 2|\hat{\mathbf{u}}_{\alpha, \beta, x}|^2 + 2|\hat{\mathbf{u}}_{\alpha, \beta, y}|^2 + 2|\hat{\mathbf{u}}_{\alpha, \beta, z}|^2 dx dy dz, \\ &= \int_{-1}^1 |\hat{\mathbf{u}}_{\alpha, \beta, x}|^2 + |\hat{\mathbf{u}}_{\alpha, \beta, y}|^2 + |\hat{\mathbf{u}}_{\alpha, \beta, z}|^2 dy, \\ &= \langle \hat{\mathbf{u}}_{\alpha, \beta} | \hat{\mathbf{u}}_{\alpha, \beta} \rangle = \|\hat{\mathbf{u}}_{\alpha, \beta}\|^2. \end{aligned} \quad (9.42)$$

We show in figure 9.3 the energy E_p of the (total) perturbation \mathbf{u}_p as a function of time, for the plane Poiseuille flow. The flow was initiated with the optimal linear initial condition for $(\alpha, \beta, t_0) = (1, 1, 45)$ with an energy $E_p(0) = E_{\alpha, \beta}(0) = 10^{-3}$. The energies E_p and $E_{\alpha, \beta}$ are initially equal since the flow is initiated solely along its (α, β) component. However, they generally depart from each other due to nonlinearities as time evolves and $E_{\alpha, \beta}$ is also represented. At the specific times corresponding to the black crosses in figure 9.3, the structure of \mathbf{u}_p is shown in figure 9.4. At this Re value and for this wavenumber, the flow is linearly stable. Yet, the initial perturbation experiences a transient growth episode with a peak in energy

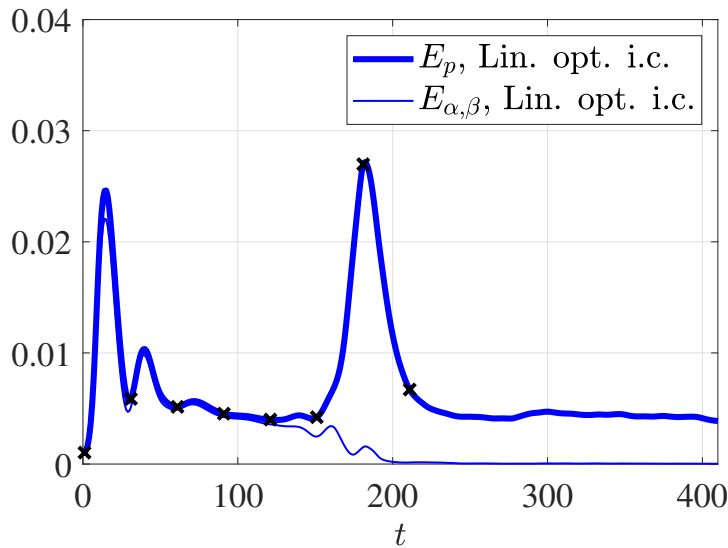


Figure 9.3: For the plane Poiseuille flow at $\text{Re} = 3000$ in a three-dimensional x -and- z periodic box (9.38), are shown the energy E_p of (total) perturbations \mathbf{u}_p (thick lines) as well as the energy $E_{\alpha,\beta}$ contained in the (α, β) -component (thin lines). It was initiated with the linear optimal initial condition for $(\alpha, \beta, t_o) = (1, 1, 45)$. The energy of the initial condition is $E_p(0) = E_{\alpha,\beta}(0) = U_0^2 = 10^{-3}$. The black crosses highlight $t \in [1, 31, 61, 91, 121, 151, 181, 211]$, times at which the flow is shown in figure 9.4

around $t = 15$, as the initial thin vorticity layers oriented against the main shear unfold in figure 9.4 (Orr mechanism). The perturbation decays only but slightly afterward, and thin wavy structures seem to develop on the top of unfolded vorticity rolls, as visible on the frames corresponding to $t = 61, 91$ and 121 in figure 9.4. These wavy structures appear to break down in the frame corresponding to $t = 151$ in figure 9.4, and the flow becomes turbulent rather abruptly, as visible in the frame corresponding to $t = 181$ in figure 9.4. This is associated with a strong surge of perturbation energy in figure 9.3. By becoming turbulent from $t = 151$ onward, the flow develops many length scales, and E_p and $E_{\alpha,\beta}$ depart from each other in figure 9.3 (whereas the energy was dominated by the (α, β) oblique wave before). This phenomenology, which consists of a perturbation that initially grows according to a non-modal mechanism, in turn bringing about nonlinearities that make the flow escape from its attractor, is typical of a bypass transition. It says nothing more than, in the phase space, the initial optimal condition for $(\alpha, \beta, t_o) = (1, 1, 45)$, with an amplitude U_0 , is outside the basin of attraction of the plane Poiseuille flow.

In the following, we implement the weakly nonlinear optimization algorithm outlined in the previous section. In the spirit of Pringle and Kerswell (2010) and Pringle et al. (2012), we hope to compute, for a given set (α, β, t_o) , an initial condition structure that is more efficient in triggering turbulence than the linear optimal one. Here, being more efficient means that the weakly nonlinear initial condition would trigger turbulence for a lower amplitude U_0 than the linear one.

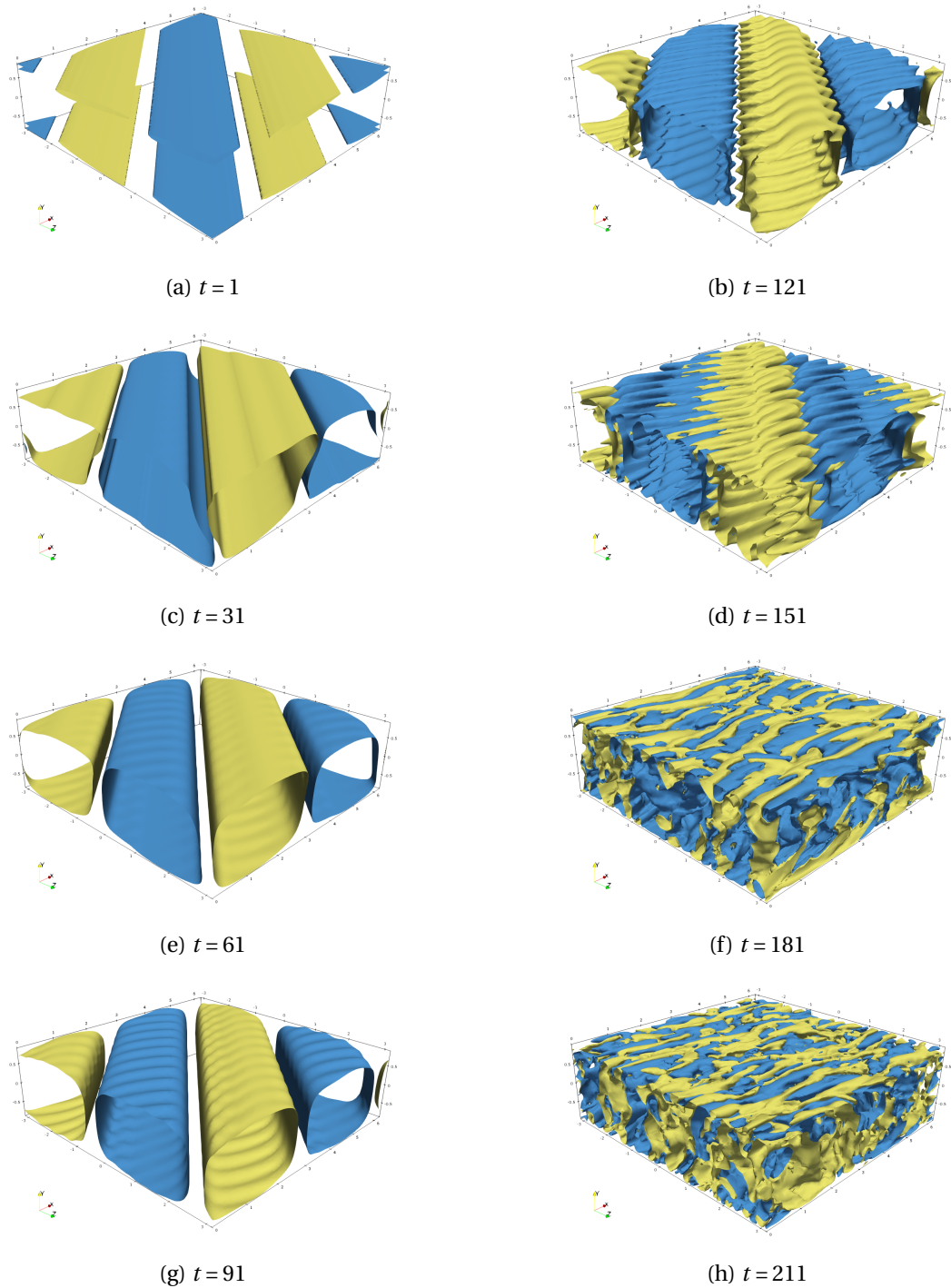


Figure 9.4: The plane Poiseuille flow at $Re = 3000$, initiated by the linear optimal initial condition for the parameters $(\alpha, \beta, t_o) = (1, 1, 45)$ and with an initial amplitude $U_0 = 10^{-1.5}$. The $\pm 10^{-2}$ isocontours of the crosswise velocity are shown. The energy of the perturbation at the corresponding times is shown with black crosses over the continuous line curve in figure 9.3.

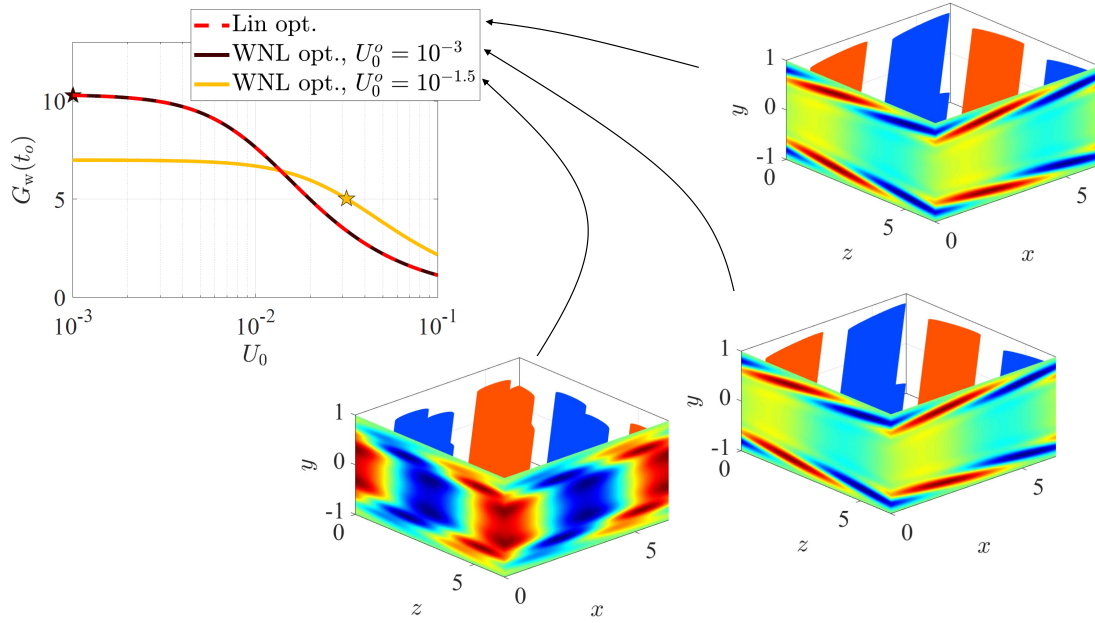


Figure 9.5: For the set of parameters $(\alpha, \beta, t_o) = (1, 1, 22)$, is shown the weakly nonlinear transient gain $G_w(t_o)$ as a function of U_0 , the amplitude of the linear optimal initial condition (red dashed line) or of the weakly nonlinear ones associated with $U_0^o = 10^{-3}$ (black continuous) and $U_0^o = 10^{-1.5}$ (yellow continuous). A star marker is placed at $U_0 = U_0^o$, i.e. when the initial amplitude is equal to that for which the structure was optimized. The corresponding structures (isocontours of the cross-wise velocity) are also shown.

Let us first consider the set of parameters $(\alpha, \beta, t_o) = (1, 1, 22)$ and different optimization amplitude of the initial condition, denoted U_0^o in what follows. The latter enters as a parameter in the weakly nonlinear optimization algorithm, in the same manner that α , β , or t_o do. By definition, when computing the evolution of $G_w(t_o)$ as a function of U_0 , that associated with the structure optimized for U_0^o should be larger than all the others at $U_0 = U_0^o$ specifically. Some results are shown in figure 9.5, where we compare the linear optimal initial structures, with the weakly nonlinear ones for $U_0^o = 10^{-3}$ and $U_0^o = 10^{-1.5}$. It appears that the optimization amplitude $U_0^o = 10^{-3}$ is sufficiently low to yield the same results as the linear optimization algorithm (which simply consists of a singular value decomposition of the propagator, without the initial amplitude entering into the calculations). Selecting the optimization amplitude $U_0^o = 10^{-1.5}$, however, significantly distorts the optimal initial structure. We check that the transient gain that was optimized for $U_0^o = 10^{-1.5}$ is larger than the linearly optimal one when $U_0 = U_0^o = 10^{-1.5}$ (i.e. the yellow curve is above the red-dashed one at the location of the yellow star).

We further consider three larger values for the temporal horizon, such that $t_o \in [22, 45, 68, 90]$ (black bullets in figure 9.2). For each value of t_o , we gradually increase the optimization amplitude of the initial condition U_0^o , and report the results in figure 9.6. For all the considered parameters, the optimization algorithm seems to be effective in maximizing the gain, in

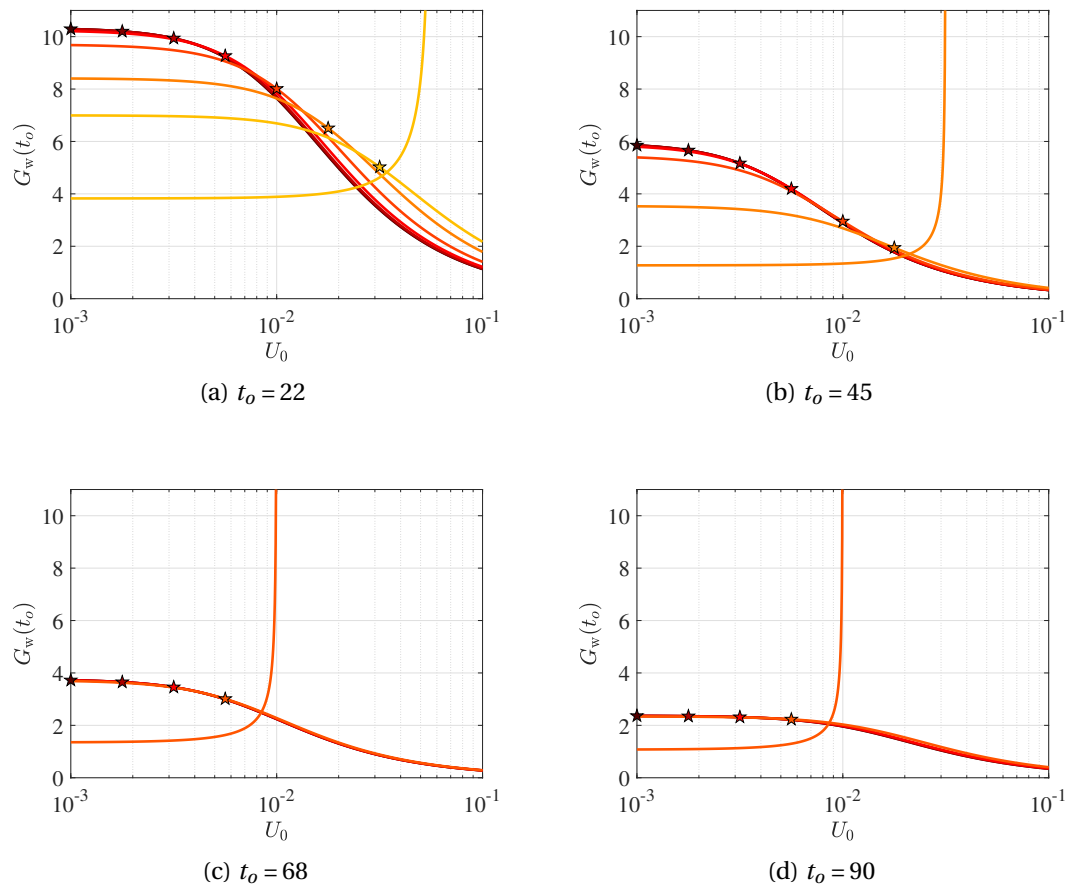


Figure 9.6: Each frame shows the evolution of the weakly nonlinear transient gain $G_w(t_o)$ with U_0 , and for several values of the optimization initial amplitude U_0^o . Different colors correspond to different values of U_0^o , and a star is placed when $U_0 = U_0^o$. Different frames correspond to different t_o . For $t_o = 22$, some results are redundant with those shown in figure 9.5.

that the $G_w(t_o)$ curve, corresponding to a given U_0^o , is above all the others at $U_0 = U_0^o$. More prosaically, in figure 9.6, the curve associated with a star is above all the others at the location of the star. This is particularly visible in figure 9.6a, corresponding to $t_o = 22$, where optimizing over increasing U_0^o seems to lead to significantly different gain variations over U_0 . Particularly, it modifies the optimal structure in a way that substantially decreases the linear gain (in the limit $U_0 \rightarrow 0$).

As seen in the previous chapter, the weakly nonlinear gain $G_w(t_o)$ is subject to a singular explosion for a sufficiently large initial amplitude U_0 . Thereby, the optimization algorithm will select the initial structure that leads to such singularity whenever the optimization amplitude U_0^o is sufficiently large to make it possible. We interpret this singularity (loss of solution) as a conservative indication that the flow has transited to another structurally different state. Otherwise, the weakly nonlinear prediction would still yield a solution. Therefore, in figure 9.6, we interpret the U_0^o at which the gain curves become singular as the minimal initial amplitude at which the flow has transited to turbulence at $t = t_o$ (i.e., the weakly nonlinear

approximation of the minimal seed energy in Pringle et al. (2012)). Such minimal U_0^o , at which the gain becomes singular and the flow presumably has bifurcated, is denoted by $U_0^{o,s}$, the superscript s for "singular". Figure 9.6 also reveals that $U_0^{o,s}$ is a decreasing function of the temporal horizon, supposedly because the initial perturbation had more time to be effective for larger t_o , thereby its amplitude can be smaller. We obtain $U_0^{o,s} = 10^{-1.25}, 10^{-1.5}, 10^{-2}$ and 10^{-2} for $t_o = 22, 45, 68$ and 90 , respectively. Note the coarse discretization in $U_0^{o,s}$, due to the rather large numerical cost of the optimization algorithm.

Note in figure 9.6 that the structures optimized for $U_0^{o,s}$ are associated with a poor linear gain close to unity, thus the asymptotic expansion used to determine the weakly nonlinear gain prolongation is hardly justified. These weakly nonlinear optimal structures, optimized for $U_0^o = U_0^{o,s}$ are shown in figure 9.7 together with the linear optimal ones (just to their respective left).

Let us now study in figure 9.10 to which extent the weakly nonlinear optimal initial perturbations are more efficient than the linear optimal ones in bringing about the transition to turbulence. To this end, we initiate a DNS with the weakly nonlinear optimal for $(\alpha, \beta, t_o, U_0^o) = (1, 1, 45, 10^{-1.5} = U_0^{o,s})$. We then compare the results with those already shown in figure 9.3, where the DNS was initiated with the linear optimal initial perturbation for the same parameters (except for U_0^o which doesn't apply). Both DNS were initiated with the same amplitude $U_0 = U_0^o = U_0^{o,s} = 10^{-1.5}$, for which the weakly nonlinear optimal initial condition should by definition lead to a larger amplification at $t = t_o = 45$ in a weakly nonlinear regime. We hope this to hold also in a fully nonlinear regime, although there are no *a priori* reasons for that. A comparison of the energies E_p and $E_{\alpha,\beta}$, as extracted from the DNS, is proposed in figure 9.8. The results are not conclusive: all along its evolution, the perturbation seeded by the weakly nonlinear optimal yields much lower energy than that seeded by the linear optimal one. In particular, the former never breaks down to turbulence whereas the latter does. We further illustrate in figure 9.9 the evolution of the perturbation flow field initiated with the weakly nonlinear optimal. If the initial evolution resembles the Orr mechanism, and the unfolded structure at $t = 61$ also tends to develop wavy structures, these latter are not energetic enough to grow and break down to turbulence as in figure 9.4, but rather relaminarize towards the plane Poiseuille flow.

We further study how generic these bad results are, by launching two fully nonlinear simulations for each of the four t_o considered. Again, the first is initiated with the linear optimal structure, shown at a given line in figure 9.7, left column. The second, with the weakly nonlinear one, at the same given line in figure 9.7, but right column. Both initial conditions have an initial amplitude $U_0 = U_0^o = U_0^{o,s}$, for which the weakly nonlinear initial condition has in principle a larger (singular) gain at $t = t_o$. The resulting gains are reported in figure 9.10, where the DNS gains relevant for the comparison are computed as $E_{\alpha,\beta}(t)/E_{\alpha,\beta}(0)$, since the amplitude equation only describes the evolution of the (α, β) component.

The results are generally not convincing, in the sense that the weakly nonlinear optimal initial

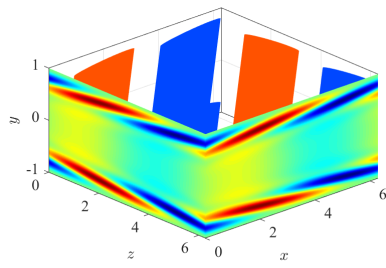
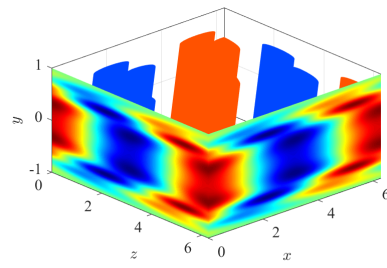
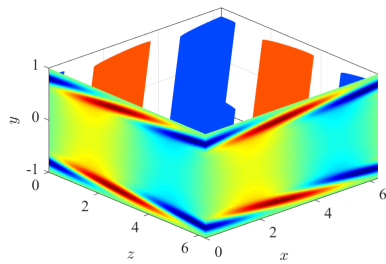
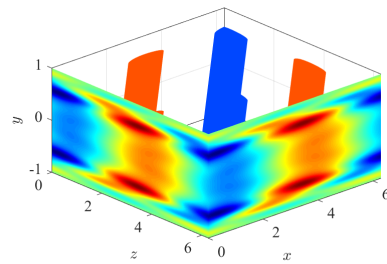
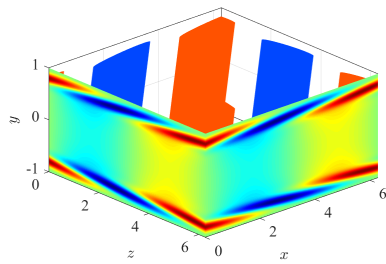
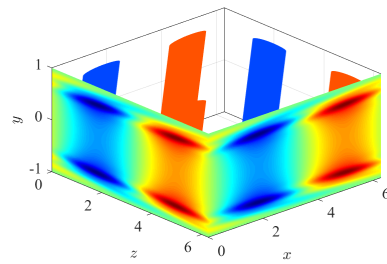
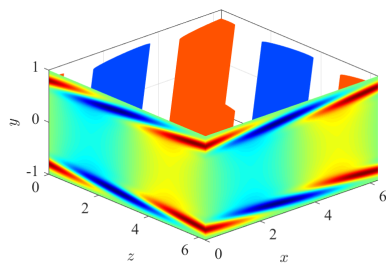
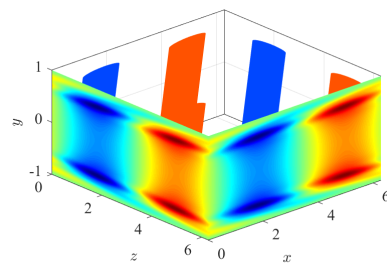
(a) $t_o = 22$, linear(b) $t_o = 22$, $U_0^o = U_0^{o,s} = 10^{-1.25}$ (c) $t_o = 45$, linear(d) $t_o = 45$, $U_0^o = U_0^{o,s} = 10^{-1.5}$ (e) $t_o = 68$, linear(f) $t_o = 68$, $U_0^o = U_0^{o,s} = 10^{-2}$ (g) $t_o = 90$, linear(h) $t_o = 90$, $U_0^o = U_0^{o,s} = 10^{-2}$

Figure 9.7: Optimal initial conditions in a linear regime (left column) and a weakly nonlinear one (right column)

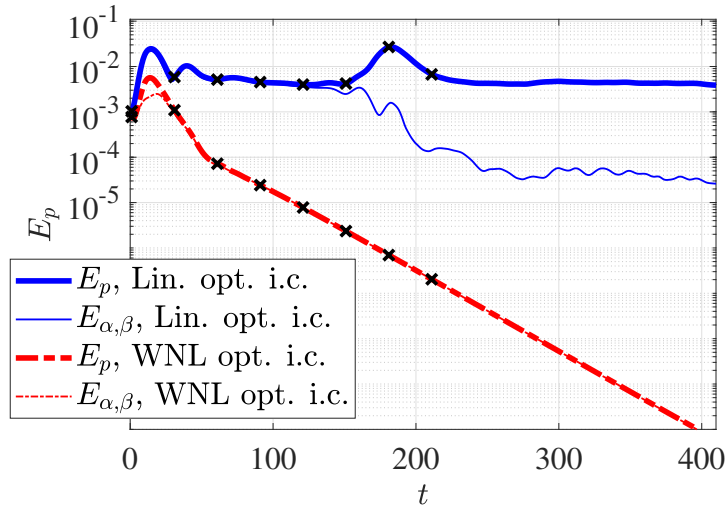


Figure 9.8: For the plane Poiseuille flow at $\text{Re} = 3000$ in a three-dimensional x -and- z periodic box (9.38), are shown the fully nonlinear energy E_p of (total) perturbations \mathbf{u}_p (thick lines) as well as the energy $E_{\alpha,\beta}$ contained in the (α, β) -component (thin lines). The continuous lines are the same as in figure 9.3 (now shown in lin-log scale). For the dashed-dotted lines, the flow was initiated with the weakly nonlinear optimal initial condition, for the same parameters together with an optimization initial amplitude of $U_0^o = 10^{-1.5}$ (the same as the initial amplitude U_0). In all cases, the energy of the initial condition is $E_p(0) = E_{\alpha,\beta}(0) = U_0^2 = 10^{-3}$. The black crosses highlight $t \in [1, 31, 61, 91, 121, 151, 181, 211]$, times at which the flow is shown in figure 9.4 (when initiated by the linear optimal) and in figure 9.9 (when initiated by the weakly nonlinear optimal)

conditions almost systematically yield a lower gain than the linear optimal ones. In other terms, in figure 9.10, the black continuous line almost systematically is above the red one. An exception is found for the frame corresponding to $t_o = 22$ in figure 9.10a, where the DNS initiated with the weakly nonlinear optimal (red continuous line) seems to yield slightly larger gain values than the DNS initiated with the linear optimal (black continuous line), for short time episodes.

It is also observed that the agreement between the DNS and the weakly nonlinear predictions, i.e. between the continuous and the dashed line for a given color, rapidly degrades as time increases. This seems particularly true for the weakly nonlinear prediction of the trajectory seeded by the weakly nonlinear optimal (i.e. the dashed red line compares particularly poorly with the continuous red line). The quick degradation of the weakly nonlinear prediction in a subcritical flow regime was also found to occur in the previous chapter in figure 8.9. It was explained by the fact that, if the considered U_0 is too large, the nonlinearly distorted mean flow became unstable to a mode that the amplitude equation was inherently unable to account for.

This seriously calls into question the approach adopted here, for the relevance of the weakly nonlinear optimal structures implicitly is based on the assumption that the weakly nonlinear amplitude equation (9.6) is an accurate model even for U_0 that are not too small. If (9.6) fails

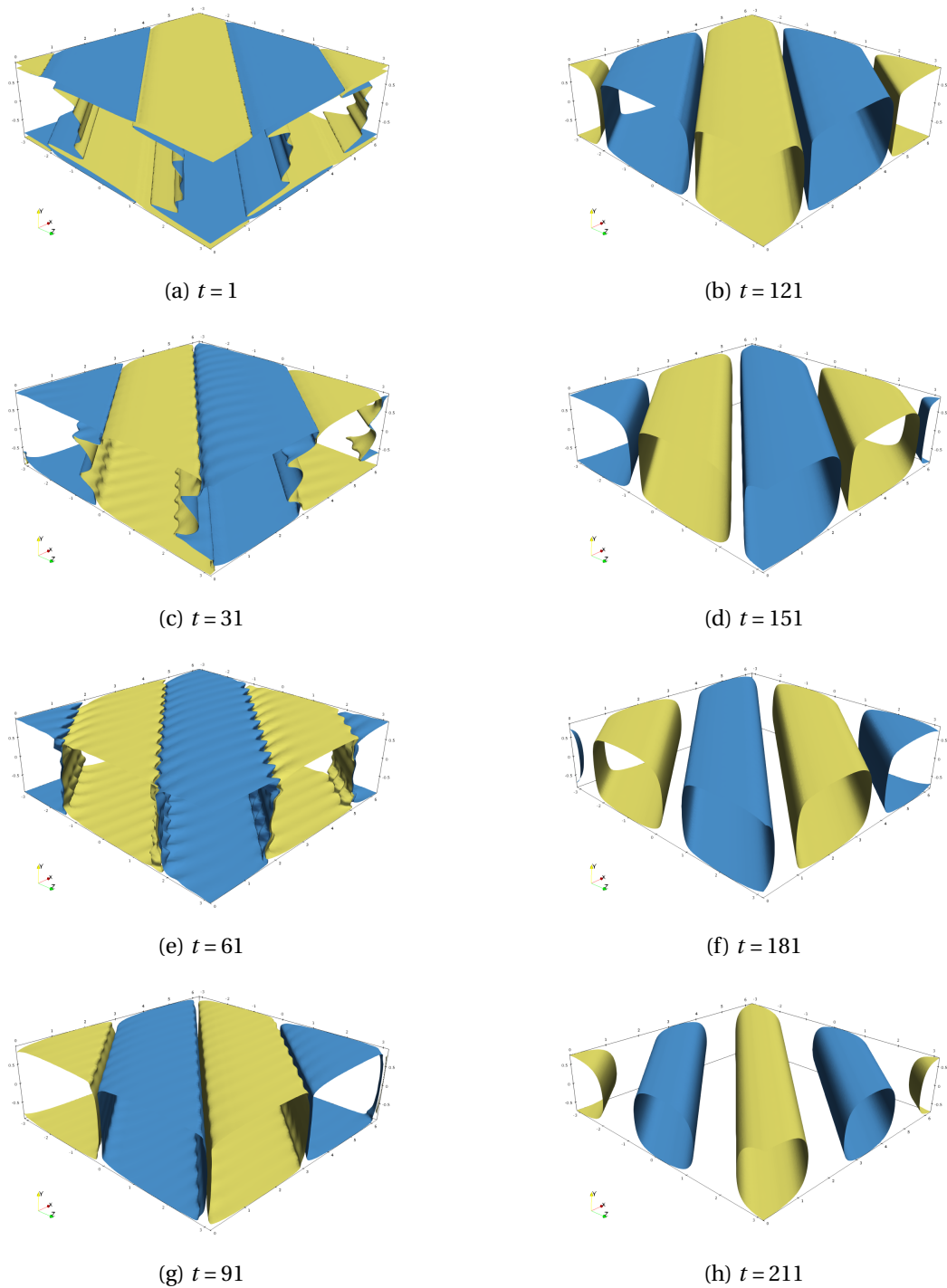


Figure 9.9: The plane Poiseuille flow at $Re = 3000$, initiated by the weakly nonlinear optimal initial condition for the parameters $(\alpha, \beta, t_0, U_0^o) = (1, 1, 45, 10^{-1.5} = U_0^{o,s})$ and with an initial amplitude $U_0 = U_0^o = U_0^{o,s} = \sqrt{E_{\alpha,\beta}(0)} = \sqrt{E_p(0)} = 10^{-1.5}$. The $\pm 10^{-4}$ isocontours of the crosswise velocity are shown. The energy of the perturbation at the corresponding times is shown with black crosses over the dashed-dotted line curve in figure 9.3.

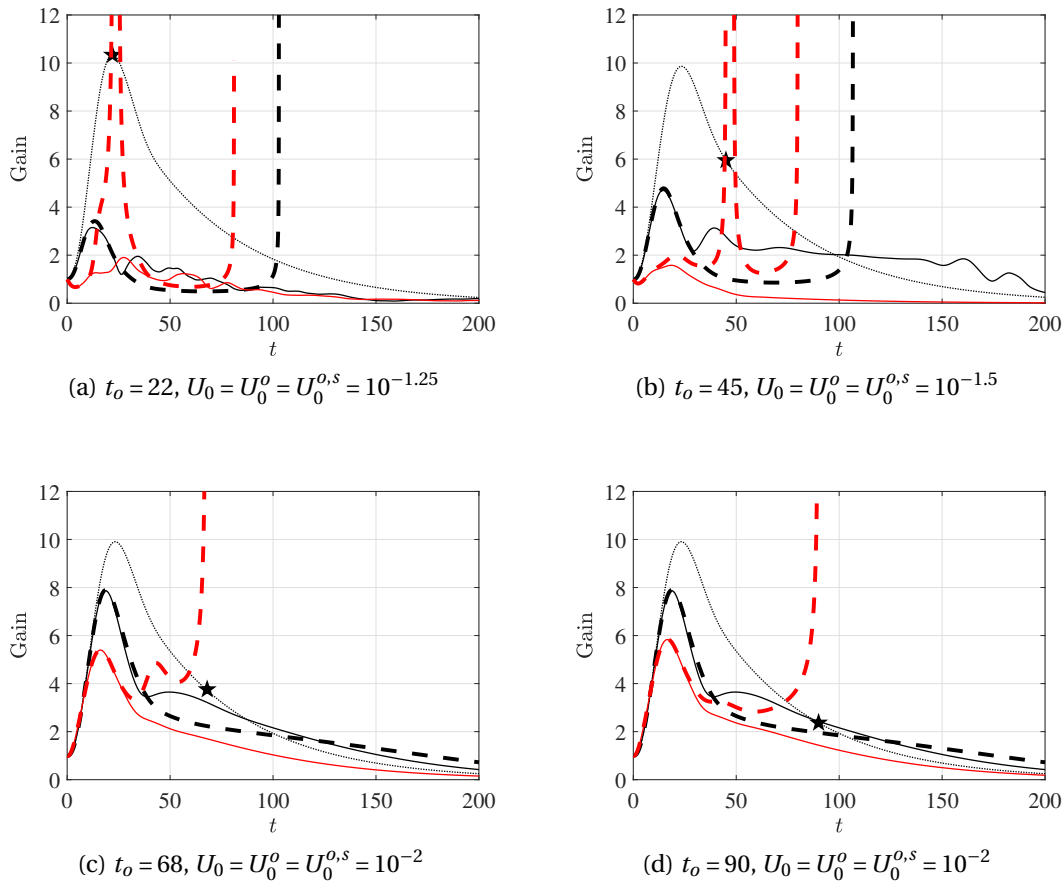


Figure 9.10: The black dotted line is the linear trajectory seeded with the linear optimal structure, with a star at the temporal horizon t_o . The continuous black line is the DNS initiated with the linear optimal and an amplitude U_0 . The dashed black line is the prediction of the weakly nonlinear amplitude equation concerning the trajectory initiated with the linear optimal. The continuous red line is the DNS initiated with the weakly nonlinear optimal and an amplitude $U_0 = U_0^o = U_0^{o,s}$ for which it was optimized, and lead to a singular explosion of the gain in figure 9.6. The dashed red line is the prediction of the weakly nonlinear amplitude equation concerning the trajectory initiated with the weakly nonlinear optimal (by construction, it should explode at the star where $t = t_o$). The DNS gain is computed on $E_{\alpha,\beta}$, after extraction of the $(\alpha,\beta)=(1,1)$ component.

to propose an accurate description for some times and/or initial amplitude U_0 , it is clear that the results of an optimization algorithm based on this model are not encouraging.

As in the previous chapter, the agreement between weakly and fully nonlinear models seems to remain good for small times, at least for the considered U_0 . Consequently, the weakly nonlinear optimal structure for $t_o = 22$, in figure 9.10a, gives the most convincing result as compared to larger t_o .

9.5 Conclusions

In this chapter, we have developed an optimization algorithm to maximize the transient gain in a weakly nonlinear regime. Specifically, the algorithm results from a Lagrangian where an amplitude equation, that describes the evolution of a linear trajectory in a weakly nonlinear regime, was included as a constraint. In its framework, the algorithm succeeds in finding a structure that yields a larger transient gain for some U_0^o than the linear one, as computed by the amplitude equation. Nevertheless, this structure was then found to be mostly irrelevant in a fully nonlinear regime of a subcritical flow. Many reasons could be advanced to explain this failure, some listed thereafter

- If the temporal horizon t_o and/or the initial amplitude U_0 are chosen too large, the predictions of the amplitude equation are found to be mostly irrelevant, for the fully nonlinear trajectory has already bifurcated at early times. Thereby, for large t_o and/or U_0 , since there the amplitude equation is an inaccurate model, the results from an optimization algorithm based on it logically also give inaccurate results. This suggests that the optimization procedure should mostly be used for small t_o , where the amplitude equation remains a good model.
- For large t_o , the weakly nonlinear initial conditions, optimized at $U_0^{o,s}$, thought of as being close to the smallest possible amplitude for the flow to nonlinearly transit, are associated with linear gains that are close to unity (see in figure 9.6 the value for the singular curve crosses the y -axis, corresponding to the limit $U_0 \rightarrow 0$). Thereby the asymptotic expansion with small parameter $\epsilon_o = 1/G(t_o)$ (the inverse of the linear gain), has no mathematical justification and the truncation error is likely to be large.
- Turbulence generates many length scales, and figure 9.3 has shown that the (α, β) Fourier component of the perturbation does not dominate the turbulence spectrum. With the current approach, however, the weakly nonlinear optimal only can optimize the y profile for a given (α, β) pair. In other terms, even is relevant in a fully nonlinear regime, the algorithm optimizes $E_{\alpha,\beta}(t)/E_{\alpha,\beta}(0)$ and not $E_p(t)/E_p(0)$, whereas it is the latter gain that matters in a turbulent regime. It is possible to compute three-dimensional weakly nonlinear optimals, that do not enforce a particular wavenumber pair for the perturbation, but this would require a computational time substantially larger.

As a perspective, the structures computed by the optimization algorithm are believed to be more relevant in supercritical flows, where the amplitude equation was found in chapter 7 and 8 to remain a good model even for large t and/or U_0 . This is simply because the fully nonlinear flow structure remained symptomatic of the linear one over which the amplitude equation was constructed.

For subcritical flows, we believe the weakly nonlinear structures to only be valid when optimized for small temporal horizons. In the spirit of Mannix et al. (2022), this could be automati-

cally coupled to a DNS routine that performs a time-marching of the flow for very large times. If it is thus found that the flow re-laminarizes, the routine repeats the optimisation procedure for a slightly larger initial condition parameter U_0^o . The procedure is stopped whenever the DNS confirms the flow to have reached turbulence.

9.6 Appendix

9.6.1 Variations with respect to the first order field.

We successively compute

$$\left\langle \frac{\delta G_w^2}{\delta \hat{\mathbf{u}}_1} \middle| \tilde{\mathbf{u}}_1 \right\rangle = \frac{B^2}{U_0^2} (\langle \tilde{\mathbf{u}}_1 | \hat{\mathbf{u}}_1 \rangle + \langle \hat{\mathbf{u}}_1 | \tilde{\mathbf{u}}_1 \rangle) = \frac{B^2}{U_0^2} \langle \tilde{\mathbf{u}}_1 | \hat{\mathbf{u}}_1 \rangle + \text{c.c.}, \quad (9.43)$$

followed by

$$\begin{aligned} & \int_0^{t_o} \left\langle \frac{\delta I_1}{\delta \hat{\mathbf{u}}_1} \middle| \tilde{\mathbf{u}}_1 \right\rangle dt \\ &= \left[\int_0^{t_o} \left\langle \partial_t \tilde{\mathbf{u}}_1 - L \tilde{\mathbf{u}}_1 \middle| \hat{\mathbf{u}}_1^\dagger \right\rangle dt + \text{c.c.} \right] - \alpha \langle \tilde{\mathbf{u}}_1(0) | \hat{\mathbf{u}}_1(0) \rangle - \alpha \langle \hat{\mathbf{u}}_1(0) | \tilde{\mathbf{u}}_1(0) \rangle \\ &= \left[\left\langle \tilde{\mathbf{u}}_1(t_o) \middle| \hat{\mathbf{u}}_1^\dagger(t_o) \right\rangle - \left\langle \tilde{\mathbf{u}}_1(0) \middle| \hat{\mathbf{u}}_1^\dagger(0) \right\rangle - \int_0^{t_o} \left\langle \tilde{\mathbf{u}}_1 \middle| \partial_t \hat{\mathbf{u}}_1^\dagger + L^\dagger \hat{\mathbf{u}}_1^\dagger \right\rangle dt + \text{c.c.} \right] \\ &\quad - \alpha \langle \tilde{\mathbf{u}}_1(0) | \hat{\mathbf{u}}_1(0) \rangle - \alpha \langle \hat{\mathbf{u}}_1(0) | \tilde{\mathbf{u}}_1(0) \rangle \\ &= \left\langle \tilde{\mathbf{u}}_1(t_o) \middle| \hat{\mathbf{u}}_1^\dagger(t_o) \right\rangle - \left\langle \tilde{\mathbf{u}}_1(0) \middle| \hat{\mathbf{u}}_1^\dagger(0) + \alpha \hat{\mathbf{u}}_1(0) \right\rangle - \int_0^{t_o} \left\langle \tilde{\mathbf{u}}_1 \middle| \partial_t \hat{\mathbf{u}}_1^\dagger + L^\dagger \hat{\mathbf{u}}_1^\dagger \right\rangle dt + \text{c.c.}, \end{aligned} \quad (9.44)$$

and by

$$\begin{aligned} \int_0^{t_o} \left\langle \frac{\delta I_2^{(2)}}{\delta \hat{\mathbf{u}}_1} \middle| \tilde{\mathbf{u}}_1 \right\rangle dt &= \int_0^{t_o} \left\langle C[\hat{\mathbf{u}}_1, \tilde{\mathbf{u}}_1] + C[\tilde{\mathbf{u}}_1, \hat{\mathbf{u}}_1] \middle| \hat{\mathbf{u}}_2^{(2),\dagger} \right\rangle dt + \text{c.c.} \\ &= \int_0^{t_o} \left\langle 2C[\tilde{\mathbf{u}}_1, \hat{\mathbf{u}}_1] \middle| \hat{\mathbf{u}}_2^{(2),\dagger} \right\rangle dt + \text{c.c.} \\ &= \int_0^{t_o} \left\langle \tilde{\mathbf{u}}_1 \middle| 2C^\dagger[\hat{\mathbf{u}}_1, \hat{\mathbf{u}}_2^{(2),\dagger}] \right\rangle dt + \text{c.c.}, \end{aligned} \quad (9.45)$$

where we have computed the adjoint advection operator, $C^\dagger[\bullet, \bullet]$, in Appendix 9.6.5. We proceed with

$$\begin{aligned} \int_0^{t_o} \left\langle \frac{\delta I_2^{(0)}}{\delta \hat{\mathbf{u}}_1} \middle| \tilde{\mathbf{u}}_1 \right\rangle dt &= \int_0^{t_o} \left\langle 2C[\hat{\mathbf{u}}_1^*, \tilde{\mathbf{u}}_1] + 2C[\tilde{\mathbf{u}}_1, \hat{\mathbf{u}}_1] \middle| \mathbf{u}_2^{(0),\dagger} \right\rangle dt \\ &= \int_0^{t_o} \left\langle 2C[\tilde{\mathbf{u}}_1, \hat{\mathbf{u}}_1^*] \middle| \mathbf{u}_2^{(0),\dagger} \right\rangle dt + \int_0^{t_o} \left\langle 2C[\tilde{\mathbf{u}}_1^*, \hat{\mathbf{u}}_1] \middle| \mathbf{u}_2^{(0),\dagger} \right\rangle dt \\ &= \int_0^{t_o} \left\langle \tilde{\mathbf{u}}_1 \middle| 2C^\dagger[\hat{\mathbf{u}}_1^*, \mathbf{u}_2^{(0),\dagger}] \right\rangle dt + \text{c.c.}, \end{aligned} \quad (9.46)$$

as well as

$$\begin{aligned}
\int_0^{t_0} \left\langle \frac{\delta I_3}{\delta \hat{\mathbf{u}}_1} \middle| \tilde{\mathbf{u}}_1 \right\rangle dt &= \int_0^{t_0} \left\langle 2C \left[\tilde{\mathbf{u}}_1^*, \hat{\mathbf{u}}_2^{(2)} \right] + 2C \left[\tilde{\mathbf{u}}_1, \mathbf{u}_2^{(0)} \right] \middle| \hat{\mathbf{u}}_3^\dagger \right\rangle dt + \text{c.c.} \\
&= \int_0^{t_0} \left\langle 2C \left[\tilde{\mathbf{u}}_1, \hat{\mathbf{u}}_2^{(2),*} \right] \middle| \hat{\mathbf{u}}_3^{\dagger,*} \right\rangle dt + \int_0^{t_0} \left\langle 2C \left[\tilde{\mathbf{u}}_1, \mathbf{u}_2^{(0)} \right] \middle| \hat{\mathbf{u}}_3^\dagger \right\rangle dt + \text{c.c.} \quad (9.47) \\
&= \int_0^{t_0} \left\langle \tilde{\mathbf{u}}_1 \middle| 2C^\dagger \left[\hat{\mathbf{u}}_2^{(2),*}, \hat{\mathbf{u}}_3^{\dagger,*} \right] + 2C^\dagger \left[\mathbf{u}_2^{(0)}, \hat{\mathbf{u}}_3^\dagger \right] \right\rangle dt + \text{c.c.}
\end{aligned}$$

and, eventually,

$$\begin{aligned}
&2 \left\langle \frac{\delta \bar{\mu}_r}{\delta \hat{\mathbf{u}}_1} \middle| \tilde{\mathbf{u}}_1 \right\rangle \\
&= \lim_{\epsilon \rightarrow 0} \frac{2}{\epsilon} \left(\Re \left[\frac{\langle \hat{\mathbf{u}}_1 + \epsilon \tilde{\mathbf{u}}_1 | \hat{\mathbf{u}}_3 \rangle}{\langle \hat{\mathbf{u}}_1 + \epsilon \tilde{\mathbf{u}}_1 | \hat{\mathbf{u}}_1 + \epsilon \tilde{\mathbf{u}}_1 \rangle} \right] - \Re \left[\frac{\langle \hat{\mathbf{u}}_1 | \hat{\mathbf{u}}_3 \rangle}{\langle \hat{\mathbf{u}}_1 | \hat{\mathbf{u}}_1 \rangle} \right] \right) \\
&= \lim_{\epsilon \rightarrow 0} \frac{2}{\epsilon} \left(\Re \left[\frac{\langle \hat{\mathbf{u}}_1 | \hat{\mathbf{u}}_3 \rangle + \epsilon \langle \tilde{\mathbf{u}}_1 | \hat{\mathbf{u}}_3 \rangle}{\langle \hat{\mathbf{u}}_1 | \hat{\mathbf{u}}_1 \rangle + \epsilon \langle \hat{\mathbf{u}}_1 | \tilde{\mathbf{u}}_1 \rangle + \epsilon \langle \tilde{\mathbf{u}}_1 | \hat{\mathbf{u}}_1 \rangle + O(\epsilon^2)} \right] - \Re \left[\frac{\langle \hat{\mathbf{u}}_1 | \hat{\mathbf{u}}_3 \rangle}{\langle \hat{\mathbf{u}}_1 | \hat{\mathbf{u}}_1 \rangle} \right] \right) \\
&= \lim_{\epsilon \rightarrow 0} \frac{2}{\epsilon} \left(\Re \left[\frac{\langle \hat{\mathbf{u}}_1 | \hat{\mathbf{u}}_3 \rangle + \epsilon \langle \tilde{\mathbf{u}}_1 | \hat{\mathbf{u}}_3 \rangle}{\langle \hat{\mathbf{u}}_1 | \hat{\mathbf{u}}_1 \rangle} \frac{1}{1 + \epsilon \langle \hat{\mathbf{u}}_1 | \tilde{\mathbf{u}}_1 \rangle / \langle \hat{\mathbf{u}}_1 | \hat{\mathbf{u}}_1 \rangle + \epsilon \langle \tilde{\mathbf{u}}_1 | \hat{\mathbf{u}}_1 \rangle / \langle \hat{\mathbf{u}}_1 | \hat{\mathbf{u}}_1 \rangle + O(\epsilon^2)} \right] - \Re \left[\frac{\langle \hat{\mathbf{u}}_1 | \hat{\mathbf{u}}_3 \rangle}{\langle \hat{\mathbf{u}}_1 | \hat{\mathbf{u}}_1 \rangle} \right] \right) \\
&= \lim_{\epsilon \rightarrow 0} \frac{2}{\epsilon} \left(\Re \left[\left(\frac{\langle \hat{\mathbf{u}}_1 | \hat{\mathbf{u}}_3 \rangle}{\langle \hat{\mathbf{u}}_1 | \hat{\mathbf{u}}_1 \rangle} + \epsilon \frac{\langle \tilde{\mathbf{u}}_1 | \hat{\mathbf{u}}_3 \rangle}{\langle \hat{\mathbf{u}}_1 | \hat{\mathbf{u}}_1 \rangle} \right) \left(1 - \epsilon \frac{\langle \hat{\mathbf{u}}_1 | \tilde{\mathbf{u}}_1 \rangle}{\langle \hat{\mathbf{u}}_1 | \hat{\mathbf{u}}_1 \rangle} - \epsilon \frac{\langle \tilde{\mathbf{u}}_1 | \hat{\mathbf{u}}_1 \rangle}{\langle \hat{\mathbf{u}}_1 | \hat{\mathbf{u}}_1 \rangle} + O(\epsilon^2) \right) \right] - \Re \left[\frac{\langle \hat{\mathbf{u}}_1 | \hat{\mathbf{u}}_3 \rangle}{\langle \hat{\mathbf{u}}_1 | \hat{\mathbf{u}}_1 \rangle} \right] \right) \\
&= 2 \Re \left[\frac{\langle \tilde{\mathbf{u}}_1 | \hat{\mathbf{u}}_3 \rangle}{\langle \hat{\mathbf{u}}_1 | \hat{\mathbf{u}}_1 \rangle} - \frac{\langle \hat{\mathbf{u}}_1 | \hat{\mathbf{u}}_3 \rangle}{\langle \hat{\mathbf{u}}_1 | \hat{\mathbf{u}}_1 \rangle} \left(\frac{\langle \hat{\mathbf{u}}_1 | \tilde{\mathbf{u}}_1 \rangle}{\langle \hat{\mathbf{u}}_1 | \hat{\mathbf{u}}_1 \rangle} + \frac{\langle \tilde{\mathbf{u}}_1 | \hat{\mathbf{u}}_1 \rangle}{\langle \hat{\mathbf{u}}_1 | \hat{\mathbf{u}}_1 \rangle} \right) \right] \\
&= \left[\frac{\langle \tilde{\mathbf{u}}_1 | \hat{\mathbf{u}}_3 \rangle}{\langle \hat{\mathbf{u}}_1 | \hat{\mathbf{u}}_1 \rangle} - \frac{\langle \hat{\mathbf{u}}_1 | \hat{\mathbf{u}}_3 \rangle}{\langle \hat{\mathbf{u}}_1 | \hat{\mathbf{u}}_1 \rangle} \left(\frac{\langle \hat{\mathbf{u}}_1 | \tilde{\mathbf{u}}_1 \rangle}{\langle \hat{\mathbf{u}}_1 | \hat{\mathbf{u}}_1 \rangle} + \frac{\langle \tilde{\mathbf{u}}_1 | \hat{\mathbf{u}}_1 \rangle}{\langle \hat{\mathbf{u}}_1 | \hat{\mathbf{u}}_1 \rangle} \right) \right] + \left[\frac{\langle \tilde{\mathbf{u}}_1^* | \hat{\mathbf{u}}_3^* \rangle}{\langle \hat{\mathbf{u}}_1 | \hat{\mathbf{u}}_1 \rangle} - \frac{\langle \hat{\mathbf{u}}_1^* | \hat{\mathbf{u}}_3^* \rangle}{\langle \hat{\mathbf{u}}_1 | \hat{\mathbf{u}}_1 \rangle} \left(\frac{\langle \hat{\mathbf{u}}_1^* | \tilde{\mathbf{u}}_1^* \rangle}{\langle \hat{\mathbf{u}}_1 | \hat{\mathbf{u}}_1 \rangle} + \frac{\langle \tilde{\mathbf{u}}_1^* | \hat{\mathbf{u}}_1^* \rangle}{\langle \hat{\mathbf{u}}_1 | \hat{\mathbf{u}}_1 \rangle} \right) \right] \\
&= \frac{\langle \tilde{\mathbf{u}}_1 | \hat{\mathbf{u}}_3 \rangle}{\langle \hat{\mathbf{u}}_1 | \hat{\mathbf{u}}_1 \rangle} - \frac{\langle \tilde{\mathbf{u}}_1 | \hat{\mathbf{u}}_1 \rangle}{\langle \hat{\mathbf{u}}_1 | \hat{\mathbf{u}}_1 \rangle} \left(\frac{\langle \hat{\mathbf{u}}_1 | \hat{\mathbf{u}}_3 \rangle}{\langle \hat{\mathbf{u}}_1 | \hat{\mathbf{u}}_1 \rangle} + \frac{\langle \hat{\mathbf{u}}_1^* | \hat{\mathbf{u}}_3^* \rangle}{\langle \hat{\mathbf{u}}_1 | \hat{\mathbf{u}}_1 \rangle} \right) + \text{c.c.} \\
&= \langle \tilde{\mathbf{u}}_1 | F(\hat{\mathbf{u}}_1, \hat{\mathbf{u}}_3) \rangle + \text{c.c.} \tag{9.48}
\end{aligned}$$

with

$$F(\hat{\mathbf{u}}_1, \hat{\mathbf{u}}_3) = \frac{\hat{\mathbf{u}}_3}{\langle \hat{\mathbf{u}}_1 | \hat{\mathbf{u}}_1 \rangle} - \frac{\hat{\mathbf{u}}_1}{\langle \hat{\mathbf{u}}_1 | \hat{\mathbf{u}}_1 \rangle} \left(\frac{\langle \hat{\mathbf{u}}_1 | \hat{\mathbf{u}}_3 \rangle}{\langle \hat{\mathbf{u}}_1 | \hat{\mathbf{u}}_1 \rangle} + \frac{\langle \hat{\mathbf{u}}_1^* | \hat{\mathbf{u}}_3^* \rangle}{\langle \hat{\mathbf{u}}_1 | \hat{\mathbf{u}}_1 \rangle} \right). \tag{9.49}$$

9.6.2 Variations with respect to the second harmonic order field.

We compute

$$\begin{aligned}
\int_0^{t_o} \left\langle \frac{\delta I_2^{(2)}}{\delta \hat{\mathbf{u}}_2^{(2)}} \middle| \tilde{\mathbf{u}}_2^{(2)} \right\rangle dt &= \left\langle \tilde{\mathbf{u}}_2^{(2)}(t_o) \middle| \hat{\mathbf{u}}_2^{(2),\dagger}(t_o) \right\rangle - \left\langle \tilde{\mathbf{u}}_2^{(2)}(0) \middle| \hat{\mathbf{u}}_2^{(2),\dagger}(0) \right\rangle \\
&\quad - \int_0^{t_o} \left\langle \tilde{\mathbf{u}}_2^{(2)} \middle| \partial_t \hat{\mathbf{u}}_2^{(2),\dagger} + L^{(2),\dagger} \hat{\mathbf{u}}_2^{(2),\dagger} \right\rangle dt + \text{c.c.} \\
&= \left\langle \tilde{\mathbf{u}}_2^{(2)}(t_o) \middle| \hat{\mathbf{u}}_2^{(2),\dagger}(t_o) \right\rangle - \int_0^{t_o} \left\langle \tilde{\mathbf{u}}_2^{(2)} \middle| \partial_t \hat{\mathbf{u}}_2^{(2),\dagger} + L^{(2),\dagger} \hat{\mathbf{u}}_2^{(2),\dagger} \right\rangle dt + \text{c.c.},
\end{aligned} \tag{9.50}$$

where we used that $\tilde{\mathbf{u}}_2^{(2)}(0) = \mathbf{0}$ in virtue of the initial condition $\hat{\mathbf{u}}_2^{(2)}(0) = \mathbf{0}$. Variation of I_3 with respect to $\hat{\mathbf{u}}_2^{(2)}$ reads

$$\begin{aligned}
\int_0^{t_o} \left\langle \frac{\delta I_3}{\delta \hat{\mathbf{u}}_2^{(2)}} \middle| \tilde{\mathbf{u}}_2^{(2)} \right\rangle dt &= \int_0^{t_o} \left\langle 2C \left[\hat{\mathbf{u}}_1^*, \tilde{\mathbf{u}}_2^{(2)} \right] \middle| \hat{\mathbf{u}}_3^\dagger \right\rangle dt + \text{c.c.} \\
&= \int_0^{t_o} \left\langle \tilde{\mathbf{u}}_2^{(2)} \middle| 2C^\dagger \left[\hat{\mathbf{u}}_1^*, \hat{\mathbf{u}}_3^\dagger \right] \right\rangle dt + \text{c.c.}
\end{aligned} \tag{9.51}$$

9.6.3 Variations with respect to the mean flow distortion field.

We compute

$$\int_0^{t_o} \left\langle \frac{\delta I_2^{(0)}}{\delta \mathbf{u}_2^{(0)}} \middle| \tilde{\mathbf{u}}_2^{(0)} \right\rangle dt = \left\langle \tilde{\mathbf{u}}_2^{(0)}(t_o) \middle| \mathbf{u}_2^{(0),\dagger}(t_o) \right\rangle - \int_0^{t_o} \left\langle \tilde{\mathbf{u}}_2^{(0)} \middle| \partial_t \mathbf{u}_2^{(0),\dagger} + L^{(0),\dagger} \mathbf{u}_2^{(0),\dagger} \right\rangle dt. \tag{9.52}$$

where it is implicit that $\tilde{\mathbf{u}}_2^{(2)}(0) = \mathbf{0}$ in virtue of the initial condition $\hat{\mathbf{u}}_2^{(2)}(0) = \mathbf{0}$. In addition

$$\begin{aligned}
\int_0^{t_o} \left\langle \frac{\delta I_3}{\delta \hat{\mathbf{u}}_2^{(0)}} \middle| \tilde{\mathbf{u}}_2^{(0)} \right\rangle dt &= \int_0^{t_o} \left\langle 2C \left[\hat{\mathbf{u}}_1, \tilde{\mathbf{u}}_2^{(0)} \right] \middle| \hat{\mathbf{u}}_3^\dagger \right\rangle dt + \int_0^{t_o} \left\langle 2C \left[\hat{\mathbf{u}}_1^*, \tilde{\mathbf{u}}_2^{(0)} \right] \middle| \hat{\mathbf{u}}_3^{\dagger,*} \right\rangle dt \\
&= \int_0^{t_o} \left\langle 2C \left[\tilde{\mathbf{u}}_2^{(0)}, \hat{\mathbf{u}}_1 \right] \middle| \hat{\mathbf{u}}_3^\dagger \right\rangle dt + \int_0^{t_o} \left\langle 2C \left[\tilde{\mathbf{u}}_2^{(0)}, \hat{\mathbf{u}}_1^* \right] \middle| \hat{\mathbf{u}}_3^{\dagger,*} \right\rangle dt \\
&= \int_0^{t_o} \left\langle \tilde{\mathbf{u}}_2^{(0)} \middle| 2C^\dagger \left[\hat{\mathbf{u}}_1, \hat{\mathbf{u}}_3^\dagger \right] + 2C^\dagger \left[\hat{\mathbf{u}}_1^*, \hat{\mathbf{u}}_3^{\dagger,*} \right] \right\rangle dt.
\end{aligned} \tag{9.53}$$

9.6.4 Variations with respect to the third order field.

We compute

$$\int_0^{t_o} \left\langle \frac{\delta I_3}{\delta \hat{\mathbf{u}}_3} \middle| \tilde{\mathbf{u}}_3 \right\rangle dt = \left\langle \tilde{\mathbf{u}}_3(t_o) \middle| \hat{\mathbf{u}}_3^\dagger(t_o) \right\rangle - \int_0^{t_o} \left\langle \tilde{\mathbf{u}}_3 \middle| \partial_t \hat{\mathbf{u}}_3^\dagger + L^\dagger \hat{\mathbf{u}}_3^\dagger \right\rangle dt + \text{c.c.}, \tag{9.54}$$

in virtue of $\tilde{\mathbf{u}}_3(0) = \mathbf{0}$ inherited from $\hat{\mathbf{u}}_3(0) = \mathbf{0}$. Furthermore,

$$2 \left\langle \frac{\delta \bar{\mu}_r}{\delta \hat{\mathbf{u}}_3} \middle| \hat{\mathbf{u}}_3 \right\rangle = \frac{\langle \tilde{\mathbf{u}}_3 | \hat{\mathbf{u}}_1 \rangle}{\langle \hat{\mathbf{u}}_1 | \hat{\mathbf{u}}_1 \rangle} + \text{c.c.} \quad (9.55)$$

9.6.5 Adjoint advection operator

In the context, the bi-linear advection operator is

$$2C[\mathbf{a}, \mathbf{b}] = (\mathbf{b} \cdot \tilde{\nabla}_{n\alpha, n\beta}) \mathbf{a} + (\mathbf{a} \cdot \tilde{\nabla}_{p\alpha, p\beta}) \mathbf{b}, \quad (9.56)$$

with $\tilde{\nabla}_{\alpha, \beta} = (i\alpha, \partial_y, i\beta)$, and where n and p are the harmonic indices of \mathbf{a} and \mathbf{b} , respectively. For instance, it is equal to 1, -1, 0, 2 for $\hat{\mathbf{u}}_1$, $\hat{\mathbf{u}}_1^*$, $\mathbf{u}_2^{(0)}$ and $\hat{\mathbf{u}}_2^{(2)}$, respectively. We define the adjoint of C as

$$\langle C[\mathbf{a}, \mathbf{b}] | \mathbf{c} \rangle \doteq \langle \mathbf{a} | C^\dagger[\mathbf{b}, \mathbf{c}] \rangle, \quad \forall \mathbf{a}, \mathbf{b}, \mathbf{c}. \quad (9.57)$$

We can compute $\langle C[\mathbf{a}, \mathbf{b}] | \mathbf{c} \rangle$ explicitly as

$$\begin{aligned} \langle 2C[\mathbf{a}, \mathbf{b}] | \mathbf{c} \rangle &= \int_{-1}^1 2C[\mathbf{a}, \mathbf{b}]^H \mathbf{c} \, dy \\ &= \int_{-1}^1 [in\alpha b_x \mathbf{a} + b_y \partial_y \mathbf{a} + in\beta b_z \mathbf{a} + (\tilde{\nabla}_{p\alpha, p\beta} \mathbf{b}) \mathbf{a}]^H \mathbf{c} \, dy \\ &= \int_{-1}^1 [-in\alpha b_x^* \mathbf{a}^H + b_y^* \partial_y \mathbf{a}^H - in\beta b_z^* \mathbf{a}^H + \mathbf{a}^H (\tilde{\nabla}_{p\alpha, p\beta} \mathbf{b})^H] \mathbf{c} \, dy. \end{aligned} \quad (9.58)$$

In particular,

$$\begin{aligned} \int_{-1}^1 (b_y^* \partial_y \mathbf{a}^H) \mathbf{c} \, dy &= \int_{-1}^1 \mathbf{a}^H b_y^* \mathbf{c} \Big|_{-1}^1 - \int_{-1}^1 \mathbf{a}^H (\mathbf{c} \partial_y b_y^* + b_y^* \partial_y \mathbf{c}) \, dy \\ &= - \int_{-1}^1 \mathbf{a}^H (\mathbf{c} \partial_y b_y^* + b_y^* \partial_y \mathbf{c}) \, dy. \end{aligned} \quad (9.59)$$

where the boundary terms vanish under the no-slip boundary condition at the rigid walls. Eventually,

$$\begin{aligned} \langle 2C[\mathbf{a}, \mathbf{b}] | \mathbf{c} \rangle &= \int_{-1}^1 \mathbf{a}^H \left[-in\alpha b_x^* - (\partial_y b_y^* + b_y^* \partial_y) - in\beta b_z^* + (\tilde{\nabla}_{p\alpha, p\beta} \mathbf{b})^H \right] \mathbf{c} \, dy \\ &= \int_{-1}^1 \mathbf{a}^H \left[-\partial_y b_y^* - (\mathbf{b}^* \cdot \tilde{\nabla}_{n\alpha, n\beta}) + (\tilde{\nabla}_{p\alpha, p\beta} \mathbf{b})^H \right] \mathbf{c} \, dy, \end{aligned} \quad (9.60)$$

which implies

$$2C[\mathbf{b}, \mathbf{c}]^\dagger = -\mathbf{c} \partial_y b_y^* - (\mathbf{b}^* \cdot \tilde{\nabla}_{n\alpha, n\beta}) \mathbf{c} + (\tilde{\nabla}_{p\alpha, p\beta} \mathbf{b})^H \mathbf{c}. \quad (9.61)$$

10 Summary and perspectives

The methods proposed in the three parts of this thesis, each being concerned with an excitation of a different nature, can be seen as particular cases of the same backbone principle. We state it as follows

- The choice of the nature of the external excitation to the system suggests a choice of an inner product whose induced norm measures the input-output amplification.

In **part I**, the applied excitation was a monochromatic sustained forcing, thereby the inner product naturally was chosen as the spatiotemporal inner product, consisting of the $L^2(\Omega)$ inner product over the spatial domain Ω , then taking the temporal average. Since the excitation was monochromatic, this was equivalent to considering solely the $L^2(\Omega)$ inner product of the Fourier component at the forcing frequency.

In **part II**, the applied excitation was a stochastic sustained forcing, thereby the inner product, whose induced norm was a relevant measure of the system state, was also selected as the spatiotemporal inner product. Generally, it also included an ensemble average over the different realizations of the stochastic forcing process.

In **part III**, the applied excitation took the form of an initial perturbation, leading to a transient response that does not persist in time. Thereby we were interested in an *instantaneous* measure of the system, and the inner product was selected as being simply the $L^2(\Omega)$ inner product over the spatial domain, without temporal integration.

- If the excited system is non-normal, it is reasonable to expect the largest attainable amplification (or "gain"), under the norm induced by the properly selected inner product, to be large. This generically results from interactions between a large number of eigenmodes of the linearized system and does not require the presence of a neutral or close-to-neutral one.

Each problem can thus be explicitly rewritten as being the excitation greatly amplified by the application of a specific operator. The latter operator typically is the resolvent for statistically steady systems subject to a sustained forcing, whereas it is the propagator for

arbitrarily time-varying systems subject to an initial perturbation. This naturally implies that the application of the inverse of this specific operator, mapping the response on its forcing, induces great mitigation under the selected induced norm.

For instance, in **part I** we have rewritten the input-output problem as

$$R(i\omega)^{-1} \underbrace{\hat{\mathbf{u}}_o}_{\|\bullet\|=1} = \underbrace{\epsilon_o \hat{\mathbf{f}}_o}_{\|\bullet\|=\epsilon_o}. \quad (10.1)$$

Therefore, the inverse resolvent generates a strong reduction under the norm induced by the $L^2(\Omega)$ inner product, since $\hat{\mathbf{u}}_o$ with $\|\hat{\mathbf{u}}_o\| = 1$, is mapped on $\epsilon_o \hat{\mathbf{f}}_o$ with $\|\epsilon_o \hat{\mathbf{f}}_o\| = \epsilon_o \ll 1$.

In **part II**, chapter 3, we have rewritten the input-output problem as

$$R(i\omega)^{-1} \underbrace{\hat{\mathbf{l}}(\omega; \theta)}_{\sqrt{\{\|\bullet\|^2\}}=1} = \underbrace{\epsilon_o \mathbf{f}_o \hat{\xi}(\omega; \theta)}_{\sqrt{\{\|\bullet\|^2\}}=\epsilon_o}. \quad (10.2)$$

In other terms, the inverse resolvent also generates a strong reduction under the norm induced by the spatio-ensemblo-frequential inner product, since $\hat{\mathbf{l}}(\omega; \theta)$ with $\sqrt{\{\|\hat{\mathbf{l}}(\omega; \theta)\|^2\}} = 1$, is mapped on $\epsilon_o \mathbf{f}_o \hat{\xi}(\omega; \theta)$ with $\sqrt{\{\|\epsilon_o \mathbf{f}_o \hat{\xi}(\omega; \theta)\|^2\}} = \epsilon_o \ll 1$.

In **part III** we have rewritten the input-output problem as

$$\Psi(0, t_o) \underbrace{\hat{\mathbf{l}}(t_o)}_{\|\bullet\|=1} = \underbrace{\epsilon_o \hat{\mathbf{u}}_o}_{\|\bullet\|=\epsilon_o}, \quad (10.3)$$

which stipulates that the inverse propagator brings about a strong reduction under the norm induced by the $L^2(\Omega)$ inner product, since $\hat{\mathbf{l}}(t_o)$ with $\|\hat{\mathbf{l}}(t_o)\| = 1$, is mapped on $\epsilon_o \hat{\mathbf{u}}_o$ with $\|\epsilon_o \hat{\mathbf{u}}_o\| = \epsilon_o \ll 1$.

- From here, the key idea, largely exploited in this thesis, is based on the following mathematical fact: if the application of an operator on a structure maps it to another with a much smaller size, "size" measured under some norm, then an operator perturbation that is small under this same norm is sufficient to make the operator singular.

In **part I**, we thus built the singular operator by manipulating (10.1) as

$$\Phi(i\omega)(\bullet) = R(i\omega)^{-1} \bullet - \underbrace{\epsilon_o \hat{\mathbf{f}}_o \langle \hat{\mathbf{u}}_o | \bullet \rangle}_{\|\bullet\|=\epsilon_o}, \quad \text{with } \Phi(i\omega)(A\hat{\mathbf{u}}_o) = \mathbf{0}, \quad (10.4)$$

for any scalar A that does not depend on space.

In **part II** the singular operator, suggested by (10.2), took the form of

$$\Phi(\omega; \theta)(\bullet) = R(i\omega)^{-1} \bullet - \underbrace{\epsilon_o \mathbf{f}_o \hat{\xi}(\omega; \theta) \{ \langle \hat{\mathbf{l}}(\omega; \theta) | \bullet \rangle \}}_{\sqrt{\{\|\bullet\|^2\}}=\epsilon_o}, \quad \text{with } \Phi(\omega; \theta)(A\hat{\mathbf{l}}(\omega; \theta)) = \mathbf{0}, \quad (10.5)$$

for any scalar A that depends neither on space, nor on the frequency, nor on the stochastic argument.

In **part III** the expression of the singular operator at $t = t_o$ comes from (10.3) as

$$\Phi(0, t_o)(\bullet) = \Psi(0, t_o) \bullet - \underbrace{\epsilon_o \hat{\mathbf{u}}_o \langle \hat{\mathbf{l}}(t_o) | \bullet \rangle}_{\|\bullet\|=\epsilon_o}, \quad \text{with} \quad \Phi(0, t_o)(A\hat{\mathbf{l}}(t_o)) = \mathbf{0}, \quad (10.6)$$

for any scalar A that does not depend on space.

- The construction of a singular operator, for which the response to the excitation constitutes the non-trivial kernel, makes it possible to bridge the gap with traditional weakly nonlinear expansion methods even in the absence of a neutral mode. It is indeed key that the operator characterizing the input-output dynamics is singular to rigorously derive an amplitude equation, for the latter precisely ensues from a non-resonance condition.

Due to the generic lack of a bifurcation point, we do not immediately have the small expansion parameter as the distance to the critical parameter. Nevertheless, due to the strong non-normality, we do have a large parameter as the gain under some induced norm. Thereby, we simply define the small parameter as the inverse of the large parameter. As shown in (10.4), (10.5) and (10.6), the former coincides with the distance to criticality, in the sense that it also is the size of an operator perturbation sufficient to make singular the operator characterising the input-output dynamics.

In each of the three parts, a multiple-scale asymptotic expansion was thus performed in terms of some power of the gain inverse. The expansion was systematically rewritten such as to make appear, at each order, the inverse of the operator characterising the input-output dynamics. The latter was then perturbed according to (10.4), (10.5) and (10.6) in **part I**, **part II** and **part III**, respectively, which could be rigorously encompassed in the expansion. Consequently, the leading order was constituted of the linearly optimal response, multiplied by some undetermined scalar that was constant with respect to the variable(s) over which the selected inner product made the integral(s). (Note that the latter fact led in chapter 4 to consider, for the perturbation operator, an inner product different from that yielding a large gain). The problem was then closed at higher orders by satisfying the Fredholm alternative. In this context, the latter stipulated that the resonant forcing terms must be orthogonal, under the selected inner product, to the adjoint of the leading-order (optimal) response. This led to an equation for the amplitude of the optimal response, which describes the weakly nonlinear evolution of the gain under the selected induced norm, while the amplitude of the excitation is increased.

The satisfaction of the Fredholm alternative had an intuitive physical interpretation in this context: to build a solution in the form of an asymptotic expansion, each of the higher-order responses must be orthogonal to the optimal (leading-order) one, under the inner product measuring a large amplification. If this is not the case, and precisely

because the expansion is made in terms of the inverse of the optimal amplification measured by such inner product, the higher-orders go up the orders of the expansion so as to find themselves at an order that is lower than that postulated. This breaks the validity of the ansatz, and must be avoided for the latter to remain relevant.

In table 10.1 we propose an exhaustive, chapter-by-chapter summary of which operator was perturbed up to singularity, according to which operator perturbation, and we also report the resulting kernel.

Table 10.1: Summary table of the operator perturbations carried out in this thesis. Each color denotes a different type of external excitation: harmonic forcing (green), stochastic forcing (lavender), and initial condition (cream).

Chap.	Perturbed operator	Gain, $\epsilon_o^{-1} =$	Perturbation operatorof norm	Kernel
2	$(i\omega I - L)^{-1}$	$\max_f \frac{\ \hat{\mathbf{u}}\ }{\ \hat{\mathbf{f}}\ }$	$\epsilon_o \hat{\mathbf{f}}_o \langle \hat{\mathbf{u}}_o \bullet \rangle$	ϵ_o	$A(\tau) \hat{\mathbf{u}}_o$
3	$(i\omega I - L)^{-1}$	$\sqrt{\max_f \frac{\{\ \hat{\mathbf{u}}(\omega; \theta)\ ^2\}}{\{\ \hat{\mathbf{f}}\hat{\xi}(\omega; \theta)\ ^2\}}}$	$\epsilon_o \hat{\xi}(\omega; \theta) \mathbf{f}_o \{ \langle \hat{\mathbf{l}}(\omega; \theta) \bullet \rangle \}$	ϵ_o	$A(\tau) \hat{\mathbf{l}}(\omega; \theta)$
4	$(i\omega I - L)^{-1}$	$\sqrt{\max_f \frac{\ \hat{\mathbf{u}}(\omega; \theta)\ ^2}{\ \hat{\mathbf{f}}\hat{\xi}(\omega; \theta)\ ^2}}$	$\epsilon_o \frac{\mathbf{f}_o}{\ \hat{\mathbf{q}}(\omega)\ ^2} \langle \hat{\mathbf{q}}(\omega) \bullet \rangle$	$\frac{\epsilon_o}{\ \hat{\mathbf{q}}(\omega)\ }$	$A(\tau; \omega, \theta) \hat{\mathbf{q}}(\omega)$
5	$(\partial_t - L_n)$	\emptyset	\emptyset	\emptyset	$A(\tau) \mathbf{q}$
6	$(\partial_t - L_n)$	$\sqrt{\frac{\ \mathbf{u}^\perp(t; \theta)\ ^2}{\ \mathbf{f}_o^\perp \xi(t; \theta)\ ^2}}$	$\epsilon_o \frac{\xi(t) \mathbf{f}_o^\perp}{\ \mathbf{f}_o^\perp\ } \langle \mathbf{l}^\perp(t) \bullet \rangle$	ϵ_o	$A(\tau) \mathbf{q} \& B(\tau) \mathbf{l}^\perp(t)$
7	$\Psi(0, t) = \exp(-Lt)$	$\max_{\mathbf{u}(0)} \frac{\ \mathbf{u}(t_o)\ }{\ \mathbf{u}(0)\ }$	$\epsilon_o \frac{H(t) \mathbf{u}_o}{\ \mathbf{l}(t)\ ^2} \langle \mathbf{l}(t) \bullet \rangle$	$\frac{\epsilon_o}{\ \mathbf{l}(t)\ }$	$A(\tau) \mathbf{l}(t)$
8	$\Psi(0, t) \neq \exp(-Lt)$	$\max_{\hat{\mathbf{u}}(0)} \frac{\ \hat{\mathbf{u}}(t_o)\ }{\ \hat{\mathbf{u}}(0)\ }$	$\epsilon_o \frac{H(t) \hat{\mathbf{u}}_o}{\ \hat{\mathbf{l}}(t)\ ^2} \langle \hat{\mathbf{l}}(t) \bullet \rangle$	$\frac{\epsilon_o}{\ \hat{\mathbf{l}}(t)\ }$	$A(\tau) \hat{\mathbf{l}}(t)$

In some sense, this thesis operated a change of paradigm from assuming a large spectral gap, making it possible to reduce the weakly nonlinear dynamics of the system to a few neutral

or close to neutral eigenmodes, to assuming a large singular value gap, making it possible to reduce the weakly nonlinear dynamics to a few largely amplified responses.

As perspectives, we sketch in sections 10.1 and 10.2 some other relevant configurations where the general principle outlined above could be applied, and we highlight in sections 10.3 and 10.4 some fundamental interrogations that the method raises, and which shall need to be clarified in the future.

10.1 Application to a harmonic resolvent analysis

A natural extension of the method outlined in chapter 2 would consist of deriving an amplitude equation for the optimal response associated with the harmonic resolvent operator (Padovan & Rowley, 2022; Padovan et al., 2020). The latter operator results from the linearization of the system around a time-periodic base flow, such that the resulting L can be expanded as a Fourier series

$$L = L(t) = \sum_{k \in \tilde{\Omega}} \hat{L}_k e^{ikt}, \quad \tilde{\Omega} = \{\dots, -2, -1, 0, 1, 2, \dots\}. \quad (10.7)$$

The harmonic resolvent applies on the whole set of Fourier components $\{\hat{\mathbf{f}}_\alpha\}_{\alpha \in \Omega}$ of the perturbative forcing $\mathbf{f}(t)$, the latter being such that

$$\mathbf{f}(t) = \sum_{\alpha \in \Omega} \hat{\mathbf{f}}_\alpha e^{i\alpha t}, \quad \Omega = \left\{ \dots, -\frac{2}{n}, -\frac{1}{n}, 0, \frac{1}{n}, \frac{2}{n}, \dots \right\}, \quad (10.8)$$

with n a natural number, and whose choice sets the fundamental forcing frequency $1/n$. Application of the harmonic resolvent gives as an output the whole set of Fourier components $\{\hat{\mathbf{u}}_\alpha\}_{\alpha \in \Omega}$ of the perturbative forcing $\mathbf{u}(t)$, the latter being such that

$$\mathbf{u}(t) = \sum_{\alpha \in \Omega} \hat{\mathbf{u}}_\alpha e^{i\alpha t}. \quad (10.9)$$

Note that, in this sense, it necessarily is of a higher dimension than the original system. It is generically not block diagonal, as it encompasses the convolution of the base flow frequencies with those of the perturbation.

Upon perturbing the inverse harmonic resolvent operator, the weakly nonlinear equation would not be for the amplitude of the optimal response structure oscillating at a single frequency, but more generally for the amplitude of the left singular mode of the harmonic resolvent operator. As said, the latter is a block vector collecting all structures $\{\hat{\mathbf{u}}_\alpha\}_{\alpha \in \Omega}$ constituting the optimal response. Thereby, the amplitude equation could predict the weakly nonlinear evolution of the harmonic resolvent gain as the amplitude of the linearly optimal $\mathbf{f}(t)$ is increased.

10.2 Application to a wavelet-based resolvent analysis

Although motivated by the pragmatic reason that it lightens the formalism in chapter 6, performing the computations in the temporal domain has another substantial advantage: they can be rather straightforwardly adapted to a configuration where the base flow evolves with time. This is particularly relevant in a case where the base flow is not statistically steady, thus where the Fourier transform is not appropriate, and the resolvent operator does not appear as the relevant one in the calculations. In other terms, the version of the method that consists of perturbing $(\partial_t - L)$ using a spatiotemporal inner product, is more general than that perturbing $(i\omega I - L)$ using a spatiofrequency inner product, precisely because moving from the temporal to the Fourier domain implies a statistically steady regime.

A forced system linearized around a time-dependent base flow writes

$$\partial_t \mathbf{u}(t) - L(t) \mathbf{u}(t) = \mathbf{f}(t) \quad (10.10)$$

where $L(t)$ highlights the temporal dependency of the linearized operator (inherited from that of the base flow). In the context where the statistics of the latter depend on time, the recent works proposed by Ballouz et al. (2022, 2023) suggest decomposing the forcing and its responses on a wavelet orthonormal basis. The wavelet transform is two-dimensional and can capture the temporal evolution of the frequency content of a signal. That is because wavelets are typically localized wavepackets, thus containing both frequency information conveyed by the carrier wave, as well as temporal information since it is localized at a specific time. This is in stark contrast with the Fourier transform, which is one-dimensional and only extracts a frequency content of the signal, precisely because it aims at capturing the persistence of a given frequency *all along* the signal. In this sense, wavelet transforms are well indicated for capturing intermittency (bursting events) in a signal, typical to some turbulent flows (Lucas & Kerswell, 2014), whereas Fourier transform is inherently unable to do so.

Let us define a wavelet family

$$\left\{ \psi_{jn}(t) = \frac{1}{\sqrt{2^j}} \psi \left(\frac{t - 2^j n}{2^j} \right) \right\}_{(j,n) \in \mathbb{Z}^2}, \quad (10.11)$$

constituting an orthonormal basis of $L^2(\mathbb{R})$. Each member $\psi_{jn}(t)$ stems from a mother wavelet $\psi(t)$ (typically resembling a wavepacket) that is shifted according to the parameter n and dilated according to the parameter j . The forcing $\mathbf{f}(t)$, even if not statistically steady, can be

decomposed in this wavelet family according to

$$\begin{aligned}
 \mathbf{f}(\mathbf{x}, t) &= \sum_{j=-M}^M \sum_{n=-N}^N \mathbf{f}_{jn}(\mathbf{x}) \psi_{jn}(t), \quad \text{with} \quad \mathbf{f}_{jn}(\mathbf{x}) = \int_0^\infty \mathbf{f}(\mathbf{x}, t) \psi_{jn}(t) dt = [\mathbf{f}(\mathbf{x}, t) \psi_{jn}(t)], \\
 &= \underbrace{[\psi_{-M,-N} I, \psi_{-M+1,-N} I, \dots, \psi_{M,N} I]}_{=\Psi(t)}(t) \underbrace{\begin{bmatrix} \mathbf{f}_{-M,-N} \\ \mathbf{f}_{-M+1,-N} \\ \vdots \\ \mathbf{f}_{M,N} \end{bmatrix}}_{=\tilde{\mathbf{f}}(\mathbf{x})}(\mathbf{x}) \\
 &= \Psi(t) \tilde{\mathbf{f}}(\mathbf{x}),
 \end{aligned} \tag{10.12}$$

where in this context $[\bullet]$ denotes the temporal integration. The response can be decomposed accordingly

$$\begin{aligned}
 \mathbf{u}(\mathbf{x}, t) &= \sum_{j=-M}^M \sum_{n=-N}^N \mathbf{u}_{jn}(\mathbf{x}) \psi_{jn}(t), \quad \text{with} \quad \mathbf{u}_{jn}(\mathbf{x}) = [\mathbf{u}(\mathbf{x}, t) \psi_{jn}(t)], \\
 &= \Psi(t) \tilde{\mathbf{u}}(\mathbf{x}),
 \end{aligned} \tag{10.13}$$

Under these decompositions, system (10.10) becomes

$$\partial_t \Psi(t) \tilde{\mathbf{u}} - L(t) \Psi(t) \tilde{\mathbf{u}} = \Psi(t) \tilde{\mathbf{f}}. \tag{10.14}$$

Equation (10.14) is multiplied from the left by $\Psi(t)^H$ and integrated over time, which, owing to the orthonormality property of the wavelet basis gives

$$[\Psi(t)^H \Psi(t)] = \begin{bmatrix} I & & & \\ & I & & \\ & & \ddots & \\ & & & I \end{bmatrix}, \tag{10.15}$$

eventually leading to

$$\begin{aligned}
 [\Psi(t)^H \partial_t \Psi(t)] \tilde{\mathbf{u}} - [\Psi(t)^H L(t) \Psi(t)] \tilde{\mathbf{u}} &= \tilde{\mathbf{f}}, \quad \text{or, equivalently} \\
 \tilde{\mathbf{u}} &= \underbrace{([\Psi(t)^H \partial_t \Psi(t)] - [\Psi(t)^H L(t) \Psi(t)])^{-1}}_{\tilde{\mathcal{H}}} \tilde{\mathbf{f}} \\
 \tilde{\mathbf{u}} &= \tilde{\mathcal{H}} \tilde{\mathbf{f}}.
 \end{aligned} \tag{10.16}$$

where we recognize equation (8) in Ballouz et al. (2022).

After discretisation, system (10.16) typically remains of very large dimension, for $\tilde{\mathbf{u}}$ and $\tilde{\mathbf{f}}$ are not response and forcing structures associated to a single wavelet pair (j, n) , respectively, but

a collection of them all according to the definition (10.12). The number of included wavelets is set by the temporal discretization. Even if the the forcing is chosen such as to only contain a single wavelet pair (j, n) , the response generically decomposes in all the other pairs. That is because the operator $L(t)$ is time-dependent and thus frequencies have no reason to uncouple.

Let us simplify the problem and force the system with the single wavelet pair, say $(j, n) = (a, b)$, such that (10.10) becomes

$$\partial_t \mathbf{u}(t) - L(t) \mathbf{u}(t) = \mathbf{f}_{ab} \psi_{ab}(t) = \mathbf{f}_{ab} \frac{1}{\sqrt{2^a}} \psi \left(\frac{t - 2^a b}{2^a} \right) \quad (10.17)$$

This amounts to considering the specific case $\tilde{\mathbf{f}} = P^T \mathbf{f}_{ab}$ in (10.16) where P is the relevant projector mapping all the wavelet component on solely \mathbf{f}_{ab} (and P^T has the reverse action, augmenting the dimension of \mathbf{f}_{ab} to that of $\tilde{\mathbf{f}}$ with the inclusion of null vectors). We are interested in optimising the structure \mathbf{f}_{ab} such as to maximise the response-to-forcing spatiotemporal induced norm

$$\begin{aligned} G_w^2 &= \max_{\mathbf{f}_{ab}} \frac{\overline{\|\mathbf{u}(t)\|^2}}{\overline{\|\mathbf{f}_{ab} \psi_{ab}(t)\|^2}} = \max_{\mathbf{f}_{ab}} \frac{\overline{\|\Psi(t) \tilde{\mathbf{u}}\|^2}}{\overline{\|\mathbf{f}_{ab}\|^2}} = \max_{\mathbf{f}_{ab}} \frac{\|\tilde{\mathbf{u}}\|^2}{\|\mathbf{f}_{ab}\|^2} = \max_{\mathbf{f}_{ab}} \frac{\|\tilde{\mathcal{H}} P^T \mathbf{f}_{ab}\|^2}{\|\mathbf{f}_{ab}\|^2} \\ &= \frac{1}{\epsilon_o^2}, \end{aligned} \quad (10.18)$$

where once again the orthonormality of the wavelet family was invoked. It is clear that the optimal wavelet structure \mathbf{f}_{ab} is the leading singular vector of $\tilde{\mathcal{H}} P^T$, and that the associated leading singular value is the largest wavelet gain under the spatiotemporal norm, as defined in (10.18)

We defined in (10.18) the parameter ϵ_o as the inverse of the wavelet gain. By assuming once again $\epsilon_o \ll 1$, the developments of chapter 6 can be adapted to derive an equation for the slowly varying amplitude of the normalized wavelet optimal response, denoted $\mathbf{l}(t)$, solving

$$\partial_t \mathbf{l}(t) - L(t) \mathbf{l}(t) = \epsilon_o \mathbf{f}_{ab} \psi_{ab}(t), \quad (10.19)$$

and being such that $\overline{\|\mathbf{l}(t)\|^2}$. Equation (10.19) suggests perturbing $(\partial_t - L(t))$ according to

$$\Gamma(t) = \partial_t - L(t) - \epsilon_o P(t), \quad \text{with} \quad P(t) = \psi_{ab}(t) \mathbf{f}_{ab} \overline{\langle \mathbf{l}(t) | \bullet \rangle} \quad (10.20)$$

and $P(t)$ is an operator with unitary spatiotemporal norm. Proceeding with the weakly nonlinear expansion and imposing spatiotemporal orthogonality of higher-order nonlinear forcing terms with the adjoint of the optimal wavelet response, is expected to lead to an equation for the slow-time variation of the amplitude of $\mathbf{l}(t)$.

In a statistically steady regime, forcing with a single wavelet that is infinitely peaked in frequency is equivalent to applying a harmonic forcing. Thereby, it should be checked that the amplitude equation that would be obtained with the procedure sketched above gives

equivalent results as that derived in chapter 2.

10.3 Some methodological clarifications

In some situations, even if not externally excited, responses along a sub-optimal structure for a given temporal basis function, and/or that project along other members of the temporal basis, can be excited *via* nonlinear interactions of the leading-order response. For instance, in the case of the harmonic forcing treated in **part I**, the selected temporal basis was constituted of time harmonic functions. There, if the leading order response was structurally optimal for the frequency ω_o , nonlinearities excited multiples of this frequency and the higher-order forcing terms projected into other members of the Fourier basis, each being associated with its own, potentially large, harmonic gain. Similarly, in the stochastic forcing **part II**, the higher-order responses had no reason to be purely along the same stochastic process as the leading-order one but generically decomposed into many other, uncorrelated, stochastic processes. Each of these processes is associated with its own stochastic gain that is potentially very large.

This fact may be problematic in a situation where these sub-optimal or "orthogonal" (in the sense that projects into other members of the orthogonal basis) gains are comparable to that of the optimal response. Indeed, in the latter case, the asymptotic hierarchy is threatened not only by the optimal response but also by the nonlinearly, endogenously excited sub-optimal or "orthogonal" ones.

This could presumably be prevented by extending the Fredholm alternative such as to also enforce orthogonality with these sub-optimal and "orthogonal" responses. For this to be formally possible, the latter responses have to be *a priori* included in the kernel of their respective operator (even though they are not externally excited). For the moment, we do not know to what extent such an extension of the Fredholm alternative, to also prevent the nonlinear excitation of largely amplified responses that are not the optimal one, improves the accuracy of the weakly nonlinear model. Indeed, if it makes sense *a priori* to derive an equation for the optimal response, since it is by construction the only one that is excited by the forcing, it is less clear to us if the other responses that it nonlinearly excites should also be included from the beginning in the analysis.

We give concrete examples in the two following subsections.

10.3.1 Coupling with sub-optimal responses

In the thesis, the question of whether or not sub-optimal responses should be included in the kernel was systematically circumvented. To do so, we assumed that the first sub-optimal gain was one order smaller in terms of the relevant power of the small parameter (the one used in the expansion), than the optimal one. For instance, in chapter 2, the optimal gain was equal to $1/\epsilon_o$ and the expansion was proposed in terms of an integer power of $\sqrt{\epsilon_o}$. Thereby the first

sub-optimal was assumed to scale like $O(1/\sqrt{\epsilon_o})$. This assumption justifies the non-inclusion of the first sub-optimal mode. Indeed, the projection of the resonant forcing appearing for the first time at $O(\sqrt{\epsilon_o}^3)$ on the sub-optimal structure yields a response potentially at $O(\epsilon_o)$. In contrast, projection on its optimal structure yields a response potentially at $O(\sqrt{\epsilon_o})$, which is the leading order. Thereby, it is primarily the latter scenario that should be avoided, for it is the one that is the most threatening to the asymptotic hierarchy.

Nevertheless, let us consider a scenario where the first sub-optimal scales like the optimal one, and yet it is only the optimal structure that is externally forced. The inclusion of the first sub-optimal response mode in the kernel, by summing two operator perturbations (the second not affecting the first since the responses are orthogonal) would lead to a system of two coupled amplitude equations that we can anticipate to be of the form

$$\begin{aligned}\frac{dA}{dT} &= a_1 A + a_2 A|A|^2 + a_3 A|B|^2 + a_4 \phi, \\ \frac{dB}{dT} &= b_1 B + b_2 B|B|^2 + b_3 B|A|^2,\end{aligned}\tag{10.21}$$

with A the amplitude of the optimal response and B that of the sub-optimal one. The equation for B is excited only through its nonlinear coupling with A , the latter being also externally excited. Whether or not the coupling with B ameliorates the predictions for A , as compared to a case where only an equation for A is derived (which also makes sense since it is only A that is externally forced), is a question that remains to be clarified.

10.3.2 Coupling with harmonic optimal responses

Along the same line of thinking, we recall that in chapter 2, in studying the response to a harmonic forcing of the BFS flow at $\text{Re} = 500$, we have considered in particular the forcing frequency $\omega_o/(2\pi) = 0.04$. For the latter frequency, the linear harmonic gain of the second harmonic (at $2\omega_o$) is larger than that of the fundamental, although of the same order of magnitude. Therefore, it would make mathematical sense to perturb $(i2\omega_o I - L)$ to singularity in addition to doing so for the inverse resolvent of the fundamental. One can then proceed with the nonlinear expansion, where the inverse of the optimal gain of the second harmonic frequency is scaled in terms of that of the fundamental, and both operator perturbations can be encompassed in the same expansion. Doing so, the leading-order response is along both the optimal response at ω_o and the optimal response at $2\omega_o$. The second order is already resonant, as the nonlinear interaction of the optimal response at ω_o with itself generates a forcing oscillating at $2\omega_o$ (whose operator was made singular as well). Furthermore, the interaction of the optimal response at $2\omega_o$, with the complex conjugate of the optimal response at ω_o , produces a forcing at ω_o . Imposing the Fredholm alternative there and pursuing the calculations up to the third order would lead to a system of coupled amplitude equations of

the form

$$\begin{aligned}\frac{dA}{dT} &= a_1 B A^* + a_2 A + a_3 A |A|^2 + a_4 A |B|^2 + a_4 \phi \\ \frac{dB}{dT} &= b_1 A^2 + b_2 B + b_3 B |B|^2 + b_4 B |A|^2,\end{aligned}\tag{10.22}$$

with A the amplitude of the optimal response at the fundamental frequency ω_o , and B the amplitude of the optimal response at the second harmonic frequency $2\omega_o$. At the cost of increasing the dimensionality of the system, having included an equation for B guarantees that the large gain at the second harmonic frequency does not break the asymptotic hierarchy, as the latter is nonlinearly excited by the interaction of the fundamental with itself.

And yet, in the (convincing) results shown in figure 2.5b, only an independent equation for A was derived, as B was not included in the expansion. The agreement with the DNS remained very good. This was explained by the naturally poor spatial projection of the second harmonic nonlinearly generated forcing on its optimal structure at $2\omega_o$. To what extent is that generic, and to what extent does the coupling with B improve the agreement of A with DNS results, is a question that was not addressed in this thesis despite its fundamental importance.

The same question would certainly arise in considering the response to stochastic forcing or wavelet forcing, sketched in section 10.2. In the latter case, the Fredholm alternative would solely prevent the projection of the higher-order fields on the optimal response associated with the member $\psi_{ab}(t)$ of the wavelet basis. Yet, these higher-order responses generically energize other wavelet members whose respective gains, as defined in (10.18), might also be large and invalidate the asymptotic expansion *ansatz*.

10.4 Mathematical clarification

This project perspective aims at linking the method proposed in this thesis, based on multiple scale expansions, with the center manifold theory, presumably more mathematically rigorous. If the equivalence between both methods has been ruled in Fujimura (1991) in the reduction of Navier-Stokes equations to modal amplitude equations, this equivalence remains to be shown for the non-modal amplitude equations derived in this thesis.

The simplest case would be to try to re-derive the simple Stuart-Landau-like amplitude equation for the non-modal response to a harmonic forcing in (2.12), by using the center manifold theory. The linearized operator being strictly (and significantly, without outstanding eigenvalue) stable, the operator perturbation would also need to be included somewhere in the calculations, for the center manifold, by definition, must be tangent to the center (neutral) subspace at the location of the fixed point in the phase space. In doing so, one could extend the works proposed in Breunung and Haller (2018), Li and Haller (2022), Li et al. (2022), and Ponsioen et al. (2020) to non-normal harmonic responses that are not directly linked to the presence of neutral or weakly damped modes.

Bibliography

- Abreu, L., Cavalieri, A., Schlatter, P., Vinuesa, R., & Henningson, D. (2020). Spectral proper orthogonal decomposition and resolvent analysis of near-wall coherent structures in turbulent pipe flows. *Journal of Fluid Mechanics*, 900, A11.
- Åkervik, E., Ehrenstein, U., Gallaire, F., & Henningson, D. (2008). Global two-dimensional stability measures of the flat plate boundary-layer flow. *Eur. J. Mech. B/Fluids*, 27(5), 501–513.
- Åkervik, E., Høpfner, J., Ehrenstein, U., & Henningson, D. (2007). Optimal growth, model reduction and control in a separated boundary-layer flow using global eigenmodes. *Journal of Fluid Mechanics*, 579, 305–314.
- Alizard, F., Cherubini, S., & Robinet, J.-C. (2009). Sensitivity and optimal forcing response in separated boundary layer flows. *Phys. Fluids*, 21, 064108.
- Amaral, F., Cavalieri, A., Martini, E., Jordan, P., & Towne, A. (2021). Resolvent-based estimation of turbulent channel flow using wall measurements. *Journal of Fluid Mechanics*, 927, A17.
- Antkowiak, A. (2005). *Dynamique aux temps courts d'un tourbillon isolé* [Doctoral dissertation, Université Paul Sabatier, Toulouse, France].
- Antkowiak, A., & Brancher, P. (2004). Transient energy growth for the Lamb–Oseen vortex. *Physics of Fluids*, 16(1), L1–L4.
- Antkowiak, A., & Brancher, P. (2007). Transition sous-critique tripolaire dans les tourbillons [Colloque avec actes et comité de lecture. Internationale.]. In A. F. de Mécanique (Ed.), *CFM 2007 - 18ème Congrès Français de Mécanique*. AFM, Maison de la Mécanique, 39/41 rue Louis Blanc - 92400 Courbevoie.
- Arratia, C., Caulfield, C.-c., & Chomaz, J.-M. (2013). Transient perturbation growth in time-dependent mixing layers. *Journal of Fluid Mechanics*, 717, 90–133.

- Asllani, M., Lambiotte, R., & Carletti, T. (2018). Structure and dynamical behavior of non-normal networks. *Science Advances*, 4(12), eaau9403.
- Baggett, J., & Trefethen, L. (1997). Low-dimensional models of subcritical transition to turbulence. *Phys. Fluids*, 9(4), 1043–1053.
- Ballouz, E., Dawson, S., & Bae, J. (2023). Transient growth of wavelet-based resolvent modes in the buffer layer of wall-bounded turbulence.
- Ballouz, E., Lopez-Doriga, B., Dawson, S., & Bae, J. (2022). Wavelet-based resolvent analysis for statistically-stationary and temporally-evolving flows.
- Balmforth, N., Llewellyn Smith, S., & Young, W. (2001). Disturbing vortices. *Journal of Fluid Mechanics*, 426, 95–133.
- Barkley, D., Gomes, G., & Henderson, R. (2000). Three-dimensional instability in flow over a backward-facing step. *Journal of Fluid Mechanics*, 473.
- Bellman, R. (1997). *Introduction to matrix analysis, second edition* (Second). Society for Industrial; Applied Mathematics.
- Bender, C., & Orszag, S. (1978). *Advanced mathematical methods for scientists and engineers i*. Springer New York, NY.
- Beneddine, S., Sipp, D., Arnault, A., Dandois, J., & Lesshafft, L. (2016). Conditions for validity of mean flow stability analysis. *Journal of Fluid Mechanics*, 798, 485–504.
- Bengana, Y., & Tuckerman, L. (2021). Frequency prediction from exact or self-consistent mean flows. *Phys. Rev. Fluids*, 6, 063901.
- Benitez, M., & Bermudez, A. (2011). A second order characteristics finite element scheme for natural convection problems. *J. Comput. Appl. Maths*, 235(11), 3270–3284.
- Berhanu, M., Monchaux, R., Fauve, S., Mordant, N., Pétrélis, F., Chiffaudel, A., Daviaud, F., Dubrulle, B., Marié, L., Ravelet, F., Bourgoïn, M., Odier, P., Pinton, J.-E., & Volk, R. (2007). Magnetic field reversals in an experimental turbulent dynamo. *Europhysics Letters*, 77(5), 59001.
- Berkooz, G., Holmes, P., & Lumley, J. (1993). The proper orthogonal decomposition in the analysis of turbulent flows. *Annual Review of Fluid Mechanics*, 25(1), 539–575.
- Bernoff, A., & Lingeitch, J. (1994). Rapid relaxation of an axisymmetric vortex. *Physics of Fluids*, 6(11), 3717–3723.

- Billant, P., & Gallaire, F. (2005). Generalized Rayleigh criterion for non-axisymmetric centrifugal instabilities. *Journal of Fluid Mechanics*, 542, 365–379.
- Blackburn, H., Barkley, D., & Sherwin, S. (2008). Convective instability and transient growth in flow over a backward-facing step. *J. Fluid Mech.*, 603, 271–304.
- Bonciolini, G., Ebi, D., Boujo, E., & Noiray, N. (2018). Experiments and modeling of rate-dependent transition delay in a stochastic subcritical bifurcation. *Royal Society Open Science*, 5(3), 172078.
- Bongarzone, A., Guido, M., & Gallaire, F. (2022). An amplitude equation modelling the double-crest swirling in orbital-shaken cylindrical containers. *Journal of Fluid Mechanics*, 943, A28.
- Bouchet, F., Laurie, J., & Zaboronski, O. (2011). Control and instanton trajectories for random transitions in turbulent flows. *Journal of Physics: Conference Series*, 318(2), 022041.
- Bouchet, F., Nardini, C., & Tangarife, T. (2013). Kinetic theory of jet dynamics in the stochastic barotropic and 2D Navier-Stokes equations. *J. Stat. Phys.*, 153, 572–625.
- Bouchet, F., Rolland, J., & Simonnet, E. (2019). Rare event algorithm links transitions in turbulent flows with activated nucleations. *Phys. Rev. Lett.*, 122, 074502.
- Bouchet, F., & Simonnet, E. (2009). Random changes of flow topology in two-dimensional and geophysical turbulence. *Phys. Rev. Lett.*, 102, 094504.
- Boujo, E., & Gallaire, F. (2015). Sensitivity and open-loop control of stochastic response in a noise amplifier flow: the backward-facing step. *Journal of Fluid Mechanics*, 762, 361–392.
- Brackston, R., García de la Cruz, J., Wynn, A., Rigas, G., & Morrison, J. (2016). Stochastic modelling and feedback control of bistability in a turbulent bluff body wake. *Journal of Fluid Mechanics*, 802, 726–749.
- Brandt, L., Sipp, D., Pralits, J., & Marquet, O. (2011). Effect of base-flow variation in noise amplifiers: the flat-plate boundary layer. *J. Fluid Mech.*, 687, 503–528.
- Breunung, T., & Haller, G. (2018). Explicit backbone curves from spectral submanifolds of forced-damped nonlinear mechanical systems. *Proceedings of the Royal Society A: Mathematical, Physical and Engineering Sciences*, 474(2213), 20180083.
- Briggs, R., Daugherty, J., & Levy, R. (1970). Role of Landau damping in crossed-field electron beams and inviscid shear flow. *The Physics of Fluids*, 13(2), 421–432.

- Butler, K., & Farrell, B. (1992). Three-dimensional optimal perturbations in viscous shear flow. *Phys. Fluids A*, 4(8), 1637–1650.
- Buza, G., Page, J., & Kerswell, R. (2022). Weakly nonlinear analysis of the viscoelastic instability in channel flow for finite and vanishing Reynolds numbers. *Journal of Fluid Mechanics*, 940, A11.
- Callaham, J., Rigas, G., Loiseau, J.-C., & Brunton, S. (2022). An empirical mean-field model of symmetry-breaking in a turbulent wake. *Science Advances*, 8(19), eabm4786.
- Camarri, S., & Mengali, G. (2019). Stability properties of the mean flow after a steady symmetry-breaking bifurcation and prediction of the nonlinear saturation. *Acta Mechanica*, 230.
- Canuto, C., Quarteroni, A., Hussaini, M., & Zang, T. (2007). *Spectral methods. evolution to complex geometries and applications to fluid dynamics*. Springer.
- Carnevale, G., & Kloosterziel, R. (1994). Emergence and evolution of triangular vortices. *Journal of Fluid Mechanics*, 259, 305–331.
- Carton, X., Flierl, G., & Polvani, L. (1989). The generation of tripoles from unstable axisymmetric isolated vortex structures. *Europhysics Letters*, 9(4), 339.
- Carton, X., & Legras, B. (1994). The life-cycle of tripoles in two-dimensional incompressible flows. *Journal of Fluid Mechanics*, 267, 53–82.
- Cates, M., & Nardini, C. (2023). Classical nucleation theory for active fluid phase separation. *Phys. Rev. Lett.*, 130, 098203.
- Cérou, F., & Guyader, A. (2007). Adaptive multilevel splitting for rare event analysis. *Stochastic Analysis and Applications*, 25(2), 417–443.
- Chen, K., Rowley, C., & Stone, H. (2017). Vortex breakdown, linear global instability and sensitivity of pipe bifurcation flows. *Journal of Fluid Mechanics*, 815, 257–294.
- Cherubini, S., De Palma, P., Robinet, J.-C., & Bottaro, A. (2010). Rapid path to transition via nonlinear localized optimal perturbations in a boundary-layer flow. *Phys. Rev. E*, 82, 066302.
- Cherubini, S., De Palma, P., Robinet, J.-C., & Bottaro, A. (2011). The minimal seed of turbulent transition in the boundary layer. *J. Fluid Mech.*, 689, 221–253.
- Chiffaudel, A., & Fauve, S. (1987). Strong resonance in forced oscillatory convection. *Phys. Rev. A*, 35, 4004–4007.

- Chomaz, J.-M. (2005). Global instabilities in spatially developing flows: non-normality and nonlinearity. *Annu. Rev. Fluid Mech.*, 37(1), 357–392.
- Chossat, P., & Iooss, G. (1994). *The Couette-Taylor problem*. Springer-Verlag.
- Constantinou, N., Farrell, B., & Ioannou, P. (2014). Emergence and equilibration of jets in beta-plane turbulence: applications of stochastic structural stability theory. *Journal of the Atmospheric Sciences*, 71(5), 1818–1842.
- Corbett, P., & Bottaro, A. (2000). Optimal perturbations for boundary layers subject to stream-wise pressure gradient. *Phys. Fluid*, 12(1), 120–130.
- Cossu, C., & Chomaz, J.-M. (1997). Global measures of local convective instabilities. *Phys. Rev. Lett.*, 78, 4387–4390.
- Crawford, J., Golubitsky, M., & Langford, W. (1988). Modulated rotating waves in $o(2)$ mode interactions. *Dynamics and Stability of Systems*, 3(3-4), 159–175.
- Crawford, J., & Knobloch, E. (1991). Symmetry and symmetry-breaking bifurcations in fluid dynamics. *Annu. Rev. Fluid Mech.*, 23(1), 341–387.
- Cross, M. (1986). Traveling and standing waves in binary-fluid convection in finite geometries. *Phys. Rev. Lett.*, 57, 2935–2938.
- Cross, M., & Hohenberg, P. (1993). Pattern formation outside of equilibrium. *Rev. Mod. Phys.*, 65, 851–1112.
- Dallas, V., Seshasayanan, K., & Fauve, S. (2020). Transitions between turbulent states in a two-dimensional shear flow. *Phys. Rev. Fluids*, 5, 084610.
- Debuysschère, R., Siconolfi, L., Rimez, B., Gallaire, F., & Scheid, B. (2021). Influence of the inlet velocity profile on the flow stability in a symmetric channel expansion. *Journal of Fluid Mechanics*, 909, A13.
- Denoix, M.-A., Sommeria, J., & Thess, A. (1994). Two-dimensional turbulence: the prediction of coherent structures by statistical mechanics. In *Progress in turbulence research* (pp. 88–107).
- Dergham, G., Sipp, D., & Robinet, J.-C. (2013). Stochastic dynamics and model reduction of amplifier flows: the backward-facing step flow. *Journal of Fluid Mechanics*, 719, 406–430.
- Ducimetière, Y.-M., Boujo, E., & Gallaire, F. (2022a). Weak nonlinearity for strong non-normality. *Journal of Fluid Mechanics*, 947, A43.

- Ducimetière, Y.-M., Boujo, E., & Gallaire, F. (2022b). Weak nonlinearity for strong non-normality. *Journal of Fluid Mechanics*, 947, A43.
- Ducimetière, Y.-M., Boujo, E., & Gallaire, F. (2022c). Weakly nonlinear evolution of stochastically driven non-normal systems. *Journal of Fluid Mechanics*, 951, R3.
- Ducimetière, Y.-M., Boujo, E., & Gallaire, F. (2024). Noise-induced transitions past the onset of a steady symmetry-breaking bifurcation: the case of the sudden expansion. *submitted to Phys. Rev. Fluids*.
- Ducimetière, Y.-M., & Gallaire, F. (2023). A weakly nonlinear amplitude equation approach to the bypass transition in the two-dimensional Lamb–Oseen vortex. *Journal of Fluid Mechanics*, 976, A10.
- Ehrenstein, U., & Gallaire, F. (2005). On two-dimensional temporal modes in spatially evolving open flows: the flat-plate boundary layer. *J. Fluid Mech.*, 536, 209–218.
- Ehrenstein, U., & Gallaire, F. (2008). Two-dimensional global low-frequency oscillations in a separating boundary-layer flow. *J. Fluid Mech.*, 614, 315–327.
- Escudier, M., & Zehnder, N. (1982). Vortex-flow regimes. *Journal of Fluid Mechanics*, 115, 105–121.
- Farano, M., Cherubini, S., Robinet, J.-C., & De Palma, P. (2015). Hairpin-like optimal perturbations in plane poiseuille flow. *Journal of Fluid Mechanics*, 775, R2.
- Farrell, B. (1987). Developing disturbances in shear. *Journal of Atmospheric Sciences*, 44(16), 2191–2199.
- Farrell, B., & Ioannou, P. (1993). Stochastic forcing of the linearized Navier–Stokes equations. *Phys. Fluids A*, 5(11), 2600–2609.
- Farrell, B., & Ioannou, P. (1994). Variance maintained by stochastic forcing of non-normal dynamical systems associated with linearly stable shear flows. *Phys. Rev. Lett.*, 72, 1188–1191.
- Farrell, B., & Ioannou, P. (1996). Generalized stability theory. part i: autonomous operators. *Journal of the Atmospheric Sciences*, 53, 2025–2040.
- Farrell, B., & Ioannou, P. (2003). Structural stability of turbulent jets. *Journal of the Atmospheric Sciences*, 60, 2101–2118.
- Farrell, B., & Ioannou, P. (2012). Dynamics of streamwise rolls and streaks in turbulent wall-bounded shear flow. *Journal of Fluid Mechanics*, 708, 149–196.

- Farrell, B., & Ioannou, P. (2019). Statistical state dynamics: a new perspective on turbulence in shear flow. In B. Galperin & P. L. Read (Eds.), *Zonal jets: phenomenology, genesis, and physics* (pp. 380–400). Cambridge University Press.
- Fauve, S. (1998). Pattern forming instabilities. In C. Godréche & P. Manneville (Eds.), *Hydrodynamics and nonlinear instabilities* (pp. 387–492). Cambridge University Press.
- Fontane, J., Brancher, P., & Fabre, D. (2008). Stochastic forcing of the Lamb–Oseen vortex. *Journal of Fluid Mechanics*, 613, 233–254.
- Freidlin, M., & Wentzell, A. (1998). *Random perturbations of dynamical systems*. New York: Springer.
- Fujimura, K. (1991). Methods of centre manifold and multiple scales in the theory of weakly nonlinear stability for fluid motions. *Proc. R. Soc. Lond. A*, 434(1892), 719–733.
- Gallaire, F., Boujo, E., Mantič-Lugo, V., Arratia, C., Thiria, B., & Meliga, P. (2016). Pushing amplitude equations far from threshold: application to the supercritical Hopf bifurcation in the cylinder wake. *Fluid Dynamics Research*, 48(6), 061401.
- Garnaud, X., Lesshafft, L., Schmid, P., & Huerre, P. (2013a). Modal and transient dynamics of jet flows. *Phys. Fluids*, 25.
- Garnaud, X., Lesshafft, L., Schmid, P., & Huerre, P. (2013b). The preferred mode of incompressible jets: linear frequency response analysis. *J. Fluid Mech.*, 716, 189–202.
- Glendinning, P. (1994). *Stability, instability and chaos: an introduction to the theory of nonlinear differential equations*. Cambridge University Press.
- Golubitsky, M., & Stewart, I. (1985). Hopf bifurcation in the presence of symmetry. *Arch. Ration. Mech. and Anal.*, 87, 107–165.
- Gor'kov, L. (1957). Stationary convection in a plane liquid layer near the critical heat transfer point. *Zh. Eksp. Teor. Fiz.*, 6, 311–15.
- Grafke, T., Cates, M., & Vanden-Eijnden, E. (2017). Spatiotemporal self-organization of fluctuating bacterial colonies. *Phys. Rev. Lett.*, 119, 188003.
- Grafke, T., Grauer, R., & Schäfer, T. (2013). Instanton filtering for the stochastic Burgers equation. *Journal of Physics A: Mathematical and Theoretical*, 46(6), 062002.
- Grandemange, M., Gohlke, M., & Cadot, O. (2013). Turbulent wake past a three-dimensional blunt body. Part 1. Global modes and bi-stability. *Journal of Fluid Mechanics*, 722, 51–84.

- Guckenheimer, J., & Holmes, P. (1983). *Nonlinear oscillations, dynamical systems, and bifurcations of vector fields*. Springer, New York, NY.
- Gustavsson, L. (1991). Energy growth of three-dimensional disturbances in plane Poiseuille flow. *J. Fluid Mech.*, 224, 241–260.
- Haller, G., & Ponsioen, S. (2016). Nonlinear normal modes and spectral submanifolds: existence, uniqueness and use in model reduction. *Nonlinear Dynamics*, 86, 1493–1534.
- Hamilton, J., Kim, J., & Waleffe, F. (1995). Regeneration mechanisms of near-wall turbulence structures. *Journal of Fluid Mechanics*, 287, 317–348.
- Haragus, M., & Iooss, G. (2011). *Local bifurcations, center manifolds, and normal forms in infinite-dimensional dynamical systems*. Springer-Verlag London.
- Hawa, T., & Rusak, Z. (2001). The dynamics of a laminar flow in a symmetric channel with a sudden expansion. *Journal of Fluid Mechanics*, 436, 283–320.
- Heaton, C., & Peake, N. (2007). Transient growth in vortices with axial flow. *Journal of Fluid Mechanics*, 587, 271–301.
- Heifetz, E., & Methven, J. (2005). Relating optimal growth to counterpropagating Rossby waves in shear instability. *Physics of Fluids*, 17(6), 064107.
- Hinch, E. (1991). *Perturbation methods*. Cambridge University Press.
- Hof, B., van Doorne, C., Westerweel, J., Nieuwstadt, F., Faisst, H., Eckhardt, B., Wedin, H., Kerswell, R., & Waleffe, F. (2004). Experimental observation of nonlinear traveling waves in turbulent pipe flow. *Science*, 305(5690), 1594–1598.
- Huerre, P., & Monkewitz, P. (1990). Local and global instabilities in spatially developing flows. *Annual Review of Fluid Mechanics*, 22(1), 473–537.
- Huerre, P., & Rossi, M. (1998). In C. Godrèche & P. Manneville (Eds.), *Hydrodynamics and nonlinear instabilities* (pp. 81–294). Cambridge University Press.
- Jain, S., Tiso, P., & Haller, G. (2018). Exact nonlinear model reduction for a von Kármán beam: slow-fast decomposition and spectral submanifolds. *Journal of Sound and Vibration*, 423, 195–211.
- Jaramillo, J., Macedo, R., & Sheikh, L. (2021). Pseudospectrum and black hole quasinormal mode instability. *Phys. Rev. X*, 11, 031003.
- Jovanović, M., & Bamieh, B. (2005). Component-wise energy amplification in channel flows. *Journal of Fluid Mechanics*, 534, 145–183.

- Kaszás, B., Cenedese, M., & Haller, G. (2022). Dynamics-based machine learning of transitions in Couette flow. *Phys. Rev. Fluids*, 7, L082402.
- Kerswell, R. (2018). Nonlinear nonmodal stability theory. *Annu. Rev. Fluid Mech.*, 50(1), 319–345.
- Kerswell, R., & Davey, A. (1996). On the linear instability of elliptic pipe flow. *Journal of Fluid Mechanics*, 316, 307–324.
- Kerswell, R., Tutty, O., & Drazin, P. (2004). Steady nonlinear waves in diverging channel flow. *Journal of Fluid Mechanics*, 501, 231–250.
- Kloosterziel, R., & van Heijst, G. (1991). An experimental study of unstable barotropic vortices in a rotating fluid. *Journal of Fluid Mechanics*, 223, 1–24.
- Knobloch, E., & Guckenheimer, J. (1983). Convective transitions induced by a varying aspect ratio. *Phys. Rev. A*, 27, 408–417.
- Kossin, J., & Schubert, W. (2001). Mesovortices, polygonal flow patterns, and rapid pressure falls in hurricane-like vortices. *Journal of the Atmospheric Sciences*, 58(15), 2196–2209.
- Kossin, J., Schubert, W., & Montgomery, M. (2000). Unstable interactions between a hurricane's primary eyewall and a secondary ring of enhanced vorticity. *Journal of the Atmospheric Sciences*, 57(24), 3893–3917.
- Kuo, H.-C., Williams, R., & Chen, J.-H. (1999). A possible mechanism for the eye rotation of typhoon Herb. *Journal of the Atmospheric Sciences*, 56(11), 1659–1673.
- Landau, H. (1976). Loss in unstable resonators. *J. Opt. Soc. Am.*, 66(6), 525–529.
- Landau, H. (1977). The notion of approximate eigenvalues applied to an integral equation of laser theory. *Quart. Appl. Math.*, 35(1), 165–172.
- Landau, L., & Lifshitz, E. (1987). *Fluid mechanics, 2nd edn*. Oxford: Butterworth-Heinemann.
- Lanzerstorfer, D., & Kuhlmann, H. (2012). Global stability of multiple solutions in plane sudden-expansion flow. *Journal of Fluid Mechanics*, 702, 378–402.
- Le Dizès, S. (2000). Non-axisymmetric vortices in two-dimensional flows. *Journal of Fluid Mechanics*, 406, 175–198.
- Lecoanet, D., & Kerswell, R. (2018). Connection between nonlinear energy optimization and instantons. *Phys. Rev. E*, 97, 012212.

- Lestang, T., Bouchet, F., & L ev eque, E. (2020). Numerical study of extreme mechanical force exerted by a turbulent flow on a bluff body by direct and rare-event sampling techniques. *Journal of Fluid Mechanics*, 895, A19.
- Li, M., & Haller, G. (2022). Nonlinear analysis of forced mechanical systems with internal resonance using spectral submanifolds, part ii: bifurcation and quasi-periodic response. *Nonlinear Dynamics*, 110, 1045–1080.
- Li, M., Jain, S., & Haller, G. (2022). Nonlinear analysis of forced mechanical systems with internal resonance using spectral submanifolds, part i: periodic response and forced response curve. *Nonlinear Dynamics*, 110, 1005–1043.
- Lowry, J., & Steen, P. (1997). Stability of slender liquid bridges subjected to axial flows. *Journal of Fluid Mechanics*, 330, 189–213.
- Lucas, D., & Kerswell, R. (2014). Spatiotemporal dynamics in two-dimensional Kolmogorov flow over large domains. *Journal of Fluid Mechanics*, 750, 518–554.
- Luchini, P., & Bottaro, A. (2014). Adjoint equations in stability analysis. *Annual Review of Fluid Mechanics*, 46(1), 493–517.
- Lundgren, T. (1982). Strained spiral vortex model for turbulent fine structure. *The Physics of Fluids*, 25(12), 2193–2203.
- Malkus, W., & Veronis, G. (1958). Finite amplitude cellular convection. *J. Fluid Mech.*, 4, 225–60.
- Manneville, P. (2004). *Instabilities, chaos and turbulence*. Imperial College Press.
- Mannix, P., Ponty, Y., & Marcotte, F. (2022). Systematic route to subcritical dynamo branches. *Phys. Rev. Lett.*, 129, 024502.
- Manti -Lugo, V., Arratia, C., & Gallaire, F. (2014). Self-consistent mean flow description of the nonlinear saturation of the vortex shedding in the cylinder wake. *Phys. Rev. Lett.*, 113, 084501.
- Manti -Lugo, V., Arratia, C., & Gallaire, F. (2015). A self-consistent model for the saturation dynamics of the vortex shedding around the mean flow in the unstable cylinder wake. *Physics of Fluids*, 27(7), 074103.
- Manti -Lugo, V., & Gallaire, F. (2016a). Saturation of the response to stochastic forcing in two-dimensional backward-facing step flow: a self-consistent approximation. *Phys. Fluids*, 1.

- Mantič-Lugo, V., & Gallaire, F. (2016b). Self-consistent model for the saturation mechanism of the response to harmonic forcing in the backward-facing step flow. *J. Fluid Mech.*, 793, 777–97.
- Mao, X., & Sherwin, S. (2012). Transient growth associated with continuous spectra of the Batchelor vortex. *Journal of Fluid Mechanics*, 697, 35–59.
- Marcotte, A., Gallaire, F., & Bongarzone, A. (2023). Super-harmonically resonant swirling waves in longitudinally forced circular cylinders. *Journal of Fluid Mechanics*, 966, A41.
- Marquet, O., Lombardi, M., Chomaz, J.-M., Sipp, D., & Jacquin, L. (2009). Direct and adjoint global modes of a recirculation bubble: lift-up and convective non-normalities. *Journal of Fluid Mechanics*, 622, 1–21.
- Marquet, O., Sipp, D., Chomaz, J.-M., & Jacquin, L. (2008). Amplifier and resonator dynamics of a low-reynolds-number recirculation bubble in a global framework. *Journal of Fluid Mechanics*, 605, 429–443.
- Marston, J., Chini, G., & Tobias, S. (2016). Generalized quasilinear approximation: application to zonal jets. *Phys. Rev. Lett.*, 116, 214501.
- Marston, J., Conover, E., & Schneider, T. (2008). Statistics of an unstable barotropic jet from a cumulant expansion. *Journal of the Atmospheric Sciences*, 65(6), 1955–1966.
- Matsubara, M., & Alfredsson, P. (2001). Disturbance growth in boundary layers subjected to free-stream turbulence. *Journal of Fluid Mechanics*, 430, 149–168.
- McKeon, B., & Sharma, A. (2010). A critical-layer framework for turbulent pipe flow. *Journal of Fluid Mechanics*, 658, 336–382.
- Meliga, P. (2017). Harmonics generation and the mechanics of saturation in flow over an open cavity: a second-order self-consistent description. *Journal of Fluid Mechanics*, 826, 503–521.
- Meliga, P. (2018). *Linear and semi-linear analysis of large-scale oscillations in laminar and turbulent open flows* [Habilitation à diriger des recherches]. Aix-Marseille Université.
- Meliga, P., Chomaz, J.-M., & Sipp, D. (2009). Global mode interaction and pattern selection in the wake of a disk: a weakly nonlinear expansion. *Journal of Fluid Mechanics*, 633, 159–189.
- Meliga, P., Gallaire, F., & Chomaz, J.-M. (2012). A weakly nonlinear mechanism for mode selection in swirling jets. *Journal of Fluid Mechanics*, 699, 216–262.

- Monokrousos, A., Åkervik, E., Brandt, L., & Henningson, D. (2010). Global three-dimensional optimal disturbances in the Blasius boundary-layer flow using time-steppers. *J. Fluid Mech.*, 650, 181–214.
- Navrose, Johnson, H., Brion, V., Jacquin, L., & Robinet, J.-C. (2018). Optimal perturbation for two-dimensional vortex systems: route to non-axisymmetric state. *Journal of Fluid Mechanics*, 855, 922–952.
- Nayfeh, A., & Serhan, S. (1990). Response statistics of non-linear systems to combined deterministic and random excitations. *International Journal of Non-Linear Mechanics*, 25(5), 493–509.
- Neubert, M., & Caswell, H. (1997). Alternatives to resilience for measuring the responses of ecological systems to perturbations. *Ecology*, 78(3), 653–665.
- Nivarti, G., Kerswell, R., Marston, J., & Tobias, S. (2022). Non-equivalence of quasilinear dynamical systems and their statistical closures.
- Nogueira, P., Cavalieri, A., Jordan, P., & Jaunet, V. (2019). Large-scale streaky structures in turbulent jets. *Journal of Fluid Mechanics*, 873, 211–237.
- Nolan, D., & Farrell, B. (1999). The intensification of two-dimensional swirling flows by stochastic asymmetric forcing. *Journal of the Atmospheric Sciences*, 56(23), 3937–3962.
- Ohm, L., & Shelley, M. (2022). Weakly nonlinear analysis of pattern formation in active suspensions. *Journal of Fluid Mechanics*, 942, A53.
- Orchini, A., Rigas, G., & Juniper, M. (2016). Weakly nonlinear analysis of thermoacoustic bifurcations in the Rijke tube. *Journal of Fluid Mechanics*, 805, 523–550.
- Orr, W. (1907). The stability or instability of the steady motions of a perfect liquid and of a viscous liquid. part ii: a viscous liquid. *Proceedings of the Royal Irish Academy. Section A: Mathematical and Physical Sciences*, 27, 69–138.
- Orszag, S. (1971). Accurate solution of the Orr-Sommerfeld stability equation. *Journal of Fluid Mechanics*, 50(4), 689–703.
- Padovan, A., Otto, S., & Rowley, C. (2020). Analysis of amplification mechanisms and cross-frequency interactions in nonlinear flows via the harmonic resolvent. *J. Fluid Mech.*, 900, A14.
- Padovan, A., & Rowley, C. (2022). Analysis of the dynamics of subharmonic flow structures via the harmonic resolvent: application to vortex pairing in an axisymmetric jet. *Phys. Rev. Fluids*, 7, 073903.

- Parker, J., Howland, C., Caulfield, C.-c., & Kerswell, R. (2021). Optimal perturbation growth on a breaking internal gravity wave. *Journal of Fluid Mechanics*, 925, A16.
- Parker, J., & Krommes, J. (2013). Zonal flow as pattern formation. *Physics of Plasmas*, 20(10), 100703.
- Petermann, K. (1979). Calculated spontaneous emission factor for double-heterostructure injection lasers with gain-induced waveguiding. *IEEE J. Quant. Elect.*, 15(7), 566–570.
- Pétrélis, F., Fauve, S., Dormy, E., & Valet, J.-P. (2009). Simple mechanism for reversals of Earth's magnetic field. *Phys. Rev. Lett.*, 102, 144503.
- Pickering, E., Rigas, G., Nogueira, P., Cavalieri, A., Schmidt, O., & Colonius, T. (2020). Lift-up, Kelvin-Helmholtz and Orr mechanisms in turbulent jets. *Journal of Fluid Mechanics*, 896, A2.
- Pickering, E., Rigas, G., Schmidt, O., Sipp, D., & Colonius, T. (2021). Optimal eddy viscosity for resolvent-based models of coherent structures in turbulent jets. *Journal of Fluid Mechanics*, 917, A29.
- Pier, B., & Schmid, P. (2017). Linear and nonlinear dynamics of pulsatile channel flow. *Journal of Fluid Mechanics*, 815, 435–480.
- Pier, B., & Schmid, P. (2021). Optimal energy growth in pulsatile channel and pipe flows. *Journal of Fluid Mechanics*, 926, A11.
- Ponsioen, S., Jain, S., & Haller, G. (2020). Model reduction to spectral submanifolds and forced-response calculation in high-dimensional mechanical systems. *Journal of Sound and Vibration*, 488, 115640.
- Pradeep, D., & Hussain, F. (2006). Transient growth of perturbations in a vortex column. *Journal of Fluid Mechanics*, 550, 251–288.
- Pringle, C., & Kerswell, R. (2010). Using nonlinear transient growth to construct the minimal seed for shear flow turbulence. *Phys. Rev. Lett.*, 105, 154502.
- Pringle, C., Willis, A., & Kerswell, R. (2012). Minimal seeds for shear flow turbulence: using nonlinear transient growth to touch the edge of chaos. *Journal of Fluid Mechanics*, 702, 415–443.
- Rajan, S., & Davies, H. (1988). Multiple time scaling of the response of a Duffing oscillator to narrow-band random excitation. *Journal of Sound and Vibration*, 123(3), 497–506.
- Randriamampianina, A., Schiestel, R., & Wilson, M. (2001). Spatio-temporal behaviour in an enclosed corotating disk pair. *Journal of Fluid Mechanics*, 434, 39–64.

- Reasor, P., Montgomery, M., Marks, F., & Gamache, J. (2000). Low-wavenumber structure and evolution of the hurricane inner core observed by airborne dual-doppler radar. *Monthly Weather Review*, *128*(6), 1653–1680.
- Reddy, S., & Henningson, D. (1993). Energy growth in viscous channel flows. *J. Fluid Mech.*, *252*, 209–238.
- Reddy, S., Schmid, P., Baggett, J., & Henningson, D. (1998). On stability of streamwise streaks and transition thresholds in plane channel flows. *Journal of Fluid Mechanics*, *365*, 269–303.
- Rhines, P., & Young, W. (1983). How rapidly is a passive scalar mixed within closed streamlines? *Journal of Fluid Mechanics*, *133*, 133–145.
- Rigas, G., Sipp, D., & Colonius, T. (2021). Nonlinear input/output analysis: application to boundary layer transition. *Journal of Fluid Mechanics*, *911*, A15.
- Risken, H. (1996). *The Fokker-Planck equation*. Springer Berlin, Heidelberg.
- Rong, H., Xu, W., & Fang, T. (1998). Principal response of Duffing oscillator to combined deterministic and narrow-band random parametric excitation. *Journal of Sound and Vibration*, *210*(4), 483–515.
- Rosenberg, K., & McKeon, B. (2019). Computing exact coherent states in channels starting from the laminar profile: a resolvent-based approach. *Phys. Rev. E*, *100*, 021101.
- Rosenberg, K., Symon, S., & McKeon, B. (2019). Role of parasitic modes in nonlinear closure via the resolvent feedback loop. *Phys. Rev. Fluids*, *4*, 052601.
- Rossi, L., Lingeitch, J., & Bernoff, A. (1997). Quasi-steady monopole and tripole attractors for relaxing vortices. *Physics of Fluids*, *9*(8), 2329–2338.
- Rusak, Z., & Hawa, T. (1999). A weakly nonlinear analysis of the dynamics of a viscous flow in a symmetric channel with a sudden expansion. *Physics of Fluids*, *11*(12), 3629–3636.
- Sarpkaya, T. (1971). On stationary and travelling vortex breakdowns. *Journal of Fluid Mechanics*, *45*(3), 545–559.
- Schecter, D., Dubin, D., Cass, A., Driscoll, C., Lansky, I., & O’Neil, T. (2000). Inviscid damping of asymmetries on a two-dimensional vortex. *Physics of Fluids*, *12*(10), 2397–2412.
- Schmeits, M., & Dijkstra, H. (2001). Bimodal behavior of the Kuroshio and the gulf stream. *Journal of Physical Oceanography*, *31*(12), 3435–3456.
- Schmid, P. (2007). Nonmodal stability theory. *Annu. Rev. Fluid Mech.*, *39*(1), 129–162.

- Schmid, P., & Brandt, L. (2014a). Analysis of Fluid Systems: Stability, Receptivity, Sensitivity: Lecture notes from the FLOW-NORDITA Summer School on Advanced Instability Methods for Complex Flows, Stockholm, Sweden, 2013. *Applied Mechanics Reviews*, 66(2), 024803.
- Schmid, P., & Brandt, L. (2014b). Analysis of Fluid Systems: Stability, Receptivity, Sensitivity: Lecture notes from the FLOW-NORDITA Summer School on Advanced Instability Methods for Complex Flows, Stockholm, Sweden, 2013. *Applied Mechanics Reviews*, 66(2), 024803.
- Schmid, P., & Henningson, D. (1994). Optimal energy density growth in Hagen–Poiseuille flow. *J. Fluid Mech.*, 277, 197–225.
- Schmid, P., & Henningson, D. (2001). *Stability and transition in shear flows*. Springer.
- Schneider, T., Gibson, J., & Burke, J. (2010). Snakes and ladders: localized solutions of plane Couette flow. *Phys. Rev. Lett.*, 104, 104501.
- Schorlepp, T., Grafke, T., May, S., & Grauer, R. (2022). Spontaneous symmetry breaking for extreme vorticity and strain in the three-dimensional Navier–Stokes equations. *Philosophical Transactions of the Royal Society A: Mathematical, Physical and Engineering Sciences*, 380(2226), 20210051.
- Shimizu, M., & Manneville, P. (2019). Bifurcations to turbulence in transitional channel flow. *Phys. Rev. Fluids*, 4, 113903.
- Shukla, P., & Alam, M. (2011). Nonlinear stability and patterns in granular plane Couette flow: Hopf and pitchfork bifurcations, and evidence for resonance. *Journal of Fluid Mechanics*, 672, 147–195.
- Sipp, D. (2000). Weakly nonlinear saturation of short-wave instabilities in a strained Lamb–Oseen vortex. *Physics of Fluids*, 12(7), 1715–1729.
- Sipp, D. (2012). Open-loop control of cavity oscillations with harmonic forcings. *J. Fluid Mech.*, 708, 439–468.
- Sipp, D., & Lebedev, A. (2007). Global stability of base and mean flows : a general approach and its applications to cylinder and open cavity flows. *J. Fluid Mech.*, 593, 333–358.
- Sommeria, J. (1986). Experimental study of the two-dimensional inverse energy cascade in a square box. *Journal of Fluid Mechanics*, 170, 139–168.
- Strogatz, S. (2015). *Nonlinear dynamics and chaos* (2nd). CRC Press.
- Stuart, J. (1958). On the nonlinear mechanics of hydrodynamic stability. *J. Fluid Mech.*, 4, 1–21.

- Stuart, J. (1960). On the nonlinear mechanics of wave disturbances in stable and unstable parallel flows, part 1. the basic behavior in plane Poiseuille flow. *J. Fluid Mech.*, 9, 353–70.
- Symon, S., Rosenberg, K., Dawson, S., & McKeon, B. (2018). Non-normality and classification of amplification mechanisms in stability and resolvent analysis. *Phys. Rev. Fluids*, 3, 053902.
- Tavallaeinejad, M., Païdoussis, M., Legrand, M., & Kheiri, M. (2020). Instability and the post-critical behaviour of two-dimensional inverted flags in axial flow. *Journal of Fluid Mechanics*, 890, A14.
- Tobias, S., & Marston, J. (2013). Direct statistical simulation of out-of-equilibrium jets. *Phys. Rev. Lett.*, 110, 104502.
- Towne, A., Schmidt, O., & Colonius, T. (2018). Spectral proper orthogonal decomposition and its relationship to dynamic mode decomposition and resolvent analysis. *Journal of Fluid Mechanics*, 847, 821–867.
- Trefethen, L., & Embree, M. (2005). *Spectra and pseudo-spectra*. Princeton University Press.
- Trefethen, L., Trefethen, A., Reddy, S., & Driscoll, T. (1993). Hydrodynamic stability without eigenvalues. *Science*, 261(5121), 578–584.
- Turner, M., & Gilbert, A. (2007). Linear and nonlinear decay of cat's eyes in two-dimensional vortices, and the link to Landau poles. *Journal of Fluid Mechanics*, 593, 255–279.
- Turner, M., Gilbert, A., & Bassom, A. (2008). Neutral modes of a two-dimensional vortex and their link to persistent cat's eyes. *Physics of Fluids*, 20(2), 027101.
- Van Heijst, G., & Kloosterziel, R. (1989). Tripolar vortices in a rotating fluid. *Nature*, 338, 569–571.
- Van Heijst, G., Kloosterziel, R., & Williams, C. (1991). Formation of a tripolar vortex in a rotating fluid. *Physics of Fluids A: Fluid Dynamics*, 3(9), 2033–2033.
- Viola, F., Arratia, C., & Gallaire, F. (2016). Mode selection in trailing vortices: harmonic response of the non-parallel Batchelor vortex. *Journal of Fluid Mechanics*, 790, 523–552.
- Waleffe, F. (1995). Transition in shear flows: nonlinear normality versus non-normal linearity. *Phys. Fluids*, 7(12), 3060–3066.
- Wan, X., Yu, H., & Weinan, E. (2015). Model the nonlinear instability of wall-bounded shear flows as a rare event: a study on two-dimensional Poiseuille flow. *Nonlinearity*, 28(5), 1409.

- Watson, J. (1960). On the nonlinear mechanics of wave disturbances in stable and unstable parallel flows, part 2. the development of a solution for plane Poiseuille and for plane Couette flow. *J. Fluid Mech.*, 9, 371–89.
- Weeks, E., Tian, Y., Urbach, J., Ide, K., Swinney, H., & Ghil, M. (1997). Transitions between blocked and zonal flows in a rotating annulus with topography. *Science*, 278(5343), 1598–1601.
- Yim, E., Billant, P., & Gallaire, F. (2020). Nonlinear evolution of the centrifugal instability using a semilinear model. *Journal of Fluid Mechanics*, 897, A34.
- Zampogna, G., & Boujo, E. (2023). From thin plates to Ahmed bodies: linear and weakly nonlinear stability of rectangular prisms. *Journal of Fluid Mechanics*, 966, A19.

Yves-Marie Ducimetière

Personal information

Born August 13, 1996, in Meyrin, Switzerland
French citizenship
yves-marie.ducimetiere@epfl.ch

Research interests

Linear stability approaches, modal and non-modal theories,
Effect of stochastic and deterministic excitations, receptivity,
Nonlinear effects, weakly nonlinear theory, asymptotic methods, semi-linear methods,
Optimal control, adjoint theory,
Statistical mechanics, large deviations theory, active matter, etc...

Education

- 2019–2023 **PhD in Mechanical Engineering at EPFL, Switzerland.**
Research activity in the Laboratory of Fluid Mechanics and Instabilities (LFMI) under the supervision of Prof. F. Gallaire. The thesis proposes a theoretical approach to derive amplitude equations governing the weakly nonlinear evolution of non-normal dynamical systems when they experience transient growth or respond to harmonic or stochastic forcing.
- 2016–2019 **MSc. in Mechanical Engineering at EPFL, Switzerland.**
Thesis title: "Absolute instabilities and the role of confinement in stratified shear flows",
advisors: Prof. C.-c. Caulfield, Prof. F. Gallaire and Dr. A. Lefauve,
Thesis mark: 6/6.
- Sept 2018 – **Research Internship at Cambridge University, UK.**
Mar 2019 Six months project at DAMTP (Department of Applied Mathematics and Theoretical Physics) on the absolute/convective discrimination of stratified shear instabilities occurring in an inclined duct.
Tutored by Prof. C.-c. Caulfield, Prof. F. Gallaire, and Dr. A. Lefauve.
- Feb 2018 – Aug **R&D Engineering Internship at Almatech, Switzerland.**
2018 Six months project in an EPFL start-up for the development of a simplified simulator for the trajectory of a hydrofoil-craft under specified waves and wind conditions.
Tutored by Dr. L. Blecha.
- Sept 2017 – Jan **Research Internship at EPFL, Switzerland.**
2018 Four months project at LFMI on the modal and non-modal stability of a thin Newtonian fluid spreading on a horizontal cylinder under the action of gravity.
Tutored by Prof. F. Gallaire, and Dr. G. Balestra.

- July 2017 – **Research Internship at University of Geneva, Switzerland.**
Sept 2017 Two months summer project at the Nonlinearity and Climate Group on statistical properties after a sudden episode of wind for water waves propagating in one direction and described by the nonlinear Schrödinger equation.
Tutored by Prof. J. Kasparian, and Dr. M. Brunetti.
- 2013–2016 **BSc. in Mechanical Engineering at EPFL, Switzerland.**
2013 **French Scientific Baccalaureate (Specialty : Mathematics) from Lycée International de Ferney-Voltaire.**

Additional schools and training

- July 2022 **Boulder School 2022: "Hydrodynamics Across Scales", University of Colorado Boulder, USA.**

Languages

- French (Native)
English (Fluent)
German (B1)

Teaching and students supervision

Teaching assistant

Analysis I Bachelor course in Mechanical Engineering at EPFL (2021), 28 hours in total.

Finite Elements Method Bachelor course in Mechanical Engineering at EPFL (2019-2023), 4×14 hours in total.

Hydrodynamics Master course in Mechanical Engineering at EPFL (2022), 28 hours in total.

Numerical Flow Simulation Master course in Mechanical Engineering at EPFL (2021), 28 hours in total.

Instability Master course in Mechanical Engineering at EPFL (2019-2023), 4×14 hours in total.

Master thesis supervisor

Tutored a student for her Master's project "Study of the Holmboe instability in an inclined duct and application of the semi-linear model".

Publications

Peer-reviewed journal articles

Eeltink, D., Armaroli, A., Ducimetière, Y.-M., Kasparian, J., and Brunetti, M. (2019). Single-spectrum prediction of kurtosis of water waves in a nonconservative model. *Physical Review*

E, 100, 013102.

Balestra, G., Badaoui, M., Ducimetière, Y.-M., and Gallaire, F. (2019). Fingering instability on curved substrates: Optimal initial film and substrate perturbations. *Journal of Fluid Mechanics*, 868, 726-761.

Ducimetière Y.-M., Gallaire F., Lefauve A., and C. Caulfield (2021). Effects of spanwise confinement on stratified shear instabilities. *Physical Review Fluids*, 6, 103901.

Ducimetière, Y.-M., Boujo, E., and Gallaire, F. (2022). Weak nonlinearity for strong non-normality. *Journal of Fluid Mechanics*, 947, A43.

Ducimetière, Y.-M., Boujo, E., and Gallaire, F. (2022). Weakly nonlinear evolution of stochastically driven non-normal systems. *Journal of Fluid Mechanics*, 951, R3.

Eghbali S., Ducimetière. Y.-M., Boujo, E., and Gallaire. F. (2023). Liquid film instability of an internally coated horizontal tube. *Physical Review Fluids*, 8, 053901.

Zhou, J., Ducimetière, Y.-M., Migliozi, D., Keiser, L., Bertsch, A., Gallaire, F., and Renaud, Philippe (2023). Breaking one into three: Surface-tension-driven droplet breakup in T-junctions. *Physical Review Fluids*, 8, 054201.

Ducimetière, Y.-M., and Gallaire, F. (2023). A weakly nonlinear amplitude equation approach to the bypass transition in the two-dimensional Lamb–Oseen vortex. *Journal of Fluid Mechanics*, 976, A10.

Papers submitted

Ducimetière, Y.-M., Boujo, E., and Gallaire, F. (2023). Noise-induced transitions past the onset of a steady symmetry-breaking bifurcation: the case of the sudden expansion. *submitted to Physical Review Fluids*.

Conferences contributed

Weak nonlinearity for strong non-normality, 74th Annual Meeting of the Division of Fluid Dynamics (APS DFD), Phoenix (AZ), USA, November 21-23, 2021.

Weakly nonlinear evolution of stochastically driven non-normal systems, 14th SIG 33-ERCOFTAC Workshop, Cadix, Spain, June 15-17, 2022.

Weakly nonlinear evolution of stochastically driven non-normal systems, 14th European Fluid Mechanics Conference (EFMC), Athens, Greece, June 13-16, 2022.

Noise-induced transitions after a steady symmetry-breaking bifurcation: the case of the sudden expansion, 15th SIG 33-ERCOFTAC Workshop, Alghero, Italy, June 28-30, 2023.

Non-modal amplitude equations, Invited speaker at Laboratoire J. A. Dieudonné (Séminaire de l'équipe EDP Analyse Numérique), Nice, France, December 7, 2023.